

Assessment of the influence of changes in land use and climate
on landslide activity in a Mediterranean environment

De invloed van veranderingen in landgebruik en klimaat
op aardverschuivingsrisico in het Middellandse zeegebied
(MET EEN SAMENVATTING IN HET NEDERLANDS)

PROEFSCHRIFT

Ter verkrijging van de graad van doctor aan de Universiteit Utrecht, op gezag van de Rector Magnificus Prof. Dr. W.H. Gispen, ingevolge het besluit van het College voor Promoties in het openbaar te verdedigen op maandag 6 mei 2002 des ochtends te 10.30 uur

DOOR
LUDOVICUS PETRUS HENRICUS VAN BEEK
GEBOREN OP 24 MAART 1969 TE BREDA

Promotor: Prof. Dr. J.D. Nieuwenhuis
Co-promotor: Dr. Th.W.J. van Asch
Vakgroep Fysische Geografie, Faculteit Ruimtelijke Wetenschappen,
Universiteit Utrecht

Dit proefschrift werd mogelijk gemaakt door financiële steun van de Nederlandse
Organisatie voor Wetenschappelijk Onderzoek (NWO-GOA 750.294.03)

**Assessment of the influence of changes in land use and climate on landslide activity
in a Mediterranean environment**

Rens van Beek

Nederlandse Geografische Studies
Netherlands Geographical Studies
NGS 294

**ASSESSMENT OF THE INFLUENCE OF CHANGES IN LAND USE
AND CLIMATE ON LANDSLIDE ACTIVITY IN A
MEDITERRANEAN ENVIRONMENT**

Nederlandse Geografische Studies 294

**ASSESSMENT OF THE INFLUENCE OF CHANGES IN LAND USE
AND CLIMATE ON LANDSLIDE ACTIVITY IN A
MEDITERRANEAN ENVIRONMENT**

Rens van Beek

Utrecht 2002

Koninklijk Nederlands Aardrijkskundig Genootschap/
Faculteit Ruimtelijke Wetenschappen, Universiteit Utrecht

This publication has been submitted in partial fulfilment of the requirements for the award of the degree of Doctor of Philosophy at Utrecht University.

Dit onderzoek werd mogelijk gemaakt door financiële steun van de Nederlandse Organisatie voor Wetenschappelijk Onderzoek, Sectie Aard- en Levenswetenschappen (NWO-ALW).

This research has been funded by the Netherlands Organisation for Scientific Research, Geosciences, Council for Earth and Life Sciences (NWO-ALW).

ISBN 90-6809-329-0 (NGS)

Copyright © L.P.H. van Beek, p/a Faculteit Ruimtelijke Wetenschappen, Universiteit Utrecht, 2002

Niets uit deze uitgave mag worden vermenigvuldigd en/of openbaar gemaakt door middel van druk, fotokopie of op welke wijze dan ook zonder voorafgaande schriftelijke toestemming van de uitgevers.

All rights reserved. No part of this publication may be reproduced in any form, by print or photoprint, microfilm or any other means without written permission by the publishers.

Gedrukt in Nederland door Labor Grafimedia b.v., Utrecht.

Printed in the Netherlands by Labor Grafimedia b.v., Utrecht.

CONTENTS

List of Tables.....	11	
List of Figures	15	
List of Plates.....	19	
Acknowledgements	21	
1	Landsliding as a geomorphic process in Mediterranean environments..... 25	
1.1	Context..... 25	
1.2	Problem definition	25
1.2.1	The role of landsliding within the hierarchy of erosion processes	25
1.2.2	Key processes	26
1.2.3	Landslide activity and hydrological triggering.....	23
1.2.4	Environmental conditions as controlling factors	28
1.3	Aims and objectives.....	29
1.4	Approach	30
1.4.1	Scale considerations.....	30
1.4.2	Environmental change	30
1.4.3	Modelling of landslide activity.....	31
1.5	Thesis structure.....	33
2	Physiography of the study area (Valles de Alcoy).....	35
2.1	Introduction	35
2.1	Geology & Geomorphology	36
2.1.1	Structural geology.....	36
2.1.2	The upper basin of the Río Serpis.....	39
2.1.3	Geomorphology of the study area.....	46
2.2	Climate.....	52
2.3	Geohydrology	54
2.4	Socio-economic development and land use.....	56
2.5	Summary.....	60
3	A coupled model of slope hydrology and stability	63
3.1	Introduction	63
3.2	Development of the coupled model of slope hydrology and stability	64
3.2.1	Scale aspects and model considerations	64
3.2.2	Modelling of slope hydrology	68
3.2.3	Modelling of slope stability.....	81
3.3	Model implementation.....	88
3.4	Concluding remarks.....	93
4	Climatic controls of landsliding: Precipitation and evapotranspiration.....	95
4.1	Introduction	95
4.2	Spatio-temporal precipitation patterns.....	96
4.2.1	Temporal rainfall patterns for Almudaina 1971-1998.....	97
4.2.2	Extreme rainfall events for Almudaina.....	102

4.2.3	Representativeness for the study area.....	105
4.2.4	Within-storm characteristics.....	109
4.2.5	Regional trends.....	112
4.3	Reference potential evapotranspiration (ET ₀).....	120
4.3.1	Penman's Equation.....	121
4.3.2	Application of the Penman equation.....	124
4.4	Hypothetical climatic conditions.....	136
4.4.1	Description of a daily weather generator.....	136
4.4.2	Parameterisation of the daily weather generator.....	140
4.4.3	Comparison of simulated vs. observed weather.....	143
4.4.4	Defining a local climate change scenario.....	149
4.5	Conclusions.....	158
5	Site Investigation and parameterisation.....	161
5.1	Introduction.....	161
5.2	Land use aspects.....	161
5.2.1	Introduction.....	161
5.2.2	Land use classification.....	162
5.2.3	Canopy interception.....	165
5.2.4	Interception measurements.....	166
5.2.5	Crop specific evapotranspiration.....	174
5.3	Soil hydrological Properties.....	176
5.3.1	Sampling Scheme.....	176
5.3.2	Porosity, bulk density and saturated hydraulic conductivity.....	178
5.3.3	Soil water retention curves.....	183
5.3.4	Relation with depth.....	185
5.4	Land use effects on hydrological properties.....	186
5.4.1	Land use effects on the saturated hydraulic conductivity and porosity.....	186
5.4.2	SWRC and porosity of the root zone.....	188
5.4.3	Infiltration and redistribution per land use unit.....	192
5.5	Topography.....	199
5.6	Soil depth.....	200
5.7	Geomechanical properties.....	207
5.7.1	Theory.....	207
5.7.2	Test procedure.....	209
5.7.3	Results.....	211
5.7.4	Discussion and conclusion.....	217
5.8	Summary and parameterisation.....	219
6	Implementation of the hydrological component of the coupled hillslope model ...	223
6.1	Introduction.....	223
6.2	Model sensitivity.....	224
6.2.1	Method of sensitivity analysis.....	224
6.2.2	Parameter sensitivity.....	226
6.3	Calibration of the hydrological model component STARWARS.....	228
6.4	Validation of the hydrological model component STARWARS.....	235
6.5	Applicability of the calibrated hydrological model component.....	241
7	Simulation of landslide activity under the present environmental conditions.....	245
7.1	Introduction.....	245

7.2	Landslide inventory	246
7.3	Simulating landslide susceptibility and slope failure.....	249
7.3.1	Implementation of the coupled hillslope model for the validation period.....	249
7.3.2	Sensitivity analysis for the slope stability model.....	250
7.3.3	Modelling of landslide susceptibility.....	251
7.4	Validation of slope stability model component PROBSTAB.....	258
7.4.1	Validation of simulated slope failure.....	258
7.4.2	Probabilistic vs. deterministic prediction.....	258
7.4.3	Measures for the validation of the simulated failure	259
7.4.4	Performance of the coupled hillslope model	260
7.4.5	Relation between landslide occurrence and the simulated probability of failure ...	263
7.4.6	Temporal characteristics of simulated failure and observed landslide activity	267
7.4	Influence of the calibrated hydrological parameter k_r on simulated failure.....	274
7.5	Environmental conditions.....	277
7.6	Summary and conclusions	283
8	Assessment of the temporal sensitivity to landsliding under changed environmental conditions by means of Scenario Modelling.....	285
8.1	Introduction	285
8.2	Development of land use scenarios	286
8.3	Scenario implementation	291
8.3.1	Scenario ensembles.....	291
8.3.2	Rainfall characteristics of the generated weather series	292
8.3.3	Correlation between simulated failure for the validation period and the BAU-CP scenario	295
8.4	Simulated changes in landslide activity under environmental change	298
8.4.1	Possible changes in landslide activity under environmental change	298
8.4.2	Changes in the area of simulated failure.....	299
8.4.3	Changes in the temporal characteristics of simulated failure	302
8.4.4	Hydrological response and temporal sensitivity	304
8.5	Discussion.....	311
8.6	Conclusions	312
Appendices		
1	Location of the study area.....	315
2	Derivation of the Penman Equation.....	317
3	Meteorological data of non-precipitation variables for Cocentaina 1991-1997	321
4	Generation of the standardised non-precipitation values.....	323
5	Infiltration and redistribution of soil moisture under different land use units as observed with TDR during broadscale rainfall simulations	327
6	Simulated hydrological response for different climate conditions	333
Summary		337
Samenvatting.....		345
References		353
Curriculum vitae.....		363

TABLES

2.1	Climatic statistics for the Valles de Alcoy	52
3.1	Model in- & output of the coupled hillslope model.....	90
4.1	Annual precipitation statistics for Almudaina 1971-1998	98
4.2	Monthly rainfall statistics for Almudaina	99
4.3	Seasonal statistics for the rainfall events at Almudaina.....	100
4.4	Expected return periods and rainfall totals for Almudaina	104
4.5	Data recovery of the tipping buckets	106
4.6	Regression of the tipping bucket data on the daily record of Almudaina....	107
4.7	Regression of the tipping bucket data from the Hollow on those of the LGM-site.....	108
4.8	Test for equality of means and variance between the long-term period 1971-1995 and the short-term period 1995-1999	109
4.9	Within-storm characteristics over the period December 1995-March 1999	110
4.10	Locations climatological stations in the Valles de Alcoy	114
4.11	Data recovery INM-stations.....	116
4.12	Cross-table of regressions for the stations of Table 4.11	116
4.13	Agreement between matched events and the total number of recorded rainfall events.....	118
4.14	Average rainfall statistics.....	119
4.15	Constants and parameters of the adapted Penman equation	123
4.16	Statistics of reference potential evapotranspiration for Almudaina and Cocentaina	132
4.17	Bias (%) introduced in the calculated ET_0 for Almudaina by the use of estimated net global radiation and wind speed	135
4.18	Transition matrix for a first-order Markov chain.....	137
4.19	Transition frequencies for the first-order Markov chain and the binomial probability for rainfall in Almudaina	140
4.20	Parameterisation of the monthly two-parameter gamma-distribution for rainfall depth.....	140
4.21	Mean and standard deviation for the standardisation of the non-precipitation values.....	141
4.22	Simultaneous and lagged correlations of the standardised non-precipitation variables.....	142
4.23	R^2 of bi- and multivariate lagged regressions of z_k	143
4.24	Lagged autocorrelations of daily precipitation totals at Almudaina	145
4.25	Comparison between the observed and generated rainfall characteristics...	148
4.26	Characteristics of the three transient GCMs considered.....	152
4.27	Average temperature and standard deviations from the monthly GCM-output and as observed at Alcoy & Cocentaina	153
4.28	Correlations between the observed and simulated monthly temperature over 1964-1997	154
4.29	Downscaled temperature values from the three GCMs considered	154
4.30	Monthly change in the mean and variance of temperature inferred from the downscaled Hadley GCM	157
5.1	Land use classification.....	163
5.2	Combination of the observed land use classes in four units	164

5.3	Regression equations of net rainfall on gross rainfall under <i>Pinus halepensis</i> for hourly and daily data	168
5.4	Regression equations of net on gross event totals under <i>Pinus halepensis</i> ..	168
5.5	Parameters for Merriam's model of canopy interception per land use unit..	173
5.6	Average crop factors per land use unit	176
5.7	Recovery from the samples with depth.....	179
5.8	Descriptive statistics for the saturated hydraulic conductivity ($m \cdot d^{-1}$).....	181
5.9	Descriptive statistics for the porosity.....	182
5.10	Descriptive statistics for the dry bulk density.....	182
5.11	Parameters of the SWRC according to Farrel & Lawson (1972) with depth	184
5.12	Test for equality of means and variance of the hydrological variables with depth.....	186
5.13	Mean and standard deviation for the lognormal distribution of the saturated hydraulic conductivity in $m \cdot d^{-1}$ per land use unit	187
5.14	Parameters of the SWRC for the rootzone of the four land use units	191
5.15	Relative amount of applied rain stored in the root zone for each land use ..	197
5.16	Optimised values of the saturated hydraulic conductivity and RMSE	198
5.17	Descriptive statistics for the soil depth interpreted from the geophysical soundings	204
5.18	Shear strength parameters for unsaturated soils (after Gens, 1993).....	209
5.19	Applied normal stresses and suction levels.....	214
5.20	Volumetric moisture contents during the suction-controlled direct shear tests	214
5.21	Shear strength, strain and dilatancy at failure	215
5.22	Shear strength relationships	216
5.23	Land use dependent soil hydrological properties for the top soil	221
5.24	Soil hydrological properties for the subsoil (2 nd and 3 rd layer)	221
5.25	Shear strength parameters	222
6.1	Parameters, mean values and variability for the sensitivity analysis	225
6.2	Available field evidence for calibration over the calendar years 1997 and 1998	231
6.3	Calibration statistics over the period 1997 – 1998.....	233
6.4	Optimised parameter values and approximate 95% confidence limits	234
6.5	RMSE between the observed and simulated groundwater depth and the VMC at the Hollow for the calibration and validation runs.....	236
6.6	Time lag, RMSE and correlation coefficient for the perched water levels measured in the Hollow	236
6.7	Statistics for the validation of the VMC for 12 locations with TDR-probes installed at 0.50, 1.00 and 1.50 m	238
6.8	Observations and simulated values of groundwater levels at the LGM-site	240
7.1	Modelled susceptibility to slope failure in relation to variations in ϕ_p'	253
7.2	Comparison of observed landslide occurrence with susceptibility	255
7.3	Agreement between modelled susceptibility and observed landslide occurrence.....	256
7.4	Areas of simulated failure and observed landslide occurrence and the resulting performance of the deterministic and probabilistic predictions of slope failure over the validation period	261
7.5	Observed landslide density as a function of the recurrence interval, persistence and average duration of simulated failure per susceptibility class.....	270

7.6	Chi ² -test for relation between simulated persistence and observed reactivation.....	271
7.7	Total area, landslide density and reactivation in relation to land use	278
7.8	Model performance per land use unit	279
7.9	Area used for the calculation of the temporal characteristics of simulated failure	280
7.10	Relative frequency of total area per land use unit and observed landslide density in relation to the average duration of simulated failure.....	280
7.11	Regression of the data of Figure 7.17	282
8.1	Changed land use based under the hypothetical scenarios on the moment of 2-CO ₂ (2060).....	290
8.2	Scenario ensembles.....	291
8.3	Rainfall characteristics for the 30-year synthetic CP- and WF-series and as observed over the validation period (1971-1998).....	293
8.4	Frequency of annual rainfall totals for the synthetic weather series and as observed over the validation period (1971-1998).....	294
8.5	Frequency of rainfall event totals and recurrence intervals in years, T _E , for the synthetic weather series and as observed over the validation period (1971-1998)	295
8.6	Similarity between the simulated failure for the BAU-CP scenario and that for the validation period.....	296
8.7	Average and the standard deviation of the maximum probability of failure for the range $P(F \leq 1) \geq 0.10$	297
8.8	Change in the area of simulated failure based on the probabilistic forecast	301
8.9	Absolute change in the area of simulated failure between the respective scenarios and the BAU-CP scenario	301
8.10	Change in the area of $P(F \leq 1) \geq 0.10$, average persistence and total duration relative to the BAU-CP scenario	302
8.11	Change in average duration relative to the BAU-CP scenario.....	303
8.12	Cumulative relative frequency of the area $P(F \leq 1) \geq 0.10$ with recurrence.	304
8.13	Correlation between the area of simulated failure and rainfall	305
8.14	Relationship between area of simulated failure and the recurrence interval, T _E , of annual rainfall.....	309
A3.1	Data recovery INM-station Cocentaina 1991-1997	321
A3.2	Seasonal and yearly statistics based on the daily averages of RH, T, V and P at the INM-station Cocentaina 1991-1997.....	322
A4.1	Beta weights of [β] for the non-precipitation variables Z _k	324
A4.2	Elements of [ζ] for properly correlated forcing of Z _k	324
A5.1	Timing and amount of water applied during the rainfall simulation on land use unit I.....	327
A5.2	Timing and amount of water applied during the rainfall simulation on land use unit II	328
A5.3	Timing and amount of water applied during the rainfall simulation on land use unit III.....	330
A5.4	Timing and amount of water applied during the rainfall simulation on land use unit IV.....	331

FIGURES

1.1	Relation between groundwater height and soil depth for rainfall-induced landslides	27
1.2	Difference in accumulated rainfall required for triggering of landslides of different depth.....	28
2.1	Location of the study area in the Valles de Alcoy	35
2.2	Simplified geological map of the Valles de Alcoy	37
2.3	Geomorphological map of the Barranco del Mollo and the Barranco de la Coloma.....	44
2.4	Depth-length ratio vs. slope angle for the reconstructed slip surfaces of 11 landslides in the Barranco de la Coloma.....	48
2.5	Mean monthly temperature, rainfall occurrence and rainfall totals for the station of Alcoy.....	53
2.6	Demographic development of Almudaina, Valles de Alcoy and Spain during the 20 th century	57
2.7	Expected development of the Spanish population	60
3.1	Schematic representation of the model concept of the hydrological component STARWARS.....	69
3.2	Flow chart of the model structure of STARWARS – surface and vegetation interactions.....	70
3.3	Flow chart of the model structure of STARWARS – unsaturated and saturated zones.....	71
3.4	Flow chart of the model structure of STARWARS – lower boundary condition	72
3.5	Cardinal directions of Local drainage direction map (LDD).....	76
3.6	Linear decrease of evapotranspiration from the unsaturated matrix	81
3.7	Definition of the infinite slope model for translational slide	84
3.8	Capacity and demand model and the probability of failure	86
3.9	Model structure	89
4.1	Average daily rainfall for Almudaina	99
4.2	Relative frequency distribution of the event totals	101
4.3	Relative frequency distribution of the event duration.....	101
4.4	Fit of the Gumbel-distribution to the yearly extremes of event totals	104
4.5	Event rainfall for Almudaina and coverage by the tipping bucket records..	106
4.6	Regression of the tipping bucket data on the rainfall from Almudaina	107
4.7	Regression of the tipping bucket data.....	109
4.8	Observed maximum storms over the period December 1995-March 1999 per season.....	111
4.9	Relation between maximum intensity and event total	112
4.10	Location rainfall stations in the Alcoy region.....	113
4.11	Spatial distribution of the expected rainfall with a recurrence interval of 10 years	115
4.12	Scatterplots of event totals for the INM stations considered	117
4.13	Annual course of the daily averages of RH, T, V and P at Cocentaina	125
4.14	Scatterplots of meteorological data, Cocentaina vs. Almudaina.....	126
4.15	Spatial distribution of the relative incoming global radiation.....	129
4.16	Cloud cover statistics for the stations of Valencia and Alicante	130
4.17	Reference potential evapotranspiration for Cocentaina and Almudaina.....	133

4.18	Scatterplots of ET_0 from biased estimates	134
4.19	Flow diagram of the stochastic weather generator.....	138
4.20	Observed and simulated frequencies of rainfall events for Almudaina	145
4.21	Relative differences in the mean and standard deviation between the observed and generated daily rainfall per month.....	146
4.22	Relative differences in the mean and standard deviations for the observed and generated annual rainfall characteristics	147
4.23	Seasonality in the average monthly temperature and standard deviation as derived from the raw GCM results	153
4.24	Monthly mean and standard deviation for the present and warmer local climate at the time of CO_2 -doubling	156
4.25	Differences in the calculated potential evapotranspiration resulting from the predicted temperature rise in the Valles de Alcoy	158
5.1	Land use in the Barranco de la Coloma in 1998.....	164
5.2	Scatterplot of gross rainfall and net rainfall under <i>Pinus halepensis</i>	167
5.3	Comparison of the event-based and aggregated interception model of Merriam (1960) for <i>Pinus halepensis</i>	170
5.4	Annual course of the crop factors of the four land use units	175
5.5	Locations along the survey lines in the 30-ha large sub-area	177
5.6	Test design inverse auger test	179
5.7	Observed frequency and fitted lognormal distributions for the saturated hydraulic conductivity	180
5.8	Observed frequency and fitted normal distributions for the porosity	181
5.9	Loglinear relationships for the SWRC according to Farrel & Larson (1972) with depth.....	184
5.10	Box & whisker plot of the saturated hydraulic conductivity per land use unit.....	187
5.11	Vegetation cover for the four land use units represented by the rainfall simulator locations.....	189
5.12	Surface cover for the land use units represented by the rainfall simulation locations.....	189
5.13	Profiles of apparent and total porosity for the root zone of the land use units.....	191
5.14	SWRCs according to Farrel & Lawson (1972) for the rootzone of the four land use units	192
5.15	Observed wetting fronts during the rainfall simulation on the four land use units.....	194
5.16	DEM of the Barranco de la Coloma	200
5.17	Lithological map of the Barranco de la Coloma.....	201
5.18	Interpolated soil depth for the 30-ha large sub-area	202
5.19	Geophysical measurements in the Barranco de la Coloma.....	203
5.20	Interpolated apparent resistivity in the Barranco de la Coloma.....	205
5.21	Simulated soil depth for the Barranco de la Coloma	206
5.22	Direct shear test results	212
5.23	Observed vs. predicted shear strength for different theoretical relationships.....	217
6.1	Sensitivity of the simulated hydrology	227
6.2	Seasonal fluctuation in VMC based on TDR-measurements.....	233
6.3	Calibration results	234
6.4	Validation results	237

6.5	Observed and simulated groundwater levels at the LGM-site: absolute depths and relative saturation.....	241
7.1	Landslide occurrence based on air photo interpretation	247
7.2	Landslide occurrence as function of time in the Barranco de la Coloma	248
7.3	Sensitivity analysis for the infinite slope model	250
7.4	Distribution of observed landslide occurrence with slope angle	253
7.5	Landslide susceptibility and correspondence with observed landslide occurrence.....	254
7.6	Observed landslide occurrence and predictions of slope failure for the entire validation period and the various sub-periods	262
7.7	Comparison between the observed landslide density and the spatial average of the maximum probability of failure	263
7.8	Threshold of critical pore pressure ratio based on the one-dimensional infinite slope model and values for eleven landslides calculated from a back-analysis using two-dimensional slope stability models in relation to slope angle	265
7.9	Probability of failure along profiles over the landslide complexes near Almudaina.....	267
7.10	Temporal characteristics of simulated failure over the validation period....	268
7.11	Chi-gram of the comparison between the observed and expected reactivation relative to persistence for 5 classes of susceptibility.....	271
7.12	Relation between observed reactivation, R, and simulated recurrence intervals per susceptibility class.....	272
7.13	Relation between observed reactivation, R, and simulated average duration and recurrence interval, RI, per susceptibility class	273
7.14	Total rainfall, area of observed landslide occurrence and simulated failure per year	275
7.15	Distribution of susceptibility in relation to land use	277
7.16	Landslide density in relation to modelled susceptibility, expressed by the critical pore pressure ratio, per land use unit	278
7.17	Spatial average of the maximum probability of failure and observed landslide density per land use unit in relation to the average duration of simulated failure (entire area $P(F \leq 1) \geq 0.10$).....	281
8.1	Relation between the area of potentially arable land and travel distance	289
8.2	Present land use configuration (BAU) and simulated land use conditions according to the CRE and PS scenarios.....	290
8.3	Simulated annual rainfall over 30 years for the CP- and WF-series.....	294
8.4	Changes in the predicted instability relative to the BAU-CP scenario, based on the deterministic model outcome ($F \leq 1$).....	300
8.5	Probability of failure against the cumulative relative frequency of the area $P(F \leq 1)$	301
8.6	Area of simulated failure per scenario and for the validation period.....	302
8.7	Hydrological response for the topsoil (< 50 cm)	306
8.8	Change in the volumetric moisture content (VMC) above the lithic contact (> 1.00 m)	307
8.9	Relation between the area of simulated failure and recurrence interval for the annual rainfall totals per scenario	310
A1.1	Topographic map of the study area (1:50,000).....	315
A1.2	Location of field equipment & tests.....	316

A2.1	Saturated vapour pressure e_s as function of temperature T_a and its first derivative δ	319
A5.1	Change in VMC as observed with TDR during the rainfall simulation for land use unit I.....	328
A5.2	Change in VMC as observed with TDR during the rainfall simulation for land use unit II	329
A5.3	Change in VMC as observed with TDR during the rainfall simulation for land use unit III.....	330
A5.4	Change in VMC as observed with TDR during the rainfall simulation for land use unit IV.....	332
A6.1	Change in volumetric moisture content for the BAU-CP and BAU-WF scenarios.....	333

PLATES

1	The incised pediment between the Sierra de Almudaina and the Benicadell	40
2	Older translational landslide with secondary activity along its scarp and toe	41
3	Rotational landslide with deposit of slid material into the barranco.....	42
4	Scars of soil slips with associated mudslides.....	43
5	Undercutting and removal of material from an unstable slope	46
6	Fissure opened by displacement during the winter and spring 1996 – 1997	50
7	Soil profile developed in weathered marl	51
8	Interception plot under <i>Pinus halepensis</i>	166
9	Rainfall simulation.....	193

ACKNOWLEDGEMENTS

This thesis is the result of research at the Department of Physical Geography of Utrecht University that started in 1995. It is written over the consecutive years when it was not always prominent but ever present. The contents of this thesis benefited from the contributions of many and I wish to thank the following persons in particular.

In de allereerste plaats wil ik mijn promotor Prof. Dr. Jan Nieuwenhuis en mijn co-promotor Dr. Theo van Asch bedanken voor hun commentaar en steun bij het voltooien van dit proefschrift. Jan, mijn dank gaat naar jou uit voor je inspiratie en je praktische aanpak en analyses die van onschatbare waarde voor dit proefschrift zijn geweest. Theo, als dagelijks begeleider ben je een grote steun en toeverlaat voor mij geweest. Met je kennis, inzicht en met je enthousiasme, zowel in Utrecht als in het veld, heb je een duidelijk stempel op dit proefschrift gedrukt.

Mijn bijzondere dank gaat ook uit naar mijn collega's binnen het NWO-programma *Hierarchy of land degradation processes in a Mediterranean Environment*, Anton Imeson, Erik Cammeraat, Hein Prinsen en Anja de Wit. Hoewel we uiteindelijk in verschillende delen van Spanje terecht kwamen, bleef de gezamenlijke interesse bestaan. Erik, ik wil jou met name bedanken voor je hulp bij de regenvalsimulaties. Hein en Anja, ik wil jullie bedanken voor jullie hulp en gezelligheid tijdens de vele veldwerken in Spanje.

Dit onderzoek was onmogelijk geweest zonder de ondersteuning van het Laboratorium en de Afdeling Electronica van de Vakgroep Fysische Geografie. Ik wil dan ook Theo Tiemissen, Marcel van Maarseveen en Bas van Dam hartelijk bedanken voor al hun professionele ondersteuning bij alles wat een batterij nodig heeft in het veld. Jullie hulp was onontbeerlijk.

Kees Klaver en Hassan Aarab ben ik erkentelijk voor al het materiaal dat mee op veldwerk ging. Kees, ik wil je in het bijzonder bedanken voor al je inspanning voor de ontwikkeling van een handzame en betrouwbare regenvalsimulator.

Veel dank ben ik verschuldigd aan Wim Haak. Wim, het is ongelooflijk hoe je het grondmechanisch lab over de jaren bestierd hebt en hoe je steeds weer met allerlei oplossingen kwam voor de meest uiteenlopende problemen. Reeds voor mijn promotieonderzoek was ik al in het grondmechanisch lab te vinden en ik wil je dan ook niet alleen bedanken voor je hulp maar ook voor alle gezelligheid over de jaren.

Materiële ondersteuning heb ik ook van andere instituten van de Universiteit Utrecht mogen ontvangen. Ik wil hier Dr. J. Bredewout bedanken voor het ter beschikking stellen van de geofysische apparatuur. Ir. Peter Mekenkamp wil ik bedanken voor de geodetische apparatuur die ik meerdere malen van hem mocht gebruiken.

Een speciaal woord van dank is bestemd voor alle doctoraal studenten die met en voor mij in Spanje veldwerk verricht hebben. In chronologische volgorde waren dit Marcel van Dorst & Berthe Brouwer, Rutger Dankers & Jan-Peter Berende, John Gossen, Bart

Overbeek, Ivan Soenario & Jurjen Bertens, Jannes Haanstra & Lea van der Last, Michiel van Straaten, en Marc van de Looij & Martijn van Drunen. Zonder jullie inzet was dit proefschrift onmogelijk geweest!

Mijn oud-collega's hebben altijd gezorgd voor een prettige en stimulerende sfeer. Met name wil ik mijn kamergenoten over de jaren bedanken. Na mijn gedwongen scheiding van Anja deelde ik met veel vreugde kamer 130 van de Zonneveldvleugel met Jelle Buma, Thom Bogaard en Karin Pfeffer. Ik ben jullie dankbaar voor al jullie hulp en gezelschap. Thom, ik geloof dat we tijdens ons promotieonderzoek elkaar goed aanvulden en ik genoot en geniet van onze inspirerende gesprekken en discussies, ook op heel andere terreinen dan de hydrologie en de grondmechanica.

Derk-Jan Karssenbergh, Kor de Jong en Cees Wesseling wil ik bedanken voor al hun ondersteuning bij de modellering in PCRaster. Ook Oscar van Dam ben ik erkentelijk voor zijn hulp en ideeën over de modellering van de inkomende straling.

Verder wil ik Ed Weiss, Henk van Steijn, Martin Hendriks en Victor Jetten bedanken voor hun hulp en commentaar. Ook Simone van Dijck ben ik zeer dankbaar voor al onze discussies over "het vak" maar ook voor de vele gezellige uren in Utrecht en in het veld.

Buiten het werk hebben mijn paranimfen Peter de Graaf en Jan de Ruiter altijd een luisterend oor gehad voor de problemen bij het schrijven van dit proefschrift. Het wordt tijd om weer eens te gaan fietsen. Tom Dijkstra en Pat Carrillo wil ik bedanken voor hun gastvrijheid en vriendschap tijdens mijn verblijf in Coventry. Het was een welkome afleiding tijdens het schrijven in het weekeinde.

Mijn ouders, zus en broer wil ik bedanken voor hun morele bijdrage aan het voltooien van dit proefschrift. Pa, Ma, Sandra en Perre, zonder jullie steun was het allemaal niet mogelijk geweest.

Special thanks I want to give to Andy Collison, Steve Wade, Mark Mulligan and Jim Griffiths of the Department of Geography, King's College London. Your contribution was essential for this research and your company and friendship much appreciated. I want to thank Andy and Steve for their help with equipment and fieldwork. Mark, I am very grateful for your climatic research that assisted me with the downscaling of the local climate from the GCM results. Jim, I still admire your nifty craftsmanship and the job you did on installing the equipment and enjoyed the pleasant times we spent together at various in Spain and the UK.

I am also obliged to Martin Dehn of the University of Bonn for his help on downscaling the rainfall patterns in the area. Although the erratic nature of rainfall in the area made the results disappointing, I am very grateful, Martin, that you applied your skills to the problem and helped me out with various questions that I had on GCMs.

The study of landslides in a Mediterranean environment raised new questions on the geomechanical behaviour of unsaturated materials. I was very lucky that the Department of Engineering Geology of the Universitat Politècnica de Catalunya participated in the NewTech project and offered me the possibilities to carry out specific tests in its

laboratory. I want to thank Jordi Corominas, Antonio Lloret and Alberto Ledesma for their support and hospitality.

Por último, quisiera agradecer a todos en Planes y Almudaina, donde he trabajado sobre sus campos, por su hospitalidad. Menciono en particular el alcalde de Almudaina, Sr. Dn. José Luis Seguí.

Además, doy mis gracias a todos mis amigos que han contribuido a esta tesis. Estoy agradecido a Alberto Llorens y Armando Gill por su información sobre el aprovechamiento y el clima. Estoy obligado a Javier Andrés por su asistencia en mantener el equipo en el campo y su información sobre la lluvia en Almudaina.

Esta tesis no estaría posible sin el apoyo Neus la Roca de la Universidad de Valencia y Inma Castelló de la Cooperativa de Labradores y Ganaderos de Planes de la Baronía. Neus e Inma, os agradezco cordialmente por vuestra ayuda y amistad por los años pasados.

Dorst, March 2002,

Rens van Beek

1 LANDSLIDING AS A GEOMORPHIC PROCESS IN MEDITERRANEAN ENVIRONMENTS

1.1 Context

The work presented in this thesis is part of the research program *Hierarchy of Land Degradation Processes in a Mediterranean Environment* and started in 1995. Funding was obtained from the Netherlands Geosciences Foundation of the Netherlands Organisation of Scientific Research (GOA-NWO, contract 750.294.03). The research program has the overall objective of developing a “new process-oriented methodology that will improve understanding of land degradation processes and patterns at different hierarchical levels...” (Imeson *et al.*, 1994). The proposed methodology consists of a model framework that hierarchically links key processes operating at different spatial and temporal scales. The research program is a combined effort of Utrecht University and the University of Amsterdam within the Netherlands Centre for Geo-ecological research (ICG).

Different land degradation processes and their relationship to environmental factors have been investigated at different scales. De Wit (2001) studied the controlling influence of environmental factors on runoff on hillslope to catchment scales. Prinsen studied the relation between vegetation patterns and surface hydrology on a plot scale. Both studies were carried out in the semi-arid Guadelentin basin (Province of Murcia). Cammeraat (in press) addresses the hierarchical linkage of the fluxes of water and sediment across different scales.

The basis of this study was included as the project *Temporal Frequency of Landsliding as an Integrated Subsystem in the Process of Land Degradation in a Mediterranean Environment* (Van Asch in Imeson *et al.*, 1994). The research was carried out in the humid to subhumid area of the Valles de Alcoy (Province of Alicante, Valencian Autonomy). In this area, La Roca (Department of Geography, University of Valencia) has carried out detailed research on mass movement activity from a geomorphological perspective. In the urbanised area of Alcoy, mass movements pose a potential risk and have been the subject of inventories made by the IGME and ITGE (1981, 1990).

1.2 Problem definition

1.2.1 *The role of landsliding within the hierarchy of erosion processes*

Mediterranean environments are characterised by the erratic distribution of high intensity rainfall events and the development of a soil moisture deficit over summer. Where neotectonics are coupled with a high-energy relief, the propensity of the system to erosion is high and determined by complex interactions between soil and vegetation. In these environments, water is the most important agents in the process of erosion. Human interference potentially disturbs the dynamic equilibrium between the biotic and abiotic components of the landscape and may result in continued deterioration or land degradation.

Within the system of erosion processes, landsliding may play an important role by its capability of removing and exposing large soil masses in relatively short timespans. Although landslides are highly localised in space in time compared to the more continuous process of surface wash, landslide activity can have a profound impact on the sediment budget on the hillslope and catchment scale when medium temporal scales (10 – 100 years) are considered (Benda & Dunne, 1997).

The rate of erosion may be limited by the incidence of significant rainfall events and by the rate by which erodible soil is produced (Dietrich *et al.*, 1984; Crozier *et al.*, 1990; DeRose *et al.*, 1991). Therefore, the hierarchy of hillslope processes can be envisaged as a cascade in which the downslope movement of material or the conversion of potential into kinetic energy is controlled by interlinked processes of surface wash, soil production and mass movement (Van Asch, 1980).

1.2.2 Key processes

In humid to subhumid Mediterranean environments rainfall suffices to support a closed vegetation cover. Under such conditions, landslides deliver a substantial share of the sediment yield, either directly by discharging slid material into the channel network or indirectly by exposing erodible material by the disturbance of the soil and vegetation cover to surface wash. Landslide activity can be taken as a relative measure for its contribution to erosion. On this premise, it is a key process and should be assessed on the appropriate spatial and temporal scales.

Within the hierarchy of hillslope processes, landsliding and surface wash are intimately linked through the hydrological system. Rainfall is the most common trigger of landslides (Sidle *et al.*, 1985; Crozier, 1986). Consequently, rainfall-induced landslides can be considered as the most important type of landslides in terms of the geomorphic work that they perform (Wolman & Miller, 1960; Gallart, 1995; Crozier, 1996).

1.2.3 Landslide activity and hydrological triggering

The term landslide is used here to describe movements by which material, either rock or soil, is displaced more or less coherently over a discrete slip surface by disturbing gravitational forces (shear stress).

Landslides are the manifestation of the inertia of the landscape to adapt to changes in the intrinsic or extrinsic factors that affect slope stability. Intrinsic factors are those that directly influence the stress distribution above the potential slip surface. Extrinsic factors influence the stress distribution indirectly. It is often difficult to distinguish the true cause of a landslide. The intrinsic factors change most times only gradually over time and can be considered as *preparatory factors* whereas the extrinsic factors are transient and can be regarded as *triggers*, i.e. the disturbance that initiates slope instability or failure. (Crozier, 1986).

Movement is resisted by the shear strength that can be mobilised along the slip surface. The shear strength consists of the cohesion and the total inter-particle friction. The friction depends on the normal stresses at the particle contacts and increases with the

weight of the soil. The cohesion is more or less constant and the resultant shearing resistance is bound by a maximum. The ratio between this maximum of available shearing resistance and the disturbing forces, or *safety factor* F , is a measure for the stability of a slope and when the two cancel each other, $F=1$, failure is imminent.

From a human perspective, landslides can also be considered as a hazard that can be defined as the likelihood of landslide occurrence within a given region over a given period (Varnes, 1984). Landslide activity can consequently be quantified in terms of frequency, duration and magnitude. This requires first of all that a thorough understanding of the mechanisms that induce distinct landslides in Mediterranean environments.

Rainfall-induced landslides are triggered hydrologically, i.e. by a rise in the groundwater depth at the slip plane. This raises the pore water pressure that carries part of the total weight that acts on the potential slip plane. The ensuing decrease in the frictional forces between particles reduces the effective shearing resistance.

Hydrological triggering can be considered as the most common mechanism of initiation and reactivation because fluctuations in the pore pressure affect stability on the shortest time scale. Because of the dependence of the frictional component of the resistance on the effective inter-particle stress, the rise in pore pressure or groundwater level that is required for triggering is proportional to the depth of the landslide mass and can be expressed by the pore pressure ratio (Bishop, 1954; Figure 1.1).

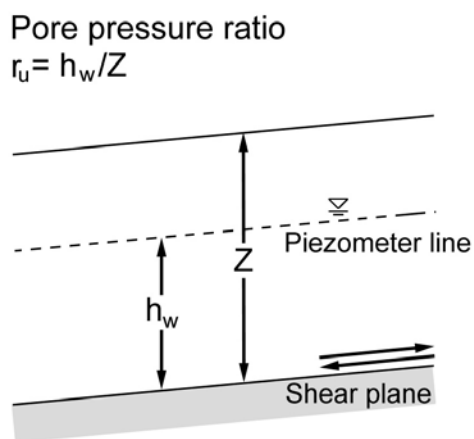


Figure 1.1: Relation, expressed as the pore pressure ratio r_u , between groundwater height, h_w , and soil depth, Z , for rainfall-induced landslides

Figure 1.1 suggests that the threshold of slope instability can be expressed as a critical increase in pore pressure, which depends on the local soil conditions and morphometry. This local threshold that defines the critical magnitude of a trigger can be denoted as the *susceptibility* (Carrara *et al.*, 1995). On graded temporal scales (Chorley *et al.*, 1984) the local *susceptibility* to landsliding can be assumed to be constant as the soil properties and the morphometry change over longer periods than the variation in rainfall events (Siddle *et al.*, 1991).

The absolute increase in pore pressures postulates that more rainfall must be accumulated to trigger a deep landslide than to trigger a shallow one, all other factors remaining equal. The amount of rainfall that is required to trigger a shallow landslides can be accumulated over one or several events, whereas the larger amount for the triggering of deeper landslides can only be amassed on a seasonal scale (Figure 1.2). The relevant

hydrological processes that influence the amount of rainfall delivered to the potential slip plane constitute the hydrological triggering mechanisms of the various landslide types (Van Asch *et al.*, 1998).

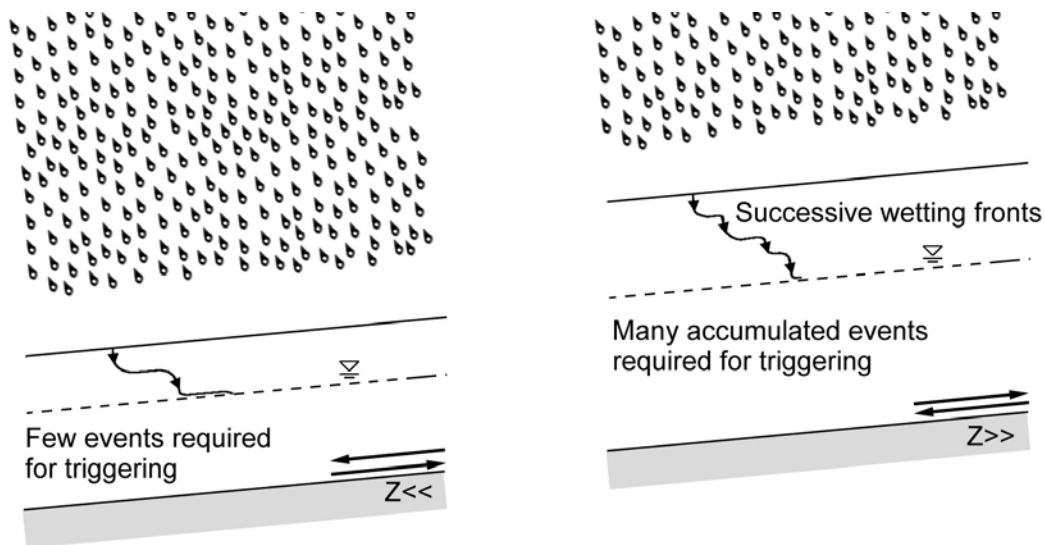


Figure 1.2: Difference in accumulated rainfall required for triggering of landslides of different depth

Due to the distinct response time of relevant hydrological processes, the hydrological triggering mechanisms will be clearly reflected in the temporal frequency of landslide types (Van Asch & Van Steijn, 1991). Combined, the susceptibility and the recurrence of potential triggering events define the *sensitivity* of the landscape to landsliding, which incorporates the spatial and temporal aspects of landslide activity.

1.2.4 Environmental conditions as controlling factors

Figures 1.1 and 1.2 imply that the activity of rainfall-induced landslides is controlled by the local conditions that determine the critical groundwater level and the frequency by which this threshold is exceeded. This frequency depends on the antecedent soil moisture conditions and the recurrence of potentially triggering rainfall events (Terlien, 1998; Crozier, 1999). In Mediterranean environments, the seasonal and interannual variation in rainfall is high and evapotranspiration is as important as the gross event rainfall for the exceedance of the critical groundwater level. Since vegetation primarily controls the loss through evapotranspiration, both land use and climate are determining factors for landslide activity. The importance of climate and land use has serious implications for landslide activity in the near future as both are subject to drastic change in the Mediterranean on moderate temporal scales of 10 to 100 years (Jeftic *et al.*, 1992; Coccossis, 1991).

Climatic change is forced by global warming as the result of the emission of greenhouse gasses (Houghton *et al.*, 1990). Potentially, it has a moderating influence on the

incidence of potentially triggering rainfall events and may possibly modify the rate at which geomorphic processes including landsliding operate (Eybergen & Imeson, 1984). Within the hydrological cycle, land use is a mediating factor by which human interference influences the activity of hillslope processes. It limits the availability of water in the soil by means of interception, evapotranspiration and infiltration. In turn, soil conditions and water availability may impose constraints on the potential land use. In European Mediterranean environments, land use change is notable, as the traditional agricultural base of sustenance has been in decline for most of the century. As a result of mechanisation, intensification and globalisation, abandonment of cultivated fields is widespread.

With respect to landslide activity, it is important to quantify it under the present and changed environmental conditions as Mediterranean environments are extremely sensitive to changes in land use and climate (Bull, 1991; Imeson & Emmer, 1992; Mulligan, 1998).

1.3 Aims and objectives

The aim of this study is to evaluate the role of landsliding within the integrated system of erosion processes in a quantitative manner. Hydrological processes that trigger landslides have a strong temporal variation that is imposed on spatial variations in susceptibility. Hence, landslide activity must be assessed in terms of its spatial extent and temporal frequency. On medium temporal scales (< 100 years), environmental conditions and the changes thereof influence the hydrology that controls landslide activity. The objectives of this study are, therefore, to

- Evaluate the spatial and temporal variations in potentially triggering rainfall events;
- Assess local variations in landslide susceptibility;
- Evaluate the role of the hydrology on landslide activity in the area;
- Assess the change in landslide activity under the impact of changes in land use and climate on medium temporal scales (10-100 years).

1.4 Approach

1.4.1 Scale considerations

The Valles de Alcoy (SE Spain), where landslides in marl slopes occur frequently, has been selected as study area.

The aim of this study to evaluate the role of landsliding within the hierarchy of erosion processes in a Mediterranean environment calls for a regional assessment of the landslide activity in which local variations in soil properties and slope conditions are incorporated. Land use is delineated at the parcel scale and, consequently, the spatial scale considered should encompass a representative part of the land use patterns. The hydrological triggers of slope instability, combining the spatial and temporal distribution of rainfall events and the redistribution of moisture, surpass the hillslope scale. To meet both demands, the

catchment scale has been preferred and a suitable area has been found in the municipality of Almudaina.

Transient hydrological conditions are the dominant triggers of landslides in the Valles de Alcoy. Because of the erratic distribution of rainfall in this subhumid Mediterranean environment, periods of considerable length should be considered (> 10 years). Land use changes also occur on similar temporal scales whilst the moment of CO₂-doubling is commonly taken as the culminating moment of the envisaged climate changes. Predictions project this moment around 2060 (Houghton *et al.*, 1990). Consequently, landslide activity will be evaluated over periods that are representative for the climatic conditions (30 years) and the consequences of land use change will be related to the expected trends of climate change (Le Hou  rou, 1992).

On the temporal scales considered, any seismic events are considered as disturbances and will not be incorporated in the analysis.

1.4.2 *Environmental change*

Inferred changes in the environmental conditions are largely hypothetical and based on extrapolations of current trends. These hypothetical conditions can be described by scenarios of varying complexity. Climate change scenarios are nowadays based on the results of general circulation models (GCMs) that are parameterised for the present climate on a continental or global scale. These models are subsequently subjected to increased concentrations of greenhouse gasses in the simulated atmosphere. The model output under these perturbed conditions is treated as a forecast for the climate conditions in the future. The model output usually consists of mean monthly or yearly statistics and the spatial resolution is generally low. In order to apply it on more detailed scales, downscaling is required. This technique has been applied for slope stability modelling at various locations in the Alps by Buma & Dehn (1998), Dehn (1999) and Dehn *et al.* (2000).

Land use conditions are usually extrapolated on the basis of social and economic statistics and observed changes in land use patterns. Alternatively, purely hypothetical scenarios of certain changes may be used to evaluate the consequences (Veldkamp & Fresco, 1996; Rodda *et al.*, 2001). In this case, land use changes are represented by changes in land cover that are associated with fixed parameter sets. A direct incorporation of the dynamics of land use change is not feasible and defies the means and scope of this research. Furthermore, only the hydrological effects of land use change are included in the land use change scenarios. Root reinforcement (Sidle *et al.*, 1985; Mulder, 1991) has been ignored as slip planes in the study area are usually located well below the root zone.

1.4.3 Modelling of landslide activity

The quantification of landslide activity under hypothetical conditions is hindered by the fact that the relation between the effective rainfall and landslide occurrence is unknown. For some time, analogue studies, in which process rates under different conditions are compared, have been popular. However, analogue comparisons under different climates or land use conditions are not necessarily representative for the expected changes. Moreover, the expected vegetation covers are not necessarily present on the slopes liable to landsliding. Given that the present climate has oscillated around a long-term mean, the landscape that represents the expected changes will have adapted itself to some degree and may deviate considerably from the inherited landscape under the true development. It is, therefore, reasonable to resort to the alternative of physically based models that are more flexible to incorporate hypothetical conditions. However, the model should be modest in its scope and its appropriateness must be corroborated on the basis of field evidence (Gleick, 1986). The disadvantage of detailed physically based models is that their data requirements are large and that they must be run at a high model resolution. These constraints limit their applicability to relatively small areas.

Because of the variation in rainfall, antecedent moisture conditions are extremely important for landslide activity in Mediterranean environments, whether it concerns shallow or more deep-seated landslides. The intended application of the model under hypothetical climatic conditions demands that the model is capable of simulating the transient hydrology under variable meteorological conditions (Brooks *et al.*, 1993). This contrasts it against the static approach that is often employed in more temperate regions (Montgomery & Dietrich, 1994; Dietrich *et al.*, 1998).

The hydrology is influenced by the vegetation and the application of different land cover configurations necessitates a distributed approach. Embedding the model in a geographical information system (GIS) has the advantage that the distributed model can be linked to land use maps and datasets of the relevant parameters whilst the topographical aspects of landslide activity are prescribed by the digital elevation model (DEM).

The simulated hydrology has to be fed into a slope stability assessment to calculate the safety factor or another measure of slope stability. Because of the dependence of the stability assessment on the simulated hydrology, it is preferred to calibrate only the hydrological component of this coupled hillslope model. Validation of the hydrological and the stability components is possible by processing the rainfall data and by comparing its results with the observed hydrology and with actual signs of slope instability.

The assessment of the coupled hillslope model is by nature deterministic, i.e. it predicts failure or not. In reality, slope failure occurs due to spatial and temporal variations in the capacity of mobilised shear strength in relation to the demand of the experienced shear stress. Discrepancies, therefore, are likely to arise between the actual landslide occurrence and simulated failure. Model performance will increase if the simulation could incorporate some of the variability in the soil properties and the temporal variations in the capacity and demand that arise from the hydrology (Ward *et al.*, 1981; Christian *et al.*, 1994).

In this case, the variability of the soil properties will be included in the analysis by means of a probabilistic slope stability model. The uncertainty in the shear strength parameters that define the landslide susceptibility will be considered.

On the basis of the validated hillslope model, changes in the temporal frequency of landsliding can subsequently be assessed by employing the model to different scenarios for land use and climate change (Scenario Modelling). The challenge is to find a concept that describes such changes in landslide activity accurately. A possible solution is the use of the sensitivity concept (Brunsden, 1999). The description of sensitivity of Section 1.2 conforms to the definition of Brunsden & Thornes (1979), that sensitivity can be expressed as the ratio of the recovery time of a system or landscape over the recurrence time of a significant disturbing event. Based on this definition, Brunsden (1993, 2001) distinguishes several types of resistance and sensitivities. According to his definitions, landslide activity can be interpreted in terms of the spatial and temporal sensitivity of the landscape to disturbing events. On graded temporal scales the spatial sensitivity can be assumed to be constant as the soil properties and the morphometry change over longer periods than those considered (Chorley *et al.*, 1984). This reduces it to a local *susceptibility* to landsliding, which is defined by the critical rise in groundwater height for failure. This susceptibility reflects the likely recurrence of the worst case condition and determines the long-term stability of a slope. Under this fundamental assumption, the sensitivity to landsliding is basically the *temporal sensitivity*, in which the frequency of potential triggering events determines the landscape response (Thomas, 2001). According to the terminology of Brunsden (2001), the model evaluates sensitivity in terms of strength resistance and filter resistance. The first is included through the variability in the shear strength parameters whilst the second is included as the hydrological influence of land use on the antecedent moisture contents and the net rainfall amounts.

The main disadvantage of the approach followed is its static nature, i.e. the simplifying assumption that the susceptibility is constant over time. In reality, the action of gradual processes implies that the susceptibility is constantly changing over time (De Boer, 1992). With respect to landsliding, these processes emerge as the preparatory factors may lower the magnitude of the required triggering rainfall event (Van Asch, 1980; Crozier & Preston, 1998). Although the approach offers an avenue to assess the changes in the temporal frequency and spatial occurrence of landsliding, it is evident that forecasts of changes in landslide activity must be treated with caution as dynamic change and complex feedback mechanisms are not considered by the coupled hillslope model.

1.5 Thesis structure

Besides this introduction (Chapter 1), which sketches the outline of the work, this thesis contains seven chapters. Chapter 2 gives a physiographic description of the study area and the Valles de Alcoy. Chapter 3 presents the coupled hillslope model that forms the basis for the subsequent modelling effort. Chapter 4 evaluates the spatial and temporal variations in the climatic controls of rainfall and evapotranspiration on landslide activity in the Valles de Alcoy. Chapter 5 describes the land use classification, which is used to interpret the soil hydrological and geomechanical properties. This Chapter also presents

the resulting parameterisation of the model. Chapter 6 treats the calibration and the validation of the hydrological model component. Chapter 7 addresses the modelled landslide susceptibility and the performance in comparison to the observed landslide activity. Finally, Chapter 8 presents the Scenario Modelling by which the influence of land use and climate change on landslide activity is assessed. The major findings and suggestions for future research stemming from this study are summarised in the concluding synthesis.

2 PHYSIOGRAPHY OF THE STUDY AREA (VALLES DE ALCOY)

2.1 Introduction

This Chapter provides a physiographic description of the study area and its surroundings in relation to landsliding. The study area itself is situated in the municipality of Almudaina, within the Spanish province of Alicante (Figure 2.1). It pertains to the district of Alcoy, which, with 60,000 inhabitants, is the largest city of the upper basin of the Río Serpis (470 km²). This basin delimits a physiographic and cultural region referred to as the Valles de Alcoy. North from the city of Alcoy, industrial and commercial activities concentrate along the banks of the Río Serpis and the parallel national road N340 from Alicante to Valencia. At Muro de Alcoy, the Río Serpis bends from its northerly course to the east and continues along the mountain range of the Benicadell. At the outlet of the basin, the reservoir of Beniarrés captures the waters of the Río Serpis after which the river continues its lower course to the Mediterranean.

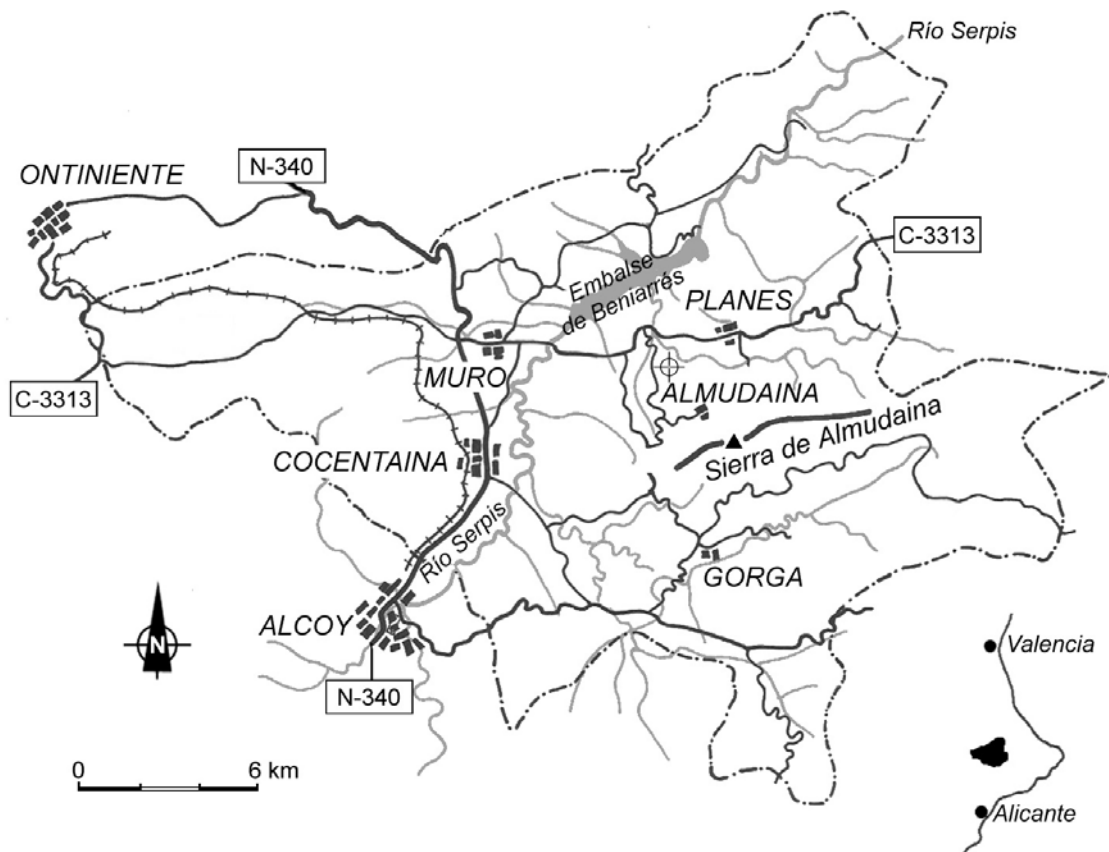


Figure 2.1: Location of the study area within the Valles de Alcoy (marked)

The study area is located on the right bank of the Río Serpis and covers the *Barranco de la Coloma*. This catchment extends on the northface of the Sierra de Almudaina. After its confluence with the *Barranco del Mollo*, the Coloma meets the larger *Barranco de Planes y Almudaina*, which drains directly into the reservoir of Beniarrés (Figure 2.1, Appendix 1). The catchments of both streams enclose approximately 4 km². North of the study area runs the secondary road from Muro to the Mediterranean coast (C3311), which forms the main route of access.

2.1 Geology & Geomorphology

2.1.1 Structural geology

The upper basin of the Río Serpis belongs to the Pre-Betic, the outer margin of the Betic Cordillera. This outer rim connects this Alpine orogenic belt to the Hercynian basement of the Spanish Meseta. In contrast to its core, the Pre-Betic is composed entirely of autochthonous sediments of Mesozoic and Tertiary age. Because of the proximity of the ancient landmass of the Meseta and the continuous shift in the position of the ancient shoreline, distal and proximal sediments alternate.

The regional structural trend of the Pre-Betic is WSW-ENE and a zone of large-scale folds and faults in this direction, the so-called *franja de los grandes ejes*, extends through the region of Alcoy (IGME, 1975; Sanz de Galdeano, 1983). Within the Pre-Betic, however, complications in the structural geology arise from the large-scale deformation of the Mesozoic and Tertiary strata over the incompetent Keuper formation that covers the Hercynian basement. Tectonic forces dislodged the plastic gypsiferous clays of Triassic age that intruded along weaker zones into the younger strata. These diapiric intrusions are generally associated with a secondary NS aligned fault-system. Although the outcrops of Triassic rocks are limited, this fault system is widespread.

In the Alcoy region, both the ENE and the N aligned fault systems have been active during most of the Tertiary (Pierson d'Autrey, 1987). At the transition from the Cretaceous to the Paleogene, no clear break in lithology is observed, an indication that the W Mediterranean basin remained distensive and the deposition of a deep-water facies of limestone and flysch-type sediments continued. From the late Eocene onwards, a shallowing-upward is present in the sequence of marine sediments. The change in facies resulted from the falling sea level and involved a lateral extension of shelf conditions (Rodríguez, 1977^a, Rebel, 1988). A hiatus in the marine sedimentation and a basal conglomerate mark the transition from the Paleogene and Neogene (Pierson d'Autrey, 1987, Rebel, 1988).

The transgression that reclaimed the area for marine sedimentation at the beginning of the Neogene coincides with a period of increased tectonic activity. As part of the foreland of the Betic Cordillera, the area experienced a general lowering while towards the south the topography was reversing under influence of the compressive NW movement. This compression forced former rift faults to scale one another and ENE aligned folds arose due to the shortening of the overlying deposits. Because of the NW compressive motion and uplift in the south, most of these fold axes are overturned in this direction (Rodríguez, 1977^b).

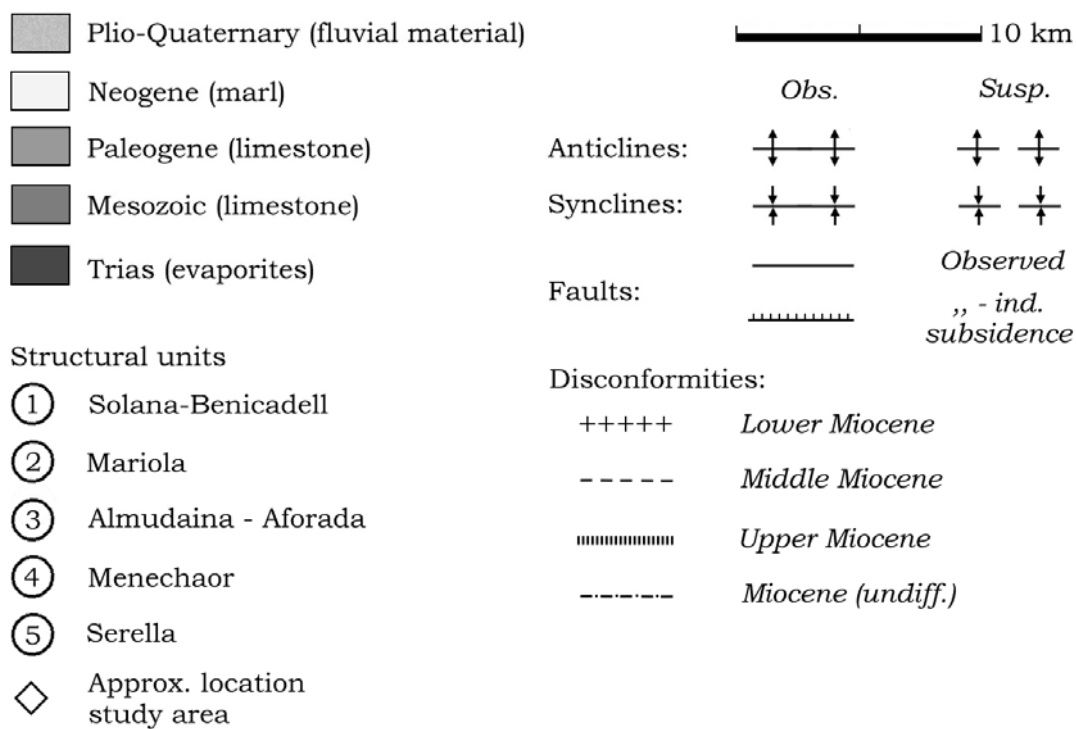
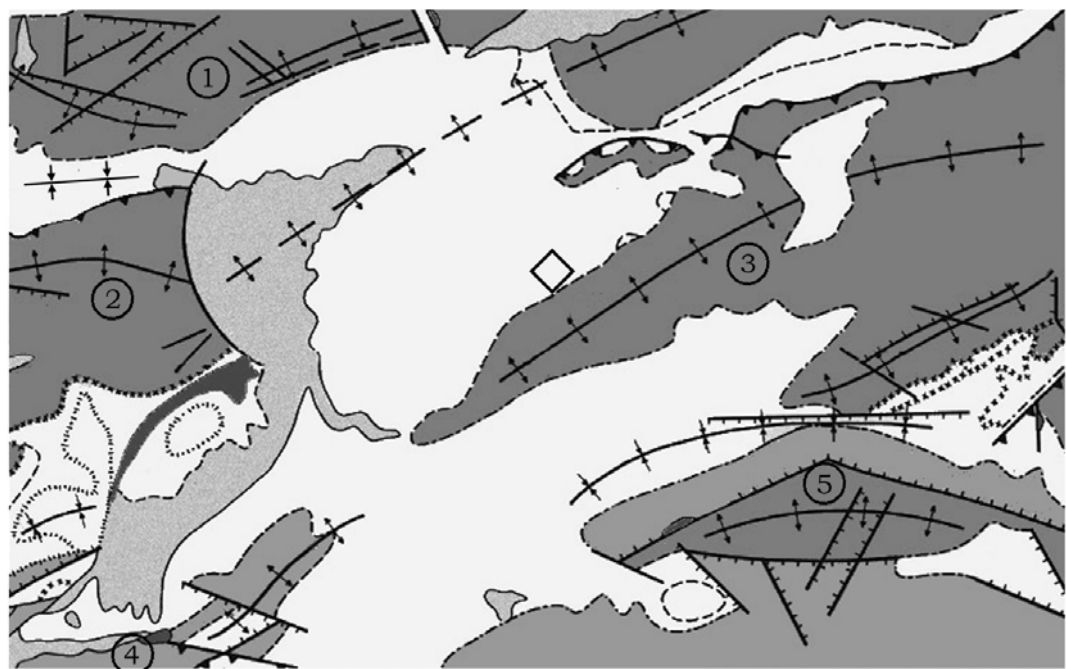


Figure 2.2: Simplified geological map of the Valles de Alcoy. Dominant lithology included in brackets. Modified from IGME (1975)

As a result of the tectonic movement, the boundary between the Neogene and the older substrate is unconformable. In the remaining basins, the increased input of eroded material led to a higher rate of sedimentation. However, the rate of subsidence apparently

matched the higher input into these basins. As a consequence, shelf conditions prevailed most of the time and thick sequences of bioclastic material and marls were deposited. These weakly consolidated sediments are similar to the deposits of the late Paleogene and are referred to as Stage 2 and 1 of one lithostratigraphical unit, called *Tap*. Because of the insecure boundaries and their vast thickness, most times no distinction has been made between the litho- or chronostratigraphy of the Miocene deposits on the geological map but, instead, they are mapped as undifferentiated Miocene (IGME, 1975).

In the middle Miocene (14 Ma), the tectonic climax was reached and the resulting uplift terminated the marine sedimentation in the area near the end of this series. From the Pliocene onwards, locally derived debris was deposited in a terrestrial environment. Tectonic activity decreased and was mostly vertical because of isostatic adjustment in the Betic system (Sanz de Galdeano, 1983). The basin of the Río Serpis has been experiencing uplift up to recent times. This is witnessed by raised Pliocene and Pleistocene terraces. Additional evidence of neotectonic activity in the area includes inclined Quaternary fluvial terraces and travertine deposits (Moseley, 1990), the seismic disruption of similar materials and the record of earthquakes in historical times (ITGE, 1990, La Roca, 1991^a). Besides isostatic adjustments, the authors attribute these signs of neotectonic activity to the continued diapiric activity, the ongoing compressive motion of the Betic Cordillera and the rejuvenation of the N-S aligned faults by distensive movement since the Pliocene.

Because of the presence of large-scale folds and faults and the succession of more resistant limestone from the Mesozoic and Paleogene by softer rocks of the Neogene, the Río Serpis follows the geological structure closely. Presently, the ENE aligned anticlines stand out as roughly parallel limestone ridges that delimit the catchment of the Río Serpis (Figure 2.2). Such anticlinal structures form the Sierra de Almudaina, the Sierra del Benicadell and the Sierra de Mariola. Towards the south, they connect to a continuous chain of mountains from the Sierra de Menechaor to the Serella that separates the Río Serpis from the coastal plain of Alicante. All mountain ranges reach heights over 1000 m. The highest summits in the region are the Plá de la Casa (1379 m.a.s.l.) and the Montcabré (1390 m.a.s.l.), in the Serella and the Sierra de Mariola respectively.

Within the upper basin of the Río Serpis, the limestone crests alternate with worn-down synclines in which the younger *Tap formation* is conserved. The dominant lithology of this formation is the less resistant marl of Miocene age. In the south-east, such a syncline, the Valle de Seta, forms a substantial sub-catchment in the upper Serpis Basin. In the northern part of the basin, three such synclines form a large plain between the Benicadell, the Sierra de Almudaina and the Mariola (Pierson d'Autrey, 1987). This plain is confined by transverse faults along which diapiric activity occurs. In the north-east, a normal fault runs through the Sierra del Benicadell. To the west, between Alcoy and Muro, such a fault terminates the Sierra de Mariola, which consequently stands out against the adjacent valley floor.

2.1.2 *The upper basin of the Río Serpis*

The resulting depression between the mountain ranges encompasses most of the course of the Río Serpis. Only where the fault through the Sierra del Benicadell meets the continuation of the northern-most syncline, the Río Serpis breaks through the confining mountain chain and continues its course towards the Mediterranean. At this narrow stretch, the course of the river has been dammed to form the reservoir of Beniarrés. At the egress, the elevation of the *Tap* is 320 m.a.s.l. and rises to 700 m.a.s.l. at the unconformity with the Cretaceous limestone.

Along the mountain ranges scree slope deposits of different age cover the *Tap formation*. The scree deposits connect to a pediment, of Plio-Pleistocene age, with a slope below 10° (Plate 1). On this pediment paleosols have formed and towards the valley an alluvial cover of increasing depth is present. This fluvial material covers a large part of the basin because of the impartial drainage directly after its emergence in the Pliocene. During the Pleistocene, raised terraces developed in this fluvial cover in response to the ongoing uplift of the area and the eustatic fluctuations in sea level (Cuenca & Walker, 1995).

After this stage of aggradation in the Plio-Pleistocene, v-shaped ravines, or *barrancos*, were cut into the pediment during the Holocene (Plate 1). This incision can be attributed to different factors (Fumanal, 1990). First of all, the sea level rise but especially the continued isostatic uplift increased the erosional gradient in the upstream parts of the river systems. Secondly, the sediment supply decreased as a result of changes in climate and vegetation. Higher temperatures and a less intense precipitation reduced the amount of debris that was extracted from the mountain ranges. Thus, the erosion of the limestone ridges decreased and the gradient between the limestone ridges and the erosion base was maintained. Deprived of their usual sediment load, the scouring capacity of the streams increased and they started to affect the older deposits. Once the older colluvial and alluvial cover deposits were removed in the basins, more fine material was eroded from the channel banks in the less resistant *Tap formation*.

Nowadays, the difference between the recent valley floor in the *barrancos* and the pediment is in the order of 50 m but locally heights in excess of 100 m can be found. The drainage network of the *barrancos* is elongated and linear. Their orientation suggests that they follow the structural geology of the area for many are aligned parallel to the ENE and N fault sets. In the *barrancos*, channel deposits are limited and often reworked. Larger alluvial deposits of Holocene age are only encountered along the Serpis and its larger tributaries.

The walls of the *barrancos* are steep and protected by overlying nearly vertical cliffs of calcreted fluvial terraces. The slopes suffer from severe erosion by surface wash and mass movements. The high erodibility of the marl should be ascribed to its fine-grained texture, the high carbonate content and the low degree of cementation and compaction. These properties induce slaking when dry material is exposed to water and the subsequent loss in strength is considerable (Section 5.7). Unloading of the material by lateral erosion results in the opening of joints along which water is able to penetrate to greater depths. Thus, the material weathers rapidly and produces a uniform and highly plastic regolith. Except for these fissures, the permeability of the marl and its regolith is

low what produces run-off during high-intensity rainfall and stagnating percolation after infiltration.

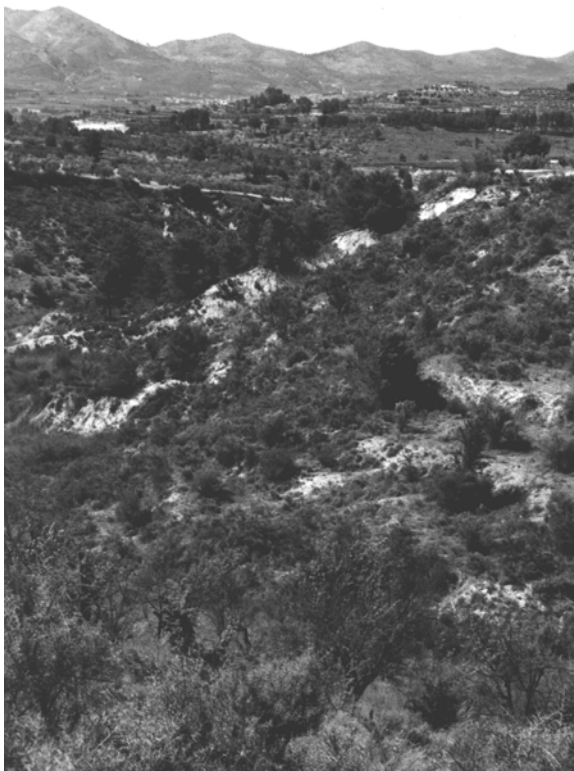


Plate 1: The incised pediment between the Sierra de Almudaina and the Benicadell

Erosion by surface wash is intense when a protective vegetation cover is absent. Since growth conditions are particularly adverse on the insolated south-exposed slopes, shallow soils with sparse vegetation develop here. On shady slopes, the higher water availability and lower transpiration favour the development of a closed vegetation cover on a more structured soil. Although the better soil structure and root density are advantageous to slope stability, the higher water retention and the accumulation of water along the slope may counter these benefits. This corresponds with the observed mass movement types in the barrancos that are generally rainfall-induced slides and flowslides along the contact between the regolith and bedrock.

In a survey of a barranco south-east of Muro, La Roca and Calvo-Cases (1988) distinguished two types of mass movements: recent mudslides and older, deep-seated landslides. Based on additional research on adjacent slopes, La Roca (1991^b) observed that the latter type of landslides concentrated on the more sensitive north-exposed slopes. These landslides are seldom active as a whole but they seem liable to secondary instability. During a period of landslide activity in 1990, 62% and 77% of the landslide activity was connected to the older deep-seated landslides on the north-exposed slopes of two barrancos (La Roca, 1991^b). In contrast, the majority of mass movements on the south-exposed slopes started as shallow slides high on the slope and continued as a flow (La Roca & Calvo-Cases, 1988, La Roca, 1991^b). The distinct landslide processes and

intensity of surface wash results in an asymmetrical shape of the valley, which is more marked when a dip slope is exposed to the north. Under those conditions, the shaded dip slope has an inclination between 14 and 20° whereas the insolated back slope generally exceeds the 20° (La Roca, 1991^b).



Plate 2: Older translational landslide with secondary activity along its scarp and toe

As a result of mass wasting on the higher parts of the slopes, colluvial soils form near the bottom of the valley. After prolonged rainfall, ephemeral streams may remove some of this material. The erosional action of these streams is, however, limited to the base of the slopes. In combination with slope instability, the episodic and localised removal of slope deposits results in an immature drainage network with hanging secondary valleys and blocked streambeds. The combined action of landsliding, surface erosion and undercutting led La Roca (1990, 1991^b) to formulate the following hypothesis for slope evolution of the barrancos in the area:

1. Dip slopes and shaded valleys favour the development of landslides. These landslides affect the entire slope, from the pediment to the valley floor. The deposition of landslide material exceeds the erosional action at the toe and the

shape will be only partly obliterated by secondary mass movements (Plate 2, Plate 3). Through this slope decline the concave valley side under the pediment converts to a convex shape near the barranco;

2. On the insolated back slopes, shallower landslides remove material from headcuts under the pediment. This material is removed as a mudslide after which the exposed material is further eroded and transported by surface wash (Plate 4). This results in gullies over the entire height of the slope with episodic periods of mass movement in the headcuts and continuous surface erosion on its walls and interfluves. Because of the constant down-wear, the transversal curvature of the slope becomes concave;
3. Fluvial erosion at the base of the slopes accelerates the degradation of the slope. Undercutting destabilises the slope and removes the older deposits, leading to parallel retreat (Plate 5);
4. Through the initiation of landslides and the continuous reactivation topographical depressions may form in the slopes that extend into the pediment. The convergence of flow paths in these depressions leads to concentration of (sub) surface water that, on its turn, stimulates the occurrence of landslides. Because of the general influence of valley incision and the mutual reinforcement of the hillslope processes, the slope in the barrancos tends to be rejuvenated in the same manner over longer periods.



Plate 3: Rotational landslide with deposit of slid material into the barranco

Potentially, earthquakes provide a trigger for landslides as well. The impact of earthquakes depends on the amount of released energy and the attenuation or acceleration due to the topography (Price, 1992). The escarpments along the pediment and the slopes in the barrancos are more vulnerable to earthquake triggered landslides because of the break of slope and the steep inclination of the weakly consolidated and semi-impervious strata (ITGE, 1990). Because of the neotectonic activity of the area, major triggering earthquakes are probable (M.S.K. \geq VII on the Mercalli scale). In Alcoy, earthquake damage was frequently reported with a largest recorded event with an intensity of IX on the M.S.K. in 1645 (ITGE, 1990, La Roca, 1991^a). A smaller event with an intensity of VIII on the M.S.K. resulted in destruction and a loss of 33 lives in the city of Alcoy whilst damage to property was reported throughout the Valles de Alcoy. On the basis of an extreme value analysis of the historical record since 1700 (Gumbel distribution, see Section 4.2), the recurrence intervals T_E for earthquakes with an intensity of VIII and IX on the M.S.K. have been determined as 60 and 150 years respectively (ITGE, 1990). However, since the end of the 19th century a seismic gap has opened over which only smaller events are recorded that passed unnoticed in the pre-instrumental record. On the premise that seismic activity can be judged as a disturbance of the continuous hydrological processes in the area and the fact that major landslides (M.S.K. \geq VII) are absent over the recent past, its role in landslide triggering will not be pursued here.



Plate 4: Scars of soil slips with associated mudslides

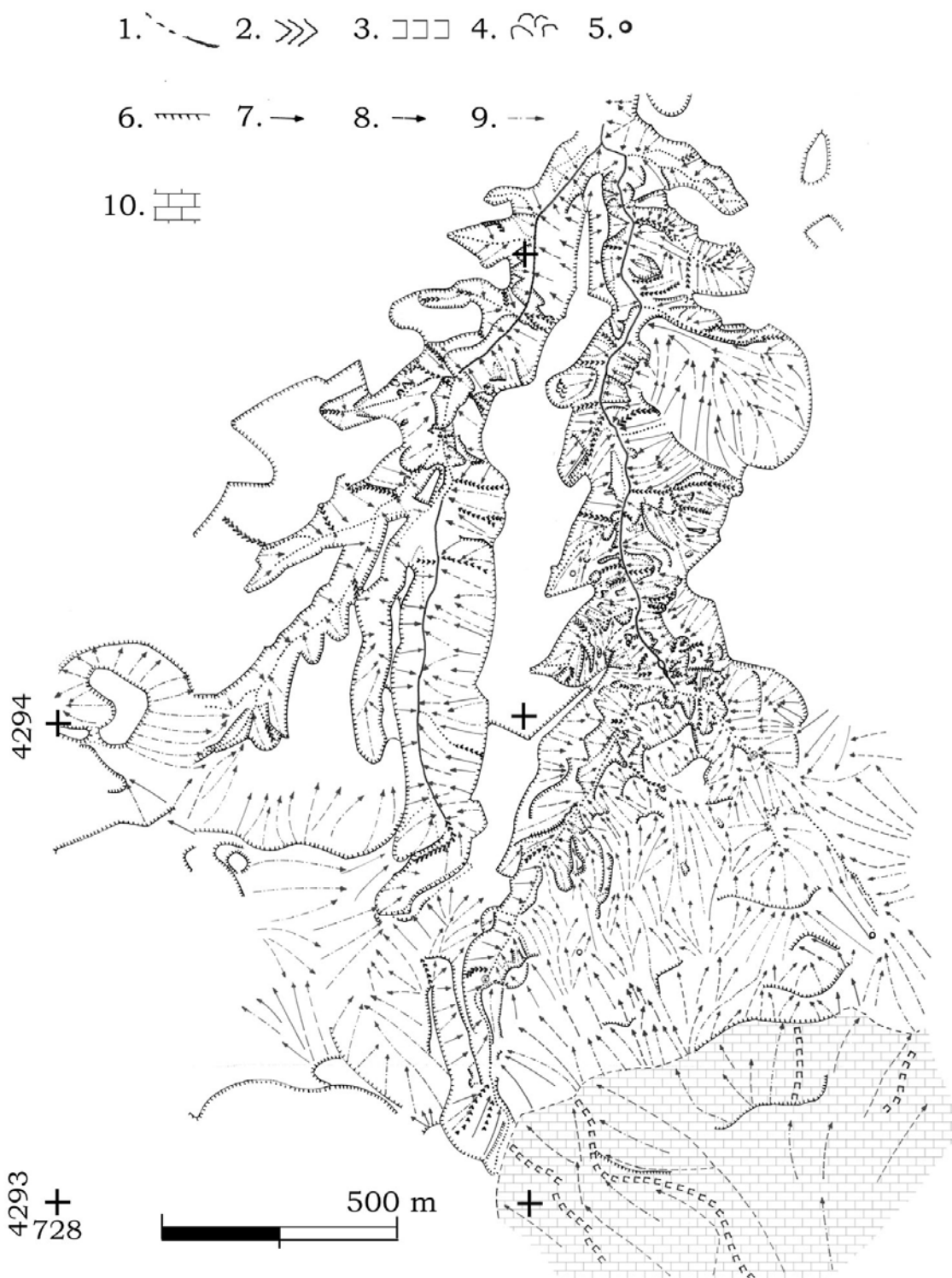


Figure 2.3: Geomorphological map of the Barranco del Mollo and the Barranco de la Coloma – 1: ephemeral stream (barranco); 2: gully; 3: dry valley; 4: piping; 5: spring; 6: escarpment; 7: rectilinear slopes; 8: convex slopes; 9: concave slopes; 10: limestone. White areas represent pediments, crosses 1000-m UTM co-ordinates.

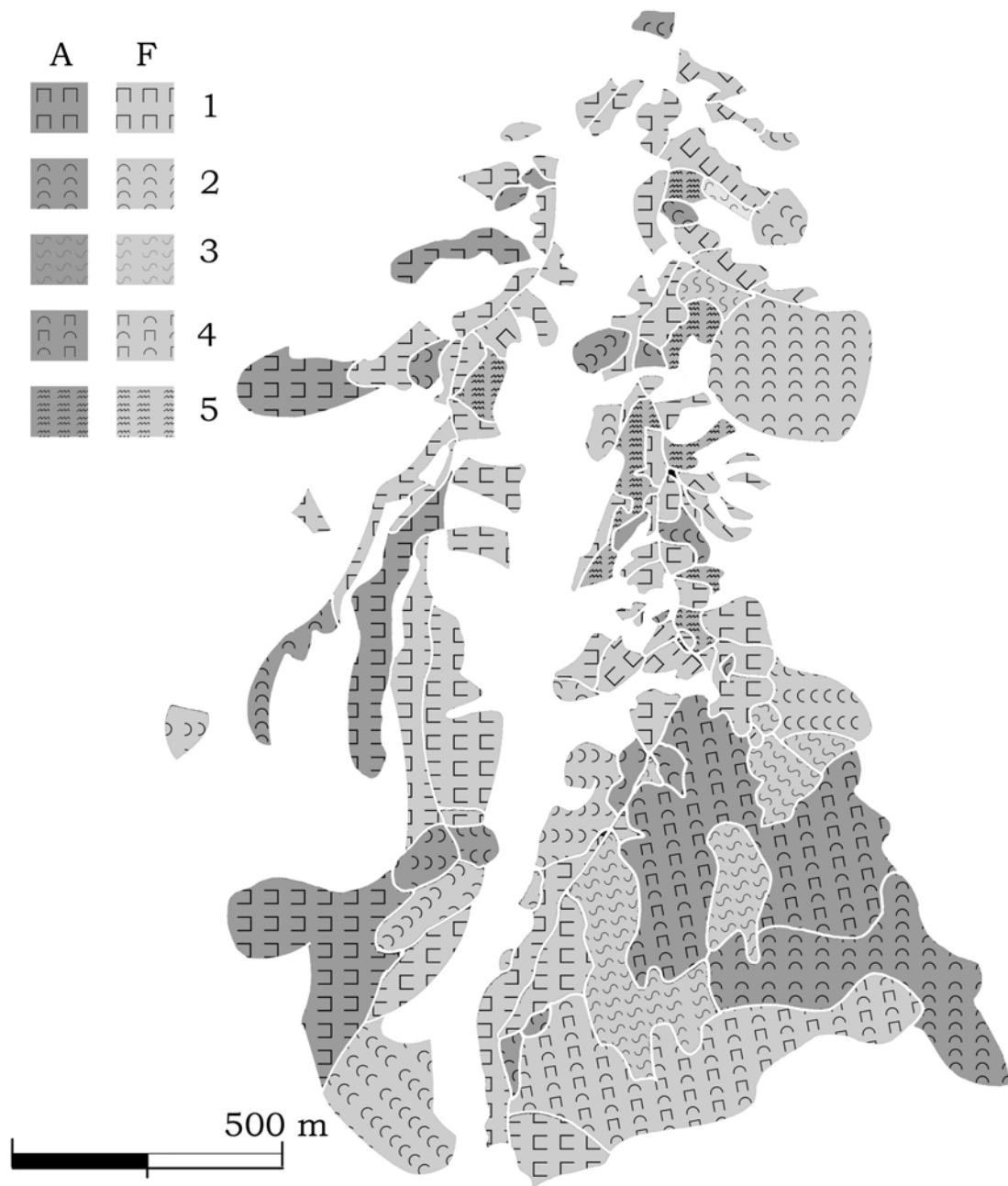


Figure 2.3 (Cont.): Geomorphological map of the Barranco del Mollo and the Barranco de la Coloma – Landslide activity: (A) active; (F) fossil; 1: translational; 2: rotational; 3: flow; 4: complex; 5: creep. Areas denote slope units rather than actual landslide size,

2.1.3 Geomorphology of the study area

The study area of the *Barranco de la Coloma* near Almudaina fits well into the general geomorphology of the upper basin of the Río Serpis. Its catchment includes a portion of the northface of the Sierra de Almudaina and runs roughly northwards until it meets the Barranco de Planes y Almudaina of which it is a tributary. Just before this confluence, it is joined by the Barranco de Mollo that intersects the Coloma due to its slightly oblique northerly course (Figure 2.3). The Coloma crosses the boundary between the Cretaceous limestone of the Sierra de Almudaina and the Miocene marl of the *Tap* formation. The total drainage area is 2.7 km² of which roughly 45% is underlain by limestone. This area is enclosed between the summit at 1013 m and the unconformity with the marl at 600 m. From here, the Coloma continues in the marl until it reaches the confluence at an elevation of 370 m. To the west, the Mollo covers an area of 1.1 km² in Miocene marl only. Its summit reaches to 640 m.



Plate 5: Undercutting and removal of material from an unstable slope

In the marl, the Mollo and Coloma are confined to ravines cut into the Pleistocene pediment. Because of the higher resistance of the limestone, the longitudinal profile of the streambed of the Coloma shows a steepening towards the Sierra de Almudaina. In the marl, the gradient along the channel decreases from 10° just below the limestone contact to values below 3° near its junction with the Barranco de Planes y Almudaina. Below the Sierra de Almudaina the marl is covered by scree originating from the limestone ridge. The scree buries the ancient topography between the 600 and 500 m contour line and

reaches a depth from a decimeter to several meters. This material is evacuated by dry-grain flows and debris flows from the limestone ridge. Presently these flows are rare; the last recorded debris flow occurred in October 1948. Yet, large debris cones testify of a more active past. In the catchment of the Coloma, two dry valleys concentrate the debris. The westerly valley connects to the main valley of the Coloma. The other valley connects to a tributary of the Coloma, which is less pronounced in its upper reach beneath the village of Almudaina (586 m). Both branches meet below the piedmont at an elevation of 420 m (Figure 2.3).

In the Sierra de Almudaina, the dry valleys coincide with transversal faults across the densely jointed and karstified limestone. In addition, three faults can be recognised parallel to the fold axis of this overthrust anticline as interruptions of the convex slope; the average inclination of the convex slope is in excess of 20° but near-vertical cliffs delimit the transversal faults. The channels of the dry valleys have been etched into the limestone along the intersecting larger discontinuities. Notwithstanding the larger tortuosity, the average inclination of the streambed remains high (15° against 6° when underlain by marl). In the marl, the linear continuation of the Coloma and the similar, N aligned course of the Mollo suggest that their shape is structurally defined by extensions of the transversal faults in the Sierra de Almudaina. Such faults explain the spur of raised marl at the summit of the Mollo. The existence of a large N-aligned fault along the Mollo is likely because of differences in the dip of the Miocene strata. However, direct evidence from the Barranco de la Coloma is lacking because few outcrops can be found and the strata have a consistent NNE dip over the catchment.

In this study, scree deposits merge with Pleistocene fluvial terraces on the remaining pediment. From the Sierra de Almudaina, the slope angle decreases to values of less than 1° on the terraces. In these flatter areas, the difference between the old aggradation level and the recent erosional base is the largest. Near the confluence of the Coloma with the Barranco de Planes y Almudaina, the old pediment has an elevation of 450 m whereas the base of the present ravine is located some 80 m lower. Consequently, steep slopes connect the remnants of the pediment to the erosion base. For the part of the area underlain by marl, pediment and ravine alike, the average slope is 13° . Of this area, 33% has a slope of less than 10° whereas 46% exceeds the average value. Hence, the distribution of slope angles is positively skewed with the maximum slope angles in excess of 40° . These steep slopes belong to those parts of the ravine walls that are undercut by the barranco and on which no soil cover is present. These slopes are relatively rare in the Coloma as less than 1% has an inclination over 34° , but more frequent in the Mollo where marl outcrops occur along the stream (Figure 2.3). In total, about 26% of the Coloma can be considered as liable to failure as the slope angle exceeds the long-term stability threshold of totally saturated material (Skempton, 1964; Carson & Kirkby, 1972).

The hillslope form in the Coloma is predominantly convex-concave from the base of the slope towards the pediment. This is consistent with the evolution by slope decline as proposed by La Roca when the upper reaches of the slope are protected by calcreted fluvial material and colluvial deposits blanket the slope. In accordance to her hypothesis, this form is truncated or obliterated by basal erosion resulting in the parallel slope retreat (see also page 41). The resulting rectilinear barren slopes with a large degree of surface

wash can be clearly recognised in the morphology of the area (Figure 2.3). Because of the alignment of the barranco, the differences resulting from insolation are less marked than postulated by La Roca (1991^b). An additional discrepancy is found between the general hillslope form in the marl and that in the area covered with scree between the two branches of the Coloma. In the latter area, the overall form is convex from the base onwards, over rectilinear to concave directly under the limestone cliff (Figure 2.3). Along the two streams, the slopes are again undercut by basal erosion and straight banks truncate the profile there. In the entire study area, a general hillslope form is a rather abstract concept for most hillsides have been shaped by man into bench terraces because of their steepness.

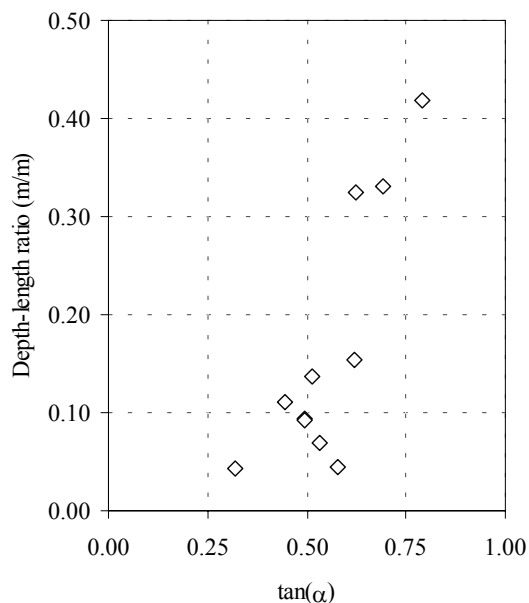


Figure 2.4: Depth-length ratio vs. slope angle for the reconstructed slip surfaces of 11 landslides in the Barranco de la Coloma. The relative increase in depth corresponds to a higher curvature of slides in steeper and undercut slopes.

Apart from surface wash by sheetflow, slope degradation occurs through rill and gully erosion and through mass movements. Both gullies and landslides tend to concentrate in topographical depressions on the slope. Gullies often start on the margin of the pediment where overland flow from this surface is concentrated. During an erosion event, the gully headwall itself often collapses what leads to the regressive expansion of the gully system into the pediment. Of the mass movements, landsliding is the dominant type but small-scale topples and falls have also been observed. Whereas the latter types are associated with natural and man-made cuts in relatively fresh marl, the landslides are rainfall-induced and affect the regolith underneath the root zone. Different degrees of complexity can be observed. Simple soil slips, often changing towards a flow when the material loses its coherence, are the most common. Their shear surfaces follow the contact of the regolith with the bedrock what giving rise to planar slides. This contact forms a hydraulic jump over which excessive pore pressures are generated that trigger these landslides. This type of landslide is shallow, with depths of one to two meters, and of modest dimensions as they do seldom occupy areas larger than a few tens of meters long and several meters wide. They occur, however, repeatedly and destroy the protective

vegetation cover after which barren material is subject to erosion. In this manner, these shallow landslides often precede surface erosion that continues over a longer time. Only once the vegetation has been re-established soil production recommences, but this can take considerable time judging the conspicuous landslide scars of the area (Plate 4). This type of landslide corresponds with the mudslides distinguished in the study of La Roca & Calvo-Cases (1988).

The curvature of the shear surface increases when the slope profile is truncated, as is the case for the undercut slopes and man-made terraces. The consequent rotational slides are characterised by their high depth-length ratio when compared to the planar slides (Figure 2.4; Crozier, 1973). The largest values are found on the man-made bench terraces but these rotational slides are extremely small and amenable to restoration. Natural rotational slides are found in undercut slopes particularly where thicker colluvial materials can be found (Plate 3). Their size and depth, however, are more similar to the planar slides and they respond to identical triggering conditions.

Some larger landslides can be found in the study area. Their full extent is difficult to recognise for they comprise older, inactive landslides that are locally reactivated on the one hand and more complex assemblies of connected slides and flows on the other. To the latter type belongs the large-scale movement between the Sierra de Almudaina and the Coloma where the more permeable scree is sliding over the semi-impervious marl base. As a result, blocks of weathered marl and scree alternate along the slope. These blocks respond differently to rainfall and the unloading due to infrequent erosion by the barranco. Depressions in this landslide complex concentrate water and the liquefied soil flows between stiffer material towards the barranco. Such flows can be identified along both branches of the Coloma that embrace this landslide complex. The movement of the complex is slow, seasonal and widespread. Movement appears to be related to the accumulated winter rainfall and damage to roads and buildings as well as the opening of transversal fissures in agricultural land were observed in the spring of 1997 (Plate 6).

The other large landslides in the area are less active. Most times, their presence must be inferred from the topography and the partial reactivation of the landslide bodies along the scarp and toe. They cover topographical hollows with a concave shape along their transversal and longitudinal profile. Although they function as tributaries of the main channel, these subcatchments are raised above the erosion level of the barranco. The step that connects these valleys to the main valley floor is subject to degradation by smaller slips and gullying by which the infill of these depressions is exposed. Dependent on the modification of the surface by terracing, the maximum depth of this colluvial soil cover varies between two and four meters over the marl bedrock.

In the Barranco del Mollo, the landslide types are identical to those in the Coloma except for the complex movement in the scree cover as this material is absent in this catchment. Moreover, in contrast to the soil-mantled slopes in the Coloma, the presence of bedrock along the channel of the Mollo limits the activity of its banks. In addition to the well-defined landslides described above, large parts of both catchments are subject to a more diffuse type of mass movement that degrades the man-made terraces and opens fissures in the soil. The affected area is large and often associated with the more recognisable landslides in the area (Figure 2.3). In the affected area, the hummocky terrain is apparently produced by creep and slow-moving, extensive sliding of the soil.



Plate 6: Fissure opened by displacement during the winter and spring 1996 – 1997

Between 1995 and 1999, in which period the field surveys were made, no soil slips were initiated in the Mollo or Coloma and the activity of the landslide complex in the scree slope was limited. Failure of the risers of bench terraces and road cuts, together with extensive gully erosion on the agricultural fields in the area, was observed as a result of a period of excessive rainfall in September 1997. For this month, 278 mm was recorded at the station of Almudaina, which is roughly three times the average monthly total. The maximum daily total was 122 mm on the 30th. No substantial landslides occurred, however, on the natural slopes along the barrancos. Here, only small-scale flows were observed. The mobilised material originated from thin soils on steep and bare slopes or from gullies on the cultivated pediment. For the preceding period, the temporal activity of the described landslide types is difficult to establish for no records of damage or maintenance work are available and revegetation and degradation affect the scars dependent on the local situation. The most recent periods of landslide activity in the Valles de Alcoy that have been reported are the years 1972 to 1974, 1986, 1989 to 1990 and 1993. Aerial photographs witness these bursts of landslide activity for the smaller landslides of which the newly formed scars are recognisable. For the larger, slow-moving landslide, however, the activity can not be readily reconstructed in this manner. An inventory of landslide activity over the period of interest is given in Chapter 7.



Plate 7: Soil profile developed in weathered marl with installed TDR-sensors

Apart from the alluvial cover of the pediments, all soil material in the study area is locally derived. Weathered marl covers most of the marl bedrock in the area. Physical weathering and dissolution of carbonate reduce the weakly cemented and compacted marl to a silty loam. Except for the steepest and barren slopes where soils are absent, typical profiles show a root zone with a maximum depth of about 50 cm below which a layer of weathered marl is present. On cultivated slopes, this root zone consists of a tillage layer of 20 cm depth. The best developed root zones are found under semi-natural vegetation where a clear distinction between this zone and the underlying cambic horizon is found. However, under all vegetation covers the content in organic material is generally below 5%. The subsequent cambic horizon of plastic material contains a high amount of precipitated CaCO_3 , which is present as mottles or concretions. This secondary carbonate accretes under the influence of evaporating soil moisture. The carbonate content, both primary and secondary together, exceeds values of 50% and is similar to the unaltered marl but both horizons are distinct because of the differentiation in CaCO_3 and clayey constituents in the cambic horizon. The accretion of secondary carbonate satisfies the definition of a calcic horizon on highly calcareous materials as specified by the USDA (1975). Because of the seasonal stagnation of water in this layer, mottles of oxidised iron and manganese are found throughout. The thickness of this layer varies from several decimeters on the top of the slope to a few meters at the foot of the slope where a colluvium has been formed by mass-wasting. In the latter case, boulders and pebbles from the alluvial cover of the pediments are mixed with the finer material. Towards the marl bedrock, the material becomes firmer. The reduction of the marl into

angular peds of several centimeters is the only sign of physical weathering. With depth, the size of the peds increases whereas the accretion of secondary carbonate becomes absent. Although the transition to bedrock is gradual, the lithological contact can be recognised by the absence of penetrating roots and secondary carbonate, a spacing of discontinuities exceeding the dimensions of individual peds that themselves do not show any alteration or displacement, and the presence of macrofossils. The consistency of this material is extremely firm and digging and augering into this material under normal soil moisture conditions is cumbersome. On slopes covered with regoliths, this bedrock is found within one to two meters below the surface (Plate 7). According to the USDA, these soils should be classified as calciorthids (USDA, 1975).

On the pediments that have not been affected by erosion, alluvium covers almost directly the marl bedrock. This alluvium of gravel and fines is sealed by a petrocalcic horizon with a depth of a few centimeters. The observed maximum depth of this alluvial layer is 1½ m. Along the barranco, recent deposits of fluvial material of limited size are found lacking a petrocalcic horizon.

On the limestone range the soils are extremely shallow. In general, scree accumulated in the debris cones is also sterile and void of any development. In contrast, scree slopes overlying the marl possess a more differentiated soil profile. It consists of angular limestone fragments of about 5 cm with etched and oxidised surfaces that are embedded in a reddish brown matrix. The entire layer is positioned on top of the Cca-horizon of weathered marl. Dependent on the depth and the weathering state of the marl, these soils should be classified as one of the variants of the group of haploxerolls (USDA, 1975).

2.2 Climate

The climate of the Valles de Alcoy is continental and Mediterranean, displaying a strong seasonality in temperature and precipitation (Table 2.1).

Table 2.1: Climatic statistics for the Valles de Alcoy (source: MAPA 1981)

Climatic variable	Average	
Mean annual temperature (°C)	12 – 18	
Mean monthly temperature, coldest month (°C)	6 – 12	
Mean monthly temperature, warmest month (°C)	20 – 26	
Length of frost period (months)	0 – 8	
Potential annual evapotranspiration (mm)	750 – 1050	
Annual precipitation (mm)	350 – 1000	
Annual moisture deficit (mm)	350 – 450	
Length of dry season (months)	4	
Contribution of seasonal rainfall (%)	Autumn	35
	Winter	31
	Spring	25

The mean temperature of the area falls within a range from 12 to 18°. The difference between the summer and winter temperature is in the order of 16°. The lowest temperatures occur in January but, because of the secluded position of the area, night

frost is frequent in the higher parts from late fall until late spring. In winter, temperature has the highest variance and the largest diurnal oscillation. In summer, the temperature is not only higher but also more stable, as the conditions of Alcoy indicate (Figure 2.5).

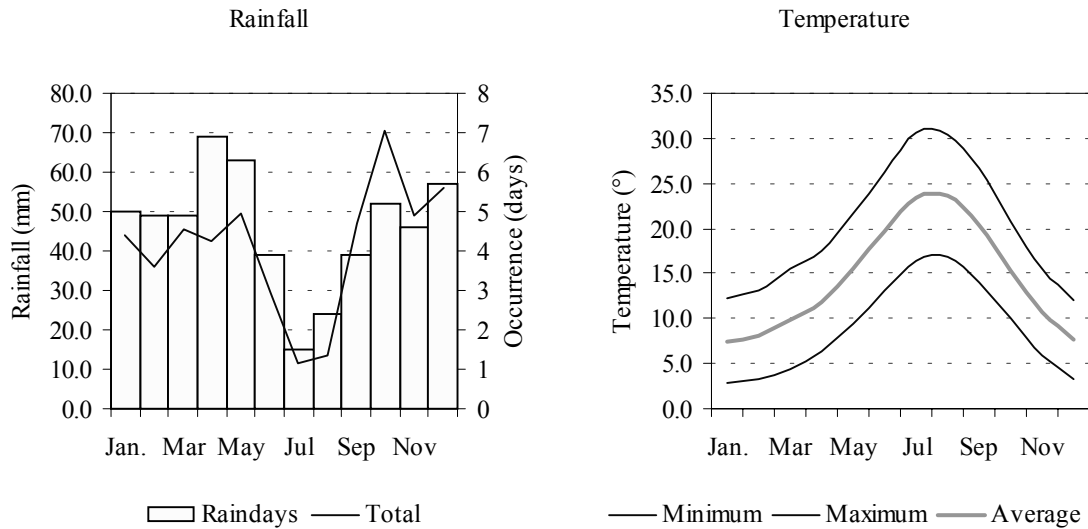


Figure 2.5: Mean monthly temperature, rainfall occurrence and rainfall totals for the station of Alcoy (data: INM)

With the annual rainfall in the range between 350 and 1000 mm the area can be characterised as semi-arid to humid. With these high values, the Valles de Alcoy form a pluviometric island between the semi-arid regions of Valencia and Alicante and the interior of the Meseta (Lautensach, 1964). The relative abundance of rainfall must be attributed to the formation of local depressions over the western Mediterranean. This weather system is often referred to as the *temporal de Levante* (La Roca, 1992, COPUT, 1994). It is generated by the penetration of cold air from the jet stream over the European landmass that becomes separated from the Atlantic by the Iberian and Cantabrian mountain ranges. Conditions for its formation are highly favourable in the autumn for then the influence of the Azores high is still significant and the higher temperatures over the Mediterranean warm the air and charge it with precipitation. The associated cyclonic NE winds direct these saturated air masses to the Levantine coast where the moisture is discharged by the relative difference in temperature and the orographic effects of the Pre-Betic mountain ranges as intense and widespread rainfall. A particular situation occurs whenever the cold air of this depression gets totally isolated and persists for several days inducing a bifurcation of the jet stream. In this situation, the bifurcation results in the development of a high over Central Europe and a low over Northern Africa that, with the Azores high, keep the depression over the Mediterranean in a stationary position. The enclosed cold air forms a convection cell in which more and more water from the Mediterranean is absorbed and delivered on the Spanish coast. This system with torrential rainfall, often exceeding daily rainfall depths of 200 mm and delivering over 50% of the total annual rainfall, is called the *gota fría* (Santos, 1991, La Roca, 1992).

The prevalence of the *temporal de Levante* is demonstrated by the statistical analyses of Romero *et al.* (1998, 1999) on the rainfall record of 410 rainfall stations over the period 1964 – 1993. They found that it was the dominant source of rainfall for the coastal area between Valencia and Murcia. Although the same weather system occurs from autumn to early spring, Romero *et al.* found that the activity of torrential rain was higher in autumn than any other season. This is caused by the unstable atmospheric situation during autumn what makes this season critical for the hydrological budget of the area. An analysis by Esteban *et al.* (1998) of the rainfall record of 40 stations covering the period between 1880 and 1992 confirms these findings; independently, both researches demonstrated that the extreme droughts in Spain during the 1920s and 1980s coincided with an absence of autumnal rainfall rather than an overall decrease.

Because of the easterly orientation of the Pre-Betic mountain ranges, the NE rain-bearing winds experience an orographic effect and deliver most of their rainfall on the exposed mountainsides. In the Valles de Alcoy, the succession of parallel mountain ranges thus produces an alternation of wetter northfaces and dryer leesides. Because of the projection of the area around the Sierra de Aitana into the Mediterranean, an additional trend is found of decreasing rainfall depths from the coast to the interior (La Roca, 1992). In the highest areas, some of the winter rainfall is delivered as snow. Although snowfall is frequent, the cover itself lasts seldom more than a few days. In spring, the conditions for precipitation from the Mediterranean become less favourable. Instead, thunderstorms develop along the mountain ranges and result in localised precipitation. In summer, the stable atmospheric conditions obstruct precipitation and a dry period from half June until the beginning of September is common (Figure 2.5). During this period, a soil moisture deficit develops that is not eliminated until substantial rainfall has occurred.

For the study area of the Barranco de Coloma, information on daily precipitation is available from the nearby meteorological station at Almudaina. This station, with a mean annual precipitation of 700 mm, is positively influenced by its position at the foot of the Sierra de Almudaina. The temporal distribution is similar to that of Alcoy as presented in Figure 2.5. On average, a year has 38 raindays. The maximum observed 24-hour total was 240.5 mm. This amount was part of an event that lasted 8 days and that delivered 553 mm out of an annual total of 967 mm. The theoretical recurrence interval of this event lies in the range of 40 to 50 years (Section 4.2). Such events of extreme rainfall, roughly in excess of 300 mm rainfall over consecutive days, could trigger small landslides, especially if some antecedent rain balances the soil moisture deficit (La Roca, 1992). In the rainfall record from 1971 until 1998, this value was exceeded in 5 out of the 27 hydrological years.

Chapter 4 addresses the climatic conditions of the Valles de Alcoy in more detail.

2.3 Geohydrology

The alternation of permeable limestone ridges with basins in which the Tap formation is preserved defines the geohydrology in the Valles de Alcoy. The succession of coarse and fine-grained deposits of the *Tap* formation in the synclines makes it to an aquitard that seals the water in the aquifers formed by the overthrust anticlines of Mesozoic and Paleogene limestone. These anticlines are bounded by large-scale transversal faults and

result in dome-like structures into which the rainfall is trapped and concentrated. Moreover, in the karstic massifs, the percolation is rapid and the losses to evaporation are at a minimum. Thus, the recharge of these aquifers like the Sierra de Almudaina is high. Notwithstanding the high recharge, the groundwater levels in these aquifers are deep. Prospective drillings were undertaken at the foot of the limestone near Almudaina at the end of the 1980s without encountering exploitable resources. Currently, a small quantity of water is extracted from the aquifer formed by the Sierra de Almudaina and the adjoining limestone massifs. Of an estimated recharge of 25 hm³ per year, 5hm³ is pumped to supply drinking and industrial water to the community of Alcoy (statistics Diputación Provincial de Alicante).

Only in the south of Alcoy, the discharge of some smaller aquifers constitutes the baseflow of the Río Serpis and its tributary, the Río Penáguila. The difference between the baseflow level and the peak discharge of the river system is marked because of the insignificance of the former and the rapid contribution of agricultural and urbanised lands along its banks after rainfall. Thus, the river system responds immediately what, in combination with the erratic occurrence of extreme rainfall, makes its behaviour highly unpredictable. Flooding occurs frequently in those areas where the river bed is confined by the natural embankment and by man-made structures as is the case in the city of Alcoy. Considerable damage following floods occurred in 1922, 1946, and 1986. In the 1990s, three smaller events of flooding occurred. In the Valles de Alcoy, the reservoir of Beniarrés, was constructed mainly in order to regulate the water supply of the Río Serpis to the coastal area.

Along the limestone ranges, the scree deposits of the piedmont form aquifers of limited depth and size in which local groundwater levels develop over the lithological contact with the underlying semi-impervious marl. Springs occur where the concentration of water in this deposit intersects the local topography or where the lithological contact surfaces. Near Almudaina, several of these springs are found. Since old, these springs provide the local water supply and nowadays two of them are captured as a source of drinking water. Yet, their discharge is variable and insecure in periods of prolonged drought. Even the spring with the largest outflow, discharging into the barranco east of the Coloma, runs dry in years of below-average rainfall. Depending on the accumulated rainfall during the wet season and the frequency of thunderstorms in spring, the yield is more substantial and prolonged. Following the wet winter of 1996 – 1997, the discharge of the larger spring was in the range of 15 to 20 litres per minute near the end of April 1997. It waned, however, rapidly after the rainfall ended. If not captured, the outflow from these sources discharges into the barrancos, making them to ephemeral streams on which the hydrological response of the marl is superimposed. Prolonged discharge of the Coloma was inferred in the early spring of 1995 and observed following the winter of 1996-1997 and 1997-1998. Over this period, the discharge of the larger Barranco de Planes y Almudaina was more secure and persisted during periods of varying length between fall and late spring.

In the study area, marl deposits form the bulk of the *Tap* formation. These strata are semi-impervious and saturated flow is observed only in some coarser layers of unsubstantial depth. Springs and wells are extremely rare. More frequent is the extrusion

of water in topographical depressions contributing to the barranco following periods of prolonged rainfall. This water stems from perched water levels that develop in the soil over the marl bedrock and converge along the slope towards the barranco. The infiltration capacity is often high on the well-developed soils of the natural slopes around the barranco but limited on the pediment where the soils are shallower. This generates run off on the agricultural lands of this pediment surface that, consequently, experience ephemeral gully erosion. This run off is concentrated and delivered to the stream, generating peak discharges during extreme rainfall events as that of September 1997.

2.4 Socio-economic development and land use

The name of Almudaina stems from the Arabic occupation of the area in the Middle Ages but the density and continuity of human occupation in the area make it likely that the settlement finds its origin in Neolithic times. After the fall of Alcoy to the Catalan crown in 1278, civic rights were bestowed onto the 120 inhabitants of Almudaina. As part of the administrative reform the village was brought under the newly established county of Cocentaina. During the consolidation of the Christian conquest, this county and the region of Alcoy were gathered under the sovereignty of Valencia. The thorough christianisation of the area followed the insurrection of the Moriscos in Andalusia and Valencia during the reign of Philip II.

Since the reconquest, the population of the area has risen until the 20th century. Agriculture, which was the main source of subsistence, appears not to have been impaired by the political changes. The increase in population led to an expansion and intensification of agriculture on all suitable lands. This traditional type of agriculture included the cultivation of fruits and cereals, partly as mixed crops, on bench terraced slopes. Dependent on the fertility of the land, cultivation was repeated after one or two years of fallow. On this fallow land and on the unproductive slopes, cattle were herded. In addition to meat, sheep herded in this manner provided wool that was processed by the textile industry that was developing in Alcoy since the 18th century. This industry and the presence of paper mills provided a base for the expansion of this city. Together with Cocentaina as a centre of administration, Alcoy became the largest concentration of population in the area. This population was maintained by the agricultural produce of the surrounding rural area that was to a large extent self-sufficient. Apart from cereals, typical crops included olives, almonds and cherries as well as vegetables in horticulture. As a result of the expansion of cultivated land and the slash-and-burn practices to achieve the renewal of pasture lands, the natural climax vegetation of holm oaks (*Quercetum rotundifoliae*) is nowadays nearly eradicated.

In the 20th century, the developments break with this trend of general expansion. The rural and urban population increased at an equal pace before the beginning of that century, but after 1920 the rural population fell rapidly. In contrast, the population of the urban centres of Cocentaina and Alcoy and the surrounding urbanised villages continued to rise. Since 1900, the population of Alcoy for example roughly doubled to 60,000, keeping pace with the national demographic trend of Spain. The total population of the Valles de Alcoy also increased but at an attenuated rate as the rural population decreased dramatically. For Almudaina, as for many of the rural villages in the area, the population

was halved over a 40 year-period twice after 1920 (Figure 2.6). After an initial population of 473 in 1900, the number of inhabitants fell to 118 in 1999, bringing it to the level at the end of the 13th century. Although some of the migration is intraregional a large part of it is directed to the larger cities of Valencia and Alicante. Because of this interregional loss and the predominantly rural nature of the region, the net demographic development of the Valles de Alcoy lags behind the national Spanish trend (Figure 2.6). In spite of this difference, the average population density of 112 inhabitants per km² exceeds the national density of 66 inhabitants per km². The latter figure matches the density of the rural area in the Valles de Alcoy, reflecting the relatively high population density in the past. The present number of inhabitants is 89,000 compared to 66,000 in 1900. With exclusion of the urban populations of Alcoy and Cocentaina (60,000 and 10,000 respectively), this brings the approximate rural population to a mere 20,000 inhabitants.

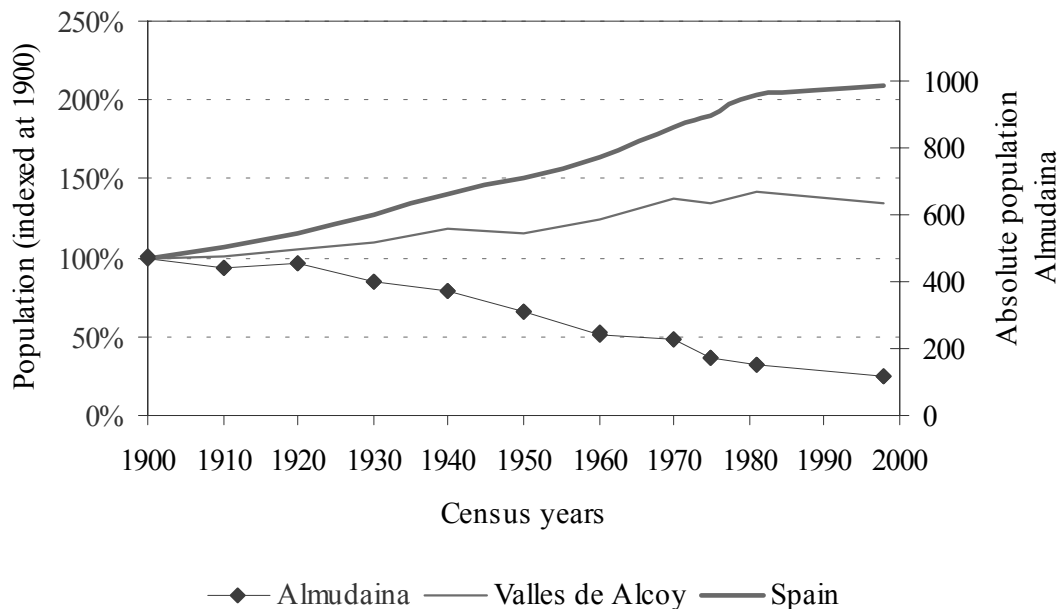


Figure 2.6: Demographic development of Almudaina, Valles de Alcoy and Spain during the 20th century indexed for 1900 (sources: MAPA 1986 & Generalitat Valenciana)

The processes explaining this dramatic drop in rural population are the decreasing family size and the rural exodus of the active labour force to the industries and services in the urban centres. Both processes are symptoms of the agricultural crisis that occurred in the wake of the Industrial Revolution. In the Valles de Alcoy, this crisis was induced by the ineptness of mechanised cultivation of cereals on the bench terraced slopes that reduced the competitiveness of the traditional agriculture. In combination with the increase in yield that could be achieved by the application of new fertilisers, pesticides and ameliorated crop types, a reorientation of agriculture in the area was imminent. The consequent smaller margins and the decreased demand of agricultural labour forced the obsolete rural population to the employment of the industries in Alcoy. Although the

change started already in the late 19th century, the effects of the Spanish civil war and the geo-political situation afterwards delayed the shift. In particular the autarky imposed in the early 1950's under Franco impeded the agricultural reform but after its lift and the entrance of Spain in the European Union, the developments occurred at a higher rate. Basically, the agriculture in the area has been adapting itself to the new market conditions by intensifying the production of marketable crops and the abandonment of marginal fields. Since the climate restricts the cultivation of profitable citrus fruits, present agriculture focuses on the traditionally grown permanent crops of cherries and olives. These crops require a minimum of mechanised labour and by the plantation of trees with varying harvest dates, agriculture is profitable under semi-traditional practices. Moreover, these crops secure a reasonable yield under the sometimes adverse climatic conditions for irrigation is only feasible on a limited scale. Of all agricultural lands, only 6% were covered by irrigated fields in 1981. The remainder of rain-fed crops took up most of the 42% of the territory dedicated to agriculture (MAPA, 1986).

Olive trees provide still the bulk of the production, which is used for oil. However, plantations of cherries are on the rise for climatic conditions ensure an early harvest and consequent high earnings on the European market. At that time, the proportion between the plantations with cherries and olives was roughly 1:1 (MAPA, 1986). Other permanent crops (almonds, peaches) are only of secondary importance.

On the fields, typical plantation densities are 6 x 6 to 8 x 8 meters for cherry trees and other drupes and 10 x 10 meters for olives. To optimise the water supply to the trees, the area between trees is kept clear of weeds by ploughing and raking. The parcellation of the area is small-scale. In the Valles de Alcoy, 58% of the parcels have a size smaller than 0.5 ha and 82% of the parcels is smaller than 1 ha (MAPA, 1986). The risers that separate these terraced fields are usually between 1 and 2 m high and have slopes of 2:1. On them, weeds and brambles are left to grow to prevent erosion. Because of the small field size and the low requirements for mechanised actions, the degree of mechanisation is relatively low with a predominance of small motorised cultivators (MAPA, 1986).

In addition to the preferred crop types, the parcellation and tenure are also very traditional. This reflects the shift in the economic importance of agriculture in the area. Nowadays, the number of full-time farmers is small. Of the employed labour in 1991, only 10.4% was directly involved in the agricultural sector compared to 51.7% in the secondary and 37.8% in the tertiary sector. However, although agriculture is no longer the main occupation for many, a large number of people still cultivates some of the fields in their possession. This is shown by the total number of small-scale exploitations: 75% of the agricultural enterprises cover less than 5 ha and 90% of all taxed grounds were held in ownership (MAPA, 1986). In 1981, the total number of exploitations was 6,798, giving a ratio of one farm per 14 inhabitants or 1:3 if only the rural population is considered. Based on these figures it should be concluded that agriculture continues to provide an additional source of income for many. Agricultural co-operations support the necessary investments and provide the infrastructure for these small-scale farmers. More important for them, however, could be the social importance of agriculture. Many of the small-scale farmers are no longer residents of the area but continue agriculture as a pastime during the weekend and holidays.

The present state of land use in the municipality of Almodaina complies well with this general picture for the Valles de Alcoy. The total acreage of the municipality amounts to 895 ha. Of these, 424 ha were under cultivation in 1977 (MAPA, 1981). At that time, olive groves formed the majority with 231 ha. The second largest crop consisted of almonds. Almonds in single cultivation covered 64 ha while a mixed crop of almonds and olives covered 22 ha. Of the remainder, 107, only 33 ha were planted with cherry trees whereas vineyards covered 50 ha at that time. Since then, the share of cherries has increased at the expense of all except the olives. At the start of this study in 1995, the ratio was roughly 1:1 and vines and almonds had nearly disappeared. An inventory of land use in 1998 showed that the cultivated land covered 63 ha out of the 154 ha under consideration in the catchment of the Barranco de la Coloma. Most of this area was located on the more accessible pediment surfaces (Figure 5.1). The remainder, 91 ha, was abandoned or covered by semi-natural vegetation. These abandoned fields take up 54% of the total area of the once bench-terraced land. Only a fraction of this was taken into production again between 1995 and 1999. In all cases it concerned relatively large and flat areas bordering the road on the pediments.

Through regeneration, a semi-natural vegetation develops on the abandoned fields. Instead of the original oak forest, the climax is an open stand of Aleppo pine (*Pinus halepensis*) with undergrowth of grasses and perennials. This full-stage development is attained within a period of 20 to 30 years dependent on the local conditions. A different type of semi-natural climax vegetation is found along the stream in the barranco. Because of the higher water availability, deciduous trees like poplars and elms replace the pines. This vegetation, however, is confined to the streambed of the barranco except for a small patch of ash trees that grows in a zone of extruding water in the eastern tributary of the Coloma.

If the conditions are more adverse, the vegetation develops towards an immature thicket of perennials of the association rosmarino-ericion (pers. com. La Roca). In this vegetation, the shrub *Ulex parviflorus* is the dominant type. The restrictive factor is often the combined effect of shallow soils and limited water availability. Such conditions also prevail on the limestone ridge south of the study area where the vegetation cover is consequently sparse and underdeveloped.

In the study area, the most degenerated vegetation can be found on slopes with a high insolation where the bedrock is constantly stripped from its soil or on the pediment where a petrocalcic horizon seals the fluvial deposits. The vegetation that establishes itself here is more patchy and consists mostly of woody herbs and heather (*Thymus vulgaris*, *Daphne gnidium*, *Erica multiflora*). Because of the adverse conditions, these less evolved types appear to be accomplished within a time span of 10 to 20 years whereas the complete revegetation of abandoned land under favourable conditions takes generally less than 10 years.

In the Valles de Alcoy, land abandonment has been symptomatic for the socio-economic developments over the last century. With the ongoing globalisation and with the expected decrease in total and agricultural population more agricultural land will probably be taken out of production in the near future (Figure 2.7). The impacts, however, will be far greater than mere abandonment for with the agriculture and the population also the liveability of the area is on the decline. In response to these changes, the economies of rural areas are reshaping themselves to remain profitable and sustainable. This process is

not only spontaneous but is also guided by policies initiated by local, national and international legislative bodies. This presents new conditions and opportunities for the existing agriculture and some probable changes in land use for the near future are discussed in Section 8.3.

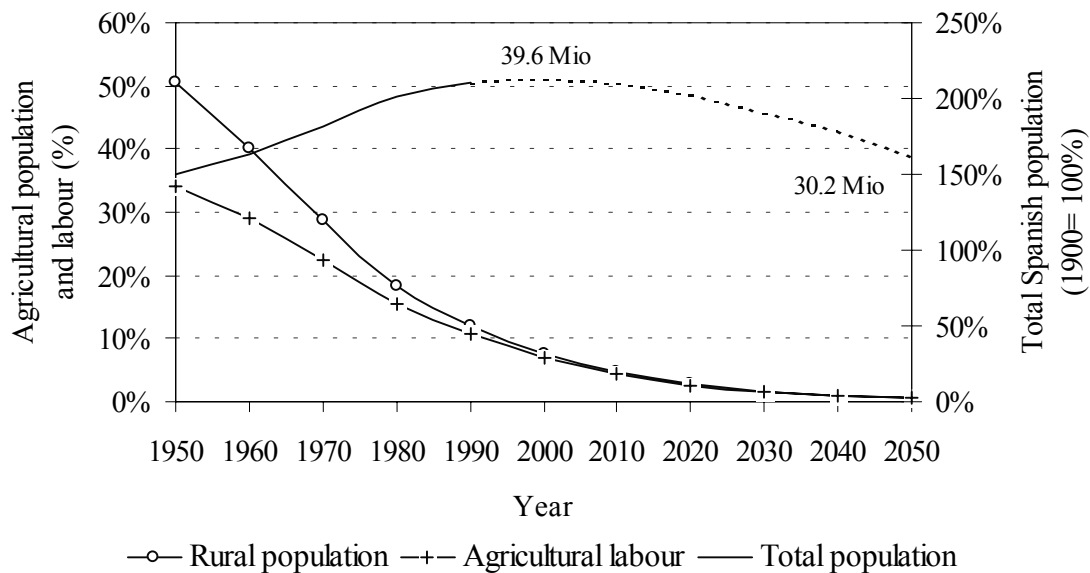


Figure 2.7: Expected development of the Spanish population. Agricultural population and labour expressed as percentage of total population (source FAO statistics)

2.5 Summary

The Valles de Alcoy are a part of the Pre-Betic orogenic belt in which overthrust anticlines of resistant Cretaceous and lower Tertiary limestone alternate with synclines of weaker Miocene marl. After the orogenic climax in the Pliocene, a stage of aggradation persisted throughout the larger part of the Pleistocene when the connection of the primeval basin of the Valles de Alcoy to the Mediterranean was still absent. Once this connection was fully established, the incision of the existing pediments and terraces started. Due to the continued uplift, this incision has persisted since the Pleistocene. As a result, v-shaped barrancos have been forming that constitute a structurally defined drainage network of ephemeral streams.

Since the summits of the drainage network are located on the resistant limestone, a strong relative relief is maintained whilst steep slopes occur along the incisions of the barrancos. On these slopes, relatively deep soils may be present or form rapidly through weathering of the weakly compacted and cemented marls. These soil-mantled slopes have a strong disposition to landsliding when the equilibrium between shearing resistance and shear stress is disturbed. The neotectonic activity in the area can lead to seismic triggering of landslides but most if not all recent landslides are rainfall-induced and caused by elevated pore pressures on the lithic contact between the soil and the marl bedrock.

Different types of landslides can be distinguished in the recent landslides. Planar slides occur higher on the slopes where a regolith of weathered marl is present whilst rotational slides occur along the channel of the barranco where more colluvium is present. Larger landslide complexes occur on the slopes under the piedmont. The toe of these slopes are destabilised by the barranco while the pore pressures are raised by the rainfall that is accumulated in the more permeable scree slope deposits.

Although these types of landslides respond differently to rainfall, triggering rainfall events can generally be said to be infrequent. Effective rainfall is strongly seasonal and the rare extreme rainfall events that cause landslides prevail in the fall and winter. The large rainfall amounts delivered by these events can to a large extent be accommodated by the root zone and tillage layers on these slopes. The infiltration capacity of these slopes can be expected to increase due to the recent abandonment of cultivated fields that are deemed marginal.

3 A COUPLED MODEL OF SLOPE HYDROLOGY AND STABILITY

3.1 Introduction

As defined in the preceding chapters, this study aims to quantify the role of rainfall-induced landslides within the hierarchy of hillslope erosion processes in a sub-humid Mediterranean environment. This hierarchy can be envisaged as a cascade- in which the downslope movement of material -or the conversion of potential into kinetic energy- is controlled by related processes of surface wash, soil production and mass movement (Van Asch, 1980).

Rainfall-induced landslides are triggered by a relative increase in pore pressure (Chapter 1). The triggering pore pressures develop often over a lithological contact, such as the transition between the soil and the underlying bedrock. Because of their limited depth, they can be triggered by rainfall that is accumulated over short periods. Thus, their occurrence can be extensive and capable of mobilising considerable volumes of material. Moreover, the destruction of the vegetation cover exposes barren material, which is the onset for surface wash processes.

Mediterranean environments, subject to erosion processes, are extremely sensitive to changing environmental conditions (Mulligan, 1998). This can be extended to include those environments where landsliding interacts with surface wash processes. The impact of environmental changes on landslide activity comprises changes in its frequency and magnitude. Under hypothetical conditions, when the changes can not be evaluated *a posteriori*, the assessment requires that the causal relation between the triggering rainfall events and landslide activity be understood. This relation is complex as the net precipitation and the antecedent moisture conditions control the triggering of landslides (Chapter 1). As a result, the evaluation of the sensitivity of an area to landsliding in the light of presumed changes in land use and climate becomes rather difficult. The use of a model may assist in the analysis whether it is directed to test a predefined hypothesis or to predict the changes in landslide activity under a presumed scenario.

The primary trait of such a model must be its capability to relate generated pore pressures to a threshold of instability. This threshold can be defined for a single landslide or for distinct type. It is either an observed pore pressure level or derived from a slope stability assessment, in which it is defined as a critical pore pressure or as a measure of overall stability (e.g. the Safety Factor; see Section 3.2.3). Irrespective of the type of threshold used, it can be compared through the model with the generated ground water. This coupling of hydrology and stability by the model makes it possible to express the sensitivity to landsliding in terms of frequency and order of magnitude. The effects of changing environmental conditions can be incorporated in the model by applying it to different scenarios.

In the following sections, a coupled hillslope model is described of which the aim is to simulate the pore pressure conditions adequately over time in order assess the activity of rainfall-induced landslides. The intended application to hypothetical scenarios postulates

that the model is physically based. Moreover, changes in the sensitivity to landsliding will only emerge on a regional scale whilst local differences in topography and land use must be considered. These requirements are the easiest accommodated by a distributed model. Adaptations of the model parameterisation that arise from environmental changes are readily accomplished when the model is embedded in a GIS environment. Consequently, the coupled hillslope model is dynamic, distributed and physically based and will be applied on a regional scale. It includes a hydrological model component named STARWARS, an acronym for Storage And Redistribution of water on Agricultural and Revegetated slopes. The stability analysis, PROBSTAB, is a limiting equilibrium model based on the Mohr-Coulomb failure criterion by which the probability of failure is assessed. The demands for the implementation of such a model are numerous and some general aspects that underlie the development of the model are considered first.

3.2 Development of the coupled model of slope hydrology and stability

3.2.1 Scale aspects and model considerations

Awareness of the possible impact of changing environmental conditions like land use and climate on the controlling pore pressures and the absence of long term observational records has led to an increase in the use of physically based hydrological models to evaluate the consequences for future landslide activity. These model approaches range from simple 1-D tank models (e.g. Buma & Dehn, 1998), over GIS embedded static and quasi-static 2- to 3-D approaches (e.g. Van Asch *et al.*, 1993; Montgomery & Dietrich, 1994; Miller & Sias, 1998) to complex numerical solutions of 2- and 3-D saturated and unsaturated flow (e.g. Brooks *et al.*, 1995; Hattendorf *et al.*, 1999). All model categories include different levels of spatial and temporal detail.

Physically based models are favoured since they are capable of predicting alterations in the hydrological behaviour by means of the constituent equations for the incorporated processes (Grayson *et al.*, 1992). The applicability of these models for future scenarios is, however, limited. Practical limitations are the related problems of spatial and temporal resolution, numerical stability and computation time. A further limitation is the large dataset that the more complex models require. Even if all model parameters can be acquired, it remains doubtful whether the changes in model output are discernible against the ensuing uncertainty (Nandakumar & Mein, 1997).

The uncertainty in parameter values derives from the natural variability and the discrepancy model-, process- and sample scale. Because of the use of the constituent physical relations, the model scale is inseparably bound to the scale at which the material properties have been sampled and at which the formulae have been defined. It coincides usually with a point scale and the support of the retrieved data is seldom larger than volumes of 1 dm³ or 1 m³ for soil properties that are taken constant over time. For soil properties, sampled over time by automated equipment, this support may even be smaller. This support may differ from the relevant process scale, often referred to as the representative elementary area or volume (REA, REV), that determines the observed behaviour (Bear, 1972; Wood, 1995).

Partly because of the spatial resolution of the data, partly because of the natural variability of the incorporated processes, the temporal scale of most models lies in the range from seconds to days. In contrast, the scale of interest is usually defined by larger natural or administrative entities (e.g. catchments and provinces) and by periods covering many years. The tendency of reducing the model resolution to cover these larger scales of interest leads to uncertainty in the estimation of parameter values (Heuvelink & Pebesma, 1999).

Further questions on the validity of these models are raised by the common practice of optimising the model performance under present conditions. This means that the tacit assumption is made that the importance and relations of the relevant processes in the modelled system will not change. Many physically based models of rainfall-induced landslides link the triggering groundwater level or matric suction in a deterministic manner to a static stability model or an observed stability threshold. This implies that the prediction of the groundwater level or matric suction as a measure of the pore pressure at the potential shear plane gives the exceedance of the critical condition. The subsequent changes after failure in the hydrological and mechanical behaviour of the system are not considered and feedback mechanisms that influence the occurrence of landslides are ignored. All in all, the model outcome gives an idea of the system response in terms of landslide susceptibility to the changing environmental conditions, with all the other factors remaining constant. For the 1- to 2-D approaches, the inferred changes in the hydrological behaviour do not surpass the domain of the modelled slope. The variability within the catchment and induced changes in the spatial and temporal distribution of landslide activity are most times neglected altogether.

Under consideration of these limitations it must be concluded that in order to evaluate the temporal and spatial alterations in landslide susceptibility under changing environmental conditions simple, physically based hydrological models are needed. These models should be modest in their aim and in their data requirements. This demand for modesty originates from the trade-off between the model's capability to simulate the real world adequately on the one side and the uncertainty that is included in the model and in the model input on the other (Hillel, 1986). All models should be applied with care and their results interpreted with scrutiny. After all, no model can predict nor assess changes beyond its original scope.

The validity of the model assumptions and boundary conditions determine the model's flexibility under the changing conditions. This excludes the use of entirely empirical models because they are based on unspecified sources of variability within the present system. In spite of this severe shortcoming of empirical models, no model can escape from a certain amount of empiricism. The simplification of the real world system leads to a neglect of factors that will be compensated by adjustment of the parameters that are included in the calibration of the model. For this reason, no model will be right in an absolute manner (Konikow & Bredehoeft, 1992), but represents rather a possible realisation of the actual system (Beven, 1989). This raises fundamental questions on the possibility to predict the behaviour of geomorphic systems at all (Haff, 1996). This limitation can be overcome by adopting a probabilistic approach in which deterministic processes on the underlying scales are replaced by random variables.

In its application, the coupled hillslope model unites partly contradictory demands on the spatial and temporal scale. The aim is to predict landslide activity over relatively long timespans and large areas. At this scale of consideration, the model must incorporate the maximum of spatial and temporal detail at a minimum of costs in terms of parameterisation and computation time. The required temporal detail of the model is dependent on the rainfall characteristics. In Mediterranean environments, this rainfall distribution is erratic and characterised by extreme rainfall events. Therefore, the temporal resolution should comply with the present rainfall distribution and with the inferred conditions from downscaled climate change scenarios. Because of the resulting short-term fluctuations in soil moisture content, the model describes transient flow instead of a static or quasi-static condition. Only for a limited number of special boundary conditions can flow under transient conditions be described by analytical functions. In the majority of cases, only numerical solutions, in which the process-domain is divided in finite increments of space and time, provide the flexibility to cover the constantly changing conditions. The hydrological component of the coupled hillslope model is for this reason based on an explicit finite difference approximation of a forward numerical scheme. The discretisation of the slope geometry has, subsequently, implications for the numerical stability of the model. Within an explicit numerical scheme, the travel distance of any flux can not exceed the distance of one spatial increment for one timestep. Thus, the choice of the spatial resolution confines the possible temporal scale at which the model can operate. A decreased spatial resolution reduces the ability of the model to represent the topographical effects on the hydrology and on the slope stability adequately (Zhang & Montgomery, 1994; Evans, 1998). In contrast, a finely grained topography needs smaller timesteps to maintain numerical stability (Bates *et al.*, 1998).

The demand for high spatial detail is based on the topographical control of the convergence of subsurface flow and slope stability (Montgomery & Dietrich, 1994; Carrara *et al.*, 1995). At the same time, the spatial resolution should also represent the spatial distribution of the important parameters –for example land use- with sufficient detail (Grayson *et al.*, 1992). This means that a distributed model is required rather than a local, 1- or 2-D approach. The detail that can be included in the 3-D model is defined by the resolution of the available data. Therefore a compromise must be found between the resolution of the digital elevation or terrain model (DEM or DTM), the spatial distribution of soil and land use properties, the temporal resolution of the available meteorological records or downscaled climate scenarios and the intended period over which the model should be applied.

The issue of model parameterisation is also related to the spatial resolution of the DEM. Distributed modelling assumes homogeneous conditions for every elemental area or volume of the DEM. Because of the required homogeneity, parameter values must be interpolated spatially. These homogeneous conditions can either be derived from a generalised set of parameter values, from a Monte Carlo simulation, from geostatistical interpolation or a combination of these. Regardless of the type interpolation, the variability within the cell is ignored.

For model scales that surpass the process scale of the original sample scale, it may be necessary to increase the support of the sample artificially. A possible solution to the discrepancy between the model scale and the sample support is to replace the field measurements by effective values, which are obtained by optimisation of the model performance. The disadvantage of this procedure with respect to predictive modelling is that parameters might lose their physical meaning and, consequently, a part of their predictive capability.

Ideally, the interpolated parameter values provide *a priori* knowledge with a minimum of unexplained variance (Grayson *et al.*, 1992). If parameters possess a strong spatial correlation or depend on a spatial attribute like soil type or land use, this information should be included in the interpolation. This improves the accurateness of the spatial prediction on the one hand and avoids that it is lumped as white noise whilst aggregating data at a lower resolution (Heuvelink & Pebesma, 1999).

Extensive testing of the model is a prerequisite for the use of any model as a predictive tool. The discrepancy between the deterministic relationships for soils obtained under controlled laboratory conditions and the highly variable processes in nature led Beven (1989, page 161) to classify distributed physically based models as lumped conceptual models. In spite of his criticism, the calibration of the model within the limits of the natural variability of the parameter set provides an internal test for the adequacy of the constituent equations that are applied in the model. Validation over a historical database gives an estimate of the predictive quality of the model for future use and, with the calibration, of the prediction uncertainty (Beven, 1989; Beven & Binley, 1992).

The exceptional and often catastrophic nature of landslide events stresses the need for model validation: since the occasional triggering conditions are underrepresented in most calibration sets, a calibrated model could represent the normal conditions adequately but might fail as a predictor of the extreme events. The validation set, which, stretching over a longer period, will include more extreme conditions, provides then an additional benchmark for the performance of the calibrated model. It should be noted that, because of the uncertainty in the parameterisation, which arises from the natural variability, measurement errors and support of the field measurements, no physically based model can provide absolute answers albeit its deterministic nature.

The uncertainty in the model performance stresses the necessity of a parsimonious parameter set for which the values can be obtained from field measurements with a certain feasibility (Hillel, 1986). It also avoids mutually dependent parameters (Beven, 1989). Their presence may result in non-unique solutions during calibration. Although these solutions have the same goodness-of-fit between the observed and simulated behaviour, their existence is in contradiction to the supposed singularity of nature. Additionally, the predictive uncertainty associated with large parameter sets will dwindle the possibility of discerning the response of the system under changing environmental conditions (Nandakumar & Mein, 1997). The crux is to prevent over-parameterisation and to reduce the indeterminacy in the process of calibration even if detail has to be sacrificed to model robustness. Or, as Beven (1989, page 165) puts it: "It is surely easier to use physical reasoning to calibrate the residence time parameter of a linear store than it is to obtain a correct combination of interacting parameters."

Based on these considerations, the coupled hillslope model has been developed. The use of simple and linear relations has been favoured when possible. The effects of land use have been captured in static parameters that are attributed to the vegetation cover. Although this excludes the dynamics in the interactions between soil, water and vegetation, the approach is simple and finds its justification in the circuitous hydrological relations between land use and slope stability.

All model parameters can be obtained from field measurements. The eventual values of the parameters can be calibrated to optimise the model performance and validated to determine its predictive ability. The exact procedure on the calibration and validation of the model is treated in the chapters on model implementation (Chapter 6 & 7).

The resulting model is distributed but its intended spatial scale of operation is the hillslope. The temporal scale of operation of the model is bound to the temporal rainfall patterns and ranges from hours to days. In the following sections, time increments of one day are used consistently.

The STARWARS and PROBSTAB model components use the embedded meta-language of the PCRaster GIS package (Van Deursen, 1995; Van Deursen *et al.*, 1996). This language allows the development of dynamic models, or *scripts*, that simulate a process or system over time but the overall structure is rather simple. It excludes, for example, the use of iterations other than the main (time) loop so no complex numerical solutions can be employed. In contrast with this disadvantage is the flexibility that the GIS environment offers to accommodate spatial and temporal variable in- and output with readily available commands. The GIS is raster-based what results in the use of cells of equal horizontal dimensions. The dynamic model uses time increments of equal length.

3.2.2 Modelling of slope hydrology

A complication in the understanding of the causal relation between the triggering rainfall events and landslide occurrence is the fact that it is obscured by the antecedent moisture conditions. Percolation through the unsaturated zone attenuates the response of the groundwater level to a large rainfall event. The importance of the antecedent net precipitation increases when the rainfall distribution becomes more erratic in time, as is the case in Mediterranean areas.

The aim of the hydrological model –simulating the spatial and temporal occurrence of critical pore pressures- stipulates that the delay and loss of percolation in the unsaturated zone are included in the model. Therefore, the model must describe the saturated and the unsaturated transient flow in the vertical and lateral directions.

In the model, the response of the groundwater to the net rainfall is direct. The saturated and unsaturated zones are taken as freely draining. Hence, the model describes only unconfined groundwater levels. The response of the groundwater is imposed on a constant groundwater level or generated over a semi-impervious lithological boundary that restricts the direct loss of soil moisture into the deeper strata. In the latter case, the resulting groundwater is a perched level, for example over the underlying bedrock. Although in theory the model is capable of simulating the response of deeper groundwater, only the latter case of perched groundwater layers is considered here. In this case, vertical flow is stagnating over the lithic contact between soil and bedrock.

The hydrological component describes the transient saturated and unsaturated flow as a function of the elevation potential only, neglecting the matric potential for the flow in the unsaturated zone. As a consequence, percolation is limited to gravitational vertical flow only. Over the saturated zone, the piezometric head defines the lateral flow. The rationale for the omission of the matric potential in the unsaturated flow is that it is generally considered of small importance in those instances when freely drainable water is available, i.e. when the soil moisture content is above the field capacity. When the moisture content is below field capacity, the flux under influence of the matric potential becomes negligible because of the sharply reduced unsaturated hydraulic conductivity at low moisture contents. The same holds even more strongly for the unsaturated lateral flow that is driven by matric potential only. Philip (1991) concluded on the basis of 2-D analytical solution of the Richards' Equation that, for a planar slope, the unsaturated lateral flux is negligible for all inclinations below 30°. Even if the lateral unsaturated flux is substantial, the large vertical gradient directs it effectively towards the saturated zone (Jackson, 1992; Van Asch *et al.*, 2001). Therefore, resulting fluxes under the gradient of the matric potential are small when compared to those of the vertical and lateral gravitational flows.

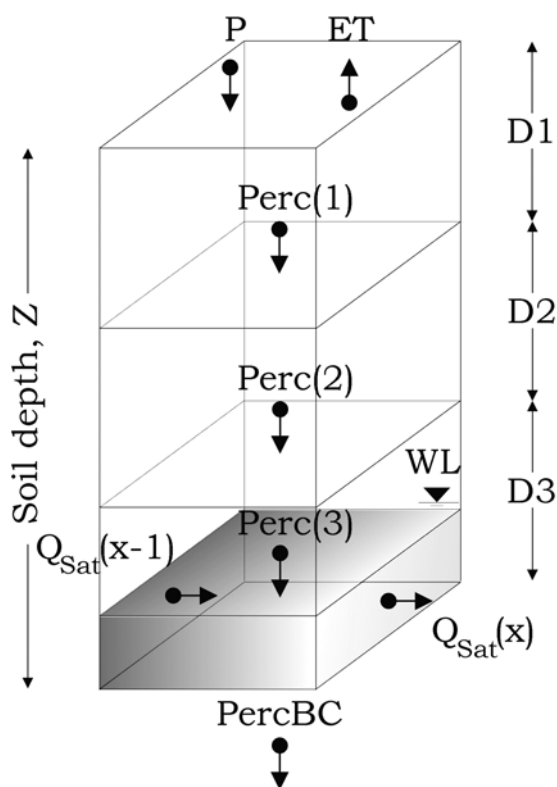


Figure 3.1: Schematic representation of the model concept of the hydrological component STARWARS. The $\text{Perc}(z)$ fluxes are defined by $\theta_E(z)$, the saturated lateral flow Q_{sat} from the gradient i of the water level.

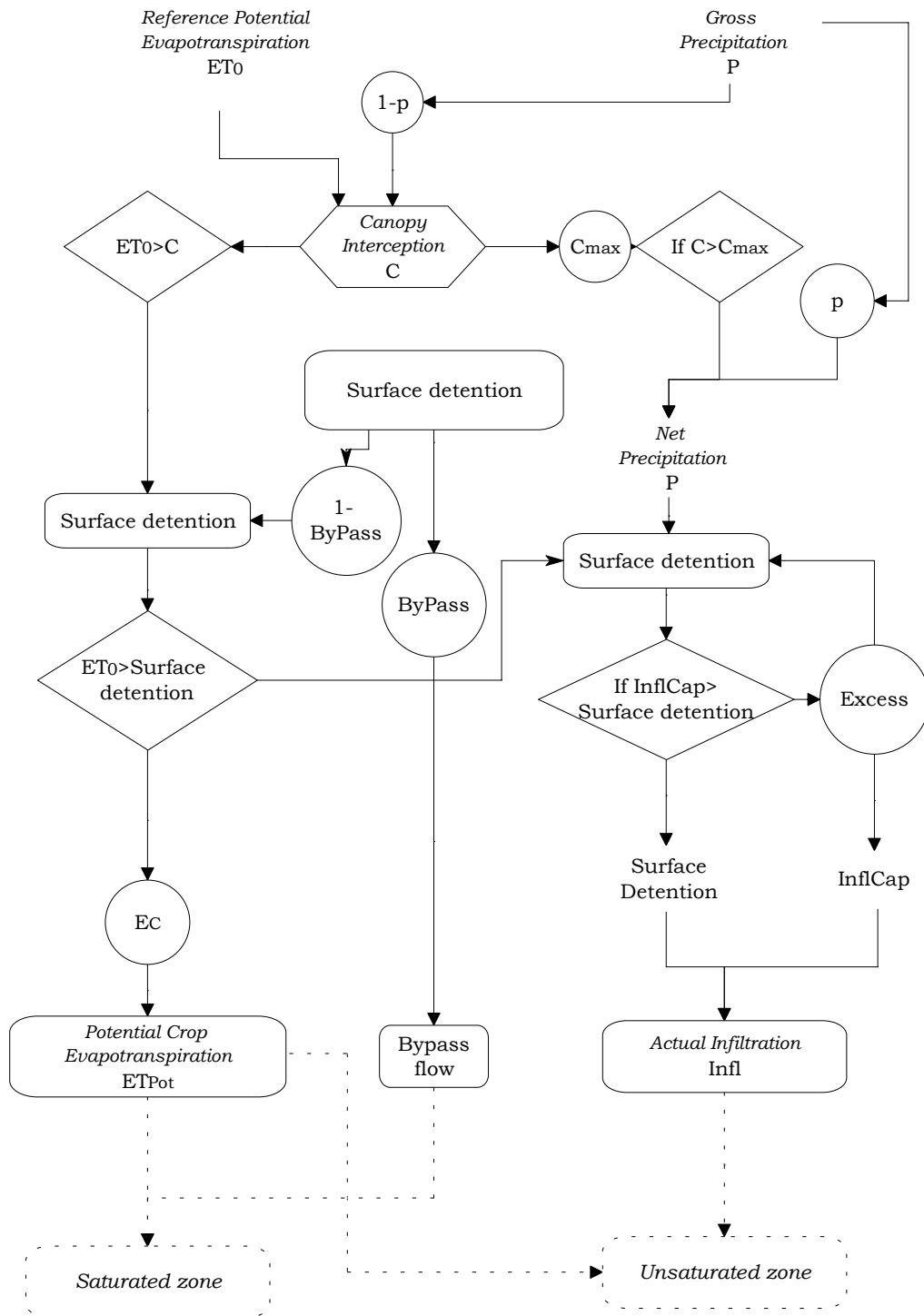


Figure 3.2: Flow chart of the model structure of STARWARS – surface and vegetation interactions. Horizontal lines signify positive decisions.

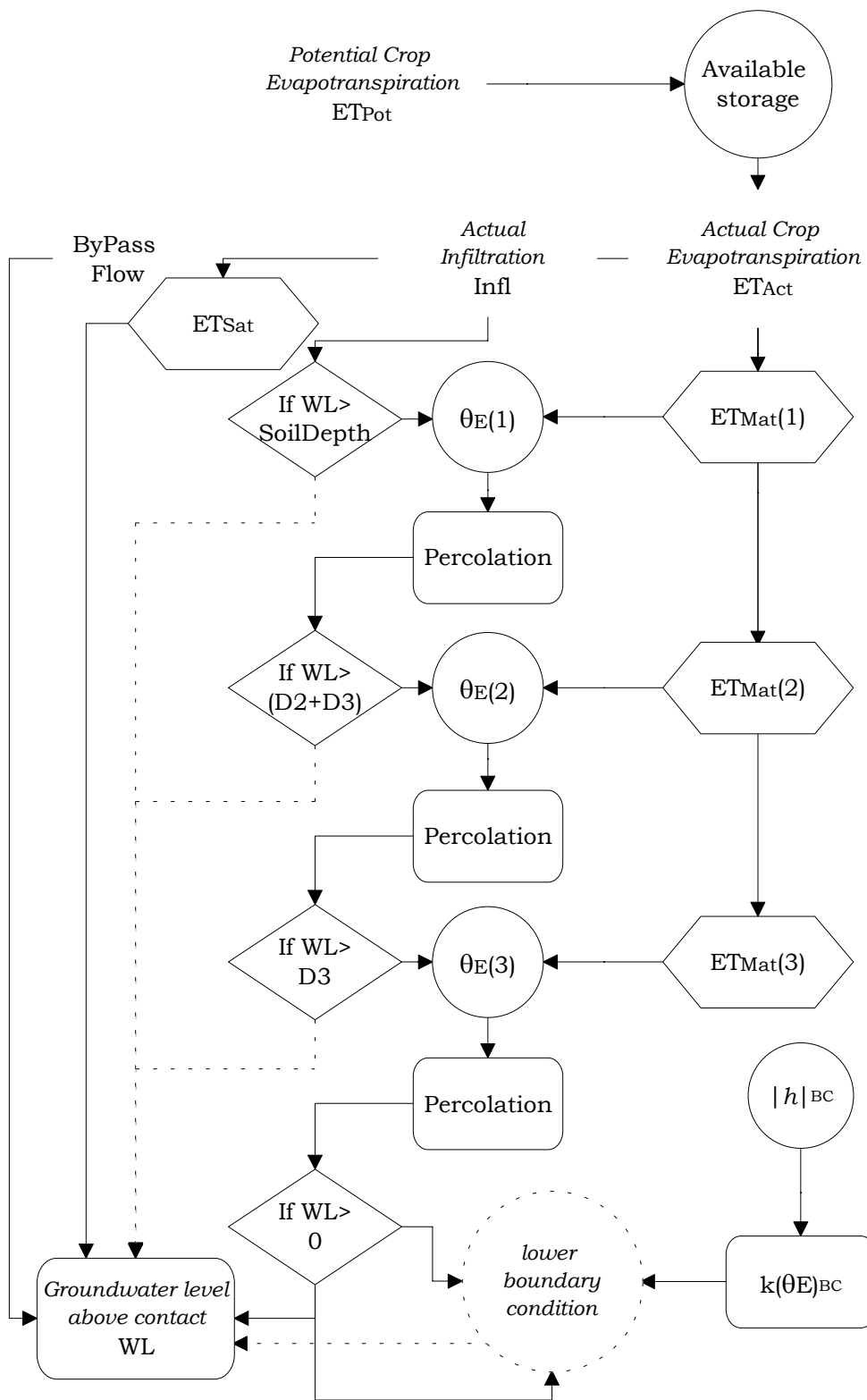


Figure 3.3: Flow chart of the model structure of STARWARS (cont.) – unsaturated and saturated zones

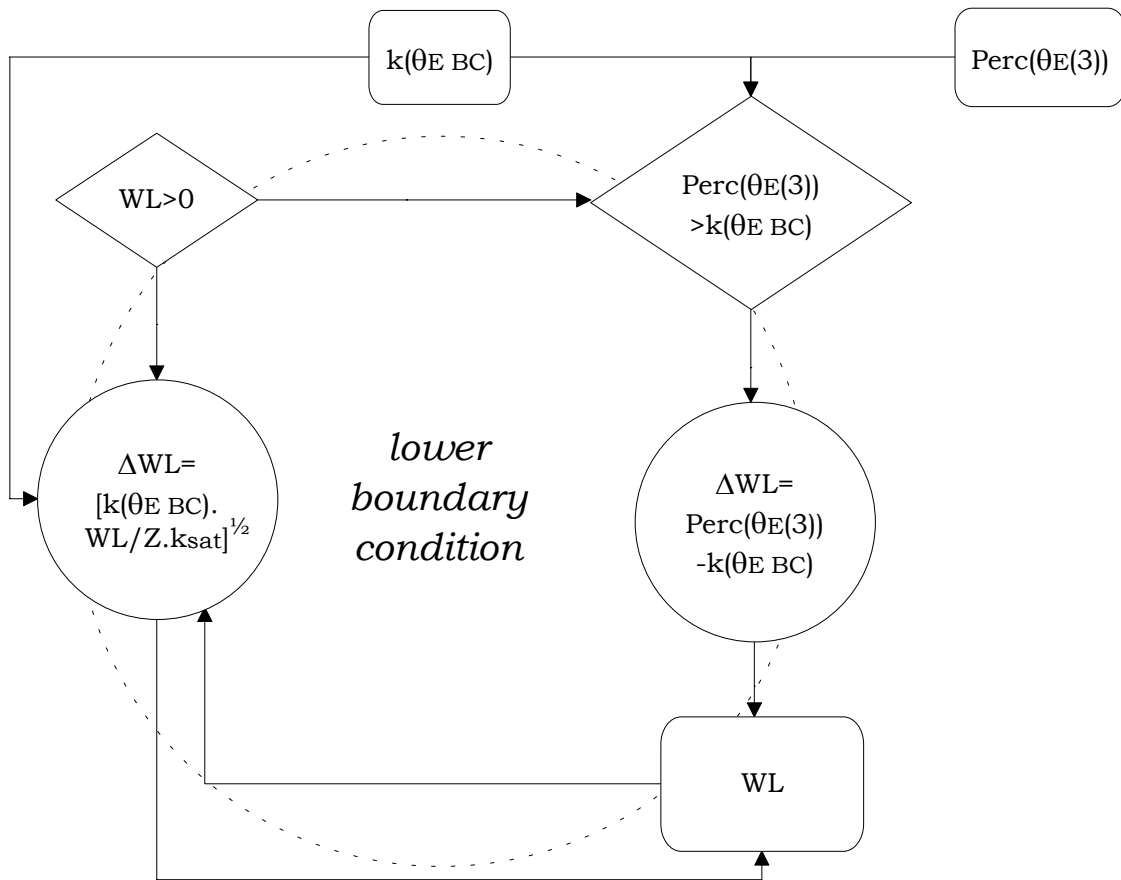


Figure 3.4: Flow chart of the model structure of STARWARS (cont.) – lower boundary condition

In most soils, the soil properties decrease with depth because of the different intensity of soil forming processes (Beven, 1982). These differences in the degree of weathering and in biological activity will result in distinct soil horizons. In order to simulate the resulting fluxes over such a differentiated soil profile above the semi-impervious lithic contact, it has been discretised into several layers. In Figures 3.2 to 3.3, a simplified scheme and a flow chart for the model are given.

For these layers, all storage and fluxes are given in units of waterslice. The advantage of this approach is that it facilitates computation as it can be converted by means of the maximum storage into the relative degree of saturation. The use of the relative degree of saturation has the advantage that it is the basis for the calculation of the percolation in the unsaturated zone. By definition, the relative degree of saturation, θ_E , is

$$\theta_E = \frac{\theta - \theta_{res}}{\theta_{sat} - \theta_{res}}. \quad (3.1)$$

In Equation 3.1, θ denotes the volumetric moisture content, θ_{sat} the saturated moisture content and θ_{res} the residual moisture content, all in units of ($m^3 \cdot m^{-3}$). The saturated moisture content is usually set to the porosity and the residual moisture content to a fraction of this maximum. The relative degree of saturation varies by definition between zero and unity when the soil is respectively at its residual and its saturated moisture content.

In Equation 3.1, the numerator and the denominator represent the actual and the maximum amount of drainable pore water. Consequently, the effective degree of saturation can be expressed in units of waterslice if both are multiplied by the thickness of the unsaturated zone above the groundwater table

$$\theta_E = \frac{D_{unsat}}{D_{unsat}} \frac{\theta - \theta_{res}}{\theta_{sat} - \theta_{res}} = \frac{StorMat}{D_{unsat}(\theta_{sat} - \theta_{res})}, \quad (3.2)$$

in which D_{unsat} is the thickness in (m) and $StorMat$ is the actual storage in ($m \cdot m^3 \cdot m^{-3}$) of the unsaturated zone. Once the initial relative degree of saturation is known, the actual volumetric moisture content is not required any more but can be obtained at any time by the formula

$$\theta = \theta_{res} + \theta_E(\theta_{sat} - \theta_{res}). \quad (3.3)$$

For each model layer z , the vertical, unsaturated matric flow, $Perc$, is based on the unsaturated hydraulic conductivity, $k(\theta_E)$. This unsaturated hydraulic conductivity is calculated from the soil water retention curve (SWRC), and the saturated hydraulic conductivity, k_{sat} . Both the saturated and the unsaturated hydraulic conductivity are defined in units of ($m \cdot d^{-1}$).

For the calculation of the unsaturated hydraulic conductivity, the mathematical formulation of the SWRC by Farrel and Larson (1972) has been used. This relation has been preferred above the well-known Van Genuchten (1980) model for two reasons. First of all, it reduces the number of parameters that describe the SWRC from three to two. The goodness-of-fit of Farrel & Larson's model is in general as good as the more complex Van Genuchten-model, especially if the number of parameters in the latter is reduced for mathematical expediency (Nielsen & Van Genuchten, 1985). Secondly, Farrel & Larson's relation is an exponential function. This can be considered as an improvement in model robustness when compared to the more complex relation of Van Genuchten. The model for the SWRC of Farrel and Larson is empirical, based on analogies in thermo-dynamics. The original model was defined in terms of θ/θ_{sat} . Rewritten in terms of θ_E , it is given by

$$|h| = h_A \exp[\alpha(1 - \theta_E)], \quad (3.4)$$

where $|h|$ is the absolute value of matric suction in (m), h_A is the absolute matric suction that corresponds to the air entry value in (m) and α is the dimensionless slope of the log-linear relationship between $\ln(|h|)$ and $(1 - \theta_E)$. This relation holds whenever the matric suction exceeds the air entry value.

The unsaturated hydraulic conductivity is calculated from the capillary analogy of Millington & Quirk (1959, 1961). According to their definition, the relative unsaturated

hydraulic conductivity, $k_r(\theta_E)$ is an analogous function of filled capillaries representing the filled pores at different suction levels. Based on the SWRC of Farrel & Larson, the relative unsaturated hydraulic conductivity becomes

$$k_r(\theta_E) = \theta_E^\tau \frac{[\exp(2\alpha\theta_E) - 2\alpha\theta_E - 1]}{[\exp(2\alpha) - 2\alpha - 1]}, \quad (3.5)$$

with the parameter of the tortuosity, τ , set to 4/3 (-). The $k_r(\theta_E)$ ranges from zero at the residual moisture content to unity at complete saturation and is dimensionless. The absolute unsaturated hydraulic conductivity, $k(\theta_E)$, is subsequently obtained by multiplying the relative unsaturated hydraulic conductivity with k_{sat} ($m \cdot d^{-1}$).

Given the thickness of the unsaturated zone and the relative degree of saturation at the beginning of the timestep, the percolation is proportional to the travel time of soil moisture over the unsaturated zone. With the vertical gradient of gravitational flow set at unity, the travel time is defined by the ratio of the depth of the unsaturated zone, D_{unsat} , over the unsaturated hydraulic conductivity ($m \cdot m^{-1} \cdot d = d$) for each model layer. The percolation is then set to the proportional loss of the unsaturated storage for layer z , StorMat, over the time increment Δt

$$Perc = StorMat \cdot \frac{k(\theta_E) \cdot \Delta t}{D_{unsat}}. \quad (3.6)$$

The loss of percolation to the groundwater table or over the semi-impervious lower boundary has consequently the dimensions of (m) waterslice and can be deducted directly from the drainable storage in the unsaturated zone and used to recalculate the resulting θ_E for the next timestep.

In the instances that the groundwater level does not reach into the model layer z , the percolation is calculated over the total depth of the layer and passed to the underlying unit. If the groundwater reaches the surface, the rate of percolation is zero and the vertical input is directly given by the evapotranspiration or the net precipitation. If the groundwater table reaches into the model layer z , the thickness of the unsaturated zone, D_{unsat} , is given by the depth to the groundwater table. An ever-increasing groundwater level will lower the thickness of the unsaturated zone and shorten the travel time for percolating soil moisture. This increases the likelihood that the fraction of Equation 4.6 exceeds unity and, drainage of the pore space would be complete. To prevent this unrealistic situation, the fraction is used to recalculate the degree of saturation first. This degree of saturation is subsequently used to project the saturated hydraulic conductivity at the end of the timestep. If the expected $\theta_E = 0$, it is set to an arbitrary value. The new unsaturated hydraulic conductivity is then used to calculate the average for the current timestep as the geometric mean, i.e. $k(\theta_E) = \sqrt{k(\theta_E)' \cdot k(\theta_E)}$. This average of the unsaturated hydraulic conductivity is then reused in Equation 3.6.

The use of the average unsaturated hydraulic conductivity also reduces the percolation close to the phreatic surface and is a surrogate for the influence of the matric potential in the vertical and for the effect of a capillary fringe. However, this conceptual approach is much simpler and reduces the problem of numerical instability if the model has to be applied over longer temporal scales. Moreover, since the model neglects the influence of

the matric potential, it does not suffer from the discontinuity in hydrological behaviour that arises from the air entry value of the SWRC of Equation 3.4.

The calculation of the percolation supposes that, for a raster cell, the percolation can be represented by the unsaturated matric flow under effective parameter values. However, for those cases that a clear dual porosity network appears to exist, an option is included to transfer a fraction of the rainfall excess directly to the lithic contact within one timestep. This will simulate the bypass flow through macropores or fissures in the regolith.

Currently, the model includes three layers that can represent the different strata over the depth of the soil mantle. Based on available knowledge, the parameterisation of the model can use spatial averages or use distributed values for the parameter values. If more geological detail or a more gradual profile of soil moisture is required, the number of model layers can be expanded. However, it must be realised that in the former case the number of parameters will increase and that in both cases the time increments has to be decreased to maintain numerical stability.

The problem of numerical stability also applies for the lateral outflow over the saturated zone. This flux is determined by the piezometric head and the effective k_{sat} and the condition must be satisfied that the flux density for a cell does not exceed the cell length over the timestep (Equation 3.10). Since both are based on a simple, explicit numerical solution, the saturated and the unsaturated flow the must comply to the Courant criterion, i.e. $V_x \ll \Delta x / \Delta t$.

In the model, the numerical solution uses a forward finite difference scheme for the discretisation of time, meaning that the fluxes in the present timestep are calculated from the state variables as obtained at the end of the previous one.

The generation of a perched groundwater table is in nature dependent on the loss of percolation across the semi-impervious lithic contact and is simulated in the model by imposing a boundary condition. If the substratum is considered impervious, no water is lost and a perched water table will form instantaneously. If this is not the case, an alternative boundary condition must be applied: at the lithic contact water is lost into an infinite fourth layer, for example bedrock. The lower boundary condition is a combination of a state-controlled, or *Dirichlet*-type, and a flux-controlled, or *Neuman*-type, boundary condition. For the fourth infinite layer, the matric suction or relative degree of saturation can be set to a fixed level, $|h|_{BC}$ or $\theta_{E BC}$. Both values are interchangeable by means of the SWRC. This results in a constant unsaturated hydraulic conductivity at the base of each element, $k(\theta_{E BC})$, in ($m \cdot d^{-1}$). Per timestep the loss to the fourth infinite store is dependent on this value and, if a saturated zone is present, on the hydraulic conductivity of the layer overlying the contact. In order to simulate the effect of the hydrostatic pressure over the contact, the height of the water level, $WL = \sum D_{sat}(z)$, is divided by the total soil depth, $Z = \sum D(z)$, and the geometric mean is used to obtain the bulk k_{sat} of the horizontal layers (Kutílek & Nielsen, 1994):

$$Perc_{BC} = \sqrt{\left(k(\theta_{E BC}) \cdot k_{sat} \cdot \frac{WL}{Z}\right) \Delta t}, \quad (3.7)$$

in units of (m) (Figure 3.1). The suffix BC has been omitted as all parameters except WL and Z refer to the fourth, infinite layer.

If no groundwater exists, the vertical loss into the fourth infinite store is dependent on $k(\theta_{E BC})$ only. This implies that the percolation from the basal layer must exceed this loss to generate groundwater. The lower boundary conditions determines for this reason the response of the hydrological system and this is in line with the physical reasoning that, in combination with the antecedent moisture conditions, above average rainfall is required to trigger landslides. The predominance of the lower boundary condition turns it in a suitable parameter for model calibration. The choice of the lower boundary condition to optimise model performance is also warranted by the fact that the characteristics of the substratum are usually less known and that it, on the temporal scales under consideration, can be presumed to be unrelated to land use and meteorological conditions.

In the model, the lower boundary condition is specified as a fixed value for the matric suction, $|h|_{BC}$ in (m). This parameter is preferred since the matric suction is continuous over space whereas the relative degree of saturation depends on the local conditions of the SWRC. Thus, $|h|_{BC}$ has to be defined after which the $\theta_{E BC}$ and $k(\theta_{E BC})$ are calculated with incorporation of any spatially varying attributes of the SWRC and the saturated hydraulic conductivity.

The lateral outflow over the saturated zone, Q_{sat} , is given by the piezometric gradient, i . This gradient is defined by the absolute elevation of the phreatic surface. This absolute elevation is obtained by summing the elevation of the lithic contact in the cell with the height of the water level, WL (both in m). Over a window of 3x3 cells (Figure 3.5), the maximum slope of the phreatic surface, $\tan(\alpha)$, is obtained for each timestep. The cell that coincides with this maximum slope is designed as the drainage direction for the saturated lateral outflow from the central cell. This type of map, in which the flow is directed in one of the eight cardinal directions, is named the *local drainage direction map* (LDD). The piezometric gradient, i , for the central cell under consideration is given by the difference in elevation over the slope parallel distance, $\Delta x/\cos(\alpha)$. Over the 3x3 window, the gradient is thus equivalent with the sine of α .

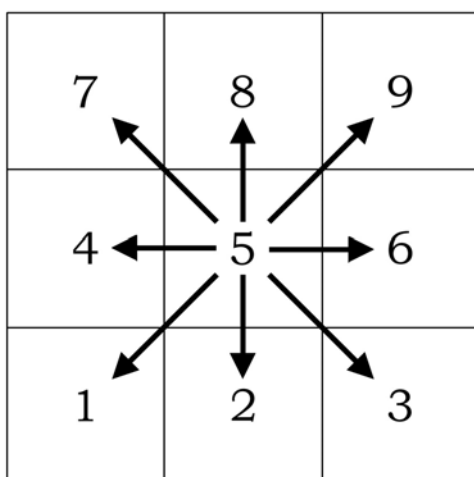


Figure 3.5: Cardinal directions of Local drainage direction map (LDD). To cells without drainage direction, pits, the value 5 is attributed.

Along the LDD, the lateral outflow, Q_{sat} , from the central cell to the downward cell passes the common height of the saturated zone and travels with the apparent velocity of the saturated lateral conductivity, $k_{lateral}$. Both are defined as the arithmetic average between the central cell x and the downstream cell $x+1$. For the calculation of the lateral saturated hydraulic conductivity, $k_{lateral}$, the bulk saturated hydraulic conductivity over the entire water table over the lithic contact is used, i.e.

$$\hat{k}_{sat} = \frac{\sum D_{sat} * k_{sat}}{WL} . \quad (4.8)$$

The average saturated lateral conductivity in the downstream direction is then

$$k_{lateral} = \frac{1}{2} \left(\hat{k}_{sat}(x) + \hat{k}_{sat}(x+1) \right) \quad (4.9)$$

and has units of ($m \cdot d^{-1}$).

Likewise, the height of the common saturated zone is averaged over the water levels. The resulting lateral flux over the saturated zone is given by

$$Q_{sat} = k_{lateral} \cdot \frac{1}{2} (WL(x) + WL(x+1)), \quad (4.10)$$

which has units of ($m^2 \cdot d^{-1}$). The use of the lateral saturated hydraulic conductivity makes the necessity that all model layers are of equal depth, superfluous.

For each cell the storage of the saturated zone is balanced for the outgoing and incoming fluxes. For the lateral flow, the change in storage, given in (m), is obtained by multiplying the net lateral flow with the time increment and dividing it over the cell length in the direction of the flow. Within a timestep, water is added to the saturated storage by the net percolation from the unsaturated zone and from bypass flow, if any occurred. The saturated storage is diminished by the loss over the semi-impervious lithic contact and by evapotranspiration. The latter loss is only substantial when the groundwater table is close to the surface (see below).

The budget for the saturated zone returns the groundwater level at the beginning of the next timestep. The inherent convergence of the LDD leads to a concentration of Q_{sat} in the downstream direction at the junctions of the LDD. As long as the model is run at timesteps that are small enough to secure numerical stability, this will not be a problem and, because the piezometric gradient is used, the flow paths will adjust themselves to the evolving situation. As a result, the groundwater on the slopes will tend to be more diffuse. Albeit its more complex nature, this is an advantage, for it avoids the rigour of models in which the flow is only driven by the topographical gradient (Dupuit-Forcheimer approximation – Beven & Kirkby, 1979; Lambe *et al.*, 1998). Although this may be a valid assumption in many cases, the method employed here is more flexible as it is able to reproduce the effects of local anomalies in the hydraulic conductivity and soil depth. The cost for the extra detail appears in the additional computational load and must be weighed against the spatial and the temporal resolution of the model. If either of these is reduced, the approaches will become more similar.

In the model, each cell is reported for which numerical stability for the saturated zone can not be maintained during the simulation. To prevent budget errors, the lateral and vertical fluxes are scaled to the available storage. The losses are summed and compared to the available storage after the incoming percolation and the bypass flow have been added. When the total loss exceeds the storage, its fluxes are reduced to match the available budget. After the local changes are balanced, the saturated lateral flow Q_{sat} is routed over the LDD to obtain the water level for the next timestep.

Any saturated storage that is in excess of the maximum storage of the soil, is removed as exfiltration. This exfiltration is passed over the LDD of the topographical surface. In the nearest downstream cell it is treated as surface detention in the next timestep and available for evaporation. This exfiltration is of little importance and it can not be routed realistically for the temporal scales under consideration. In the model, the user has the option to evacuate it directly from the entire area.

After a layer has become completely saturated, subsequent drainage may lower the groundwater level under its upper boundary. If the relative degree of saturation of the overlying layer is used as the initial value for the draining layer. In case that total saturation of the soil profile were to occur, the initial value has to be defined arbitrarily. In the model, this value is taken as the relative degree of saturation at field capacity, the amount of water the soil retains against the forces of gravity after 24 hours of drainage. For temporal resolutions shorter than one day, a value is used that is interpolated linearly between saturation and field capacity. For timesteps of more than one day, the field capacity itself is used. The choice of the θ_E at field capacity is free but for convenience the absolute matric suction is used as input, from which the θ_E is calculated. As for the definition of the lower boundary condition, this avoids the troublesome definition of the relative degree of saturation from spatially varying soil properties (porosity and SWRC).

In addition to the processes of percolation and saturated, lateral flow, STARWARS also includes infiltration and evapotranspiration. These last mentioned processes are determined to a large extent by land use and vegetation and they define the boundary condition that is imposed at the surface of the soil. The upper boundary condition for the model is flux-controlled and concerns the meteorological input at the surface consisting of the precipitation and the evapotranspiration. Both values are given as daily totals, which can be split over smaller time increments if this is required to maintain numerical stability. Alternatively, more detailed records can be included when available. In the latter case, a better infiltration module may be needed. Currently, the infiltration capacity is defined as a ratio, k_0 , of the saturated hydraulic conductivity of the top layer. Infiltration excess occurs if the rain that reaches the surface exceeds the infiltration capacity.

The amount of rainfall that is available for infiltration is limited by the evapotranspiration on one hand and by interception on the other. All rainfall is subject to interception by the vegetation, which is included in the model as a canopy store of finite capacity.

Interception is here defined as the gross interception (Zinke, 1965). This is the amount of water that is detained by the canopy and lost to evaporation. This loss is proportional to the gross precipitation rate, P , over a certain time span. All water that is not intercepted by the canopy, will be passed to the surface. A part of this water will be intercepted by the vegetation and litter that cover the soil and is not available for infiltration. However,

in the model this loss is expected to be included by the evapotranspiration of the soil and is not covered by canopy interception. This choice is based on the notions that the canopy interception is easier to measure in the field and that the conditions of the vegetation can vary independently at the two levels over time (e.g. in the case of deciduous forests). In the hydrological component of the model, the evaporation loss of the interception at the surface is accommodated by the actual evapotranspiration. For the canopy, the precipitation balance is

$$C = (1 - p) \int P dt - \int D dt - \int E dt, \quad (3.11)$$

where p is the fraction of not intercepted rainfall, P is the rainfall intensity, D is the drainage rate from leaves and stem, E is the rate of evaporation and C is the quantity of water detained on the canopy (Aston, 1979). All rates are in units of waterslice over time and defined over a unit area of the projected canopy.

The first two terms of Equation 3.11 define the amount of water that reaches the surface. In practice, the distinction between the direct throughput, conditioned by the proportion p , and the drip of the foliage can not be separated. So, both fluxes are lumped into one quantity, the throughfall (P_t). The term of D then comprises only the concentrated routing of water along the stem and branches, the stemflow (P_s). Written as a budget of the sum of these terms, the gross interception loss of the canopy, I_c , becomes

$$\Sigma I_c = \Sigma P - \Sigma P_t - \Sigma P_s. \quad (3.12)$$

Thus, the net rainfall, ΣP_n , that is available for infiltration equals $\Sigma P - \Sigma I_c = \Sigma P_t + \Sigma P_s$.

All interception, which is not indirectly passed on to the topsoil, can be lost due to evaporation. Since the maximum storage capacity, C_{\max} , is finite, the effective rainfall intensity, including the loss due to evaporation, determines the moment at which saturation is reached. Only when saturation is reached, the drainage process, D , will become fully operative (Rutter *et al.*, 1971). If the canopy does not reach saturation, no drainage will occur and the total gross interception equals a proportion $(1-p)$ of the integrated intercepted rainfall (Equation 4.11; Lankreijer *et al.*, 1992). Because both the time to saturation and the drainage processes are related to the effective rainfall intensity, most interception equations have the general appearance of a curvilinear relation that is bounded by C_{\max} .

The description of the interception is simplified if the evaporation during the rainfall is neglected. This is a reasonable assumption as the rate of evaporation is strongly reduced when the temperatures are low and the relative humidity is high. A simple conceptual model is that of Merriam (1960) that defines the detained water at a given time as an exponential function of the maximum storage capacity and the accumulated rainfall

$$C = C_{\max} [1 - \exp(-(1-p)\Sigma P / C_{\max})]. \quad (3.13)$$

Aston (1979) replaced the fraction of intercepted rainfall, $(1-p)$, by an empirical coefficient k , increasing the number of parameters to two. For six out of eight *Eucalyptus* species, he found a close agreement between this empirical parameter and the physically rationalised value $(1-p)$.

In Chapter 5, the performance of Merriam's model and that of a linear regression are evaluated for inclusion in the model. Both functions are described by two parameters. For

the linear regression these are the slope and intercept which give the rainfall dependence and the maximum storage capacity respectively. For Merriam's model, the parameters are the maximum storage capacity, C_{max} , and the factor $(1-p)$ (Equation 3.13). Because the fraction p specifies the amount of direct throughfall, it is also referred to as the *free throughfall coefficient*. When not used as a fitting parameter, it can be estimated from measurements of the leaf area index, the ratio of the leaf surface over the projected canopy area (LAI , $m^2 \cdot m^{-2}$).

Because most interception models are event-based, their performance will be poor on the temporal scale of days. This limited skill is explained by the fact that the sum of rainfall provides no information on the rainfall intensity and that the discretisation leads to an artificial division of prolonged rainfall events. This limitation will reduce the general interception function effectively to an invariable maximum storage capacity. The definite form of the interception model is based on the findings of Section 5.2.2. To some extent, the functionality of all interception models will be limited by the natural variability in rainfall intensity, by the temporal differences in vegetation conditions and by the spatial variability of vegetation (open stands).

After the interception has been deducted, the net rainfall is passed to the surface and stored as surface detention. Both interception and surface detention are subject to evaporation. The evapotranspiration that is used as input for the model is the reference potential evapotranspiration, ET_0 . It is entered separately as a timeseries into the model and can consist of observed or calculated values. In this case, Penman's equation has been used to calculate it, which is treated in detail in Section 4.3.

Because of the importance of the evapotranspiration in the Mediterranean, a detailed module to simulate the loss to evapotranspiration has been incorporated in the model. In the model, any interception can be lost directly to the potential reference evapotranspiration over the current timestep. The deduction from the surface detention affects only the excess from the previous timestep, after which the surface detention over the present time step, becomes available for infiltration. If the new surface detention exceeds the infiltration capacity, the excess is stored will become available for direct evaporation in the next timestep.

Any remaining reference potential evapotranspiration, ET_0 , may be lost from the water that is stored in the soil. However, a limited soil water availability and the presence of vegetation may reduce this potential rate. In the model, simple, dimensionless scaling factors or *crop factors*, k_c , relate this reference potential evapotranspiration, ET_0 , to the actual evapotranspiration for specific vegetation covers. The decline of the actual evapotranspiration, ET_{Act} , with decreasing water storage in the soil is simulated by scaling the remainder of the potential evapotranspiration with the ratio between actual and the maximum storage of an element

$$ET_{Act} = k_c \cdot ET_0 \cdot \frac{(\sum StorMat + \sum StorSat)}{\sum StorMax}, \quad (4.14)$$

where $StorMat$, $StorSat$ and $StorMax$ represent respectively the unsaturated, saturated and the maximum storage in units of waterslice (m).

The actual loss due to evapotranspiration is proportional to the available storage in each layer. Over the unsaturated zone, the loss to evapotranspiration is divided over sink terms, S_z , for every layer, z . The rate of evapotranspiration in each layer is calculated with the aid of the gradient, this being the slope of evapotranspiration over the depth of the unsaturated zone (Figure 3.6). At the same time, the amount of evapotranspiration of each unsaturated layer is limited by the difference in the relative degree of saturation between the layer under consideration, z , and the overlying layer, $z-1$. Bearing in mind the implicit assumption that the relative degree of saturation is a substitute for the continuity of matric suction in the unsaturated zone, this condition assures that the soil moisture content deeper in the soil can not decrease below that of the top layer due to evapotranspiration, as is usually the case in nature.

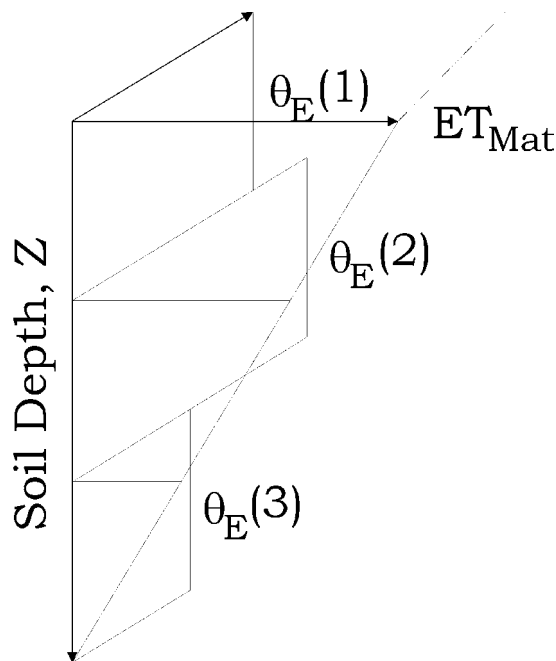


Figure 3.6: Linear decrease of evapotranspiration from the unsaturated matrix. Maximum evapotranspiration from layer z is limited by the relative degree of saturation of the overlying layer.

3.2.3 Modelling of slope stability

On slopes, the soil above a potential shear plane is subject to a driving force, or *demand* (D), that includes the downslope component of the own weight of the soil and any additional loads acting on it. Movement is resisted by the reaction force of the mobilised shear strength. The mobilised shearing resistance is finite and can be considered as the capacity, C , of the soil to resist failure. Failure is to occur as soon as the demand exceeds the capacity. This principle is the basis for the limiting equilibrium approach, which forms the basis for the slope stability assessment in the coupled hillslope model; the

maximum shearing resistance that can be mobilised is equal to the disturbing forces at imminent failure (hence the name limiting equilibrium).

With the limiting equilibrium method, the stability can be expressed as the ratio or the difference between the capacity and the demand. The first measure is known as the safety factor, F ,

$$F = \frac{C}{D} . \quad (3.15)$$

At $F= 1$, failure is imminent and the situation critical. When $F < 1$, the slope should theoretically have failed. The difference is known as the safety margin, SM ,

$$SM = C - D . \quad (3.16)$$

For critical situations, SM equals zero whilst positive values indicate stable conditions. The safety factor is dimensionless whereas the safety margin has the units of the demand and capacity, which can be defined as forces, moments or stresses. It is the most convenient to define the conditions at the potential shear plane as stresses, the average of the inter-particle forces over an elementary area., i.e. $f = \Sigma F/A$.

The limiting equilibrium approach only considers yielding by plastic failure. The maximum shearing resistance can then be described by the Mohr-Coulomb failure criterion

$$\tau_f = c + \sigma \tan \phi , \quad (3.17)$$

where τ_f is the shearing resistance at failure ($F= 1$), c is the cohesion σ is the total normal stress and ϕ is the angle of internal friction. The latter is defined as an angle whilst the other variables have units of stress ($N \cdot m^{-2}$ or kPa). The contribution of the cohesion is considered constant and consists of all inter-particle bonds such as those between clay minerals or cementation by salts or metal oxides.

The frictional component of the shearing resistance varies with the average inter-particle stress normal to the potential shear plane, σ . If the weight of the soil, W , is the only load acting at the potential shear plane, the total normal stress for an area of unit width and length is given by

$$\sigma = W \cdot \cos^2 \beta , \quad (3.18)$$

where β is the slope angle. W equals $Z \cdot \gamma \cdot 1 \text{ m}^2$, respectively the depth (m) and the bulk density of the soil ($kN \cdot m^{-3}$). Under the same assumptions, the disturbance is given by the shear stress, τ ,

$$\tau = W \cdot \sin \beta \cos \beta . \quad (3.19)$$

When part of the imposed load is carried by the water that is present in the pores, the frictional component of the shear resistance depends on the effective normal stress, σ' , which is the total normal stress reduced with the pore pressure, u

$$\sigma' = \sigma - u . \quad (3.20)$$

The use of effective conditions is indicated by primed symbols for the normal stress and the shear strength parameters, c' and ϕ' . Under the assumption that the occurring groundwater levels are unconfined, the effective stress is affected by the buoyancy of the particles below the groundwater level, so

$$\sigma' = [(Z - WL) \cdot \gamma + WL \cdot \gamma'] \cos^2 \beta, \quad (3.21)$$

where WL represents the groundwater height above the shear surface and, respectively, γ and γ' are the moist and buoyant bulk unit weight ($\text{kN} \cdot \text{m}^{-3}$).

For the calculation of the slope stability, the model uses the same schematisation of the soil mantle over a lithic contact as depicted in Figure 3.1. The depth of the potential shear plane determines the weight acting on it. In the field, such potential shear planes include planes of structural weaknesses as bedding planes or horizons in the soil profile, like lower boundary of the root zone or the lower end of the weathering profile. When the depth of landslides is defined by such structural weaknesses, their form can be described as planar or translational, and their length will be much greater than their depth (Crozier, 1973). For this type of landslides the curvature of the shear plane is negligible and inclined almost parallel to the topographical surface. This approaches an situation in which the soil mantle is of infinite length. Under homogeneous soil conditions, it can then be argued that, at equilibrium, all forces acting on the upslope part of an element are balanced by downslope forces that are equally large but opposite in sign. This slope stability model is known of the *infinite slope model* (Nash, 1987). In a raster-based GIS this has the advantage that the interactions between cells can be neglected and the calculated stability is dependent on the local cell attributes only. This one-dimensional approach will make the stability model less dependent on the actual cell size and the error that otherwise results from adding generalised attributes over multiple cells, is avoided. It allows a tight coupling of the model with the GIS environment which is impossible to achieve with 2- and 3-D models (Van Asch *et al.*, 1993). A loose coupling, in which the output of the hydrological model is exported to a 2-D or 3-D slope stability model, is possible but requires a high resolution DEM to avoid discretisation errors in the landslide morphology. The usefulness of this option is limited when the stability has to be assessed over larger areas and when no landslides or landslide prone areas are distinguished in advance. The data transfer and the recurring calculations make a slope stability assessment by loosely coupled 2-D or 3-D models on a regional scale unwieldy.

In the infinite slope model, the local values of the demand and the capacity govern the stability. On natural slopes, these quantities are primarily influenced by the own weight of the soil above the potential shear plane (Equation 3.17 and 3.19). The stability is assessed in terms of effective stress, with the frictional component of the shear strength set to $(\sigma - u) \tan(\phi')$. To determine the pore pressure, the assumptions of the infinite slope model impose the condition that the seepage is parallel to the shear plane and topographic surface. As an alternative to Equation 3.21, the pore pressure that is needed for the calculation of the effective normal stress is given by

$$u = \gamma_w WL \cdot \cos^2 \beta, \quad (3.22)$$

where WL represents the groundwater height above the shear surface, γ_w is the density of water ($\text{kN}\cdot\text{m}^{-3}$) and β is the inclination (Figure 3.7).

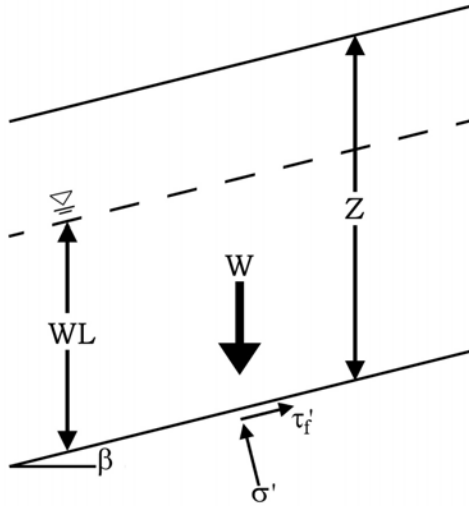


Figure 3.7: Definition of the infinite slope model for translational slides

If no groundwater is present, the matric suction provides an additional interstitial force that adds to the shear strength. According to the model of Fredlund (Fredlund, 1987), this force is additional to the frictional shear strength and not an intrinsic part of it. Over a unit area, it can be represented as an apparent cohesion term $\Delta c'$

$$\Delta c' = |h| \tan \phi^b, \quad (3.23)$$

which is positive and consists of the absolute matric suction, $|h|$ (kPa), and ϕ^b , the friction angle that describes the increase in shear strength at higher values of suction.

Both can be included in the equation of the infinite slope model. With stability expressed by the factor of safety, F , this equation is derived by substituting Equations 3.17, 3.19, 3.20 and 3.23 into Equation 3.15. This results in

$$F = \frac{c' + \Delta c' + [(Z - WL) \cdot \gamma + WL \cdot \gamma'] \cos^2 \beta \tan \phi'}{[(Z - WL) \cdot \gamma + WL \cdot \gamma_s] \sin \beta \cos \beta}, \quad (3.24)$$

where c' and $\Delta c'$ are respectively the true and the apparent cohesion, ϕ' is the angle of internal friction, Z is the depth to the potential shear plane, β is the slope angle, WL is the water level above this plane and γ , γ_s and γ' are respectively the moist, saturated and buoyant bulk densities.

The slope stability assessment is deterministic and requires the input of the soil depth, Z , and the other parameters. The model has the option to calculate the critical depth, at which $F=1$, but for the present case the depth has been fixed to that of the third layer and the lithic contact is taken as the potential shear plane (Section 5.7). The hydrologic input consists of the absolute matric suction, $|h|$, and the groundwater height, WL , which stem from the hydrological model component STARWARS.

The safety factor and the safety margins are deterministic measures for the slope stability. They predict instability if the driving forces exceed the available resistance locally. On this scale, i.e. for a slope or cell, the safety factor and the safety margin can be used to predict instability. However, these measures are poor estimators of landslide activity on a regional scale because they are linear scaling methods that relate the actual demand to the potential capacity (Christian & Beacher, 1999). Since both do vary with local conditions, identical values of F or SM do not provide information on the amount of capacity that is required to ensure stability and can not be compared. This limits their usefulness if landslide activity must be forecasted under hypothetical conditions. Moreover, the deterministic measures of F and SM are unable to explain any discrepancy between the observed landslide occurrence and simulated failure as they ignore local variations in the capacity and the demand.

These problems can be partly overcome by the probability of failure, which reflects the likelihood that the demand exceeds the available capacity given the variability in the variables of Equation 3.24. This probability of failure is directly comparable and the probabilistic approach thus provides a better statistic to compare landslide activity on the one hand, and addresses the problem of natural variability on the other.

The probability of failure can be envisaged as the overlap between the distributions of the capacity and demand (Lee *et al.*, 1983; Figure 3.8). Mathematically, the probability that the true safety factor is smaller than unity, $P(F \leq 1)$, for known distributions of the capacity, C, and demand, D, is given by

$$P(F \leq 1) = \int G_C(D)g_D(D)dD, \quad (3.25)$$

where G_C and g_D are respectively the cumulative probability function of the capacity and the probability density function of the demand.

The distributions are defined by the mean and variance of the capacity and the demand. Assuming that both the demand and capacity are normally distributed, the probability of failure is given by (Lee *et al.*, 1983)

$$P(F \leq 1) = 1 - G_F \left(\frac{M[C] - M[D]}{\sqrt{V[C] + V[D]}} \right), \quad (3.26)$$

where G_F denotes the cumulative probability of the standard normal distribution, $G_F(z)$, and $M[\cdot]$ and $V[\cdot]$ denote respectively the arithmetic mean and variance of the demand and the capacity.

A probabilistic approach can be followed to calculate the mean and variance of the capacity (Mood *et al.*, 1974; Mulder, 1991). The mean and the variance of the sum of two independent variables is given by

$$M[a_1x + a_2y + a_3] = a_1M[x] + a_2M[y] + a_3, \quad (3.27A)$$

$$V[a_1x + a_2y + a_3] = a_1^2V[x] + a_2^2V[y], \quad (3.27B)$$

where a_1, \dots, a_3 denote constants and x and y are variables with arithmetic average $M[\cdot]$ and the variance $V[\cdot]$.

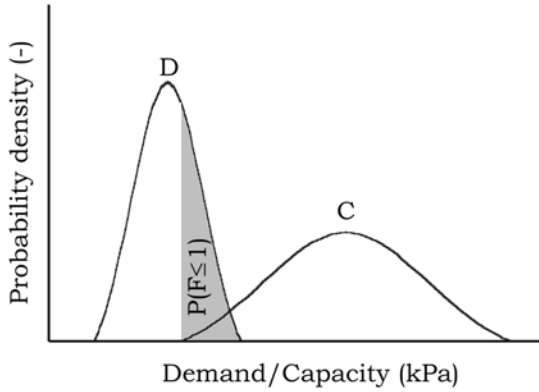


Figure 3.8: Capacity and demand model and the probability of failure (Lee *et al.* 1983)

The mean and variance for the product of two independent variables is given by

$$M[x \cdot y] = M[x] \cdot M[y], \quad (3.28A)$$

$$V[x \cdot y] = M[x]^2 \cdot V[y] + M[y]^2 \cdot V[x] + V[x] \cdot V[y]. \quad (3.28B)$$

These rules (Equations 3.27 and 3.28) can be applied to the infinite slope model of Equation 3.24. For the capacity, given by the Mohr-Coulomb Failure Criterion, the mean and variance become

$$M[C] = M[c'] + M[\sigma'] \cdot M[\tan \phi'], \quad (3.29A)$$

$$V[C] = V[c'] + M[\sigma']^2 \cdot V[\tan \phi'] + M[\tan \phi']^2 \cdot V[\sigma'] + V[\tan \phi'] \cdot V[\sigma'] \quad (3.29B)$$

The terms of c' and σ' can be expanded by use of the theorems to include the variability in the underlying variables (e.g. $\tan \phi^b$, γ , z and u or WL). The same holds for the demand, although the variability in the demand is generally smaller than that in the capacity. The probabilistic theorems also permit the inclusion of other distributions than the normal or Gaussian distribution if the parameters that describe them are converted to the arithmetic mean and the variance, $M[\cdot]$ and $V[\cdot]$. Successively, the probability of failure can be calculated using 3.26 assuming a normal distribution of the factor of safety.

The choice of the normal distribution is not evident for natural variables as the limits of the integral of Equation 3.25 can range from $-\infty$ to ∞ . In reality, many natural variables and the factor of safety will be censored as the shearing resistance can not be negative. This limits the range of the integral of F in Equation 3.25 from 0 to ∞ . If the variability is small, the error due to the fraction $F < 0$ of the area under the normal curve will be negligible. When it is large, however, another distribution may be needed. Commonly

used statistical distributions that may restrict the distribution to the range $F \geq 0$ are the uniform and the lognormal distribution. Especially the lognormal distribution has been used to describe the shear strength parameters of c' and ϕ' and the factor of safety (e.g. Lumb, 1970; Mulder, 1991). If the mean and variance of the safety factor are calculated directly, the probability of failure can be calculated for any probability density function g_F

$$P(F \leq 1) = \int_0^1 g_F(F) dF. \quad (3.30)$$

This solution is more flexible than the approach of Equation 3.25 as only the distribution of F has to be assumed. The distributions of the variables that are included as sources of uncertainty in F are considered to be known from field measurements. For the normal distribution, the probability of failure is then given by the integration of the standard normal curve for the range $-\infty < F \leq 1$, where the z -score is given by

$$z = \frac{x - M[F]}{\sqrt{V[F]}}. \quad (3.31)$$

For the lognormal distribution, the z -score is based on the logtransform $y = \ln(F)$ and takes the form

$$z = \frac{\ln(x) - M[y]}{\sqrt{V[y]}}. \quad (3.32)$$

In both cases is x the value of the safety factor for which the probability of failure is determined, i.e. $x = 1$.

The probability density function $g_F(z)$ for the standard normal curve is

$$g_F(z) = \frac{1}{\lambda} \exp\left(-\frac{1}{2} z^2\right), \quad (3.33)$$

where λ is $\sqrt{(V[F] \cdot 2\pi)}$ for the normal distribution, and $x\sqrt{(V[y] \cdot 2\pi)}$ for the lognormal distribution.

The integrated value of $g_F(z)$ is usually determined numerically. In PCRaster, however, iterations outside the main dynamic loop are not possible. Alternatively, a parameterised function is used which approximates the cumulative standard normal curve by

$$G_F(z) = \frac{1}{2} + \frac{\text{atan}\left\{z \cdot (C_1 + C_2 \cdot z^2)\right\}}{\pi}, \quad (3.34)$$

where $C_1 \approx 1.253$ and $C_2 \approx 0.579$. This function deviates slightly from the true probability at the extremes of the curve but the difference is negligible (< 0.01).

The slope stability model component uses Equation 3.32 with Equations 3.30 and 3.31 to determine the probability of failure for the normal and the lognormal distribution of F .

The probabilistic assessment is straightforward but can involve many variables for which the distributions have to be specified. The conversion from the parameters from distributions that are not normally distributed to the arithmetic mean and variance involves some error. From this point of view, it would be better to use a Monte Carlo simulation that offers more flexibility to establish the probability of failure for a cell (Christian *et al.*, 1994). However, with the coupling of the slope stability assessment to the hydrological model component, a deterministic approach is more appropriate for validation purposes as the similarity in the simulated and actual hydrological triggering mechanisms must be assessed. For this reason, a probabilistic approach for the stability assessment has been followed in which the probabilistic element has been restricted to the shear strength parameters. These are the cohesion, and the angles of internal friction, ϕ' and ϕ^b . The variability in the bulk density has been ignored as it has a only a very limited influence on the calculated slope stability (Section 7.2). The added information does not outweigh the complexity it introduces in the calculations.

Because only the intrinsic soil properties are included in the probabilistic slope stability assessment, it merely assesses the variability in the susceptibility (Section 7.3). The hydrological input into the stability analysis is kept deterministic and assesses the worst-case scenario over the period considered, both over the validation period and for the hypothetical conditions of the scenarios. This choice is based on the dependence of slope failure on critical pore pressure conditions and for ease of comparison of simulated landslide sensitivity under the current and hypothetical environmental conditions, which is the main objective of this study.

3.3 Model implementation

In a raster GIS, such as PCRaster in which the coupled hillslope model is embedded, calculations take place on the level of the individual cells. Therefore, all parameters must be specified at the level of the individual cell. Since it is not feasible to specify the input for the individual cell, some form of generalisation or interpolation is required. Dependent on the assumptions that are made on the spatial distribution of the parameters, the input can be defined as spatially constant, linked to known spatial attributes (e.g. land use), or estimated by geostatistical techniques. PCRaster supports these different options. Parameters can be entered as constants in the model script or included in tables, which relate the parameter value to a spatial attribute. The program GSTAT provides geostatistical interpolation techniques that are fully integrated with PCRaster (Pebesma & Wesseling, 1998).

If a parameter is dynamic, it has to be specified for every moment in time. Spatially distributed parameters have to be provided as stacks of maps, with one map for every timestep. If the spatially distribution can be ignored or simplified to several units, timeseries can be used to enter dynamic model input.

Model output can also be generated in the form of maps and timeseries. Spatial information is well represented by maps, but often difficult to analyse over a longer period. For this purpose, the condensed information of timeseries, which give the temporal information for a limited number of points, is more suited.

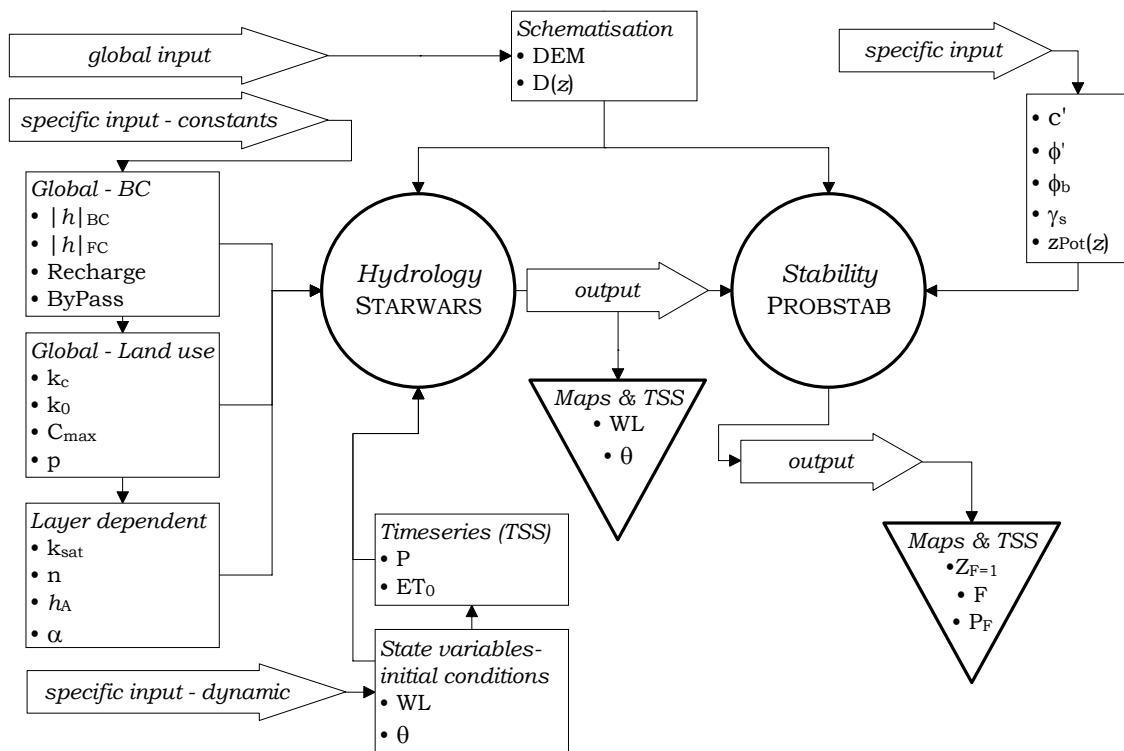


Figure 3.9: Model structure: in - & output

For the application of the coupled model, the overall structure defines that the hydrological model component precedes the stability assessment. So, the hydrological model component needs the input of the precipitation and the reference potential evapotranspiration over time. Because of the precedence of the hydrological model component, it also requires initial values for some of its state variables. These state variables are subsequently changed dynamically in the simulation of the hydrological processes. This contrasts them against the constant parameters of the model that are used throughout a model run to schematise the topography and soil profile and to parameterise the constituent equations (Figure 3.9).

The schematisation of the topography is based on the DEM, and the depth of the different layers above the semi-impervious lithic contact. This schematisation is identical for the hydrological and the slope stability model component and has been used to specify the input for these modules. For the topsoil, the influence of the vegetation on the hydrological processes of interception, infiltration and evapotranspiration will be linked to land use units that are considered as internally homogeneous.

Table 3.1: Model in- & output of the coupled hillslope model for hydrology (STARWARS) and stability (PROBSTAB)

Model component:	Hydrology – STARWARS	Stability – PROBSTAB	
<i>Model Input</i>			
Schematisation	<ul style="list-style-type: none"> • High resolution DEM (m) • Layer depth D(z) (m) 		
Constant parameter values	<i>Global boundary conditions</i> <ul style="list-style-type: none"> • Matric suction for lower boundary condition $h _{BC}$ (m) • Matric suction at field capacity, 1st layer $h _{FC}$ (m) • Residence* of surface detention Recharge (-) • Fraction of bypass flow* ByPass (-) 	<i>Layer-dependent</i> <ul style="list-style-type: none"> • Cohesion c' (kPa) • Internal friction angle ϕ' (°) • Angle of unsaturated shear strength contribution ϕ^b (°) • Dry bulk density of the soil γ_s (kN·m⁻³) • Depth of potential shear plane*** $z_{Pot}(z)$ (m) 	
	<i>Global – land use dependent</i> <u>Evapotranspiration</u> <ul style="list-style-type: none"> • Crop factor k_c (-) <u>Infiltration</u> <ul style="list-style-type: none"> • Infiltration constant K_0 (-) <u>Interception</u> <ul style="list-style-type: none"> • Max. storage capacity C_{max} (m) • Direct throughfall ratio p (-) 		<i>All parameters can be considered as layer and land use dependent</i>
	<i>Layer-dependent**</i> <ul style="list-style-type: none"> • Saturated hydraulic conductivity** k_{sat} (m·d⁻¹) • Porosity n (m³·m⁻³) • Air entry value** h_A (m) • SWRC slope** α (-) 		
	<i>All parameters of the top layer can be considered as land use dependent</i>		
Dynamic input – All timesteps	<ul style="list-style-type: none"> • Reference potential evapotranspiration ET_0 (m·d⁻¹) • Precipitation P (m·d⁻¹) 	<ul style="list-style-type: none"> • Groundwater level WL (m) • Volumetric soil moisture content θ (m³·m⁻³) 	
Initial conditions - state variables	<ul style="list-style-type: none"> • Groundwater level WL (m) • Volumetric soil moisture content θ (m³·m⁻³) 		
<i>Model Output</i>			
Maps and Timeseries	<ul style="list-style-type: none"> • Groundwater level WL (m) • Volumetric soil moisture content θ (m³·m⁻³) 	<ul style="list-style-type: none"> • Factor of safety F (-) • Probability of failure P_F (-) • Critical depth $Z_F=1$ (m) 	

*: not considered (by default all water is transferred over the LDD and no bypass flow occurs)

** : also required for lower boundary condition

***: optional if the potential shear planes do not coincide with the layer boundaries

Of the model layers, z , only the first layer is taken as land use dependent in the hydrological model component. For these layers, input per layer consists of the parameters for the porosity, SWRC and the saturated permeability. These parameters are listed in Table 3.1. Per layer, the hydrological model thus requires the 5 parameters mentioned in Equations 3.3 and 3.4 and k_{sat} . When the tortuosity is set to the constant value of $4/3$, as used by Millington & Quirk (1959, 1961), this number reduces to 4 parameters, of which the SWRC characteristics h_A and α are mutually dependent. So, for z model layers, the required number of parameters becomes $4z$, and this may increase if, the upper layer, is divided over n land use units. Since only the first layer is taken as land use dependent, the number of required parameters becomes $4(z-1)+4n$.

The hydrological model component requires several parameters for the definition of the upper and lower boundary conditions. For a semi-impervious lower boundary, one parameter is needed, the matric suction $|h|_{\text{BC}}$, to define the unsaturated hydraulic conductivity, $k(\theta_{\text{E BC}})$, of the infinite store under the lithic contact. As intended, the SWRC and the k_{sat} are considered as identical to that of the overlying layer, thus trading three parameters for one general assumption.

For the upper boundary conditions of the hydrological model component, four parameters are needed to define the flux-controlled interactions between land use and soil moisture at the surface (Table 3.1). These parameters are the fractions and constants defining actual evapotranspiration, infiltration capacity and interception. Dependent on the number of land use classes, this adds $4n$ constants to the list of parameters.

The last parameters, which can be specified in the model, define the residence of surface detention and the bypass flow (respectively *Recharge* and *Bypass*; Section 3.2.2). The first defines the fraction of the surface detention that is routed over the LDD of the topographical surface. The remainder is transferred to the next timestep. The second factor defines the fraction of the surface detention that is passed directly as bypass flow to the lithic contact. They can be used to simulate the presence of a fissure network in unstable areas but are not applied in this study. All surface detention is routed and available for evapotranspiration and infiltration in the downstream pixel during the next timestep while all vertical flow towards the lithic contact is confined to matric pores.

To illustrate the sample requirements of the hydrological model component STARWARS the following example is given. For a schematisation of three layers and four land use classes, ($z= 3$, $n= 4$), $4(z-1) + 4n + 4n= 40$ values are needed to parameterise the processes above the lithic contact. If $|h|_{\text{BC}}$ is considered as constant and the only unknown for the lower boundary condition and the fractions of recharge and bypass flow are specified, 3 more parameters are needed. This brings the total for this configuration to 43 parameters, or 41 if the latter two are ignored.

To this number, the initial values for the state variables must still be added. Initial values must be specified for the initial groundwater level and for the surface detention at the start of any new simulation. Per layer, the volumetric soil moisture content, θ_z , has to be specified, from which the matric suction and the degree of saturation can be derived. Therefore, $2+z$ initial values must be added to the total number of parameters. All in all, this leads to the rather disappointing conclusion that, even for a simple model, the data

requirements are high: 47 parameters are needed when the morphology is not included. Distinct parameters for the different land use units are the main source for the large data requirements. Ideally, the in- & output will be defined according to the relevant detail for the intended use. In reality, data availability will restrict the available options.

The probabilistic stability component, PROBSTAB, is less demanding and requires the specific input of the shear strength parameters and of the dry bulk density. For the calculation of the probability, the variance for these parameters must be specified as well (Table 3.1).

If the potential shear planes do not coincide with the layer boundaries, the depth of the potential unstable soil mantle can be included. If the stability has to be calculated for a layered soil profile, the total number of parameters equals $4z$.

For the calculation of the effective normal stress and the shear stress, the input of the groundwater level and the soil moisture for each timestep is required. Likewise, the matric suction is needed to calculate its contribution to the unsaturated strength, but this variable is interchangeable with the soil moisture through the SWRC. In the coupled hillslope model, thus $z+1$ dynamic variables are derived from the hydrological component.

The output of the stability assessment typically consists of the degree of safety, in this case of the safety factor, and the probability of failure over time. Together with the preceding output of the hydrological model component, the output of the coupled model comprises

- Groundwater levels;
- Soil moisture content for z layers;
- Average or expected factor of safety at specified locations, $E[F]$, for example the base of z layers;
- Probability of failure at the above specified locations;
- The critical soil depth for which $F=1$ ($Z_{F=1}$).

All output is basically composed of stacks of maps, reported at each timestep. The option exists to limit the output to maps that are generated at pre-set timesteps, or to limit the output to a continuous timeseries for predefined locations in the area of interest. Because of the tight coupling and the topographical control on landslide occurrence, both models are bound to the same spatial scale. The temporal scale for the stability assessment is not necessarily confined to the high resolution that the hydrological component dictates. It can be run at a coarser temporal resolution, using the aggregated output of the hydrological model component. This option is desirable if one wants to assess the most critical situation that is defined by the highest pore pressures for a given period (worst case scenario). In most cases, however, it is more economic if the temporal scales of both components coincide. The results must then be analysed and aggregated over the scales of interest afterwards.

3.4 Concluding remarks

Before the model is applied, it is helpful to enumerate its limitations and possibilities. They define, above all, the potential of the model to evaluate the impact of changing environmental conditions on landslide sensitivity.

The coupled hillslope model is physically based and is in principle capable to simulate the landslide activity under present and hypothetical environmental conditions. Changes in landslide activity, however, are only reflected in the temporal sensitivity as the susceptibility is not changed for the scenarios. The meaning of these changes depend entirely on the agreement of the model with the present processes and the extent to which the importance of these processes remain unchanged. This demands that the validity of the model is assessed. Moreover, it implies that, even for a valid physically based model, the environmental changes that can be imposed on the model must be moderate and based on the present situation.

The model validity is affected by operational and model errors. Operational limitations concern rounding errors and data limitations that originate from the discretisation of the model. Model input may also be affected by the available data, which will be presented and discussed in the chapter on data acquisition and model parameterisation (Chapter 5).

A manifest limitation of the scenarios is the incapability to capture all changing environmental conditions into one valid scenario. The definition of scenarios including consistent change in all related, environmental factors, requires knowledge that in all cases will surpass the available information for the construction and implementation of the model. In general, only the broad outlines of the present situation and its heterogeneity are known. As a consequence, the predefined scenarios are more or less artificial for only the changes in a limited number of environmental conditions are inferred while all others factors remain constant (Chapters 4 and 8).

Discretisation and simplification put a further restraint on the potential of the model. Because the scope of the model stretches beyond the event-scale, runoff can not be included realistically in the model. Over time increments of days, runoff can cover large distances whereas this is limited to a mere cell size of several meters in the simulation. If runoff is considerable or surface erosion has to be assessed, another approach becomes compulsory.

Similar limitations originate from the use of distinct model layers and from the definition of the relative degree of saturation at field capacity. The latter, used to initiate drainage after complete saturation, supposes a linear decrease in moisture, regardless of the elapsed time, and simplifies the initial conditions to one general value for every situation. The use of model layers poses a specific lower limit to the response time. With three model layers, the transfer of water from the surface to the lithic contact lasts at least three time steps. Depending on the duration, the response is more or less retarded. Consequently, the optimum model configuration may change if different time increments are used.

Oversimplification also affects the land use characteristics that are incorporated in the model as the spatial and temporal variability is lumped over larger units or periods. Such land use dependent parameters will be adequate descriptors for the mean land use conditions but over short periods and on local scales they may be in error and influence

the capability of the model to predict the occurrence of actual landslides. For evaluation purposes, time-dependent relations could replace the constant land use parameters. Sidle (1992) used such an approach to model the temporal variation of shear strength under the impact of timber harvesting. For the hydrological properties, however, these relations are difficult to quantify and not always clearly discernible against the background noise. For this reason, the simpler approach has been favoured, in spite of the ensuing limitations. A clear model limitation is the static nature of the slope stability model. The model does not simulate changes in landslide susceptibility, which could arise from adaptations in the morphology and the soil properties of a slope. This simplification is valid under the assumption that changes in the temporal sensitivity precede those in the susceptibility (Chapter 1).

Still, the infinite slope mode offers a simple means to assess the stability but other measures of instability than the traditional measures of the factor of safety or the safety margin are required as the main interest lies in the assessment of landslide sensitivity on a regional scale and over longer period. The probability of failure is a good alternative that takes the local variability into account and its values can be compared and analysed on a regional scale. The eventual accuracy of the infinite slope model is determined by the degree to which the underlying assumptions are met and the confidence by which the actual topography and soil properties can be represented on the chosen spatial resolution. This can be evaluated from a comparison of the observed activity with simulated failure, which is covered in Chapter 7.

The uncertainty that results from the model structure and its implementation poses, in combination with the oversimplified relationships, limitations to the reliability of the model outcome. To evaluate the consequences of these limitations, the model should be tested on its sensitivity, before an attempt at calibration and validation is made. From the sensitivity analysis, some preliminary ideas on the performance of some optimisation parameters can be obtained. Sensitivity analyses of the hydrological model component and of the stability assessment are considered in Chapters 6 & 7.

4 CLIMATIC CONTROLS OF LANDSLIDING: PRECIPITATION AND EVAPOTRANSPIRATION

4.1 Introduction

The net precipitation input is the primary factor that controls the activity of rainfall-induced landslides. Apart from the intermediate influence of land cover, which is treated in the following chapter, this net input is defined by the climatic variables of precipitation and evapotranspiration. The relevance of the respective climatic inputs for landsliding is defined by the initial stress distribution above a potential shear plane. Dependent on the geometry and strength of the slope materials increasing net rainfall depths are required to induce failure (Chapter 1). Whilst such amounts may be delivered by single rainfall events in some occasions, most landslides require a more substantial period of rainfall to attain critical pore pressures. Under those circumstances, evapotranspiration becomes more important for it uses up the available soil moisture storage and thus attenuates the response following new rainfall events. Hence, the activity of most landslides is not merely controlled by the gross rainfall but, as it must accumulate over a longer period to balance evapotranspiration, also by its temporal characteristics, in casu the duration of alternating periods of wet and dry spells.

Both precipitation and evapotranspiration exhibit a temporal variability on a seasonal and an interannual scale but evapotranspiration, acting continuously, is the more steady process of the two and the less susceptible to extreme events. In contrast, precipitation as a trigger of otherwise stable slopes is characterised by its extreme events. These extreme events are loosely defined as the positive deviations in the rainfall distribution that are likely to trigger landslides. Since, according to the quantitative magnitude-frequency approach of Wolman and Miller (1960; Chapter 1), the high geomorphic power of the more extreme events is compensated by their rare occurrence, the relative work done by events of intermediate frequency (once every 5 to 100 years) is the more important (Gallart, 1995). All in all, this implies that the activity of rainfall-induced landslides is not only controlled by the short-term and seasonal characteristics of precipitation but also by the expected return periods of extreme events.

On a local scale, the temporal variability of the precipitation and evaporation explains the activity of rainfall-induced landslides. Over larger areas, the emerging spatial patterns blur this influence. For this reason, any generalisation of landslide activity is confined by the representativeness of the local temporal variability for larger areas. The temporal variability in precipitation and evapotranspiration must be related to spatial patterns if the assessment of the landslide susceptibility is intended to have more than a local meaning. In practice, this problem is only aggravated by the sparse and uneven distribution of meteorological stations with observational records of considerable length. So, the causes of the spatio-temporal variation must be understood in order to reduce the uncertainty in the interpolated climatic input.

Under consideration of the importance of precipitation and evapotranspiration as controls of landsliding, the first objective of this Chapter is to characterise their spatial and temporal patterns in the study area. This characterisation must provide the information to

make generalisations on the climatic control of rainfall-induced landslides as included in the historical dataset for the calibration and validation of the model. The characteristics of interest are the variation in rainfall depth and duration within and between seasons and the recurrence intervals of extreme rainfall. The main interest is given to the characteristics of daily and event rainfall at Almudaina but some attention will be paid to the within-storm characteristics as well for they provide essential information on the seasonal differences in rainfall intensity, duration and persistence that control surface processes like interception and infiltration (Chapter 5).

Subsequently, these characteristics are compared to observations made in the study area of the Coloma itself and in neighbouring meteorological stations. These comparisons are intended to increase the support of the observations and to place the climatic controls in a regional context. A similar approach will be followed for the derivation of the potential evapotranspiration as covered in Section 4.3.

The description of the meteorological record serves an additional purpose. Because of its relatively short length and the implied order of events, the historical dataset is of little use in the diagnosis of the landslide susceptibility under changing environmental conditions in the future. In order to prevent the bias in the frequency of potential landslide triggers, hypothetical datasets, based on the available record, are constructed as model input. These hypothetical datasets are based on a weather generator for daily precipitation. This weather generator is conditioned on the present climatic conditions and on downscaled scenarios for the average daily temperature for future conditions, stemming from general circulation models (GCMs). The use of downscaled GCM-scenarios for daily rainfall has been abandoned because of their limited success in simulating present-day Mediterranean precipitation patterns. Their use would not increase the confidence in the future scenarios, nor would it remove the basic assumption that in the near future the dynamics and local phenomena of the weather system remain the same. The construction of the hypothetical datasets of rainfall and temperature and their relation to the net precipitation in the study area are addressed in the final section of this Chapter.

4.2 Spatio-temporal precipitation patterns

A high degree of spatial and temporal variability in precipitation characterises most Mediterranean climates. Because of its high intensity and erratic occurrence, this precipitation has often an extreme nature. Along the Levante, the origins of this large variability are the predominance of the meso-scale weather system of the *temporal de Levante* (Quereda, 1989; Section 3.2), and local convection cells (Camarasa, 1991), in combination with the orographic effects induced by the SW-NE aligned ridges of the Pre-Betic (La Roca, 1992).

The study of La Roca addresses the problem of the spatio-temporal distribution of precipitation in the coastal area between Valencia and Alicante in detail and refers in particular to its role in landslide activity in the upper basin of the Río Serpis. For this region, which overlaps the study area, the erratic character of the precipitation is witnessed by the spatial and temporal differences in rainfall depths. Precipitation data are available as 24-hour totals from the Instituto Nacional de Meteorología (INM) for ten

locations, in several cases since the 1950s onward (La Roca, 1992). Of these, the climatic station at Almudaina is the nearest to the study area with a maximum distance of 2 km. In contrast with the other stations, it is located at the base of the N-exposed face of the Sierra de Almudaina, at an elevation of 586 m above sea level. Thus, it is exposed in a similar manner as the study area to the rain-bearing winds that enter from the Mediterranean by westward winds. Hence, it can be assumed that from the available stations this location would be the most representative.

Here, the climatic record of the station of Almudaina is used to analyse the temporal distribution of precipitation in the study area. The representativeness of the climatic station for the study area is addressed by a comparison of the long-term record of Almudaina with a detailed but short record from the field with the 24-hour totals over the years 1995-1999. This record also provides the information on the within-storm characteristics.

The spatio-temporal rainfall patterns on a regional scale are studied by the subsequent comparison of the long-term record of Almudaina with the records of neighbouring stations. In combination with the findings of La Roca (1992), some generalisations on the occurrence of extreme rainfall on a regional scale are made.

4.2.1 Temporal rainfall patterns for Almudaina 1971-1998

For the IMN-station of Almudaina (Nr. 8066), precipitation data are available since March 1954. Although the record until 1998 covers 45 years, it contains several gaps in the years preceding 1971. Before this year, 78% of the record is available, with no recovery from March 1962 until October 1964. To avoid the presence of missing values, the analysis of precipitation at Almudaina has been limited to the period between 1971 and 1998. The length of the record is thus 28 years, which is close to the conventional 30 years used in climatic research.

Over the period 1971-1998 the precipitation has been measured at the same location near the village of Almudaina. Precipitation is collected by a simple rain gage with a resolution of 0.1 mm, situated a 1.5 m above the ground. The accumulated precipitation over 24 hours is measured at 8:00 hours approximately, after which the collector is emptied. The precipitation total is noted in units of 0.1 mm of equivalent water depth. In addition to this quantity, qualitative information on the type of precipitation, the wind direction and the time of occurrence are noted. If the equivalent water depth is low and can not be quantified it is noted as imperceptible. In the record, the lowest entry of rainfall is 0.2 mm, which can be considered as the accuracy of the analysis that only includes the actual values and ignores the qualitative entries. In this manner, the precipitation record includes only direct rainfall and snow. This latter type forms a minority. Over the years 1971-1998, only 18 days have been recorded for which the precipitation consisted of snow. The majority of these days occurred in January and February but exceptional events were recorded in November and March as well. This snow cover persisted never for more than two days. Consequently, precipitation is directly available for the hydrological processes in the topsoil.

The precipitation totals for Almudaina vary strongly over the years. This is partly caused by the incongruence between calendar and hydrological years. By definition, a hydrological year in Spain starts in the month of September and includes the period over

which the precipitation and evapotranspiration amplitudes alternate. The rainfall record over the 27 hydrological years that are present over the period from 1971 till 1998 has a minimum of 336 mm in the year 1983-1984 and a maximum of 1186 mm in the year 1972-1973. Still, the variability remains high: the range of 851 mm is 120 % of the mean annual precipitation of 698 mm (Table 4.1). For the complete hydrological years in the period 1954-1971 (N= 6), the mean annual precipitation reduces to a value of 608 mm. This reduction is entirely due to the extremely low amount of 122 mm over the year 1960-1961. Based on the available information it appears that the average annual sum of precipitation is constant but highly variable. Given the erratic nature of the rainfall record and because of the gaps prior to 1971 no trends can be discerned. However, the observed minimum and maximum coincide with marked periods of drought and above-average rainfall that were observed along the entire Mediterranean coast of Spain (Esteban *et al.*, 1998, Romero *et al.*, 1999).

Table 4.1: Annual precipitation statistics for Almudaina 1971-1998. A hydrological year covers the period between the 1st of September and the 31st of August.

Values in mm	Calendar years	Hydrological years
Mean	692	698
Median	696	671
Standard Deviation	289	244
N (years)	28	27
Range	991	851
Minimum	190	336
Maximum	1180	1186

The large differences between the individual hydrological years are reflected by the seasonal variability. The average daily precipitation (calculated from the daily totals over the period 1971-1998) exhibits a large range over the period of 27 year. This variability is only partly reduced when a central 31-days moving average is taken (Figure 4.1): the shape of the curve remains irregular because of the infrequent occurrence of rainfall.

On average only 10.5% of the year can be considered as raindays (Table 4.2). These wet days are spread unevenly over the year. Dry spells last for most of the summer and in more than 50% of the cases, no rainfall occurred in July and August. During the wetter months of the year, the average percentage of rainfall days exceeds the yearly statistic. The distributions are positively skewed for most months. Clear exceptions are the months of April and May for which the median concurs with the mean. These months seem to have a fair change on a constant amount of raindays, what must be attributed to the occurrence of local thunderstorms in this period. This does not apply to the amount of rainfall, as standard deviation for these months is similar to the other monthly values (Table 4.2).

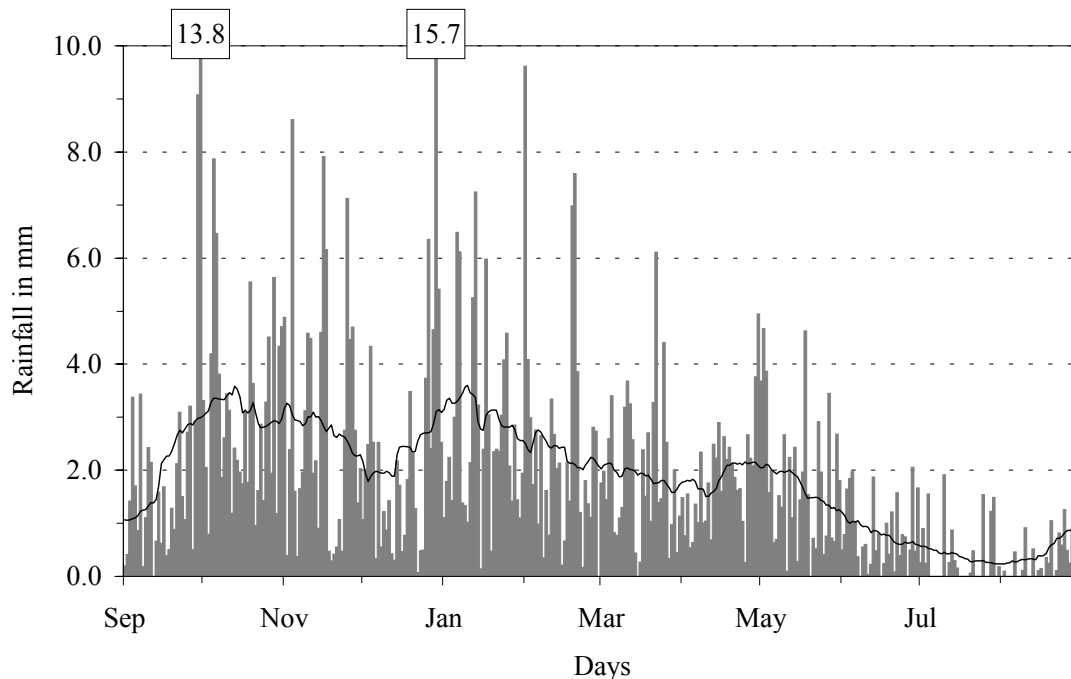


Figure 4.1: Average daily rainfall at Almudaina over the hydrological years 1971-1998. Drawn line represents the 31-days central moving average.

Table 4.2: Monthly rainfall statistics for Almudaina (hydrological years 1971-1998)

	Sep	Oct	Nov	Dec	Jan	Feb	Mar	Apr	May	Jun	Jul	Aug	Tot.
<i>Rainfall totals (mm)</i>													
Mean	65	96	86	76	86	72	60	55	55	24	12	12	698
St. Dev.	98	98	91	91	92	123	63	48	54	27	17	21	244
Skewness	2.5	1.7	1.2	2.3	1.3	4.0	1.2	1.2	1.4	1.3	1.2	3.1	0.4
<i>Rainfall occurrence (days)</i>													
Mean	2.5	4.3	3.9	4.3	4.2	3.5	3.6	4.4	3.9	1.9	0.8	1.1	38.2
St. Dev.	2.2	2.7	2.3	4.4	3.6	2.9	2.2	2.4	3.2	1.8	1.2	1.5	10.1
Skewness	0.6	0.7	0.0	1.0	1.2	1.5	0.5	-0.1	0.3	0.9	1.8	1.2	0.1

The bulk of rainfall is delivered in the period between October and February. On average, these months contribute each more than 10% of the mean annual precipitation (415 out the total of 698 mm). This seasonality is the result of the occurrence of the *temporal de Levante*. The dominance of this system for the rainfall in Almudaina can be traced in the rainfall records as most of the rainfall events are accompanied by easterly winds stemming from the Mediterranean. In the fall this phenomenon is relatively short-lived but results in secure and high-intensity rain as the intrusion of cold air over the warm Mediterranean may lead to extremely unstable atmospheric conditions (the so-called *gota fría*). In the winter months the weather system is more tenacious but results in less intensive rain as can be seen in Figure 4.1.

The importance of the *temporal de Levante* is underscored by the fact that a significant correlation exists between the total annual precipitation and the largest rainfall event ($R^2=0.50$, $N=27$, $P < 0.001$). The largest rainfall event is defined as the maximum collected during a single event of prolonged rainfall for each hydrological year. Such events of prolonged rainfall or *tandas* are capable of delivering substantial parts of the total annual rainfall (in the range of 30 to 50%, La Roca, 1992). In Almudaina, this was the case for the above average wet years of 1986-1987 and 1992-1993. With the last event that occurred in the month of February, the monthly total rainfall of 638 mm was nearly as large as the average annual rainfall over the period 1971-1998.

Table 4.3: Seasonal statistics for the rainfall events at Almudaina (hydrological years 1971-1998)

	SON	DJF	MAM	JJA	Entire period
<i>Number of events</i>					
	169	159	191	76	595
<i>Duration (days)</i>					
Mean	1.7	2.1	1.7	1.4	1.7
Standard deviation	0.9	1.5	0.9	0.6	1.1
Maximum	5	9	5	3	
Contribution (%)	27	32	31	10	
<i>Event total (mm)</i>					
Mean	37.7	41.4	23.8	17.4	31.7
Standard deviation	66.0	69.0	32.4	15.7	54.3
Maximum	441.0	553.2	207.1	80.1	
Contribution (%)	34	35	24	7	
<i>Maximum over 24 hours (mm)</i>					
Mean	25.1	25.1	16.7	14.8	21.1
Standard deviation	34.0	31.4	18.0	12.2	27.1
Maximum	204.0	240.5	128.8	59.8	
<i>Rainfall period intensity RPI (mm·d⁻¹)</i>					
Mean	18.2	16.1	12.5	12.6	15.1
Standard deviation	21.9	16.5	11.0	9.4	16.2
Maximum	147.2	105.0	66.2	41.5	
SON: September, October, November					
DJF: December, January, February					
MAM: March, April, May					
JJA: June, July, August					

The longest duration was 9 days for an event in February 1980 with a total of 122 mm. The largest event, in February 1993, delivered 553 mm divided over 8 days (Table 4.3). The lowest annual maximum for the period 1971-1998 was observed during the same month in the extremely dry year of 1983-1984. In this year only 30 mm fell, divided over two days.

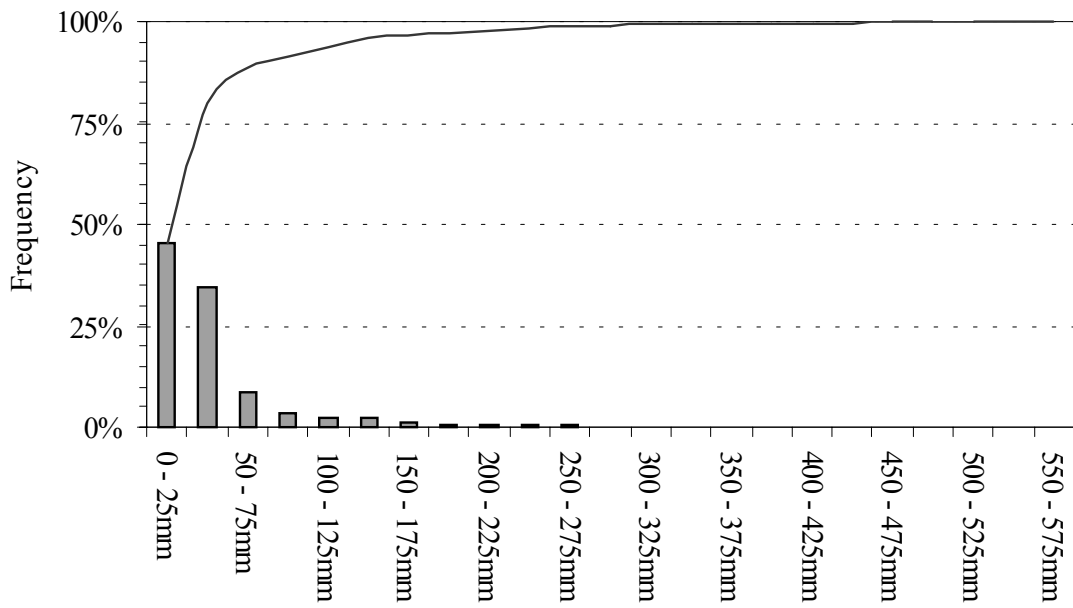


Figure 4.2: Relative frequency distribution of the event totals over the hydrological years 1971-1998

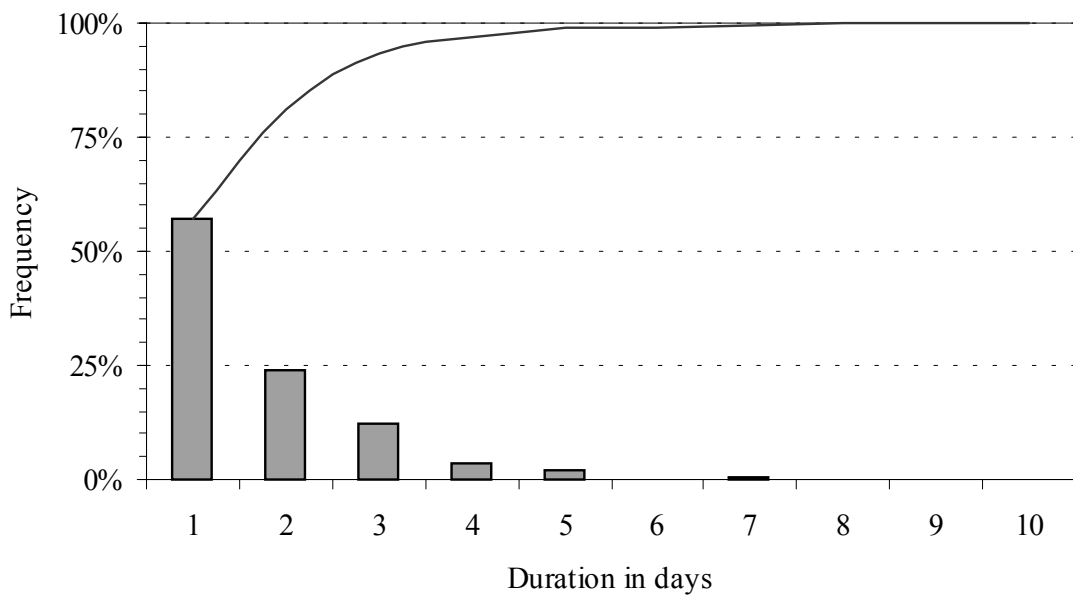


Figure 4.3: Relative frequency distribution of the event duration over the hydrological years 1971-1998

The 595 events of Table 4.3 represent 1032 raindays over a total duration of 9862 days. Of these events, only 437 experienced rain for more than one day. Consequently, the

mean duration of a wet spell (*MDWS*) is 1.7 days. The average event total over the same period amounts to 31.7 mm but seasonal differences are manifest in the average duration and the rainfall totals (Table 4.3). In winter, the rainfall totals and duration are on average the highest but also the most variable. If the average rainfall intensity per event or *rainfall period intensity (RPI)* is considered, the winter rainfall has a lower intensity and a smaller variation than the rainfall during the fall. During the spring and summer, the average duration and accumulated rainfall decrease. This reflects the relative increase of more sparsely occurring short-lived, high-intensity events (thunderstorms) at the expense of the more persistent rainfall. Combined with the frequency distributions of Figure 4.2 and Figure 4.3, it must be concluded that, regardless of the season, most events are short-lived and that the collected rainfall totals are highly variable.

Because of the short lifespan of the rainfall periods, a good relation exists between the 24-hour maximum and the event total. For the maximum event totals of each individual hydrological year, the total amount explains 82% of the variance for the maximum 24-hour rainfall. This supports the contention of La Roca (1992) that the events are usually short and dominated by a high-intensity rainstorm.

4.2.2 *Extreme rainfall events for Almudaina*

No trends or deviations can be found by the evaluation of the precipitation record of Almudaina over the years 1971–1998 and by its comparison with the incomplete antecedent record over the years 1954–1971. By absence of such a trend, the probability on triggering rainfall can be estimated from the frequency distribution of extreme rainfall. It is obvious that the main interest is placed in the positive deviations, i.e. the larger rainfall depths, since these extremes are more likely to induce critical pore pressure conditions than average circumstances. The likelihood of extreme events is based on the observations over the available record. In this manner, it is possible to define the statistically expected average time between events of a similar magnitude, the *return period* or *recurrence interval*. Evidently, the length of the observation record and the appropriateness of the technique and assumptions determine the possibility of deriving meaningful statistics. It is always questionable to extrapolate the findings beyond the length of the available record as the findings of Patton & Baker (1977) demonstrate. Therefore, the aim of this section is merely to characterise the events in the recent past by their magnitude and frequency.

All frequency histograms of the rainfall duration and depth can be approximated by positively skewed or logarithmic distributions. Whereas the length of a dry or wet spell is a discrete variable, the rainfall total can be considered as continuous. For the highest values that are present in the tail of its distribution, the observations will be more or less independent and can be evaluated by an *extreme value series* in which only the extremes for a given length of time are included (Buishand & Velds, 1980). The extreme value series specifies the period that a given quantity is on average exceeded once.

One of the asymptotic probability distributions for extreme value series is the widely used Gumbel-distribution (Clarke, 1994; Buishand & Velds, 1980). The base of the Gumbel-distribution is a logarithmic transform of the time axis and on this transformed

scale a linear shape of the distribution is assumed. Because it is a special and simplified form of a more general distribution of extreme events, it is also referred to as the *Type I*-distribution to distinguish it from other particular types that are described by the Cauchy- and the Weibull-models (respectively Type-II & Type III; Buishand & Velds, 1980). The Gumbel-distribution is, however, capable of describing the data of Almudaina adequately and has been preferred because of its simpler form.

For the cumulative Gumbel-distribution, the frequency of a rainfall depth of magnitude x , $F(x)$, is equal to the cumulative probability, P , on all depths $\leq x$, or

$$F(x) = P(x \leq x) = \exp(-\exp(-y)), \quad (4.1)$$

where $y = a(x-u)$, which is the *reduced variate*. Whenever the reduced variate $y \approx 0$ ($x \approx u$), the average frequency of x is less than once every year (Buishand & Velds, 1980). The parameters a and u define the shape of the Gumbel-distribution.

The maximum, observed for each time increment in the extreme value series, is denoted by \underline{x} . The return period, T_E , for \underline{x} exceeding an arbitrary level x is given by

$$T_E = 1 / P(\underline{x} > x) = 1 / [1 - F(x)]. \quad (4.2)$$

This return period is applicable to the extreme value series in which only the maxima are considered.

The Gumbel-distribution has been fitted to the data by rearranging the observed maxima in ascending order. For the unknown frequency distribution of the population, the estimated frequency, $E\{F(x)\}$, can be calculated by dividing the rank number of an event, i , in the ascending extreme value series by the number of observations that is increased by one

$$E\{F(x)\} = \frac{i}{(N+1)}. \quad (4.3)$$

So, by introducing the estimated frequency of Equation 4.3 into Equation 4.1, the reduced variate y for the observed maximum event, x_i , can be expressed by a function of the form

$$y = a(x_i - u) \approx -\ln\left(-\ln\frac{i}{N+1}\right). \quad (4.4)$$

By plotting x_i versus $y \approx -\ln[-\ln\{i/(N+1)\}]$, all data points should fall on a straight line if the observations comply with a Gumbel-distribution. Subsequently, the parameters a and u of Equation 4.4 can be determined from the best fit of a linear regression of x_i on y . This offers the possibility to relate the observed rainfall depth to an average return period. Alternatively, the total for an extreme event with an arbitrary return period within the observation period can be obtained.

In Figure 4.4 the maximum rainfall depth that was collected during a single event for each individual year over the period 1971-1998 has been plotted as the variable x_i against the reduced variate y as given in Equation 4.4. The observed events are well approximated by a Gumbel-distribution that is represented by the drawn line. The dashed lines represent the 95% confidence interval. The stretch of this confidence interval is

narrow since more than 98% of the variance is explained by the Gumbel-distribution. The return periods and the associated rainfall depths are listed in Table 4.4 and Figure 4.4.

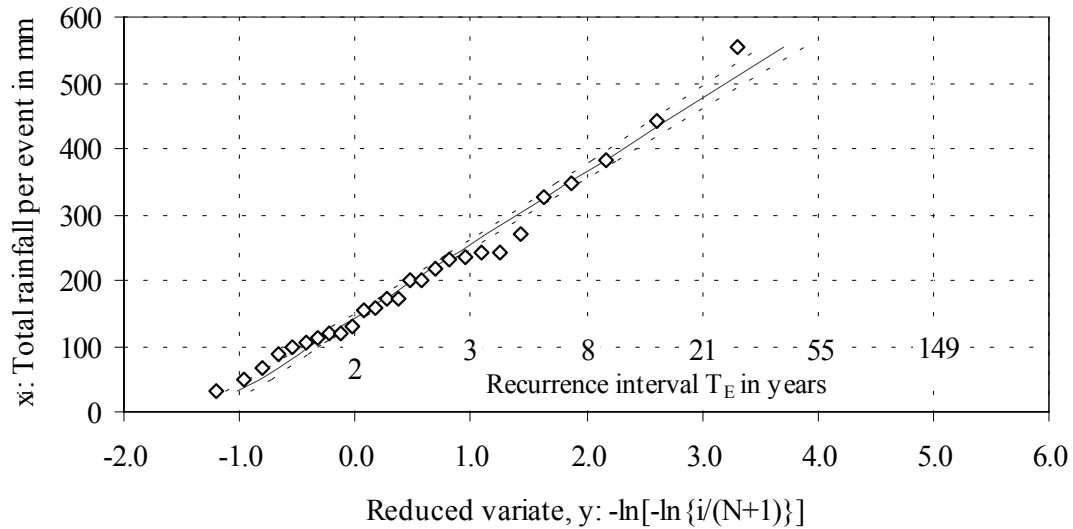


Figure 4.4: Fit of the Gumbel-distribution to the yearly extremes of event totals over the hydrological years 1971-1998 ($N=27$, $R^2=0.98$)

Table 4.4: Expected return periods and rainfall totals as calculated from the Gumbel-distribution for Almodaina over the hydrological years 1971-1998 (all relations $N=27$ and $R^2=0.98$)

Return period T_E (years)	Expected Extreme rainfall (mm)		
	24-hours	Event	Annual
2	96	184	662
3	120	242	777
4	135	280	851
5	146	307	905
10	178	389	1067
15	197	435	1158
20	209	468	1222
25	219	493	1271
50	250	569	1422
100	280	645	1573

The Gumbel-distribution can be applied to other extreme value series as well. In Table 4.4, the return periods are given for the 24-hour maxima and the annual rainfall. La Roca (1992) calculated the return periods for these statistics and for the maximum events, which she defined as the rainfall sums over 2 to 6 days, by means of the same distribution. Because her analysis is based on differently grouped data for a different record length, her results deviate from those in this study. The most marked differences are found for the return periods for the annual rainfall, which in her case are much shorter than the intervals calculated here. This should be attributed entirely to the shorter record

length and the calendar years she used. For the maximum rainfall per event and for the 24-hour totals, the differences are less marked. Overall, the return periods presented here are similar to those presented by La Roca (1992) or are slightly lower.

4.2.3 *Representativeness for the study area*

The long-term record of daily precipitation provides the basic model input. The significance of the model input is, however, dependent on the representativeness of the long-term record for the nearby study area. Here, the representativeness will be analysed by relating the daily rainfall of the station at Almudaina with data collected by tipping bucket pluviometers in the study area during the years 1995-1999.

In the study area, the rainfall is recorded automatically by two tipping bucket pluviometers. Both devices have a resolution of 0.2 mm and the rainfall is registered as multiples or *tips* over a fixed period. The accuracy of the rainfall intensity is dependent on the time over which the rainfall is aggregated. One of the tipping buckets records the number of tips every minute, if rainfall occurs. It is located at 450 m.a.s.l. on the W exposed side of the barranco (referred to as the LGM-site; Appendix 1). The other tipping bucket records the accumulated tips for every hour. It is part of an automated meteorological station and it is located in the open at an elevation of 435 m.a.s.l., on a ridge south of a topographical depression known as “the Hollow” (Appendix 1). From the LGM-site, data are available since December 1995. At the Hollow, the meteorological station is in function since September 1996. In order to allow a comparison between the three locations – LGM-site, Hollow & the station at Almudaina proper – the data of the tipping buckets have been aggregated to daily and event rainfall totals.

In the analysis of the tipping bucket data, all available data until the 31st of March 1999 are included. Over this period, both stations have considerable gaps in their records as can be seen in Table 4.5. The available records represent around 60% of the continuous record of Almudaina. The observed events at Almudaina are given in Figure 4.5. Over the entire period of 3 years and 4 months, 2149 mm fell over 161 raindays. Over the period, the average collected annual rainfall was below average (640 against 698 mm), but the total of the hydrological year 1996-1997 was above average (810 mm). Because of the regular occurrence of events from the fall of 1996 till the spring of 1998, the frequency of raindays over this period is higher than the average over the period 1971-1998 (13.2 vs. 10.5%). As observed in the long-term record, most of the rainfall is concentrated in the fall and winter. With regard to the comparison of the available data over the available period this means that most of the rainfall results from events that are more prolonged and less intense than the average conditions over the long-term period between 1971-1998 (a MDWS of 1.8 compared to 1.7 days and an average RPI of 11.8 compared to 15.1 mm.d⁻¹).

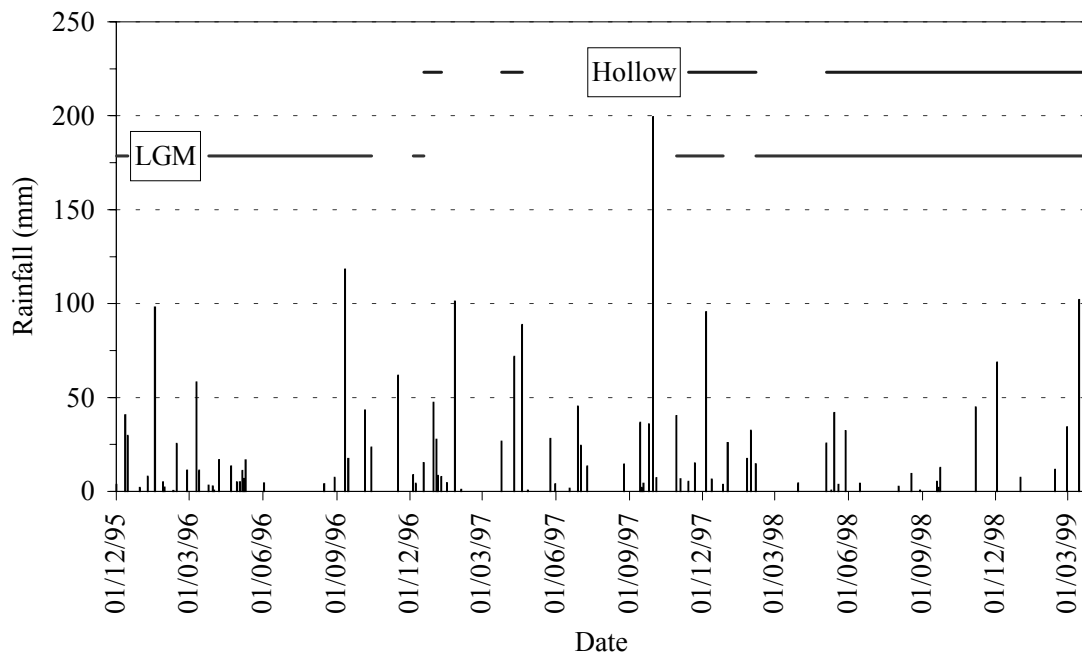


Figure 4.5: Event rainfall for Almudaina over December 1995-March 1999 and coverage by the tipping bucket records from the study area

Table 4.5: Data recovery of daily rainfall data from the tipping buckets in the study area relative to the INM-station of Almudaina

	Duration days	Recovery in %	Period
LGM-site	1217	69	12/1995 – 03/1999
Hollow	851	63	09/1996 – 03/1999

When the daily data from the tipping buckets and from the station at Almudaina are matched, the difference in resolution between automated pluviometers and the hand-read station becomes apparent. The automated pluviometers record more days with precipitation than the station of Almudaina. Over the period from December 1995 until March 1999, the tipping bucket at the LGM-site recorded 190 days with one or more tips while only 69% of the record is present, compared to 161 raindays at Almudaina over the entire period. Likewise, the tipping bucket at the Hollow recorded 159 raindays from December 1996 onwards. This inconsistency is partly explained by the difference in resolution. Any precipitation in excess of 0.2 mm will result in tips that are duly recorded by the equipment. A large proportion of these unmatched tips is, however, insignificant as they result from condensation and dew. In contrast, the data of the station at Almudaina do not show values smaller than 0.5 mm over this period. Smaller amounts may be recorded as imperceptible or may be neglected altogether. Consequently, they are not entered in the quantitative analysis. This is not the only explanation, however. Even when the events with less than 0.4 mm of rainfall are excluded from the record, the tipping buckets record still more raindays than the station of Almudaina. The probable

cause is the tendency to note the accumulated rainfall over an event to one specific day whereas the automated equipment is rigorous in the division. This is reflected by the increasing agreement between the different locations when the event totals are compared, rather than the mere 24-hour totals. The regressions of the tipping bucket data on those of the station at Almudaina are summarised in Table 4.6 and depicted in Figure 4.6. All events that precede or succeed days with missing values have been omitted from the analysis.

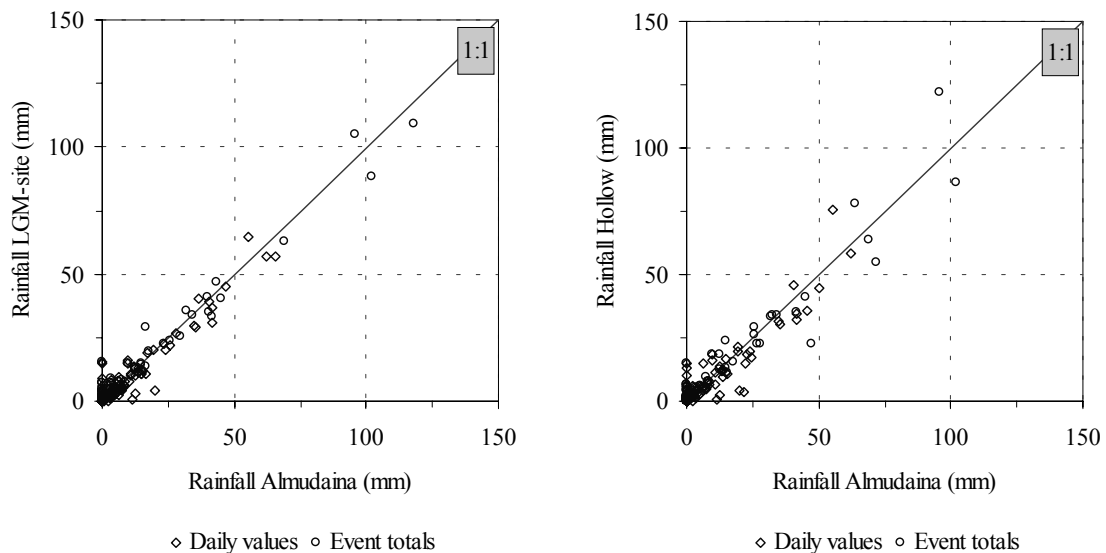


Figure 4.6: Regression of the tipping bucket data on the rainfall from Almudaina: A) LGM-site, B) Hollow

Table 4.6: Regression of the tipping bucket data on the daily record of Almudaina

	Slope (-)	Intercept (mm)	R ² (-)	N (-)
LGM-site: December 1995 – March 1999				
Daily	0.89	0.64	0.92	190
Event	0.93	1.06	0.97	102
LGM-site: September 1996 – March 1999				
Daily	0.88	0.89	0.88	127
Event	0.93	1.27	0.97	70
Hollow: September 1996 – March 1999				
Daily	0.89	0.62	0.87	159
Event	0.95	0.97	0.93	79

From the comparison of the daily and event-totals of the different station, it appears that the rainfall at the LGM-site is more similar to that of Almudaina than the rainfall at the Hollow. The difference in similarity is, however, small and the agreement between the locations is generally high. The closer agreement between the rainfall at the LGM-site

and at the station at Almudaina is not entirely the result of the longer data record. Although the explained variance and the slope and intercept of the regression on the daily values are comparable for both locations from December 1996 onwards, the regression of the event-totals remains better for the LGM-site (Table 4.6). The obvious reason for the similarity between the rainfall at Almudaina and at the LGM-site is the proximity of both locations and the equally large influence of the Sierra de Almudaina. Because of its sheltered position, the rainfall totals at the LGM-site tend to be smaller than those collected at Almudaina. At the Hollow, the deviations from the 1:1-slope are larger and less systematic. The largest positive deviation occurred between 3 and 6 December 1997. The collected rainfall amounted to 105.1 and 122.2 mm at the LGM-site and the Hollow respectively. At Almudaina a total of 95.7 was collected over the same period. The situation was more or less reversed between 11 and 13 March 1999, when 102.1 mm was collected at Almudaina against 88.1 and 86.2 mm at the LGM-site and the Hollow respectively. The event between 28 and 30 December 1996 resulted in a similar absolute difference as a total of 47.3 mm was collected at Almudaina against a mere 22.4 mm at the Hollow.

Because of the discrepancy in the temporal resolution of the collected data, the unmatched daily values are in the order of 15 mm. The only event recorded by both tipping buckets, without match at the station of Almudaina has a similar order and occurred on the 16th of May 1998 (15.6 and 14.6 mm at the LGM-site and at the Hollow respectively). At Almudaina, this event was possibly added to the preceding rainfall on the 14th of May as the total on that day is 41.9 mm compared to 33.3 and 35.2 mm at the respective tipping bucket locations.

A closer agreement is observed between the two locations with tipping buckets (Table 4.7 & Figure 4.7). For the daily and event-totals the regressions are consistent and explain over 99% of the observed variance with a slope near unity. The values are located directly on and around the 1:1-slope. The largest deviation is the already mentioned event of December 3-6, 1997. For this particular event, the rainfall depth seemingly decreased in the direction of the Sierra de Almudaina.

Table 4.7: Regression of the tipping bucket data from the Hollow on those of the LGM-site

	Slope (-)	Intercept (mm)	R ² (-)	N (-)
Daily	0.92	0.11	0.99	138
Event	1.07	-0.02	0.99	78

Based on these comparisons, the rainfall totals appear not to be different over the available period. All linear regressions explain over 90% of the variance between the event-totals and all slopes are close to unity what suggests that the daily rainfall data from the stations are interchangeable.

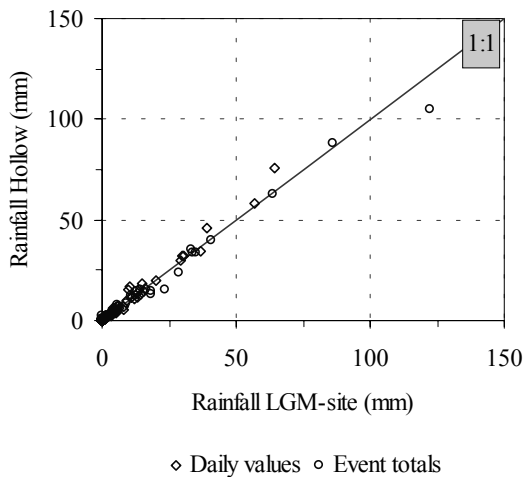


Figure 4.7: Regression of the tipping bucket data - Hollow vs. Al mudaina: A) daily and B) event totals

4.2.4 Within-storm characteristics

The hourly tipping bucket data can be applied to describe the within-storm characteristics over the period 1995-1999. These statistics will not serve as direct model input but provide information on the seasonal differences in rainfall intensity, duration and persistence that control the surface processes of interception and infiltration.

The tipping bucket records can be considered as representative for the entire study area but suffer from a limited temporal support. This raises the question to what extent the more detailed records of the tipping buckets are representative for the within-storm dynamics over longer periods. As remarked above, the overall conditions at Al mudaina differ over the period December 1995 – March 1999 from the average conditions over the 27 hydrological years between 1971 and 1998.

Table 4.8: Test for equality of means (t-test) and variance (F-test) between the long-term period September 1971-August 1995 and the short-term period December 1995-March 1999 as covered by the rainfall record from the station of Al mudaina. Significant deviations from H_0 at the 95% confidence level are italicised.

	Mean	Variance	N	F	$F_{crit.}$	t	$t_{crit.}^*$
	<i>RPI ($mm.d^{-1}$)</i>						
Long-term	15.7	285.7	507	2.23	1.33	-2.68	1.97
Short-term	11.9	128.3	89				
	<i>Duration (days)</i>						
Long-term	1.73	1.29	507	1.02	1.29	0.68	1.96
Short-term	1.82	1.26	89				

Based on the test statistics of Table 4.8, both the mean and variance of the rain period intensity (RPI) differ significantly at the 95% confidence level. For the duration, no significant differences are found. The probable cause for the difference in the RPI

between the two records lies in the more homogeneous (or less extreme) conditions that prevailed during the shorter period. The fact that there is no apparent difference in duration suggests that this quantity is less biased than the event total. This is confirmed by the maximum duration of 5 days in the short-term record, representing 99% of the cumulative frequency distribution over the long-term period. All by all, the short-term record represents rainfall events with on average smaller rainfall intensities than those of the long-term record.

For the analysis, the records from the Hollow and the LGM-site have been merged into one data set in which the data from the Hollow replenish the latter. Rainfall is represented by the hourly totals, which are grouped into events of prolonged rainfall. These are periods with intermittent showers of more than 0.2 mm within 24 hours of each other. Because of the difference in temporal resolution, the tipping bucket record also includes many low-intensity short-duration events that are absent in the record of Almudaina. To eliminate the influence of these insignificant rainfall events, all events with a total of less than 1 mm have been excluded. The resulting data set includes 74 events that match with 70% of the record from Almudaina.

From the data set, the statistics for the prolonged rainfall events have been calculated (Table 4.9). These statistics include the duration and rainfall total, the observed maximum intensity and the persistence. Persistence is defined here as the ratio between the total duration of an event, including the dry period between rainfall, and the period with actual rainfall. It has units of hours over hours and gives the average duration of dry periods within one event.

Table 4.9: Within-storm characteristics over the period December 1995-March 1999

	SON	DJF	MAM	JJA	Entire period
<i>Number of events</i>					
	17	25	24	8	74
<i>Duration (days)</i>					
Mean	11.9	15.2	15.1	5.5	13.4
St. Dev.	12.8	11.2	17.0	4.3	13.4
Maximum	53	40	58	15	
<i>Total (mm)</i>					
Mean	20.5	17.2	20.4	9.8	18.2
St. Dev.	27.2	22.7	23.9	11.7	23.2
Maximum	108.9	105.1	88.1	37.1	
<i>Persistence (hr·hr⁻¹)</i>					
Mean	3.7	3.6	2.7	1.9	3.2
St. Dev.	2.7	2.0	1.9	1.8	2.2
<i>Hourly intensity (mm·hr⁻¹)</i>					
	20.9	7.9	13.4	15.0	

Due to missing data, the data set underestimates the contribution of the summer and fall between December 1995 and March 1999. Yet, even when the number of events and the

total collected rainfall are adjusted to the different record lengths, the winter and spring still have the largest contribution, although the differences in rainfall depth between these seasons and the fall are small. For all seasons, the variability in duration and rainfall depth is high (Table 4.8). Yet, from the comparison of the within-storm characteristics it appears that some seasonal differences exist. Particularly the observed winter rainfall deviates through its longer duration and below-average rainfall total. This implies that, during the winter, rainfall is delivered as a more continuous low-intensity shower as the observed maximum intensity testifies. Although the spring rainfall has an equally large average duration, its variation is larger and the persistence lower. This means that an event most times includes a single rainfall period and that the atmospheric conditions repeatedly lead to similar event totals. As a possible explanation for these characteristics, the occurrence of isolated thunderstorms during this season could be mentioned. For the other seasons, the absence of rainfall in the summer is manifest. The autumnal rainfall is above all characterised by its variability. It consists of a succession of high-intensity rainfall separated by dry periods of different length. Of the available events, the largest event of every season is represented in Figure 4.8, which represents these seasonal differences. On a monthly and seasonal scale, the accumulated rainfall and number of raindays reflect the differences in intensity whilst the mean duration of a wet spell reflects the differences in persistence and duration (Table 4.2 & Table 4.3).

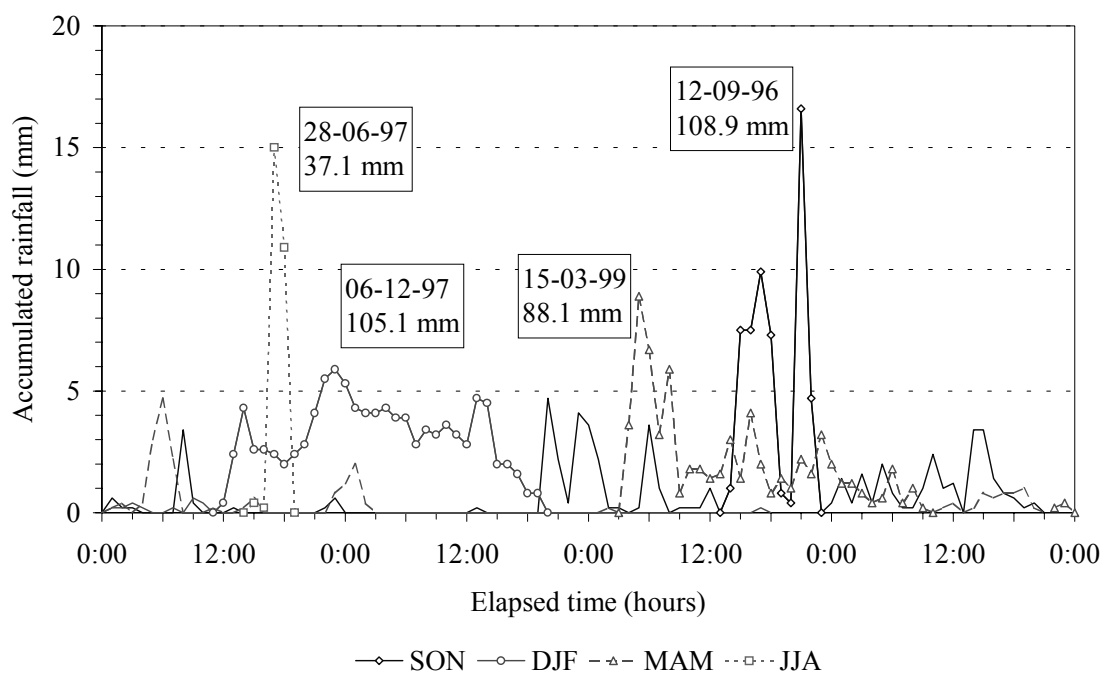


Figure 4.8: Observed maximum storms over the period December 1995-March 1999 per season. Symbols demarcate the period of the maximum continuous rainfall.

The seasonal differences in the within-storm characteristics have several implications for the hydrological processes in the study area. The low-intensity rainfall during the winter contrast with the high-intensity events in the period from the late spring till early fall. In

summer, the relative difference in intensity within an event is the highest. Yet, the importance of these events is low since the delivered rainfall totals are much smaller in the spring and fall. On average, prolonged rainfall does not extend beyond 40 hours or the 1.7 days of the MDWS for the daily data. Each period of prolonged rainfall contains some intermittent showers that constitute around 60 to 70% of the event time. Because the rainfall is well-distributed over an event, the 24-hour totals, as available at Almudaina, provide a reasonable estimate of the average rainfall intensity during an event. The daily data, however, provide no information on the maximum intensity that controls most of the hydrological surface processes. For the hourly tipping bucket data, the maximum intensity can be plotted against the event total (Figure 4.9). On a log vs. log-scale, the relation is linear, with an explained variance of 71.8%. The predicted maximum intensity, I_{Max}^* , is given by

$$\ln(I_{Max}^*) = -0.4097 + 0.6644 \cdot \ln(Tot_{Event}). \quad (4.5)$$

If the event totals from the tipping bucket are considered as a substitute of the event totals of the daily rainfall record at Almudaina, the relation could be applied to approximate the maximum hourly rainfall intensity.

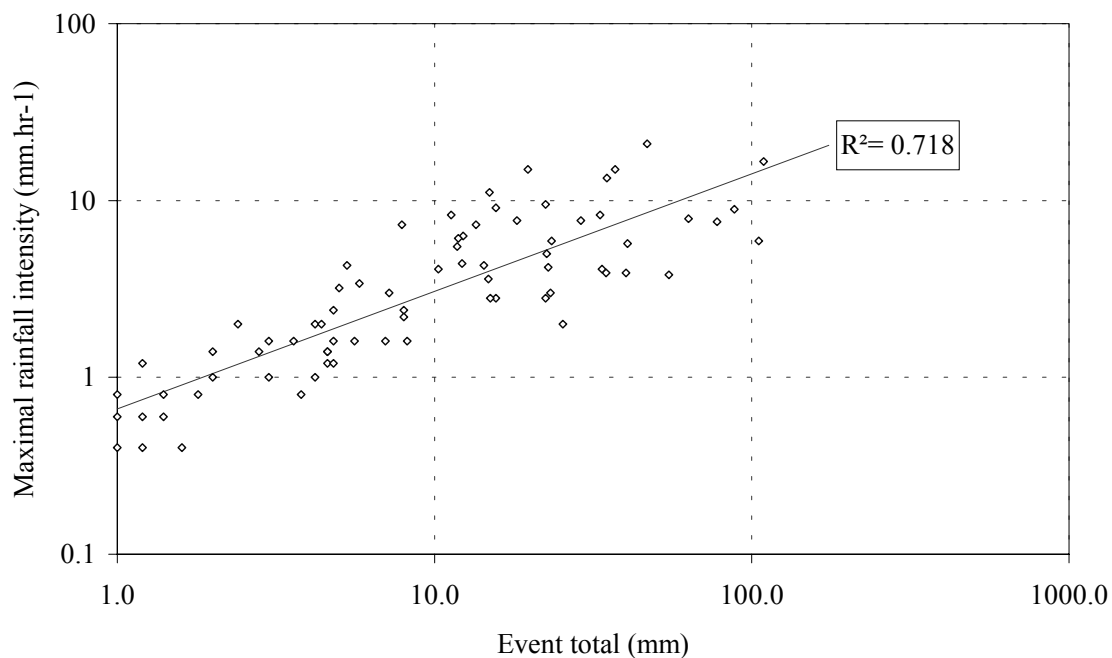


Figure 4.9: Relation between maximum intensity and event total

4.2.5 Regional trends

In the previous section, the temporal characteristics of rainfall at Almudaina and its extremes have been evaluated. The question that remains to be answered is to which extent the local statistics are part of a spatial pattern in the upper basin of the Río Serpis.

This question concerns the rainfall totals, its frequency and persistence and the recurrence interval of extreme events.

In her study of 1992, La Roca processed the data of 81 stations that cover a considerable part of the coast and inland between Valencia and Alicante. These included ten stations in the upper basin of the Río Serpis, where 24-hour totals of rainfall are collected. La Roca applied the Gumbel distribution to nine of these ten stations with records of variable length in order to define the return periods of different rainfall totals. Five stations have a record length that is comparable to that of Almudaina. The information for these stations has been summarised in Table 4.10, the locations are given in Figure 4.10.



Figure 4.10: Location of rainfall stations in the Alcoy region

Because of the perpendicular orientation of the Pre-Betic mountain ranges on the NE rain-bearing winds of the Mediterranean, the distribution of rainfall in the Valles de Alcoy is characterised by a strong orographic influence (Section 2.2). Lower annual rainfall totals are found in the lee of the mountain ranges and in the floodplain of the Río Serpis (Table 4.10). In general, a gradient is found that increases the mean annual rainfall with 60 mm for every 100 m of added elevation but it remains unknown whether this relationship holds for the higher elevations where observations are absent (Figure 4.11C; La Roca, 1992). The swell in annual precipitation is the result of the increasing probability on extreme rainfall events that are associated with the *temporal de Levante*. Along the northface of the Sierra de Aitana, the amount of daily and event rainfall with an expected return period of 10 years increases as the graphs illustrate (Figure 4.11A & B). A similar relation between the local weather system, extreme rainfall and annual rainfall totals was observed by Romero *et al.* (1998, 1999).

Table 4.10: Locations and summary statistics for the climatological stations in the Valles de Alcoy (sources: La Roca, 1992; COPUT: Atlas Climàtic, 1994). Location numbers refer to Figure 4.10.

Nr.	Station	INM station Nr.	Mean annual rainfall in mm	Gumbel-Distribution	
				Record length (years)	Goodness-of-fit (-)
44	Agres	8064	659	24	0.98
49	Alcoy	8059, 8059b	495	29	0.99
73	Alcoleja	8060	706	18	0.82
46	Almudaina	8066	630	20	0.97
37	Beniarrés (reservoir)	8067	643	27	0.98
51	Gorga	8063	586	35	0.98

*: based on event rainfall totals

Similar to the rainfall in Almudaina, the majority of the precipitation falls in the autumn and winter. In contrast to the rainfall patterns at Almudaina, however, La Roca (1992) observed some persistent low-intensity winter rainfall in the daily records for the stations of Alcoy and Gorga. She attributed this to the direct exposure of these stations to western winds from the Atlantic.

During the later spring and early summer, rainfall is limited to a localised thunderstorm that forms from the convection of warm and moist air from the Mediterranean. During the remainder of the summer, conditions are extremely stable and no considerable rainfall occurs.

The findings of La Roca (1992) can be evaluated by plotting the observed event rainfall over the available period in a scatterplot. Albeit the missing values, the records are considered complete enough to warrant this approach. This is based on the fact that for the missing periods, which over-represent the month of August, rainfall is usually negligible. Hence, the sample size should be large enough to provide an unbiased estimate of the rainfall distribution. By aggregating the daily rainfall into event totals, the error that could stem from the artificially discretised values is reduced. Thus, the rainfall of two stations can be compared and deviations, other than a random scatter, can be discerned from the departure of the 1:1-slope (Figure 4.12). This method has the additional advantage that the entire rainfall record is analysed instead of the extremes only. The records of four stations, listed in Table 4.11, have been examined of which La Roca (1992) states that they are subject to different rainfall conditions. The distance between the stations is less than 15 km and all are located at elevations between 545 and 586 m above sea level. Of the available records, the record of Gorga is the shortest and suffers from the missing values that are present in the data from the other stations for the period before 1971. With the available data, five comparisons between stations can be made. In order to use all consistent data in the comparison between Almudaina and Gorga, the combined series of 1954-1958 and 1965-1968 have been used.

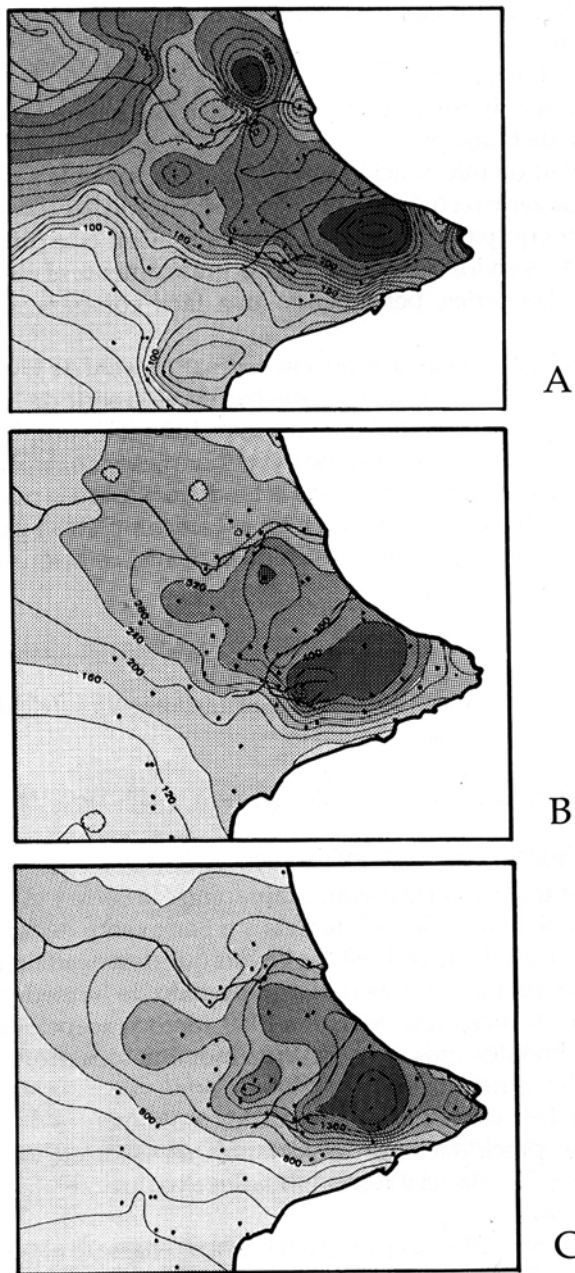


Figure 4.11: Spatial distribution of the expected rainfall with a recurrence interval T_E of 10 years for A) 24-hour maximum, B) event total, C) annual total (La Roca, 1992)

The results of the comparisons are given in Table 4.12. The relationships are depicted graphically in Figure 4.12. The relations exhibit a relatively large scatter in the lower range of the data (<100 mm). Over the entire dataset, the relationships tend to be linear. The goodness-of-fit of the linear regressions, of which the intercept has been set to zero, ranges from 72.5 to 93.1%. In the relation between Almudaina and Alcoy Juan XXIII, extreme events have a large influence on the slope of the linear regression. In all cases, the event rainfall in Alcoy is on average the lowest and, as a result, the slope is below unity. The event rainfall in Almudaina is on average the highest. The relationship between Almudaina and Gorga has a slope that is the closest to unity, indicating that the

rainfall at these two locations is the most similar. The goodness-of-fit is, however, the lowest. This is caused by the large spread in extreme events what reflects the influence of the Sierra de Almudaina separating both locations. The outliers for which the rainfall in Gorga is the double of the rainfall in Almudaina, occurred in the months of November and December. In contrast, the relation between Gorga and Alcoy is consistent but, in Gorga, extreme rainfall is always higher. Between the two stations located in Alcoy, the relation is strongly linear but exceeds the 1:1-slope. Hence, the nature of rainfall in Alcoy and at the station Alcoy Juan XXIII is similar but the latter collects higher totals.

Table 4.11: Data recovery INM-stations

Station	Nr.	Record length	Recovery	Complete series
Alcoy	8059	1950-1987	88	1963-1985
- Juan XXIII	8059b ¹	1978-1997	96	1978-1996
Almudaina	8066	1954-1998	91	1971-1998
Gorga	8063	1954-1971	96	1954-1971

¹: Station Alcoy Juan XXIII (8059b), operative since 1978

Table 4.12: Cross-table of regressions for the stations of Table 4.11

Station		R ²	α	N
Almudaina	Gorga	0.725	0.966	195
	Alcoy Juan XXIII	0.787	0.756	319
	Alcoy	0.731	0.582	500
Alcoy	Gorga	0.747	1.344	265
	Alcoy Juan XXIII	0.931	1.251	197

The relationships of Table 4.12 and Figure 4.12 include only the events that are felt in more than one of the analysed stations. This implies that only the events with a larger spatial distribution are included. Yet, some of the rainfall will not be felt in all locations and this may form an equally important part of the spatio-temporal distribution of precipitation. In Table 4.13 the total number of events and the number of matches are given. The agreement between the paired stations is expressed as the ratio between the number of matches and the total number of observed events. If the agreement is high, the two values will approach 100%. If the values are low and disproportionate, the variation is high and the records have a poor resemblance. Of the unmatched events the maximum rainfall depth is given.

From the comparison of the data it appears that the stations located in Alcoy are the most similar. This was to be expected since the distance between them is the shortest and, consequently, the variation in rainfall stems from the same sources. Still, about 20% of the rainfall events are not matched in the records. This concerns mainly small rainfall events in the months of November till February and high-intensity events of short duration (thunderstorms) in the later part of spring. This is witnessed by the unmatched maximum event that occurred in May.

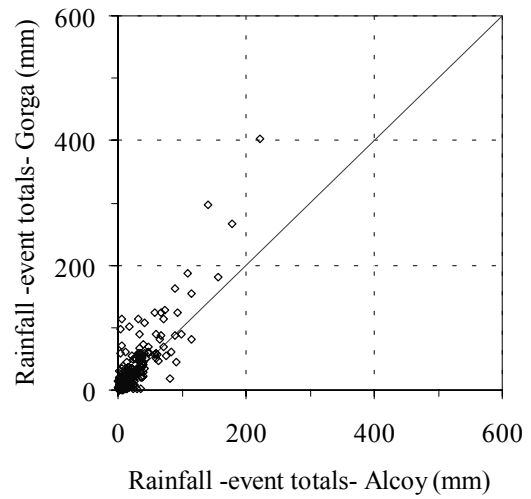
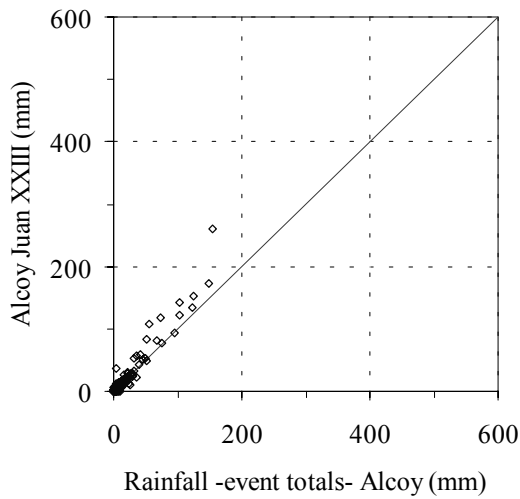
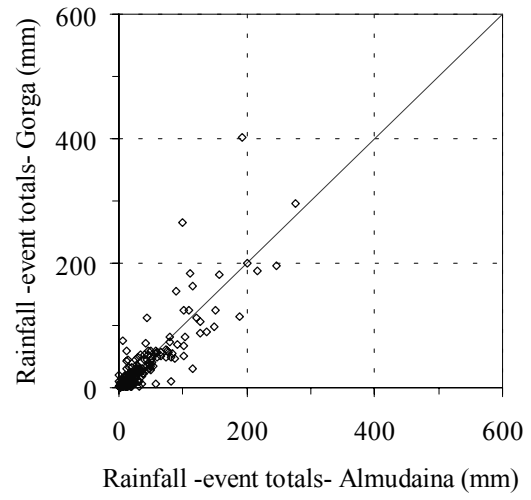
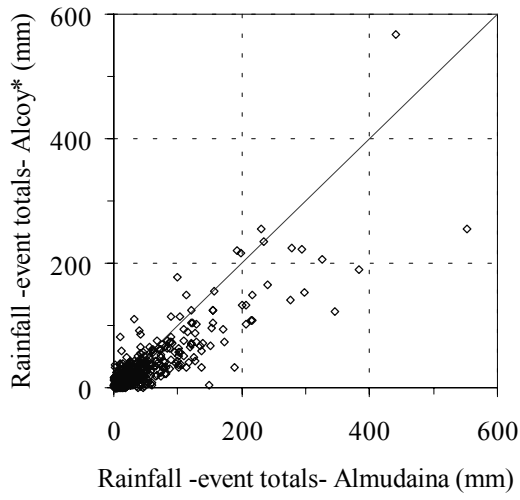
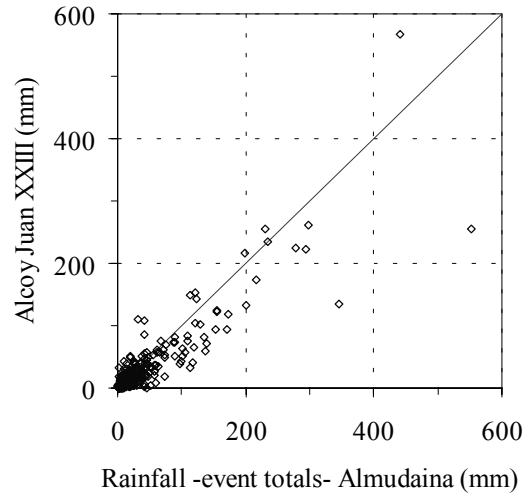
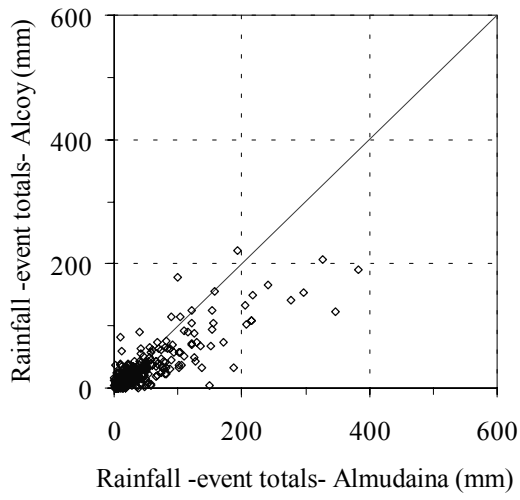


Figure 4.12: Scatterplots of event totals

A similar agreement is found between the stations at Gorga and Almudaina. For them the agreement is respectively 71 and 79%. This stems basically from the prolonged events of rainfall in the fall and winter, which give large rainfall totals. In Almudaina, the unmatched events consist mostly of thunderstorms, which appear to be more frequent here than in Gorga over the analysed period, but a considerable number of unmatched, small rainfall events are also observed during the winter and fall. Given the fact that most of these events are recorded in Alcoy it must be concluded that the station in Gorga is sheltered to some extent by the Sierra de Almudaina against events entering the area from the N and NE.

Table 4.13: Agreement between matched events and the total number of recorded rainfall events

Station Y	N			A		Not matched B			Complete series	
	X	Y	X&Y	X	Y	Max.	Occ.	C		
<i>Station X: Almudaina</i>										
Gorga	155	139	110	71	79	88.0	October	Y	1954-1958, 1965-1968	
Alcoy Juan XXIII	370	566	319	56	86	52.7	April	Y	1978-1997	
Alcoy	282	488	265	54	94	54.3	May	X	1971-1985	
<i>Station X: Alcoy</i>										
Gorga	255	172	150	59	87	31.0	October	X	1963-1971	
Alcoy Juan XXIII	205	215	171	80	83	32.8	May	Y	1978-1985	
	A:	Agreement in %								
	B:	Maximum event								
	C:	Station at which maximum event occurred								

In Gorga, the largest share of events that are not observed in Almudaina occurs also in the fall. The largest unmatched event was recorded in October. It lasted for four days and delivered 88 mm of rainfall with a maximum of 42 mm in 24 hours. Since for this and similar events no rainfall was collected in Almudaina, in contrast to the stations in Gorga and Alcoy, it must be concluded that the northface of the Sierra de Almudaina is sheltered in a corresponding manner against events that enter the basin by the Valle de Seta.

The agreement of the respective stations at Gorga and Almudaina with the stations of Alcoy is much poorer. Despite an agreement of over 85% for the first two stations, the percentage of matched events for Alcoy does not pass the 60%. With the relationships of Figure 4.12, this implies that the zone near Alcoy is less exposed to extreme rainfall than the stations of Gorga and Almudaina. This must be explained by the stronger orographic influence that is felt by the rainfall that enters the basin of the Río Serpis from the Mediterranean (Figure 4.10). When the events approach Alcoy, they are already dampened and the influence of the Sierra de Mariola is felt less. In Alcoy, less than 300 of the mean annual rainfall of 495 mm can be attributed to these events that deliver most of the rainfall in Gorga and Almudaina. The events that are recorded in Alcoy but that are absent in the other stations are probably related to a direct influence of depressions over the Atlantic as proposed by La Roca (1992). This Atlantic influence is larger for the station of Alcoy than for the station Alcoy Juan XXIII and the latter is more exposed to

the high intensity rainfall that dominates in Gorga and Almudaina. As a consequence, the event totals are here larger than for Alcoy proper and have a larger variability. This is clearly shown by the relationship of Figure 4.12 and by the statistics on duration and rainfall totals, which have been summarised in Table 4.14. The influence of high intensity -or more extreme- rainfall can be deduced from the fewer events and higher average intensity in combination with the larger variability.

Table 4.14: Average rainfall statistics for the INM stations considered

Station	Record length* (years)	Events per year (mean)	MDWS (days)		RPI (event totals in mm)			Max. event
			Avg.	St. Dev.	Avg.	Median	St. Dev.	
Alcoy	22	34	1.7	1.2	14.1	24.2	5.5	206.5
-Juan XXIII	19	30	1.9	1.3	18.8	41.6	6.3	567.6
Almudaina	27	22	1.7	1.2	32.9	56.3	15.0	553.2
Gorga	17	22	1.7	1.1	27.3	43.2	12.4	403.0

*: length of the complete rainfall record in hydrological years

The relations and statistics between the various stations appear to confirm most of the findings of La Roca. Towards the west, the annual average rainfall decreases. This is the result of a dwindling contribution of high intensity rainfall associated with the *temporal de Levante*. The lower frequency and magnitude of these events are in the western part of the upper basin of the Río Serpis only partially compensated by a larger influence of Atlantic depressions. Towards the east, the same conditions seldom result in rainfall as can be seen in the records of Gorga and Almudaina. Hence, the Atlantic influence on the rainfall record of Gorga, as mentioned by La Roca (1992), must be of a different order than that in Alcoy. The 26% of the events, observed in Gorga, that are not matched by rainfall in Almudaina, occur in the same period and have similar characteristics as the rainfall in Almudaina. This suggests that, over the period analysed, the differences between these stations are not caused by distinct weather systems but by different entries of saturated air from the Mediterranean into the upper basin of the Río Serpis. In combination with the easier access along the Río Serpis from the NE, the orographic effect by the Sierra de Almudaina results in a net higher precipitation on its northface. No differences exist, however, in the distribution of extreme rainfall for the two stations.

Recapitulating, the spatio-temporal distribution of rainfall in the upper basin of the Río Serpis is characterised by the occurrence of infrequent high intensity rainfall, of which the influence decreases to the west, i.e. at a greater distance from the Mediterranean coast. This rainfall is associated with the temporary presence of a depression above the W Mediterranean. This weather system is known as the *temporal de Levante* and delivers most of the annual rainfall in the period between the September and February. The totals collected during these events constitute an important part of the annual total. The events are short-lived. Even if they extend over several days, a clear maximum event delivers often most of the event rainfall.

In contrast, inland the number of small rainfall events increases. These events are related to depressions over the Atlantic. Although their persistence is similar to the events that are associated with the *temporal de Levante*, they deliver less rainfall. Where they occur,

they may partly compensate for the attenuated influence of the *temporal de Levante*. This means that in the western part of the Valles de Alcoy, the variability in the annual rainfall will be lower. The areas exposed to more frequent high-magnitude events are possibly more prone to the formation of landslides. In the areas with more secure rain, the availability of water could lead to a more prolonged activity. An additional factor in this respect is the occurrence of thunderstorms in the spring and early summer. On top of a wet winter, these events of short duration and average intensity are potential triggers that, because of the convection of unstable air over the mountainsides, operate on a local scale.

4.3 Reference potential evapotranspiration (ET_0)

Over longer time scales, the momentary input of precipitation has to be balanced against the loss of soil moisture by evapotranspiration. This loss of soil moisture is defined by the rate at which water can evaporate at the surface and transpire through the vegetation. Potential evapotranspiration usually refers to the maximum amount of water that can be evaporated from a uniform soil or water surface when the water supply is not a limiting factor (Doorenbos & Pruitt, 1977, Brutsaert, 1982). Eventually, the actual loss due to evapotranspiration is defined by the presence of limiting factors like stomata closure or advection. Because of the complexity that is involved, the relation between the local evapotranspiration by a soil under a vegetation cover and the potential evaporation is most times represented by simple empirical constants, which are commonly known as *crop factors* (k_c). Following this approach, the potential evapotranspiration is a reference potential evapotranspiration, ET_0 , that is defined as the “rate of evapotranspiration from an extensive surface of 8 to 15 cm tall green grass cover of uniform height, actively growing, completely shading the ground and not short of water” (Doorenbos & Pruitt, 1977). This ET_0 depends only on the atmospheric conditions. The specific loss, ET_c in $\text{mm}\cdot\text{d}^{-1}$, by a disease-free crop is then given by

$$ET_c = k_c \cdot ET_0. \quad (4.6)$$

The crop factor combines all effects of the vegetation on the evapotranspiration including those of ground cover and surface roughness. Although the approach is coarse, it is often in balance with the available data. The k_c can be defined as a constant or vary over the year to simulate the crop development during the growth season. In the latter case, different values for the crop factor are specified over 10- to 30-days periods. These values are usually obtained from the comparison of the actual evapotranspiration under a certain crop type at different stages of maturity to the potential evapotranspiration. If this information is unavailable, the crop factors can be obtained from standard values and local information. The values for the various crop factors are discussed in the section on land cover parameters in Chapter 5. In this section, the objectives are to quantify the potential evapotranspiration ET_0 under recent climatic conditions and to provide a framework for its extrapolation in the future. The effect of the topography on the energy budget that results in a spatial variance is discussed as well.

The reference potential evapotranspiration is calculated by the physically based model of the Penman Equation (Penman, 1948). In this model, the potential rate of

evapotranspiration is determined by causal relations and equations that are considered to represent the involved processes accurately. This means that given the meteorological condition -or the average climatological conditions- the potential evapotranspiration can be calculated under certain assumed boundary conditions. Because this implies a truthful representation of the process, such a physically based model has been preferred in order to estimate the potential evapotranspiration under recent and presumed future condition. The calculated potential evaporation shall be related to measurements or to crop factors to predict the actual evapotranspiration. Although expanded equations, like the Penman-Monteith equation, are better equipped to include vegetation effects, the basic form of Penman's equation is used to reduce the number of variables. The equation is described in short below and applied to climatological data from the Alcoy area. The derivation of the equation is described in Appendix 2.

4.3.1 Penman's Equation

The Penman equation and its adaptations are commonly denoted as the *combination methods* as they combine the principles of both aerodynamic and energy balance approaches. Such methods assume isothermal conditions, what implies that both the temperature and the vapour pressure at the surface are identical to the values prevailing at a certain height (Brutsaert, 1982, Dingman, 1994). So, climatic data from meteorological stations can be used to calculate the reference potential evaporation from Penman's equation. It has been applied successfully in many instances and part of its success must be attributed to the fact that it is a robust method, which uses easily measurable quantities.

In its basic form, Penman's equation combines a radiation term for evaporation, ET , with a mass transfer term:

$$ET \propto \frac{\delta \times \text{"net radiation"} + \gamma \times \text{"mass transfer"}}{\delta + \gamma}, \quad (4.7)$$

where the mass transfer term represents the effectiveness of the vertical transport of the water vapour under the gradient in vapour pressure between the evaporating surface and the overlying air. In this relation, δ is the slope of the function of the saturation vapour versus the air temperature T_a and γ is the psychrometric constant (both in units of $\text{Pa} \cdot ^\circ\text{C}^{-1}$; Dingman, 1994).

The net radiation, R_N , is given by the total of absorbed incoming global short-wave radiation R_S and long-wave radiation, R_L :

$$R_N = R_S(1 - \rho) + R_L, \quad (4.8)$$

where ρ is the albedo (-) and the radiation is expressed as flux in units of $\text{W} \cdot \text{m}^{-2}$.

Usually the influence of the long-wave radiation is considered of little importance compared to that of the global radiation. If the net radiation is known, the energy budget equation can be written as:

$$R_N = H + \lambda \cdot \rho_w \cdot ET + G, \quad (4.9)$$

in which G is the quantity of radiation used to heat the soil or water body (*ground flux*) and H that for heating the air, often called the sensible heat. This contrasts it against the term $\lambda \cdot \rho_w \cdot ET$ or *latent heat*, L , which represents the amount of energy that is used to evaporate or transpire water from the soil and vegetation. Most of the incoming net energy is consumed as latent heat for evapotranspiration when the water supply is unrestricted. In the study area, this condition will prevail during the cooler and wetter parts of the year. During the summers, the water supply is restricted and more energy will be transferred as sensible heat.

Under the assumed isothermal condition, the effectiveness of the mass transfer term of relation Equation 4.7 depends on the vertical transport capacity of the turbulent air. This turbulence is induced by the canopy and can be quantified by means of the canopy resistance term, R_a , which has units of $s \cdot m^{-1}$:

$$R_a = \frac{\ln\left[\frac{(Z_m - Z_d)/Z_0}{k^2 \cdot V_m}\right]^2}{k^2 \cdot V_m}, \quad (4.10)$$

where Z_0 and Z_d are roughness parameters dependent on the vegetation height (Z_{veg} in m). R_a describes an idealised parabolic wind profile over the evaporating surface. V_m and Z_m denote the wind speed ($m \cdot s^{-1}$) and the height (m) at which this value is measured respectively. The factor k is a dimensionless constant, called the *von Karman* constant, with a value of 0.41. When R_a is included in the mass term, E_a , the Penman equation is given by

$$ET = \frac{\delta \cdot R_N + \gamma \cdot E_a}{L(\delta + \gamma)}, \quad (4.11)$$

where the evapotranspiration rate is given in units of $m \cdot s^{-1}$ (see also Appendix 2).

The nature of the available climatological data and the validity of the underlying assumptions limit the applicability of the Penman equation. In general, daily records are detailed enough to calculate the potential evapotranspiration adequately. Data with a higher temporal resolution may be used, if available and required. The application of the equation to data averaged over longer periods is not advisable as it levels the influence of the more extreme conditions. Hence, longer periods are better covered by summing the potential evapotranspiration as calculated on a daily basis.

The calculation of the daily potential evapotranspiration supposes that the meteorological data, as listed in Table 4.15, are known. Given the sensitivity of the Penman equation to wind speed and incoming solar radiation these quantities must be known accurately. For the total global radiation, standard functions can be used but these theoretical values will overestimate the actual radiation most of the time as the incoming light is partially reflected and scattered in the atmosphere. Likewise, actual values should be used for the temperature and the relative humidity as they may experience a clear cyclicity over the day and over the seasons. The Penman equation is, on the other hand, relatively insensitive to the atmospheric pressure. This value can be taken as a constant, whether at

sea level or for the local elevation, without introducing a serious error in the model results. In the following section, locally measured values are used whenever possible.

Table 4.15: Constants, parameters and meteorological variables for the adapted Penman equation

Symbol	Value	Units	Description
<i>Constants</i>			
C_p	1004	$J \cdot kg^{-1} \cdot K^{-1}$	specific heat of air
ϵ	0.622	(-)	ratio molecular weight dry and wet air
k	0.41	(-)	<i>von Karman</i> constant
ρ_a	1.205	$kg \cdot m^{-3}$	density of air
ρ_w	998	$kg \cdot m^{-3}$	density of water
$e_s(0)$	611	Pa	saturated vapour pressure at $T=0^\circ C$
<i>Parameters</i>			
ρ	0.11	(-)	Albedo
Z_m	2.0	m	Measurement height wind speed
Z_{veg}	0.10	m	vegetation height
Z_d	$0.75 Z_{veg}$	m	zero plane displacement
Z_0	$0.10 Z_{veg}$	m	roughness height
<i>Meteorological variables</i>			
RH	var.	%	relative humidity
T	var.	$^\circ C$	Temperature
P	var.	Pa	atmospheric pressure
V	var.	$m \cdot s^{-1}$	wind speed
R	var.	$W \cdot m^{-2}$	incoming radiation flux

Concerning the assumed boundary conditions, the isothermal condition is a potential source of error. The largest deviations will occur when the evapotranspiration from the surface is restricted by the availability of soil moisture and more energy is transferred as sensible heat. This condition will exist mainly during the summer and the high potential rate of evapotranspiration that follows from the Penman equation will exceed the actual rate considerably. Similar deviations between the actual and potential rate will result from the advection from energy and from local anomalies in the generalised wind profile (Hanks & Ashcroft, 1986; Brutsaert, 1982). The performance of the model may increase by the incorporation of more information on the fluxes of sensible heat, G and H, and on the aerodynamic profile over the area under consideration. However, these measurements are difficult to obtain and do not fundamentally alter the limitation that the Penman equation predicts potential evapotranspiration under ideal conditions. Under consideration of the theoretical nature of the calculated potential evapotranspiration and the lack of the additional data, the use of the standard formula of Equation 4.9 has been preferred.

4.3.2 Application of the Penman equation

Data availability

In the study area, measurements of the relevant climatic variables have been made with an automatic weather station, of which the location coincides with the tipping bucket at the Hollow (Appendix 1). Relative humidity, temperature, wind speed and radiation have been sampled every 5 minutes and the average hourly values are recorded. The data have been collected from September 1996 till the end of March 1999. Over this period, 91% of the data have been recovered. Given the short period over which data have been collected, it is difficult to generalise the observed seasonal fluctuations. To complement the local data, additional information from nearby stations has been sought. In the upper basin of the Río Serpis, the station of Cocentaina (8059E; No. 45 in Figure 4.10) provides climatic data on temperature, atmospheric pressure, relative humidity and wind speed. At the automatic station, measurements over the in-between periods are summarised at 0, 7, 13 and 18 hours. Daily extremes or totals are given as well. The data have been analysed over the period 1991-1997. For this period, 90% of the individual data are recovered. When the variables are considered jointly, nearly 75% are recovered. The low recovery can be partly attributed to the lack of pressure data. Since this is the parameter to which the Penman equation is the least sensitive, the overall availability is effectively higher than the 75%. A summary and description of the seasonal statistics of Cocentaina are given in Appendix 3.

The resolution of the two stations is comparable but the station of Cocentaina is located at 560 m.a.s.l. whilst the elevation of the study area ranges between 400 and 586 m at Almudaina. An error is consequently introduced by the use of the raw data of the atmospheric pressure. However, the resulting error will be small and unlikely to exceed the error that arises from the local differences between the two stations. The data from Cocentaina are consequently only an indication of the regional conditions that affect both locations.

Representativeness for the study area

The assumption that the data of Cocentaina are representative for the meteorological conditions of the study area should be evaluated. Both stations exhibit the same seasonal trend, which for the variables of Cocentaina is represented in Figure 4.13.

All variables display a diurnal and seasonal course. The relative humidity, RH, and the temperature, T, and are negatively proportional. The latter has also the largest seasonal variability, whereas that of the other variables is more limited.

The data of study area near Almudaina and Cocentaina have been compared by plotting them in scatterplots. As was the case for the regional comparison of the rainfall records (Section 4.2.5), these scatterplots give an indication of the similarity of the climate at the locations (Figure 4.14).

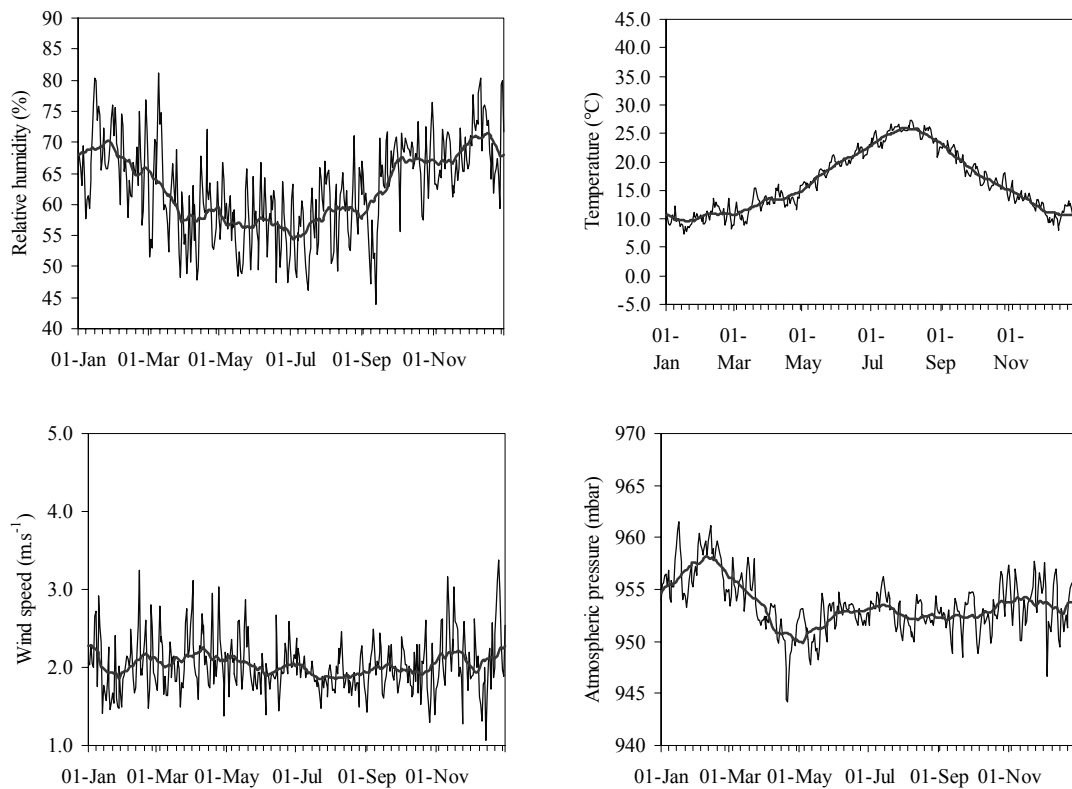


Figure 4.13: Annual course of the daily averages of RH, T, V and P at Cocentaina. Drawn line represents the 31-days central moving average.

The scatterplots for the relative humidity and for the temperature show clearly the close similarity between Almudaina and Cocentaina. In both cases the slope of a linear function, forced through the origin, is near to unity and the goodness of fit exceeds the 85% (respectively $\alpha = 1.00$ (-) and $R^2 = 86\%$ for RH, $\alpha = 1.03$ (-) and $R^2 = 97\%$ for T). From the scatterplot of Figure 4.14, the wind speed at the two locations appears to be less similar. The average daily wind speed in Cocentaina is, overall, higher than the value of the study area. Only 54% of the variation is explained by the R^2 , and the slope through the data has a clear intercept with a value of $0.45 \text{ m}\cdot\text{s}^{-1}$. Apparently, the wind regime in Cocentaina differs from that in Almudaina what may be caused by the sheltering effect of the Sierra de Almudaina on the study area for W and S winds. This local effect of the wind direction, on which no data are available, has the consequence that the wind speed data from Cocentaina have a limited validity for the study area.

A linear regression of the wind speed of Almudaina on that of Cocentaina may be applied to estimate the wind speed for the study area. The regression, forced through the origin, estimates the wind speed at Almudaina at

$$\hat{V}_{Almudaina} = 0.694 \cdot V_{Cocentaina} \quad (4.12)$$

The relation explains 52% of the variance and has been used to transform the data when the wind speed at Almudaina has to be estimated from the long-term climatic data of Cocentaina.

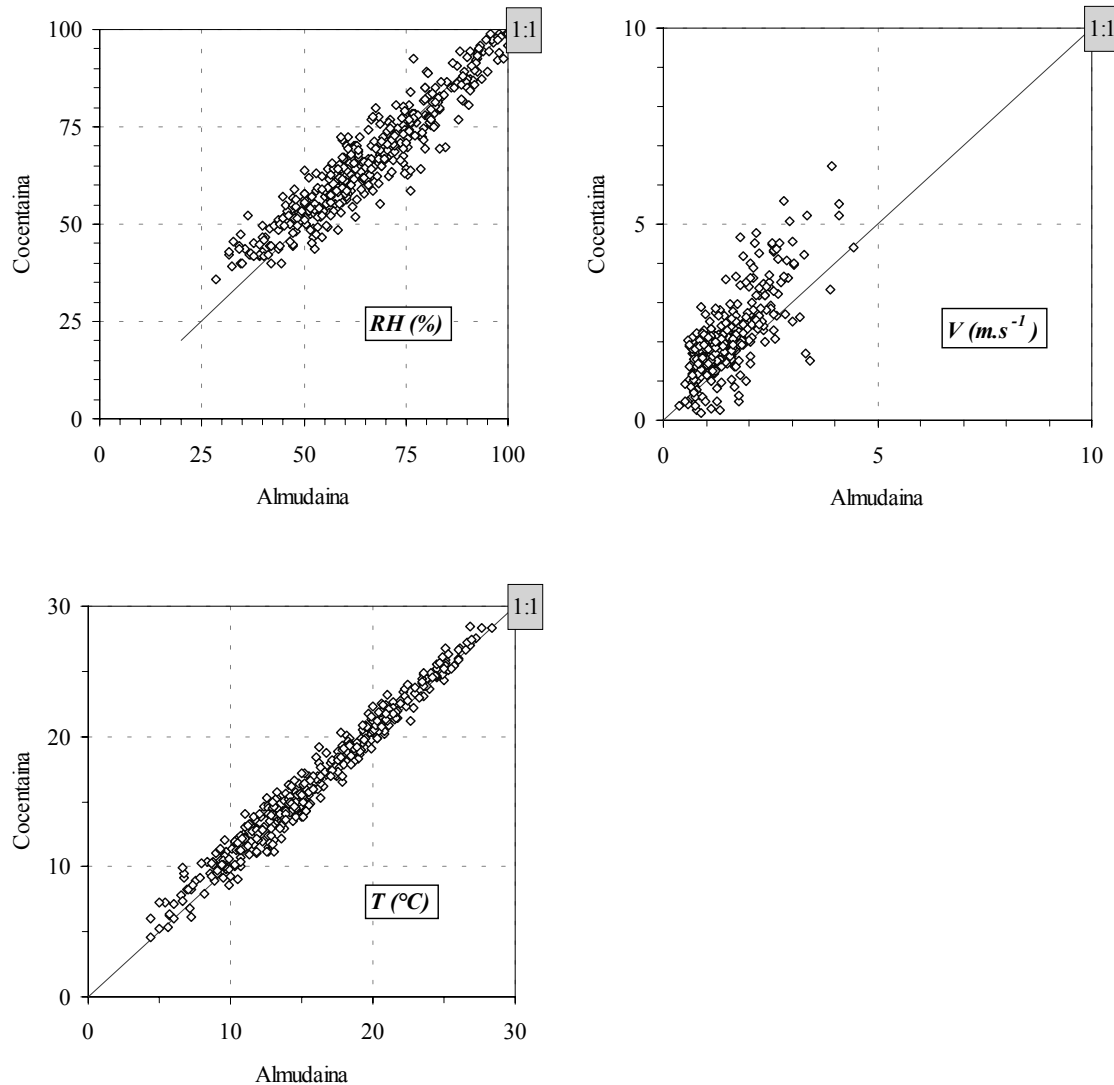


Figure 4.14: Scatterplots of meteorological data Sept. 1996-Dec. 1997

Local estimate of net global radiation

A shortcoming of the station of Cocentaina is that no data on the actual incoming global radiation R are available, which is required for the Penman equation. Data on the actual radiation are available from the local meteorological station in the study area but the record is too short to estimate the evapotranspiration for longer periods.

If the global radiation is unknown, standard functions can be used, which estimate the maximum energy on the basis of the latitude of the station and the date and time. Van

Dam (2001) describes the calculation of available net global radiation comprehensively. Here, it suffices to state that the incoming radiation depends on the total radiation from the sun that reaches the outer atmosphere, the so-called extraterrestrial solar flux or S_{out} . The extraterrestrial flux is given by the solar constant, the radiation flux of $1360 \text{ W}\cdot\text{m}^{-2}$, the declination of the sun between the tropics and the latitude. The fraction of the radiation flux that reaches the surface is dependent on the atmospheric conditions and the length of the travel path. The opacity of the atmosphere to the incoming sunbeams is called the transmissivity, (-). The radiation on a surface normal to the incoming beam, S_{normal} , is given by

$$S_{normal} = S_{Out} \cdot Trans^{Mh}, \quad (4.13)$$

where Mh is the relative path length through the atmosphere (-).

This radiation is scattered and reflected by the atmosphere and only a part will hit the surface as direct sunlight if not prevented by clouds. Of the scattered light, a part will still reach the surface as diffuse radiation. The total incoming global radiation is the sum of both quantities.

Usually, the transmissivity is set to a fixed level between 0 and 1, with typical values between 0.6 and 0.8 (-). It is obvious, however, that this value might change with time, dependent on the atmospheric conditions.

At the surface, a part of the global radiation is reflected. This reflection is defined by the albedo, ρ (Equation 4.8). Again, the albedo is unlikely to be constant with time as the reflection may change with different factors, e.g. with the wetness of the soil or with the condition of the vegetation cover, but the range over which this factor varies is usually small.

To obtain reliable estimates for the transmissivity and the albedo, data on the actual radiation from the study area from 1996 onwards have been used. In order to determine the albedo, the reflected radiation flux was measured with the incoming flux for three months in the fall of 1996. From these data, the albedo could be determined by a simple linear regression. The albedo, ρ , equals 0.11 for the daily radiation flux, with a R^2 of 0.98 and with the intercept forced through the origin. This value lies within the range of 0.10 to 0.20 (-) that is commonly reported as the albedo of dry to wet loamy and clayey soils (Dingman, 1994; Hanks & Ashcroft, 1986).

The transmissivity has been tuned to match the observed maxima of the measured radiation. When the overall transmissivity is set to 0.80 (-), the theoretical curve coincides with most of the observed maxima.

The theoretical curve of maximum global radiation provides with the albedo the basic information for the calculation of the net global radiation. The incoming global radiation can be further reduced if the direct beam radiation is obstructed by clouds or the topography. The former type of obstruction will act on a more regional scale and may, on the scale under consideration, be taken as ubiquitous and random whereas the latter is entirely determined by the local conditions. Neglect of both factors would lead to an overestimation of the potential evapotranspiration and, so, their influence should be accounted for if an accurate estimate is required.

The influence of the topography on the incoming radiation extends beyond the point under consideration. The incoming flux of direct beam radiation is not only projected differently on sloping surfaces, the point may stand in the shadow of the surrounding relief as well. The projection of the shadow of the surrounding relief varies over the day and over the year with the fluctuation in the zenith of the sun. It has been modelled with the SHADE function of PCRaster (Van Dam, 2001). The shading influence of the relief is larger in the winter than in the summer (Figure 4.15). For the entire study area, the direct sunlight is obstructed by the shade of the Sierra de Almudaina during the first hours of daylight in winter. Within the study area, differences arise from the presence of the *barrancos*. The slopes and bottoms of these incised valleys and their tributaries stay in the shade for most of the year and even during summer direct radiation is excluded on some northfacing slopes. For the spatial modelling, both topographical influences have been included. The distribution was calculated on an hourly basis to simulate the diurnal course and subsequently aggregated to daily values.

The annual course in the distributed, incoming radiation is expressed relative to the maximum at the meteorological station. Thus it can be combined with the net global radiation.

The influence of the cloud cover on the maximum net global radiation is directly included in the measured radiation from the meteorological station. If information on the actual incoming radiation under clouded conditions is lacking, it has to be estimated. Readily available statistics to substitute for the missing data include those on the hours of direct insolation and the degree of cloudiness. Cloudiness has been preferred because it does not discriminate between the direct and backscattered radiation. Over the period that the actual incoming global radiation flux has been measured in the area, cloudiness has been calculated as the ratio of the actual incoming radiation over the potential global radiation. This ratio can be compared to the long-term statistics of cloud cover. For the Levante, monthly statistics on cloud cover are available from Alicante and Valencia (Atlas Climàtic, COPUT 1994). In the observations, a distinction has been made between clear, cloudy and overcast skies. No apparent differences have been found and the values have been averaged and presented in Figure 4.16.

These monthly statistics on cloud cover have been used as a proxy for the global radiation throughput on a daily basis. Under cloudy and overcast skies, the direct throughput of the potential global radiation has been set arbitrarily to a fraction of respectively a half and none, whereas all incoming radiation will reach the surface unhampered under clear skies. On a monthly scale, the fractions of direct and backscattered radiation are determined by the frequency of the observed cloud cover conditions. The average values of the recorded actual radiation from the meteorological station over the period September 1996 – March 1999 have been used to tune the proportion of indirect radiation that reaches the surface with the monthly averages from the stations at Alicante and Valencia. Based on the values from the meteorological station, the proportion of radiation, scattered by clouds, that reaches the surface indirectly has an optimal value of 50.8%. In this case, the average absolute error between the observed and calculated radiation throughput is 6.2%.

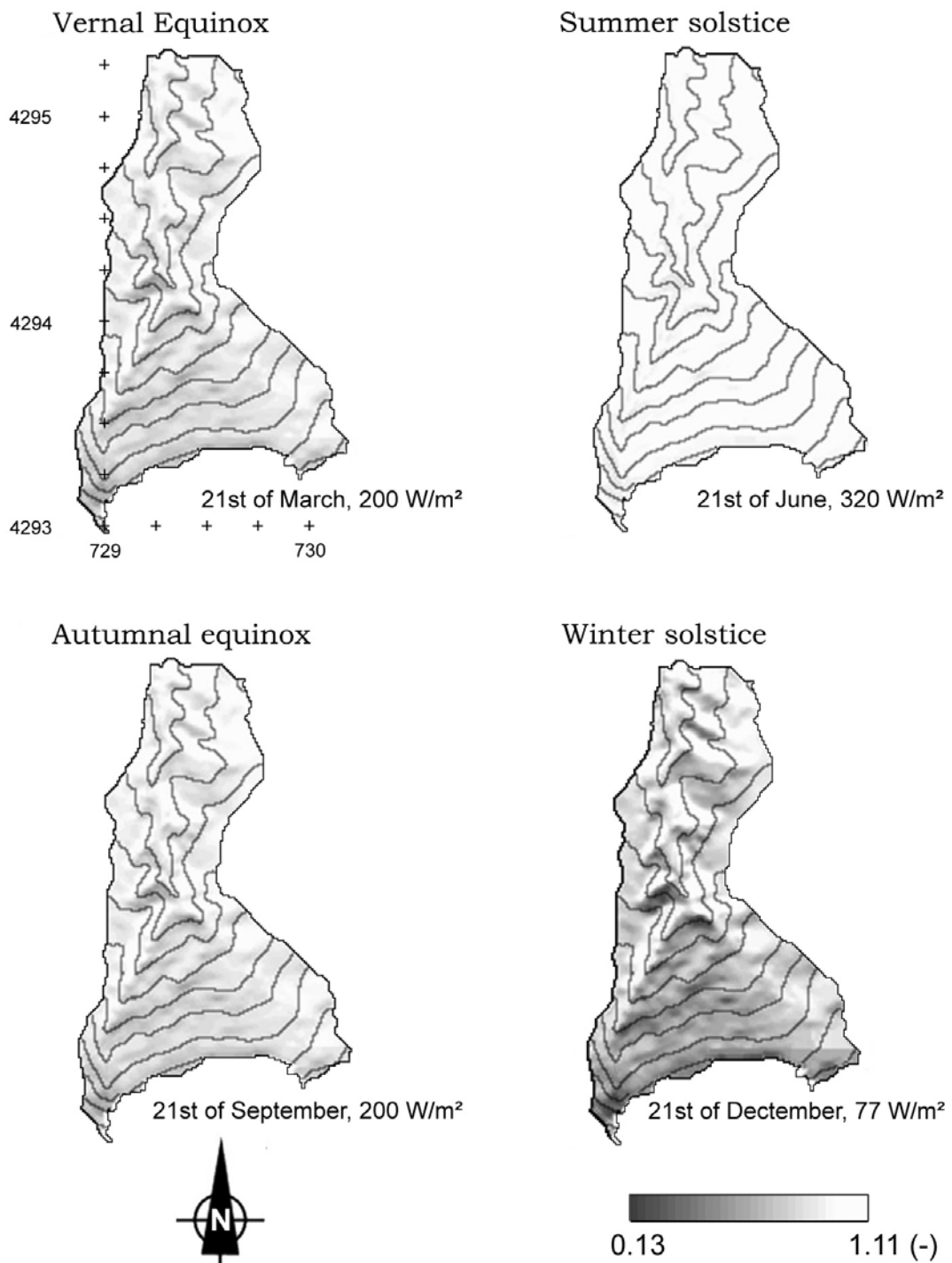


Figure 4.15: Spatial distribution of the relative incoming global radiation for the study area

Because of the shorter length of the record of Almudaina, the cloudiness will be more variable here than at the stations at Alicante and Valencia. Also, the cloudiness will vary

over periods shorter than one month. However, from the comparison it appears that the calculated net global radiation and the observed values are similar and that the best estimate of the proportion of indirect radiation falls within a small range. The largest errors are to occur when the atmospheric conditions vary from the average conditions over a longer period. The error that arises from the generalised cloud cover will be discussed in detail below.

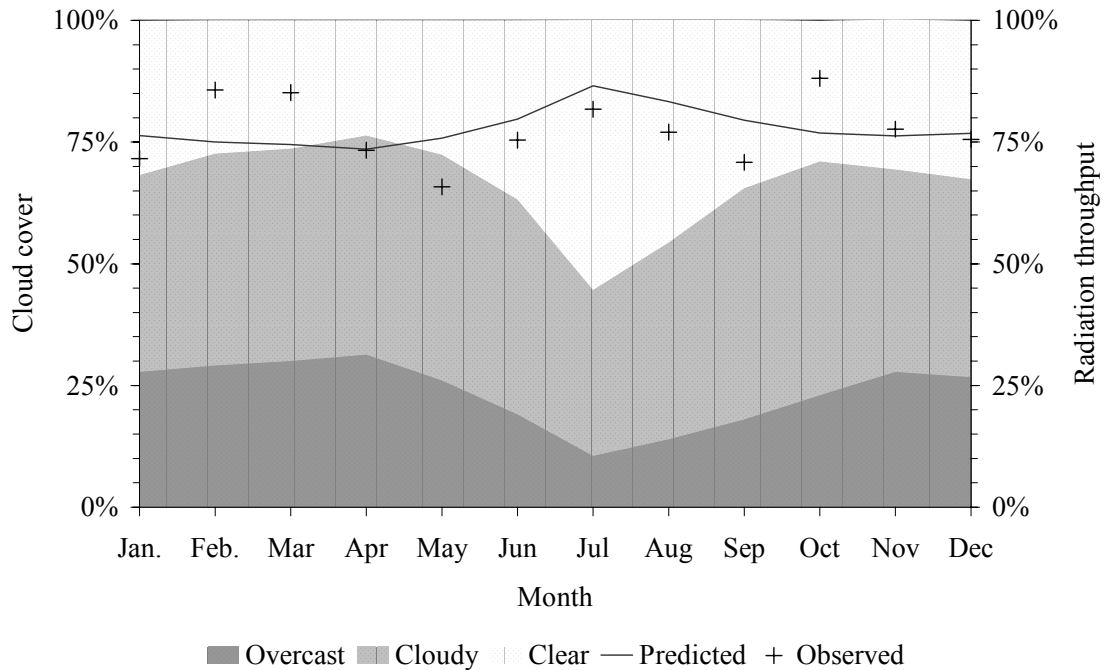


Figure 4.16: Cloud cover statistics for the stations of Valencia and Alicante (source: Atlas Climàtic, 1994) and the optimised monthly average of incoming global radiation

Constants and assumptions

In the preceding sections, some assumptions have been made, which, before the potential evapotranspiration is calculated, will be restated here together with the constants that are used in the parameterisation of the Penman equation.

In addition to the assumptions that the potential evapotranspiration is calculated for a reference vegetation cover for which the water supply is not restricted and that all vegetation effects can be lumped in empirical crop factors, it has been assumed that

- No energy is advected through the air or soil;
- The net ground flux, G , is small on a day-by-day basis and negligible over the year;
- The gradient of the water vapour pressure can be derived from the isothermal condition;
- The evapotranspiration occurs in a stable atmosphere where the diffusivity of water vapour is equal to the diffusivity of momentum caused by wind turbulence;
- The shape of the wind velocity profile is parabolic;

- The turbulence is defined by the average height of the surface roughness, in casu a reference vegetation cover;
- The course of the extraterrestrial radiation flux is the same for all years;
- The transmissivity is constant over time and space;
- The albedo is constant over time and space;
- The local meteorological data are valid for the entire study area; regional values can be applied when local data are lacking.

Most of the constants used in the Penman equation, as listed in Table 4.15, will not be truly constant as they vary over a small range, dependent on factors like temperature and humidity. Yet, they are considered as constant for the resulting error in the estimated potential evapotranspiration is much smaller than that resulting from the general assumptions (Dingman, 1994). As mentioned before, the largest sources of error will arise from the assumption that averaged local and regional meteorological values can be used as substitute for missing values. Another potential source of error is the assumption on the ground flux G . In spite of the obvious daily and seasonal trend in warming and cooling of the soil, this flux has been neglected. On a daily basis, a part of the net global radiation will be absorbed, which will be emitted as heat, both sensible and latent, during the night. A typical value for the proportion of net global radiation lost as ground flux is 10% during summer but values as high as 50% have been reported for the upper 10 mm of the soil under wet conditions (Rosenberg *et al.*, 1983). The penetration of the energy as heat into the soil is, however, often very shallow and the amplitude of the stored temperature decreases strongly on both a daily and seasonal scale (Hanks & Ashcroft, 1986). Setting the integrated ground flux on a daily basis to zero will overestimate the net global radiation leading to evapotranspiration during summer and underestimate it during winter. Without data that specify the actual ground flux, an error is introduced which may be considerable under conditions that clearly deviate from the normal conditions. However, this consideration ensures that no drift in the energy budget is introduced over longer periods.

Dependent on the choice of the reference surface, assumptions are to be made on the influence of the surface roughness on the aerodynamic profile. With the exchange of Penman's original empirical function with the physical relation of the wind profile by Van Bavel (1966), the height of the surface roughness has to be included. For a reference vegetation cover, usually a lawn of short grass, this is the average height of the vegetation. If the zero plane displacement, Z_d , is not considered, this height is used directly as the value for the surface roughness, Z_0 . For the reference vegetation of grass, this value ranges from 0.01 to 0.03 m. With the zero plane displacement, Z_d , and the roughness height, Z_0 , set to empirical values of 0.75 and 0.10 (-) of the vegetation height respectively, the first value of 0.01 m corresponds to a vegetation height of 0.10 m when the zero plane displacement is considered. This height corresponds with the definition of Doorenbos & Pruitt (1977; see also page 120). This latter value is used here for the calculation of the reference potential evapotranspiration in the study area over a surface with the measured albedo of 0.11 (-).

Daily potential evapotranspiration

For the available data of the meteorological stations in the study area near Almudaina and at Cocentaina, the potential daily evapotranspiration has been calculated (Figure 4.17). For both stations, the original records have been used but periods with missing values have been replenished by the 31-day central-moving average of Figure 4.13. From these average data also the interannual, mean potential evapotranspiration has been calculated. For Cocentaina, the potential evapotranspiration is based on the average annual course in the global radiation. For the study area, the measured actual radiation has been used when available.

The potential evapotranspiration exhibits a clear seasonal trend. It is the highest for the summer when temperatures are high and the relative humidity lower. For the ET_0 calculated from the actual daily values, the signal is rather noisy. But also for the smoother series of the average, smaller fluctuations occur. They result from extreme values that are not straightened out over the sampling period of 7 years. The larger peak that occurs in the months of July and August is due to the use of the monthly average of the cloud cover.

Table 4.16: Statistics of reference potential evapotranspiration for Almudaina and Cocentaina

Location:	Cocentaina		Almudaina
Period:	1992-1997		1997-1998
	Daily	Mean Daily*	Daily
	<i>Total data recovery (days)</i>		
Length	2192	Not Available	730
Recovery (%)	74	NA	88
	<i>ET₀ (mm.d⁻¹)</i>		
Average	6.5	6.3	5.7
COV	0.4	0.4	0.6
Min.	1.3	2.8	0.2
Max.	17.9	10.8	14.4
Annual total** (mm.yr ⁻¹)	2330	2283	2068
Average**	6.4	6.3	5.7
	<i>Ratio mass transfer/radiation</i>		
Average	0.6	0.6	0.4
COV	0.8	0.4	1.2

*: based on the average annual meteorological record of Cocentaina over the years 1991-1997

** : includes the replenished periods of impartial data recovery

The calculated potential evapotranspiration is summarised in Table 4.16. The calculated annual ET_0 ranges from 2068 mm for Almudaina to 2330 mm for Cocentaina. The potential evapotranspiration of Almudaina is the most variable as the actual incoming radiation has been used rather than the average course over the year. This has a stronger influence on the variability than the use of the averaged non-precipitation values as the coefficient of variation (COV) does not change in the latter case. The similarity of the two curves is displayed by their coincidence in Figure 4.17. The effect on the extremes is shown by the reduction in the calculated range from 16.6 to 8.0 mm.d⁻¹.

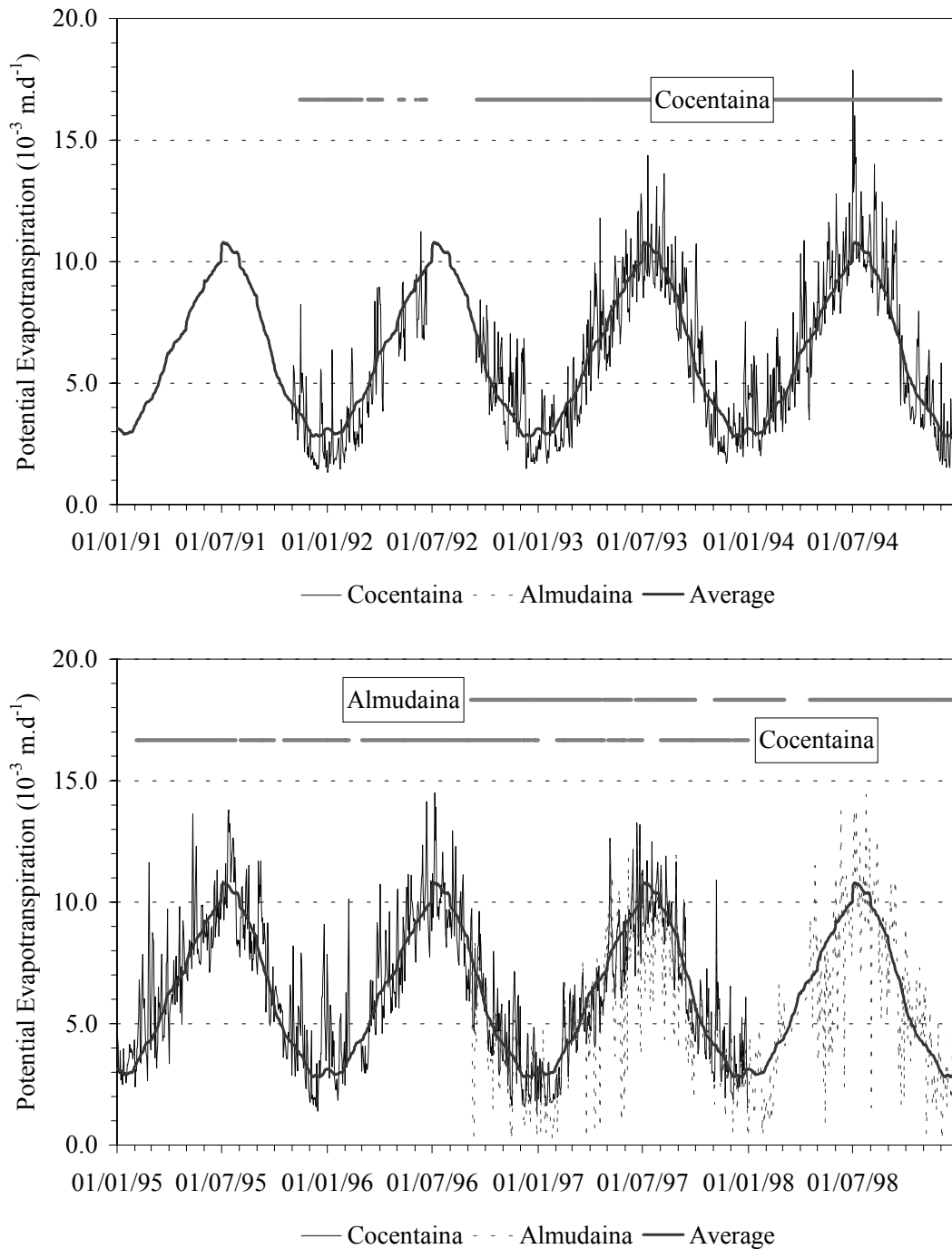


Figure 4.17: Reference potential evapotranspiration for the INM-station at Cocentaina and the field site at Almudaina over time. The horizontal bars mark the periods of complete data retrieval.

The differences between Almudaina and Cocentaina do not only arise due to the use of the actual radiation data. The difference in wind climate also plays a role (Section 4.3).

This is evidenced by the lower and more variable ratio between the contributions of the mass transfer term, governed by the diffusivity, and the radiation term to the potential evapotranspiration (Table 4.16).

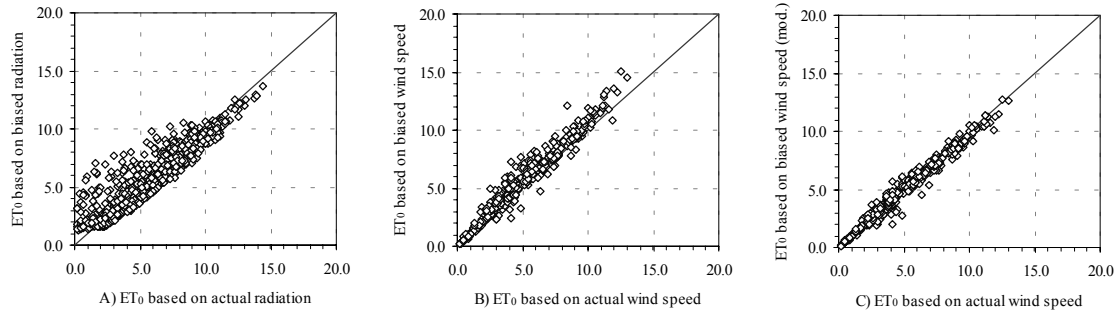


Figure 4.18: Scatterplots of ET₀ from biased estimates: A) incoming global radiation, B) wind speed - unadapted values Cocentaina, C) adapted wind speed Cocentaina

The use of the uniform radiation curve and the transfer of the wind speed data from Cocentaina to Almudaina will introduce a bias in the estimates of the potential evapotranspiration over longer periods. The errors have been explored by comparing the calculated ET₀ from actual values to the biased data. For the radiation, the entire period from September 1996 until March 1999 has been used. For the wind speed, the period from September 1996 until December 1997 has been used. Both the raw and modified wind speed data have been used as an estimate for Almudaina (see Equation 4.12). The ensuing bias is expressed the relative difference between the approximate and the actual value of ET₀ (Table 4.17). Hence, negative values signify an underestimation and positive values an overestimation relative to the actual value.

For the biased radiation, there is a close agreement between the actual and the biased data (Figure 4.18). Both the mean and median are reproduced accurately and the variability is only partly reduced (Table 4.17). The net difference in the annual potential evapotranspiration is thus small (-2 mm), but an overestimation of the evapotranspiration in the cooler and wetter periods is favoured.

The direct application of the wind speed data of Cocentaina leads to an overestimation (Figure 4.18). The bias is the largest for the average and the median. Relatively, the variability in the wind speed is similar at Cocentaina and Almudaina, which explains the low bias in the coefficient of variation (Table 4.17). The error in the annual evapotranspiration is large with an overestimation of 197 mm.

The error is reduced when the modified wind speed is applied. As can be seen in Figure 4.18.C, the values are compressed along the 1:1-slope. Because of the linear regression used, the positive extremes have a larger influence, what results in a slight underestimation. The modified data are thus by far a better approximation, with an underestimation of the potential evapotranspiration by 24.9 mm on a yearly basis. This bias is consistent over the entire range of the potential evapotranspiration and not related to any season.

Based on the evaluation of the bias, it can be concluded that the modified wind speed and the uniform radiation curve are reasonable estimators for the reference potential evapotranspiration over periods ranging from several days to years. The statistics are comparable to those based on the daily potential evapotranspiration as calculated from the actual record of the meteorological station near Almudaina (Table 4.17). The estimates can therefore be used with the other data from Cocentaina as a reliable substitute when actual data from Almudaina are absent.

Table 4.17: Bias (%) introduced in the calculated ET_0 for Almudaina by the use of estimated net global radiation and wind speed

Statistics	Net global radiation Sep. 1996 – March 1999		Wind speed Sep. 1996 – Dec. 1997		
	Actual	Bias	Actual	Bias ^A	Bias ^B
N (days)	850		432		
	<i>ET₀ (mm.d⁻¹)</i>				
Average	5.3	-0.1	5.1	10.7	-1.3
COV	0.6	-7.6	0.6	-2.6	-2.3
Median	4.7	-1.7	4.6	17.2	3.4

A: unadapted wind speed data Cocentaina

B: adapted wind speed data Cocentaina ($0.694 \cdot V_m$)

The reference potential evapotranspiration is high for both Cocentaina and Almudaina. The values are comparable to the potential evapotranspiration as measured by pan evapometers at Moncada and Alquería del Niño Perdido (respectively in the provinces of Valencia and Castellón). Thus, with the spatial distribution of the incoming global radiation (Figure 4.15), the distributed values of ET_0 pose a clear upper limit to the potential evapotranspiration in the field. As its value exceeds the rainfall three times on an annual scale (2068 vs. 698 mm), the actual evapotranspiration must be much lower and is one of the problems addressed in the coming chapters. The reduction in ET_0 due to the local vegetation will be included through empirical crop factors (Section 5.2.4). However, crop factors apply only to a healthy vegetation under optimal conditions of soil moisture and fertility. The actual rate of evapotranspiration depends heavily on the available soil moisture. This relation is simulated by the hydrological model (Equation 3.14). Additional reductions may be necessary to compensate for the remaining deviations for which sufficient information is lacking. Among others, these deviations can be attributed to the topography and to local vegetation- and soil conditions. The topography and differences in vegetation spacing and height will generally reduce the potential evapotranspiration that is due to the mass transfer term (Equation 4.7). Besides the vitality of the vegetation, rooting depth and leaf area, which vary with the maturity of the vegetation, will also affect the actual water uptake and the transpiration. The soil conditions, like crusting and moisture content, will influence the actual loss of incoming radiation as ground flux. Although these deviations result from processes that operate on a local scale, they are lumped in one factor that is taken as constant over time and space. This factor is determined as part of the calibration of the hydrological model component (Chapter 6).

4.4 Hypothetical climatic conditions

The meteorological record of the study area is of little use as direct model input for the assessment of the sensitivity of landslide occurrence to the climatic variability under the present and inferred future climatic conditions. Because of the implied order of events over a comparatively short period the direct use of the available record would make the analysis liable to bias in the frequency of potential landslide triggers. Moreover, the use of this record would by its deterministic nature intuitively clash with the uncertainty that is involved in forecasting future climatic conditions. To overcome this problem a stochastic daily weather generator is used to provide many synthetic timeseries of precipitation and temperature. The many realisations of the weather for series of individual years can be seen as a Monte Carlo simulation.

The daily weather generator is parameterised on the basis of the available record and adapted to the future climatic conditions from general circulation models (GCMs).

4.4.1 Description of a daily weather generator

Most daily weather generators simulate rainfall occurrence as the key parameter. The occurrence of rain, in its basic form a dichotomy representing a wet or a dry day, conditions subsequently the state of the other meteorological variables of interest as rainfall depth, temperature *et cetera* (Wilks & Wilby, 1999). Daily weather generators of this type are based on the work of Gabriel & Neumann (1962) and Richardson (1981). The stochastic daily weather generators simulate the weather conditions by means of a random number generator in combination with probability density functions (PDFs) and statistical relationships that are parameterised on the basis of the available meteorological record. This assumes that the record on which the daily weather generator is parameterised, is characteristic for the local climate and representative for the area under consideration. Because the daily weather generator is driven by a mere statistical fit, it has no physical basis whatsoever (Gabriel & Neumann, 1962). Seasonality is imposed on the generator by varying the probabilities on a monthly or seasonal basis. Although the probabilities change continuously over time, the discrete PDFs are reasonable estimates under most conditions. According to their goodness-of-fit, the weather generator reproduces a substantial part of the observed seasonal and interannual variation. Yet, although the daily weather generator approximates the average conditions adequately, it is by definition incapable of reproducing a series of events in the past or present exactly (Wilks & Wilby, 1999).

For the simulation of rainfall occurrence, daily weather generators generally employ geometric distributions that describe the length of wet and dry spell. A simple model that follows the geometric distribution is the first-order Markov chain as proposed by Gabriel & Neumann (1962). This simple model has the advantage that the probable occurrence of rainfall on day (t) is dependent on the condition on the directly preceding day ($t-1$) only. This succession of dry and wet days is conditioned by two probabilities

$p(1|0)$: the probability that a rainday follows a dry day;
 $p(1|1)$: the probability that a rainday follows a rainday.

These conditional probabilities are derived from the observed relative transition frequencies. In Table 4.18, the off-diagonal elements represent the probability of the transition of the one state to the other. The diagonal elements represent the probability on the persistence of either state.

Table 4.18: Transition matrix for a first-order Markov chain

Condition on day (t)	Condition on day ($t-1$)	
	0: No rain	1: Rain
0: No Rain	$p(0 0)$	$p(0 1)$
1: Rain	$p(1 0)$	$p(1 1)$

The probability on either diagonal element $p(0|0)$ or $p(1|1)$ is usually higher than that on the off-diagonal elements, what emphasises the persistent nature of rainfall in most climates. Rainfall occurrence is simulated by drawing a random number u from a uniform distribution between 0 and 1. Rainfall is to occur whenever $u \leq p_c$ where p_c is the probability in the right-hand column of Table 4.18 given the state on the preceding day ($t-1$). This is represented schematically in the flow diagram of Figure 4.19.

After establishing the state of the rainfall occurrence, the dependent meteorological variables are simulated in the appropriate sub-models (Figure 4.19). These include first of all the rainfall on raindays. Additionally, non-precipitation variables may be included like temperature and cloudiness. The rationale for coupling the non-precipitation variables to the simulation of rainfall occurrence lies in the fact that both are conditioned by the same overall meteorological situation and that rainfall occurrence, as a discrete variable, is the more suitable decision variable. Yet, due to the largely indirect relationships, the causal relation may be poor in many cases.

On a rainday, the non-zero precipitation amount is drawn from a cumulative PDF from which a new, independent random seed u returns the upper boundary x of the area enclosed under the curve, i.e.

$$F(x) = \int_0^u f(i) di. \quad (4.14)$$

The PDF is parameterised on the frequency distribution of the 24-hour rainfall totals from the available meteorological record. Rainfall is often positively skewed, with the bulk of observations in the domain of lower daily precipitation amounts and a long tail towards the more extreme events. Different types of PDFs that are generalisations of the exponential distribution have been proposed to fit these skewed populations. The most widely used is the two-parameter gamma-distribution of the form (Buishand, 1978)

$$f(x) = \frac{1}{\beta^\alpha \Gamma(\alpha)} \cdot x^{\alpha-1} \exp\left[-\frac{x}{\beta}\right]. \quad (4.15)$$

In this function, $f(x)$ is the frequency of the 24-hour rainfall total x , α is the shape parameter and β the scale parameter. $\Gamma(\alpha)$ is the value of the gamma-function at α (e.g. Boas, 1983). Low values of α result in rapidly decreasing frequencies while high values of β lead to distributions with long tails in the region of the higher precipitation amounts. The parameters α and β can be estimated by maximum-likelihood or from the sample population of the 24-hour rainfall totals since an ideal two-parameter distributions displays the following properties

$$\alpha = \frac{\mu^2}{\sigma^2}, \quad (4.16A)$$

and,

$$\beta = \frac{\sigma^2}{\mu}, \quad (4.16B)$$

where μ and σ are the population's mean and standard deviation. When $\alpha=1$ (i.c. $\mu=\sigma$), $\Gamma(\alpha)=1$ and the gamma-distribution reduces to a simple exponential distribution with $\beta=\mu$.

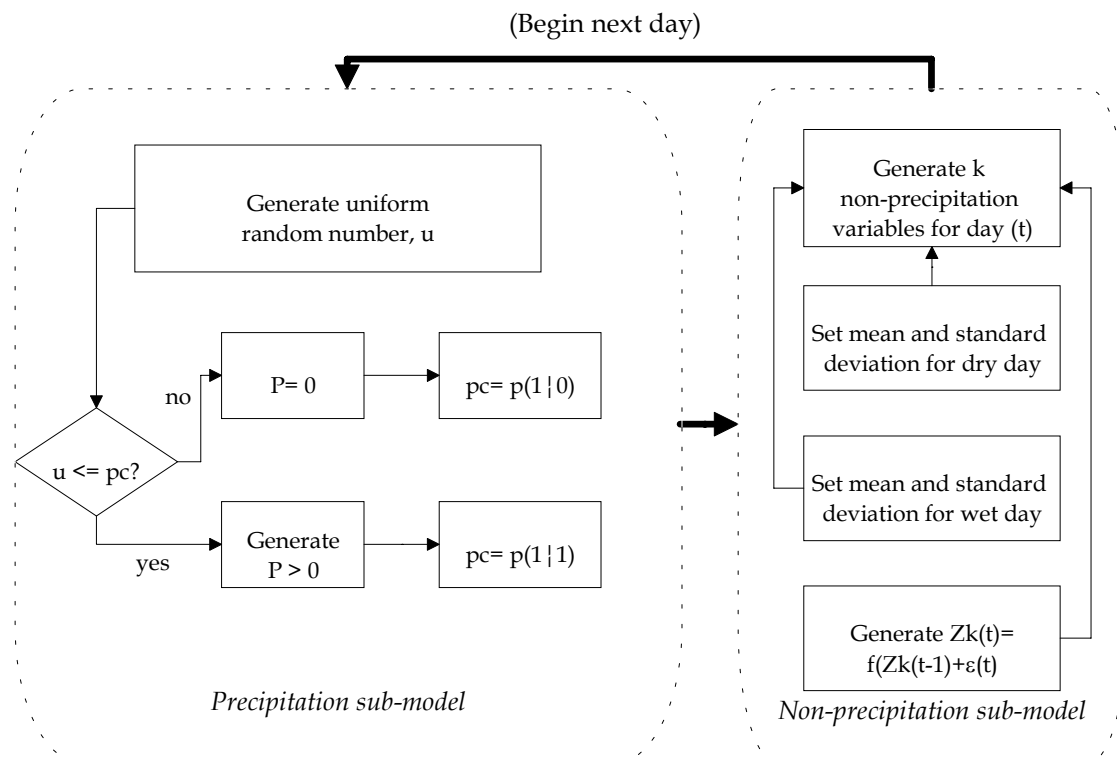


Figure 4.19: Flow diagram of the stochastic weather generator

Both the exponential and two-parameter gamma-distribution that can be used to generate the precipitation amount x on a simulated rainday, are continuous functions in the domain $x > 0$. This implies that for $F(x) = 1$, $x \rightarrow \infty$. To avoid the generation of unrealistic rainfall depths, the random number u can be limited to a range that corresponds to the observed rainfall depths.

According to Richardson (1981), the k non-precipitation variables, T_k , that are to be simulated, are generated through their standard normal values z_k . Dependent on the state of rainfall occurrence on day (t), the observed $T_k(t)$ is standardised to $z_k(t)$ by

$$z_k(t) = \frac{T_k(t) - \mu_{k,0}}{\sigma_{k,0}}, \quad (4.17A)$$

or,

$$z_k(t) = \frac{T_k(t) - \mu_{k,1}}{\sigma_{k,1}}, \quad (4.17B)$$

where μ_k and σ_k are the mean and standard deviation of the variable k over the observational record for days without rainfall (0) or with rainfall (1) which can be calculated on a monthly or on a seasonal basis.

When the seasonal trend is removed, the statistical relations between the observed z_k are used to generate new realisations of z_k (first-order linear autoregression model). The new standard normal variable $z_k(t)$ is determined partly by the state of all variables at the previous day ($t-1$). It is also subject to a random external forcing of white noise, $\varepsilon(t)$, which will generate new weather sequences. In matrix notation, this can be written as

$$z(t) = [\beta] \cdot z(t-1) + [\zeta] \cdot \varepsilon(t), \quad (4.18)$$

where $z(t)$ and, $z(t-1)$ are k -dimensional vectors of the standard normal variable z_k for the present and the previous day and $\varepsilon(t)$ is the k -dimensional vector of uncorrelated, standard normal white noise. The $k \times k$ -dimensional matrices $[\beta]$ and $[\zeta]$ are coefficients relating the vector $z(t)$ to those of $z(t-1)$ and $\varepsilon(t)$ respectively. The elements of $[\beta]$ are the beta weights that indicate how much change in the dependent variable $z_k(t)$ is produced by a standardised change in either independent variable $z_k(t-1)$ when the others are controlled (multiple correlation, Blalock, 1981). So, similar to the first-order Markov chain for the simulation of rainfall occurrence, the state of z_k at day (t) is related through matrix $[\beta]$ to the weather conditions on the previous day only. The elements of $[\zeta]$ are coefficients that ensure that the linear combination of the elements of $\varepsilon(t)$ results in properly correlated random contributions to $z_k(t)$ (Wilks & Wilby, 1999). The correlation in the error term of Equation 4.18 represents the degree to which new weather conditions affect the variables z_k simultaneously. The entries for the matrices $[\beta]$ and $[\zeta]$ are computed from the simultaneous and lagged correlations between the standard normal non-precipitation variables z_k (Matalas, 1967; see Appendix 4).

Dependent on the state of the rainfall occurrence, the simulated non-precipitation variables T_k are subsequently obtained from the inverted Equation 4.17 (Figure 4.19).

4.4.2 Parameterisation of the daily weather generator

For the simulation of the precipitation variables – rainfall occurrence and 24-hour totals-, the daily weather generator has been parameterised using the 27-year long record of Almudaina (Section 4.2.1). The PDFs for the rainfall depth and occurrence have been fitted on a monthly basis. This should provide enough detail to simulate the seasonal differences in rainfall in the study area while the record is long enough to provide reasonable estimates of the variance of the population.

The transition frequencies of rainfall occurrence provide maximum-likelihood estimates for the conditional probabilities $p(0|1)$ and $p(1|1)$ in the first-order Markov chain (Gabriel & Neumann, 1962; see Table 4.19). When compared to the binomial probability on rainfall - the unconditional chance π_1 -, the observed frequencies clearly demonstrate that, during the wetter months of the year, the conditional probability on the transition from a dry to a wet day is much lower than could be expected if the change was purely random ($p(1|0) < \pi_1$; Table 4.19). In contrast, the observed transition frequency $p(1|0)$ approaches π_1 during the dryer months of July and August, reflecting the feeble persistence of rainfall during summer.

Table 4.19: Transition frequencies ($\times 10^{-3}$) for the first-order Markov chain - $p(0|1)$ & $p(1|1)$ - and the binomial probability π_1 for rainfall in Almudaina

	Sep	Oct	Nov	Dec	Jan	Feb	Mar	Apr	May	Jun	Jul	Aug	Year
$p(1 0)$	63	91	86	77	74	69	80	91	96	45	22	29	67
$p(1 1)$	339	420	430	517	527	511	378	482	324	321	143	226	423
π_1	87	135	131	137	136	123	114	149	124	62	25	36	105

Table 4.20: Parameterisation of the monthly two-parameter gamma-distribution for rainfall depth

Month	N	Average (mm)	St. Dev (mm)	α (-)	β (-)	R^2 (-)
September	68	25.8	36.1	0.511	50.477	0.898
October	115	22.4	28.5	0.621	36.146	0.889
November	104	22.4	34.5	0.423	52.988	0.764
December	117	17.5	23.7	0.545	32.162	0.942
January	113	20.4	22.0	0.864	23.640	0.938
February	94	20.6	31.7	0.425	48.610	0.728
March	96	17.0	20.6	0.676	25.083	0.954
April	118	12.6	12.0	1.090	11.525	0.987
May	105	14.1	17.4	0.661	21.368	0.896
June	51	12.7	9.8	1.665	7.601	0.959
July	21	14.7	13.5	1.196	12.315	0.838
August	30	10.8	11.3	0.905	11.925	0.925

On raindays, the precipitation amounts are generated from a probability density function that reproduces the observed frequency distribution at Almudaina. Here, the two-parameter gamma-distribution has been tried. The shape and scale parameter α and β are derived from the properties of an ideal distribution (Equation 4.16) and estimated from the sample mean and standard deviation μ and σ on a monthly basis (Table 4.20). The

fits of this distribution are reasonable for most months. Exceptions are months with scattered events of high-magnitude, what results in skewed distributions with long and “ragged” tails (e.g. November and February). These skewed and dispersed distributions are characterised by a low α and a high β , which is typical for the wet season. For the spring and summer, the distribution of the 24-hour rainfall totals is more homogeneous. This is consistent with the rainfall characteristics of the study area as described in Section 4.2.

Table 4.21: Mean and standard deviation for the standardisation of the non-precipitation values

	Jan	Feb	Mar	Apr	May	Jun	Jul	Aug	Sep	Oct	Nov	Dec
<i>Relative humidity (%)</i>												
N	135	111	152	113	142	136	144	146	133	134	171	95
$\mu_{k,0}$	66	62	59	54	55	54	56	58	58	65	64	69
$\sigma_{k,0}$	11	13	12	11	12	11	13	13	14	11	11	11
N	38	26	22	27	21	22	7	9	30	36	34	23
$\mu_{k,1}$	80	84	78	72	71	73	59	74	78	77	79	79
$\sigma_{k,1}$	14	15	13	16	10	13	15	13	13	12	12	15
<i>Temperature (°C)</i>												
N	129	123	155	118	145	143	140	144	136	135	174	126
$\mu_{k,0}$	10.1	11.3	12.2	14.1	18.0	21.4	24.9	25.1	21.2	17.0	13.9	11.3
$\sigma_{k,0}$	3.0	3.0	3.0	2.8	2.6	2.7	3.2	2.6	2.9	3.1	3.4	2.9
N	23	26	22	28	21	23	7	9	30	36	34	26
$\mu_{k,1}$	7.6	8.8	10.0	12.2	14.4	18.1	23.1	24.0	18.0	14.8	12.0	10.3
$\sigma_{k,1}$	3.9	3.1	2.9	3.0	2.2	2.4	2.6	2.9	2.7	2.8	2.2	3.3
<i>Wind speed ($\sqrt{m \cdot s^{-1}}$)</i>												
N	117	123	155	119	145	143	146	146	136	135	161	126
$\mu_{k,0}$	1.36	1.42	1.40	1.44	1.42	1.39	1.37	1.37	1.41	1.38	1.45	1.42
$\sigma_{k,0}$	0.33	0.34	0.26	0.27	0.23	0.17	0.15	0.14	0.20	0.28	0.36	0.40
N	37	26	22	28	21	23	7	9	30	36	34	26
$\mu_{k,1}$	1.30	1.38	1.56	1.43	1.43	1.40	1.41	1.24	1.34	1.30	1.38	1.40
$\sigma_{k,1}$	0.49	0.45	0.35	0.31	0.30	0.26	0.11	0.13	0.21	0.27	0.40	0.47
<i>Atmospheric pressure (mb)</i>												
N	119	112	154	119	145	143	107	116	113	114	152	70
$\mu_{k,0}$	957.4	958.5	955.5	952.0	951.9	953.2	953.4	952.4	952.9	953.4	955.1	950.6
$\sigma_{k,0}$	8.8	6.3	6.7	5.4	4.2	3.9	2.8	2.5	3.8	5.1	6.1	6.3
N	33	24	22	28	21	23	4	8	23	26	27	23
$\mu_{k,1}$	951.8	956.4	948.9	946.8	947.3	950.2	953.0	951.6	950.6	950.3	949.3	947.6
$\sigma_{k,1}$	6.7	7.7	5.4	5.7	4.1	2.9	1.5	2.2	4.0	4.3	7.7	7.1

For the parameterisation of the non-precipitation variables, the data record of Cocentaina has been used as described in Appendix 3. This record includes information on the average daily value for four non-precipitation variables (average daily relative humidity, temperature, wind speed and atmospheric pressure). These variables are simulated by the daily weather generator with the purpose of computing the reference potential evapotranspiration by means of the Penman equation. In contrast to the original generator

proposed by Richardson (1981), solar radiation is excluded from the simulation because reliable data are absent. Instead, the curve of potential global radiation is used in combination with the average cloud cover statistics (Section 4.3.2). Although this choice was shown to result in an underestimation of the interannual variability, the average radiation conditions provide a reasonable estimate over longer periods. This matches the findings by Richardson (1985) that the output of a crop model of wheat was similarly insensitive to the daily variations in global radiation.

For the generation of new values of the standard normal non-precipitation variables z_k , the coefficients of the matrices $[\beta]$ and $[\zeta]$ of Equation 4.18 have to be known. These coefficients are calculated from the simultaneous and lagged (by one day) correlations between the standardised k non-precipitation variables T_k over the observation period (Appendix 4). The overall monthly averages and standard deviations are used as the basis for the standardisation although few raindays are present during the dryer months (Equation 4.17). This should be attributed to the comparatively short period that the INM data of Cocentaina cover (just over 6 years).

The standard normal values of z_k are calculated from the overall monthly averages and standard deviations as listed in Table 4.21. A square-root transformation has been applied to the wind speed data in order to obtain a better representation of its skewed distribution. The reduction that is needed to convert the wind speed from Cocentaina to values that are representative for the conditions at Almudaina has been applied afterwards.

Table 4.22: Simultaneous and lagged correlations of the standardised non-precipitation variables

A) Simultaneous correlations, r_{vx} , and number of observations, N (lower half)					
		X, t			
		RH	T	V	P
Y, t	RH	1.000 1907	-0.415	-0.435	0.145
	T	1867	1.000 1953	0.136	-0.050
	V	1873	1912	1.000 1951	-0.365
	P	1673	1686	1684	1.000 1726
B) Lagged correlations (lag= 1 day), r_{vx} , and number of observations, N					
		$X, t-1$			
		RH	T	V	P
Y, t	RH	0.551 1860	-0.230 1864	-0.352 1869	0.117 1666
	T	-0.184 1855	0.670 1930	0.006 1893	0.049 1668
	V	-0.278 1863	0.156 1894	0.455 1929	-0.352 1669
	P	0.154 1660	-0.097 1669	-0.242 1668	0.778 1704

The lagged and simultaneous correlations between the standard normal variables are given in Table 4.22. The correlations are generally weak but significant. Notable exceptions of significance are the lagged correlation between temperature and wind speed and the lagged and simultaneous correlations between temperature and atmospheric pressure. Because of the strong interaction between the non-precipitation variables, the explained variance increases only slightly by adding variables (Table 4.23). The beta weights of matrix $[\beta]$, which correct for this interaction, are derived from these correlations. They give the actual change in the values $z_k(t)$ that is produced by the conditions on the previous days, $z_k(t-1)$. The elements of $[\beta]$ are listed in Appendix 4. Most of the change results from the variable under consideration, although the average wind speed on the preceding day has a considerable influence on the relative humidity on day (t) whilst the atmospheric pressure on its turn influences the wind speed.

Table 4.23: R^2 of bi- and multivariate lagged regressions of z_k

Lagged correlation, R^2	$Z_k(t)$			
	RH	T	V	P
Bivariate R_{xx}^2	0.303	0.449	0.207	0.606
Multivariate R^2	0.319	0.465	0.259	0.614

The lagged correlations explain between 26% and 61% of the variance in the variable $z_k(t)$ (Table 4.23). The remainder of the variance is included by the simultaneous correlations in the error term of Equation 4.18, given by the matrix $[\zeta]$. The entries of this matrix are listed in Appendix 4.

4.4.3 Comparison of simulated vs. observed weather

Criticism on the validity of weather generators focuses on the simplified representation of persistence by the first-order Markov chain of Equation 4.19 and the lagged autocorrelation of Equation 4.18. Especially under temperate and humid conditions, first-order Markov chains have been demonstrated to underestimate the frequency of rainfall events of above average duration. To overcome this, several alternative approaches have been proposed to adapt the conditional probability $p(1|1)$. Already Gabriel & Neumann (1962) tried higher-order Markov chains but concluded for the data of Tel Aviv that the influence of the second and third preceding day was insignificant. More recent adaptations include - amongst others - the application of a persistence parameter (Bardossy & Plate, 1991) and the enforcement of long-term persistence by downscaling the observed monthly totals in the simulation by means of linear regression (e.g. Wilks, 1992; Van der Wateren – De Hoog, 1996). Moreover, the generator is primarily trained to simulate the duration of wet spells. Hence it is unable to simulate the duration of dry spells with an extreme length adequately. This has been the general objection against their use in agricultural studies in which water stress is a more limiting factor than actual rainfall occurrence. An alternative forms the spell-length model (Semenov & Barrow, 1997) in which the dry and wet spell length are drawn successively from the observed frequency distributions. This type of generator, however, is less suitable for the

modelling for rainfall-induced landslide occurrence for they are unable to reproduce the more extreme rainfall events. Therefore, the Markov chain model has been preferred here as the generated spell length is not directly dependent on the observations.

An additional weak point of the described stochastic weather generator is that it lumps the observations into one general parameter set. As a consequence, it tends to underestimate the observed interannual variability that arises from the year-to-year variations in atmospheric conditions. The recognition of this weakness led towards the development of weather-type simulation (Hay *et al.*, 1992; Wilby, 1994). In weather type simulation, the rainfall occurrence - and thus all other conditional variables - are made dependent on the regional state of the atmosphere. This state can be simulated or obtained directly from regional and global circulation patterns. By means of the variation in this state, a better reproduction of the interannual variability in the locally simulated variables is achieved. For the study area, however, weather-type simulation is not feasible since the local, relatively sparse datasets of Almudaina and Cocentaina lack any reference to regional atmospheric conditions; the effort of increasing the spatio-temporal support of the stochastic weather generator for the study area clearly surpasses the scope of this study. This means that the effectiveness of the limited parameter-set to reproduce the temporal behaviour and the interannual variability of the local weather must be considered before the synthetic meteorological timeseries can be used as reliable model input.

In the evaluation of the performance of the stochastic weather simulator, two related topics must be considered. The first is the effectiveness of the parameterisation of the generator and concerns the goodness-of-fit of the implemented PDFs and the coefficients of the first-order linear autoregression model. The second, depending on the first, is the generator's capability to reproduce the interannual variability over the observation period.

In the generator for Almudaina, the occurrence of rainfall is conditioned by a first-order Markov chain. The simpler first-order Markov chain can be considered as a reasonable estimator when the probability of a wet spell of n days is simulated adequately over the observation period. The probability of a spell of n continuous raindays is for a first-order Markov chain given by (Gabriel & Neumann, 1962)

$$p(n) = [1 - p(1|1)] \cdot p(1|1)^{n-1}. \quad (4.19)$$

With the conditional probabilities of Table 4.19, the distribution of wet spells can be simulated for the observation period of 27 years and compared to the actual distribution as shown in Figure 4.20. The simulated distribution follows the observed duration closely although some discrepancies exist for events with a length of 3, 4 and 6 days as the χ -gram indicates. The goodness-of-fit has been calculated by means of the generalised likelihood ratio test (Wilk's $-2 \log \Lambda$ test; Rice, 1995). Because of the deviations between the observed and expected frequencies, the first-order Markov chain has a probability of 0.13 ($\Lambda=11.1$, DF= 7).

The theoretical curve of spell length, generated by the first-order Markov chain, decreases continuously with an increasing n . Since the deviations at $n= 3$ and $n=4$ are mirrored, it can be argued that the observed discrepancies - at least in part - can be attributed to the discrete nature of the observations. However, the deviation at $n= 6$ is

isolated and must result from the ineptness of the model to reproduce the reality as this spell length was observed only once over the period 1971-1998. The observed events with a duration longer than $n=6$ are well approximated. Generally, a higher order Markov chain gives a better description of persistent rainfall but the enhanced performance should be judged against the increased model complexity (Wilks & Wilby, 1999). Second- and third-order Markov chains have been tried but this did not result in a better representation of the persistent events ($n > 5$) and, evaluated by the approach described by Tong (1978), the added complexity did not enhance the predictions made by the model.

Within the weather generator, the daily rainfall amounts are simulated independently over successive raindays. This violates reality for, at Almudaina, the lagged autocorrelation of daily precipitation totals is high for the period 1971-1998 (Table 4.24). Slightly lower but still highly significant autocorrelations were found for the period before 1971 and for the other stations analysed (Section 4.2.5). The significant autocorrelations are positive. Because of their weight on the linear regression, rare events of consecutive 24-hour rainfall totals larger than 150 mm define the high lag(1)-correlation. Commonly, the lagged autocorrelations of daily rainfall are weak and are conveniently neglected in most stochastic rainfall generators (Wilks & Wilby, 1999).

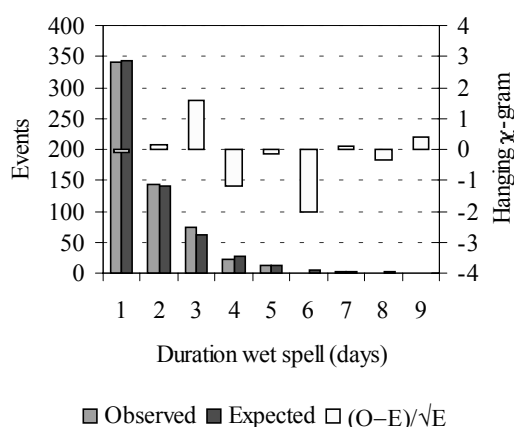


Figure 4.20: Observed and simulated frequencies of rainfall events for Almudaina 1971-1998

Table 4.24: Lagged – by n days – autocorrelations of daily precipitation totals at Almudaina over 1971-1998. Probability refers to the random change that the observed lag(n)-correlation is exceeded.

n (days)	1	2	3	4
$\rho_n (-)$	0.441	0.206	0.078	-0.006
$P(\rho)$	0.00	0.04	0.18	0.40

To analyse the likelihood of the lagged autocorrelations, 100 random combinations of the observed rainfall were made for Almudaina over the period 1971-1998. The lag(1)-correlation of 0.441 was only approximated once. Lag(1)-correlations in excess of 0.2 were only observed in 5% of the random combinations. In contrast, the random combinations indicate that the lagged correlations over periods longer than two day are more likely. These weaker correlations over the longer lags are mostly defined by the

similarity of the bulk of small rainfall amounts. Thus, the strong autocorrelations at Almudaina over lags (1) and (2) are caused by extreme rainfall events that deliver intense rainfall for two or more consecutive days. Such events are likely to be related with the local weather system of the *temporal de Levante* (Sections 2.2 & 4.2). These events are of the utmost importance for the temporal activity of landslides in the area. However, a direct empirical relation could not be included in the stochastic weather generator because of the underrepresentation of the longer rainfall events in the record.

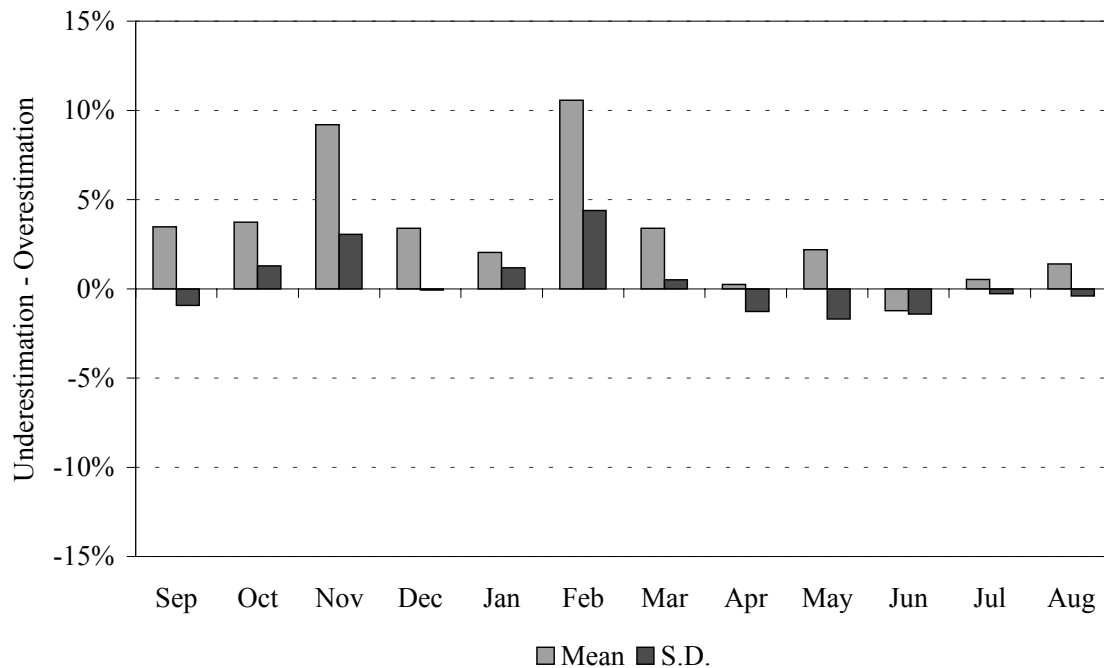


Figure 4.21: Relative differences in the mean and standard deviation between the observed and generated daily rainfall per month

It is known that the tails of the two-parameter gamma-distributions tend to underestimate the observed frequencies of the larger rainfall depths (Wilks & Wilby, 1999). However, the observed frequencies in the tail were not better represented by exponential and mixed exponential probability density functions. Therefore, the parameterised gamma-distribution of Table 4.20 that reproduce the mean and variance of the sample population accurately have been maintained. The goodness-of-fit of these distributions, expressed as the R^2 , is given in this table as well. The errors that arise from the uncertainty in these PDFs can be estimated by the approximation of the observed mean and variance by the generated values. For 10,000 realisations, the relative differences in the mean and standard deviation are shown in Figure 4.21. The months that are the least well approximated are the months of November and February. For these months, the mean is overestimated by some 10%. This is caused by the bias that is introduced by infrequent high rainfall events in the two-parameter gamma-distribution. The mean and variability of all other months are better approximated by the weather generator.

The frequency distribution of the wet spell length of Figure 4.20 and the differences in daily rainfall depth of Figure 4.21 only indicate how well the weather generator approximates the frequency and magnitude of precipitation. They provide no information on the simulation of the interannual variability by the generator that is the benchmark of its performance. Therefore a comparison has been made between the observed and simulated annual rainfall characteristics from 10,000 realisations that are presented in Figure 4.22.

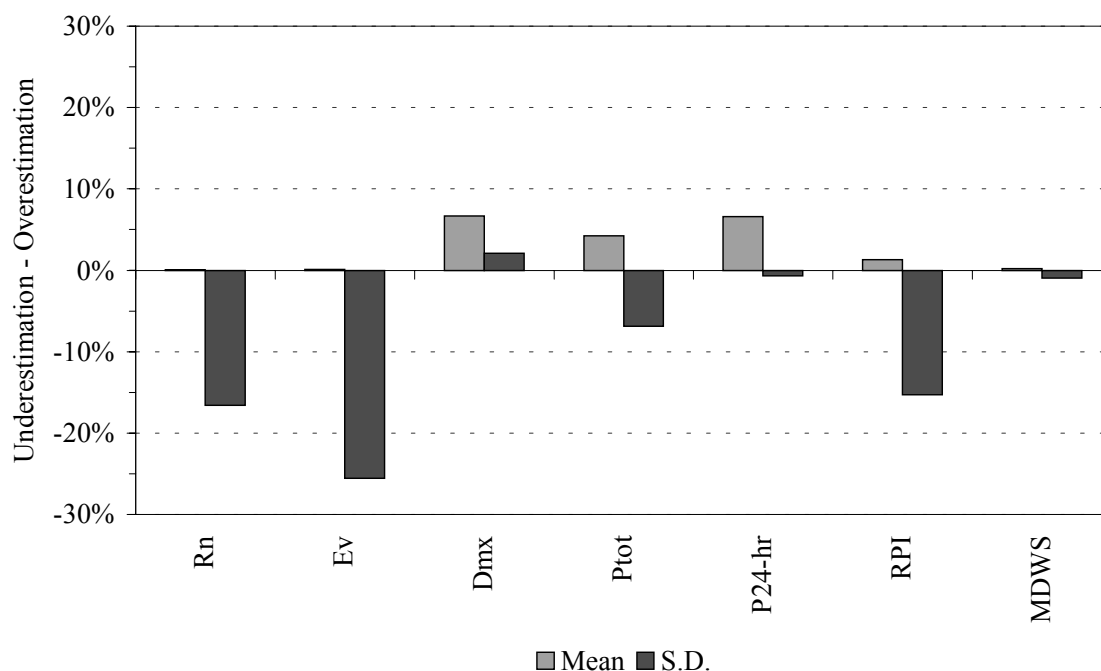


Figure 4.22: Relative differences in the mean and standard deviations for the observed and generated annual rainfall characteristics

Deviations from the expected means occur for the maximum duration and some statistics that are related to the rainfall depth (maximum 24-hour rainfall total, P_{24-hr}, and the total annual rainfall, P_{tot}). The deviations are all positive. The explanation lies in the relative overrepresentation of more extreme events due to the application of continuous PDFs over a period longer than the observation period. Most means are, however, well approximated.

The approximation of the interannual variability by the stochastic weather generator is much poorer. The largest differences are found for the characteristics related to rainfall occurrence. Of these, the number of raindays, R_n, the numbers of events, E_v, and the rainfall period intensity, R_{PI}, the interannual variability is underestimated by 15 to 26%. Since the mean duration of wet spells, MDWS, and the rainfall depth are well estimated, the discrepancies must be entirely explained by the year-to-year variability. Apparently, the stochastic weather generator fails by its structure and parameterisation to simulate the observed droughts (e.g. 1983 –1984). This is illustrated by the minimal

annual rainfall total of 113 mm over the 10,000 simulated years while the similar amount of 122 mm was recorded for the hydrological year 1960-1961.

The underestimation of the interannual variability over the 10,000 realisations raises the question to what extent the observed rainfall characteristics are approximated over shorter periods. To test the agreement between the simulated and observed values, 10 series of 27 year each were generated and compared with the observed mean and variance.

On a monthly scale the generated mean rainfall is significantly different from May until August ($\alpha= 5\%$, two-tailed). For these months, differences occurred at least 8 times out of the 10 generated short-term series. The deviations are the result of the limited rainfall occurrence in these months. All the wetter months are better simulated. Significant deviations occurred only once for December and February. On average, the monthly average of daily rainfall depth falls within 5% of the observed values. Only for the more variable months of November and December and for the summer month of August lies the difference in the order of 10%. No significant differences in the simulated rainfall variance exist between the observations and the 10 generated series.

The simulated annual characteristics of Figure 4.22 differ significantly from the observed values once in every series of 27 years. In all but one case, these deviations are overestimations of the observed values. Significant differences in the interannual variability are only found for the means of four out of the seven considered characteristics (Table 4.25). Between the simulated and observed variances no significant differences were found. The deviations from the observed interannual variability confirm the trend of Figure 4.22. Given the small differences in the mean, it can be concluded that despite, the signalled shortcomings of the stochastic weather generator, it is capable of simulating the observed means and interannual variability for precipitation satisfactorily.

Table 4.25: Comparison between the observed and generated rainfall characteristics. Marked values indicate significant deviations at $\alpha= 0.05$.

	Average				
	Observed 1971-1998	Generated 10 x 27 yrs	Generated minimum	Generated. maximum	Significant deviations
Raindays	38.2	38.9	37.1	41.1	0
Events	22.0	22.4	21.5	23.3	0
D_{\max} (days)	4.7	4.9	4.2	5.4*	2
P_{tot} (mm)	697.7	732.6	677.0	802.6*	1
$P_{\max 24\text{-hr}}$ (mm)	103.6	107.2	93.4	127.9*	1
RPI (mm)	18.6	18.5	17.6	19.7	0
MDWS (days)	1.7	1.7	1.7	1.9*	1

The generated non-precipitation values are above all dependent on the performance of the multivariate linear autoregression model of Equation 4.18. For 10,000 realisations, the generated mean and variances are not significantly different from the standard normal distribution. The standardised non-precipitation variables approximate the expected mean and variance of zero and unity respectively within 0.01 (-). For dry and wet days, the error in z_k increases for the raindays in the dry months of July and August. This could have a negative effect on the non-precipitation variables T_k generated for relatively short periods.

With the stochastic weather generator, synthetic timeseries have been generated for seven years, roughly the period covered by the record of Cocentaina, which was used to parameterise the non-precipitation module. The autocorrelation, both lagged by one day and simultaneous, was most times similar to the observed values. Exceptional differences occurred in some instances but these always concern the insignificant correlations without any weight. The significant correlations are all approximated within 10% of the observed values. For the generated monthly means and variances, only once in June the variance of the standardised wind speed for raindays was significantly lower than unity. This must be attributed to the low frequency of raindays for this month. Because of the agreement between the expected standard normal distribution and the generated standardised non-precipitation variables z_k all non-precipitation variables T_k are well approximated by the generator. It can therefore be concluded that the multivariate linear regression model provides a valuable complement to the rainfall module of the weather generator. It generates internally consistent synthetic timeseries of precipitation and non-precipitation variables that determine the available net precipitation for the study area near Almudaina.

4.4.4 *Defining a local climate change scenario*

The increase of greenhouse gasses by human activities is likely to induce higher global temperatures. This global warming may give rise to local changes in climatic conditions like temperature, relative humidity, rainfall occurrence and rainfall intensity. Through the hydrological cycle, these changes could have a profound impact on net precipitation that controls landslide activity.

Model studies that evaluate the hydrological impact under climatic change infer the future conditions from scenarios. This description clearly stresses the involved uncertainty. Different approaches have been applied to define these future conditions. One is the *analogue* method in which historical records reflecting the presumed changes are used as model input. An alternative that has become increasingly popular is the use of the output of *general circulation* models (GCMs). These GCMs simulate the interactions between the atmosphere, the oceans and the earth masses on a global to continental scale. They are calibrated and validated on the available historical dataset, typically the 100 years preceding 1980 or 1990. From then onwards, the model is projected to obtain future climatic conditions under an assumed forcing of the atmospheric system by a compound increase of greenhouse gasses over time. Initially, the model projections consisted of new equilibrium conditions under increased concentrations of greenhouse gasses, but with increasing computational power transient predictions have become available since the mid 1990s. Comparisons of the two types of models for the Mediterranean basin show that both predict similar patterns and magnitudes of climatic change (Palutikof & Wigley, 1996).

Because of the complexity of the atmospheric interactions simulated by the GCMs, their spatial representation is coarse to achieve feasible calculation times. Most GCMs resolve their numerical solutions for relatively few gridpoints that are spaced hundreds of kilometres apart. Moreover, because little credibility can be placed in the temporal detail of the GCM, the final output is usually given as the monthly mean. As a result, the

GCMs have a limited potential to reproduce local weather for they lack the spatial and temporal resolution to include the local effects of orography, vegetation and landmass distribution. To overcome this problem, GCM results are usually downscaled to obtain the support for local predictions (Wilby & Wigley, 1997). A major distinction can be made between empirical and physical downscaling techniques. In the physical techniques, a high-resolution physical model is nested within a GCM that provides the necessary boundary conditions. In the empirical techniques, the local observations are related directly to the model output for the available period. Most of the empirical techniques are all variants of regression approaches whether they include simple linear regressions (e.g. Semenov & Barrow, 1997) or multivariate techniques like canonical correlation (e.g. Von Storch *et al.*, 1993). Because of their amenability to local and regional conditions, statistical techniques have been applied in many studies to derive scenarios of climatic change.

In model studies on the impact of climatic change, stochastic weather generators play an important role. For transient GCMs, they can be used to disaggregate the monthly climatic output to daily values (Wilks, 1989). For the transient and equilibrium GCMs alike, stochastic weather generators can be adapted to generate long synthetic weather series as unbiased estimates of extreme conditions for a changed local climate, just as they were applied for the present conditions. This offers the possibility to evaluate the effects of the changed occurrence of extreme events. For the sensitivity of hydrological processes to the changed variability could be far more important than the changes in the mean (Katz & Brown, 1992).

The adaptation of the stochastic weather simulator requires an approach to adapt its parameters to the changed climatic conditions as reflected by the mean and variance of the downscaled GCM output. Once simplifying assumptions are made, its adaptation is relatively straightforward although the distinction between conditioning, in this case rainfall occurrence, and conditional variables can have unexpected results (Katz, 1996). It is obvious that for the generator depicted in Figure 4.19 changes in rainfall occurrence will affect the mean of the non-precipitation variables. However, they may also alter the variance and correlation of these variables.

Given a presumed increase in greenhouse gasses, the development of a climate change scenario depends on the aim of the exercise and the reliability of the GCM to make local predictions. With respect to the triggering of rainfall-induced landslides, both the occurrence and amount of rainfall as well as the changes in evapotranspiration are of importance. Unfortunately, attempts to downscale precipitation for the Spanish Mediterranean coast are seldom successful. The indefiniteness of most downscaled precipitation scenarios must be attributed to the importance of regional weather systems, the occurrence of local convective cells and the orographic effects. The predicted trends in precipitation are often opposed and vary with the downscaling approach used. Cubash *et al.* (1996) applied both the statistical analogue method and the physically based timeslice method to downscale the output of transient simulations from the ECHAM GCM (see below). The statistical method predicts an increase in winter rainfall in the order of 0.5 mm per day for the Mediterranean coast at the time of CO₂-doubling. Under the same circumstances, the high-resolution timeslice experiment produces a decrease of the same order. The only consistency between the two approaches is that both indicate an

increasing variability in rainfall occurrence and depth. For the analogue method, the probability on a dry spell at Alicante increases slightly. For the timeslice experiment, the occurrence and intensity of rain decreases for all seasons except the winter. In the latter season, an increase in high-intensity rainfall is predicted. It should be stated that the statistical support for the analogue method for Alicante is insignificant with a mere correlation of $\rho = 0.26$ (-). Similar low correlations were obtained by analogue downscaling of the ECHAM GCM with data of Almudaina for this research. Over the period 1954-1994, the seasonal correlation coefficient varies between -0.1 and $+0.1$. When calibrated and validated over the split record, the method gives only coherent results for the autumn (data courtesy M. Dehn).

In their study of 1992, Giorgi *et al.* demonstrated by the use of a physical limited area model (LAM) that at the time of CO₂-doubling the prognosis differed significantly from the parent GCM. The most interesting point of this model exercise is that they found a weakening of the jet stream and the associated rainfall in October. This is of importance for the occurrence of the typical *temporal de Levante* that results in most of the rain in the study area.

A recent and rather successful attempt to downscale rainfall for the Spanish Mediterranean coast was made by Goodess & Palutikof (1998). They transferred the weather-type classification of Hay *et al.* (1992) to the Guadelentín basin in SE Spain. In this area, most of the rainfall stems from the same meso-scale weather system as that in the Valles de Alcoy although the annual rainfall depth is much lower ($P_{\text{tot}} < 350\text{mm}$). They found that in the perturbed state, the frequency of the different weather types did not change except for the summer. For this season, the significant changes resulted in a relative increase in rainfall depth of 10 to 18%. This is, again, in contradiction to the parent GCM that predicts a decrease of summer rainfall of 60%. However, because summer rainfall is negligible, its contribution to the annual rainfall remains unimportant. If their results may be transferred to the Valles de Alcoy, the possibly reduced spring rainfall could be more important for the occurrence of landslides. This removes potential triggers after winter rainfall and advances the soil moisture deficit that the increased summer rainfall can not compensate.

Downscaling of rainfall at the station of Sella, located on the southface of the Sierra de Aitana, by means of regression techniques is equally inconclusive on the expected changes in precipitation and the annual rainfall totals under a warmer climate remain approximately the same (pers. com. J. Griffiths).

Based on the limited success of the local downscaling exercise and on the ground of the observed contradicting tendencies in other studies, it has been assumed that the rainfall characteristics in the study area will not be different in a future warmer climate.

It is evident that with a global increase in temperature, the rate of potential evapotranspiration will increase if it were not tempered by negative feedback mechanisms. Reduction could occur either through a lower gradient in the mass transfer term of Equation 4.7 or by a lowering of the net global radiation. Without evidence to specify these interactions, the local increase in average daily temperature is the only variable of interest and can be used to calculate the rate of potential evapotranspiration under a warmer climate. This simple approach is followed here. It appears to be justified by the findings of Palutikof *et al.* (1994). This study, the only one addressing the effect of

climatic changes on the potential evapotranspiration and soil moisture availability in the Mediterranean basin, distinguishes rainfall and temperature as most influential factors. Hence, the increased local temperature at CO₂-doubling for Almudaina is derived here and included in the stochastic weather generator with the aim of generating consistent synthetic timeseries for the non-precipitation variables of relative humidity, wind speed, atmospheric pressure and altered temperature. These variables will be used to derive from the reference potential evapotranspiration ET₀ that with the generated precipitation enters the hydrological model.

For the prediction of the effect of global warming on the local temperature conditions, the results of three different transient GCMs have been evaluated. These are the HadleyCM2 model of the UK Meteorological Office, the ECHAM2 model of the Deutsches Klimarechenzentrum and that of the Geophysical Fluid Dynamics Laboratory. All three GCMs are gridbased and are subject to an increase in an ensemble of greenhouse gas and sulphate that is expressed as an equivalent of CO₂. The rates of increase differ per model and result in dates of expected CO₂-doubling between 2050 and 2060 (Table 4.26). These forcings of increased concentrations of greenhouse gasses are consistent with the trend projected by the Intergovernmental Panel on Climate Change (IPCC; Houghton *et al.*, 1990).

Table 4.26: Characteristics of the three transient GCMs considered

GCM	HadleyCM2	ECHAM2	GFDL
Forcing	Ensemble of greenhouse gasses and sulphate		
CO ₂ -increase	1 %.yr ⁻¹ compounded	IPCC A	1 %.yr ⁻¹ compounded
Date 2·CO ₂ (+ 1990), yr	70	60	70
Length (+ 1990), yr	100	60	70
Local ΔT 2·CO ₂ (°C)	1.7	1.3	4.7

From the GCMs, the data of the nearest grid point to the study area has been analysed. Since the results of the GCMs are not directly transferable to the local situation, the temperature differences between the present conditions and those at CO₂-doubling are more meaningful than the absolute temperature levels. This also facilitates the comparison between the different models that are based on different rates of CO₂-increase. The difference per model in Table 4.26 are calculated by subtracting the 20-year average before 1990 from the 20-year average preceding the date of CO₂-doubling. The difference in temperature rise for the various models can partly be explained by the inertia of the modelled ocean-atmosphere interactions. Particularly the GFDL model shows a rapid increase in temperature towards the date of 2·CO₂.

An important feature of a Mediterranean climate is its seasonality. This provides an additional tool to evaluate the performance of the GCMs as predictor for the local climate. In Figure 4.23, the seasonal fluctuation in the average monthly temperature with its standard deviation is given over the period 1964-1997. For this period temperature data from the stations of Cocentaina and Alcoy are available and are represented as well. Data from the latter station over the period 1964-1987 were added to provide additional statistical support for the short record of Cocentaina. Since no overlap in the records

exists, the complementary nature of the record of Alcoy to that of Cocentaina has been evaluated by comparing the lagged correlation ρ_1 of the standardised daily temperature. The correlations are similar for Alcoy and Cocentaina (respectively 0.698 and 0.670). Yet, because of the disparity in record length, the correlations are significantly different (7954 vs. 1930 observations, $Z= 2.069$, $p= 0.02$). Under consideration of the similarity, however, and on the ground of the high correlation between Almudaina and Cocentaina, it has been assumed that the data of Cocentaina, Alcoy and Almudaina are interchangeable (Section 4.3).

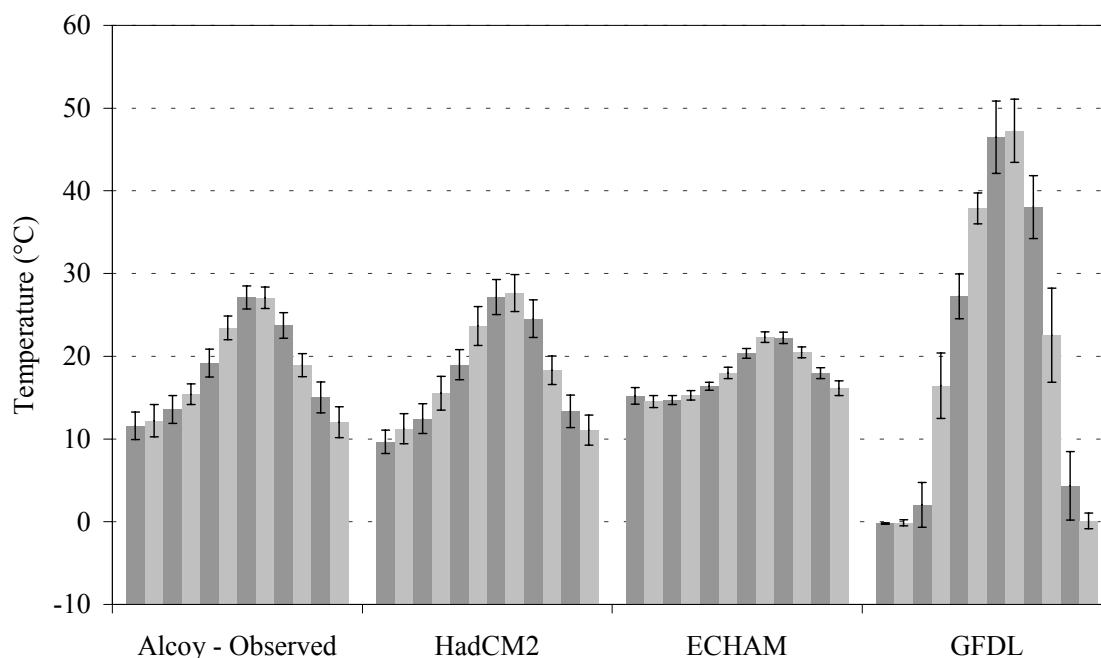


Figure 4.23: Seasonality in the average monthly temperature and standard deviation as derived from the raw GCM results

Table 4.27: Average temperature and standard deviations from the monthly GCM-output and as observed at Alcoy & Cocentaina

	Observed	GCM		
		HadleyCM2	ECHAM2	GFDL
Annual average	18.2	17.8	17.8	20.2
Monthly standard deviation	5.8	6.6	2.9	18.4

Since the GCMs simulate temperature at sea level, 0.006°C per m elevation have been added to the observed temperature for Alcoy and Cocentaina. Despite the fact that all average annual temperatures are similar to the observed value (Table 4.27), the seasonality is reproduced with varying success. Of the GCMs, the Hadley model is the more similar in its mean and deviation on an annual and on an average monthly scale. The other models have on average some seasonality but deviate clearly from the observations.

According to the simple regression approach applied by Semenov & Barrow (1997), the GCM output can be calibrated to the observations by regressing the standardised observations on the standardised predictions. Following this approach, the dataset of observations has been divided in two periods of 17 years each. The period 1964-1981 has been used to define the linear regression, which subsequently was used to downscale the model results. The downscaled temperature over the period 1982-1997 was verified against the observed values. The GFDL model has statistically the same predicting power as the Hadley model that performs better in the colder months (Table 4.28). Because of its low variability (Table 4.27), the ECHAM model has the lowest predictive power on a monthly basis.

Table 4.28: Correlations between the observed and simulated monthly temperature over 1964-1997

GCM	HadleyCM2	ECHAM2	GFDL
	<i>Total period 1964-1997</i>		
Correlation (-)	0.92	0.79	0.93
	<i>Calibration period 1964-1981</i>		
Correlation (-)	0.92	0.79	0.94
	<i>Validation period 1982-1997</i>		
Correlation (-)	0.92	0.80	0.93
RMSE (°C)	2.3	3.6	2.2

RMSE: Root mean squared error

Table 4.29: Downscaled temperature values from the three GCMs considered

	HadleyCM2	ECHAM2	GFDL
Date 2·CO ₂	2060	2050	2060
Annual average	19.4	20.1	19.6
Local ΔT 2·CO ₂ ^A	1.2 ± 0.06	2.0 ± 0.17	1.4 ± 0.06
Monthly standard deviation	5.3	4.8	6.0

^A: ± 95% confidence level

Downscaling brings the highly variable simulated temperatures of the GCMs within the range of the observed values. The average temperature is reproduced within 0.1 °C. The standard deviation of the downscaled monthly temperatures is slightly below the observed value of 5.8 °C (Table 4.27). This statistic becomes 5.0, 4.4 and 5.2 °C for the downscaled Hadley, ECHAM and GFDL model respectively. Accordingly, the expected rise in temperature at the time of CO₂-doubling becomes more homogeneous. Calculated again as the mean of the 20 years preceding the date of 2·CO₂, the average increase in temperature is 1.5 °C. In addition, an increase in variability is observed (Table 4.29). The change in the standard deviation is the largest for the GFDL model. This is mainly due to its steep increase in temperature near the date of 2·CO₂. In this case, the ECHAM model predicts the largest rise in temperature. This can be partly explained by its lower variability. This model has also the largest uncertainty. The uncertainty around the

downscaled temperature increase is for the ECHAM model three times as high than that of the Hadley and GFDL models. The relative error in the downscaled temperature rise lies between 4 and 8%.

On the ground of the statistics of Table 4.29, a local change in temperature due to an increase in greenhouse gasses is highly likely. The temperature rise lags with the predicted global change. This agrees with the downscaled predictions by Palutikof & Wigley (1996) for the Spanish Mediterranean coast. Both their findings and the results of the timeslice-experiment by Cubasch *et al.* (1996), predict different rises in the mean seasonal temperature. It has long been recognised that the effects of global warming on the mean and variability of the temperature will differ per season. Since the calibrated Hadley model represents the observed seasonality and variability adequately, it has been preferred for scenario building.

The scenario describing the local effects of global warming includes the 20-year mean preceding the moment of CO₂-doubling rather than applying the transient model outcome directly. The rationale for this is inspired by the constraints that the disaggregation of the predicted monthly temperature values imposes on the generated timeseries of rainfall. As the latter variable is deemed as the more important landslide trigger, its unbiased estimate is preferred above the simulation of a hypothetical monthly temperature. Thus the climate change scenario can simulate the expected changes in temperature and its variability but does this without any deterministic order.

Because of the design of the stochastic weather generator, the downscaled daily mean and standard deviation are required to parameterise it for a warmer climate. The resolution of the GCM output, however, is monthly and must be used to approximate the underlying daily variability. For large samples, the relation between the variances of monthly and daily values can be estimated by

$$\text{var}(T_a) = \frac{\sigma_d^2}{N} \left(1 + 2 \sum_k \rho_k \right), \quad (4.20)$$

where $\text{var}(T_a)$ is the aggregated variance over N daily values with variance σ_d^2 . ρ_k represents the daily correlation coefficients of the k non-precipitation variables. Hence, changes in $\text{var}(T_a)$, as observed in the downscaled GCM predictions, can be the result of changes in the daily variability and the persistence as simulated by the multivariate linear autoregression applied in the generator (Wilks, 1992). According to Wilks, evidence from GCM simulations does not indicate a large change in the autoregression function, and the simplifying assumption can be made that the correlations between the standardised non-precipitation remain the same. Since no changes are made to the generated rainfall occurrence under the future climate and the standardised non-precipitation values have only a relative weight in the autoregression function, the synthetic weather series will be consistent. This implies that under the changed climatic conditions only the absolute characteristics of the daily temperature are changed. Its relation with the other variables and its persistence remain the same. This assumption leads to

$$\sqrt{\frac{\text{var}(T_a')}{\text{var}(T_a)}} = \frac{\sigma_d'}{\sigma_d}, \quad (4.21)$$

where the primed variances refer to those under the changed climate that are obtained from the downscaled GCM results.

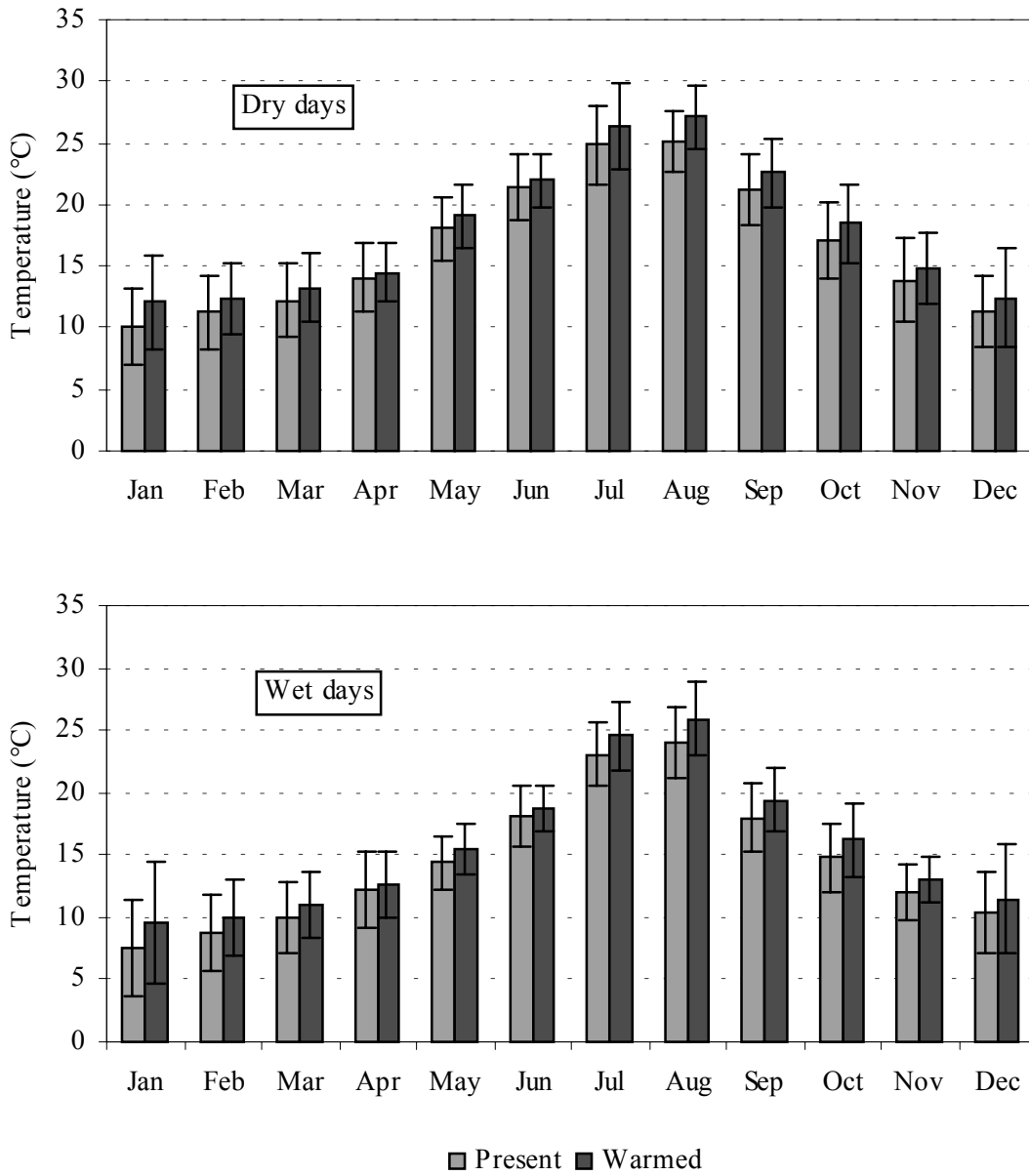


Figure 4.24: Monthly mean and standard deviation for the present and warmer local climate at the time of CO₂-doubling

Consequently, changes in the monthly temperature variability are controlled by the underlying variability of daily temperature only. From the ratio between the downscaled monthly variance in temperature for the present and warmed local climate, the changed daily standard deviation can be calculated and implemented in the weather generator. Since an addition to the mean does not alter the variance, the estimated difference in temperature between the present and the warmed climate can be summed with the observed temperature. In this manner, the parameters of the stochastic weather generator can be adapted to the warmer climatic conditions near the date of CO₂-doubling. Without evidence to the contrary, the changes on the dry and raindays are assumed to be equally large. In Table 4.30, the difference between the downscaled monthly values and the ratio of their standard deviation are given for the 20-year period preceding the date of CO₂-doubling. The resulting differences with respect to the parameterisation of the present climate are visualised in Figure 4.24.

Table 4.30: Monthly change in the mean and variance of temperature inferred from the downscaled Hadley GCM

	Jan	Feb	Mar	Apr	May	Jun	Jul	Aug	Sep	Oct	Nov	Dec	Yr.
ΔT (°C)	2.0	1.1	1.0	0.4	1.0	0.6	1.4	2.0	1.4	1.5	1.0	1.1	1.2
σ^2/σ (-)	1.3	1.0	0.9	0.9	1.0	0.8	1.1	1.0	0.9	1.0	0.9	1.4	1.2

The downscaled GCM output indicates that the changes in the winter and summer temperature are the largest. Especially the winter months of December and January experience an above-average increase in the mean temperature and its variance. Since the variability was already high in this season, the expected range of winter temperature values becomes only larger. The induced change in evapotranspiration could have a large influence on the antecedent moisture conditions and thus on the triggering potential for a given rainfall event. For the summer, the changes are also large. Any increase in summer rainfall, as inferred from the downscaling of precipitation for the Guadelentín area by Goodess & Palutikof (1998), will certainly be compensated by it. The only season for which the changes are less far-reaching is the spring, for which the increase in temperature is the lowest and the variability apparently experiences a slight decrease. Overall, the projected change in temperature increases the annual potential evapotranspiration by 55 mm for Cocentaina (Figure 4.25). At Almudaina, the change is 48 mm, which is due to the lower, local wind velocities. Therefore the soil moisture deficit will generally deepen and extend itself over the year if it were not compensated by increased rainfall.

The predicted change in evapotranspiration for the Valles de Alcoy agrees with the large-scale changes found by Palutikof *et al.* (1994). The warmer climate leads to a consistent raise of evapotranspiration over the year with the largest absolute changes in summer. In winter, they found that the absolute changes are smaller. However, relatively the average change is equally large or even larger if under the present climate the seasonal difference in evapotranspiration is large. In their analysis, the effects of climatic change on the variability or extreme values of evapotranspiration were not considered (Palutikof *et al.*, 1994). Yet, this study indicates that more variable conditions are to occur in winter. This has a profound impact on the hydrological cycle in the Mediterranean since the surplus in

winter rainfall is essential to replenish the soil moisture deficit and for the recharge of aquifers. Due to the larger variability, however, the increase in evapotranspiration does not necessarily eliminate those soil moisture conditions that favour the triggering of landslides. This is demonstrated by Figure 4.25, which gives the average curves of potential evapotranspiration and their minima and maxima for the present and warmed climate in the Valles de Alcoy. Although the predicted curves generally exceed those of the present climate, the minimal evapotranspiration rate is not very different from that under the present conditions.

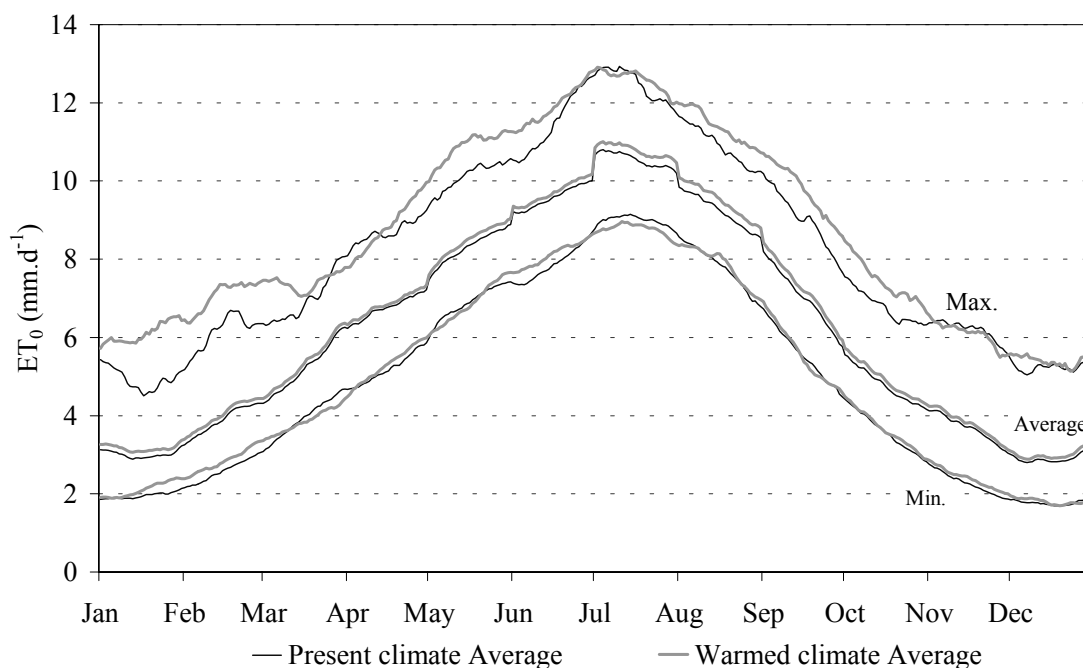


Figure 4.25: Differences in the calculated potential evapotranspiration resulting from the predicted temperature rise in the Valles de Alcoy. The observed values over 1991-1997 and those generated over 7 years have been compared.

4.5 Conclusions

The local weather system of the *temporal de Levante* – a depression over the Mediterranean that directs moist air towards the Iberian Peninsula – defines the temporal activity of rainfall in the Valles de Alcoy. Under certain conditions the depression may deepen and result in a *gota fría* that brings extreme rainfall. Although this system is not the only source of rainfall, it is the more important as droughts resulting from its absence demonstrate.

On a regional scale, the orographic effect of the parallel aligned mountain ranges leads to a spatial difference between the northfaces that are exposed to the incoming rain from the Mediterranean and the leesides. It also favours the seclusion of fronts and the formation

of convection cells that explain spatial differences in rainfall occurrence as the analysed stations of Gorga and Almudaina indicate.

At the scale of the study area near Almudaina, no spatial differences in rainfall depth or occurrence could be found. Apparently the distribution is fairly homogeneous as long as the same exposure in the same valley is considered.

Over the period 1954-1998, the rainfall data from the station of Almudaina show no tendencies other than a large interannual variability. With the observed extreme events that deliver a large share of the annual total, this variability must be attributed to the activity of the *temporal de Levante*. On a seasonal scale, differences in the daily rainfall characteristics can be observed that are more prominent in the within-storm characteristics for the study area. These characteristics show a more persistent low-intensity rainfall in winter that is contrasted by the more intermittent rainfall in autumn. This autumnal rainfall is highly variable and characterised by intense rainfall. In spring, intensities are also high but the rainfall is constrained to more similar, single-storm events that can be attributed to thunderstorms. The fall and winter deliver most of the rainfall whilst the contribution of summer rainfall is negligible. Because of the relative short duration of most events and the similarity of the rain-bringing conditions, a good relation exists between the duration, intensity and the accumulated rainfall depth that can be used to disaggregate rainfall data to smaller temporal scales.

Because of the large seasonal differences in temperature and radiation, the potential evapotranspiration mirrors the temporal distribution of rainfall over the year. Hence a soil moisture deficit is built up during summer that is not compensated until substantial rainfall in the fall or winter has occurred. Although most of the meteorological variables determining evapotranspiration can be considered as homogeneous over the study area or even on regional scales, the topography has again a strong influence. Based on a spatial model for incoming global radiation, it can be concluded that strong differences in the received radiation exist between the shadowed dells of the barranco and the exposed valley sides and pediment. This difference is the highest when the solar altitude is low, namely during winter. As a result, spatial differences in the net precipitation will occur that might favour the landslide activity in those depressions where more water is accumulated and less lost to evapotranspiration. Therefore, the spatial distribution of global radiation must be included in the hydrological model. This could equally apply to the effects of the topography on the wind profile but except for the direct influence of the Sierra de Almudaina, these could not be quantified.

For the estimation of the net precipitation in the hydrological model, the potential evapotranspiration is calculated by means of the Penman equation (Penman, 1948). A problem arises because detailed meteorological information is seldom available. By comparison of the short-term records of Almudaina and Cocentaina it can be concluded that the bias introduced by the use of transformed or averaged data in the Penman equation is acceptable for longer periods.

The expected global warming by the emission of greenhouse gasses is likely to have a great impact on the net rainfall that triggers landslides. Both changes in the rainfall characteristics and in the meteorological variables defining evapotranspiration will affect the net difference between them. These changes can be inferred from the output of GCMs that simulate the global weather adequately. Their application, however, on the local scale is not straightforward. The output can not be transferred directly because of the

low-resolution of GCMs, the uncertainty incorporated by the simulated atmosphere-ocean-landmass processes at this resolution and the absence of local effects of vegetation and topography. Hence the outcome must be downscaled – here by a simple regression model – before the GCM output can be applied at the higher local resolution. Based on the downscaled output of three GCM models, the local warming in the 20-year period before CO₂-doubling is in the order from 1.2 to 2 °C. The increased temperature is not evenly divided over the year but predicts larger rises in winter and summer. The temperature rise in winter is relatively the largest and associated with an increase in variability. Thus, the higher temperature range will strengthen the moisture deficit in the area but the variability will not entirely eliminate those soil moisture conditions favouring landslide occurrence in the wetter part of the year between autumn and spring. The net effect of climatic change will depend on the accompanying changes in rainfall. However, downscaling of precipitation for the Mediterranean is generally unsuccessful because of the local character of the weather systems and the topographical effects that define rainfall in this region. Based on literature, it appears that the pertinent changes are slight although all analyses indicate an increase in variability. In this respect it is of interest that the influence of the jet stream towards the Mediterranean could probably decrease. Since the jet stream transports cold polar air to the Mediterranean that gives rise to unstable atmospheric conditions and extreme rainfall, this will certainly alter the temporal activity of landslides in the Valles de Alcoy. However, because of the limited success of the downscaling of precipitation at Almudaina, the climate change scenario has been limited to a rise in temperature only with the precipitation remaining unchanged.

The application of the coupled hillslope model under future conditions clashes with the deterministic nature of the historical rainfall record of Almudaina and it could introduce bias in the estimation of the potential landslide triggers of extreme rainfall events. To overcome this problem, a stochastic weather generator has been constructed that simulates the daily weather for the study area. In addition to rainfall occurrence and daily rainfall totals, the non-precipitation variables of relative humidity, temperature, wind speed and atmospheric pressure are simulated to calculate the potential evapotranspiration. Since global radiation is mostly defined by the atmospheric conditions and it could be shown that by absence of long-term data the use of averaged values did not result in faulty estimates of evapotranspiration, this variable is introduced as the long-term seasonal trend for the Valles de Alcoy.

The weather generator is designed to produce internally consistent timeseries meaning that it reproduces the observed characteristics and correlations between the variables. To this end, the generator has been parameterised on the present climate of Almudaina and adapted to the inferred rise in temperature as the result of global warming. For the present-day climate, it has been demonstrated that the weather generator fails to simulate the observed autocorrelation of the precipitation totals and the occurrence of prolonged dry spells. However, the observed interannual variability was satisfactorily reproduced by the stochastic weather generator. This makes it a valuable tool to obtain unbiased, synthetic timeseries of the climatic conditions controlling landslides for the recent past and the near future.

5 SITE INVESTIGATION AND PARAMETERISATION

5.1 Introduction

For the calibration and validation of the coupled hillslope model over the historical period from 1971 until 1998 and its eventual application to the assumed scenarios of environmental change, a parameterisation describing the material and vegetation properties is required (Table 3.1). This parameterisation should represent the spatial distribution adequately whilst generalising the data to keep the implementation of the model feasible.

The relevant hydrological and geomechanical properties of the soils and vegetation have been determined in the field and laboratory. In the following sections, the methodologies and results of the various field and laboratory tests are presented and discussed. When appropriate, these characteristics have been analysed with respect to land use. To this end a land use classification has been defined that is covered in Section 5.2.

The measured properties have been determined on samples from different locations in the *Barranco de la Coloma* and the *Barranco del Mollo*. The coupled hillslope model shall be applied to the Barranco de la Coloma on which consequently the emphasis has been placed. The concluding section of this Chapter gives a synthesis of the data and the parameter set for the calibration and validation of the model.

5.2 Land use aspects

5.2.1 Introduction

Land use has a strong influence on soil moisture availability and by that on the activity of rainfall-induced landslides in the Mediterranean. Besides the effects of direct human action (e.g. tillage practices), the influence of land use on the water balance is the result of the vegetation cover that has evolved under the human exploitation in the past. The effects of the vegetation cover can be subdivided in the loss of precipitation by interception and the removal of soil moisture by transpiration.

In the study area, the cultivated fields are distinct from the abandoned terraces and the semi-natural vegetation. On the cultivated fields, the intention is to make as much water as possible available to the crops. Hence, the crop density is low and all weeds are removed to reduce the interception and evapotranspiration. To increase infiltration and to reduce erosion, all slopes have been terraced. The soils are ploughed -at least three times per year- to increase the infiltration capacity and to preserve water: once at the start of the autumnal rains, once at the beginning of the spring and after the harvest. Often ploughing is repeated after rainfall events to reduce evaporation and to restore the damage of superficial erosion. The tillage itself is shallow and does not extend beyond the upper 20 cm of the soil.

For the abandoned and semi-natural fields, the transpiration will be higher due to the greater expanse covered by vegetation. According to Eagleson (1982), the natural vegetation in water-limited systems produces an optimum canopy density that limits

water stress and provides a maximum biomass for the species present. Because of the soil moisture deficit over summer, the competition for water will be intense. In the present case, where the cultivated area is abandoned, the development of the semi-natural vegetation occurs at the expense of the neglected crop types. The competition for water delays the revegetation at first but when well underway the semi-natural vegetation is often more successful because of its better access to the available water in the winter. Consequently, the abandoned crops wither and give way to a more evolved semi-natural vegetation. The development of the semi-natural vegetation proceeds by a succession of perennial grasses, herbs, evergreen shrubs and Pine trees. The crisp bench terraces degrade gradually during this process.

With respect to the hydrological triggering of landslides, the difference in vegetation may have ambiguous results (Greenway, 1987; Chapter 1). Although the annual water use will be higher under natural vegetation, the water yield to the deeper regolith is not necessarily lower as the more developed root zone may increase the infiltration and storage capacity of the soil. Consequently, the yield could be higher than that of the cultivated fields whenever the available rainfall exceeds the demands of the vegetation over a certain period. This increase in water yield to a potential shear zone could counteract the beneficiary effects of the higher water consumption and the increased shear strength due to the presence of roots. The stabilising effect of roots, however, is easily downgraded if the roots do not penetrate the potential shear surface (Tsukamoto & Kusakabe, 1984). This is the case in the study area where the sound marl bedrock is unattractive for vegetation. As a result, all observed shear planes pass for most of their length through the regolith, well below the root zone.

Because of the presumed influence of land use on landslide activity, the spatial configuration of land use and related parameters should be known. This requires a land use classification that is defined here. Also, the direct vegetation effects of interception and evapotranspiration are covered in this Section.

5.2.2 Land use classification

The main objective of the land use classification is that it should provide relevant information on vegetation cover and generalise the available data as model input. Given the ongoing abandonment of cultivated fields in the study area, it should include the successive stages of revegetation. The refinement of the classification is not only limited by its intended use for model parameterisation but also by the available data. It is evident that the information on land use conditions in the past or in the future inherently lacks detail.

To meet these requirements, a land use classification has been designed that is hierarchical, in the sense that it represents land use on different spatial and temporal scales. Table 5.1 summarises the different levels in the classification. The four main categories, denoted by capitals, distinguish the level of human involvement with decreasing intensity. For each of these categories an additional subdivision is made in crop or vegetation types and signs of degradation or the establishment of climax vegetation. In this manner, land use is classified by determining the main category and the appropriate subgroups of crop, revegetation and area coverage.

Table 5.1: Land use classification

Level I	Land use classes	Level II	Primary vegetation (crops)
	<i>Primary land use classes</i>		<i>All crops, ranked with coverage</i>
B:	Built-up area	o:	no primary vegetation
C:	Cultivation	f:	fallow (tilled/no crops)
A:	Abandoned	h:	horticulture (annual crops)
S:	Semi-natural	v:	vines
		i:	isolated and dispersed permanent crops (fruit trees)
		s:	scarce plantation with permanent crops (fruit trees)
		p:	plantation with permanent crops (fruit trees)
		_c:	mixed crops: recognisable produce of annuals between permanent crops (suffix)
		_l:	lawn of grass or other sown weeds to protect soil (suffix)
Level III	Secondary vegetation	Level IV:	Climax vegetation
	<i>The secondary vegetation includes all types of weeds that emerge naturally when agricultural practices has stopped</i>		<i>This category includes types of vegetation - or their absence - relating to the development of a climax vegetation</i>
g:	grasses and herbs; secondary vegetation of grasses, herbs and heather-like perennials	B:	Barren areas of degraded soil present and clearly visible in vegetation cover
s:	Shrub vegetation and dwarfed trees; canopy extending approx. 0.2 - 1 m above the soil	D:	Deciduous trees, tall-growing species (poplar and elm)
g/s:	Patches of (g) and (s) without further distinction	P:	Coniferous trees (pine and larch)
		Q:	Oak, natural climax vegetation

According to the classification, land use has been mapped from aerial photographs. These photographs are available from the years 1956, 1965, 1973, 1984, 1989 and 1994. All photos were taken in the period between May and July. Except for the years 1956 and 1984, the vegetation types can be recognised at the level of the individual parcels. The derived land use configuration of 1994 has been compared with the field situation of 1998. The mapped units agreed well with the field situation except for the restoration of cultivation on some abandoned fields.

Several land use changes can be recognised in these photos. Firstly, the abandonment and consequent revegetation is apparent in most photographs. The greatest change occurred in the period between 1956 and 1973. The rate of revegetation varies per location but generally the vegetation cover closes within 10 years after abandonment. Aleppo pine (*Pinus halepensis*) establishes itself as semi-natural climax vegetation within 30 years. On the cultivated bench terraces, the clearest changes appear between 1956 and 1965. Compared to 1956, the more interesting fields are better kept and enlarged in 1965 while some fields that were still rudimentarily used in 1956 are abandoned. Over the years, the

change in the ratio between annual and permanent crops is also visible. Nowadays, most of the area is covered by permanent crops whereas in 1956 a large area was used to grow annual crops or kept fallow at the time of the photographs.

Between 1973 and 1998 the differences are less pronounced except for abandonment and the conversion of vineyards to cherry and olive trees. Grapes formed an important commercial crop until 1977 when the bulk of the agricultural land was mapped as mixture of vines with olives (MAPA, 1981). Yet, vines had vanished in the study area by 1989.

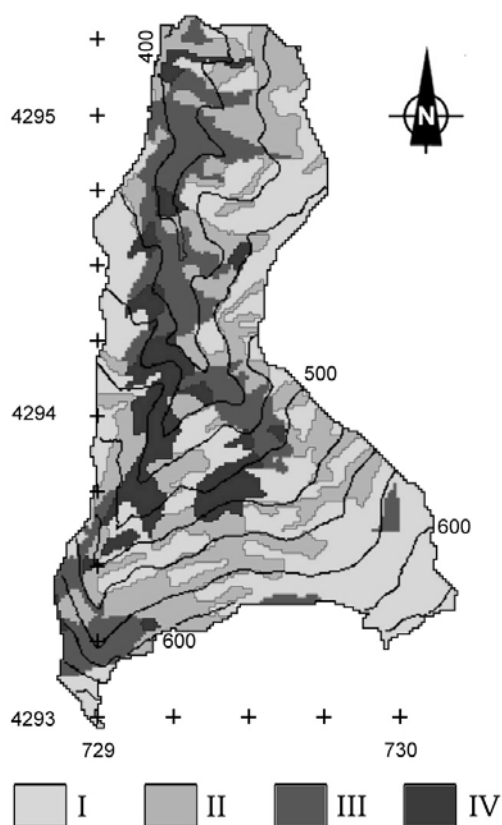


Figure 5.1: Land use in the Barranco de la Coloma in 1998. See Table 5.2 for units

Table 5.2: Combination of the observed land use classes in four units

Unit I	<i>Cultivated fields</i>									
	Bo	Cf	Cp							
Unit II	<i>Abandoned, first succession of grasses and weeds</i>									
	Aog	AogB	Aogs	AosB	Apg	ApgB	ApsB			
Unit III	<i>Abandoned, secondary succession of shrubs</i>									
	Aos	AosPB	Aps	AssB	Ss	SsB				
Unit IV	<i>Semi-natural climax vegetation</i>									
	AogD	AogP	AogP	AogsP	AosP	ApsP	SoD	SoP	SsP	SsPB

In the land use classification of 1998, 26 units were identified. This number is too high for the parameterisation and some classes must be combined. Of these, the area of human

occupation was negligible and can be merged with the cultivated fields without problem. The same holds for all agricultural areas not covered by permanent crops.

In addition to the clearly distinct agricultural fields, some generalisations can be made for the revegetated and natural areas as well. Considering that vegetation cover and type define the losses to interception and transpiration and the development of the root zone, the primary succession of crops on the abandoned fields will be different from the complete cover attained by the second phase of revegetation (shrubs) and by the semi-natural vegetation. Hence, the classified land use has been merged in the units of Table 5.2, which are characterised by the vegetation types described in Section 2.4.

The generalisation of the land use classification offers the possibility to include the relevant vegetation and soil properties per unit in the parameterisation of the model. Since land use is a spatial attribute (Figure 5.1), all parameters will be distributed accordingly and the mean and variance are assigned to the areas of this choropleth map.

5.2.3 *Canopy interception*

Canopy interception has a direct influence on the net rainfall available for infiltration. Canopy interception is defined as gross interception (Zinke, 1965). This is the amount of interception that is detained by the canopy and lost to evaporation. Thus, the net precipitation consists of all water that passes through the canopy either as direct throughput or as the delayed transfer of intercepted water. As explained in Section 4.3 it could be treated distinctly from the interception storage at the surface level in order to allow varying vegetation conditions at the two levels over time. Moreover, canopy interception can be more effectively monitored and included in the model parameterisation.

In Chapter 3, linear regression equations and conceptual models were mentioned as the simpler approaches to quantify the influence of canopy interception on the net rainfall. Linear regression models are directly applicable to the temporal scale on which they are defined. They specify an invariable deduction on the basis of independent variables that can be interpreted as the loss to evapotranspiration from the intercepted rain during an event. Such linear regression models are entirely empirical and mainly the gross rainfall is used to predict interception. Thus, regression equations are usually unable to accommodate the specific conditions per event. As a solution, distinct regressions for periods that reflect these differences may be required. Compared to such empirical linear relationships, conceptual models, such as those of Rutter *et al.* (1971) and Gash (1979), have the advantage that they can be parameterised with *a priori* knowledge and adapt to different initial conditions and rainfall events. Because these models are event-based, however, they need detailed temporal information and must be aggregated to accommodate data with a lower temporal resolution.

For the parameterisation of the model, the flexibility and the simplicity of respectively the conceptual model and the linear regression equation must be evaluated. To this end, both models are applied to measurements of net precipitation in the study area and compared with cited values for similar vegetation covers in Mediterranean environments.

5.2.4 Interception measurements

In the study area, canopy interception was measured by rainfall experiments under different vegetation types and monitored continuously under a stand of Aleppo pine (*Pinus halepensis*).

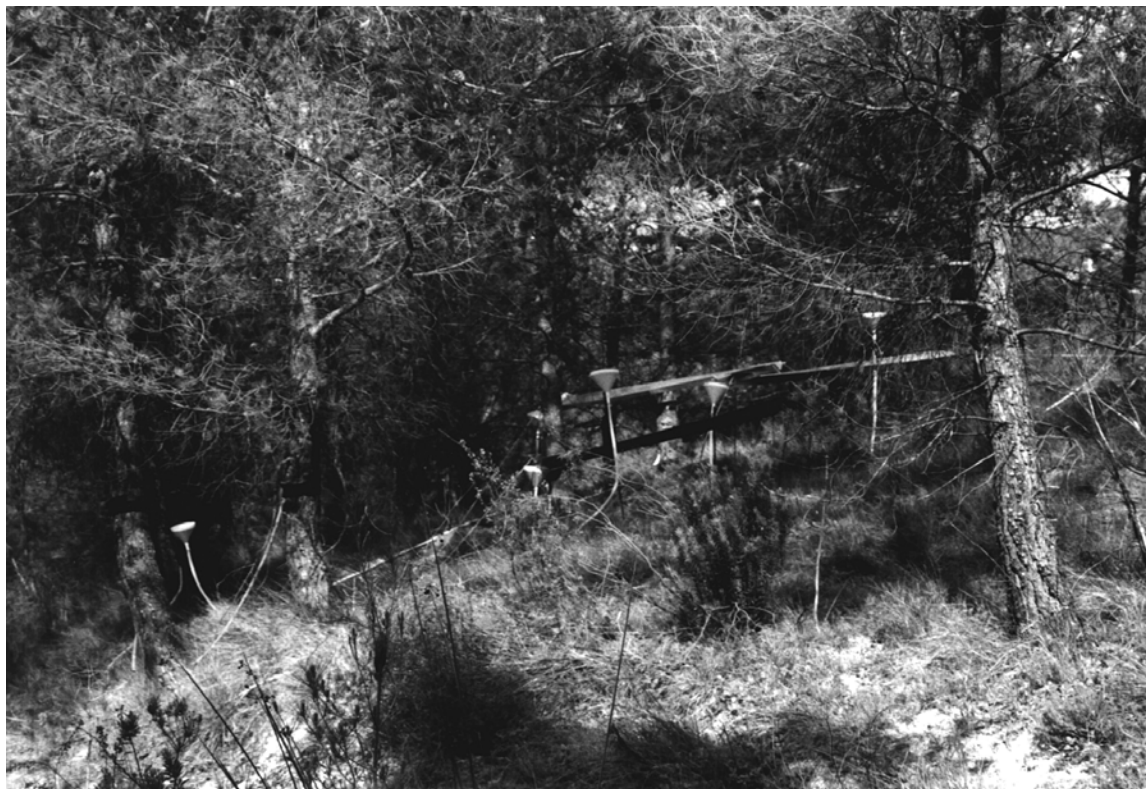


Plate 8: Interception plot under *Pinus halepensis*

The plot for monitoring the interception under Aleppo pine is located at the LGM-site (Appendix 1). The plot is operative since December 1996 and records the stemflow and throughfall under natural conditions over an area of 100 m² on the W-exposed side of the Barranco de la Coloma. On this site, 7 individuals are present of which the projected canopies cover 111 m². Tree diameters at breast height range between 9 and 21 cm and tree heights vary from 4 to 10 m.

All seven trees have been fitted with collars to collect stemflow. Between the trees, zinc sheets, which cover nearly 3.5 m², collect the throughfall at approximately 1 m above the ground (Plate 8). Both stemflow and throughfall are collected and recorded by separate tipping buckets. Gross rainfall is available from the tipping bucket at the LGM-site. To avoid incongruence between the discretely sampled data, all data have been sampled at 10-minute intervals and have been summed to hourly and daily values afterwards.

Between December 1996 and February 1998, 15 events in excess of 1 mm within 24 hours have been recorded for which the gross rainfall at an hourly scale is available. These 15 events represent a recorded total of 36 at the station of Almudaina. The absence

of data for a substantial part of this period is explained by the malfunctioning of the equipment in the period between February and April 1997 and the lack of gross precipitation data in the subsequent period till October 1997. When daily totals are considered and the missing rainfall is replenished by the daily record at Almudaina, the total of recovered events increases to 20.

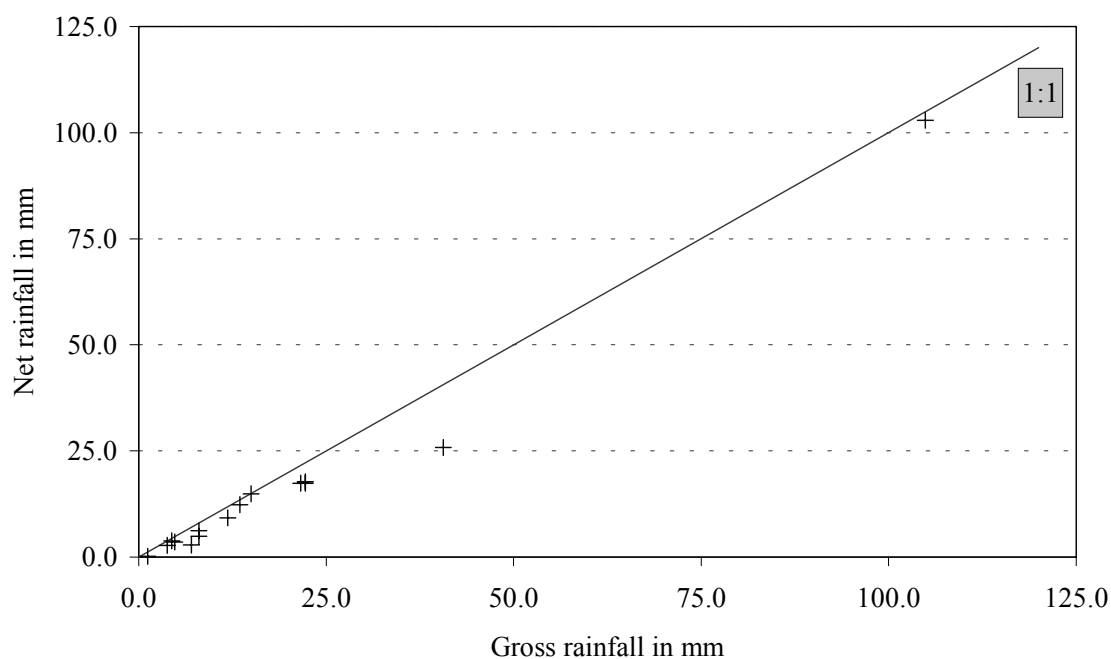


Figure 5.2: Scatterplot of gross rainfall and net rainfall under *Pinus halepensis*

Because of the fragmented data records, most events cover the months from November till February and thus represent low-intensity and prolonged rainfall (Section 4.2.4). The shortest event, stretching from the first until the last recorded tip, lasted 6 hours and delivered 1.2 mm of rainfall. The longest event lasted 54 hours and delivered 22.2 mm. The largest event delivered 104.9 mm in 43 hours. Overall, Figure 5.2 shows that the net precipitation is close to the gross rainfall for the larger events. Stemflow, expressed as waterslice over the projected area, is as a rule negligible and only perceptible for the larger storms.

With net rainfall being defined as the sum of throughfall and stemflow, the total interception loss is easily defined. For the 15 events, the net precipitation amounts to 241.8 mm or 84% of the gross total of 289.1 mm. This fraction does not change when the 20 events available from daily values are considered ($P_{\text{net}}/P_{\text{gross}} = 85\%$).

For the hourly and daily values, the linear regression equations have a slope close to 0.80 ($\text{mm}\cdot\text{mm}^{-1}$) (Table 5.3). This suggests that on average some 20% of the gross precipitation could be lost to interception. Both linear regression equations have a slightly positive intercept that incorporates part of the error. The error in the estimated interception loss result partly from sampling errors that occur when the recorded net and

gross rainfall amounts are distributed unevenly over two hours. A structural error, however, is also present as the linear regressions deduct a fixed, proportional amount from the gross rainfall at every timestep, irrespective of the intensity and the antecedent rainfall during the event.

Table 5.3: Regression equations of net rainfall on gross rainfall under *Pinus halepensis* for hourly and daily data

Measurements	Y_0 (mm)	α (-)	R^2 (-)	N
Hourly	0.01	0.81	0.89	228
Daily	0.14	0.79	0.84	48

The performance of the linear regression equations increases when the event-totals are considered. The aggregation of the data removes the measurement error from the data and includes the effects of accumulated rainfall (Table 5.4). It is the total gross rainfall that is the best predictor in an absolute sense although duration and maximum intensity have some relative predictive power as well. The event-based regression equations give estimates for the net precipitation that fit well to the observed values.

Table 5.4: Regression equations of net rainfall on gross event totals under *Pinus halepensis*. Based on on-site data and daily rainfall totals from Almudaina

Measurements	Y_0 (mm)	α (-)	R^2 (-)	N
Hourly	-2.47	0.96	0.98	15
Daily	-2.01	0.96	0.99	20

According to both linear regression equations of Table 5.4, the net rainfall amounts to 96% of the gross precipitation from which an amount in the order of 2 mm is deducted. These equations hold well for the larger events that deliver most of the rainfall and that have a larger weight in the regression analysis. They fail to estimate contribution of smaller events or prolonged events, however, for the negative intercept results in negative net rainfall for all events smaller than 2.5 mm. Still, these events may produce some throughfall. Thus, whilst the event-scale regressions provide a better model to predict net precipitation, it inherently is not applicable to discrete temporal data, as processed by the model, and it underestimates the contribution of the smaller events. A solution to these shortcomings can be found in a conceptual model as that proposed by Merriam (1960). His model defines the detained water, C , at a given time as an exponential function of the maximum canopy storage capacity, C_{\max} , and the accumulated rainfall, P ,

$$C = C_{\max} [1 - \exp(-(1 - p)\Sigma P / C_{\max})]. \quad (5.1)$$

where p is a dimensionless throughfall partitioning coefficient and where rainfall P and canopy storage C are given in mm.

Merriam's model considers the accumulated rainfall, meaning that the saturation of the canopy storage can vary over time. It can consider evaporation from the canopy storage when it is considerable during intermittent periods of ceased rainfall. Unlike the

regression equations, the parameters C_{\max} and p have some direct physical explanation and can be estimated from field measurements. Because only the fraction $(1-p)$ of the rainfall is intercepted, some rainfall passes the canopy in all circumstances. In this respect, the model is more appropriate for the smaller events than the event-based regression equations of Table 5.4. Compared to the regressions on the discrete data of Table 5.3, the model has the advantage that its canopy storage is limited to a maximum, C_{\max} . In this manner, rainfall is not stored infinitely by the canopy but is passed on unhampered whenever the canopy store is fully saturated.

Merriam's model has been applied to the recorded events on an hourly basis. These events stretch over periods of intermittent rain and the potential evaporation has been included to obtain a reliable estimate of the maximum canopy storage capacity. The potential evaporation has been calculated from the data of the meteorological station (Section 4.3), and is available for 14 of the 15 events.

For the 14 analysed events it has been assumed that the canopy conditions do not vary with time, so p and C_{\max} are regarded as constant. Moreover, canopy storage is only dependent on the rainfall and evaporation. The latter quantity is small, amounting to 30.0 mm compared to 249.1 mm of rainfall over the 14 events.

The fraction of intercepted rainfall has been set to the inverse of the leaf area index (LAI), the ratio of the leaf area over the total surface area. The LAI has been determined by means of Beer's Law that gives the relation between the global radiation flux over and under the canopy. Both radiation fluxes were measured with pyranometers during a one-hour lasting experiment in April 1997. Under the canopy, the radiation flux was measured at the ground surface at random positions. The total incoming radiation was measured at the meteorological station. Measurements were made at a sampling rate of 30 s after which the values were aggregated to 5-minute averages. The value of the LAI was determined at 1.67 ($\text{m}^2 \cdot \text{m}^{-2}$). The bulk throughfall coefficient, being the difference between unity and the inverse of the leaf area index, then equals 0.40 (-; fraction of $\text{mm} \cdot \text{mm}^{-1}$ rainfall per unit surface area) for the interception site.

The common opinion is that Merriam's model should preferably be fitted on an event-basis (Aston, 1979; Klaassen *et al.*, 1998). Notwithstanding, the predicted values approximate the observed values well, both on an hourly as on an event-scale (Figure 5.3). Using the root mean squared error (RMSE) as the optimisation criterion, the maximum canopy storage capacity has a corresponding value of 1.9 mm in both cases.

For the event-totals, the RMSE amounts to 1.3 mm. Figure 5.3 shows that the model underestimates the net precipitation in 8 of the 14 cases. Generally, the model performs well except for the smallest event. On the total budget, the net precipitation is only slightly underestimated (215.5 vs. 216.1 mm).

If applied to daily totals of gross rainfall, Merriam's model needs to be aggregated. Aggregation to the daily scale is easily achieved as the fraction p of the gross daily rainfall reaches the surface unhampered whilst the intercepted precipitation is only passed on when the canopy store is fully saturated. In that case, the interception loss is only dependent on the evaporation. As a consequence, the losses from small, prolonged rainfall events are relatively large. When rainfall continuously exceeds the available canopy storage capacity, C_{\max} , the reduction of the gross precipitation is finite and the losses predicted by the aggregated Merriam model resemble those made by the event-

scale linear regressions. However, as the Merriam model is more flexible than the linear regressions applied, it should give better approximations in all regions with little more modelling effort. This has been tested by applying the aggregated Merriam model to the daily interception data. When the aggregated Merriam model is applied to the daily data, without considering evaporation, the RMSE amounts to 3.3 mm. Most of this error is attributable to an event that lasted 3 days in October 1997. During this event, 41.2 mm of gross precipitation resulted in 26.1 mm of net rainfall whereas the predicted net precipitation amounts to 39.3 mm. Overall, the aggregated model approximates the observed net precipitation well except for the smallest of events in which the evapotranspiration has a relatively large influence (Figure 5.3).

With exclusion of the event of October 1997, the aggregated Merriam model performs well; it overestimates the accumulated net rainfall over the events by 10.9 mm (312.8 against 301.9 mm observed). On an event-scale, the linear regression model of Table 5.4 underestimates the net rainfall by the same order of magnitude. However, Merriam's model performs better than the simple regression on an hourly and daily scale. This makes Merriam's model the more appropriate to estimate the amount of intercepted rainfall from the daily rainfall data of Almudaina.

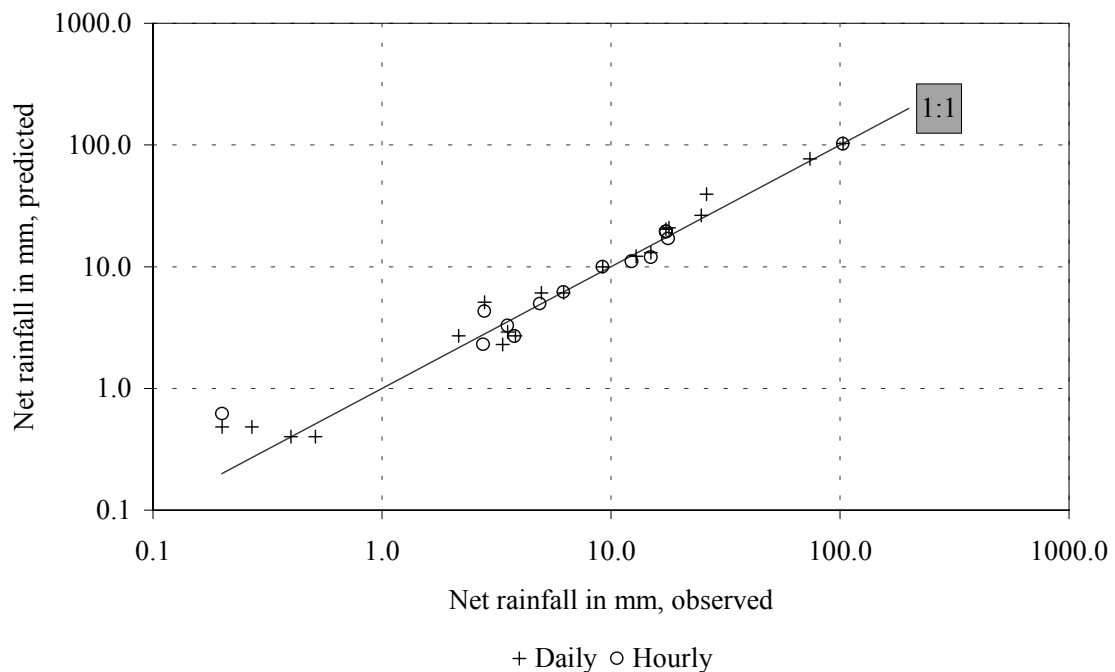


Figure 5.3: Comparison of the event-based and aggregated interception model of Merriam (1960) for *Pinus halepensis*

For the other vegetation types, data on interception are less detailed. The available information stems from simple rainfall experiments on canopies of olive trees and thorn shrubs (*Ulex parviflora*). For each type, two experiments are available. The applied rain was compared with the accumulated throughput during and following the experiment. The measurements were made with a tipping bucket device with a sampling rate of once

every 10 seconds. In each experiment, artificial rain was applied until a constant rate of tips was achieved. The applied intensities were high, with values of 142 – 146 mm·hr⁻¹ and 33 mm·hr⁻¹. The experiments lasted for 20 to 45 minutes.

Because of the coarse design of the experiments, the results are poor and suffer from their limited scale and sample size. The most obvious conclusion is that the actual throughfall under the canopy is small. At the conclusion of the experiments, the ratio of collected total throughfall was 44% and 40% for the shrub and olive canopy respectively. Owing to the delay of the throughput, the amount of water stored in the canopy decreased during the experiments. In the first phase, the ratio was often well below the final version and seldom exceeded the 20%. The low throughfall ratio is confirmed by hand-made measurements of the collected throughfall under olive trees from natural rainfall in spring 1997. It appears that for short-duration rainfall the throughfall is negligible under this type of vegetation.

In contrast to the data from the interception-site under the Aleppo pine, the rainfall experiments do not give a bulk value for the throughfall but measure it for a specific part of the projected canopy. Consequently, the data can not be transferred directly to a larger area. Corrections for the density and the projected area must be made if area-averages are required. In that case, the interception by olive trees and the comparable cherry trees is strongly reduced because of the large spacing of the crops in the area. Typically, cherry trees and olive trees are spaced respectively 8 and 10 m apart. With a canopy radius in the order of 2½ m, 70 to 80% of the rainfall reaches the bare surface unhampered on the cultivated fields. Thus, the amount of intercepted rainfall is relatively small and a value in this range can be used as the throughfall partition coefficient for the cultivated orchards. The maximum canopy storage capacity can be obtained from the observed difference between the applied rainfall and the collected net precipitation. For the two olive trees tested this value is in the order of 40 mm. Multiplied with the projected canopy area (20 m²) and divided by the total area per individual tree this gives a maximum canopy storage capacity of 8 mm.

For the shrubs, the scaling is less straightforward since the vegetation density varies locally. The observed loss in terms of net precipitation is the same as for the olive trees. So, the interception at the plant level is roughly the same but will be distinct and variable on the field site because of the variable vegetation density and plant size.

In comparison to literature values for interception by pine trees, the fits of the various linear regression equations and the Merriam model agree well. Typical values for the fractional loss of gross precipitation by canopy interception are in the range from 10 to 35% (Dingman, 1994). The loss, however, falls in the lower range and is much lower than the value for Aleppo pine found by Belmonte at a location in SE Spain (Belmonte, 1997). There, the fractional loss was 27%. The large difference between the locations can be explained by the differences in canopy density and in annual rainfall. The measurements by Belmonte were made under and around the canopy of several isolated trees and not under a complete but sparse cover. Regarding the difference in rainfall, the largest annual total was 330 mm over the period 1992 – 1995. This is only half the average at Almudaina. Hence the evapotranspiration by the vegetation under water stress will be larger than that under the more moist conditions at Almudaina (Klaassen *et al.*, 1998). This is evident from the large fractional loss of 35% in the extremely dry year of

1995 and from the lower slopes of the regression equation found by Belmonte (0.91 compared to $0.96 \text{ mm}\cdot\text{mm}^{-1}$ at Almudaina; Belmonte, 1997).

Given the parameters of the Merriam model, the throughfall partitioning coefficient of 0.4 (-) is comparable to the value of 0.36 (-) estimated by Valente *et al.* for *Pinus pinaster* in Portugal (1997). This value was estimated for the Rutter model that subdivides the canopy storage in that of the trunk and canopy. Since from both water is lost to evapotranspiration, the values are incomparable to the maximum canopy storage capacity in Merriam's model. The observed loss to interception is more similar to that at Almudaina, namely 17% (Valente *et al.*, 1997).

The data from the rainfall experiments on the olive and shrub canopy are less reliable. The high fractional loss of 40 to 45% of the applied high-intensity rain is not representative for the natural conditions. Also, stemflow was ignored. For the olive trees, this quantity is negligible compared to the rainfall lost on the canopy but for the shrubs stemflow is considered an important process (Belmonte, 1997). Thus the amount of collected throughfall may be an erroneous estimate of the net precipitation under shrubs (Burgy & Pomeroy, 1958).

In order to obtain more reliable data on interception, literature values have been used for all vegetation other than pine. For the permanent crops of olive and cherry trees, values for deciduous trees are used. For them, the fractional loss of gross precipitation is generally less than 20%. For small eucalyptus trees, not unlike olives, the loss is around 10% (Aston, 1979; Valente *et al.*, 1997). Under the canopy, the throughfall partitioning coefficient is in the order of 0.4. The maximum canopy storage capacity for the projected canopy area varied between 1 and 2 mm for eight small trees of different eucalyptus species (Aston, 1979).

Deciduous trees with dormancy, like oaks, provide some information on the interception by cherry trees. A study by Dolman (1987) on interception by a closed canopy of oaks showed saturation storage capacities of 0.8 and 0.3 mm for summer and winter respectively. The absence of foliage explains the lower winter value. This value is lower than expected on ground of the reduced fractional loss by interception after defoliation reported in literature (Noirfalise, 1959; Dingman, 1994). Generally, a 30% decrease is mentioned whereas the storage capacity mentioned by Dolman (1987) decreases with 60%. Considering that the latter value is obtained from modelling and accompanied by an opposite 60% decrease in the throughfall partitioning coefficient, it is likely that the change in both parameters account for the seasonal difference in rainfall and evapotranspiration rates rather than for changes in plant physiology. Hence the throughfall partitioning coefficient and the maximum canopy storage capacity are estimated to be 0.4 and 2 mm over the projected canopy area. Since this area covers only a mere 40 to 20% of the area between the individual trees, the values are scaled accordingly. Hence, the throughfall partitioning coefficient is increased to 0.8 and the maximum canopy storage capacity reduced to 0.6 mm. Consequently, interception will be small under permanent crops. The parameters are considered as constant as the effect of defoliation from the cherry trees will be small. Consequently, no distinction between olives and cherries has been made.

For shrubs of different size, *in casu* junipers, thyme and rosemary, Belmonte (1997) mentions fractional interception losses of 28%, 28% and 25% respectively. These values are spatial averages. Under mixed vegetation types, the actual throughfall varied between

35 and 95% of the incoming rain. For the shrubs, a substantial part of the net precipitation is delivered by stem flow (20 to 40%). Since the Merriam model does not include this process explicitly, a relatively large error is introduced in comparison with the pine and fruit trees. For the smaller shrubs, the travel-time of the stemflow is reasonably short but transfer of the intercepted water to the branches and trunk may be delayed by the intricate structure of the shrubs. Consequently, relatively large losses could occur for the smaller rainfall events when no stemflow is generated. This is consistent with the regression equations obtained by Belmonte. In all cases, the slope of the regression equations was relatively constant at 0.85, indicating a constant loss once storage capacity is exceeded. Similarly, a constant negative intercept exists that represents the initial loss due to canopy storage. The largest value was 1.5 mm for the larger juniper shrubs. This value compares well with the maximum canopy storage capacity of shrubs mentioned in the literature (Burgy & Pomeroy, 1958). For all types, the intercept is smaller during periods of water stress. This is probably caused by a loss of foliage. As an approximation of the interception by shrubs, the parameters of the linear regression equation for juniper have been used as the maximum canopy storage capacity and the throughfall partitioning coefficient ($C_{\max} = 1.5$ mm, $p = 0.9$ -).

In addition to canopy interception, a part of the gross rainfall can be caught and evaporated by the understorey. On cultivated terraces any undergrowth of weeds is removed frequently and can conveniently be ignored. On the areas covered by shrubs, the canopy levels can not be distinguished and are treated as one. However, a secondary level of vegetation, mostly grass and herbs, is present under the stands of pine and on recently abandoned terraces. On the abandoned terraces, this vegetation layer increases interception and the maximum canopy storage capacity has been set to the value of 1.2 mm. This value was obtained by Burgy & Pomeroy from laboratory experiments (Burgy & Pomeroy, 1958). Including the abandoned crops, this gives an equivalent maximum canopy storage capacity of 1.5 mm and a throughfall partitioning coefficient of zero (i.e. all storage must be replenished for net rainfall to become available). Burgy & Pomeroy (1958) argue that this loss of gross precipitation is not directly proportional to the net precipitation as the moistened vegetation will transpire less moisture. This effect will be small, however, on the more exposed abandoned fields where the turbulence around the trees will increase the evapotranspiration. In contrast, the loss of interception due to the presence of understorey under a closed pine canopy will be less marked because of the higher humidity during and after a rainfall event. Because of this reduced evapotranspiration, the presence of an understorey has been ignored for the pine stands in the study area. The parameterisation for the different land use units is listed in Table 5.5.

Table 5.5: Parameters for Merriam's model of canopy interception per land use unit

Representative for:	Unit I Cultivation of permanent crops	Unit II Abandoned crops with grass cover	Unit III Shrubs	Unit IV Pine
p (-)	0.8	0.0	0.9	0.4
C_{\max} (mm)	0.6	1.5	1.5	2.0

p (-): Throughfall partitioning coefficient
 C_{\max} (mm): Maximum canopy storage capacity

5.2.5 Crop specific evapotranspiration

The crop factor, k_c , is a dimensionless adjustment factor that specifies the portion of the potential evapotranspiration that can be removed through the vegetation (Doorenbos & Pruitt, 1977). It reduces the maximum rate of potential evapotranspiration to a rate allowed by the vegetation, the crop specific evapotranspiration, ET_c , which is estimated from the calculated reference potential evapotranspiration ET_0 , by

$$ET_c = k_c \cdot ET_0. \quad (5.2)$$

The crop specific evapotranspiration lumps all vegetation effects that arise through the characteristics of the individual plant or the plant community. The crop factors defined by Doorenbos & Pruitt (1977) apply to disease-free crops under an optimum supply of water and nutrients but local and regional environmental factors can be considered. It is important to realise crop factors do not take the soil moisture availability into account, which will be simulated independently by the model.

If the evapotranspiration by plants were to be measured under such ideal conditions, the crop factor is simply obtained by dividing the actual evapotranspiration by the crop over the reference potential evapotranspiration. However, the measurements are difficult and prone to error. The best measurements are made by sapmeters but this is only feasible for the larger plants and trees and must be transferred to larger areas with heterogeneous plant communities. Simple lysimeter experiments give again a highly localised estimate and suffer from their small size. Often their size is too small to contain representative samples of the vegetation and it makes their results inaccurate. Water balances for the root zone under different vegetation types suffer from the heterogeneity of the soil and require large sample sizes to obtain meaningful results. Any of these direct measurements were beyond the scope of this research. As an alternative, literature values have been used to define the crop coefficients according to the approach specified by Doorenbos & Pruitt (1977).

Although the crop factor approach was developed originally for real crops, it can be expanded to natural vegetation. The crop factors described here apply to the generalised land use units of Table 5.2, regardless whether they are agricultural or not. The values provide area-averages and cover the evaporation from the bare soil and the transpiration through the vegetation alike. The reason for this simplification is that transpiration is often more substantial than the evaporation from a dry soil surface (Hooghart & Lablans, 1988).

In the study area, most of the fields are planted with perennial crops of drupes and olives. Olives and drupes differ in evapotranspiration as the latter trees drop their leaves and experience dormancy what reduces evapotranspiration outside the growing season. In contrast, olives are ever-green and consequently the evapotranspiration is more constant over the year. Since the actual distribution of the two crops is unknown except for a total area ratio of approximately 1:1, the two factors have been averaged to obtain one monthly value for the composite crop that is applicable to all presently cultivated orchards. For the agricultural practices in the Valles de Alcoy, the seasonal change in

crop factors is given in Figure 5.4. The few fields that are planted with annual crops have been ignored and made subject to the crop factor for the permanent crops.

After abandonment, semi-natural vegetation develops at the expense of the original crop types. Consequently, the influence of the latter dwindles and the seasonal variations in the crop factor are dampened for most of the natural vegetation consists of perennial grasses, herbs, evergreen shrubs and pine trees. It is plausible that with the achievement of the semi-natural vegetation by the units III and IV the crop factor will not vary over the year. Seasonal differences will exist in the early phases of revegetation when the area between the abandoned crops is colonised. For the annual and perennial grasses the grow season starts directly after the autumnal rain but remains low in the period of germination between the die-back in late summer and the start of the growing season in February (Joffre & Rambal, 1993). Yet, the early start of the growing season gives the new vegetation an advantage over the former crops that are dormant over winter. At first, most evapotranspiration is lost by the abandoned crop but as time proceeds more and more of the loss is caused by the emerging natural vegetation. In the growing season the crop factor is high because of the competing demands on the available soil moisture by the vegetation components. The increase due to the presence of a vegetation cover between the trees is in the order of 0.05 (-) and based on the values provided by Doorenbos & Pruitt (1977; Figure 5.4).

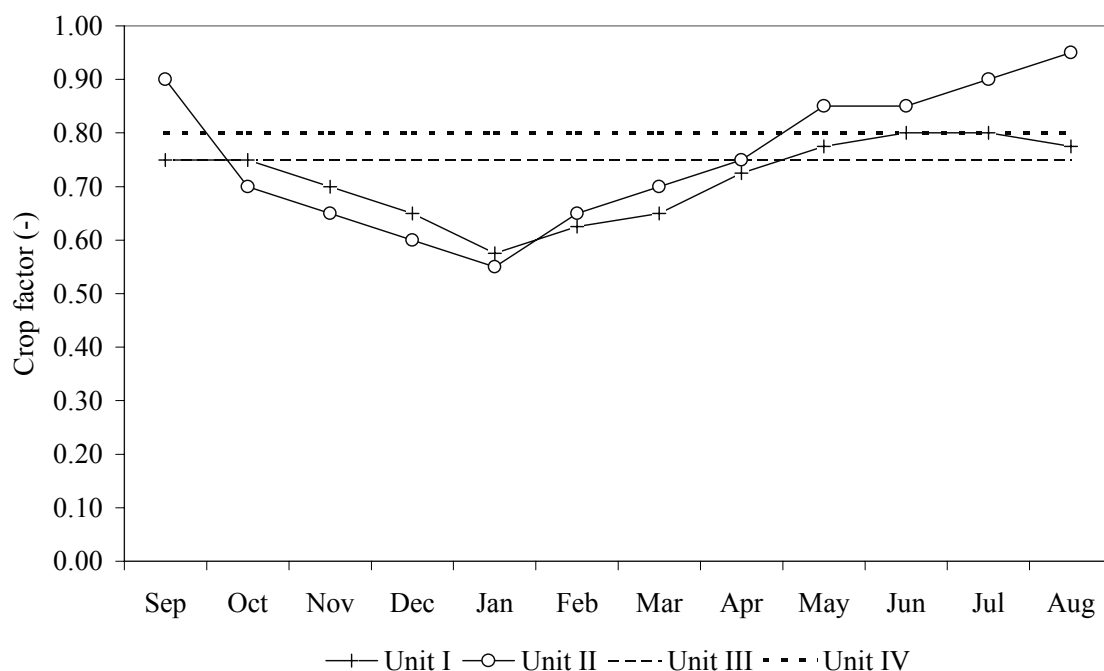


Figure 5.4: Annual course of the crop factors of the four land use units

At the next stage in the revegetation, the vegetation cover is complete and dominated by shrubs (Unit III). For this type of vegetation, any seasonal trend in the uptake of water is absent. Hence the crop factor is at its constant maximum that is equal to the average value for the mixed vegetation of perennials and trees on the abandoned fields. Similar

considerations apply to the climax vegetation of Aleppo pine (Unit IV). For two different stands of Aleppo pine in Israel, Schiller & Cohen (1995, 1998) measured maximum ratio between ET_c and ET_0 in the order between 0.3 and 0.6 (-) by sapflow experiments. The differences between the two sites were the result from the disparity in the annual rainfall and potential evapotranspiration. Because of the higher soil moisture availability, a higher tree density (1600 vs. 600 trees per hectare) was sustained on the site with the larger crop factor. The described stands are well-kept and frequently trimmed. In this respect they are distinct from the spontaneous revegetation in Almudaina. However, adopting from the authors the approach of comparing the maximum ratio of ET_c over ET_0 by means of the leaf area index, the value for the K_C at Almudaina would be in the order of 0.6 (-). In comparison to the Israeli sites, the site at Almudaina has a longer growing season and a more developed undergrowth. Moreover, the higher turbulence around the isolated pine stands would result in a higher evapotranspiration. For these reasons, the crop factor for the land use Unit IV dominated by Aleppo pine has been raised to 0.8. The average value and the range of the crop factors for the four land use units have been summarised in Table 5.6.

Table 5.6: Average crop factors for the four land use units: average and range

Unit	I: Cultivated	II: Abandoned	III: Abandoned	IV: Semi-natural
Vegetation type	Orchards Olives 1:1 Cherries	Idem, mixed with abandoned crop trees	Dominated by shrubs (<i>Ulex</i> <i>parviflora</i>)	Dominated by Aleppo pine (<i>Pinus halepensis</i>)
k_c (-) - average	0.70	0.75	0.75	0.80
k_c (-) - range	0.58 – 0.80	0.55 – 0.95	constant	constant

The use of crop factors has the advantage that the actual evapotranspiration is easily estimated from the reference potential evapotranspiration. However, because of its simplified representation of the plant, the method has been criticised. With respect to Mediterranean environments, this criticism is justified because of the water stress that recurs annually. During prolonged droughts, the rate of transpiration becomes negligible. However, in these environments the vegetation often endures these adverse conditions without harm and recovers to its former level once substantial rainfall has occurred (Gindel, 1964). So, although the criticism on the use of crop factors is valid in the light of plant physiology, the crop factor approach can offer an effective an simple manner to include the vegetation effects on the rate of evapotranspiration for this model application.

5.3 Soil hydrological Properties

5.3.1 Sampling Scheme

For the marl slopes, the soil profile has been subdivided in three layers of 50 cm depth to account for the effects of decreasing weathering. The upper part of 50 cm is considered to represent the fully developed root or tillage zone. Below 100 cm from the surface, observations in the field show a tendency from slightly weathered marl with fissures and

peds towards sound marl bedrock (Section 2.1). The profile between 50 and 100 cm depth is considered as a transition zone.

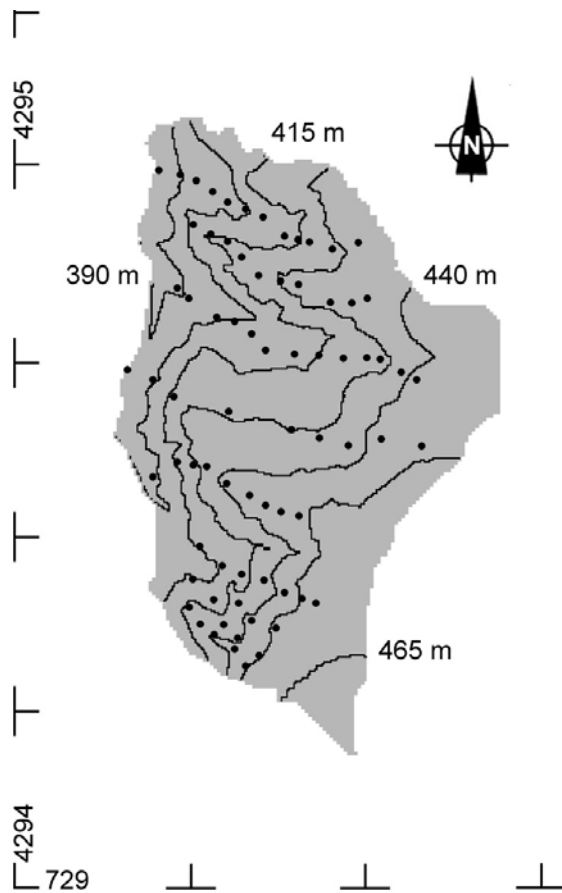


Figure 5.5: Locations along the survey lines in the 30-ha large sub-area

For the defined layers, the saturated hydraulic conductivity, the porosity and the dry bulk density of the soil have been studied systematically along 9 survey lines in a sub-area in the *Barranco de la Coloma* of 30 ha (Figure 5.5). It comprises a part of the westerly exposed hillslopes in this barranco. Most of the area is covered by regoliths and colluvial soils developed over marl. Only on the pediment some alluvial deposits are present.

The area includes the test-site of the “Hollow”, where FDR-probes, the meteo-station and piezometers have been installed in the fall of 1996 (Appendix 1). A total of 76 locations have been sampled in the springs of 1996 and 1998. Along the survey line the distance between sample locations varies between 30 and 40 m. The spacing between the survey lines is approximately 60 m, with a denser coverage of 3 lines at the Hollow. The position of each sample location has been positioned with reference to the local UTM-grid by a theodolite survey.

At each location the bulk density of the oven-dry material and the porosity have been obtained from undisturbed samples at 50, 100 and 150 cm depth. For this purpose, stainless steel sample rings with a volume of 100 cm³ were driven into the matrix. The samples were subsequently saturated and weighed with an accuracy of 0.1 g. After a period of 24 hours at 105°C, the oven-dry samples were weighed again. The data on the

dry bulk density are presented in Section 5.7 on the geomechanical properties of the regolith.

The saturated hydraulic conductivity has been determined in situ by means of the inverse auger hole method (Kessler & Oosterbaan, 1974). The main advantage of this method is that it tests the saturated hydraulic conductivity over an intact soil profile that is assumed to be homogeneous over its entire depth. Thus, it avoids the disturbance commonly encountered in sampling laboratory experiments. It also incorporates the soil variability which increases the accuracy of the measured value. The main drawbacks of the method are that the test is performed in an uncased bore-hole, what makes the bore-hole liable to collapse and sealing. Over the depth tested, successive soil strata of varying permeability influence the final value considerably and violate the assumption of an ideal homogeneous material. This may be recognised by the anomalous behaviour that arises in such cases. However, when the layers of different permeability are small and alternate, the measured horizontal infiltration will be an erroneous estimate of the actual vertical movement of the soil without this being recognised.

In the field, the test procedure consisted of drilling uncased holes with a hand-held 70 mm auger, up to the required 50 cm increment. The bore-hole was then saturated two times, in order to reduce the influence of the suction at the boundary of the saturated and the dry soil. In order to avoid the collapse and sealing of the bore-hole, it was saturated through a hose pipe, from the bottom upwards. A ring of PVC, inserted in the aperture, provided a fixed reference datum. The saturated hydraulic conductivity was eventually determined from the draw-down of the water level after a third entire saturation of the bore-hole. The depth of the water column with reference to the datum was measured by a steel tape dipmeter with a resolution of millimeters. The time of the observations was recorded with a resolution of seconds.

Additional data are available from the scree slope under Almudaina and from the *Barranco del Mollo*. The data from the scree have been determined in the same manner and are presented here. However, because of the varying depth of the scree cover over the marl, the sampling has been less structured and only profiles including a scree cover of sufficient depth have been used.

The data from the Mollo are used to relate the saturated hydraulic conductivity to land use as treated in Section 5.4.1.

5.3.2 *Porosity, bulk density and saturated hydraulic conductivity*

For the 76 sampling locations in the test area, the total number of successful experiments at 3 depths would be 228. Because of the presence of bedrock and other unfavourable sampling conditions, however, missing values occur within the sample population. Both for the inverse auger hole tests and the porosity and dry bulk density sampling a decrease in success is observed with depth (Table 5.7). For the inverse auger hole tests, a total of 202, or 88.6 %, of successful experiments was obtained. For the recovery of the sample rings for the determination of the porosity and dry bulk density, this total was 176 or 77.2 %.

Table 5.7: Recovery from the samples with depth

Depth (m)	Inverse Auger Hole Tests		Porosity & Bulk Density	
	Absolute	Relative (%)	Absolute	Relative (%)
0.00 – 0.50 cm	74	97.4	73	96.1
0.50 – 1.00 cm	73	96.0	67	88.3
1.00 – 1.50 cm	55	72.4	36	47.4
Total	202	88.6	176	77.2

The saturated hydraulic conductivity, or k_{sat} , has been derived from the final draw-down of the water table in the bore-hole after the third entire saturation. For the calculation of the hydraulic conductivity, Kessler & Oosterbaan's method has been used (1974). Under the assumption that the gradient within the saturated column is equal to the height of the water table above the bottom of the hole – hence $dh/dz = 1 \text{ m}\cdot\text{m}^{-1}$, the combination of the continuity and momentum equation gives (Kessler & Oosterbaan, 1974; Figure 5.6):

$$Q(t_i) = 2k_{sat}\pi r \left[h(t_i) + \frac{r}{2} \right] = -\pi r^2 \frac{dh}{dt}, \quad (5.3)$$

where t_i denotes the time since the start of the experiment, h denotes the water height, and r is the radius of the bore-hole (all units expressed in m and s).

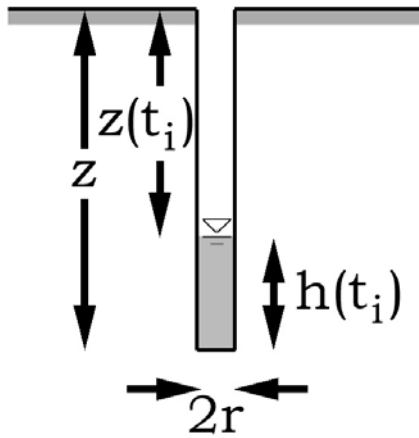


Figure 5.6: Test design inverse auger test (Kessler & Oosterbaan, 1974)

According to Equation 5.3, the saturated hydraulic conductivity can simply be derived by determining the slope between the term $\ln(h(t_i) + \frac{1}{2}r)$ and the time (t_i) and multiplying it with $-\frac{1}{2}r$. It was observed that in all bore-holes the reference rings with a diameter of 75 mm could easily be inserted. Thus, the radius has been set to 37.5 mm.

For the processing of the inverse auger hole tests, all slopes have been determined by the least square method. All available data points for the 50 cm interval under consideration have been included in the analysis. In 9 cases, however, data were scarce and the slope had to be determined for the available data points, whether the water columns extended above the interval of interest or not. Without exception this concerns less permeable soils

for which the difference in processing does not seem to influence the final value for the saturated hydraulic conductivity.

For the experiments, the goodness-of-fit, R^2 , is generally high. For a total of 181 experiments, the R^2 exceeds the value of 0.95. Only 5 experiments have a R^2 that is below 0.90. In these cases, it concerns the upper 50 cm of the soil profile with a high permeability for the root zone. If the measurement of the depth, both of the bore-hole and the water column, is taken as the only source of error, with a maximum deviation of 5 mm, the maximum error for the lowest and highest observed permeability is within 2%. The same uncertainty arises from errors in the time observation of 10 seconds.

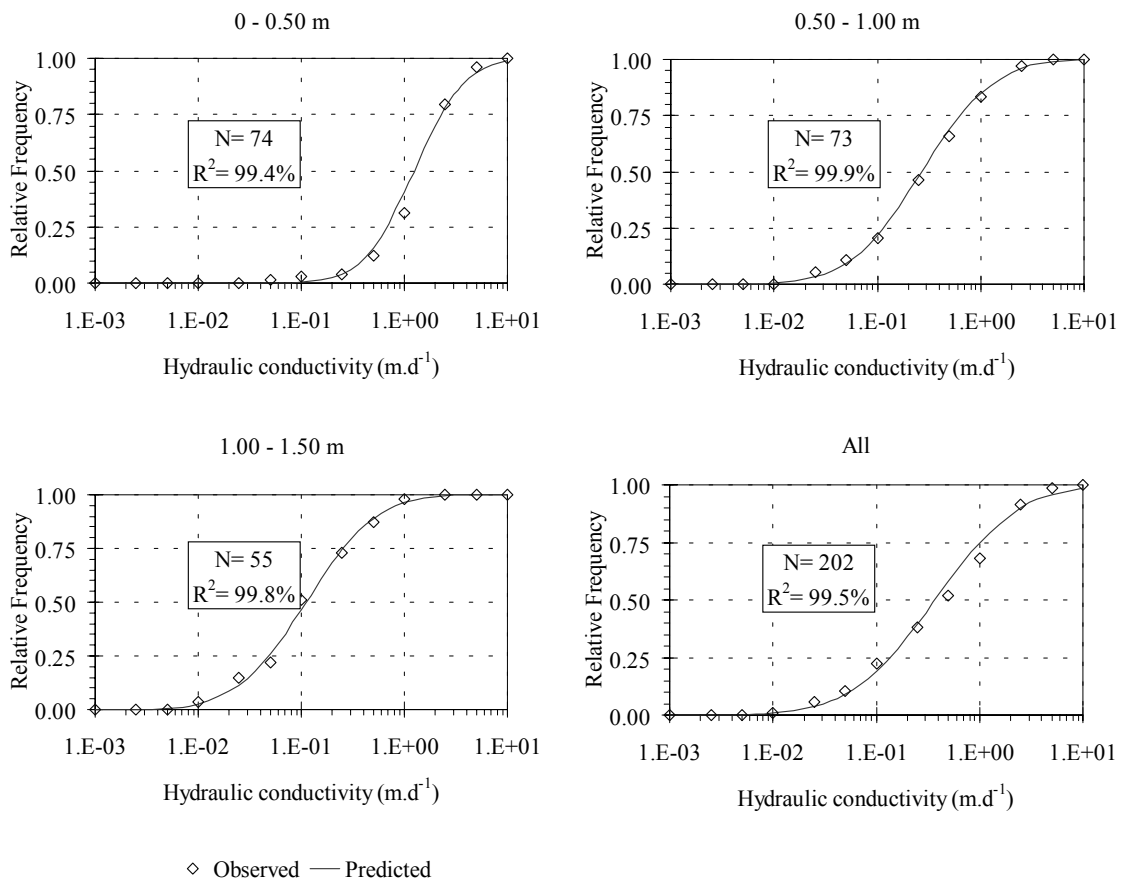


Figure 5.7: Observed frequency and fitted lognormal distributions for the saturated hydraulic conductivity

In Table 5.8, the descriptive statistics for the sample populations at 50, 100 and 150 cm depth are given. As expected, the highest permeability is found for the upper 50 cm of the soil profile, the root zone where the activity of roots and burrowing animals is the highest. With depth, the permeability tends to decrease, although the variance for the observation increases. This can be explained by the typically, negatively skewed frequency distributions: a large number of relatively low permeability values suppresses the median, whereas the larger extremes have a strong influence on the average permeability. As a consequence, the distribution is best approximated by a lognormal

distribution, as is consistent with most distributions of the saturated hydraulic conductivities (Kutilek & Nielsen, 1996). For the upper 50 cm, the amount of variance explained by the lognormal distribution, expressed by the R^2 , is the lowest, with 99.4%. For the underlying layers at 100 and 150 cm depth, the R^2 amounts to 99.9% and 99.8% respectively (Figure 5.7). A possible explanation for the relatively poor fit for the upper 50 cm is that the saturated hydraulic conductivity is more evenly spread around the arithmetic mean. For the normal and lognormal distributions the values of the skewness are equally large but opposed in sign (Table 5.8). For the lognormal distributions, the geometric mean decreases from $1.248 \text{ m}\cdot\text{d}^{-1}$, to 0.267 and $0.111 \text{ m}\cdot\text{d}^{-1}$ with the increasing depth of the 50 cm intervals (Table 5.8).

Table 5.8: Descriptive statistics for the saturated hydraulic conductivity ($\text{m}\cdot\text{d}^{-1}$)

Depth	0.0 – 0.5 m		0.5 – 1.0m		1.0 – 1.5 m	
	k_{sat}	Log-transform	k_{sat}	Log-transform	k_{sat}	Log-transform
Average	1.703	1.248	0.530	0.267	0.213	0.111
Standard Deviation	1.335	2.455	0.675	3.583	0.243	3.424
Skewness	1.971	-1.198	2.953	-0.297	1.715	-0.197
Minimum	0.044		0.015		0.008	
Maximum	7.552		3.987		1.081	
N	74		73		55	

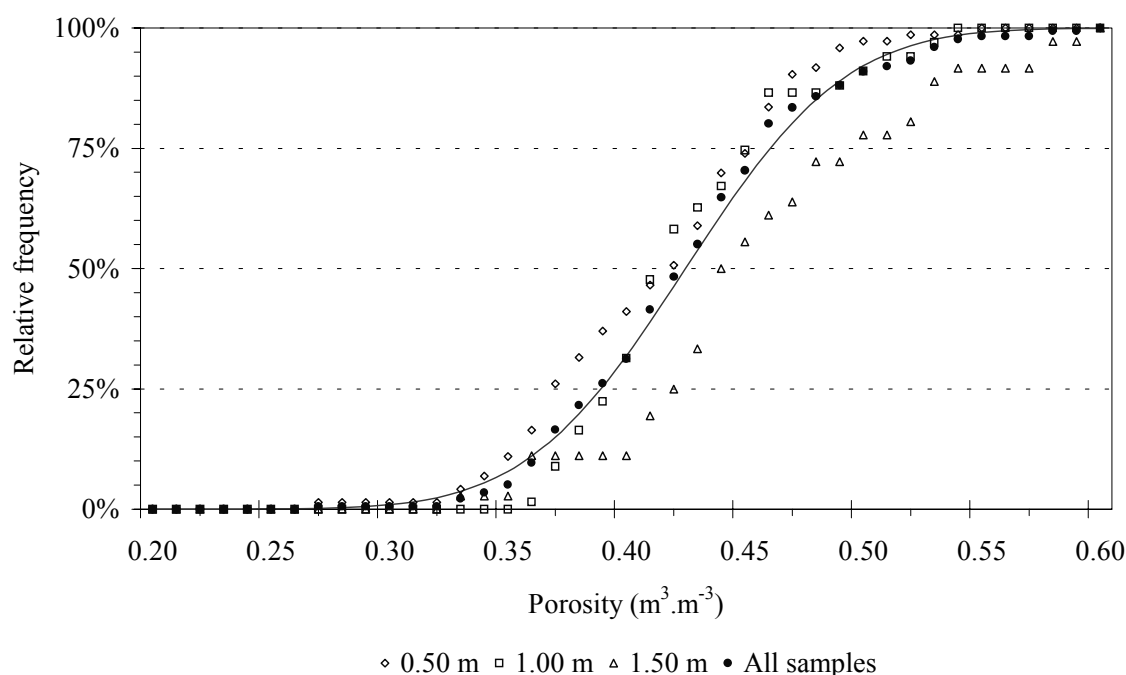


Figure 5.8: Observed frequency and fitted normal distribution for the porosity

For the porosity, the descriptive statistics, both for the entire sample population and subdivided over the three sample depths, show little variation. The frequency distributions of the sample populations can be reproduced adequately by the normal

distribution for the sample mean and variance: in all cases the goodness-of-fit exceeds the 99%. The same holds for the entire sample population (Figure 5.8). When the relative frequencies and statistics for the different sample depths are compared, it becomes apparent that the population at 150 cm displays the largest variation. This is probably due to the limited number of samples that is available for this depth (N= 36). Although the observed range at this depth is similar to the values at 50 and 100 cm depth, the larger sample populations for the latter depths provide a better approximation of the actual distribution of the porosity in the field.

For the entire sample population, the porosity ranges between 0.266 and 0.596 $\text{m}^3 \cdot \text{m}^{-3}$. The average value for all samples is 0.425, which is within 7% deviation of the mean values for the different depths (Table 5.9).

Table 5.9: Descriptive statistics for the porosity

Depth	0.0 – 0.5 m	0.5 – 1.0m	1.0 – 1.5 m	All depths
Average	0.413	0.424	0.455	0.425
Standard Deviation	0.051	0.045	0.063	0.053
Skewness	-0.111	0.848	0.327	0.440
Minimum	0.266	0.352	0.325	0.266
Maximum	0.542	0.539	0.596	0.596
N	73	67	36	176

The dry bulk density is closely related with the porosity. The values for the different layers are similar to the overall average of $14.4 \pm 1.3 \text{ kN} \cdot \text{m}^{-3}$. As was the case for the porosity, only the value of the third, deepest layers differ (Table 5.10).

Table 5.10: Descriptive statistics for the dry bulk density

Depth	0.0 – 0.5 m	0.5 – 1.0m	1.0 – 1.5 m	All depths
Average	14.6	14.5	13.8	14.4
Standard Deviation	1.3	1.2	1.4	1.3
Skewness	0.2	-0.9	-0.7	-0.4
Minimum	12.1	10.4	9.7	9.7
Maximum	18.6	16.8	18.6	18.6
N	73	67	36	176

For the scree slope, data are available from 10 locations. In these bore-holes to 1.5 m depth a layer of scree of maximum 80 cm covers the marl. The scree was mixed with fines, which partly derived from a colluvial layer covering the scree. Compared to the marl, the scree was more permeable; in some bore-holes the saturated conductivity was ten times higher than that of the underlying marl. The saturated conductivity of the scree was also less variable. Over the entire scree layer, the geometric mean of the saturated hydraulic conductivity was $2.7 \text{ m} \cdot \text{d}^{-1}$ with a standard deviation of $1.4 \text{ m} \cdot \text{d}^{-1}$. The observed minimal and maximum values were 1.8 and $3.5 \text{ m} \cdot \text{d}^{-1}$.

Few porosity samples were recovered from these bore-holes due to the stoniness of the scree. For the 6 recovered samples, the mean porosity was $0.49 \text{ m}^3 \cdot \text{m}^{-3}$. These values

were confirmed by several larger bulk samples that showed a porosity in the order between 0.45 and 0.60 m³·m⁻³.

5.3.3 Soil water retention curves

The soil water retention curve (SWRC) has been determined by laboratory experiments. Sample rings of 100 cm³ were saturated and subjected to a constant matric suction. The suction was maintained until the suction and the retained water were in equilibrium. Subsequently, the suction was increased and the procedure repeated. The absolute matric suction, $|h|$, applied ranged between 0.01 and 158 m. This suction was obtained in maximum 12 stages. Up to 5 m, the suction was applied as an actual suction at the base of an air entry plate. For these suctions, the individual samples were weighed daily and equilibrium was considered to be achieved if the successive values differed less than 0.1 gram. For the suctions of 25 and 158 m, the suction was applied by increasing the air pressure in a pressure pan to a level equivalent to the required suction. For these measurements, the total drainage from the pressure pan was collected. The samples were considered to be in equilibrium when the total loss in moisture was less than 0.1 gram.

At every suction, the retained water content has been expressed as the volumetric moisture content (VMC). Since this measure is dependent on the absolute porosity of the sample, it has been transformed into the relative degree of saturation, θ_E (Nielsen *et al.*, 1980)

$$\theta_E = \frac{\theta - \theta_R}{\theta_S - \theta_R}, \quad (5.4)$$

where θ is the actual volumetric moisture content and θ_S and θ_R are the saturated and the residual volumetric moisture content respectively. The saturated VMC is used as the porosity. The residual moisture content, the amount of water bounded to the soil particles that can not be released by suction, has been set to a constant fraction of 5% of the porosity. This fraction is based on the observed average VMC of 46 air-dry samples from the Coloma

By transforming the VMC to the relative degree of saturation, the variation of the porosity has been removed and the samples are directly comparable. A model for the SWRC can be fitted to these data to obtain the relative degree of saturation for a given matric suction and vice versa. Here, the SWRC of Farrel & Larson (1972) has been used (Section 3.2.2). This function describes the SWRC as an exponential relationship

$$|h| = h_A \exp[\alpha(1 - \theta_E)], \quad (5.5)$$

where α is the shape factor describing exponential relationship and h_A is the air entry value. By definition, matric suction is taken as positive. The model has no real physical basis but the air entry value could be interpreted as the minimal matric suction that is required to start drainage from fully saturated pores. At suctions smaller than the air entry value, the soil remains saturated and will behave accordingly. The shape factor α can be interpreted as a measure for the pore size distribution. High values of α are associated

with heterogeneous porous media that experience a more gradual loss of pore water as the matric suction increases.

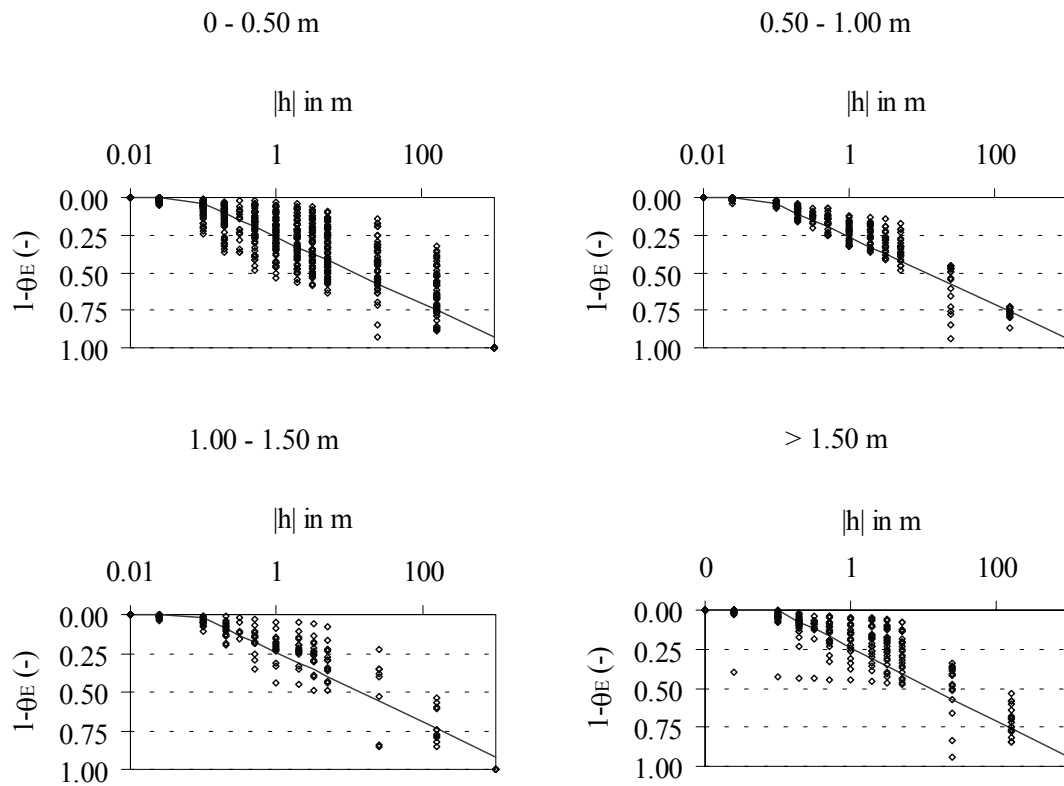


Figure 5.9: Loglinear relationships for the SWRC according to Farrel & Larson (1972) with depth

The model of Farrel & Larson can be fitted to the data as a simple loglinear relationship. This is shown by the SWRCs of Figure 5.9 that plot as straight lines once the logarithm of the matric suction $|h|$ is taken. The SWRCs shown have been fitted for all soils of weathered marl in the Coloma. Data are available from 124 samples. The SWRCs have been fitted to the entire sample population and to sub-samples per 50 cm depth for which all samples from depths greater than 1.5 m have been merged. The fitted parameters are listed in Table 5.11.

Table 5.11: Parameters of the SWRC according to Farrel & Lawson (1972) with depth

Depth (m)	N of samples	α (-)	$\Delta\alpha$ (%) (95%)	h_A (m)	Δh_A (%) (95%)	R^2 (-)
0.0 - 0.5	62	10.332	± 4	0.067	-15 / 17	0.856
0.5 - 1.0	23	10.258	± 5	0.067	-16 / 19	0.937
1.0 - 1.5	15	10.264	± 8	0.081	-24 / 31	0.889
> 1.5	24	9.777	± 6	0.097	-20 / 25	0.878
All	124	10.168	± 3	0.074	-10 / 11	0.880

The SWRCs fit reasonably well for the different sample populations. The samples from the upper 50 cm have the largest range in the θ_E per matric suction and consequently the poorest fit. This should be attributed to the more variable pore size distribution for this layer as a result of the biological processes in the root zone. With depth, the capacity of the soil to retain water increases as the rising air entry value and the lower shape factor indicate.

As the intercept of the loglinear relationship, the air entry value is the more sensitive parameter of the SWRC. Within the 95% confidence limit, the shape factor α does not vary more than 8% for all fitted models (Table 5.11). The air entry value accommodates most of the error and varies by 10% when all samples are considered. For the subpopulations, the lesser fit and the lower number of samples result in larger deviations. Since the fit is logarithmic, these larger deviations are not symmetrical. The error in the air entry value will result in a horizontal displacement of the curve. Consequently, both the region of saturation ($h < h_A$) and the unsaturated region are wrongly estimated. At the 95% confidence level, the bias is 5% of the θ_E at field capacity (≈ 3.3 m) for the entire sample population. For the least successful fit (1.0 – 1.5 m), this increases to 15%.

For the scree slope, data are available from one sample only. The SWRC for this material has a lower air entry value and a higher shape factor ($h_A = 0.022$ m, $\alpha = 11.221$ (-)). This agrees with the expected values for this coarser and less sorted material.

5.3.4 Relation with depth

In order to test the hypothesis that the layers do have different hydrological properties, Student's difference-of-means test has been applied (t-test). The underlying assumption is that the large number of samples permits the use of parametric tests. The difference-of-means test has been applied to the sample populations of the porosity and the saturated hydraulic conductivity for the respective depths. Tested is the hypothesis that the difference between the mean values is equal to zero ($H_0: \mu_1 = \mu_2$). Prior to testing this hypothesis, the equality of variance of the two sample populations is tested by means of an F-test ($H_0: \sigma_1^2 = \sigma_2^2$). When the variances appears to be equal, the t-test has been performed with the pooled variance and $(N_1 + N_2 - 2)$ degrees of freedom. When the null hypothesis is rejected, the pooled variance and the degrees of freedom have been obtained by means of the procedure described by Blalock (1981). The critical level has been set to 0.05 for the F- and t-test (two-tailed in case of the latter). For the saturated hydraulic conductivity, the tests have been performed on the logtransformed values. This allows the use of normal test procedures in the case of lognormal distributions (Davis, 1986). The outcome of these tests is summarised in Table 5.12.

In the tests, significant differences at the 0.05 critical level were found for the mean and variance of the k_{sat} at all depths and for the mean porosity at 1.5 m. This result is obvious as the saturated hydraulic conductivity decreases with depth. This tendency is confirmed by the strong loglinear relationship of the k_{sat} values on the depth of each layer. ($R^2 = 0.43$). The saturated hydraulic conductivity associated with this relationship is

respectively 1.18, 0.32 and 0.09 m·d⁻¹ at the depths of 0.5, 1.0 and 1.5 m. This agrees well with the observed geometric means of 1.25, 0.27 and 0.11 m·d⁻¹ for these layers.

Table 5.12: Test for equality of means and variance with the probability of the test statistic (respectively pt and pF). ° and * denote significant deviations from the expected equality at the 0.05 critical level

Layer	1: 0.00 – 0.50 m	2: 0.50 – 1.00 m
2: 0.50 – 1.00 m	Ksat ^{°*} (pF= 0.00, pt= 0.00) Por (pF= 0.17, pt= 0.18)	
3: 1.00 – 1.50 m	Ksat ^{°*} (pF=0.01, pt= 0.00) Por* (pF= 0.06, pt= 0.00)	Ksat* (pF= 0.39, pt= 0.00) Por ^{°*} (pF= 0.00, pt= 0.01)

The decisions for the porosity are identical to those for the dry bulk density. The tests show that the sample population at 150 cm is significantly different from those at 50 and 100 cm. This observation makes it possible that the upper two layers are lumped, whereas the lower layer has to be treated as a different population. For the lumped samples at 50 and 100 cm depth (N= 140), the average value of the porosity is 0.418 m³·m⁻³ with a standard deviation of 0.048. The average dry bulk density is 14.5 ± 1.3 kN·m⁻³. It is possible that the differences of the lower layer do not reflect the natural situation. It is possible that the firmer marl at this depth is more disturbed by sampling. The lower density could then be explained by the opening of the fissures between the peds. Overall, the distributions of the sample populations have the same shape, although the distribution of the porosity for the lower layer is shifted to the right and is more irregular because of the limited sample size (Figure 5.8).

For the SWRCs, the tested hypothesis states that the slopes of the loglinear fits are equal (H₀: α₁= α₂). As could be expected from the similarity of the regression equations and the large error bands associated with it, no significant differences at the 0.05 critical level could be found.

5.4 Land use effects on hydrological properties

5.4.1 Land use effects on the saturated hydraulic conductivity and porosity

The spatial distributed data on the saturated hydraulic conductivity and porosity of the marl slopes have been analysed with respect to the four land use units of Table 5.2. Because of the limited occurrence of Unit IV of semi-natural climax vegetation, none of the locations falls within this unit. Data from this unit are available from the Mollo and have been added to the data set. This brings the total number of sample points to 93, 75 within the 30 ha large sub-area of the Coloma and 18 in the Mollo.

For the different land use units, the statistics on the saturated hydraulic conductivity are summarised in Table 5.13. No apparent differences have been found in the porosity for the units at the different depths. In contrast, the different land use units seem to represent different saturated hydraulic conductivities at the 50-cm depth (Figure 5.10). For this

layer, the logtransformation fails to stabilise the variance of the saturated hydraulic conductivity for Unit I. This could be the result of the small sample populations. In the sample population of Unit I, the larger variance is due to the presence of lower values than those observed for units II, III and IV. As a result the saturated hydraulic conductivity is distinctly lower at 50 cm. For the units II, III and IV, the range in the saturated hydraulic conductivity is higher but the logtransformed data represent the expected lognormal distributions better (Figure 5.10).

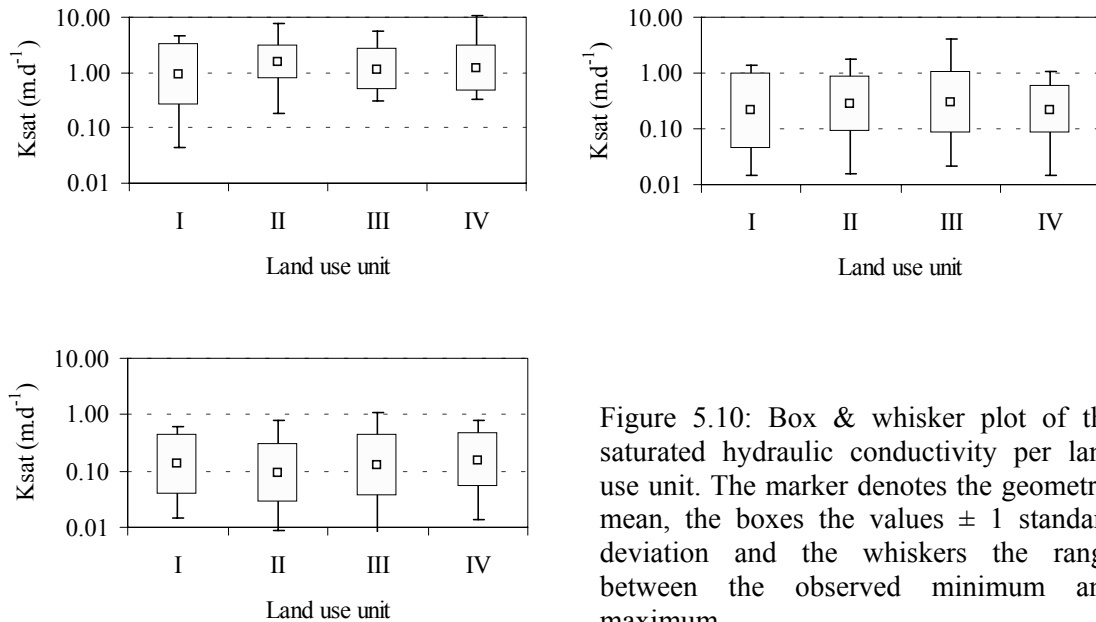


Figure 5.10: Box & whisker plot of the saturated hydraulic conductivity per land use unit. The marker denotes the geometric mean, the boxes the values ± 1 standard deviation and the whiskers the range between the observed minimum and maximum

Table 5.13: Mean and standard deviation for the lognormal distribution of the saturated hydraulic conductivity in $m \cdot d^{-1}$ per land use unit

Layer	Land use unit			
	I	II	III	IV
0.0 – 0.5 m	0.91 ± 1.74	1.53 ± 1.35	1.14 ± 1.45	1.22 ± 1.52
0.5 – 1.0 m	0.21 ± 1.96	0.28 ± 1.66	0.29 ± 1.74	0.22 ± 1.54
1.0 – 1.5 m	0.13 ± 1.71	0.09 ± 1.68	0.13 ± 1.74	0.16 ± 1.62

With depth, the saturated hydraulic conductivity becomes more similar although the logtransformation is still less successful for Unit I at 100 cm. At 150 cm depth, the saturated hydraulic conductivity is identical for all units.

The different behaviour of Unit I can be explained by differences in soil depth. At 150 cm depth, only 60% of the samples have been recovered for Unit I. For the remaining 40%, bedrock was present within 100 cm from the surface. These conditions are found on the pediment and associated with lower hydraulic conductivities. The deeper soils have a higher saturated hydraulic conductivity: the locations with full recovery under Unit I, the saturated hydraulic conductivity for the upper 50 cm increases with 42% to $1.29 m \cdot d^{-1}$. In comparison, the recovery for units II, III and IV was 68%, 92% and 100%

respectively and the conductivity of the top 50 cm was more similar to that of the entire population (-3%, -4% and 0%).

To test whether the measured hydraulic conductivity was significantly different, an ANOVA was performed. Because of the small sample size of units I and IV, the assumption of normality has been relaxed and the non-parametric Kruskal-Wallis test has been used. The saturated hydraulic conductivity was not significantly different between the units ($H= 3.47$, $DF= 3$, $p< 0.33$). This must be attributed to the large variability of Unit I. Given the similarity of the saturated hydraulic conductivity at the depths of 100 and 150 cm and of the porosity at all depths, tests for these variables have been forfeited. The relation between the saturated hydraulic conductivity of the scree and the land use conditions have not been considered because this coarse material is less susceptible to land use influences.

The data on the saturated hydraulic conductivity of the upper 50 cm indicate that the influence of land use do not extend beyond the shallow root zone and that the differences between the land use units is not significant when the saturated hydraulic conductivity is aggregated over this depth. within the root zone. Important differences in the hydrological response between the land use units, however, may still arise from variations in the infiltration and percolation within the root zone that are controlled by the vegetation cover and land use practices. These differences have been studied more directly by means of rainfall simulations (Section 5.4.3). As supplement to these experiments, detailed information was gathered on the characteristics of the vegetation cover and on the porosity and SWRC of the root zone under the four land use units, which is discussed below.

5.4.2 SWRC and porosity of the root zone

The porosity and the SWRC have been determined at different levels of the root zone. They have been determined at the sites of the four rainfall simulations in the 30-ha large sub-area (Appendix 1). Each location represents one of the land use units of Table 5.2. The successive units have an increasing vegetation cover and a more developed soil surface (Figure 5.11 & Figure 5.12).

For the four locations, the total porosity has been determined from bulk samples. This total porosity includes both larger, structural pores (macropores), partly formed by roots and burrowing animals, as smaller textural pores (micropores). Macropores can not be representatively sampled with conventional 100 cm³ sample rings (Section 5.3.2). Thus, the porosity that is determined in this manner should be treated as an apparent porosity that reflects the microporosity of the sample only. So, the contribution of macropores is defined as the difference between the total porosity of a larger volume of soil and the apparent porosity as determined from smaller sampling rings. Comparisons between the total and apparent porosity can therefore help to discern the influence of the vegetation on soil development. To this end, the total porosity and apparent porosity have been plotted with depth for the four land use units (Figure 5.13).

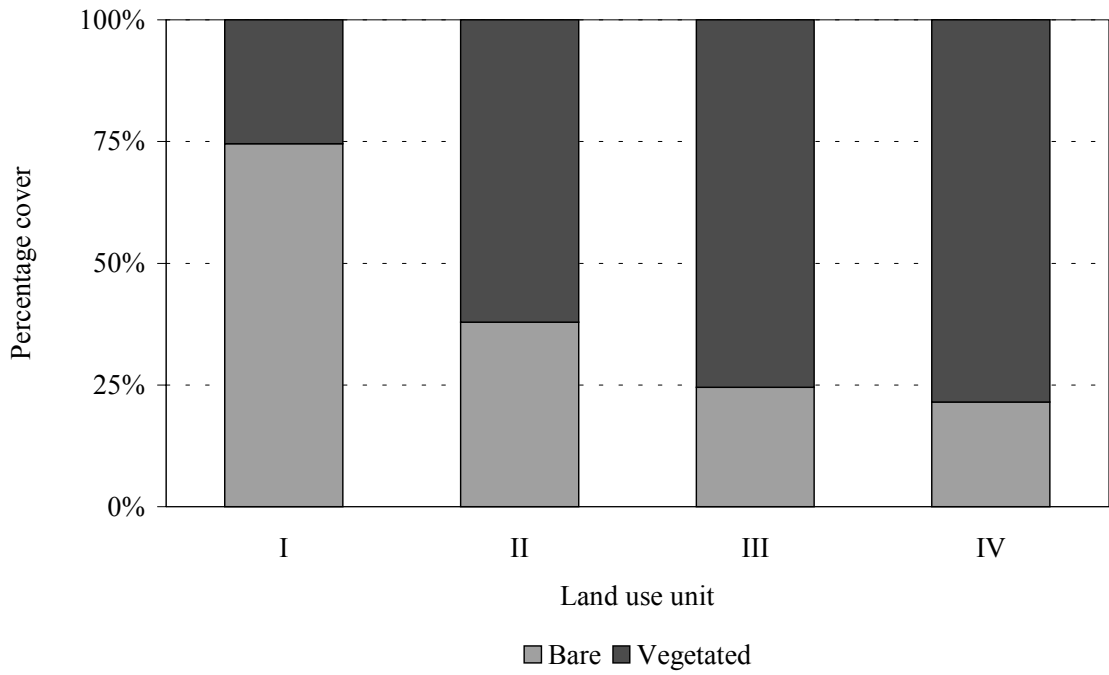


Figure 5.11: Vegetation cover for the four land use units represented by the rainfall simulation locations

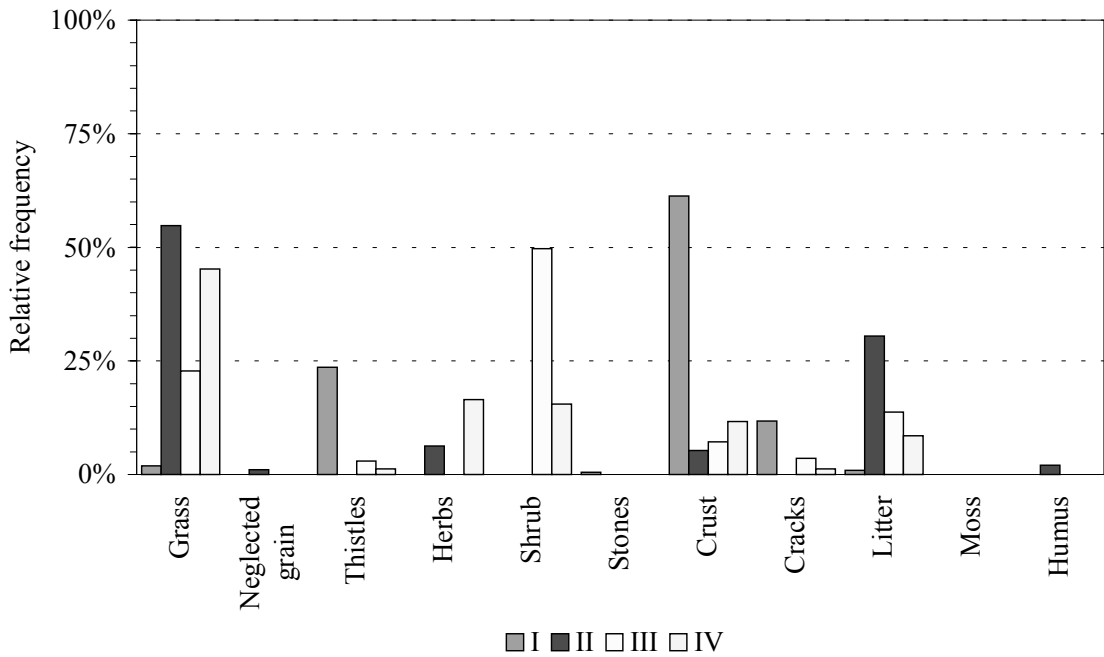


Figure 5.12: Surface cover for the land use units represented by the rainfall simulator locations

The total porosity was determined from bulk samples consisting of small, cubic trial pits with a size of 40 cm in all directions. The excavated material was retrieved and labelled for different depths, after which the exact dimensions of the pit were measured with a resolution of 5 mm. The retrieved material was weighed with mechanical scales at 250 g accuracy. The gravimetric moisture content was determined for subsamples of the large volume of soil. After the correction for soil moisture, the total porosity and bulk density have been calculated by relating the mass of the soil to the volume of the pit. Although this technique is coarse, the results are detailed enough to compare it with the apparent porosity. From each location, between 5 and 10 samples at varying depths are available.

For Unit I, a marked change in the porosity occurs at the lower end of the tillage layer. In the tillage layer, both the total and apparent porosity are above $0.63 \text{ m}^3 \cdot \text{m}^{-3}$ whereas they drop to average values in the order of $0.45 \text{ m}^3 \cdot \text{m}^{-3}$ below 30 cm depth (Figure 5.13).

For the units II, III & IV, the apparent porosity is still higher closer to the surface, but the difference is less pronounced than for Unit I. Both the apparent and total porosity decrease gradually with depth due to the lower degree of weathering and biological activity. For the units III and IV, the apparent porosity is fairly constant ($\approx 0.45 \text{ m}^3 \cdot \text{m}^{-3}$). The total porosity is higher over the entire depth or a part of the profile; for Unit III, the total porosity is over $0.60 \text{ m}^3 \cdot \text{m}^{-3}$ for the upper 20 cm. For Unit IV, the macroporosity increases with depth. A possible explanation for this phenomenon would be that, at greater depth, parts of slightly weathered bedrock are incorporated into the root zone that gradually are fragmented until a homogeneous soil has been obtained. Based on these observations, the conclusion should be that on units III and IV clear macropores exist between peds of slightly weathered matrix, in contrast to the units I & II where no difference in matric and macroporosity has been found. The high porosity at the top of Unit I would be the result of tillage.

For the four locations, the SWRC has been determined as described in Section 5.3.3. A sample of 100 cm^3 was taken for each 5 cm of the root zone, up to a depth of 50 cm. The model of Farrel & Larson (1972) has been fitted on these data for each unit (Figure 5.14). The fitted models are summarised in Table 5.14. The average matric porosity was used to determine the saturated and residual volumetric moisture content as macropores can by definition not retain any capillary water (Beven & German, 1982).

The best fit for the SWRC is obtained for Unit IV. For all other units, the fit is poorer, with a minimal R^2 of 0.37 for Unit I. The explanation for the poor fit lies in the stratification of the root zone for the topsoil is generally more porous than the deeper layers. Only for Unit IV is the soil more evenly developed. The ploughed soil of Unit I has the poorest water retention and this porous material drains easily (Figure 5.14). The sudden drop in moisture content experienced by the soil of Unit I is reflected by the high air entry value. Once this fraction of the soil moisture has been released, the drainage continues at steady rate. The fitted model parameters lump the variation with depth as the more compact soil of Unit I has the strongest water retention capacity if the individual layers are considered. Based on the poor fit for the overall SWRC of Unit I, it should be concluded that the model of Farrel & Larson is unable to represent the disparate behaviour of the tilled soil adequately. For the other units, the fitted SWRCs perform better. When the SWRCs of the different units are compared to the overall fit, it appears

that the SWRCs are distinct for the root zone. This disagrees with the homogeneous SWRCs found over the deeper soil profile (Section 5.3.3).

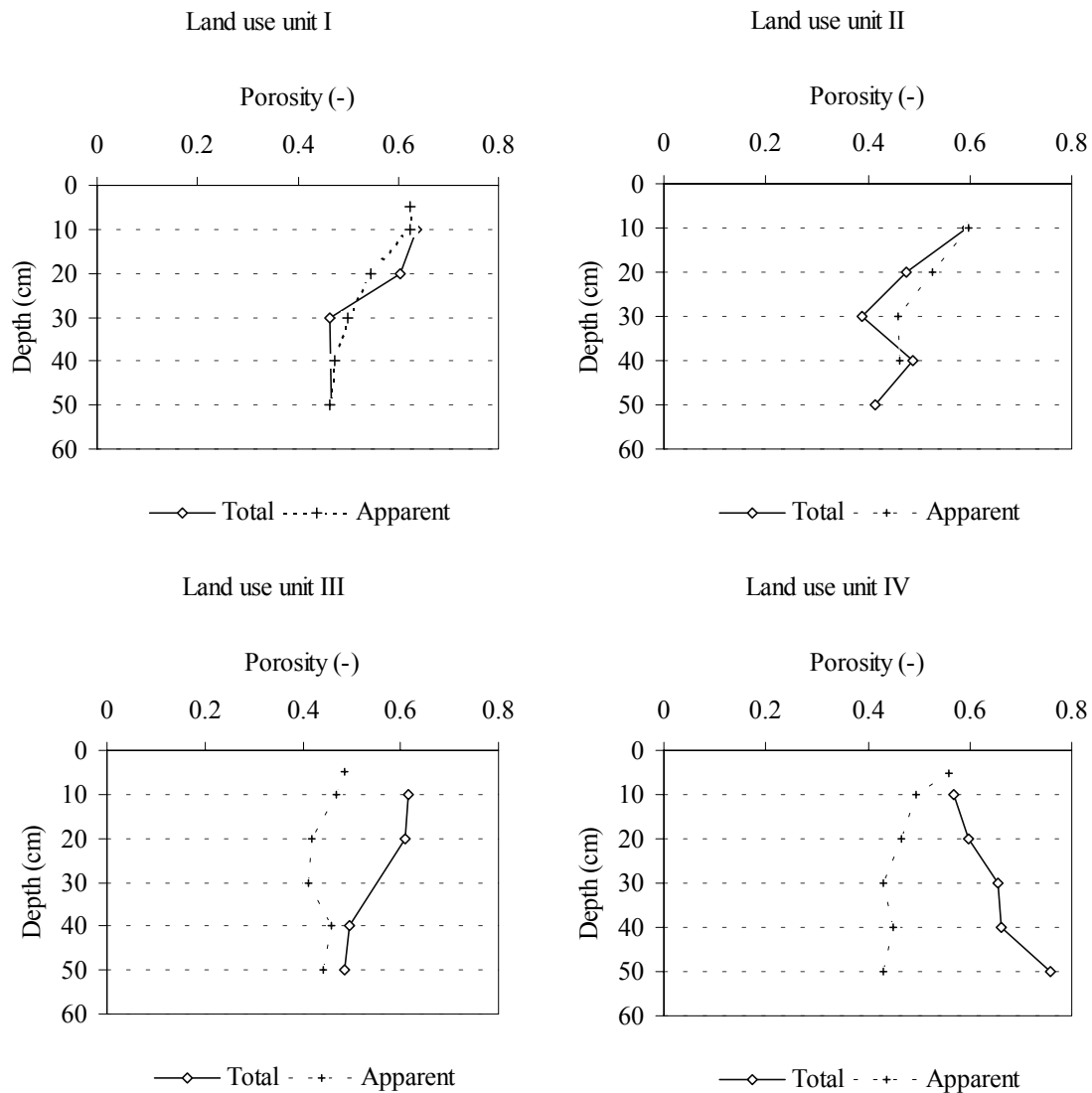


Figure 5.13: Profiles of apparent and total porosity for the root zone of the land use units

Table 5.14: Parameters of the SWRC for the root zone of the four land use units

Land use unit	θ_{Sat}	θ_{Res}	h_A (m)	α (-)	R^2
I	0.501	0.031	0.161	9.204	0.366
II	0.511	0.026	0.049	11.089	0.722
III	0.444	0.022	0.145	12.258	0.681
IV	0.528	0.026	0.020	12.907	0.961
All units	0.493	0.025	0.088	10.539	0.619

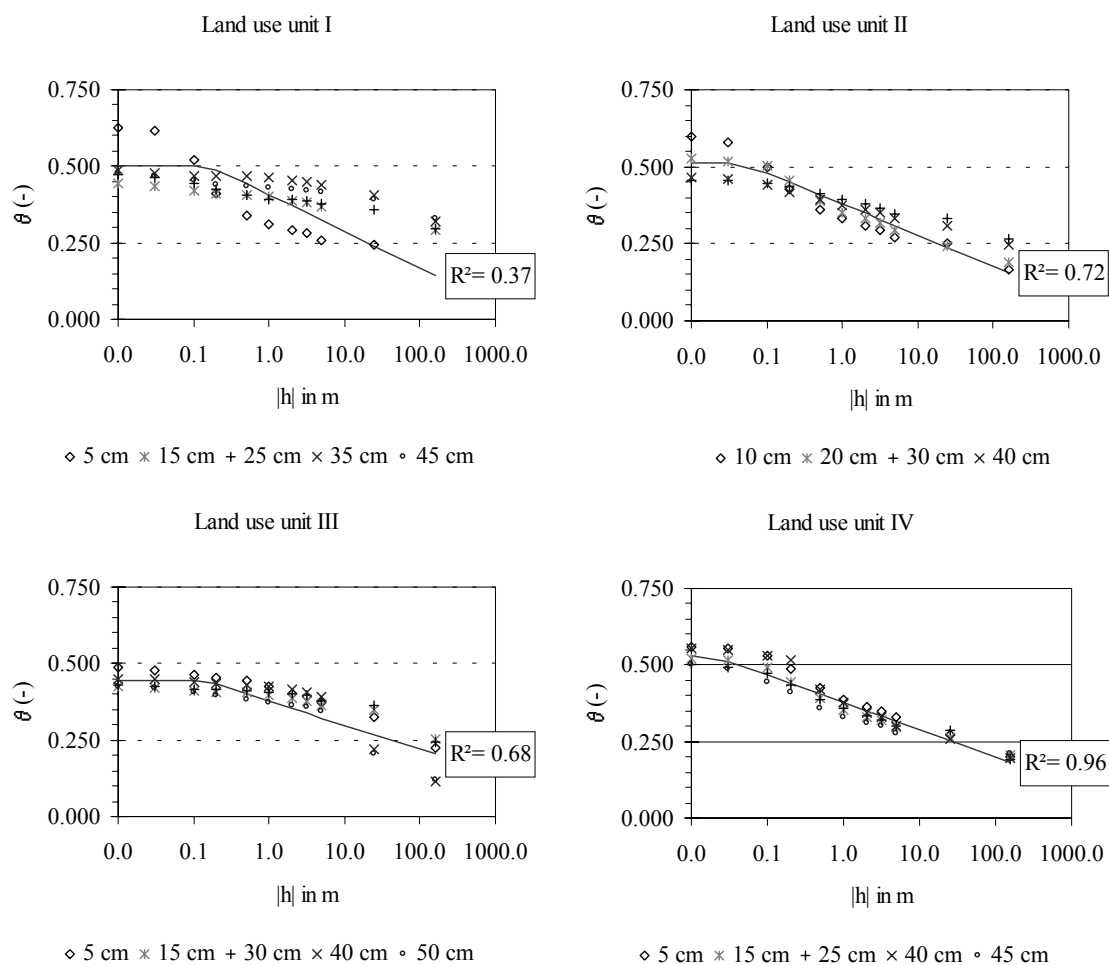


Figure 5.14: SWRCs according to Farrel & Lawson (1972) for the root zone of the four land use units. The drawn line represents the best fit for all samples per land use unit.

5.4.3 Infiltration and redistribution per land use unit

Under the different land use units, the infiltration and the subsequent redistribution of soil moisture in the root zone has been studied by broadscale rainfall simulations. Rainfall simulations offer controlled conditions under which these processes can be studied in detail with a minimum of disturbance. Broadscale rainfall simulations represent larger volumes of soil and hence the variability of the soil can be lumped on a scale that is consistent with the model representation.

The rainfall simulations address two related objectives on the soil moisture redistribution in the root zone. Firstly, the experiments will be used to describe the patterns of preferential flow in the root zone and to calculate the water balance during the simulation. Secondly, the processes of infiltration and redistribution are simulated by a one-dimensional model for the Richards' equation that describes vertical unsaturated Darcian flow (Kutílek & Nielsen, 1994). If no large horizontal gradients or preferential

flow paths exist, the equation should be able to simulate the observed infiltration and redistribution adequately. By applying the equation to the data and optimising the model performance for the observed volumetric moisture contents, bulk values for the relevant static soil properties can be obtained. If the model fails to reproduce the observed values adequately, the appropriateness of Darcian flow is falsified.

In the early summer of 1996, four broadscale rainfall simulations have been performed that represent the four land use units. The simulations covered an area of 6 by 2.75 m. The area outside this perimeter was not considered to eliminate boundary effects.

During the simulations, the total duration of rainfall was in the order of 2 hr 20'. This rainfall was divided in five to six runs that lasted between 15 to 45 minutes. Separated by several hours, the runs extended the total duration of a simulation to one day. A tent sheltered the plot to avoid disturbance by wind and to reduce evapotranspiration (Plate 9). To the same end, the plot was covered with plastic sheets between the runs.

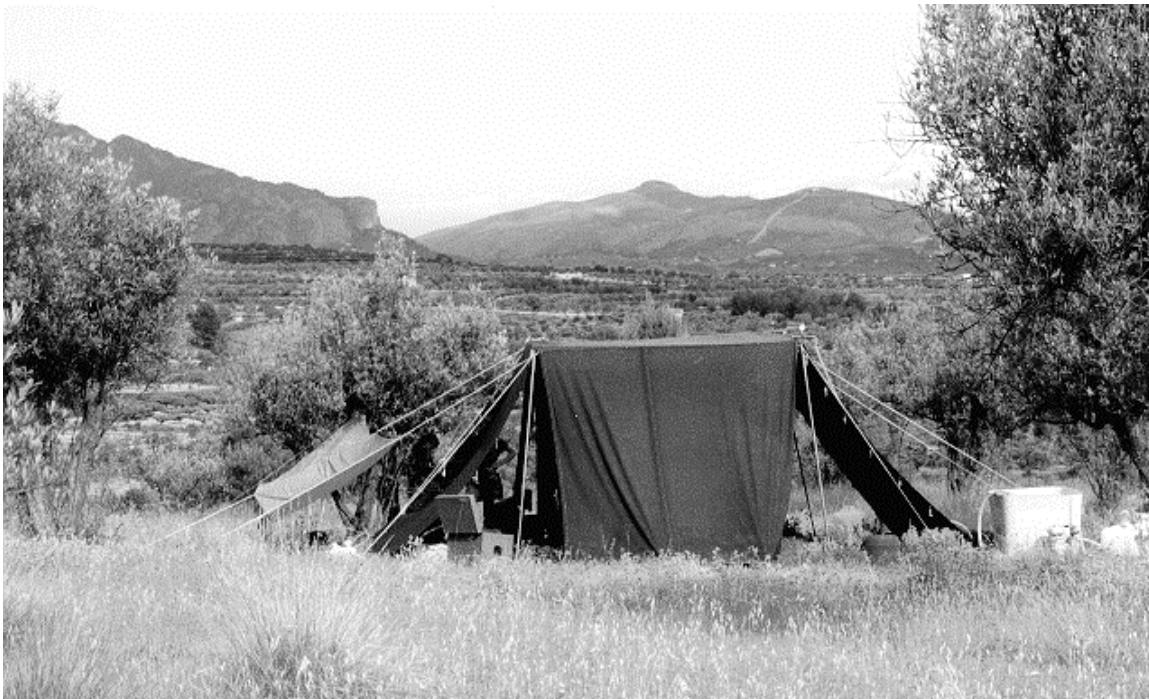
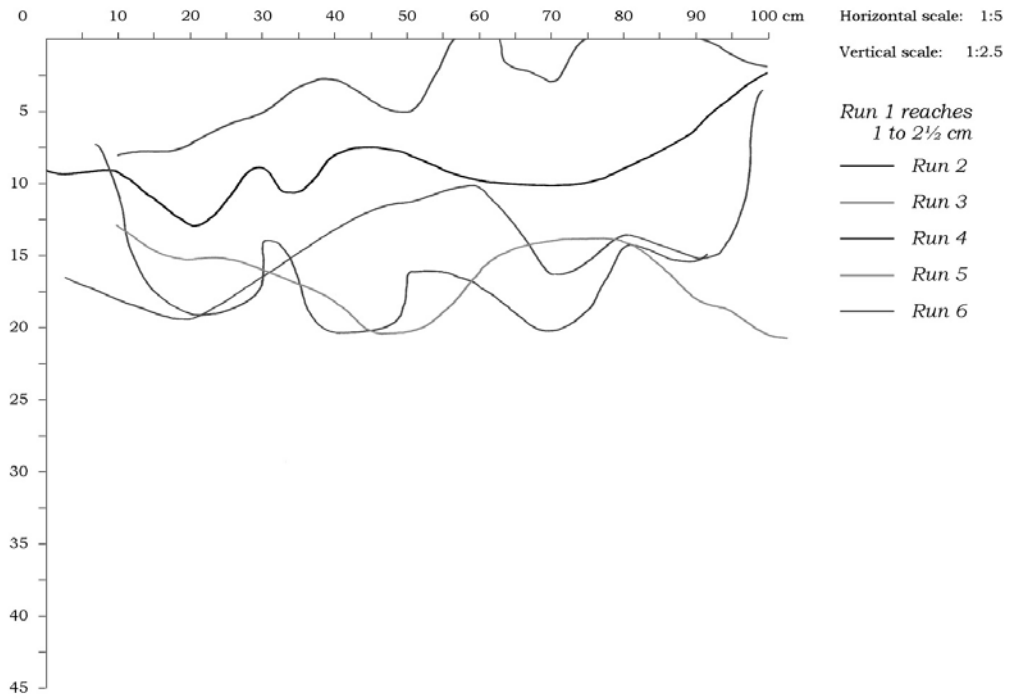


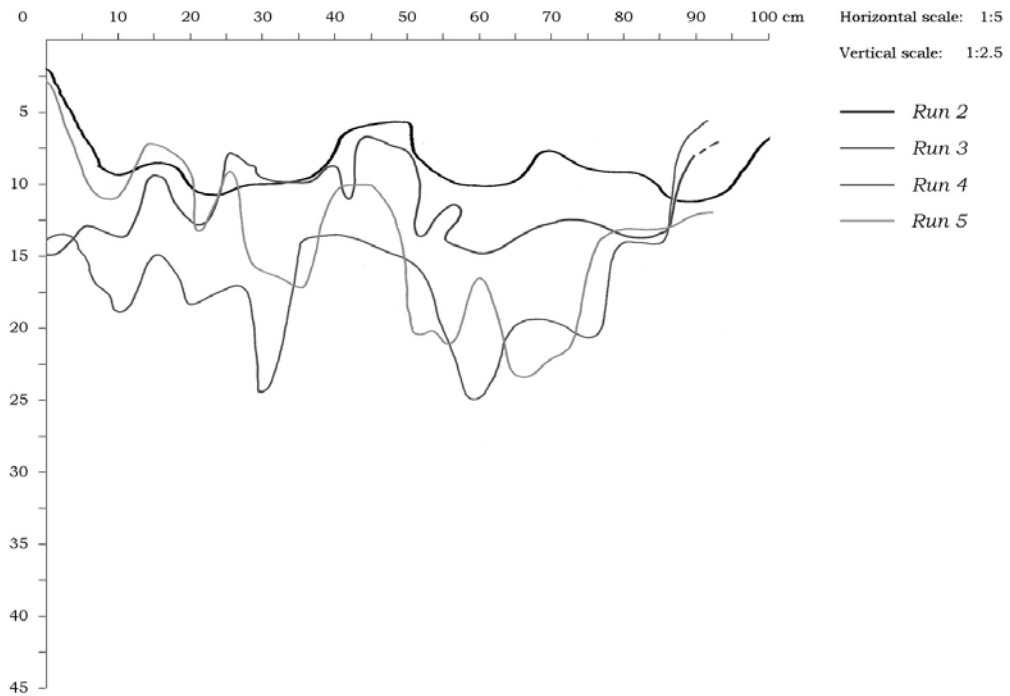
Plate 9: Rainfall simulation

Rainfall was applied by two nozzles hanging from the 2.25 m high frame. Water was pumped through these nozzles by petrol-fuelled pumps. Because of fluctuations in the pressure, the average intensity during the simulations varied between 28.1 and 37.5 $\text{mm}\cdot\text{hr}^{-1}$. The average intensity was $34.4 \pm 3.7 \text{ mm}\cdot\text{hr}^{-1}$. The spatial distribution of the rainfall over the selected area was homogeneous except for a small zone of overlap for the two nozzles. About 1500 l of demineralised water was applied during each simulation.

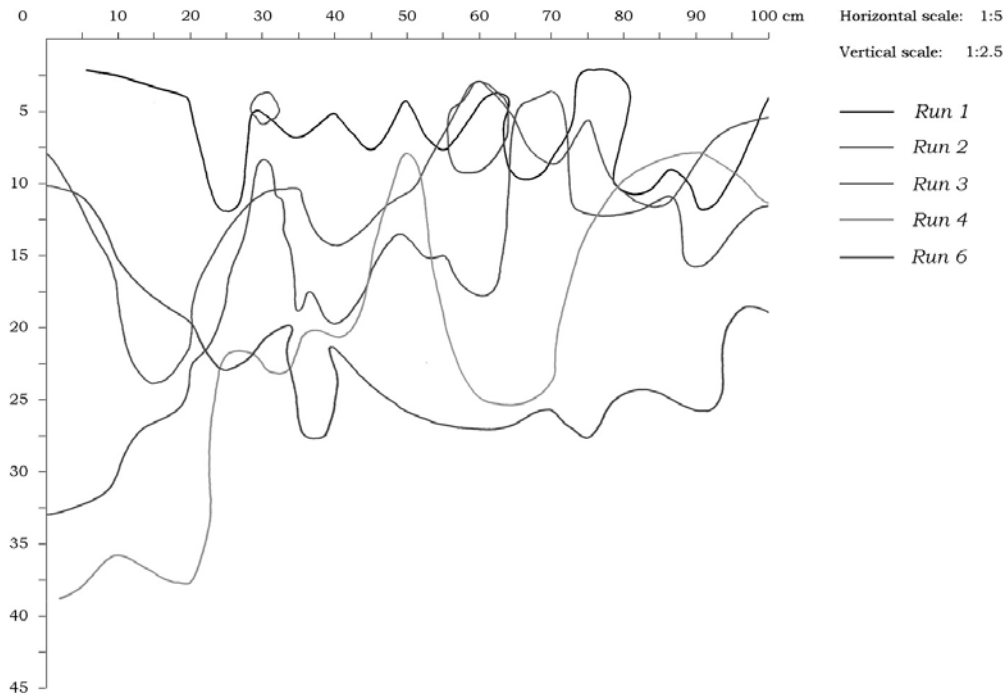
Land use unit I



Land use unit II



Land use unit III



Land use unit IV

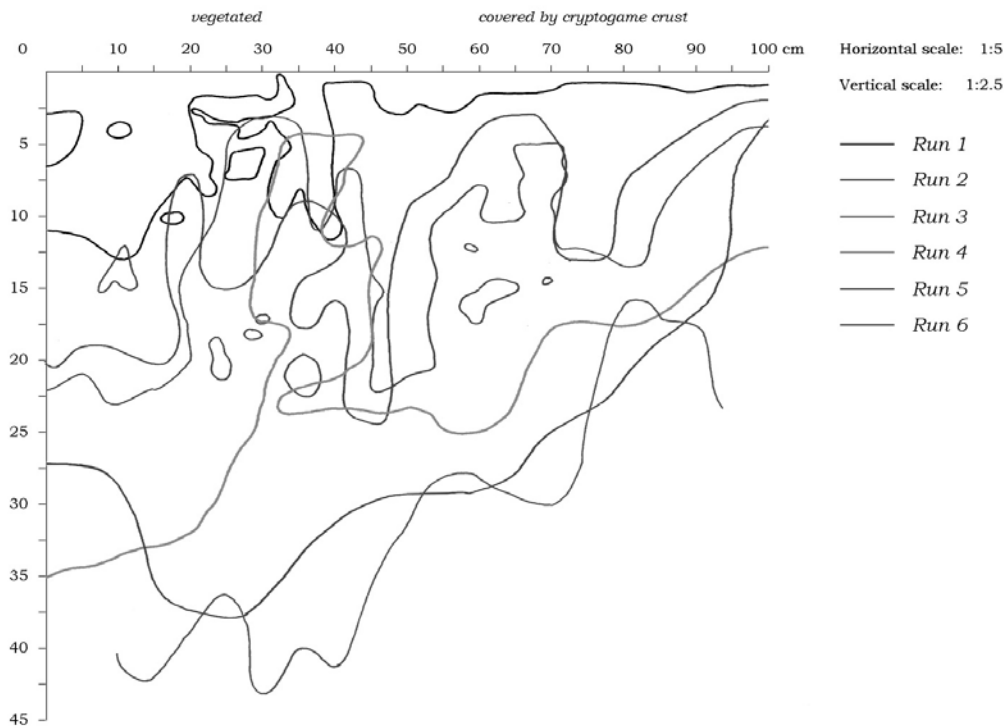


Figure 5.15: Observed wetting fronts during the rainfall simulation on the four land use units

At the lower end of the enclosed area, a gutter was installed to measure the possible run off. At three locations, spaced regularly from the centre of the plot, the volumetric moisture content (VMC) was monitored using Time Domain Reflectometry (Topp *et al.*, 1980). In this method, the dielectric permittivity of the material at different moisture contents is used as a measure for the VMC. The TDR-probes used were of the three-pronged type described by Heimovaara (1993), with a length of 100 mm and a width of 20 mm between the outer earthed pins. The probes were installed by digging a small pit of 10 by 20 cm and backfilling it afterwards with the excavated material. The probes were inserted horizontally and pointing slightly upwards to prevent the effects of disturbing seepage through the installation pit. At the three locations, four probes were installed at 5, 10, 20 and 30 cm depth. Measurements on the VMC were made by these probes with a Tektronix 1502B cable tester. The measurements of the dielectric permittivity have been processed by the software developed by Heimovaara to obtain the VMC by the use of the general calibration curve of Topp *et al.* (1980). Compared to gravimetrically determined VMCs from random locations at the plot, the relation explains 42% of the variance for the individual TDR-readings. The VMC determined from the TDR readings overestimates the gravimetrically determined VMC generally by 17%. This is due to the large scatter in the gravimetrically determined VMC. If the averages of the observations are taken, the R^2 increases to values between 0.60 and 0.93 for the different land use units.

After each run, the wetting front was directly excavated over a length of one meter and mapped. To increase the contrast between the dry soil and the wetted material, pyranine dye was applied on the surface at the beginning of each run.

No overland flow has been observed during any rainfall simulation. All infiltrated water was stored in the wetting zone that reached to maximum 50 cm below the surface. The excavated wetting fronts for the four simulations are represented in Figure 5.15. These profiles demonstrate qualitatively the effects of land use on the infiltration and redistribution in the soil. As expected, the complexity of the wetting front increases with vegetation cover. Redistribution along a uniform wetting front prevails for the units I and II. For the more developed vegetation – units III and IV - the initial runs show infiltration along preferential flowpaths although the profiles become smoother as the simulation continues. These qualitative observations are confirmed by the TDR-observations (Appendix 5). For the topsoil of the presently cultivated field, the initial VMC was low and no response occurred until the end of the second run. Redistribution was slow and most of the water was stored in the upper 20 cm that has a higher storage capacity due to tillage.

The response of the Unit II was the most homogeneous of the four units studied. In contrast, the units III and IV had a constant initial VMC over the 30 cm of the root zone tested but responded very irregularly once rain was applied. Only at the end of the experiments, an uniform soil moisture content had been achieved.

Because of the difference between the gravimetrically determined VMCs and the VMC-readings from the TDR, the results of the water balance calculations are inconclusive (Table 5.15). Only for Unit I, some water is apparently lost. However, at the end of the

experiments, most of the water is still stored in the upper 30 cm of the root zone for each unit.

Table 5.15: Relative amount in percent of applied rain stored in the root zone for each land use as measured by the two methods applied

Method	Land use unit			
	I	II	III	IV
TDR	89	148	94	119
Gravimetical	90	100	108	99

The Richards' equation has been applied to model the redistribution of soil moisture quantitatively. An explicit forward-finite difference numerical scheme was used with a schematisation according to Table 5.14. By inverse modelling, the saturated hydraulic conductivity was optimised. This parameter is not the most sensitive parameter and hence optimisation requires large adaptations. The choice to optimise the saturated hydraulic conductivity, however, is inspired by the notion that this parameter only changes the rate of Darcian flow and not the dependence of the relative unsaturated hydraulic conductivity on the SWRC. If the assumption of Darcian flow is appropriate for the redistribution of water through the network of matric and macropores alike, successful optimisation by adapting the saturated hydraulic conductivity provides a bench mark test.

The Richards' equation has been optimised by minimising the root mean squared error, RMSE, between the observed and the simulated VMC from the 3 x 4 TDR-probes. The RMSE has been determined from all available readings at the end of the successive runs and for the intermediate periods with redistribution. As initial VMC, the average reading at each depth at the start of each run has been taken. For the four simulations, five or six runs or wetting periods are available. Each simulation has one dry period less. So, a maximum of 72 or 60 points are available for the wetting or drying periods of a simulation.

The optimisation strategy has the disadvantage that the more similar readings during the wetter runs near the end of the experiment have a larger weight but at the same time it provides one consistent value for the k_{sat} for each land use unit. The success of the optimised model can be determined from the RMSE of the drying part of the simulation. This RMSE may be higher for the optimised saturated hydraulic conductivity must accommodate the possible hysteresis that is introduced by the SWRC, which has been determined for the drying limb of the curve.

The discretisation of the soil profile consisted of 16 nodes at regular 5 cm intervals (0.75 m depth). The timesteps varied in length depending on the duration of the simulation or intermediate period. Below the root zone, the saturated hydraulic conductivity was set for all model runs to a fixed level of $0.267 \text{ m}\cdot\text{d}^{-1}$ as determined from the inverse bore hole tests.

Initially, uniform values of the saturated hydraulic conductivity were assigned to the top 50 cm and the underlying 25 cm. Only the value of the upper layer was adapted in order to optimise the model performance assuming a homogeneous root zone. Because of the insensitivity of the model to changes in the saturated hydraulic conductivity, it is impossible to obtain adequate fits for the observations.

Table 5.16: Optimised values of the saturated hydraulic conductivity and root mean squared error (RMSE) of the volumetric moisture content

Land use	Curve	ksat(m·d ⁻¹)		α^{***} (-)	ρ (-)	RMSE (-)	N ****
		top*	avg.**				
I	Wetting	25.8	5.6	0.914	0.826	0.066	68
	Drying			0.908	0.737	0.069	60
II	Wetting	783.6	54.7	0.821	0.787	0.078	58
	Drying			0.897	0.705	0.053	48
III	Wetting	30.4	6.3	0.880	0.886	0.063	70
	Drying			0.883	0.826	0.066	60
IV	Wetting	876.0	58.6	0.933	0.757	0.062	64
	Drying			0.919	0.660	0.060	59

- *: Optimised value at surface
- ** : Geometric mean
- ***: Slope of linear regression, forced through origin
- ****: Number of observations

As an alternative, an exponential distribution of the root density was assumed and related to the saturated hydraulic conductivity. At the lower end of the profile, the saturated hydraulic conductivity was set to the fixed value of 0.267 m·d⁻¹. A higher saturated hydraulic conductivity was assigned to the surface. No optimisation was performed except that maximum moisture contents near the end of a run were interpreted as representing a Neuman boundary condition. A saturated hydraulic conductivity was sought that satisfied the condition that the rainfall intensity equalled the unsaturated conductivity for the imposed soil conditions and rainfall intensities. This optimised surface conductivity and the average value for the upper 50 cm, based on the geometric mean and the statistics on the model performance are given in Table 5.16.

The optimisation results in a reasonable approximation of the observations for the wetting periods and the drying periods even when the latter accumulate the errors over a longer period (hourly to daily scales). In both cases, the predicted values tend to underestimate the larger moisture contents and the scatter is equally large and evenly distributed.

As expected, the saturated hydraulic conductivity for the upper 50 increases with abandonment. Generally, the optimised values over the upper 50 cm are an order of magnitude higher than those determined by the inverse bore-hole method (Table 5.13). For land use units I and III, the values are not improbable for they fall within the range of values observed in Figure 5.10. For land use units II and IV, however, the values fall outside the observed range. In the inverse bore-hole tests, however, the lateral propagation of saturated wetting front over the entire profile is used to determine the saturated hydraulic conductivity whereas during the rainfall simulation unsaturated flow predominates. Consequently, the bore-hole test will tend to overestimate influence of the deeper layers of lower conductivity in the average k_{sat} , whereas the optimised k_{sat} of the rainfall simulation accommodates errors that arise from the SWRC. Still, the estimated saturated hydraulic conductivity over 50 cm is in the same order of magnitude for both methods.

On the scale of the rainfall simulations, the VMCs of the one-dimensional Richards' equation approximate the observed values on average reasonably well. This also applies to the land use units II and IV, for which the TDR-observations point towards a rapid redistribution of soil moisture. However, this redistribution appears to be larger than observed from the gravimetric measurements (Table 5.15). This should be attributed to the smaller sample volumes of TDR-sensors, which makes them more susceptible to local variations in the moisture content. Despite the larger redistribution, the simulated loss across the 30 cm node is in all cases less than 15% and negligible at the 50 cm node. This strengthens the observations of Table 5.15 that transfer to the underlying regolith is slowly initiated under summer conditions.

The results from the rainfall simulation indicate that there is no ground to doubt the aptness of concept of Darcian flow to describe the transfer of water from the root zone to the regolith on the scale of the rainfall simulations. All optimised values for the saturated hydraulic conductivity are higher than the averages for the land use units of Table 5.13. For all units, the high intensity is readily accepted by the soil and the transfer is limited by the underlying regolith for no large losses in the water budget have been observed at the end of the simulation. Therefore it must be concluded that for the rainfall intensity and duration tested, the concept of Darcian flow is appropriate and that the infiltration is not limited by infiltration rate but rather by the storage capacity of the root zone.

5.5 Topography

In the model, the topography is represented by a digital elevation model (DEM). The model uses the DEM as the source for the topographical attributes that determine the elevation head, the slope and aspect and the shading of slopes by the surrounding topography. Because of the raster-structure of PCRaster in which the model is embedded, the resolution of the DEM influences the precision at which these attributes can be represented (Evans, 1998). For the rasterised DEM, this precision is superimposed on the accuracy at which the measurements or map data represent the real world. Large cell sizes smooth the data and lead to an underrepresentation of the larger topographical gradients (Zang & Montgomery, 1994). Although this favours numerical stability, it leads to an inaccurate representation of the steeper slopes prone to landsliding. Thus, it appears to be advisable to select the smallest cell size supported by the original data. However, this could result in unruly large maps from a computational point of view. Hence, an optimum between cell- and map size should be found. Zang & Montgomery (1994) concluded that a cell size of 10 m offered a good balance between precision and manageability.

The study area consists of a steep slopes along the barranco that connect to gently inclined pediments. Due to the presence of the bench terraces and scarps, the resulting topography varies over short distances. A detailed DEM is required if these small-scale features should be represented. To this end, an intense survey was made of the 30-ha large sub-area. From a network of triangulation points, the linear features in the area were surveyed. The error of closure of the triangulation network is less than 5 mm. The

maximum error in the height of the survey points is 30 cm and 10 cm in the XY-plane. From these data, a high-resolution DEM was made with a cell size of 5 m. Because of the linear features represented by the data, interpolation was done using a triangular irregular network (TIN).

This detailed survey could not cover the entire Barranco de la Coloma because of poor lines of sight within the barranco and across the wooded area, this survey. For this area, a DEM with a resolution of 10 m has been derived from a digitalisation of the 1:10,000 topographical map (Generalitat de Valencia). This map, with equidistant contour lines of 10 m, is based on an air photo reconnaissance from 1994. The DEM based on TIN of the data from this map is presented in Figure 5.16.

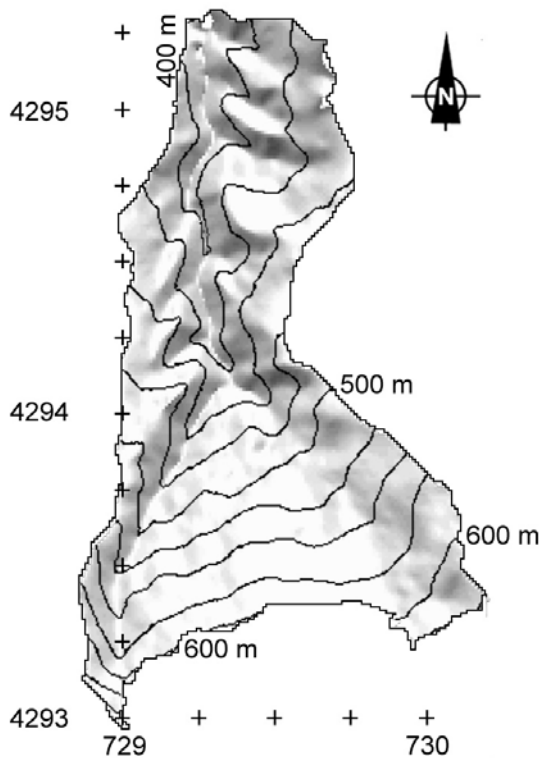


Figure 5.16: DEM of the Barranco de la Coloma (10 m resolution, based on 1:10,000 topographical map of the Generalitat de Valencia, 1995)

5.6 Soil depth

Soil depth is an important parameter for the simulation of the hydrological and geomechanical behaviour of the slopes in the area. Yet, it is difficult to quantify it exactly at every location because of the various soil forming processes. Hence spatial data on soil depth suffer from the inherently large variability. In the study area, most of the soils have developed in or are deposited over the Miocene marl. The scree deposits and the alluvial cover of the pediment are distinct from the autochthonous soils in the marl. Along the barranco, the soils consist of regoliths and colluvial deposits of weathered marl (Figure 5.17).

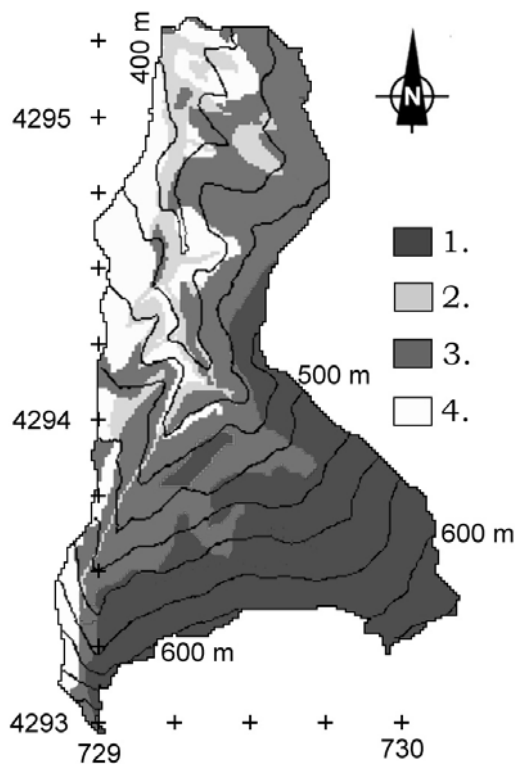


Figure 5.17: Lithological map of the Barranco de la Coloma. 1: Scree; 2: Alluvium; 3: Colluvium; 4: Regolith.

Data on soil depth in the area are available from augering and from geophysical research. For the 30-ha large sub-area, the 75 bore-holes provide information on the actual depth. In 27 of the 75 cases, the intended profile depth could not be reached because bedrock was encountered within 1.4 m. The shallowest depth recorded is 0.85 cm. Empirical relationships between the observed soil depth from the bore-holes and geomorphological attributes have a limited predictive power. For the individual survey lines, the relation between the downslope distance from the divide and the soil depth explains a maximum of 78% of the variance. For these local predictions, the total R^2 amounts to 58%. When the entire sample population is analysed, the simplest multivariate regression of the soil depth on the slope angle and the natural logarithm of the upstream area explains 19% of the variance. The average absolute error in this case is 0.18 m with a maximum deviation of 0.47 m. The prediction is not enhanced if more complex relationships are considered; when, in addition to the local slope and upstream area, the relative elevation and position in the catchment are considered, the R^2 increases to a mere 21%. The errors between the predicted and observed values remain the same. For the dataset of soil depths smaller than the intended 1.5 m, the R^2 increases to 40% but the mean absolute error rises to 0.66 m. Thus, empirical relationships have a very limited capability to predict soil depth.

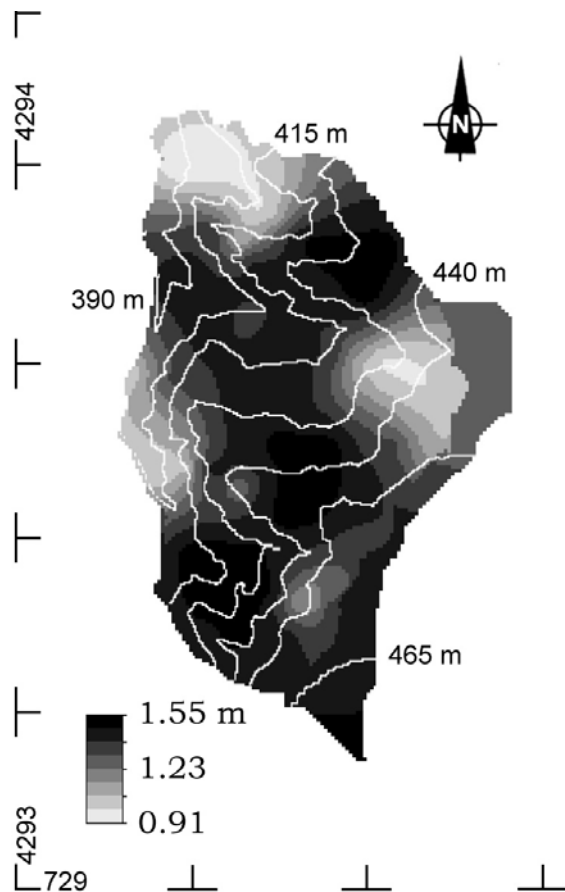


Figure 5.18: Interpolated soil depth for the 30-ha large sub-area

Spatial interpolation provides a better estimate of soil depth. The standardised soil depth has been interpolated using ordinary kriging in GSTAT (Pebesma & Wesseling, 1998). The soil depth has been kriged over 50 x 50 m block averages to increase the support of the observation (block kriging). This results in lower variances and smoother predictions. Compared to ordinary kriging the maximum variance within the area of interest is reduced from 0.98 to 0.66 (-) for the standardised soil depth. The smoother representation still approximates the observed values well. The average absolute error in the soil depth is 0.09 m. The means of the predicted and observed values are identical (1.33 m) but the standard deviation of the predicted soil depth is lower (0.17 compared to 0.23 m). The maximum deviation is 0.27 cm, which is lower than for the empirical models. The interpolated soil depth is represented by Figure 5.18. The deepest soils are found as colluvial fills in depressions. Relatively shallow soils are found on the pediment and on the steeper slopes along the barranco.

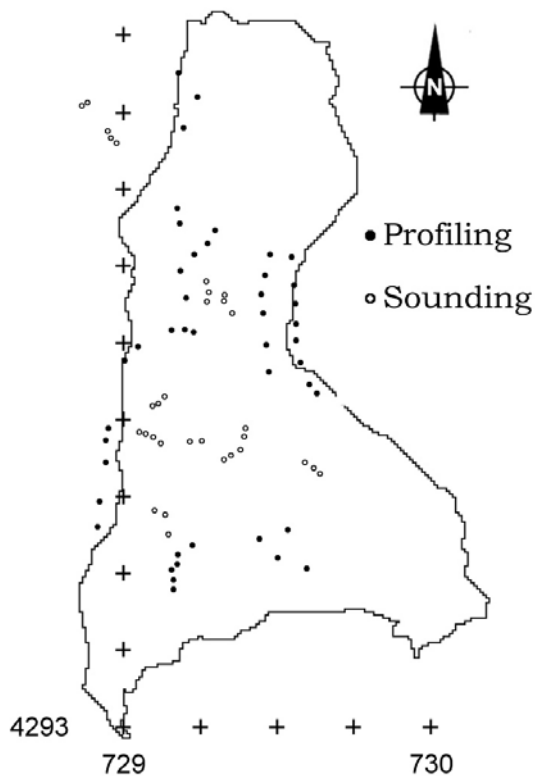


Figure 5.19: Geophysical measurements in the Barranco de la Coloma

The data from the 30-ha large sub-area are detailed but they are applicable to a small area only. Moreover, they could underestimate the soil depth in some of the colluvial areas. To obtain a better spatial representation of soil cover, geophysical measurements were made in June and early July 1998. Within the catchment of the Coloma, the apparent resistivity of the soil was determined with a Schlumberger array. In total, the resistivity was measured at 76 locations in and around the Coloma (Figure 5.19). In 73 cases, the resistivity was measured over a fixed current electrode spacing, L , of 20 m, while half the electrode spacing, $\frac{1}{2}L$, is directly proportional to the depth of penetration. This technique is known as profiling and supplies information on the bulk resistivity of the soil. Zones with a high resistivity represents areas where the currents transverse low-conductivity zones like dry soils or bedrock. Zones of low resistivity represent mostly wetter and fine-grained soils.

Repeated measurements at different electrode spacings give information on the successive resistivity of the soil. Such expanded measurements are known as soundings and interpreted by plotting the apparent resistivity against half the electrode distance. The resulting curve of the apparent resistivity includes the actual resistivity of all layers and must be interpreted by means of a generalised model of the soil geometry. This interpretation is not objective and requires *a priori* knowledge on the geometry and the resistivity in the area.

In the study area, 31 soundings were made. The measurements with the Schlumberger array have been interpreted by applying a two-layer model with the lower, infinite layer set to the resistivity of marl bedrock (typically between 10 and 15 Ωm) at first. For the

root zone, a depth of 0.5 m is assumed, after which the depth and resistivity of each layer has been altered until the observed and predicted apparent resistivity curves coincided. The root mean squared error (RMSE) has been used to express the mismatch between the fitted curve and the observations. In most cases, the error has been reduced by several adaptations to less than 1% (28 locations). For three locations, no satisfactory fit could be obtained because of anomalous readings which have been ignored. The statistics for the modelled soil depth are presented in Table 5.17. The distribution is positively skewed and suggests that a lognormal distribution may be appropriate.

Table 5.17: Descriptive statistics for the soil depth interpreted from the geophysical soundings

N	Average	St. Dev.	Min	Max	Median
31	2.6	1.8	0.5	6.5	2.9

In comparison to the data from the bore-holes, the average soil depth is much higher. This is caused by the higher values obtained for the marl slopes under the Sierra de Almudaina. The observed maximum of 6.5 m is found in an area mapped as regolith in Figure 5.17. Although the curve has been fitted with a small RMSE of 0.1%, it is doubtful whether it represents the actual soil depth. It may equally result from a weathered material that is not unlike bedrock or from a lower resistivity at greater depth that decreases the discernment over the upper soil mantle.

The resistivity from the available 73 locations has been interpolated spatially by ordinary kriging over blocks of 50 x 50 m. In the Coloma, the emerging patterns reflects the mapped lithology of Figure 5.17. The highest resistivity appears to coincide with the presence of bedrock close to the surface or where the stoniness of the top layer is high. The latter is the case where alluvium or scree cover the underlying marl. The presence of bedrock, in this case limestone, is apparent from the dome of high resistivity near Almudaina. On the marl slopes, patterns of more conductive layers emerge along the barranco and in its tributaries. This is the result of the greater soil depth and higher soil moisture contents in these depressions (Figure 5.20).

The original intention was to relate the soil depth of the interpreted soundings to the spatially interpolated apparent resistivity from the more numerous observations made with profiling. Geostatistical techniques, such as universal kriging and co-kriging (Pebesma & Wesseling, 1998; Burrough & McDonnell, 1998), can then be used to obtain local estimates of the soil depth for the entire study area. However, the spatial relation between the results from sounding and profiling, on which these techniques rely, was weak and prohibited their application. The small number of joint data points (N= 28) and the relatively complex geology explain this failure. Attempts to include the observed relation with the upstream area and local slope angle did not improve the performance ($R^2= 0.12$).

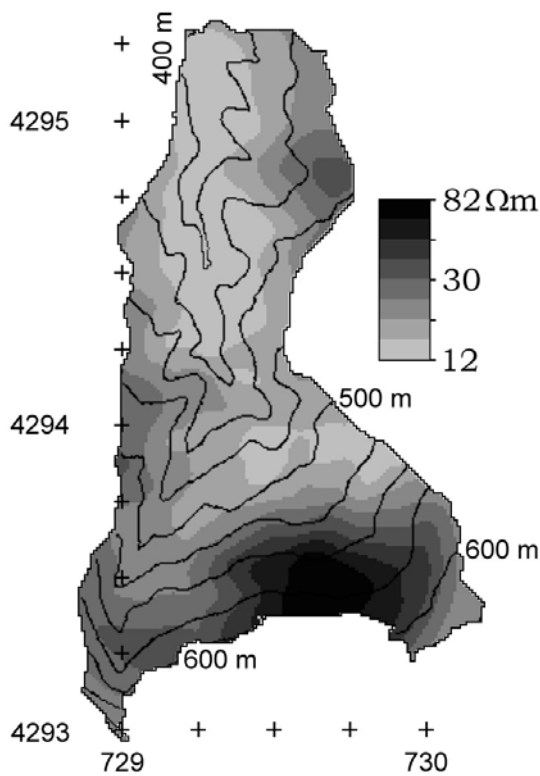


Figure 5.20: Interpolated apparent resistivity in the Barranco de la Coloma

As an alternative, the spatial distribution of the apparent resistivity from the profiling has been used to obtain estimates of the local soil depth qualitatively. To this end, the apparent resistivity has been subdivided over three classes, being $\rho_a < 15$, $\rho_a < 30$, $\rho_a \geq 30$ Ωm . Of these classes, the first represents those slopes that consist entirely of weathered marl. The second category represents similar slopes but with shallow covers of alluvium or scree. The last category represents exclusively slopes close to the Sierra de Almudaina that are covered with scree. The spatially interpolated apparent resistivity has been obtained by conditional simulation (Pebesma & Wesseling, 1998). For the resulting three categories, a soil depth was assigned randomly from a uniform distribution describing the observed soil depths. Ten realisations of the apparent resistivity and the associated soil depth were generated and averaged over a window that ranged in size from 20 to 100 m squared, dependent on the upstream area of a location. Small window sizes have been assigned to points near the divide as to simulate the smaller spatial dependence of slope formation here. In contrast, large window sizes have been applied for the downstream parts of the drainage network where slope formation is strongly influenced by upslope processes. Thus, a compromise has been found between a smooth spatial distribution of the apparent resistivity as represented by Figure 5.20 and the variability in soil depth (Figure 5.21).

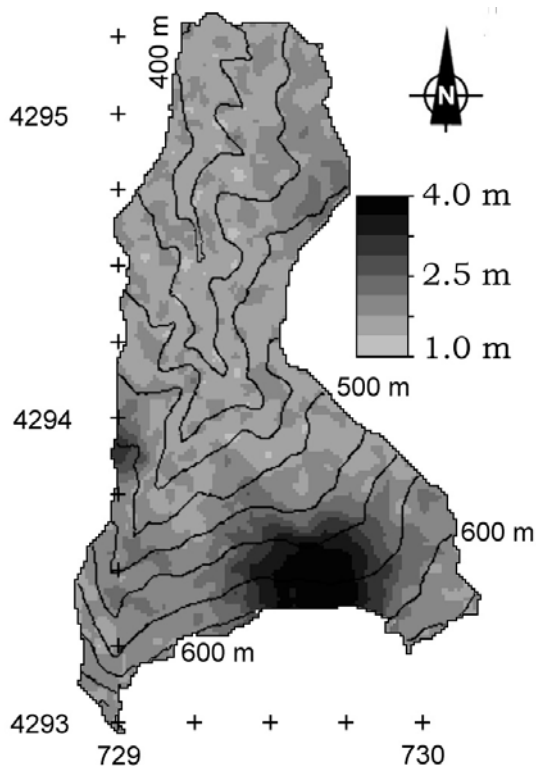


Figure 5.21: Simulated soil depth for the Barranco de la Coloma

The resulting spatial distribution is not a direct reproduction of the actual soil depth; it merely simulates some of the spatial trends that may influence the occurrence of landslides. Still, the simulated soil depth approximates the lower values of the soil depth reasonably well. Of the soil depth derived from the geophysical measurements, the geometric mean and the median are underestimated by 0.24 and 0.38 m respectively (12% and 18%). However, the simulated soil depth fails to reproduce the standard deviation and the arithmetic mean accurately. Both are underestimated by 1.61 and 0.84 m respectively (92% and 33%). This mismatch can be explained by the skewed distribution of the soil depth as determined from the soundings.

Compared to the less variable observations from the auger holes, the simulated soil depth performs better. All measures of central tendency are overestimated by less than 0.3 m ($\pm 30\%$). The standard deviation is reproduced more accurately and only underestimated by 30%. It should be noted that the observations are artificially bounded to the 1.5 m maximum and the natural variability could be larger. If the observations with a soil depth less than 1.4 m are considered, the soil depth is on average overestimated by 0.6 m. Therefore it should be concluded that the simulated soil depth provides no more than an approximation of the actual soil depth in the area.

5.7 Geomechanical properties

5.7.1 Theory

For most slopes, the long-term stability is controlled by the drained shearing resistance that can be mobilised along a potential slip plane under positive pore pressures (Chapter 1). This shearing resistance is commonly described by the Mohr-Coulomb Failure Criterion that states that the strength resisting movement equals the cohesive force per unit area and a frictional term under the experienced normal stress, denoted by σ .

Terzaghi expanded this equation for effective stresses, by replacing the total normal stress by the effective normal stress, σ' , acting on the soil skeleton (Craig, 1987):

$$\tau = c' + \sigma' \tan(\phi') \quad (5.6)$$

where τ is the maximum amount of mobilised shear strength in kPa, c' is the effective cohesion in kPa, σ' is the effective normal stress in kPa, equal to $(\sigma - u_w)$, u_w is the pore water pressure in kPa, and ϕ' is the effective angle of internal friction, in $^\circ$.

According to the Mohr-Coulomb Failure Criterion, slopes inclined at angles above the angle of internal friction are unconditionally unstable as they do not require positive pore pressures to achieve failure if insufficient cohesive strength is present. However, on some unconditionally unstable slopes, a soil mantle can be observed to remain stable. The additional strength that stabilises such slopes can be explained by the stronger inter-particle bonds due to matric suction under unsaturated conditions. In Mediterranean environments, the often erratic occurrence of potentially triggering rainfall events prevents the matric suction from attaining critical levels over longer periods. This renders the inclusion of the additional strength under unsaturated conditions important as the otherwise unstable slopes are highly sensitive to landsliding and the material stored here provides an easily exhaustible source of soil.

The first to expand this effective shear equation to unsaturated soils was Bishop (1955). He introduced an empirical parameter, χ , into the effective normal stress equation that accounts for the influence of the pore water pressure on the strength in soils that are partly filled with air:

$$\sigma' = \sigma - u_a + \chi(u_a - u_w), \quad (5.7)$$

where χ is a dimensionless parameter and u_a and u_w are respectively the pore air and pore water pressure in kPa.

Because of the surface tension, the pore water pressure must always be less than the pore air pressure under unsaturated conditions. It has been shown that the parameter χ is dependent primarily on the degree of saturation. It ranges between $\chi = 0$ when the soil is entirely dry, and $\chi = 1$ when the soil is entirely saturated. Under atmospheric conditions the pore air pressure is zero, what reduces Equation 5.7 to the effective normal stress defined in Equation 5.6 for saturated conditions and to $\sigma' = \sigma - \chi u_w$ under unsaturated conditions. Although Bishop's equation describes the often observed effect of increased

strength under suction, it has found little entrance because of the inconvenience of defining χ empirically.

At the end of the 1970s, the continuous demand for unsaturated shear strength equations for slope stability analysis led to new formulations. Anderson & Howes (1985) defined the contribution of suction to the shear strength of a regolith in Hong Kong simply by incorporating the negative pore water pressure in the effective stress equation. They hold that this approach is valid whenever the suction of the soil is low. The largest effort in describing the shear strength of unsaturated soils should be attributed to Fredlund who in 1978 defined a unsaturated shear strength equation that extended the linear Mohr-Coulomb equation into another dimension by introducing the matric suction as a new independent stress state variable (Fredlund, 1987). Thus, the failure envelope is expanded to a three-dimensional failure surface. In comparison to Bishop's earlier definition, this has the advantage that the increase in shear strength under unsaturated conditions can be considered regardless of the normal stress conditions. If the shear strength is thought to increase linearly with the matric suction, Fredlund's equation becomes:

$$\tau = c' + (\sigma - u_a) \tan(\phi') + (u_a - u_w) \tan(\phi^b), \quad (5.8)$$

where ϕ^b is the friction angle that describes the increase in strength at higher values of suction (Fredlund, 1987).

At all levels of suction, the effective angle of internal friction is taken to be constant. So, the effect of suction on the shear strength, when represented in the two-dimensional σ - τ plane, is to increase the offset of the failure envelope, so that the failure envelopes for different suctions become parallel lines. As a consequence, the contribution of the ϕ^b -term can, at a known level of matric suction, be reduced to an apparent cohesion, c , which is given by:

$$c = c' + (u_a - u_w) \tan(\phi^b). \quad (5.9)$$

In Fredlund's original formulation, the contribution of the ϕ^b -term is taken to be linear. Recent studies have questioned whether ϕ^b is really constant. The slope of the τ -(u_a - u_w) relation in general seems to flatten at higher suctions, at which in some cases an absolute drop in shear strength has been noted (Escario & Sáez, 1986). To overcome these shortcomings, the use of empirical bilinear, multilinear and curved ϕ^b -relationships has been advocated (Gan *et al.*, 1988). Escario & Sáez (1986) plead for the reintroduction of Bishop's parameter χ in the ϕ^b -term as $\tan(\phi^b) = \chi \tan(\phi')$. The advantage of χ is that it can account for the total absence of suction effects at high level of suctions. It should be realised, however, that the introduction of these empirical relationships might lead to a more accurate description of the shear strength behaviour of the soil but that none adds to a better understanding of the underlying mechanisms. Until no better theoretical relationships between the matric suction and the unsaturated shear strength has been provided, the soundest approach of defining it is possibly to determine the angle ϕ^b only over the suction range of interest. Although this may introduce some inaccuracy, the main advantage is that it is a basically simple equation that can be introduced without great difficulty in most limiting equilibrium slope stability models. Moreover, the error

due to this simpler equation is probably low as most literature values for the unsaturated shear strength show consistent values of ϕ^b that vary only in a small range (Table 5.18).

Table 5.18: Shear strength parameters for unsaturated soils (after Gens, 1993)

Soil type	c' (kPa)	ϕ' (°)	ϕ^b (°)	Test procedure	Reference
	<i>Compacted shale</i>				
w= 18.6%	15.8	24.6	18.1	Constant water content; triaxial	Bishop, Alpan, Blight & Donald (1960)
	<i>Boulder clay</i>				
w= 11.6%	9.6	27.3	21.7	Constant water content; triaxial	Bishop, Alpan, Blight & Donald (1960)
	<i>Dhanauri clay</i>				
w= 22.2%, BD= 15.5 kN·m ⁻³	37.3	28.5	16.2	Constant water content; triaxial	Satija (1978)
w= 22.2%, BD= 14.5 kN·m ⁻³	20.3	29.0	12.6	Constant water content; triaxial	
w= 22.2%, BD= 15.5 kN·m ⁻³	15.5	28.5	22.6	Constant water content; triaxial	
w= 22.2%, BD= 14.5 kN·m ⁻³	11.3	29.0	16.5	Constant water content; triaxial	
	<i>Madrid grey clay</i>				
w= 29%, BD= 12.9 kN·m ⁻³	23.7	22.5 ^a	16.1	Consolidated drained; direct shear	Escario (1980)
	<i>Undisturbed decomposed granite: Hong Kong</i>				
	28.9	33.4	15.3	Consolidated drained; multistage triaxial	Ho & Fredlund (1982)
	<i>Undisturbed decomposed rhyolite: Hong Kong</i>				
	7.4	35.3	13.8	Consolidated drained; multistage triaxial	Ho & Fredlund (1982)
	<i>Tappen-Notch Hill silt</i>				
w=21.5%, BD= 15.6 kN·m ⁻³	0	35.0	16.0	Consolidated drained; multistage triaxial	Krahn, Fredlund & Klassen (1987)

a): average value

5.7.2 Test procedure

In this study, the shear strength has been determined by strain-controlled, consolidated and drained direct shear tests. This is the simplest test to determine the drained shear strength. The test is performed in a shear box, a device that is divided in half over the height of the sample. In this manner, an area is formed over which the sample is loaded vertically, resulting in the normal stress σ , and strained horizontally. This deformation is imposed by keeping the upper half of the box in a fixed position and displacing the lower half. As a consequence, an artificial shear plane develops. Over this shear plane, the mobilised shear strength is easily measured as the reaction force under the applied strain. Since the shear strength of the material is finite, the material will fail and the shear stress

recorded at this stage, τ_f , must be considered as the maximum shear strength that can be mobilised under the applied normal stress σ_f . By determining the shear strength at failure for various levels of normal stress the Mohr-envelope can be constructed and the intrinsic parameters of cohesion and angle of internal friction can be determined from least-squares or graphically.

Compared to other tests, the advantages of the direct shear test are its simple design, the small sample size and its rapid execution. Because of the relatively small sample size, the dissipation of pore pressures in the deforming shear plane is quick and thus effective stress conditions are readily ensured as long as the strain rate is sufficiently low. This makes the test also more appropriate for the determination of the unsaturated shear strength. Many tests can be performed in a relatively short time and the number of samples that can be tested often exceeds that of other methods. Disadvantages arise through the small sample size and the artificial nature of the imposed shear surface. As a consequence, the results from direct shear tests are often more variable and tend to overestimate the actual angle of internal friction in the order of 2° (Lambe & Whitman, 1988).

For the determination of the saturated, effective shear strength, the standard direct shear equipment – as present at Utrecht University - has been used. This equipment, however, can not comply with the requirements for sophisticated unsaturated tests. The additional strength due to matric suction can only be approximated by testing partly saturated material to which no suction can be applied during the tests. To test the actual contribution of matric suction to the shear strength, material has been determined at the Department of Engineering Geology of the Universitat Politècnica de Catalunya (UPC) where an adapted direct shear apparatus is available.

The direct shear equipment at the UPC follows the traditional design except that a matric suction can be applied and controlled at the base of the sample during the test. The set up of the equipment as used at the UPC has been extensively described by Escario & Sáez (1986) and by Gens (1993). The equipment complies with the ASTM standard for direct shear testing *ASTM D 3080/79*.

During the unsaturated test, the sample is enclosed in an airtight steel container except for the base of the sample that is placed on a semi-permeable membrane that covers an air entry disk. The matric suction is applied by means of the axis-translational technique (Fredlund & Rahardjo, 1993). In contrast to the direct technique, in which a negative head is applied to the air entry disk, the matric suction is generated by applying a larger pore air pressure on the sample over the semi-permeable membrane at the base of the sample. The membrane prevents the pore air pressure, u_a , to dissipate and has the effect of an artificial increase in the atmospheric pressure. As a result a relative matric suction, $u_a - u_w$, acts on the sample and soil water is free to move through the membrane until equilibrium has been reached. The indirect technique has the advantage that any matric suction can be applied without the risk of the cavitation of air under the air entry disk. Fredlund & Rahardjo (1993) have shown, using Bishop & Blight's (1963) results that the obtained material strengths under equal conditions of matric suction are identical for both the direct and indirect technique.

Except for the applied suction, the saturated and unsaturated direct shear tests have been performed under normal stress conditions, dimensions and a strain rate that were as similar as possible. For the saturated tests, the sample size was larger and the strain rate lower; they were respectively 60 x 60 x 20 mm and 0.2 mm·hr⁻¹ for the saturated tests compared to 50 x 50 x 22 mm and 0.3 mm·hr⁻¹ for the unsaturated tests. From these samples, the bulk density, porosity and gravimetric moisture content have been determined before and after the test. The samples were consolidated under the intended normal stress prior to the test. For the saturated tests, the samples were submerged in water and the consolidation maintained until the phase of secondary consolidation was achieved. For the unsaturated test, consolidation was continued until the volumetric moisture content of the initially saturated sample and the applied suction were in equilibrium. To this end, the drainage from the sample was recorded by means of a burette.

5.7.3 Results

All observed shear planes were located at or near the lithic contact between the marl bedrock of the Tap formation and its weathered product. So, only tests on the weathered marl are described here and compared to the strength of the marl bedrock

The saturated and unsaturated shear strength of the weathered marl has been determined by consolidated-drained tests on samples from two locations on opposite sides of the Barranco de la Coloma. In total, 27 samples have been tested for their saturated shear strength. Ten samples have been subjected to unsaturated tests in the direct shear apparatus of the Department of Physical Geography of Utrecht University while 6 samples have been tested unsaturated in the more appropriate apparatus of the Universitat Politècnica de Catalunya.

The samples have been taken at the bedrock contact near two landslides. Between the two sites, the materials seem to differ. On one site, where the material was taken at 70 to 90 cm depth, the material is slightly coarser, better rooted and more reworked than at the second site. Here, the material from 70 to 110 cm depth consists of sub-angular peds up to 20 mm in size. Yet, the results of the saturated direct shear tests are highly similar and thus the data are presented without any distinction.

All 27 saturated shear tests have been performed single-stage. The applied normal effective stress, σ' , varied in the range between 23 and 122 kPa. The material exhibits a slightly negative cohesion of -1.3 kPa and an angle of internal friction of 35.4° ($R^2= 0.91$; Figure 5.22). When the slope $\tan(\phi')$ is forced through the origin, the angle of internal friction equals 34.8°. The standard error of the regression with $R^2= 0.90$ is 0.9°. This corresponds to a standard deviation of 4.8° ($\tan(\phi')= 0.694 \pm 0.084 (-)$).

Nine samples experienced an additional strain of 25% after failure had occurred. From the final shear strength readings, the residual strength has been calculated. Under the assumption of a residual cohesion of 0 kPa, the residual angle of internal friction, ϕ'_r , is 30.2° with a standard error of 1.4°.

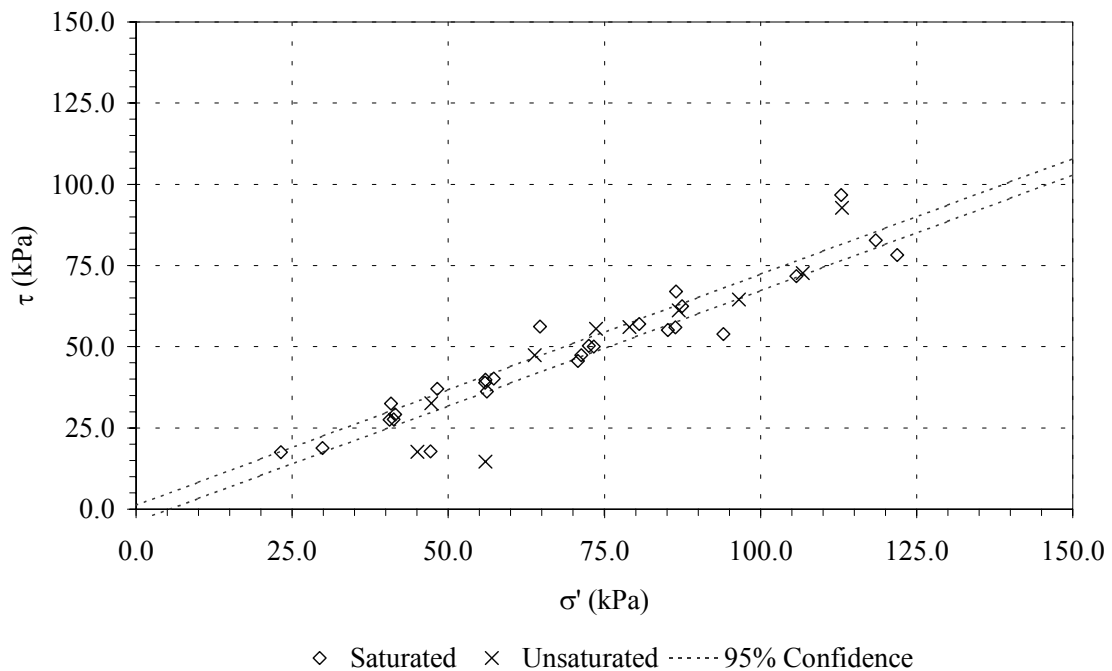


Figure 5.22: Saturated and unsaturated direct shear test results and the Mohr envelope for the saturated shear strength for the weathered marl. $c' = -1.3 \pm 3.4$ kPa, $\tan(\phi') = 0.71 \pm 0.04$ ($R^2 = 0.91$).

Similar strain-controlled direct shear tests have been performed on unsaturated samples. Before testing the material in the direct shear apparatus, the sample was placed on a suction plate on which an actual suction of 1.0 m ($pF = 2$) was applied. After equilibrium in the gravimetric moisture content of the sample had been reached, it was consolidated in a traditional direct shear apparatus for 24 hours without, however, immersing the sample in water. After the consolidation horizontal strain was applied and the sample failed. During the test, a soaked cotton cloth was placed over the sample to prevent any moisture loss due to evaporation. In total 10 single-stage tests have been carried out with effective normal loads in the range between 45 and 113 kPa.

On the basis of the results, the unsaturated shear strength is, when the slope $\tan(\phi')$ is forced through the origin, 34.7° . The standard error of the regression is 2.4° , with $R^2 = 0.70$. This is more or less consistent with the saturated shear strength, as described previously, and the slightly lower value and low goodness-of-fit are clearly due to two deviating points which generate extremely low shear stresses under the applied normal stresses of 45 and 55 kPa. For all other points, the observed mobilised shear strength is in line with the saturated strength. Most deviations fall within the 95% confidence band or are close to it (Figure 5.22).

During these shear tests on unsaturated samples, the moisture content stayed relatively constant, the maximum recorded change of the gravimetric moisture content (GMC) is 3%. The degree of saturation during the tests was approximately 80%, with GMCs ranging between 0.25 and 0.30. This high degree saturation and the absence of suction during the test itself probably explain the behaviour of the material during the unsaturated tests. So, it should be concluded that direct shear tests at constant soil

moisture contents are inappropriate to determine the possible gain in shear strength under unsaturated conditions when the applied suction is relatively low and the moisture contents are close to saturation.

The analysed material has reasonably uniform geotechnical properties. Of the analysed 37 samples, the mean porosity is $0.51 \text{ m}^3 \cdot \text{m}^{-3}$ with a standard deviation of $0.05 \text{ m}^3 \cdot \text{m}^{-3}$. The porosity ranges from 0.42 to 0.65. The average dry and saturated bulk densities are respectively 15.0 ± 1.0 and $20.0 \pm 1.1 \text{ kN} \cdot \text{m}^{-3}$. These values agree with the bulk density and porosity of the 176 samples from the 30-ha large sub-area (Section 5.3.2). Consistent with the trend observed for these 176 samples, the differences in the porosity and the bulk density are negligible with depth for the direct shear samples tested.

The weathered marl lacks the cementation that is preserved in the case of the sound marl bedrock. Consequently, the strength of the weathered marl is much lower. Samples of sound marl were taken from an outcrop in a road cut between the Coloma and the Mollo. This material consists of a porous siltstone and a denser, more calcareous marl. The unconfined compressive strength, q_u , for 5 samples of this denser material is an order higher than that for 8 samples of the less compacted siltstone (14.2 MPa vs. 1.3 MPa). The difference is also reflected in the bulk density. The stronger material has also a higher density ($20.8 \text{ kN} \cdot \text{m}^{-3}$ vs. $16.7 \text{ kN} \cdot \text{m}^{-3}$).

In the softer material, slaking has been observed when it had been left to absorb water. Although the material appears homogeneous, expansion takes place along the bedding planes. No slaking has been observed for the denser material.

The effect of the sedimentary structure is also present in the results of the saturated consolidated-drained direct shear tests on these types of sound marl bedrock. Samples tested perpendicular to the lamination are more resistant than those tested with the shear plane parallel to the lamination. Seven samples have been tested, four parallel and three perpendicular to the lamination. The cohesion, as determined by a best linear fit, is similar with respectively 31.0 kPa vs. 27.9 kPa for the samples tested parallel and perpendicular to the bedding planes. The difference in strength is more strongly reflected in the angle of internal friction; for the first group, this is 38.9° , for the second 53.3° . This last value is too high to be explained by friction along a uniform slip plane only. Notwithstanding, it demonstrates that considerable additional resistance can be mobilised when strain occurs across bedding planes.

All seven bedrock samples exhibited considerable strain-softening. After failure, the strength of the marl drops to cohesion of 5.6 kPa and a angle of internal friction of 37.1° .

Proper direct shear tests on material under suction are relatively time-consuming. Therefore, only a limited number of tests has been executed under suction-controlled conditions at the Universitat Politècnica de Catalunya (UPC). Moreover, several of these tests have been performed multistage. This means that the same sample is tested under different conditions; at reaching the maximum amount of mobilised shear strength (*peak strength*), the test is stopped, relaxed, and the consolidation and testing are repeated under new values of the normal stress and suction. The feasibility of this method is limited by the strain limits of the equipment and by the behaviour of the material. Despite the savings in time and material, the obvious drawback of this method is that the decision

to interrupt the test is highly arbitrarily. In this case, considering the material as cohesionless, the ratio between the corrected σ and τ has been used to decide whether the sample had reached its maximum strength as objectively as possible, and the test was stopped when consecutive, constant values had been recorded. A solution to prove the validity of the tests is to repeat some stages in common, single-stage tests. Because of the limited time available, however, no tests have been duplicated, although two single-stage tests have been carried out.

Table 5.19: Applied normal stresses and suction levels

Test No.:	Sample	Test	Effective normal stress, σ' , in kPa	Suction, $(u_a - u_w)$, in kPa
1	B1 Sq. 1	single	100	35
2	A1 Sq. 1	multi- (I)	50	100
3	A1 Sq. 1	multi- (II)	50	65
4	A1 Sq. 2	multi- (I)	75	100
5	A1 Sq. 2	multi- (II)	75	35
6	A1 Sq. 3	single	125	100

Table 5.20: Volumetric moisture contents during the suction-controlled direct shear tests as calculated from the burette readings and from observed gravimetric moisture contents

Test No.:	Suction, $(u_a - u_w)$ (kPa)	Volumetric Moisture Content (VMC; $m^3 \cdot m^{-3}$) \Rightarrow	
		Calculated	Observed
1	35	0.357	0.361
2	100	0.263	-
3	65	0.308	0.298
4	100	0.284	-
5	35	0.318	0.320
6	100	0.278	0.278

Of the six tests carried out at the UPC, four were multistage tests, with two tests on one sample each. During the multistage tests, the normal stress was maintained constant, but suction was decreased at the beginning of the second stage to simulate the effect of wetting on the soil, and the consolidation was repeated. Practical and geomorphologic considerations form the base for the selection of the ranges of normal stress and suction that have been applied during the tests. The normal stress ranged from 50 to 125 kPa, thus copying largely the range of the saturated direct shear tests. For the suction levels, winter conditions are assumed to govern the long-term stability of the unsaturated slopes. As the minimum suction level, the field capacity, at a value of 35 kPa, was chosen. This equals a negative head of approximately 3.5 m. The maximum suction level was set to 100 kPa. Higher suctions can clearly be expected, especially during summer conditions, but under these conditions instability of most slopes can be considered of no concern. In Table 5.19 the applied normal stresses and suction levels are listed for the 6 tests.

Before and after the test the gravimetric moisture content and dry bulk densities have been determined for each sample. From them, the volumetric moisture content (VMC) has been derived. Table 5.20 summarises the calculated VMC and the observed values at the end of the test, if available. In general the observed and calculated VMCs are the

same within a small band of error. Compared to the fit of the soil water retention curve (SWRC) of the material, the values are also in close agreement. The R^2 for the VMC predicted from the SWRC and the observed values is 0.90. The close agreement suggests that, during the test, the moisture contents were in equilibrium with the applied suction.

Table 5.21: Shear strength, strain and dilatancy at failure

Test No.:	Sample	$u_a - u_w$ (kPa)	Strain, ϵ (10^{-3} m)	Dilatancy (10^{-3} m)	σ' (kPa)	τ (kPa)	τ/σ' (-)
1	B1 Sq. 1	35	4.121	-1.614	109.0	89.0	0.816
2	A1 Sq.1 (I)	100	3.716	-0.049	54.0	69.9	1.295
3	A1 Sq.1 (II)	65	4.831	0.152	55.3	69.5	1.256
4	A1 Sq.2 (I)	100	3.443	-0.204	80.5	95.7	1.188
5	A1 Sq.2 (II)	35	3.896	-0.283	81.3	85.1	1.046
6	A1 Sq.3	100	4.834	-0.287	138.4	143.4	1.036

The maximum shear strength ratio τ/σ' has been determined as a function of the experienced strain. For the 6 tests, these points are considered to represent the moment of failure at which the maximum shear strength or peak strength has been mobilised. In Table 5.21 the shear strength ratio, the corresponding normal stress and shear stress values, together with the strain and dilatancy, are given at failure. It becomes clear from these data that all samples failed between 3.4 and 4.8 mm and no marked difference between peak and residual strength was observed. Similar behaviour was found for the saturated tests.

To the test results of Table 5.21, the relationships of Section 5.7.1 that describe the unsaturated shear have been applied. These relationships are:

- I. The Mohr-Coulomb Failure Criterion for the total normal stress, σ ;
- II. The Mohr-Coulomb Failure Criterion for effective normal stress σ' , as modified by Anderson & Howes (1985), with $\sigma' = \sigma + (u_a - u_w)$;
- III. Fredlund's unsaturated shear strength model (Equations 5.8 & 5.9), which relates the increased strength under suction to the slope $\tan(\phi^b)$;
- IV. Bishop's model (1955), in which the effective stress is defined by a proportional contribution of the applied suction, depending on an empirical parameter χ .

All models have been fitted by means of least-squares methods. In the case of Bishop's model, the parameter χ has been calculated for each test under the assumption that the strength of the material equals the saturated shear strength ($\phi' = 34.8^\circ$). The values of χ have subsequently been regressed on the suction levels applied during the test using a loglinear relationship.

The shear strength parameters of the different models are given in Table 5.22. The goodness of fit of all models is expressed by the squared correlation coefficient, R^2 . For the three direct regressions of τ on σ , a 95% confidence level was applied to the regression variables and the lower and upper levels have been listed. These confidence levels are also represented in the graphs of Figure 5.23. For Bishop's model, the represented error stems only from the regression of χ .

Table 5.22: Shear strength relationships; $\sigma_{y|x}$ is the standard error of the regression.

Shear strength parameters			Confidence levels	
			lower 95%	upper 95%
<i>I) Based on total stress, σ</i>				
$c' =$	26.2	kPa	-17.5	70.0
$\phi' =$	37.3	°	15.8	51.1
$R^2 =$	0.83			
$\sigma_{y x} =$	12.57			
<i>II) Based on effective stress, σ' (Anderson & Howes, 1985)</i>				
$c' =$	7.9	kPa	-55.4	71.1
$\phi' =$	27.9	°	8.2	42.5
$R^2 =$	0.78			
$\sigma_{y x} =$	14.13			
<i>III) Fredlund's model for ϕ^b</i>				
$c' =$	5.1	kPa	-37.4	47.5
$\phi' =$	37.4	°	22.0	48.4
$\phi^{b'} =$	16.1	°	-4.4	33.2
$R^2 =$	0.94			
$\sigma_{y x} =$	8.24			
<i>IV) Based on Bishop's parameter χ (using the saturated shear strength)</i>				
$c' =$	0.0	kPa	$Y_0 =$	3.10
$\phi' =$	34.8	°	$B =$	-1.27
$R^2 =$	0.93		$R^2 =$	0.88
$\sigma_{y x} =$	6.23		$N =$	5

Figure 5.23 shows that the reliability of the relationships is seriously impaired by the limited number of tests, although it is evident that a correlation exists. For all regressions, testing the hypothesis that no correlation would exist ($\rho = 0$), the critical significance level at which this hypothesis can not be rejected is between 1 and 2%. So, all relationships are significant at $\alpha = 0.05$. It is, however, troublesome to determine which of the models gives the most accurate description of the unsaturated shear strength of the material. Fredlund's model clearly has the highest goodness-of-fit with a R^2 of 0.94, and has the smallest band of error for the shear strength parameters of Table 5.22. The slopes of $\tan(\phi')$ and $\tan(\phi^b)$ are significant at $\alpha = 0.05$, although the t-test statistic for ϕ^b is only slightly above the critical value. The slope $\tan(\phi^b)$ in Fredlund's model explains a fraction of 67.7% of the variance in addition to the 82.9% already explained by the effective normal stress alone, bringing the multiple R^2 to 0.94.

For the two other direct regressions of τ on σ , the error is higher. The large amount of error resulting from the limited number of tests is most clearly reflected by the cohesion. All direct regressed relationships have a positive intercept but the associated error is high, stretching the confidence band to a considerable width (Figure 5.23). This explains why for none of these models the cohesion is significant at the 95% confidence level.

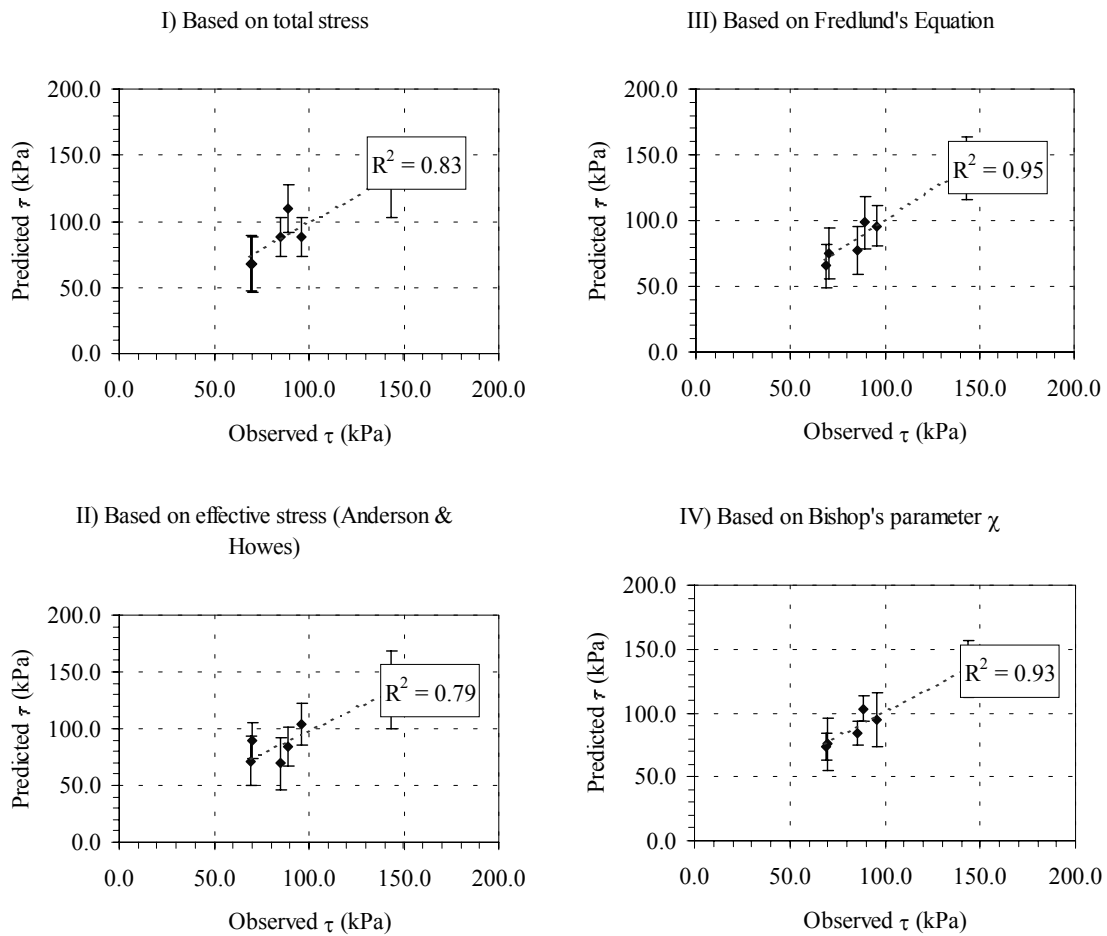


Figure 5.23: Observed vs. predicted shear strength for different theoretical relationships

For Bishop's model, incorporating the parameter χ , the uncertainty in the relation between the applied suction and this parameter leads to an equally large band of error around the shear strength relation (Figure 5.23). The explained variance, however, is reasonably high, $R^2 = 0.93$, and approaches Fredlund's model. In addition, the use of the well-defined saturated shear strength restricts the main source of error to the loglinear relation between the suction and the parameter χ only. The overall error, expressed as the average of the deviations from the expected values, is the lowest for Bishop's model, with the maximum error being only slightly above the maximum for Fredlund's model.

5.7.4 Discussion and conclusion

From the correlations of Table 5.22 and Figure 5.23, it is evident that Bishop's and Fredlund's models have the best predicting capacities over the ranges of the applied shear stresses and suction levels. However, as a consequence of the associated error and their different nature, it is difficult to judge their respective usefulness. Fredlund's model has

the computational advantage that the strength increase due to suction is explained by the slope $\tan(\phi^b)$ that expands the normal Mohr-Coulomb Failure Criterion simply into a third plane. All parameters can then be derived directly from the test results, what reduces the associated error for the shear strength equation. If ϕ' and ϕ^b are assumed to be constant, an additional advantage is that the increased shear strength under suction leads to linear behaviour, which facilitates the interpretation of model results. However, this advantage will be lost if curved empirical relationships are used to describe the decreased effect of ϕ^b at higher matric suction level. Under these restrictions, Fredlund's model is entirely empirical and not different from Bishop's model, incorporating χ . According to Escario & Sáez (1986), the empirical parameter χ has the advantage that it by nature reduces the gain in shear strength to zero, when large suctions are applied. Moreover, χ is linked directly to the stress and capillary history of the soil and could be more informative with regards to the behaviour of the soil (Escario & Sáez, 1986). However, these advantages are hypothetical as the increase in shear strength is determined by the matric suction and the relationships between matric suction and the stress- and pore space conditions are highly uncertain.

On the basis of the present results, the linear shear strength equation as proposed by Fredlund (1987) is preferred (Equation 5.8). Over the range of matric suction between 35 and 100 kPa, the slope $\tan(\phi^b)$ equals 16.1° . The shear strength at the zero suction plane is given by an effective cohesion of 5.1 kPa and an angle of internal friction, ϕ' , of 37.4° for effective normal stress conditions ranging from 50 to 125 kPa. This strength at the zero suction plane is similar to the strength obtained from the conventional direct shear test that pointed towards a cohesionless material. The cohesion for the unsaturated results is entirely due to a reduced shear strength ratio for the higher values of normal effective stress, which are emphasised by the limited number of tests. Consequently, the shear strength of the weathered marl of the Tap formation at the zero suction plane is based on the results of the saturated direct shear test ($c' = 0$ kPa, $\phi' = 34.8^\circ$). The contribution of the matric suction to the shear strength is described by the value of ϕ^b from the 6 suction-controlled direct shear tests. Its value fits well within the range of ϕ^b as given in Table 5.18. The proposed set of shear strength parameters for the weathered marl of the Tap formation in the study area are in close agreement to the values for the Tappen-Notch Hill silt as tested by Krahn *et al.* (1987, *op. cit.* Gens, 1993). The agreement between results of the suction-controlled and saturated direct shear tests on the one hand and between the results and the literature values on the other implies that the obtained parameters provide a good estimate of the saturated and unsaturated direct shear test alike, despite the limited number of suction-controlled tests that could be performed.

With $\phi^b = 16.1^\circ$, suction appears to have a considerable influence on the stability of soils on slopes inclined at angles steeper than ϕ' . At a matric suction of 35 kPa, the apparent cohesion at the potential slip plane would be 10.1 kPa (Equation 5.9). This means that at, the critical slope angle $\alpha = \phi'$, the factor of safety of a uniform soil layer of 6 m would be 1.25 (see also Section 3.2.3). With increasing soil depth, the safety factor approaches asymptotically to $F = 1$, the level of stability if no apparent cohesion due to matric suction would be present. When the slope angle increases to 40° , the factor of safety drops to 1.1.

For slopes inclined at this angle, the critical soil depth, at which $F=1$ at an apparent cohesion of 10.1 kPa, is 8.2 m.

For slopes at lower inclinations than ϕ' , elevated, positive pore pressures are required for failure. The marl bedrock of the Tap formation has a variable strength and is weak in comparison to other rocks but in its original state is sufficient to resist failure. The low degree of compaction and cementation, however, makes the marl prone to slaking and weathering and it can be considered as a soil from an engineering perspective. The residual strength of the failed bedrock is just above the saturated peak strength of the weathered marl ($\phi'=37.4^\circ$ compared to 34.8°). After failure, the residual strength of the weathered marl is lowered but still in the order of 30° . In all cases, the test results do not unambiguously manifest any true cohesion.

Apparently, weathering makes the marl slopes rapidly susceptible to landsliding. This can also sustain prolonged landslide activity once the soil cover has been stripped. This regeneration of the soil cover may be enhanced by the horizontal unloading of the marl after the incision of the barrancos in the Valles de Alcoy. The resulting fissures and intrinsic discontinuities offer pathways along which weathering can attack the remaining bedrock (Taylor & Crips, 1987).

5.8 Summary and parameterisation

A land use map was produced from air photo reconnaissance and field mapping (Section 5.2). In addition, land use was mapped from air photographs since 1956. This inventory shows a clear trend of abandonment. This notion has been used to merge the 26 classes of the land use situation of 1998 into larger units. Four units have been distinguished that represent the successive stages of abandonment (Table 5.2).

The four land use units have been employed to describe the land use dependent processes of interception and evapotranspiration and to analyse and assign soil hydrological properties to the topsoil.

Interception under *Pinus halepensis* (semi-natural vegetation or Unit IV) has been monitored continuously over a year. For the other units, interception was studied by rainfall simulations only and less detailed information is available. The determined values of the throughfall partitioning coefficient and the maximum storage capacity are conformant with literature values for Mediterranean vegetation (Table 5.5). Cultivated areas have a large storage capacity but a high throughfall coefficient and a large fraction of the rainfall will reach the surface unhampered. For the other units, the canopy interception is higher, with the strongest influence under semi-natural vegetation.

Crop specific evapotranspiration is related to the potential reference evapotranspiration by means of crop factors (Doorenbos & Pruitt, 1977). These crop factors assume that the vegetation is healthy and grows under optimum conditions of water and nutrient supply. Consequently, they represent merely the relative influence of the vegetation. They are based on literature values. For the evergreen vegetation of the land use units III and IV, the crop factor is constant over time. The dormancy of cherry trees and the die-back of grasses are simulated by dynamic crop factors for respectively the land use units I and II (Figure 5.4).

For the parameterisation of the model, the crop factors and the interception variables have been assigned to the land use units under the general assumption that the units are static and homogeneous.

The soil hydrological properties have been studied for an adopted schematisation of three layers of equal depth (0.5 m). This schematisation corresponds with the observed soil profile in the study area. A root zone is present that varies in depth but does not exceed 0.5 m. The underlying layers represent the pristine soil and a decrease in weathering may be expected with depth (Section 5.3).

The saturated hydraulic conductivity and the porosity have been determined for 76 sampling locations in the Barranco de la Coloma. An exponential decrease in the saturated hydraulic conductivity was observed. The variability decreases also and both mean and variance are significantly different (Table 5.12). For the porosity, which is reciprocal to the dry bulk density, only differences between the deepest layer and the two upper layers were found. However, the values of the bulk density and the porosity are very similar and it may be argued that the difference is due to sampling disturbance.

The soil water retention curve (SWRC) has been determined from sampling rings and described with the simple formula of Farrel and Larson (1972). For the various depths, the formula performs well and the differences are small. Consequently, the SWRC of the weathered marl can be represented by a single function as given in Table 5.11.

The description of the soil hydrological properties does not describe the influence of land use. To determine this influence, the available data have been re-interpreted using the land use units of Table 5.2 (Section 5.4). The data demonstrate that the influence on the saturated hydraulic conductivity does not extend beyond the root zone. No differences have been found for the sampled porosity between the land use units at any depth.

The absence of an influence of land use on the porosity can be explained by the small sample size that fails to include structural pores, e.g. root canals or fissures. Excavations of trial pits have been used to determine the total porosity, which includes those structural pores. A comparison of both shows an increase in total porosity in the case of land use units I and II. For land use unit II, no difference has been found. Unit I shows a clear difference for the topsoil, which must be attributed to tillage.

Tillage also affects the fit of the SWRC for land use unit I. For the other units, the fits perform better and these data have been used to parameterise the SWRC for the topsoil. For the porosity, the VMC at saturation has been used.

Infiltration and redistribution are important hydrological process with respect to landsliding that are potentially influenced by land use. These processes have been studied by means of broadscale rainfall simulations in which attention has been paid to the development of preferential flow and the validity of the concept of Darcian flow. No run off was observed under the imposed intensities. Infiltration appears to be limited by the storage capacity rather than by the infiltration capacity under the intensity and quantity of the applied rainfall (respectively $34.4 \text{ mm}\cdot\text{hr}^{-1}$ and 55-69 mm).

Redistribution was rapid within the root zone but budgets are inconclusive on the amount of water that is transferred to the underlying soil (Table 5.15). Preferential flow was observed for the land use units III and IV whereas the units I and II are dominated by a more uniform wetting front (Figure 5.15). However, because of the development towards

more homogeneous moisture distribution near the end of the simulation Darcian flow, as simulated by a one-dimensional solution of the Richards' equation, performs reasonably well (Table 5.16). The average saturated hydraulic conductivity exceeds the values of Table 5.13 by an order of magnitude but the concept of Darcian flow seems appropriate on the scale of the rainfall simulations. Given the lower spatial and temporal resolution, at which the coupled hillslope model is applied, any preferential flow has been ignored. The rainfall simulations were performed under dry initial conditions and the amount of redistribution is small as it is limited by the conductivity of the underlying layer. Under consideration of the low sensitivity of the model to the saturated hydraulic conductivity, the measured values of Table 5.13 have been preferred over the optimised values from the rainfall simulations to represent the saturated hydraulic conductivity of the top layer. The infiltration capacity has not been restricted and all rainfall can enter the soil provided that neither the storage capacity nor the saturated hydraulic conductivity is exceeded. The subsequent land use dependent parameterisation for the topsoil is given in Table 5.23.

Table 5.23: Land use dependent soil hydrological properties for the topsoil

Unit		k_{sat} ($\text{m}\cdot\text{d}^{-1}$)	Porosity ($\text{m}^3\cdot\text{m}^{-3}$)	SWRC	
				$ h _{\text{A}}$ (m)	α (-)
I	Cultivated	0.91	0.501	0.161	9.204
II	Abandoned	1.53	0.511	0.049	11.089
III	Abandoned	1.14	0.520	0.145	12.258
IV	Semi-natural	1.22	0.528	0.020	12.907

The soil hydrological properties of the second and third layer are given in Table 5.24. Only the saturated hydraulic conductivity varies between the layers. For the porosity, this is contrary to the field evidence but the choice can be defended on the ground that does not conform to the expectation that the degree of weathering would decrease with depth. The decline in the saturated hydraulic conductivity with depth makes the existence of such a trend likely.

According to the description of the coupled hillslope model, the saturated hydraulic conductivity and the SWRC that define the lower boundary condition have been set to those of the third layer. The matric suction, $|h|_{\text{BC}}$, that defines the loss across the lithic contact is insufficiently known and subject to calibration (Chapter 6). The matric suction that prescribes the incipient moisture content after complete saturation, $|h|_{\text{FC}}$, has been set to 1.00 m. The residual moisture content, θ_{res} , is 5% of the porosity in all cases.

Table 5.24: Soil hydrological properties for the subsoil (2nd and 3rd layer)

Layer	Depth	k_{sat} ($\text{m}\cdot\text{d}^{-1}$)	Porosity ($\text{m}^3\cdot\text{m}^{-3}$)	SWRC	
				$ h _{\text{A}}$ (m)	α (-)
2	0.50 – 1.00 m	0.27	0.425	0.074	10.168
3	> 1.00 m	0.11			

For the parameterisation, the thickness of the first layer has been fixed at 0.5 m. The second layer also has a maximum thickness of 0.5 m but can be less if limited by the soil

depth. The same applies for the third layer, which is defined by the difference between the joint thickness of the first and second layer and the specified soil depth. In the present case, the soil depth was determined from field observations (Section 5.6). Geostatistical interpolation was not feasible and an attempt was made to obtain representative estimates of soil depth stochastically (Figure 5.21). The estimates are not able to reproduce the mean and variance accurately but reproduce some of the spatial trends that may influence the occurrence of landslides. Since soil depth is a key variable in landslide activity and its contribution to hillslope degradation, a better estimate is required. Notwithstanding, soil depth is often taken as constant and homogeneous and may be considered as one of the principal areas of interest to improve the accuracy of assessments of landslide activity on a regional scale.

The digital elevation model representing the topographical surface has a resolution of 10 x 10 m and has been based on the 1:10,000 topographical map of the area (Section 5.5).

Generally, the slip surfaces of landslides in the field pass through the regolith below the rooted topsoil. Most times, it follows the contact between the unweathered marl and the regolith. Therefore, the potential slip surface of the soil mantle coincides with the lower boundary of the third layer in the model. The geomechanical properties that are used for the parameterisation of the shearing resistance along this lithic contact are presented in Section 5.7. Material was tested under saturated and unsaturated conditions. The best description of the shear strength was given by the adapted Mohr-Coulomb Failure Criterion of Fredlund (1987). A summary is given in Table 5.25. In the stochastic model, only the variability in the shear strength parameters, ϕ' and ϕ^b will be considered (Section 3.3.3). The standard deviation is approximate and based on the error in the slope of the linear regression. The standard deviation of ϕ^b is based on literature values because only a limited number of samples has been analysed. For the entire profile the dry bulk density is kept constant at $14.4 \text{ kN}\cdot\text{m}^{-3}$.

Table 5.25: Shear strength parameters

Shear strength parameter	Average	Standard deviation
Cohesion, c' (kPa)	≈ 0	
Angle of internal friction, ϕ' ($^\circ$)	34.8	4.8
Fredlund's suction friction angle, ϕ^b ($^\circ$)	16.1	5.2

Much effort has been invested into the parameterisation of the model. The capability of the model to simulate the hydrology and the accurately will be investigated in the following chapters. In Chapter 6, the calibration and the validation of the hydrological model component are discussed. Chapter 7 covers the performance of the slope stability model to assess landslide activity from simulated failure.

6 IMPLEMENTATION OF THE HYDROLOGICAL COMPONENT OF THE COUPLED HILLSLOPE MODEL

6.1 Introduction

The coupled hillslope model is intended to quantify the change in sensitivity of the marl slopes to landsliding under present and altered climatic and land use conditions in the Alcoy region. For this purpose, the coupled hillslope model will be implemented for the catchment of the Barranco de la Coloma (Chapter 2). The implementation of the model requires that its performance is optimised and evaluated as an implicit proof of the model validity (Chapter 1). Here, model performance is defined as the accuracy of the model to reproduce the observations from the simulation.

So far, the coupled hillslope model and the parameterisation have been defined without paying attention to the eventual model performance. Consequently, the performance will be impaired by uncertainty as the model contains processes that are insufficiently known or understood. Since an increase of model complexity is not desired, the performance can only be increased by optimisation, i.e. the reduction of the difference between the observed and simulated values to the smallest possible value by parameter adjustment. Ideally, this is achieved by adjusting the parameter within the observed or expected natural limits (calibration). The use of the more influential parameters makes it more likely that the optimum parameter set will comply with the expected limits. Suitable parameters for calibration can be identified through a sensitivity analysis (Section 6.1).

Since the hydrology is assumed to be the primary cause of landslides in the Alcoy region, it is an obvious choice to calibrate the hydrological component of the hillslope model in order to increase its performance. Moreover, hydrological processes can be considered as continuous over time and space. Monitoring of the hydrological field conditions, therefore, provides a possible end to calibrate the hydrological component of the coupled hillslope model even if direct information on the hydrological triggering conditions is absent.

Calibration, however, does not warrant that the optimised model will perform equally well at other places or over different periods. The assumption that the calibrated hydrological model is generally valid and can be extrapolated to simulate the hydrological conditions at the moment of failure must be proven. To this end, the calibrated model is validated against a second set of field observations. Although this provides no exclusive proof of the validity of the model (Konikow & Bredehoeft, 1992; Oreskes *et al.*, 1994), it tests the consistency of the model's performance. Sections 6.2 and 6.3 cover the calibration and validation of the hydrological model component STARWARS.

Validation of the hydrological model is important as, under the hypothetical conditions of climate and land use, the degree of success will inherently be dependent on the general applicability of the optimised model parameters. Therefore, the implementation of the hydrological model component and its applicability under the expected change in the environmental conditions are discussed in Section 6.4.

6.2 Model sensitivity

The sensitivity of the model to changes in the parameterisation can be studied by means of a sensitivity analysis (Kirkby, 1993). In a sensitivity analysis, parameters are varied in consecutive model runs and the model outcome is compared to that for the reference parameterisation. Since most models consist of a succession of physical or empirical relationships, the absolute or relative changes in model outcome are seldom straightforward. So, for clarity, usually only one parameter is perturbed in each run.

From the results of a sensitivity analysis, the most influential parameters can be identified. These factors can consequently be employed to calibrate the model. This is the main purpose of the sensitivity analysis in this study. Since the model performance will be calibrated by means of the simulated hydrology only, the sensitivity of the hydrological model component will be treated in detail.

Alternatively, the results of the sensitivity analysis can be used to induce the effect of environmental change, if the model is considered as a satisfactory replicate of natural behaviour (Boorman & Sefton, 1993).

6.2.1 Method of sensitivity analysis

The sensitivity of the hydrological model component STARWARS to parameter change has been analysed by comparing the simulated hydrology of a 250 m long and 50 m wide slope transect at a resolution of 5 x 5 m. This ideal slope transect has a slope of 12° in the direction of the slope length and drains through the central axis. Starting with the same initial conditions, the response of the volumetric moisture content and of the perched water levels has been modelled over a period of two average hydrological years with 698 mm of rainfall each. For the reference potential evapotranspiration, the average conditions for Almudaina as described in section 5.4 have been used. The potential global radiation has been reduced to account for the effect of cloud cover but no topographical effects on the insolation have been included.

In the sensitivity analysis, only parameters have been considered which do not directly restrict the input of rainfall in the model. So, the modelled hydrological response has been analysed for changes in six parameters, which are listed in Table 6.1, whereas the parameters describing fissure flow, interception and infiltration capacity have been kept at constant values that eliminate the influence of these processes. Furthermore, the model has been simplified by removing the land use dependency of the parameters for the topsoil. Instead, the average value for the entire sample population has been used. The schematisation of the parameters over layers of 0.5 m depth, however, has been maintained for the saturated hydraulic conductivity and the porosity.

The parameter change that has been imposed on the model has been calculated by subtracting or adding 25%, 50% and 100% of the standard deviation to the mean parameter value. If the variability is unknown, an estimate has been used (Table 6.1). For the saturated hydraulic conductivity, this change is based on the log-transformed data. A problem arises for the soil water retention curve (SWRC), which is parameterised by two variables, namely the air entry value h_A and the shape factor α that can not be varied independently. To circumvent this problem, the relative degree of saturation at field

capacity ($|h|= 3.3$ m) and its standard deviation have been used. This value determines the amount of drainable water content and thus provides a single value to relate the SWRC to the redistribution of soil moisture in the model. Thus, the parameters of the SWRC are varied to meet the changed relative degree of saturation at field capacity at the pre-set increments. To this end, the less certain air entry value is changed by the appropriate levels within its 95% confidence interval ($h_A= 0.074 \pm 0.008$ m). These values determine then the shape factor α . Using the total SWRC as the basis of the parameterisation, the perturbed SWRCs fall within the observed range (Section 5.3).

An important parameter is k_r . This is a general parameter that, with the crop factors of Section 5.1.4, reduces the reference potential evapotranspiration to a rate sustained by the vegetation and the available moisture content in the soil, the actual evapotranspiration. In the same manner as the crop factor k_c , it is defined as a fraction of the reference potential evapotranspiration. To distinguish this general reduction from the land use dependent crop factor k_c the subscript r has been used.

The loss of soil moisture to the underlying bedrock is restricted by the unsaturated hydraulic conductivity below the lithic contact (Equation 3.8). This unsaturated hydraulic conductivity is specified by a lower boundary condition, defined as matric suction. The theoretical matric suction at field capacity has here been used as an estimate ($h= 3.3$ m). Its variability is set to 2.0 m, what brings the relative unsaturated hydraulic conductivity, $k_r(h)$, within the range from 10^{-3} to 10^{-5} (-).

Table 6.1: Parameters, mean values and variability for the sensitivity analysis. Italicised values represent estimates. The first two layers are fixed to 0.5 m depth, the lower, third layer depends on the remaining soil depth.

Layer	k_{sat} ($m \cdot d^{-1}$)			n (-)			$\theta_{E \text{ FC}}$ (-)	$ h _{BC}$ (m)	k_r (-)	z (m)
	I	II	III	I	II	III	All	All	All	Total
Mean	1.25	0.27	0.11	0.41	0.43	0.43	0.63	3.30	0.50	1.75
St. Dev.	2.45	3.58	3.42	0.05	0.05	0.05	0.12	2.00	0.25	0.50

- k_{sat} : Saturated hydraulic conductivity
- n: Porosity
- $\theta_{E \text{ FC}}$: SWRC, soil moisture content at field capacity ($|h|= 3.3$ m)
- $|h|_{BC}$: Lower boundary condition, suction of infinite bedrock store
- k_r : Reduction in ET_0
- z: Soil depth

As a general measure of the simulated hydrology, the total drainable storage has been used. This value lumps the active water in the soil over the entire slope. Initially, the storage consists entirely of the moisture stored in the unsaturated zone. As initial settings for all model runs, the average summer profile in volumetric moisture content has been used as measured at different locations in the period 1996 – 1998 (Figure 6.2). The absolute volumetric moisture contents are therefore the same for all model runs. The amount of drainable pore space, however, alters for the runs in which the porosity and the soil depth have been changed. Changes in the soil depth affect the thickness of the lowest layer in the profile and thereby its influence on the initial value of the drainable storage. The total soil depth ranges between 1.25 and 2.25 m, which reflects the depths encountered in the marl slopes of the area. The decision to keep the two upper layers

constant is consistent with the schematisation that was defined in Chapter 5. Changes in porosity affect the drainable pore space directly and result in different initial values as the residual moisture content, taken at 5% of the porosity, varies with it. For the altered porosity, the changes in initial storage are less than 1.2%. For the altered soil depth, the difference between the reference value condition and the cases ± 1 standard deviation is in the order of 33%.

In total, the model has been applied to the 36 variants of the parameterisation and to the average condition as reference. In all but one case, the final storage was below the initial value as the average rainfall could not maintain the high initial moisture contents. This loss is mainly due to evapotranspiration. The loss to the infinite bedrock store is small and the model responds in a normal manner to the winter rainfall surplus. In all runs, perched water tables occurred at some stage during the two model years.

The change in model response has been expressed as the ratio between the initial and the final storage. This removes the inequality between the initial settings and allows a general comparison between the results of the reference parameterisation and the perturbed parameter sets. The different ratios have been normalised by deducting the ratio for the reference parameter set. Hence negative values denote a relatively larger decrease in storage whereas positive values indicate a relative increase in storage. The reference case represents a decrease of 28% over the two model-years.

6.2.2 *Parameter sensitivity*

In Figure 6.1, the normalised changes in modelled storage are given for the respective parameter increments. In terms of total storage, the hydrological model is the most sensitive to the reduction of the reference potential evapotranspiration, k_r . A change by 25% in k_r results in a deviation of 11% in the final storage. The changes in k_r produce proportional changes in the final storage except for the largest reductions, which result in relatively smaller deviations (Figure 6.1). The storage increases with decreasing evapotranspiration but more water is consecutively lost to outflow over the saturated zone. This also affects the hydrological response as it will take more time to drain the saturated zone. For decreased values of k_r , the mean change over time is between 5 and 7% when expressed relative to the reference condition. This value is not related to the change in final storage, indicating that the additional storage is contained by the saturated zone and lost entirely once the rainfall stops. In contrast, the mean change over time is proportional to the change in final storage for increased values of k_r . This implies that, relative to the final storage of each run, the simulated response remains similar.

Porosity is the parameter with the second largest influence. The deviations in final storage are more or less identical to the relative changes in the parameter value. Over time, the average deviation in storage is identical to that for the final storage. Apparently altering the effective degree of saturation through the porosity has the effect that the soil moisture percolates at a different but relatively constant rate, as is to be expected.

The relation of the porosity with the SWRC and its role in the attenuation or accentuation of the saturated conditions along the lithic contact explain its importance. In the sensitivity analysis, the other parameters have less influence and behave in a less orderly manner. The deviations in final total storage are less than 5%. Among these parameters,

the SWRC has the highest influence. The final total storage is lower when the field capacity, as described by the SWRC, is increased. More water is retained by the top layer in the model that is not transferred to the deeper layers but, instead, is lost to evapotranspiration. The deviations due to variations in the saturated hydraulic conductivity are in the same range but negative under all circumstances. This is caused by the rapid drainage of water, both saturated and unsaturated, when the k_{sat} is increased. When reduced, the larger loss is the result of the higher rate of evapotranspiration.

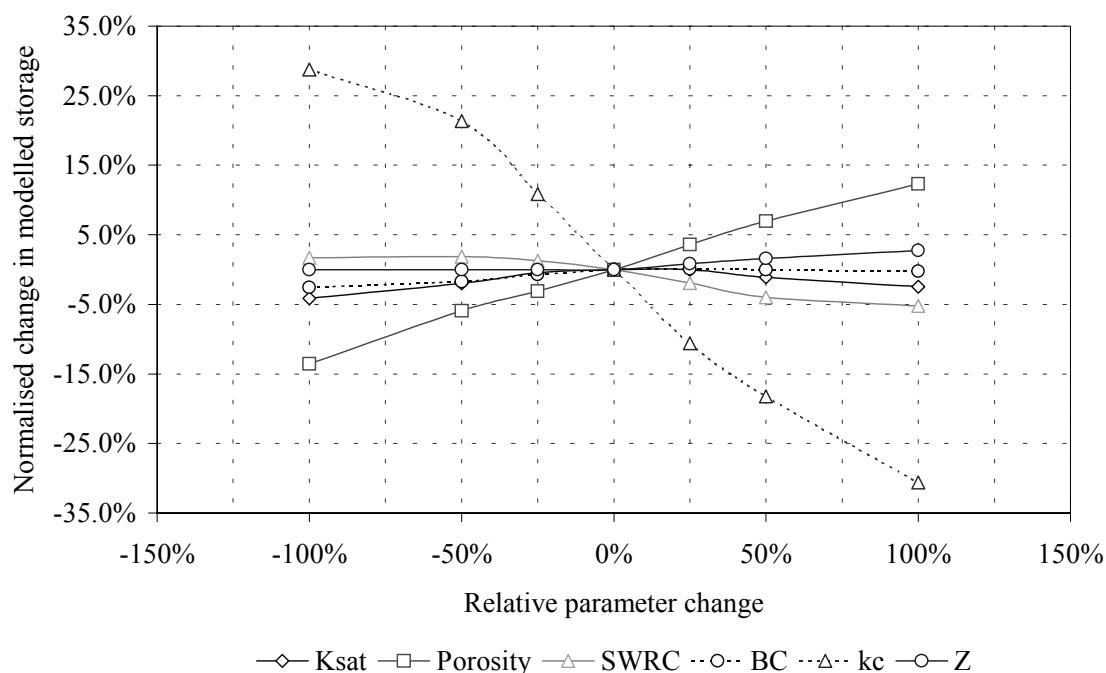


Figure 6.1: Sensitivity of the simulated hydrology, expressed as the change in total storage, to changes in six model parameters (see Table 6.1 for abbreviations)

Over the interval analysed, the influence of changes in the boundary condition is small as the resulting loss over the lithic contact is either small or very small. Yet, the parameter is of importance for it prevents the formation of saturated conditions over the lithic contact for the run with the lowest suction ($|h|_{BC} = 1.30$ m) while they occur in most other runs. The model is insensitive to changes in the soil depth for they affect the processes in the lowest and less responsive layer. Only for the largest soil depth in the analysis (2.25 m), the final total storage increases for less water is transported by saturated lateral flow through this relatively impermeable layer.

The sensitivity analysis indicates that the porosity and the reduction of the potential evapotranspiration, ET_0 , k_r , are the more suitable parameters for calibration. Changes in both parameters lead to more or less proportional differences in the modelled hydrology. As a calibration parameter, however, the porosity suffers from the small range over which this parameter may be expected to vary in reality. Since the model is more sensitive to the changes in the parameter k_t , this parameter gives an option to calibrate the

model by making only minor adjustments. This is important as the possible changes in this parameter are restricted; although the soil moisture deficit may vary over time, the evapotranspiration can not exceed the available rainfall over longer periods without changes in the vegetation type or density.

An additional complication is that changes in the k_r alter the response of the model to the available rainfall. With a decrease of the relative degree of saturation, the redistribution of soil moisture and hence the generation of perched water tables are attenuated. In contrast, increases in the relative degree of saturation lead to a more rapid response. This is demonstrated by the deflection of the modelled response of Figure 6.1 when the reduction in k_r is very large. Thus, if all other factors remain equal, the analysis indicates that the simulated hydrological behaviour is the most sensitive to changes in the evapotranspiration. This implies that changes in the actual evapotranspiration, whether these are the result of an absolute increase of the reference potential evapotranspiration under a warmer future climate or a relative change under different land use conditions, will have a large impact on landslide activity.

6.3 Calibration of the hydrological model component STARWARS

On the temporal scale considered in this study, pore pressure is regarded as the dominant trigger of landslides. Thus, calibration of the simulated hydrology could enhance the performance of the coupled hillslope model. This postulates that the calibrated model is expected to have predictive power for the unknown hydrological conditions under which landslides are triggered. This requires that the physically based model describes the relevant processes and that these processes are continuous in time and space.

Calibration involves the adaptation of the model parameters in order to reduce the discrepancy between the observed and simulated hydrological response. The success of the calibration will depend on the uncertainty in the model parameters and the simplification of the natural system. The uncertainty that is associated with the model parameters includes natural variability and sampling errors. In addition to these sources of error, the simplification introduces an unknown amount of ignorance (Casti, 1990). In most cases, the two sources of uncertainty can not be distinguished in the process of calibration. The plausibility of the solution can only be indirectly proven by validating the simulation with observed behaviour at locations or periods that have not been included in the calibration process (see Section 6.3). The robustness of a physically based model generally increases when the number of parameters is restricted (Hillel, 1986). Although the success of the calibration will increase if more parameters are released for optimisation, this increases the likelihood of encountering non-unique solutions (Refsgaard, 1997). Non-unique parameter sets have an equal predictive power but some are not robust and the parameter values may fall outside the natural limits. The use of the most influential parameters increases the likelihood that the optimised parameter set falls within the expected range whilst the risk of encountering non-unique solutions decreases. Suitable parameters for calibration have been identified through a sensitivity analysis (Section 6.1). The subsequent set of optimised parameters will lump all the uncertainty whether it stems from ignorance or variability at the process- and model-scale.

The parameters included in the calibration are the matric suction of the infinite bedrock store that underlies the soil mantle and a factor that reduces the potential evapotranspiration to a level sustained by the actual rainfall.

The matric suction defines the loss over the lithic contact and thus the response of the perched water table to the percolation from above. The actual loss varies with the height of the perched water table (Equation 3.8) or with the percolation from the lowest model layer. In the latter case, the loss can not exceed the maximum imposed by this lower boundary condition. Although the sensitivity analysis showed that this parameter has only a limited influence on the model outcome, it has been included in the calibration for a good reason. The loss to bedrock, which is relatively unknown, may be of limited importance on a day-by-day scale, the accumulated error may be substantial if the hydrology is simulated over longer periods as is required for this study.

In the study area, the average annual rainfall is only a third of the potential evapotranspiration. The actual evapotranspiration, therefore, must be reduced to a level that can be sustained by the rainfall over a prolonged period without harming the present vegetation cover. This reduction has the highest influence on the model outcome as it directly affects its amount of storage and the rate of percolation. Its selection as a calibration factor is, therefore, evident.

After the deduction of any available surface detention, the reduction of the reference potential evapotranspiration to the actual evapotranspiration comprises two steps. The first involves the multiplication by the crop factors as specified in Section 6.1.3. These crop factors incorporate the transpiration by vegetation under optimal soil moisture and nutrient conditions for an area that represents the entire plant community at a given stage in its development. The actual evapotranspiration is further limited by the availability of water in the soil mantle. This reduction is linearly dependent on the depth of the water table, if present, and the available soil moisture (Equation 3.14). This reduction is multiplied by an absolute fraction that limits the evapotranspiration loss to levels that are sustained by the precipitation in the long run and that is determined from the calibration. This absolute reduction in the evapotranspiration by which the model performance is optimised can be interpreted as a general measure of the rate of evapotranspiration through the topsoil. In its value, it combines some of the unexplained variance that arises from sub-grid surface conditions as vegetation density and sealing.

In the calibration, the reductions in the evapotranspiration as the matric suction of the infinite bedrock store are treated as constant over time and space. This is probable the case for the entire store of marl of which the conditions do not change for the temporal scale under consideration. It is more questionable whether these assumptions hold for the reduction in the evapotranspiration. It postulates that the calibrated parameter value represents a long-term average. It is doubtful whether the parameter is spatially constant at all. This means that local variation is lumped into a general value that has limited predictive power for specific locations. However, information to incorporate this local detail is absent and it could be too finely grained to be incorporated at the present model scale. Thus, the calibrated model will represent an average solution. It will approximate the local field evidence only if the local, actual evapotranspiration is proportional to the imposed general reduction of the reference potential evapotranspiration.

Because of the many calculations needed, calibration of a distributed hydrological model is time-consuming. The repeated simulation is unwieldy if it has to be performed by hand. Automated processing may help to facilitate the calculation and to obtain a more objective result but even then limitations must be imposed to reduce the calculation time to feasible dimensions. To this end, the calibration of the model has been confined to a small sub-catchment, named *the Hollow* (see Appendix 1), for which data on the perched groundwater levels and the soil moisture conditions are available over the years 1997 and 1998 from automated sampling. Additional information from this and other locations has been kept in reserve to validate the model performance.

The choice for this limited area is not only dictated by the resolution of the available data. It is also inspired by the notion that the effects of model changes are more predictable for a smaller sized catchment. Thus, the likelihood of non-unique or oscillating solutions would be reduced.

For the calibration, the hydrological model component STARWARS has been applied to *the Hollow* with the parameterisation as specified in Chapter 5. The spatial resolution of the model was 10 x 10 m. The actual area under consideration has been kept larger than the topographical watershed since the routing of the saturated lateral flow is variable. The model input had a temporal resolution of days but in the calculation the data have been split in half to prevent numerical instability.

The period over which the model performance is optimised stretches over the years 1997 and 1998. The model, however, requires initial conditions that are equally important for its performance. Hence, the period over which the hydrology is simulated must be longer in order to warm up the model. This period should be as long as possible but this contradicts the need of calculation expediency as the entire period must be recalculated in the next iteration of the optimisation process. Because of the soil moisture deficit during summer, the model performance is not seriously hampered if an average profile of volumetric moisture contents is imposed, as long as there is sufficient time between the initial model year and the period of interest to eradicate the introduced error and to lighten the local differences that govern the response of the distributed hydrological model. Under these considerations, the average summer soil moisture profile as measured by TDR or time domain reflectometry (Topp *et al.*, 1980; Heimovaara, 1993) has been used. By TDR, the volumetric moisture content (VMC) has been measured at 12 locations throughout the Barranco de la Coloma at various moments in the years 1996 – 1998. This information has been used to provide the initial conditions at 0.5, 1.0 and 1.5 m depth (respectively VMC= 0.21, 0.24 and 0.28 ($\text{m}^3 \cdot \text{m}^{-3}$); see Appendix 1 for locations). Under such average conditions, the initial values of the perched water table and the surface detention are set to zero. Subsequently, the model has been run for five consecutive hydrological years from the 1st of September 1991 onwards. This period is long enough to neutralise the influence of the initial conditions, especially since the period starts with relatively wet conditions that are followed by a period with below-average rainfall (1993 – 1995 with 1580 mm in total). So, a total of eight hydrological years is simulated of which only the last three are considered in the optimisation. For the entire period, the daily rainfall as recorded at the station of Almudaina has been used (Section 4.2). The reference potential evapotranspiration has been calculated from the daily data from the meteorological data at Cocentina for the years 1991 – 1995 and from the meteorological station in the study area for the years 1996 – 1998.

The field evidence against which the model is calibrated stems from two locations. At these locations, *theta-probes* had been installed (Delta-T Devices, 1995). The theta-probes operate according to a principle similar to TDR except that a signal of a known frequency is used (frequency domain reflectometry or FDR). These probes monitor the volumetric moisture content continuously over time. One location, FDR-1, is located on a south exposed slope whilst the other, FDR-2, is placed at the bottom of the valley floor (Appendix 1). Both have four probes installed at 10, 25, 50 and 70 cm depth. These values have been averaged proportionally to obtain the volumetric moisture content for the layer between 0.0 and 0.5 m and the one between 0.5 and 1.0 m. The perched water table is measured in two separate piezometer tubes at virtually the same location as FDR-2. Both piezometers have a vented electronic Druck pressure gage installed in them. Their depths are 2.62 and 1.58 m respectively. The deeper piezometer has been installed with great effort and reaches partly into the sound marl bedrock. The shallower one is installed in the colluvial soil and rests on the contact with the bedrock. Both piezometers show the same response which indicates that the deeper one is filled from the perched water table that develops over the lithic contact. For this reason, the existence of perched water levels is only included if the pressure gauge in the shallower piezometer records a water height of more than 0.02 m. If both piezometers exceed this level, the values are averaged. To avoid duplication in the observations, the VMCs of location FDR-2 are excluded whenever the observed or averaged water height exceeds the lower boundary of a model layer. To avoid inconsistencies as a result of the differences in soil depth and water height, the comparison between the simulated and observed perched water levels is made with reference to the topographical surface, i.e. as a water depth. At location FDR-1, no information is duplicated and all available data are used. The total dataset of field evidence includes 2287 observations of 12-hour averages that are based on the original measurements that had been sampled at intervals between 10 and 60 minutes. Because of the exclusion of data and the malfunctioning of the equipment between 25% and 40% of the data are available (Table 6.2). For the calibration, the field evidence is represented at a resolution of 0.01 m for the perched water levels and of 0.01 (m³·m⁻³) for the VMC.

Table 6.2: Available field evidence for calibration over the calendar years 1997 and 1998

Variable	Perched water level (m -ref.)	Volumetric moisture content (m ³ ·m ⁻³)			
		FDR-1	FDR-1	FDR-2	FDR-2
Location	Piezo	FDR-1	FDR-1	FDR-2	FDR-2
	FDR-2	0.0 – 0.5 m	0.5 – 1.0 m	0.0 – 0.5 m	0.5 – 1.0 m
Data availability (%)	27%	39%	39%	35%	25%

For the actual calibration, the program PEST has been used (Watermark Computing, 1994). This program is capable of optimising all models of which the in- and output can be read and written in ASCII. It uses a finite difference method to calculate the partial derivatives of the model output over the calibration parameters and adapts the parameters consequently with the aim to minimise the objective function, Φ , by means of the Marquardt theorem. The objective function is defined as the squared sum of the deviations between the generated model output and the actual observations, i.e.

$$\Phi = \sum w_i (b_o - \beta_o)^2, \quad (6.1)$$

where b and β stand for the generated and actual value for observation o . If the square root of the objective function divided by the total number of observation were taken, one obtains the root mean squared error (RMSE) as defined before. In Equation 6.1, the squared residual is multiplied by a weighing factor, w_i . This weighing factor can be specified for each variable i considered in the optimisation. These weighing factors can balance the objective functions whenever the resolution of the considered variables is very different or if one of them is deemed more reliable or more important than the others. For the calibration of the hydrological model component no weighing factor has been specified. Yet, the perched water level varies by 0.01 over 1.58 m whereas the soil moisture content varies by 0.01 over a smaller range to an approximate maximum of $0.45 \text{ m}^3 \cdot \text{m}^{-3}$. This suggests that absolute deviations in the moisture content should be given a larger relative weight. Since this is omitted, the perched water level is given a decisive influence on the calibration process. This decision is based on the notion that the perched water level is the most important trigger of landsliding.

PEST's optimisation process applies a finite difference solution and requires that the settings for the calculation of the derivatives and the termination criteria are specified for the particular problem. The calculation of the derivatives directs the model by the Marquardt theorem towards optimisation. The termination criteria provide the limits to stop the optimisation process whenever the model is apparently incapable of reducing the objective function over several iterations. If this meets a pre-set value for the change in the objective function Φ , in this case 0.01, the model can be considered to have converged to an acceptable solution that provides the optimal parameter set. If this criterion is not met over a specified number of iterations, optimisation is considered to be unattainable. In such a case, the optimal value for a calibration parameter lies outside the expected natural range or the derivatives are badly defined and the optimal values are not approximated. This last problem can be solved by changing the settings for the calculation of the derivatives or, equally important, by defining initial parameter estimates that lie close to the optimal values. Both problems in the optimisation, however, stress the importance of reliable estimates on the parameter values and their variability. For the calibration of the hydrological model component, the initial value for the matric suction under the lithic contact was estimated from the average volumetric moisture content at the 12 TDR-locations at 1.5 m depth. This value shows little seasonal variation compared to the topsoil (Figure 6.2). Hence, it has been taken as an approximation of the conditions deeper in the marl bedrock. At 1.5 m, the average VMC was $0.31 \text{ (m}^3 \cdot \text{m}^{-3})$ what corresponds with a matric suction of 1.26 m. The observed range from 0.27 and $0.38 \text{ (m}^3 \cdot \text{m}^{-3})$ corresponds to a variation in matric suction between 0.25 and 3.77 m. For the calibration, the interval of tolerated values was relaxed to a range from 0.1 to 25 m of matric suction.

For the reduction in reference potential evapotranspiration, no data are available, except the prior knowledge that the long-term average of the product between crop factors and the reduction factor must be in the order of one third. The initial value has been set to 0.5 (-) and the tolerated range of values to between 0.01 and 0.99 (-).

The model converged to a minimal objective function of 21.32 (see Equation 6.1). The agreement between the observations, i.e. the field evidence, and the simulated hydrology is represented graphically in Figure 6.3. For the individual observations, the results are summarised in Table 6.3. Overall, the simulated hydrology agrees well with the observations although the simulated VMC of the second layer underestimates the observed values. Apparently, more water is lost to evapotranspiration from this layer during the dryer periods in the simulation. Compared to the RMSE for the FDR readings, the larger discrepancy between the simulated and observed groundwater level can be explained by the larger absolute errors and the cumulative effect of upstream errors (Table 6.3).

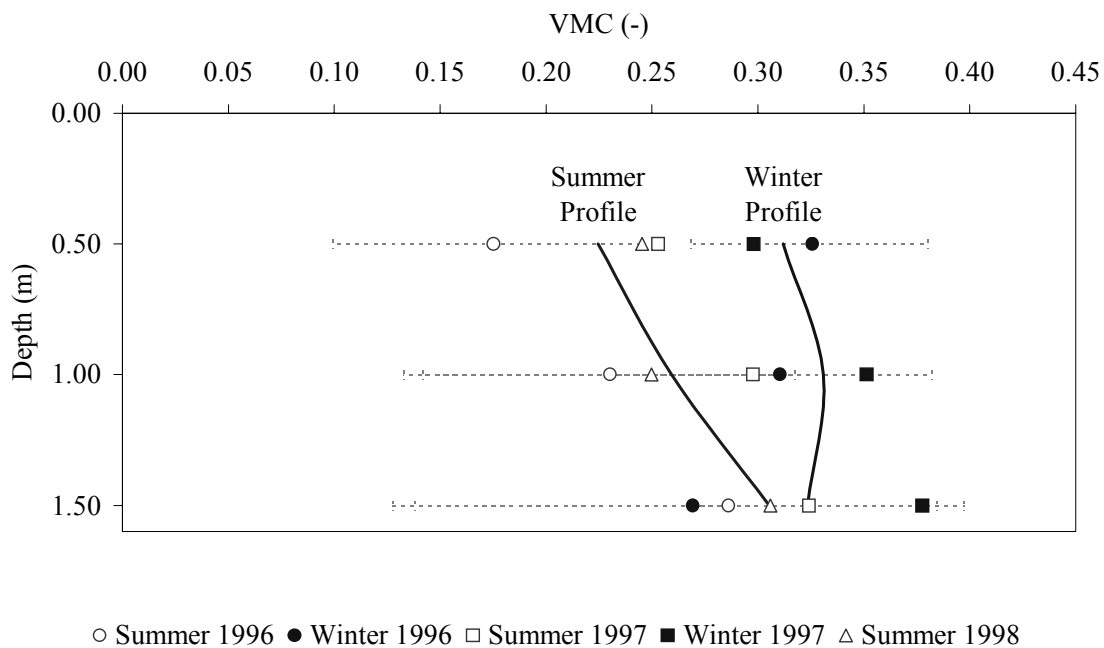


Figure 6.2: Seasonal fluctuation in VMC based on TDR-measurements

Table 6.3: Calibration statistics over the period 1997 – 1998. Simulated values have been regressed on the observations with intercept Y_0 , slope α , and explained variance R^2 . Units vary with the respective variables

	GWL (m)	FDR – 1 ($m^3 \cdot m^{-3}$)		FDR – 2 ($m^3 \cdot m^{-3}$)	
		0.5 m	1.0 m	0.5 m	1.0 m
Φ	13.91	1.35	2.37	1.44	2.77
RMSE	0.189	0.049	0.065	0.053	0.086
α (-)	0.94	1.62	1.13	1.30	1.42
Y_0	-0.02	-0.11	-0.10	-0.11	-0.22
R^2 (-)	0.84	0.92	0.67	0.84	0.71

The optimal values for the calibration parameters are given in Table 6.4. The confidence levels are small and fit well with the expected values. The lower boundary condition of a

general and constant matrix suction of 2.13 m corresponds with a VMC of 0.29 ($\text{m}^3 \cdot \text{m}^{-3}$) (all other parameters except the evapotranspiration reduction factor remaining fixed to the values specified in Chapter 5). This suction is higher than the initial value of 1.26 m that still varied seasonally. Thus, the water loss to the underlying bedrock is less than originally estimated.

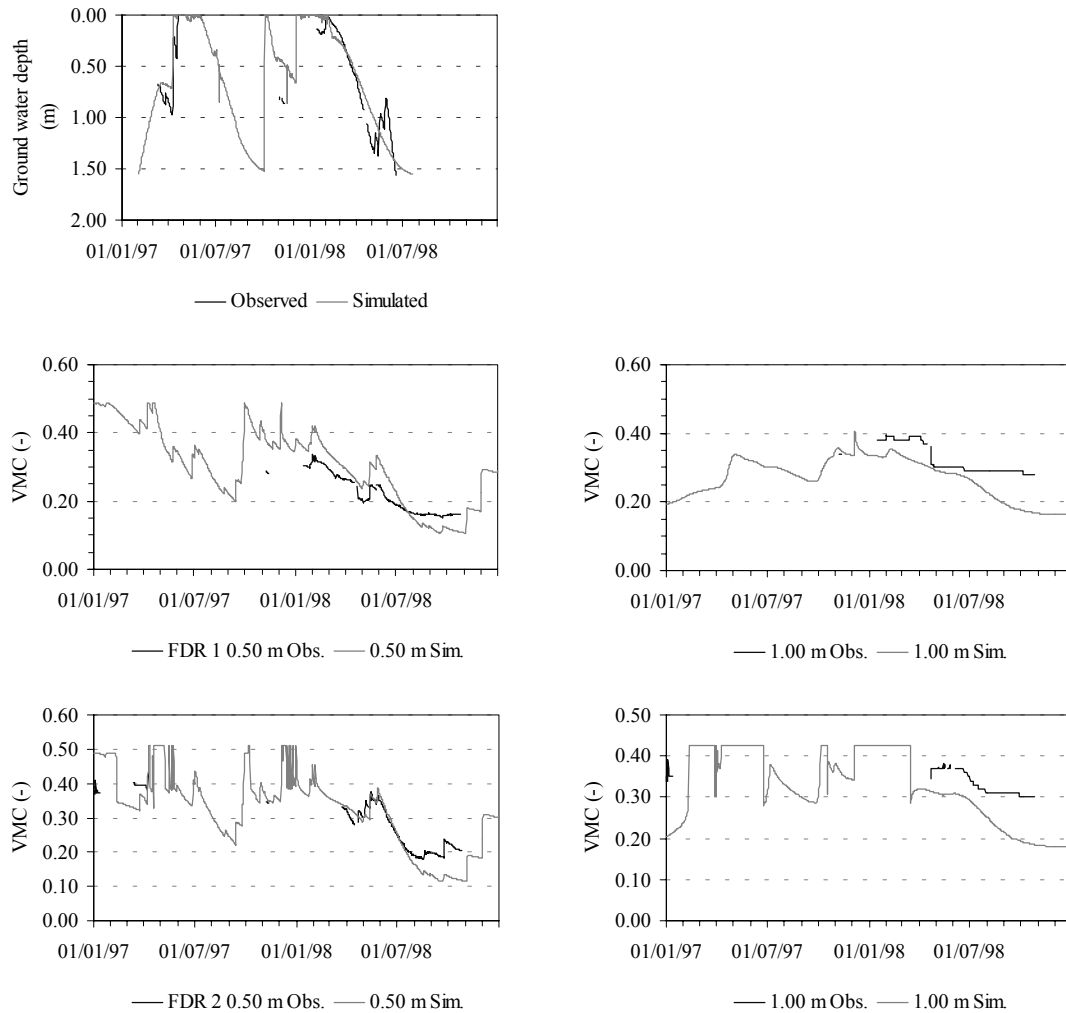


Figure 6.3: Calibration results: Observed and simulated perched water levels and volumetric moisture contents at the Hollow 1997 – 1998

Table 6.4: Optimised parameter values and approximate 95% confidence limits

Parameter	Optimal value	Lower 95%	Upper 95%
$ h _{BC}$ (m)	2.126	2.117	2.135
Reduction ET_0 (-)	0.4589	0.4585	0.4593

The optimal value of the evapotranspiration reduction is 0.459. Multiplied with the crop factors of the various land use units, this reduces the actual evapotranspiration to a range

between 0.32 and 0.37 (-) of the reference potential evapotranspiration, what corresponds with the expected actual evapotranspiration loss of one third of the reference potential evapotranspiration.

6.4 Validation of the hydrological model component STARWARS

Even if the model has been calibrated successfully, it remains questionable whether it can be generalised over a larger area or a longer period. This question pertains in particular to the simulation of rainfall-induced landslides in a Mediterranean environment. The actual triggering occurs under extreme meteorological conditions and affects only few locations with varying antecedent soil moisture conditions. Thus, the field data against which the model is calibrated are unlikely to cover any triggering rainfall event, as is the case in this study. The question whether the model is generally applicable can be partly answered by trying the spatial representativeness of the calibrated model. Although this provides no proof of the validity of the model, it gives an assessment of the consistency in the success to simulate the hydrology under different conditions. Notwithstanding, the performance of the coupled hillslope model to predict landslides should be analysed as well and this is treated in detail in the next chapter (Chapter 7).

For the calibration, the model was run repeatedly for a small area over a period of eight hydrological years in order to reduce the calculation load in the optimisation process. In contrast, the validation of the model has been based on a single run for the entire study area of the Barranco de la Coloma over a period of 27 consecutive hydrological years. There are three interrelated reasons for simulating the hydrology and the resultant landslide activity over such a long period. Firstly, it offers a possibility to compare the simulated with the observed landslide activity as addressed in the next chapter. Secondly, the period includes more extreme weather conditions, such as high-intensity rainfall or prolonged droughts, which put the consistent behaviour of the hydrological model to the test. Thirdly, it offers an indirect manner to validate the simulated landslide occurrence of the scenarios. In the synthetic precipitation series, the decreased variability could influence both the reaction time and the magnitude of landslide events. The comparison of the validated model with the scenario results under the present climate and the present land use conditions will reveal how the reduced variability of the synthetic precipitation affects the simulated landslide occurrence.

The period covered by the validation run spans the period 1971 – 1998 for which continuous rainfall data are available. At the beginning of this period, the abandonment of the marginal fields along the barranco was more or less complete and the static situation as mapped in 1998 has been used throughout. The grid size and the timestep of the validation run have been kept identical to those for the calibration, respectively 10x10 m and 12 hours. Because of the larger upstream area and the larger amounts of accumulated rainfall over the 27-year period, rainfall excess and exfiltration occur. Since the coarse timesteps of the models inhibit the realistic simulation of surface run off, all excess surface water is removed once it enters the streambed of the barranco. Subsequently, this excess water has no influence on the hillslope hydrology.

For the validation of the hydrological model component, the same readings of the volumetric moisture content and the ground water levels have been used. For the validation of the model, these readings have been complemented by hand-read observations from the TDR-sensors, open standpipe piezometers and automated recordings of pore pressures. Although the hand-read observations are infrequent and sparse, they have been made at various locations that represent different environmental conditions.

In the calibration measured, but spatially constant VMCs have been used as initial conditions for each run. In contrast, spatially varying steady state conditions have been used as the initial setting for the validation. These conditions have been obtained from a 20-year long run with average weather series. In the validation, these imposed conditions are modified by the nearly 25 years that precede the period for which the measurements of groundwater levels and moisture contents are available. As a result, the simulated hydrology in the validation run will be different from that from the calibration. In addition to the mismatch stemming from the spatial variability, the deviation between the simulated hydrology and the field evidence accumulates all the errors over time. Therefore, the validation tests the combined effects of spatial differences and the consistent behaviour of the model over a timespan that is comparable to the intended length of its application.

Table 6.5: RMSE between the observed and simulated groundwater depth and the VMC at the Hollow for the calibration and validation runs. RMSE is in m for the groundwater depth, in $\text{m}^3\cdot\text{m}^{-3}$ for the VMC.

	GWL	FDR 1		FDR 2	
		0.5 m	1.0 m	0.5 m	1.0 m
Calibration	0.189	0.049	0.065	0.053	0.086
Validation	0.847	0.049	0.069	0.056	0.115

Table 6.6: RMSE and correlation coefficient for the perched water levels measured in the Hollow. Original data give the results of the original validation run, translated values give the enhanced performance with the corresponding time lag

Piezometer	Original validation data		Translated data		
	Correlation, ρ (-)	RMSE (m)	Time lag (days)	Correlation, ρ (-)	RMSE (m)
A+B	0.40	0.53	-33	0.53	0.39
C	0.70	0.76	-44	0.40	0.60
D	0.02	0.59	-85	0.64	0.45
E	0.78	0.76	-81	0.56	0.57
F	0.74	0.85	-75	0.09	0.64
G	0.76	0.72	-37	0.73	0.67

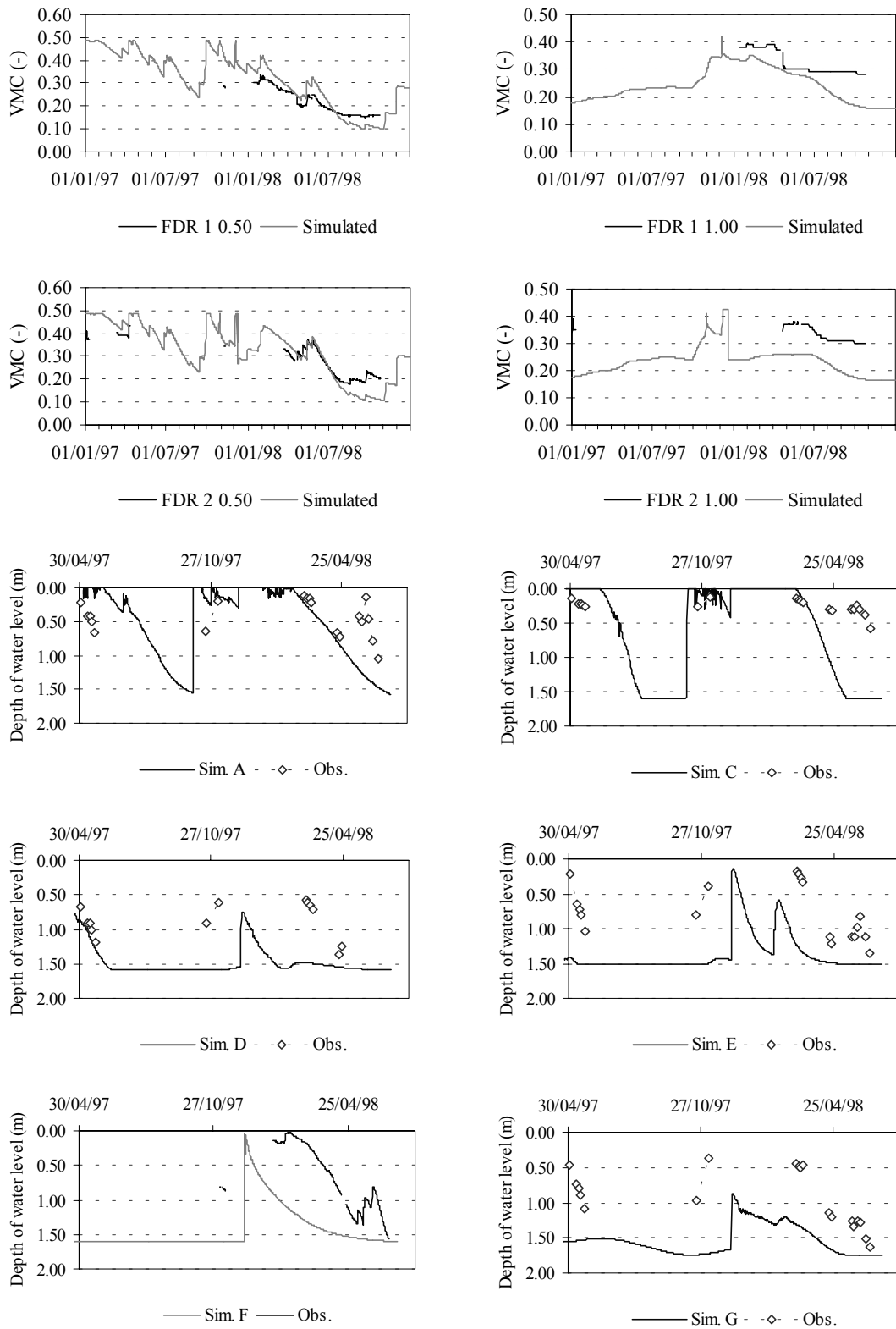


Figure 6.4: Validation results: Observed and simulated perched water levels and volumetric moisture contents at the Hollow 1997 – 1998

Table 6.7: Statistics for the validation of the VMC for 12 locations with TDR-probes installed at 0.50, 1.00 and 1.50 m. Simulated values have been regressed on the observations with intercept Y_0 , set to 0.

Location	Depth (m)	ρ (-)	α , $Y_0=0$	RMSE (-)	N
1.01	0.5	0.886	1.437	0.14	20
	1.0	-0.120	0.657	0.12	20
	1.5	-0.386	0.584	0.12	20
1.02	0.5	0.311	1.655	0.19	20
	1.0	0.316	0.718	0.09	20
	1.5	0.140	0.499	0.16	20
1.03	0.5	0.456	1.445	0.14	19
	1.0	0.005	0.824	0.09	20
	1.5	0.163	0.862	0.09	20
1.04	0.5	0.669	1.424	0.14	20
	1.0	-0.216	0.664	0.13	20
	1.5	-0.784	0.497	0.17	20
2.05	0.5	0.598	1.331	0.12	19
	1.0	-0.062	0.736	0.11	19
	1.5	0.293	0.756	0.09	19
2.06	0.5	0.706	1.157	0.07	18
	1.0	0.327	0.899	0.05	18
	1.5	0.169	0.839	0.08	18
2.07	0.5	0.492	1.324	0.11	18
	1.0	0.252	0.978	0.04	18
	1.5	0.699	0.890	0.05	18
3.08	0.5	0.755	1.293	0.10	19
	1.0	No data			
	1.5	0.240	0.755	0.11	19
3.09	0.5	0.794	1.241	0.08	19
	1.0	0.018	0.962	0.05	19
	1.5	0.568	0.991	0.04	19
3.10	0.5	0.605	1.520	0.14	19
	1.0	0.828	1.197	0.06	19
	1.5	No data			
3.11	0.5	0.719	1.485	0.14	19
	1.0	0.629	1.247	0.08	19
	1.5	0.832	1.446	0.12	19
3.12	0.5	0.863	1.520	0.13	19
	1.0	0.395	1.273	0.08	19
	1.5	0.770	1.110	0.05	16

When the simulated hydrology from the validation run is related to the field evidence originally used in the calibration of the model, the poorer performance of the model to simulate perched groundwater levels becomes apparent (Figure 6.4 & Table 6.5). In this graph, the simulated and observed perched water levels are given for six open standpipe piezometers along the axis of the Hollow (see Appendix 1; labelled A-G in upslope direction). This includes the automated site, F, used in the calibration. At this location, the simulated perched water level responds late and enters the falling limb too soon in comparison with the observed water level. Despite the maximum is simulated in accordance to the observed water level, there is an offset between the simulated and the

observed peak. A similar displacement in time is witnessed by all hand-read open stand-tube piezometers and is in the order of one to three months (Figure 6.4). Nearly all are successful in simulating the observed levels, yet fail to reproduce the exact timing. The RMSE can be reduced by translating the simulated water levels forward in time, although this does not necessarily increase the correlation coefficient (Table 6.6). This is partly due to the observed secondary peaks that are absent in the simulation. Compared to the calibration, the RMSE for the groundwater level increases four-fold in the validation (Table 6.5). In contrast, the volumetric moisture content is simulated more adequately. The RMSE is just above the values obtained after calibration. The poorest performance is obtained by the second layer of location 2, which starts at a lower VMC than observed and does not recover to the observed levels during the measurement period.

Hand-held TDR-readings, taken at 12 locations on marl slopes with different vegetation types, confirm these observations. For each location, about 20 readings at three depths – 50, 100 and 150 cm- are available over the period 1996 – 1998. In general, the RMSE is of the same order as that at the calibration locations (Table 6.7). However, larger deviations are found at the more insulated locations (e.g. locations 1.01 and 1.04). At these locations, the simulated VMC of the top layer overestimates the actual values whereas for the deeper layers the simulated VMCs fail to reach the observed VMCs. A probable source of error explaining this failure lies in the invariant reduction of the reference potential evapotranspiration as determined from the calibration. For the exposed slopes, the excessive loss to evapotranspiration reduces the moisture content over the entire profile after periods of prolonged droughts like that over 1993 – 1995 preceding the measurement period. As a consequence, the unsaturated hydraulic conductivity drops and insufficient moisture percolates from the topsoil into the deeper regolith during the following wetter periods. The single value for the topsoil porosity of each land use class aggravates this problem. Since these values are higher than the maximum VMC of the matrix as measured by the FDR- and TDR-probes, the calibration process leads to an artificially higher loss of water from the topsoil in order to reduce the mismatch between the observed and the simulated VMC. In reality, the exposed locations may support a sparser vegetation cover with limited water demands. In addition, shrinkage cracks may develop in the soil that offer a direct pathway for the rainfall into the deeper parts of the soil that bypasses the slower matric percolation after periods of prolonged drought. Other macropore networks that become operable when free-draining water is available may explain some of the secondary peaks in the observed ground water levels. The model offers the possibility to include this by-pass flow in the simulation. However, in this case it was opted against its inclusion as it would increase the number of parameters to be optimised. Moreover, the influence of the macropore network could be time-dependent what without *a priori* knowledge seriously reduces its usefulness as an optimisation parameter. Although the use of a high total porosity for the topsoil is not an ideal solution, it is the best in terms of model simplicity and functionality. Despite this simplification of the hydrological processes in the topsoil, the model performs acceptably well for most conditions. The fact that the lag between the observed and simulated VMC is small for either the TDR-readings and the FDR-observations used in the calibration substantiates this claim (Figure 6.4).

Table 6.8: Observations and simulated values of groundwater levels at the LGM-site. Absolute depth to groundwater from the topographical surface and the relative saturation of the soil mantle are given. Note the difference in the real and simulated soil depth. Correlation coefficients refer to the agreement between simulated and observed values for the groundwater depth

ID	Depth (m)	Min. GW depth (m)	Saturation (%)	Correlation, ρ (-)
<i>Toe</i>				
1.O	4.38	1.60	63	0.03
2.O	3.70	2.45	34	0.56
Simulated	1.87	0.27	86	
<i>Uphill</i>				
1.B	4.42	1.77	60	-0.02
2.B	4.30	1.32	69	-0.05
Simulated	1.64	0.39	76	

In the simulated perched water levels, these local errors are added to those stemming from biased estimates of soil depth and incorrect values for the upstream area and local slope angle. Although the routing of the lateral saturated flow is not confined to fixed topographical paths, the combined effect of these errors in the hillslope geometry affects the simulated groundwater levels regardless. This is clearly the case for the piezometers F and G in Figure 6.4, which are located in the upper part of the Hollow. Hence, they are only connected to short lengths of steep slope and suffer from the lower amount of water that is transferred along the axis of this sub-catchment in comparison to the calibration run. The effect of the soil depth on the simulated hydrological response is also illustrated by the readings of four closed-type piezometers near the interception plot (LGM-site; see Appendix 1). They had been installed, all spaced some 30 m apart, on a marl slope underneath the scree cover. Two were located at the bottom, above the streambed of the barranco, and two halfway the hillslope. By means of these piezometers, the pore pressures at this location have been recorded automatically once every hour. 78% of the data have been recovered over the period between December 1995 and March 1999. For this period, the observations are summarised in Table 6.8.

The piezometers were based on the sound marl bedrock. A layer of colluvial soil and weathered marl covers the bedrock and has a thickness between 3.7 and 4.4 meter. This agrees with the geo-resistivity measurements at the site which indicate an average depth of 3.5 m. In the parameterisation of the model, however, the estimated soil depth is shallower. The section of the slope draining into these piezometers was given soil depths within the range from 1.8 to 2.5 m. As a consequence, the simulated perched water levels fail to achieve the observed peaks in absolute terms. Relatively, the agreement is better and the timing between the simulated and the observed peaks is reasonable (Figure 6.5). Although the simulation will, therefore, not reproduce the actual critical groundwater levels over the validation period, the relative agreement can still simulate landslide occurrence as a result of the local susceptibility to slope failure (see Section 7.3).

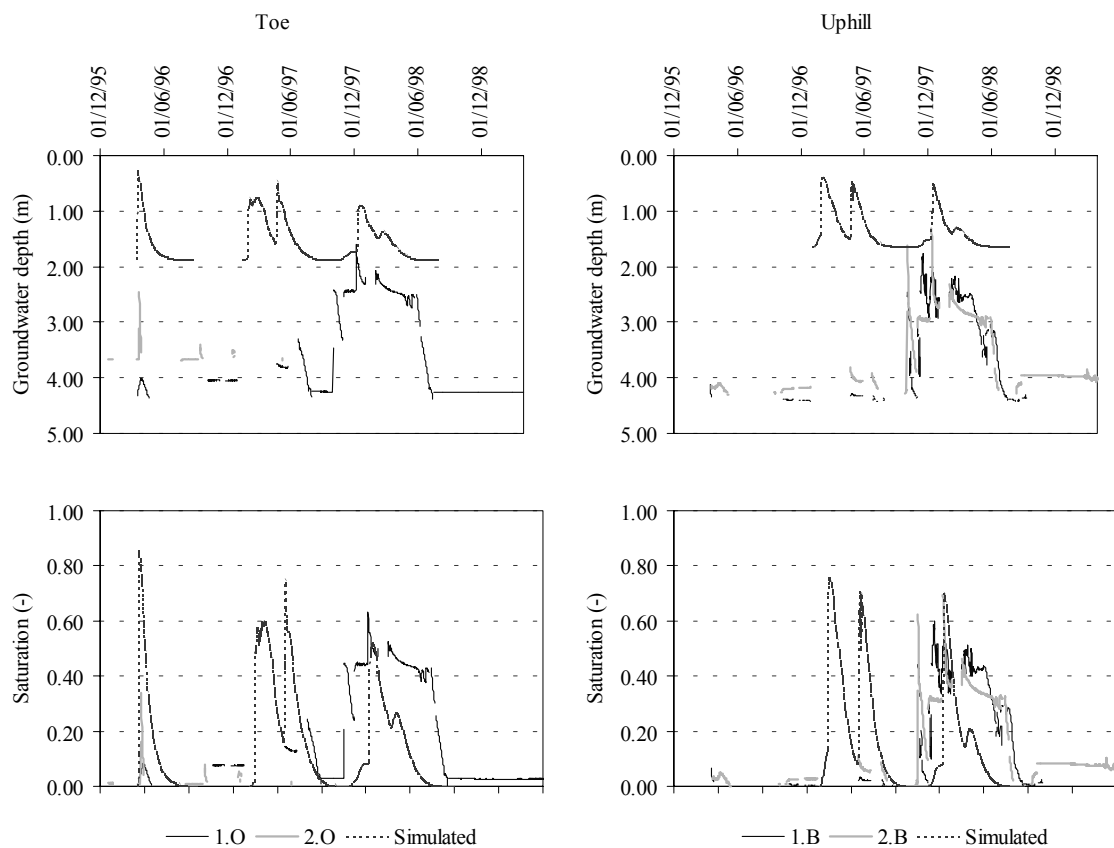


Figure 6.5: Observed and simulated groundwater levels at the LGM-site: absolute depths and relative

Notwithstanding, it is clear that its performance is limited by the poor estimate of the soil depth. Although this leaves much to be desired, it is evident that such discrepancies are inherent to the application of a distributed model and pose serious limitations to the capability of the model as an absolute predictor of local landslide phenomena. The mismatch between the simulated and the observed hydrological response, however, can be attributed largely to the parameterisation of the model. The systematic errors within the hydrological model component itself are small as the comparison between the calibration and validation runs confirms. The model has in general a sound hydrological basis to evaluate landslide activity. The groundwater levels that trigger most landslides are reasonably reproduced and the observed time lag between the simulated and observed water levels does not affect the capability of the model to simulate the spatial occurrence of landsliding, although the model fails to regenerate the soil moisture and groundwater levels as rapidly as observed after periods of prolonged droughts.

6.5 Applicability of the calibrated hydrological model component

The calibrated parameters of the hydrological model component are considered as constant in time and space. The calibrated values, therefore, reflect the average

conditions of land use and climate. Consequently, some mismatch will occur as the actual conditions will vary locally and temporally from these average conditions. This is clearly the case for periods of prolonged drought as the validation of the hydrological model demonstrated (Section 6.3). Such deviations will affect the overall performance of the coupled hillslope model as evaluated in the next chapter. This evaluation provides a test for the long-term validity of the adopted parameter values under the present conditions of land use and climate. For the scenarios of inferred climatic and land use change, however, it is necessary to establish whether the calibrated parameters are generally applicable.

The calibrated parameters, although theoretically independent, influence each other and can not be considered separately. The use of a constant value means that local variation is lumped into a mean value. Because of the incorporation of unexplained variance in the optimised values, care must be taken with their extrapolation to the hypothetical conditions of land use and climate scenarios. The small confidence limits around the optimised parameters indicate that the amount of incorporated unexplained variance is limited (Table 6.4). Moreover, the parameters are not directly related to the present land use configuration. Nonetheless, it is evident that the calibrated parameters will only be valid under limited amounts of environmental change.

Of the calibrated parameters, the loss to bedrock is relatively insensitive to environmental change because of the large volume involved. The reduction factor for the evapotranspiration, k_r , is more sensitive. Firstly, the hydrological model component reacts strongly to this parameter and, consequently, small deviations have a relatively large influence on the model outcome (Section 6.1.2). Secondly, the actual evapotranspiration varies with the available rainfall and other meteorological variables. Consequently, the simulated value will be biased when the governing conditions differ strongly over a prolonged period from the average conditions (Section 6.3).

For the present land use classes, the total reduction of the potential evapotranspiration falls in the order between 0.32 and 0.37 (-) (see Section 6.2). The actual rainfall is on average 698 mm per year whilst the potential reference evapotranspiration is respectively 2068 and 2116 mm for the present 1·CO₂- and the expected 2·CO₂-climates (Sections 4.3 & 4.4). Thus, the available rainfall is just below the actual evapotranspiration under the more adverse land use conditions, in which case respectively 765 and 783 mm will be lost ($0.37 \cdot ET_0$). If one takes the spatial distribution of the global radiation into account, it is likely that the net annual rainfall is sufficient to sustain this loss without affecting the vegetation cover. Larger losses, however, will be intolerable without a reduction in the density or vitality of the vegetation cover. Under such conditions, the calibrated parameter, k_r , will no longer be applicable as this value lumps surface conditions like vegetation density and sealing.

It may be concluded, therefore, that the optimised model parameters will be applicable to the hypothetical conditions of land use and climate as long as these conditions comply to the down-scaled 2·CO₂-climate of Sections 4.3 & 4.4 and the reduction of the potential evapotranspiration, i.e. the overall reduction factor and the crop factors, remains similar. This applicability concerns the entire study area and the entire periods under consideration. Due to local and temporal variations, this applicability may be violated if the simulated actual evapotranspiration exceeds the available net rainfall considerably. It

is to be expected, therefore, that, in spite of the assumed similarity for the hypothetical land use conditions, the actual density in the vegetation cover will be different from the present conditions.

7 SIMULATION OF LANDSLIDE ACTIVITY UNDER THE PRESENT ENVIRONMENTAL CONDITIONS

7.1 Introduction

This Chapter covers the validation of the slope stability component of the coupled hillslope model. It evaluates its performance in simulating landslide activity under the present environmental conditions. Eventually, the performance of the coupled hillslope model aggregates all the errors that arise from the simulated hydrology and the slope stability analysis. The performance of the coupled hillslope model is, therefore, evaluated for two reasons. Firstly, the evaluation is intended to delimit the validity of the calibrated parameters of the hydrological model component STARWARS. Whereas extreme meteorological conditions like droughts and extreme rainfall events (*tandas*) are characteristic for the Mediterranean climate and essential for the explanation of the occurrence of slope instability in the study area (Chapter 4), they are in principle irreconcilable with the constant values that have been assigned to the calibrated parameters. Discrepancies between the simulated and observed landslide activity would serve to establish whether the limited validity of the calibrated parameters impairs the model performance.

Conform Gleick (1986), the calibrated hillslope model will be applied to scenarios of environmental change (Chapter 1). In Section 6.4 it was demonstrated that the calibrated values are applicable under the limited environmental change that is envisaged in these scenarios. On its own, the change in the forecasts of landslide activity under these hypothetical conditions provides primarily a qualitative measure for the relative change in landscape sensitivity to slope instability. For the interpretation of the actual changes that may be expected, it is necessary to have a good understanding of the limitations of the coupled hillslope model under various environmental conditions. This is the second reason for the evaluation of the model performance under the present environmental conditions. It is highly unlikely that the simulated slope failure will correspond unconditionally with the observed landslide activity over the validation period. Under the present land use conditions, the agreement between the simulated failure and the observed landslide activity will demonstrate whether the calibrated model is capable of making accurate predictions of landslide activity. On the basis of this agreement, some general conclusions on the expected landslide activity under the changed environmental conditions can be made in the next chapter on Scenario Modelling (Chapter 8).

Together with the limited validity of the calibrated parameters, this limits the changes that can be applied in the hypothetical scenarios. Whereas the consequences of limited changes in the environmental conditions can be predicted on the basis of the extrapolation of the present process-response systems, radical and complete changes affect the landscape through processes that extend beyond the model scale of conventional physically based models.

Because of the deterministic relationship between simulated hydrology and slope failure, only the hydrological model component STARWARS has been calibrated (Chapter 6). It is not deemed appropriate to optimise the slope stability model PROBSTAB by adjusting the

intrinsic shearing resistance of the material as it could bias the model towards the prediction of a particular type of landslide. Thus, the slope stability model has been parameterised with *a priori* knowledge only.

In the slope stability model, the uncertainty in shearing resistance is incorporated by means of a probabilistic analysis. (Section 3.2.3). This returns the probability of failure that can be interpreted as the confidence limit around the predicted factor of safety. The probabilistic approach, therefore, avoids the rigid prediction of deterministic slope stability models that fail to take the variation in shear strength into account (Section 7.3). Although the simulated hydrology is equally prone to uncertainty in the parameters, the pore pressure conditions that act as potential triggers of slope failure are treated as absolute values for the ease of comparison. The simulated probability of failure only reflects the uncertainty in the landslide susceptibility of the study area. The effect of the temporal sensitivity, i.e. the incidence of potentially triggering conditions (Brunsden, 1993 & 2000), can be determined by means of the temporal component of landslide activity (see also Chapter 1). Thus, two levels of comparison between simulated slope failure and landslide activity are available. The first is based on mere coincidence between observed landslide occurrence and areas of simulated failure, the second is based on the temporal agreement between them. For the probabilistic slope stability model PROBSTAB, these comparisons are covered in Section 7.4 on validation. Subsequently, the validity of the calibrated hydrological parameters and the influence of the environmental conditions on the model predictions are discussed respectively in Sections 7.5 and 7.6.

Prior to the validation of the simulated slope failure, the implementation of the coupled hillslope model and the susceptibility of the landscape to slope failure are discussed in Section 7.3. Firstly, in Section 7.2, the landslide inventory is presented that describes the observed landslide activity over the validation period

7.2 Landslide inventory

For the study area no record of landslide activity is readily available. Damage by landslides to roads and the drainage network in the area is repaired by the municipality and the Valencian Transport Council (COPUT) who do not keep records that are detailed enough to specify landslide occurrence on the spatial resolution of the model. Damage to the bench terraces in the area is repaired by the farmers themselves and forms part of their routine in spring and fall. Thus, a detailed record of landslide occurrence is missing and an alternative must be found to validate the performance of the coupled hillslope model. As a substitute, a map of landslide occurrence has been used that has been based on air photo interpretation and geomorphological mapping (Figure 2.3). For the matching of the actual landslides and simulated failure, only the affected area is traced from air photographs over the validation period from 1971–1998 (Figure 7.1). Notwithstanding the fact that this is the only opportunity to obtain a complete spatial coverage of landslide occurrence, it is obvious that the quality of the record will be impaired by the frequency of the flights and by the visibility of the landslides. Three flights are available that incorporate sufficient detail to distinguish the individual landslides. These are the flights of 1973, 1989 and 1994 that have an approximate scale of 1:25,000. Given the available

flights, it is obvious that the initial conditions for 1971 are missing. The most appropriate flight dates back to 1965. Taking this flight as the null-situation, most of the study area is vegetated completely without apparent signs of instability. Notable exceptions are two south exposed slopes that seem to be stripped entirely of vegetation and soil. However, these slopes are already well revegetated in the photos of 1973 without signs of continued degradation. The only other areas clearly affected by landslides are three rotational slides that remain active during the validation period. Some of the steeper slopes, subject to mass wasting, also remain barren over the entire period. Apparently, the extent of landslides is at a low at the beginning of the validation period.

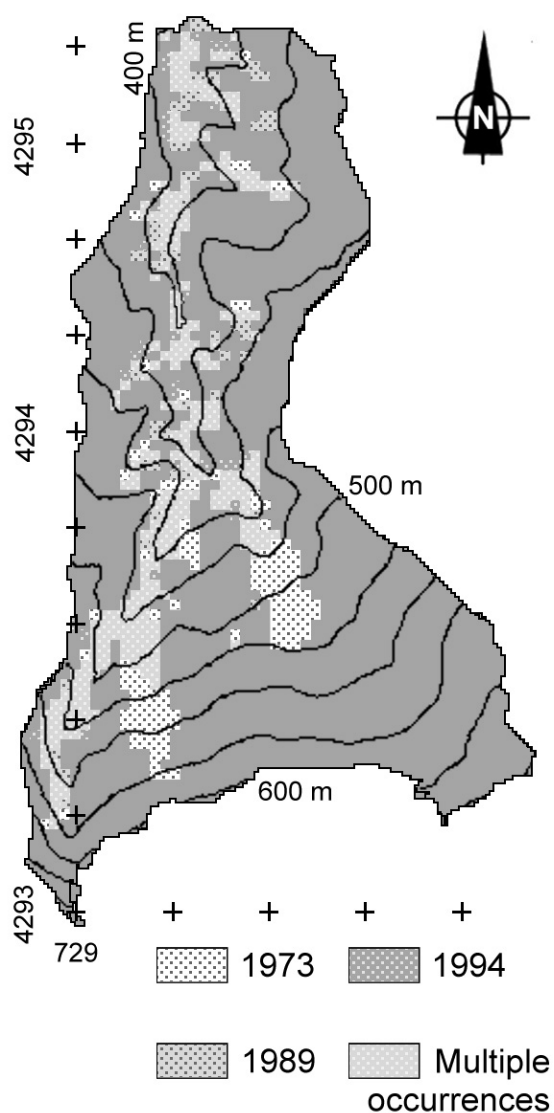


Figure 7.1: Landslide occurrence based on air photo interpretation for the years 1973, 1989 and 1994

The condition of the vegetation cover raises the subject of the second limitation, namely landslide visibility. In the air photographs, the recognisable landslides are those in which the scar is exposed as barren soil or bedrock or those in which the surface is sufficiently reworked to form a typical topography of hummocky ground with an immature drainage.

The latter terrain type is discernible on the mudflows of the landslide complexes near Almudaina (Section 2.2). Landslide occurrence may be overestimated when no distinction can be made between reactivation and the degradation of scars by superficial erosion. This is particularly the case for shallow landslides in semi-natural vegetation of which the scarp is the dominant feature for their recognition. In contrast, landslide occurrence could be underestimated in the case of deep-seated rotational landslides, small failures of bench terrace risers and landslides in cultivated fields. In the case of rotational slides, the soil is displaced more or less coherently and a relatively small scar is exposed. In cultivated fields, tilled, barren soil may mask the features of all landslides occurring here and the small-scale failure of bench terrace risers is easily repaired. Although the geomorphological mapping provides ground truth to corroborate the air photo interpretation, the landslide inventory lacks essential information on the triggering moments of landslides.

The observed landslides have been mapped without any further interpretation on the type or activity. This results in simple Boolean representation of landslide occurrence for the three flights that can be combined into a total map of landslide occurrence over the validation period (Figure 7.1). This landslide occurrence has been represented on a coarser resolution (25x25 m) than the original model scale (10x10 m). This decrease originates from the lower resolution at which landslide occurrence could be mapped on the basis of the aerial photographs and represents the uncertainty in the landslide boundaries which not only encompass the area of failure but also the run-out of the material on otherwise stable slopes.

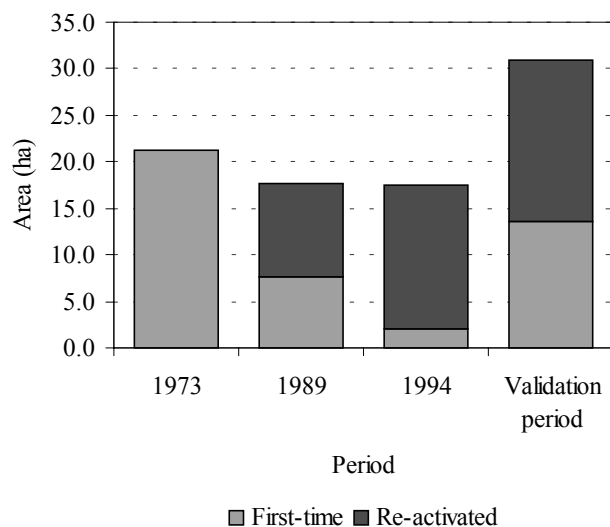


Figure 7.2: Landslide occurrence as function of time in the Barranco de la Coloma

The total area with recognisable landslide occurrence amounts to 30.9 ha. From the three air photographs, the temporal activity can be determined over the preceding period (Figure 7.2). For the three periods, the area covered by recognisable landslides is roughly similar but, over time, the area of landslides subject to reactivation increases. The distinction between first-time failures and reactivated landslides, however, is artificial as it is based on the absence of recognisable landslides in the 1965 photograph, which is

taken as the null-situation. Despite this absence, it is likely that some of these areas had experienced instability in the recent past (< 100 years).

Although the area of instability is very similar for the three periods, the distribution varies over the years (Figure 7.1). Whereas most of the reactivation occurs along the steep slopes adjacent to the main course and tributaries of the Barranco, the single events witnessed by the 1989- and 1994 photographs are concentrated on the upper parts of these slopes and represent predominantly a retrogressive destabilisation above landslide prone areas in colluvial soils. In 1973, activity concentrated on the scree-covered slope under Almudaina, where large landslide complexes developed after 1965. According to the local population, the total movement since the end of the 1960s amounts to several tens of meters. After 1973, reactivation was limited and only some residual seasonal activity, e.g. the opening of fissures and deformation of road works, was observed during the field campaigns since 1995 (Plate 6). Overall, the level of landslide activity has been low since the events witnessed by the flight of 1994. No substantial landslides have been observed in the Barranco de la Coloma since 1995. Following prolonged rainfall in September 1997, some small failures in road cuts and the risers of bench terraces occurred. However, their extent does not compare to the observed landslide occurrence over the preceding period and can be neglected.

7.3 Simulating landslide susceptibility and slope failure

7.3.1 Implementation of the coupled hillslope model for the validation period

The validation of the simulated slope failure is identical to that of the hydrological model component of Section 6.3. The validation period covers a period of 27 hydrological years from 1971 onwards, from which date continuous rainfall data from the station of Almudaina are available (Section 4.2.1). The simulated failure can be compared to the actual landslide occurrence from 1973 onwards.

The initial conditions for 1971 are steady-state conditions of groundwater levels and volumetric moisture contents based on 20 years of average weather series. The change in land use conditions to the present configuration has been considered as complete at the start of the validation period (Section 6.3).

The coupled hillslope model simulates slope failure, of which the spatial and temporal components of simulated failure are reported in the form of yearly and overall maps of failure, probability of failure and duration. For the observed landslide activity, this information is available from the landslide inventory that provides the touchstone for the validation of the model over the period 1973-1994 (Section 7.2). Yet, the temporal information of the landslide inventory is poor and, consequently, the possibilities to compare the temporal component of landslide activity in the validation will be limited. This is particularly the case for the period preceding the aerial photograph of 1973 for which the comparison is tentative as failure is simulated only from 1971 onwards, rather than from the previous flight of 1965. The difference in land use conditions between 1965 and 1973 and the absence of reliable rainfall data prohibit the modelling of this period.

7.3.2 Sensitivity analysis for the slope stability model

The slope stability component of the coupled hillslope model is based on the infinite slope model (Section 3.2.3). For the infinite slope model, many examples of sensitivity analyses are available from literature (e.g. Gray & Megahan, 1981; Mulder, 1991). These sensitivity analyses may assist to identify the more important factors for slope failure. These sensitivity analyses are based on the deterministic version of the infinite slope model, rather than the probabilistic version used in PROBSTAB. However, the results are interchangeable if the coefficient of variation is kept constant to ensure that the probability of failure will not be influenced by the absolute levels of parameter change. The sensitivity analysis has been used to evaluate the influence of eight parameters and variables on slope stability. These parameters can be subdivided into three groups that are represented in Figure 7.3: morphometry, soil properties and transient factors. These transient factors are those related to hydrology (pore pressure, matric suction) and the surcharge, which could be imposed by vegetation.

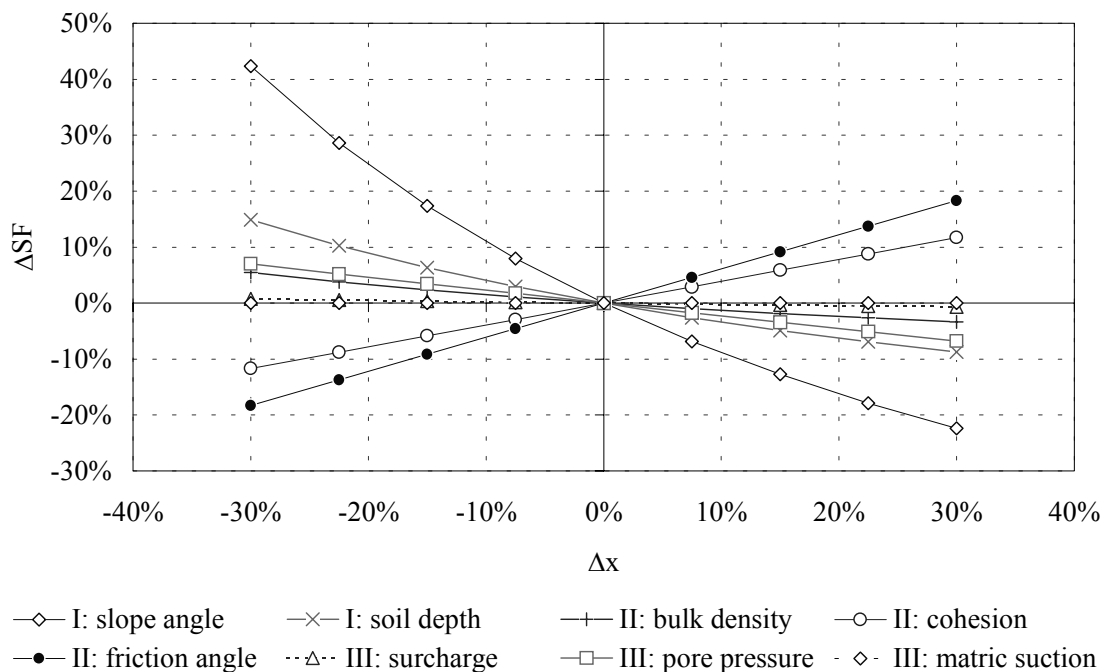


Figure 7.3: Sensitivity analysis for the infinite slope model: I) morphometry; II) soil properties; III) transient factors

The sensitivity analysis shows that the slope angle has the clearest and largest influence on the safety factor (Figure 7.3). With decreasing slope angles, the safety factor increases rapidly. In contrast, the reduction in the safety factor is less dramatic for increasing slope angles.

For shallow soils in cohesive soils, the influence of the slope angle is followed closely by that of the soil depth and – to a lesser extent – the cohesion itself. The cohesion imposes an invariant strength over the length of the potential shear plane that must be exceeded by the shear stress. The shear stress is primarily a function of the soil depth and slope angle. If the soil mass is relatively deep, the influence of the soil depth and cohesion is reduced and the frictional component of the shear strength becomes more important. In the case of mere frictional strength, the pore pressure and the angle of internal friction ϕ' have a similar but opposed influence. Variables directly related to the weight acting on the potential shear plane (bulk density and surcharge) have only a very limited influence as they act partially on the resistance and partially on the driving forces. Whenever the soil depth is large enough to compensate the cohesion, the safety factor, as calculated by the infinite slope model, is the most sensitive to the slope angle, followed by the pore pressure conditions and the angle of internal friction. Although the pore pressure conditions come only second if one considers the absolute sensitivity of the infinite slope model, it is important to note that it is the only influential variable that is prone to changes over short periods.

7.3.3 *Modelling of landslide susceptibility*

The findings of the sensitivity analysis show that pore pressure is an important trigger of slope instability. The occurrence of slope instability is, however, primarily defined by the susceptibility of the landscape on which the fluctuations in pore pressure are superimposed. These fluctuations explain the temporal sensitivity of the Alcoy region to environmental change that is assessed in this study (Chapter 1).

For the susceptibility, the slope angle and to a lesser degree the soil depth, which vary locally, are the more influential factors. Other variables are of less importance because of their low weight on the model outcome and the limited range over which their values vary.

For this simulation, the susceptibility is assumed as constant. This supposes that preparatory factors *cf.* Crozier (1986) and Van Asch (1980) are not of importance on the temporal scale considered in the simulation. Thus, the temporal sensitivity is assessed on the basis of a static level of the susceptibility.

Since this susceptibility will not change from one scenario to the other, a short description is appropriate, as it will aid to interpret the results of the scenario modelling. Moreover, the modelled susceptibility is based on a simplification of the natural process system and its description can explain some of the shortcomings of the slope stability model PROBSTAB that will become apparent in the validation.

The landscape susceptibility to slope failure is defined here as the threshold of the critical pore pressure at which the soil mantle for a given slope angle becomes unstable. At limiting equilibrium (Section 3.2.3), this threshold of failure can be expressed by the critical pore pressure ratio (Montgomery & Dietrich, 1994; Van Beek & Van Asch, 1998). The pore pressure ratio is defined as the ratio between the actual pore pressure and a maximum on a potential slip plane (Bishop, 1953). For an unconfined water table, this maximum is taken to be the pore pressure generated under total saturation, in which case

the height of the water table, h_w , is equal to the depth, z , of the soil above the potential slip plane, i.e. $r_u = h_w/z$.

By definition, the critical pore pressure ratio is the value at which the slope is at limiting equilibrium. If the critical pore pressure ratio of a slope exceeds unity, the pore pressure required for triggering is larger than that which can be generated under the assumed unconfined water table with seepage parallel to the topographical surface. Thus, the slope can be considered as being not susceptible to failure.

For frictional materials, the stability of a slope is independent of the soil depth due to the absence of cohesion. Thus, the modelled susceptibility is equivalent with the slope angle. The critical pore pressure ratio is given by

$$r_{u \text{ crit}} = \gamma \cdot \frac{\tan \phi / \tan \alpha - 1}{\gamma_{\text{sat}} - \gamma + (\gamma - \gamma') \cdot \tan \phi / \tan \alpha}, \quad (7.1)$$

where α is the slope angle, ϕ' is the effective angle of internal friction and γ , γ_{sat} , and γ' , represent respectively the moist, saturated and the buoyant bulk unit weight. For a maximum of $r_{u \text{ crit}} = 1$ and $\gamma_{\text{sat}} \approx 2 \cdot \gamma'$, this implies that the minimum slope for which the deterministic model can predict failure is approximately (Skempton, 1964; Carson, 1973)

$$\tan \alpha \approx \frac{1}{2} \tan \phi'. \quad (7.2)$$

This threshold is taken as dependent on the peak strength of the material and post-failure behaviour is not considered. So, it only assesses occurrence of first-time failure.

The predictive capacity of the infinite slope model, which forms the basis of PROBSTAB, is further limited by its one-dimensional nature. Consequently, the fluctuations in the lateral stresses that affect the stability are ignored. The threshold of the critical pore pressure ratio is, therefore, constant over time and only dependent on the local slope conditions and material properties.

Based on the effective angle of internal friction at peak strength, ϕ_p' , of 34.8° and Equation 7.1, the model only simulates first-time failure for slopes steeper than 18° ($\tan \alpha \geq 0.33$). This is a deterministic assessment and all slopes below this threshold are unconditionally stable in the simulation ($F > 1$). For the Barranco de la Coloma, 21% or 32.8 ha of the total area of 153.7 ha exceeds this threshold (Figure 7.4). The slopes above this threshold represent 43% of the observed landslide occurrence of the inventory (13.4 out of 30.9 ha).

As the distribution of the observed landslide occurrence reveals, slope failure is not bounded by this deterministic topographic threshold. The available shearing resistance may err on the unsafe side as a result of local variations in the shear strength or the presence of lateral stresses. Prolonged destabilisation may even lead to the development of residual strength. Subsequently, slope failure becomes more frequent and the steady-state threshold modelled on the peak strength will underestimate this reactivation.

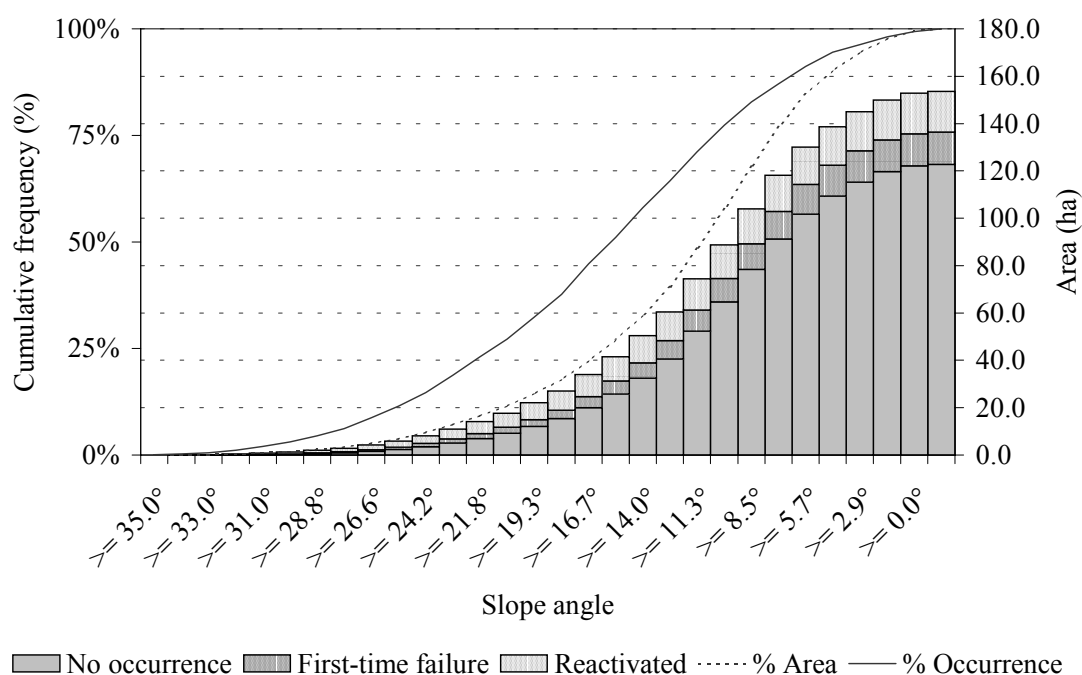


Figure 7.4: Distribution of observed landslide occurrence with slope angle

As a result of the distribution of slopes and landslide occurrence in the study area, a large number of landslides occur on slopes just under the topographic threshold. The probabilistic analysis has the advantage that the rigour of this deterministic threshold is partly overcome. With the uncertainty in the shear strength parameters, the calculated threshold may vary as limiting equilibrium can be achieved for gentler slopes and vice versa. For the threshold of slope instability, the effect of the uncertainty in the shear strength parameters can be illustrated by calculating the critical slope angle for the 95%-confidence limits around the angle of internal friction (Table 7.1). It should be noted that the resulting spread in the threshold value reflects in theory only the uncertainty in the peak strength of the material; the possible effects of residual strength and lateral stress distributions are not considered.

In the probabilistic analysis, the resulting uncertainty in the calculated safety factor is reflected in the probability of failure, $P(F \leq 1)$. This is the statistical likelihood that, given the variability in the shear strength parameters, the factor of safety actually falls below unity (Section 7.4.3).

Table 7.1: Modelled susceptibility to slope failure in relation to variations in ϕ_p' (95% confidence limits)

	$\tan(\phi')$	ϕ'	$\tan(\alpha_{crit.})$	$\alpha_{crit.}$	Total area $> \alpha_{crit.}$		Observed landslide occurrence	
	(-)	(°)	(-)	(°)	(ha)	(%)	(ha)	(%)
Min.: $\phi' - 2 \text{ S.D.}$	0.526	27.7	0.250	14.0	44.5	39	19.9	64
Avg.: ϕ'	0.694	34.8	0.330	18.3	32.8	21	13.4	43
Max.: $\phi' + 2 \text{ S.D.}$	0.862	40.8	0.410	22.3	23.0	11	7.8	25

Based on the average value for the peak friction angle, 21% of the total area of the Barranco de la Coloma is modelled as susceptible (32.8 out of 153.7 ha; Table 7.1). This fraction of 21% covers 43% of the observed landslide occurrence. When the lower end of the peak friction angle is considered, 64% of the observed landslide occurrence fall within the category of slopes susceptible to instability. So, the agreement between simulated failure and the observed landslide occurrence can increase by 50% when the variability in the peak shear strength is considered.

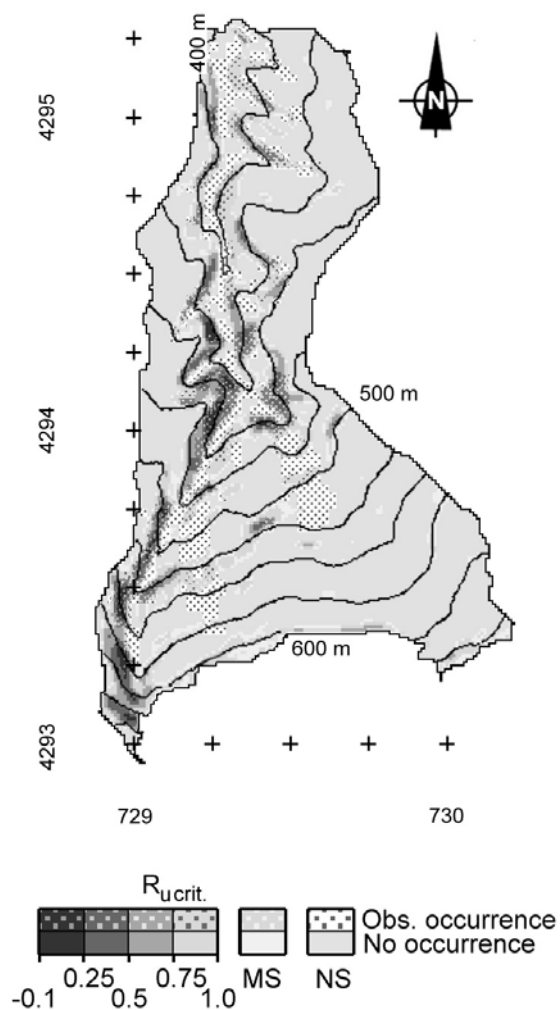


Figure 7.5: Landslide susceptibility as modelled with the critical pore pressure ratio and correspondence with observed landslide occurrence. See text for explanation.

In Figure 7.5, the distribution of the critical pore pressure ratio is given for the Barranco de la Coloma. This distribution is based on the average shear strength parameters. The negative values for the critical pore pressure ratio relate to the most susceptible areas. Here, the slope angle exceeds the mean friction angle. These areas are unconditionally unstable unless matric suction provides additional shearing resistance that can keep the material in place.

The variation of the soil properties on the unsafe side results in marginally susceptible areas that require below-average shearing resistance and nearly complete saturation for failure. These are indicated separately on the map (*MS*).

Areas that are not susceptible to failure, i.e. having a critical pore pressure ratio above unity, are indicated as well (*NS*). For this category, observed landslide occurrence can not be matched. So, the susceptibility map with the exception of the category *NS* constitutes the upper limit for the performance of the coupled slope model. The total area of observed landslide occurrence can be compared to the area susceptible to failure. This is represented graphically in Figure 7.5, where the rasterised areas represent areas with observed landslide occurrence. The comparison of the observed landslide occurrence and modelled susceptibility is worked out in Table 7.2.

Table 7.2: Comparison of observed landslide occurrence with susceptibility

Susceptibility,	NS	MS	$1.0 \geq$	$0.75 \geq$	$0.5 \geq$	$0.25 \geq$	All
$r_{u \text{ crit.}}$			$x > 0.75$	$x > 0.5$	$x > 0.25$	$x > -0.1$	
Threshold slope, α	14°	18°	23°	27°	31°	36°	
<i>Landslide activity</i>							
<i>Absolute occurrence (ha)</i>							
Total area	93.2	28.0	17.1	9.9	4.2	1.3	153.7
First-time failure	5.9	3.4	2.1	1.3	0.8	0.1	13.6
Reactivated	5.1	3.1	3.7	2.9	1.6	0.9	17.3
Landslide density	0.12	0.23	0.34	0.42	0.57	0.75	0.20
<i>Relative occurrence (%)</i>							
First-time failure	43	25	15	9	6	1	100
Reactivated	30	18	22	17	9	5	100
All landslides	36	21	19	13	8	3	100

The classified data of Table 7.2 also demonstrate that, with an increase in susceptibility, the landslide density rises (see also Equation 7.4, Section 7.4.3) and that the recurrence of slope instability becomes more frequent. In absence of other major triggers like seismicity, this is consistent with the premise that the occurrence of excessive pore pressures is the dominant triggering mechanism of landslides in the study area.

Despite the consistent behaviour of the modelled susceptibility, the observed uncertainty in the peak value of the shearing resistance is insufficient to explain 36% of the observed landslide occurrence. The probabilistic model may perform marginally better because of the additional 2.5% of uncertainty that is contained by the lower tail of the distribution but additional reasons must be found for this unexplained fraction.

In addition to Figure 7.5 the agreement between the observed landslide occurrence and the modelled susceptibility is given in Table 7.3. The diagonal elements represent the agreement between the observation and the simulation, the off-diagonal elements represent the mismatch. The agreement is based on the average friction angle as the inclusion of the marginally susceptible areas would result in a large overestimation of the observed landslide occurrence by the modelled susceptibility. The category, which contains the susceptible area not matched by observed landslide occurrence, represents a

worst-case assessment as it presumes complete saturation of the soil mantle. In the dynamic situation of the hydrology, it is probable that these extreme pore pressure conditions will not be achieved for the entire area and the overestimation will consequently be lower than the values presented here. Notwithstanding, the off-diagonal elements that contain the mismatch represents areas that are larger than that of matched landslide occurrence. Consequently, the dynamic simulation of the hydrology and the inclusion of the marginally susceptible areas by means of the probabilistic slope stability analysis are necessary to obtain a better agreement between simulated failure and observed landslide activity. The performance of the coupled hillslope model and the influence of the hydrology on the simulated failure will be evaluated in Section 7.4.

Table 7.3: Agreement between modelled susceptibility and observed landslide occurrence.

Area (ha) Observed	Modelled		Total Observed
	Non-susceptible	Susceptible	
	<i>Absolute area (ha)</i>		
No occurrence	103.6	19.1	122.7
Occurrence	17.6	13.3	30.9
Total susceptible	121.2	32.5	153.7
	<i>Relative frequency (%)</i>		
No occurrence	84	16	100
Occurrence	57	43	100

Localities of marked discrepancies are the large landslide complexes near Almudaina (Section 7.2), the streambed of the barranco and the SW slope along it. In the first two cases, landslide occurrence is underestimated as these areas are not susceptible to failure in the simulation. In the latter case, failure is overestimated as no landslide occurrence is observed in this highly susceptible area.

A fundamental reason for the underestimation is the fact that the modelled susceptibility simulates failure. This is not synonymous with the extent of the landslide deposits, which are included by the landslide inventory (Montgomery *et al.*, 1998). In addition, erroneous observations will arise due to the lower resolution of the landslide inventory. Consequently, landslide deposits are present in the streambed of the barranco. Because of its low slope angle, the streambed remains unconditionally stable in the simulation. The landslide occurrence in this area can therefore be considered as spurious. However, steeper slopes border directly to the channel and 90% of the slopes in or next to the streambed have a slope of less than 8.5°. If these slopes along the barranco are barred from the landslide inventory, 3.5 ha or 11% of the observed occurrence would be excluded from the comparison. For the present model, this exclusion increases the agreement between the modelled susceptibility and observed landslide occurrence from 64% to 73%.

The 27% of landslide occurrence that are not matched by the modelled susceptibility occur on the least susceptible slopes for which no failure can be simulated. Still, the landslide occurrence on these least susceptible slopes is always connected to areas where the observed landslide occurrence is matched by modelled susceptibility. Thus, the modelled susceptibility is capable to reproduce the spatial distribution of landslide

occurrence although it only takes the local conditions into consideration. However, the modelled susceptibility is too optimistic as the susceptible area underestimates that of landslide occurrence.

An explanation for the observed discrepancy between modelled susceptibility and the observed landslide activity is the possible influence of preparatory processes like weathering and strain softening or past landslide occurrence. These preparatory processes can result in local variations in the material properties that invalidate the static susceptibility that has been used here. Such local variations could include the development of residual strength in the landslide complexes near Almudaina.

Where the soil is stripped away, the potential for landslide occurrence is exhausted (Crozier, 1996). Consequently, the susceptibility is overestimated and only after a certain period of time will the preparatory processes have reduced the threshold sufficiently for slope failure to recur under the prevalent hydrological triggers. Evidence for such temporal variations in landslide activity has been reported by Crozier *et al.* (1990), Dietrich *et al.* (1984), and Dietrich *et al.* (1992).

Although there is no record of landslide activity for the Alcoy region to test the hypothesis that preparatory processes control landslide activity on the temporal scale considered, it is plausible that the rate of recovery of the susceptibility is a dominant factor for landslide activity in the study area. In combination with the resistant limestone ranges, the base level lowering of the Río Serpis probably maintains sufficient relative relief that allows for the repeated destabilisation of the soils that develop on top of the marl bedrock. At least, exhaustion of the soil mantle could explain part of the overestimation of landslide occurrence. The modelled susceptibility presumes a constant soil cover, which is no longer present on the steep SW slopes along western branch of the Barranco de la Coloma. Here, marl bedrock crops out close to the contact with the limestone of the Sierra de Almudaina and the rate of soil production limits the landslide activity. This area covers 4.0 ha or 12.1% of the total susceptible area of 32.8 ha when based on the average value for the friction angle (Table 7.1).

On the basis of the comparison between the modelled susceptibility and the observed landslide occurrence it should be concluded that the marginally susceptible slopes and the simulated hydrology should be included to increase the agreement between simulated failure and observed landslide activity. The inclusion of the marginally susceptible slopes by means of the probabilistic analysis would bring 64% of the observed landslide occurrence within the range of the modelled susceptibility. For the remaining 36%, corresponding to all landslide occurrence on slopes below 14°, failure can not be simulated (Table 7.1).

This fraction of 36% includes landslide deposits that probably do not represent slope failure. This area constitutes 11% of the observed occurrence and could be excluded from the comparison. This would increase the overall agreement between the modelled susceptibility and the observed landslide occurrence to 73%. Thus, the model is too optimistic as 27% of the observed landslide occurrence on the least sensitive slopes is not matched by the modelled susceptibility. However, the modelled susceptibility provides a reasonable estimate for the spatial distribution of the observed landslide occurrence. This raises the essential question whether simulated failure in one-dimension can be equated

with landslide occurrence. The performance of the coupled hillslope model will, therefore, depend on the interaction between the simulated hydrology and the spatial variability in the susceptibility. In the next section, it will be assessed whether the coupled hillslope model simulates the observed landslide activity adequately in terms of spatial and temporal occurrence.

7.4 Validation of slope stability model component PROBSTAB

7.4.1 Validation of simulated slope failure

No important landslide events occurred during the period 1995-1998 over which the hydrological model component STARWARS has been calibrated. Thus, the predicted instability has been compared with the landslide inventory to assess the performance of the calibrated model. This landslide inventory comprises the landslide occurrence over the period 1973 - 1999 as observed from geomorphological mapping and air photo interpretation (Section 7.2).

The validation of the slope stability model evaluates to which degree the model predicts observed landslide activity. Ideally, it should provide a perfect match. In reality, there will be a certain mismatch comprising all model errors, whether these originate from the simulated hydrology or the modelled susceptibility. In addition, this mismatch incorporates observational errors stemming from both mistakenly recorded and overlooked landslides. In spite of the spatial and temporal detail of any available record, none can provide a completely accurate inventory of the actual landslide activity.

As defined in Chapter 1, landslide activity can be subdivided into a temporal and a spatial component. The validation of the slope stability model will focus on the spatial distribution or the occurrence of simulated failure. Less weight is given to the temporal aspects of landslide activity since they are subordinate to observed landslide occurrence or simulated failure. Moreover, the temporal resolution of the landslide inventory is low and only approximate data on reactivation or duration of the observed landslides could be obtained. It is, however, obvious that the response time should be simulated well enough to guarantee a match with the observed occurrence in the landslide record.

7.4.2 Probabilistic vs. deterministic prediction

The performance of the model is evaluated for the deterministic and the probabilistic versions of the infinite slope model, which is implemented in PROBSTAB. The deterministic version is based on the average values for the shear strength parameters, $\tan\phi_p'$ and $\tan\phi^b$ (Section 3.2.3). Slope failure is predicted when the factor of safety falls below limiting equilibrium ($F \leq 1$). The factor of safety gives a measure for the stability of the slope. The factor of safety is defined as the ratio between the available shearing resistance and the disturbing forces. This ratio can be envisaged as the ratio between the actual pore pressure conditions or groundwater level and the critical level at which the

slope is at limiting equilibrium (Equation 7.1). The output of the deterministic model comprises the area of slope failure and its frequency and total and average duration over the validation period.

The factor of safety is a linear scaling method (Section 3.2.3). Its value provides no information on the amount of shearing resistance that can still be mobilised to counter the disturbing forces and how this amount varies from place to place. Consequently, it is a poor statistic to evaluate the hazard of slope failure on a regional scale. Intuitively, the probability of failure, as returned by the probabilistic version of the infinite slope model, is easier to interpret. The probability of failure, denoted as $P(F \leq 1)$, represents the likelihood that given the variability in the shear strength parameters the disturbing forces exceed the available shearing resistance and the factor of safety deviates on the unsafe side. For the assumed normal distribution, the probability of failure is 50% at limiting equilibrium ($F = 1$, $P(F \leq 1) = 0.5$). This implies that there is an equal chance that the factor of safety falls below unity and the soil fails. Thus, the probability of failure can be compared over space and time.

The probabilistic version uses the average values and the standard deviations of the shear strength parameters. The output of the probabilistic version of PROBSTAB includes the mean and maximum probability of failure, both per year and over the entire validation period. The duration of the probability of failure has been reported as the period over which it exceeded pre-set levels per year (range $0.1 \leq P(F \leq 1) < 1.0$ with an increment of 0.1). The range of $P(F \leq 1) \geq 0.1$ is based on the observation that this range covers the majority of the susceptible slopes. The subdivision is, however, arbitrary and only intended to isolate the area of interest. From the reported duration, the total and average duration and the frequency for the entire validation period can be calculated.

7.4.3 Measures for the validation of the simulated failure

The performance of the coupled hillslope model with respect to the simulation of landslide occurrence can be expressed as the ratio of the area over which the simulated failure corresponds with the observed occurrence over the total area for which failure is simulated or landslide occurrence observed. So, the model performance, mp , is

$$mp = \frac{\text{matched landslide occurrence}}{\text{total landslide occurrence} + \text{simulated failure only}} \quad (7.3).$$

Poor performance can be due to both over- and underestimation of the landslide occurrence in an area as the statistic is penalised for either of them. Its value ranges from zero, when none of the observed landslide occurrence is matched, to 100%, when all occurrence is matched by the simulated failure. It can be applied to the simulation over the entire validation period or various sub-periods. In the latter case, it provides a means to assess the model performance with respect to the temporal activity of landsliding.

The probability of failure can be regarded as the likelihood that simulated failure results in recognisable landslides for a specific area. This presumes that simulated failure equates landslide occurrence. In this light, it is interesting to compare the probability of

failure with the observed landslide density, ld , which is the area of observed landslide occurrence per unit area.

For the calculation of the landslide density, it is necessary that the area of interest is defined *a priori*. This area can be defined on the basis of the susceptibility (critical pore pressure ratio or slope angles) or a classification of the probability of failure. In the former case, it can be compared with the spatial average of the probability of failure over the area of interest. In the latter case, the landslide density can be related directly to the class-mid of the limit values x_1 and x_2 for the probability of failure $P(F \leq 1)$. So,

$$ld = \frac{\text{area of observed landslide occurrence}}{\text{total area}}, \quad (7.4)$$

for which $x_1 < P(F \leq 1) \leq x_2$.

A range of statistics can be defined to describe the temporal characteristics of simulated failure or observed landslide activity. These are based on pre-set states or levels. These include observed occurrence, simulated failure ($F \leq 1$) or arbitrary levels of the simulated probability of failure, x .

The simplest temporal characteristic is *persistence*, the fraction of the validation period that $P(F \leq 1) \geq x$,

$$\text{persistence} = \frac{\text{total period with } P(F \leq 1) \geq x}{\text{total duration}}. \quad (7.5)$$

Recurrence, which is comparable to frequency, is defined as the number of hydrological years that the conditions exceed the pre-set state or level. From the recurrence, the average recurrence interval or return period can be calculated, which is the number of hydrological years without recurrence divided by those of years with recurrence. This recurrence interval is identical to that for the partial duration series that is defined as the average period separating two events (Buishand and Velds, 1980).

The average duration is the ratio between total duration and recurrence. For the validation of the temporal activity, all three statistics have been used.

7.4.4 Performance of the coupled hillslope model

The performance of the calibrated coupled hillslope model with respect to the prediction of landslide occurrence has been assessed for the deterministic and probabilistic versions of PROBSTAB.

For the calculation of the model performance, the area of simulated failure is required (see Equation 7.3). For the deterministic version, this equals the area for which the factor of safety fell below limiting equilibrium ($F = 1$) at any moment during the validation period. For the probabilistic version, the area of simulated failure is given by the product of the total area and the spatial average of the probability of failure. This spatial average is calculated from the maximum probability of failure over the validation period. The maximum probability of failure can be deemed as the decisive factor in the triggering of landslides and corresponds with the highest pore pressure in the simulation.

The calculation of the model performance for the probabilistic version of the infinite slope model has tacitly touched upon the incongruity between the prediction of local landslide occurrence and the forecast of landslide activity as part of a regional assessment. The area with a given probability of failure will always exceed that of the observed landslide occurrence. Only a fraction of this area can be expected to fail due to variations in stabilising and destabilising factors. Assuming that the probability of failure reflects the chance that a soil mass with $F \leq 1$ results in a recognisable landslide, the probability of failure can be used to forecast landslide occurrence on a regional scale. However, it can not be used to predict landslide occurrence locally. At any location, the actual occurrence of landslides is only a particular realisation out of a large number of possibilities. Therefore, it is impossible to predict the local landslide occurrence from the probability of failure in any manner other than that made by the deterministic model.

The model performance has been calculated for the entire validation period and for the sub-periods delineated by the aerial photographs of 1973, 1989 and 1994 (Table 7.4). Since the validation period extends beyond 1994, this period has been included in the comparison. Over this period, no substantial landslides have been recorded and all simulated failure after 1994 can be considered as erroneous. The performance of the model over the entire validation period is, however, not affected by these errors as the simulated failure recurred in areas that had been predicted as unstable during the previous period.

Table 7.4: Areas (in ha) of simulated failure and observed landslide occurrence and the resulting performance (in %) of the deterministic and probabilistic predictions of slope failure over the validation period

Period	Pre-1973	1973-1989	1989-1994	Post-1994	Entire validation period
Total occurrence (ha)	21.3	17.6	17.5	NA	30.9
<i>Deterministic prediction</i>					
Matched occurrence (ha)	2.3	2.1	8.9	5.4	13.1
Simulated only (ha)	4.2	5.7	22.4	5.6	18.2
Model performance (%)	8.9	8.9	22.3	49.1	26.7
<i>Probabilistic prediction</i>					
Matched occurrence (ha)	7.1	5.9	13.2	9.4	18.9
Simulated only (ha)	3.2	5.2	20.7	4.0	15.0
Model performance (%)	28.9	26.0	34.6	70.2	41.2

For both the deterministic and probabilistic version, the infinite slope model performs better over the entire validation period than for any of the sub-periods (Table 7.4). Due to reactivation, the areas for the validation period are lower than the sums of the sub-periods. For the period before 1973, the poor model performance can be explained by the fact that not all of the triggering rainfall has been included in the comparison. For the other sub-periods, the poor model performance requires clarification. It can be explained by the simulated hydrology, which will be discussed in detail in Section 7.5.

The probabilistic version of the infinite slope model performs better than the deterministic version for all periods (Table 7.4). For the entire validation period, the model performance of the probabilistic version is some 50% higher than that of the deterministic version (respectively 41.2 and 26.7%). This difference hardly changes for the periods before and after the flight of 1994. For the periods preceding 1973 and 1989, however, the probabilistic version performs better with a relative increase in the order of 200%.

The explanation for the difference in model performance lies in the use of the probability of failure, which leads to the inclusion of the marginally susceptible areas. So, the performance of the probabilistic version of the infinite slope model is not affected by the topographic threshold that impairs the performance of the deterministic version. Furthermore, the use of the probability of failure reduces the area for which failure is predicted but no landslide occurrence is observed (Figure 7.6). These factors also account for the differences in the model performance of the probabilistic version for the various periods. For the period before 1994, the high proportion of the area with simulated failure only explains the relatively low rise in the model performance with respect to the period before 1989. Between these two periods, the model performance rises with 8.4% compared to a rise of 13.4% for the deterministic version.

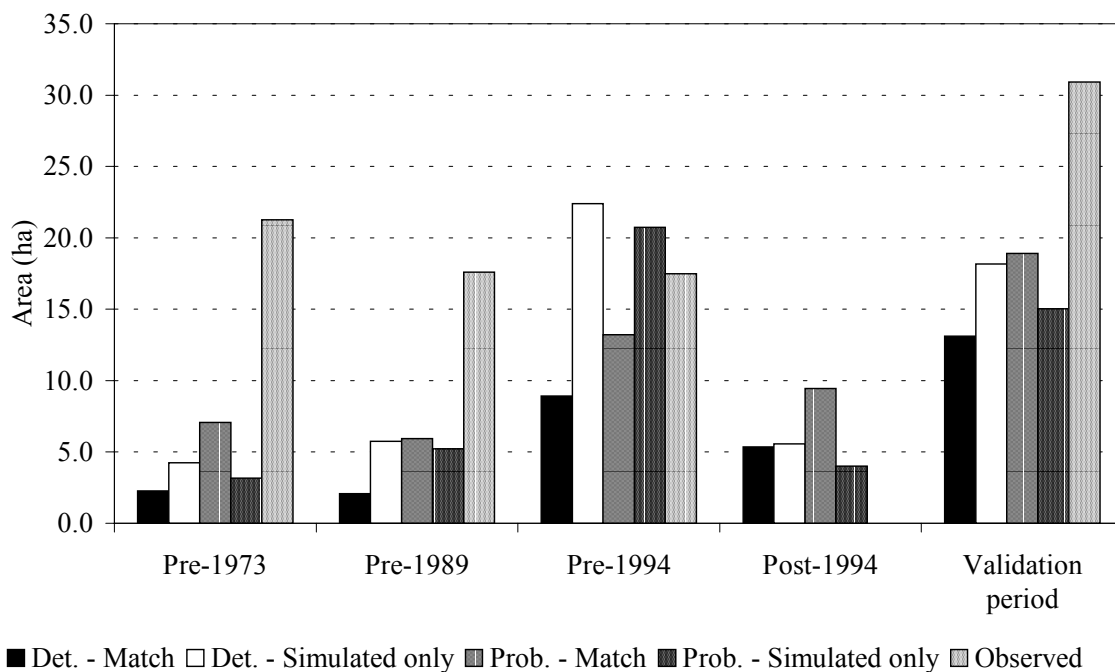


Figure 7.6: Observed landslide occurrence and predictions of slope failure of the deterministic and probabilistic model versions for the entire validation period and the various sub-periods

The calculated model performance is penalised for the mismatch between simulated failure and observed landslide occurrence. As the values of Table 7.4 are calculated on the basis of the total areas with observed landslide occurrence and simulated failure, they are conservative estimates of the model performance. More realistic values can be

obtained when the areas with erroneous landslide occurrence and simulated failure are excluded. The former areas comprise the landslide deposits in the streambed of the barranco, the latter the areas that are modelled as susceptible but where no soil cover is present (7.3.3). Their exclusion would bring the area of observed landslide occurrence to 27.4 ha in stead of 30.9 ha and it would reduce the area with simulated failure only by 4.0 ha. This increases the model performance over the entire validation period to 31.5% and 49.2% for respectively the deterministic and probabilistic versions of the infinite slope model. For the probabilistic model, this brings the fraction of matched landslide occurrence to 69% out of a maximum of 73% that was achieved by matching the observed landslide occurrence with the modelled susceptibility (Section 7.3.3). The small difference suggests that the simulated failure reflects predominantly the static susceptibility. This is confirmed by the fact that the model performance over the entire period exceeds that over the various sub-periods; the simulated failure agrees better with the spatial component than the temporal component of the observed landslide activity.

7.4.5 Relation between landslide occurrence and the simulated probability of failure

Although the area of simulated failure for the probabilistic model is similar to that of observed landslide occurrence (respectively 33.9 and 30.9 ha), there is only a limited amount of agreement between the expected and the observed areas of landslide occurrence. This is caused by the overestimation of observed landslide occurrence above the topographic threshold for landslide susceptibility and the underestimation for the non-susceptible and the marginally susceptible categories below it (*NS* & *MS*; Figure 7.7).

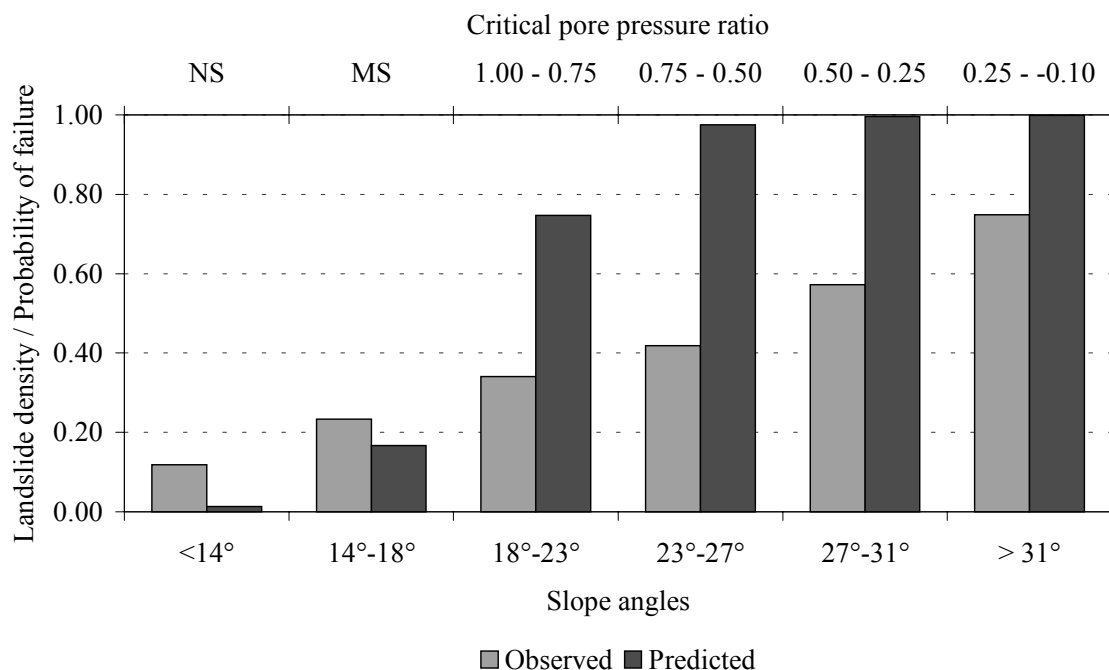


Figure 7.7: Comparison between the observed landslide density and the spatial average of the maximum probability of failure for the 6 susceptibility classes

The maximum probability of failure and the observed landslide density have also been compared directly for 40 equal classes of $P(F \leq 1)$ between 0 and 1. This shows the same reversal from under- to overestimation of the observed landslide density with an increase in the probability of failure. This reversal occurs at $P(F \leq 1) \geq 0.275$, after which the overestimation is consistent. This boundary splits the observed landslide occurrence in half, with 48% occurring above it. Most of the landslide occurrence below this limit, however, occurs in the first class of $P(F \leq 1) < 0.025$, which accounts for 30% of the observed landslide occurrence and corresponds to the non-susceptible class, *NS*, of Figure 7.7 ($ld = 0.12$). Even if the 3.5 ha of spurious landslide observations are excluded, the landslide density remains 0.07 which accounts for 22% of the observed landslide occurrence. At the same time, 20% of the observed landslide occurrence falls in the most critical class of $P(F \leq 1) > 0.975$ that accounts for 37% of the simulated failure. The use of the maximum probability of failure produces this bimodal distribution.

For $P(F \leq 1) \geq 0.275$, the ratio between the observed landslide density and the maximum probability of failure is on average 0.55 (-). It ranges between 0.30 and 0.91 but only 12 of the 29 classes exceed it. Over the validation period, this consistent overestimation implies that the normal distribution, assumed to describe the uncertainty in the shear strength parameters, is not the primary source for the overestimation. It is, therefore, plausible to conclude that factors other than the uncertainty in the shear strength are likely to explain it.

The dichotomy of underestimation and overestimation for the less and more susceptible areas is found in many probabilistic studies (Mulder, 1991; Terlien, 1996). Mulder (1991) used a worst-case estimate for the pore pressure conditions by assuming complete saturation of the soil mantle. He concluded that this conservative estimate of the pore pressure conditions could account for the observed disparity. It could indeed explain the overestimation, as it is unlikely that the soil on the steeper slopes could become fully saturated. However, it is unable to explain the underestimation as complete saturation can be considered as the worst-case condition for any soil cover.

Terlien (1996) also applied a probabilistic slope stability to static pore pressure conditions. He found that the observed landslide occurrence was overestimated 5 to 10 times. Only the landslide density for the class with the lowest probability of failure was reproduced correctly. He concluded that the uncertainty in the input data for the model and the faulty observation of landslide occurrence over the verification period explain the observed disparity. This implies that, with an increase in the observed landslide occurrence, a similar underestimation can be expected for the class with the lowest probability of failure.

The uncertainty in the input data is the second explanation for the poor performance given by Terlien (1996). He asserts that slope stability assessments are unable to predict actual landslide occurrence because the input data do not reflect the local variations in soil depth and mobilised shearing resistance that determine failure. In the light of the overestimation, the estimated soil depth appears to be a crucial factor for the parameterisation of slope stability models, especially when coupled to a simulation of the hydrology. The soil depth is prone to several sources of error, which are equally applicable in this case. Firstly, the estimated soil cover is supposed to be complete and therefore the area that is liable to failure is overrepresented in the model. This is

illustrated by the overestimation of the area susceptible to failure as discussed in Section 7.3.3. Similarly, areas with more resistant soils are present where weathering is generally slow (e.g. under calcified fluvial deposits, Section 2.2). In these instances, the adopted shear strength parameters and the larger water storage capacity of the soil will favour instability. Secondly, a tendency exists to underestimate the actual soil depth in the model (Section 5.5). This results in an overestimation of the simulated hydrological response during the wetter periods and an underestimation of the shear resistance that could be mobilised (see Section 6.3). These errors increase the likelihood that failure is simulated and the part of the predictions of $P(F \leq 1) \geq 0.275$ can therefore be considered as conservative as the simulated failure overestimates the actual occurrence.

In addition to the spurious observations of landslide occurrence in the streambed of the barranco, it is probable that part of the underestimation for the range $P(F \leq 1) < 0.275$ arises from the limitations of the slope stability model. These limitations are the steady-state assumption of landslide susceptibility and the one-dimensional nature of the infinite slope model. Consequently, the slope stability model is unable to simulate any changes in the maximum available shearing resistance or to take any unbalanced lateral stresses into account. Because of its limited validity, Aleotti & Chowdhury (1999) have questioned the use of the infinite slope model in hazard assessments.

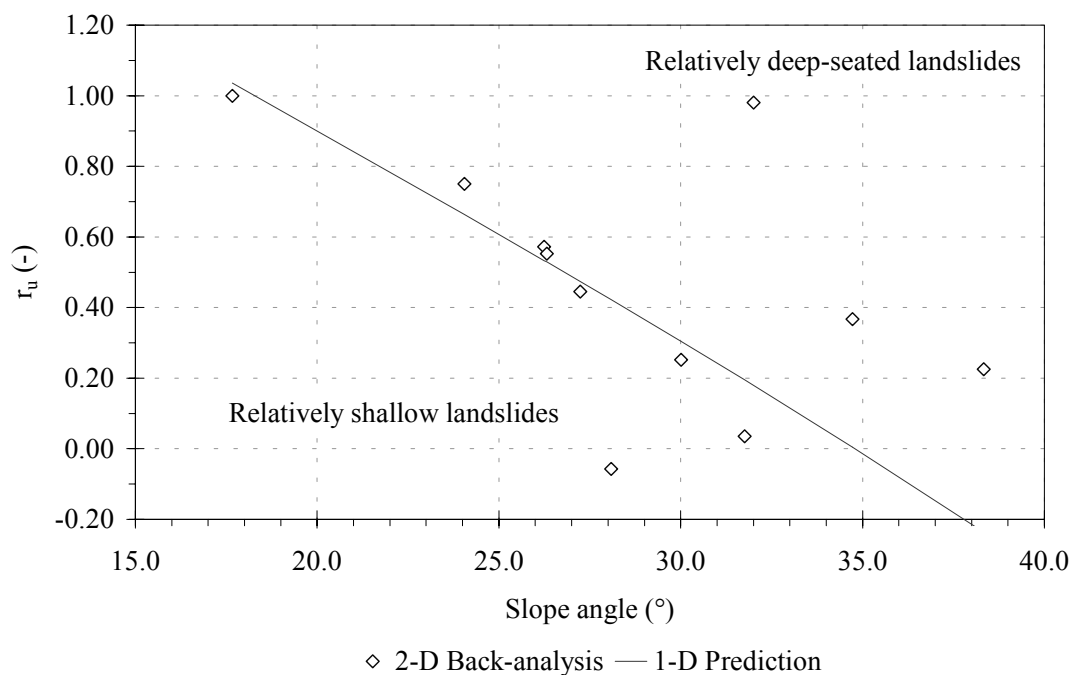


Figure 7.8: Threshold of critical pore pressure ratio based on the one-dimensional infinite slope model and values for eleven landslides calculated from a back-analysis using two-dimensional slope stability models in relation to slope angle

Since the error that is introduced by the infinite slope model could be directed in either direction from the actual factor of safety, it can provide an explanation for both the

underestimation and the overestimation for the ranges below and above $P(F \leq 1) = 0.275$. However, the error in the factor of safety, as calculated by the infinite slope model, can be expected to be small if the depth of the potential landslide is shallow in comparison to its length (Megahan & Gray, 1981). For the Barranco de la Coloma, a comparison has been made of the critical pore pressure ratio, calculated from the infinite slope model, with values based on a back-analysis of the critical groundwater conditions for a total of 11 landslides using two-dimensional slope stability models (Van Beek & Van Asch, 1998). This shows that there is little difference between the two approaches except for the smallest of landslides that have a strongly curved slip plane (Figure 7.8). Such landslides occur generally along the steep risers of bench terraces where the soil is relatively deep. For these landslides, the one-dimensional model underestimates the critical pore pressure ratio. The slopes that are associated with the failure of bench terrace risers are not adequately reproduced by the DEM. The errors that are introduced by the infinite slope model will be small for the landslide occurrence that is included in the inventory. Hence, the simplifying assumption of the infinite slope model can not explain the difference in model performance on either side of $P(F \leq 1) = 0.275$.

For the observed landslide occurrence, the maximum probability of failure is 0.43 on average. This value is below the value of 0.50 that can be expected as a long-term minimum for limiting equilibrium. Thus, the stability of the observed landslide occurrence is overestimated under the assumption that the simulated maximum probability of failure equates landslide occurrence. The explanation for this overestimation is the fact that the adopted peak strength that is characteristic for first-time failure is not applicable to the two landslide complexes near Almudaina. For these complexes, the spatial average of the maximum probability of failure is respectively 0.20 and 0.19. For the first complex, the profile over the maximum slope of the landslide is rectilinear and the local probability varies with a maximum of 0.50 near the toe. For the second complex, the profile is more varied and the peaks in the local probability of failure higher. The maximum, again at the toe of the complex, amounts here to 0.96 (Figure 7.9). This suggests that undercutting has been an essential process for the lateral destabilisation of these slopes. The slopes fall just below the lower topographic threshold of the class of marginally susceptible slopes with overall angles of 13.6° and 12.2° . Subsequent activity on the steeper parts of these slopes may have led to the general development of a lower, residual, strength over time. According to IGME (1981), the residual friction angle can lower than 26° for the marls of the Alcoy region. This value equals the lower limit of the 95%-confidence interval of the peak angle of internal friction of 34.8° , which was used to define the susceptibility of Section 7.3.3.

If the landslide complexes near Almudaina are excluded from the calculation, the overall probability of failure for the observed landslide occurrence in the Barranco de la Coloma rises to 0.53, which is still influenced by the spurious observations of landslide occurrence. Of the total area of 30.9 ha of observed landslide occurrence, only 4% occurs in landslides for which the maximum probability of failure does not exceed $P(F \leq 1) = 0.5$. These landslides are, however, always bordered by cells that have been simulated to have failed. Consequently, they can be attributed to inaccuracies that arise due to the spatial resolution of the simulation and the landslide inventory. It can be concluded, therefore,

that the simulated failure replicates the observed spatial distribution of landslide occurrence but is not an exact estimator for the observed landslide density.

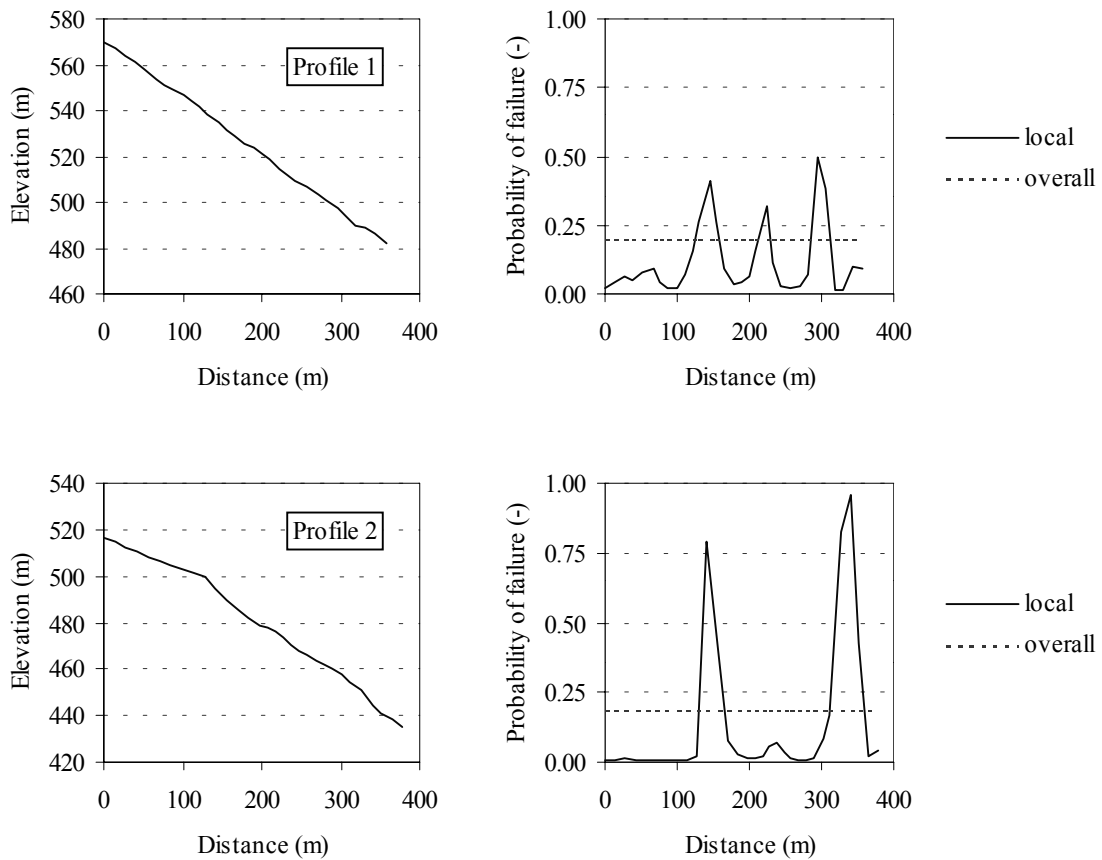


Figure 7.9: Probability of failure along profiles over the landslide complexes near Almudaina

The agreement between simulated failure and observed landslide occurrence is first of all the result of the modelled susceptibility. Although the model simulates first-time failure adequately, it must be concluded that this static threshold is unable to predict slope instability in areas where the susceptibility has changed as a result of persistent activity. This deficiency is particularly conspicuous in the case of the landslide complexes near Almudaina.

7.4.6 Temporal characteristics of simulated failure and observed landslide activity

The maximum probability of failure for the observed landslide occurrence is on average 0.43. This is significantly different from that of the area without landslide occurrence, which is only 0.17 ($Z = -3.14$, $P < 0.001$). Because of the overestimation of slope failure, however, there is little difference between the average of the maximum probability for the susceptible slopes $> 18^\circ$. For the area with landslide occurrence, the average amounts

to 0.87, compared to 0.82 for the slopes without landslide occurrence. These high values can be explained by the fact that the maximum probability of failure, as extreme, is sensitive to short-lived peaks in the simulated pore pressures, which are not necessarily representative for the hydrological triggering conditions.

It seems plausible that the likelihood of triggering increases when critical pore pressures are more frequent and persistent. Both the frequency and the persistence of critical pore pressures would be included implicitly if the average probability of failure for a locality over the entire validation period were used. However, this statistic is affected by the low value of the probability of failure for most of the time. Consequently, the overall values are low (respectively $P(F \leq 1) = 0.016$ and 0.008 for the unstable and stable areas) and the effect of persistence on slope failure is not readily discernible. For the unstable area, its value is largely determined by the more susceptible slopes for which the probability of failure is usually high and persistent. For the less susceptible slopes, for which the triggering pore pressures occur less frequently and persist over shorter periods, the determining influence is lost. Thus, the average probability of failure is of little use for the forecast of landslide activity.

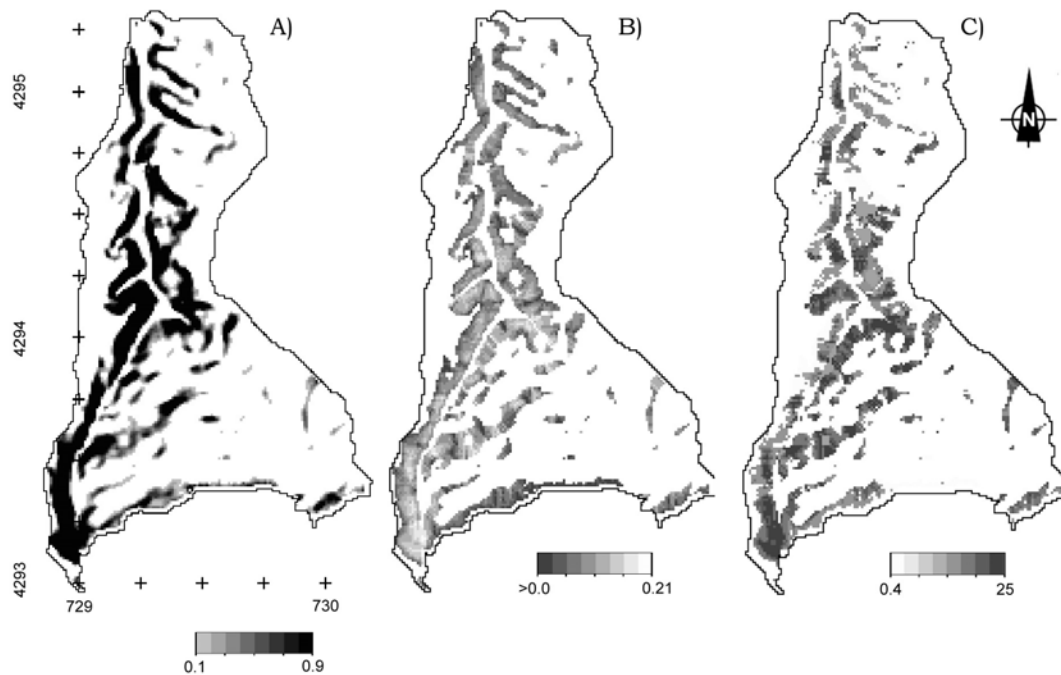


Figure 7.10: Temporal characteristics of simulated failure over the validation period: A) probability of failure (-); B) persistence (logarithmic scale; -); C) Recurrence interval (years)

The temporal characteristics of simulated failure are the persistence, recurrence interval and the average duration, which represents the combined effect of persistence and recurrence (Section 7.4.3). They represent the time that the pore pressure was above the critical level in the simulation. They are calculated from the number of timesteps or hydrological years that a pre-set level of the probability of failure in the range $0.1 \leq$

$P(F \leq 1) < 1.0$ is exceeded (Section 7.4.2). This range covers all slopes with a critical pore pressure ratio, $r_{u \text{ crit.}} \leq 1.0$, and the marginally susceptible slopes (*MS*).

The temporal characteristics have been compared directly with the observed landslide occurrence. This provides additional information to the comparison of the area of simulated failure and the observed landslide occurrence. To eliminate the absolute influence of the probability of failure, the temporal characteristics have been normalised with respect to its maximum over the validation period. So, the temporal characteristics represent the duration or frequency for which the probability of failure approached the maximum. The critical level has been set to the first decimal of the simulated maximum. For example, for a cell with a maximum probability of failure of 0.46, the level is set to 0.4. This level is not unbiased as it fails to take the relative decrease in class width into account. Still, it allows for the compilation of the temporal characteristics of simulated failure into single maps (Figure 7.10).

For the calculation of the temporal characteristics, the observed landslide occurrence for which no failure has been simulated has been ignored. This excludes the class of the non-susceptible slopes, *NS*, in its entirety and all susceptible slopes for which the probability of failure did not exceed the onset of $P(F \leq 1) = 0.1$. As a consequence, the total area under consideration is 48.4 ha of which 17.6 ha represent observed landslide occurrence ($ld = 0.36$).

The relation between landslide occurrence and the temporal characteristics of simulated failure is presented in Table 7.5. The observed landslide density has been calculated for different categories of the recurrence interval, persistence, and average duration of simulated failure and the modelled susceptibility. The more susceptible slopes have been grouped in a joint class $r_{u \text{ crit.}} \leq 0.75$. The susceptibility classes represent equal shares of the total area for which $P(F \leq 1) \geq 0.10$.

The landslide density generally increases with more frequent or persistent triggering conditions in the simulation. This trend is the least clear for the recurrence interval, which can be explained by the intervals used. For all susceptibility classes, the categories with high recurrence intervals, i.e. ≥ 5 years, represent more than 70% of the area under consideration. For the persistence and the average duration, the area is more evenly spread over the categories.

With respect to the recurrence interval, the more susceptible slopes, with $r_{u \text{ crit.}} \leq 0.75$, form an exception as the landslide density does not tend to increase with shorter recurrence intervals. All values are closely spaced around the mean landslide density of 0.49 for this class as a whole. However, a positive trend between landslide density and the persistence or duration of simulated failure is observed. For the category of the highest persistence ($\geq 3.93 \cdot 10^{-2}$ (-), $ld = 0.26$), the drop in landslide density is due to the exhaustion of the soil mantle. These slopes have also the longest simulated duration and exhaustion explains the relatively low landslide density for the category ≥ 25 days in the class $r_{u \text{ crit.}} \leq 0.75$.

For the individual susceptibility classes, the like increase in landslide density implies that the attempt to standardise temporal characteristics for the maximum probability is

successful. The relation between the simulated temporal characteristics of Table 7.5 and the observed landslide density implies that the likelihood of landslide occurrence increases, regardless of the absolute level of the simulated probability of failure.

Table 7.5: Observed landslide density as a function of the recurrence interval, persistence and average duration of simulated failure per susceptibility class

Temporal characteristics, lower limits	MS	$1.00 \geq r_{u \text{ crit.}} > 0.75$	$r_{u \text{ crit.}} \leq 0.75$	All susceptible slopes
<i>Recurrence interval</i>				
≥ 12 years	0.21	0.32	0.51	0.34
≥ 5 years	0.24	0.32	0.46	0.33
≥ 3 years	0.33	0.44	0.50	0.42
≥ 2 years	0.49	0.42	0.48	0.47
> 0 years	0.62	0.48	0.46	0.51
<i>Persistence (-)</i>				
$\geq 4.54 \cdot 10^{-5}$	0.08	0.23	0.14	0.16
$\geq 2.46 \cdot 10^{-4}$	0.19	0.30	0.42	0.29
$\geq 1.33 \cdot 10^{-3}$	0.33	0.40	0.51	0.42
$\geq 7.23 \cdot 10^{-3}$	0.48	0.48	0.57	0.53
$\geq 3.93 \cdot 10^{-2}$	0.84	0.58	0.26	0.58
<i>Average duration (days)</i>				
> 0	0.08	0.20	0.23	0.16
$\geq 2\frac{1}{2}$	0.20	0.33	0.40	0.29
≥ 5	0.30	0.41	0.44	0.39
≥ 10	0.45	0.45	0.54	0.50
≥ 25	0.60	0.58	0.60	0.60
<i>Spatial distribution (48.4 ha = 100%)</i>				
Simulated area (%)	33	35	32	100
ld per class (-)	0.27	0.34	0.49	0.36

Apparently, the temporal characteristics of simulated failure mimic the effect of frequent or persistent hydrological triggering conditions on landslide occurrence. The validity of the simulated hydrological triggering mechanisms could be determined if the temporal characteristics of the observed landslide activity and those of simulated failure could be compared directly. However, because of the poor temporal resolution of the landslide inventory, such a direct comparison is not possible. The only possible comparison is that of Table 7.4, which relates the area of simulated failure to the observed landslide occurrence at different moments in the validation period (see also Section 7.5).

Alternatively, the observed reactivation has been used as an approximation of the temporal activity of landsliding. A comparison of the reactivation with the persistence of simulated failure provides an indirect test of the hypothesis that the simulated hydrology explains the observed landslide activity. It is expected that the fraction of reactivation, R , will increase with the persistence. Falsification of the null-hypothesis that R is constant for the entire range of the simulated persistence would make it plausible that the

simulated hydrology represents the triggering pore pressure conditions to some degree. The null-hypothesis is evaluated by means of a χ^2 -test.

Table 7.6: Chi²-test for relation between simulated persistence and observed reactivation. H₀: fraction of reactivation is independent of simulated persistence. Two degrees of freedom are lost from N, the number of persistence classes, to complement the total number of observations and to estimate R from the data.

Susceptibility, $r_{u,crit}$	MS	1.00 - 0.75	0.75 - 0.50	0.50 - 0.25	0.25 - -0.10
Occurrence (m ²)	42900	57750	41300	23975	9950
Reactivation, R (%)	50	64	70	66	86
N	5	5	5	4	4
χ^2	29.21	22.95	8.72	17.81	4.06
$\chi^2(\alpha=0.05)$	7.81	7.81	7.81	5.99	5.99
Probability	$2 \cdot 10^{-06}$	$4 \cdot 10^{-05}$	0.03	$1 \cdot 10^{-04}$	0.13

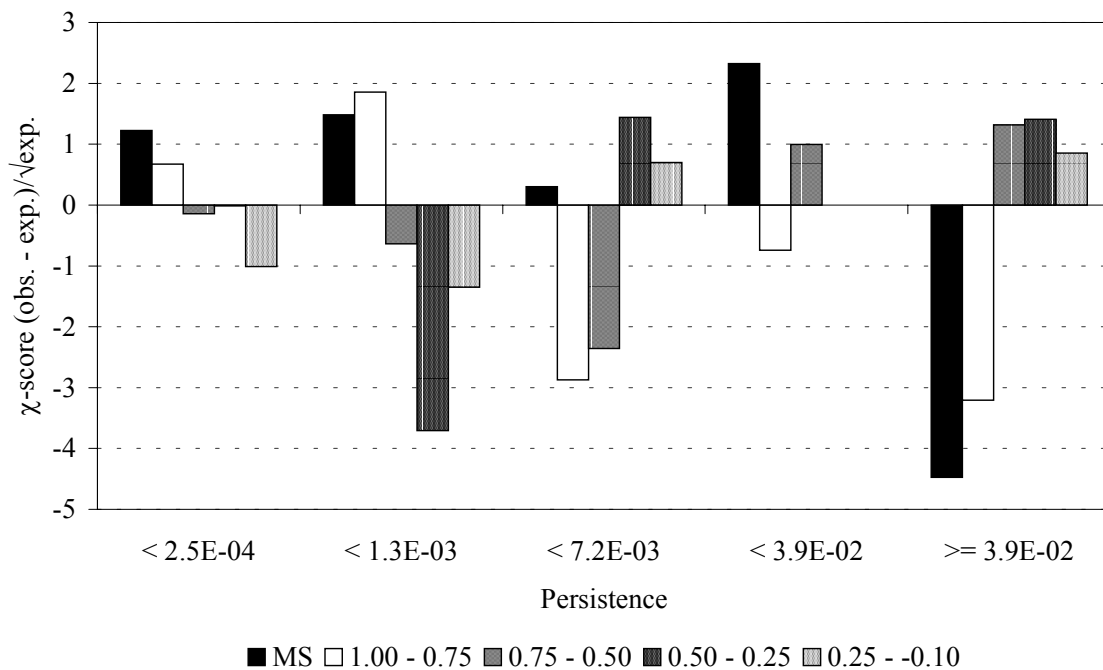


Figure 7.11: Chi-gram of the comparison between the observed and expected reactivation relative to persistence for 5 classes of susceptibility (see Table 7.5)

The distribution of the persistence is approximately lognormal when all areas are excluded for which the simulated persistence is zero. The range of the persistence between $5 \cdot 10^{-5}$ to 0.21 (-), has been subdivided into equal classes using the lognormal distribution of Table 7.5. To eliminate the dominant effect of susceptibility, the data have been analysed separately for the classes of Table 7.2. The χ^2 -test has been based on the number of cells rather than the area they represent. The results of the χ^2 -test for the five susceptibility classes are summarised in Table 7.6. The χ -gram of Figure 7.11 shows the tendency per susceptibility class. In this graph, the χ -scores are plotted for which

negative values signify an overestimation and positive values an underestimation of the observed reactivation by the expected values.

The null-hypothesis should be rejected at the 0.05 significance level for all classes except for the most susceptible slopes (Table 7.6). For this class an increase in reactivation is observed with increasing persistence (Figure 7.11), but the null-hypothesis can not be rejected. This implies that the simulated hydrology is of limited influence on the triggering of the steepest slopes since the required rise in pore pressure to trigger these slopes is absolutely small and readily exceeded. This conclusion is supported by the high proportion of reactivated landslides for this category (86%).

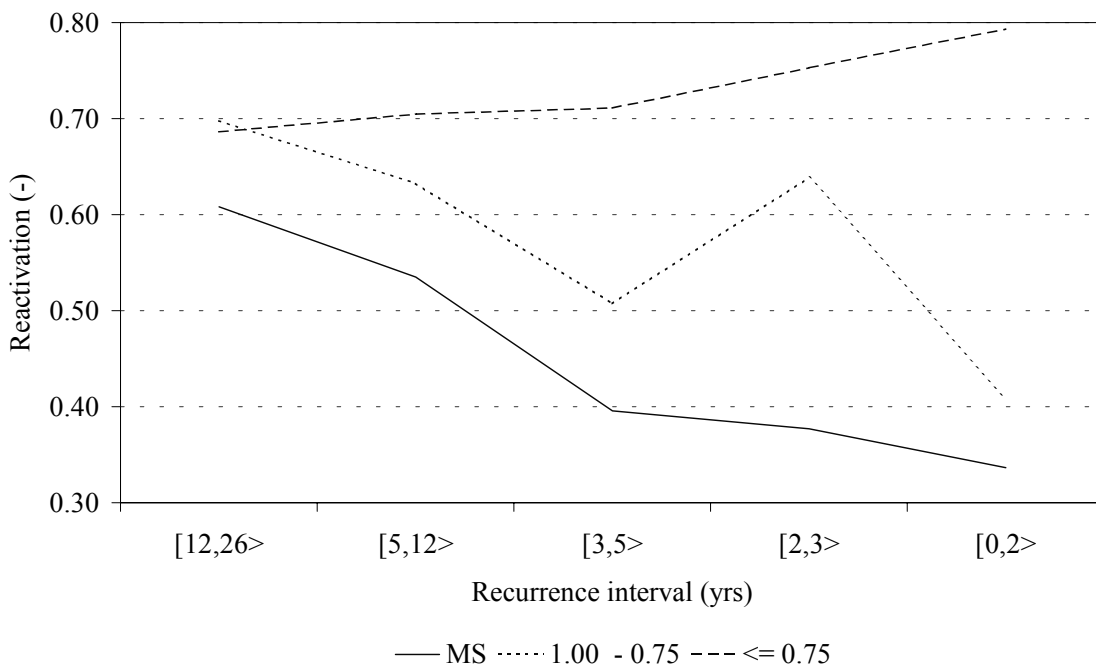


Figure 7.12: Relation between observed reactivation, R , and simulated recurrence intervals per susceptibility class

For the classes between $0.75 \geq r_{u \text{ crit.}} > 0.25$, the χ -score complies with the expectation (Figure 7.11); the constant fraction of reactivation, R , underestimates the observed reactivation for the classes with a higher persistence. However, for the less susceptible slopes contained by the classes MS and $1.00 \geq r_{u \text{ crit.}} > 0.75$, the tendency is contrary to the expectation and reactivation is preferentially associated with the classes of lower persistence. This can be explained by the relatively large increase in pore pressure that is required to trigger these slopes. Consequently, reactivation is associated with high recurrence intervals for the classes MS and $1.00 \geq r_{u \text{ crit.}} > 0.75$ (Figure 7.12). The proportion of reactivation, R , increases more strongly with the average duration for the highest recurrence interval (≥ 12 years) than for all recurrence intervals combined (Figure 7.13). In contrast, reactivation is negatively proportional to the recurrence interval for the remaining susceptibility classes with $r_{u \text{ crit.}} \leq 0.75$ as triggering pore pressure conditions occur more often (Figure 7.12). Thus, the persistence reflects

primarily the recurrence interval for the more susceptible slopes. The relation between the proportion of reactivation and the average duration does not change markedly between the different recurrence intervals (Figure 7.13).

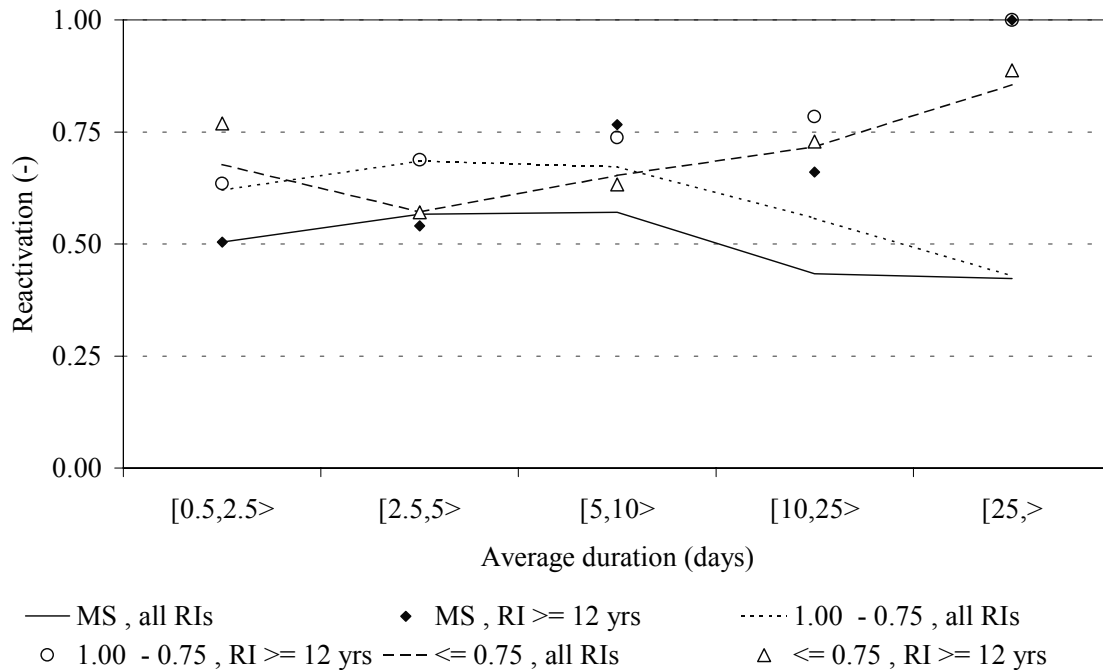


Figure 7.13: Relation between observed reactivation, R, and simulated average duration and recurrence interval, RI, per susceptibility class

The conclusion is that the temporal characteristics of simulated failure reflect the causal relationship between the persistence of critical pore pressure conditions and landslide activity for which the observed reactivation was used as a proxy. Thus, coupled hillslope models simulate the influence of persistent hydrological triggering conditions on landslide activity in an explainable way.

The temporal characteristics are based on the probability of failure. Whereas the probability of failure can be regarded as a direct estimator of landslide occurrence, the temporal characteristics can only provide information for slopes that are modelled to be susceptible (Section 7.3.3). An additional disadvantage is that the temporal characteristics are indissolubly linked to the validation period through its length and the incidence of potential triggering rainfall events. Therefore, extrapolation of the landslide density on the basis of the temporal characteristics of simulated failure will result in flawed estimates of landslide occurrence. Notwithstanding, they can be used as relative indicators of landslide activity as they provide valuable information on the role of persistent triggering conditions that is not included in the maximum probability of failure. The average duration appears to be a reasonable measure for the effect of the hydrology as it disconnects the total duration from the recurrence of potential triggering events over the period under consideration. The relationship between landslide activity and the temporal characteristics of simulated failure, as evidenced by Table 7.5, is

therefore an essential means to assess the influence of changing environmental conditions on the temporal sensitivity of the landscape to landsliding.

7.5 Influence of the calibrated hydrological parameter k_r on simulated failure

The only temporal comparison possible, as represented by the sub-periods of Table 7.4, reveals that the performance of the coupled hillslope model for any of these sub-periods is poorer than that based on the occurrence over the entire validation period alone. In addition to the insufficient temporal resolution of the landslide inventory, the poor performance can be explained by errors in the simulated pore pressure conditions (see also Section 6.3). Temporal variations in susceptibility that are neglected as a result of the steady-state assumption provide an additional explanation although the resulting error can be presumed to be small relative to the errors in the simulated hydrology.

For the period before 1973, the poor model performance might be acceptable as not all of the triggering rainfall might be included. After 1973, however, it must be evaluated as part of the validation of the coupled hillslope model. A possible explanation for the observed model performance lies in the simulated hydrology, which is influenced by the calibrated parameters. These parameters are the reduction of the reference potential evapotranspiration, k_r , and the matric suction of the infinite bedrock store, $|h|_{BC}$.

The calibrated parameters are representative for the present conditions and it was demonstrated that they remain equally applicable to limited changes in climate and land use conditions (Section 6.4). However, this concerns the average annual totals of rainfall and reference potential evapotranspiration. Interannual variability in these meteorological variables could lead to large deviations in the annual totals of the net rainfall that through the calibrated variables affect the performance of the coupled hillslope model to simulate landslide activity. Since the hydrological model component STARWARS, is the most sensitive to the parameter k_r (Section 6.1), its calibrated value will have the largest influence on the validity of the coupled hillslope model.

The influence of the calibrated parameter k_r can be evaluated by relating the meteorological input over the validation period to the observed landslide activity and the simulated failure. From this information, the limits of its validity can be defined. Eventually, these limits can be used to ascertain that the validity of k_r is not violated by the synthetic weather series that are used in the Scenario Modelling (Chapter 8).

The validation of the hydrological model component demonstrated that the simulated hydrological response is attenuated after periods of drought. Furthermore, the simulated groundwater levels lag with the observations (Section 6.3). Both problems could result in erroneous predictions of simulated failure for the closely spaced observations of 1989 and 1994. From the late 1970s till the middle of the 1980s, rainfall was well below average. This period of prolonged drought ended with extreme rainfall in 1986 (Figure 7.14). With the sustained rainfall in the hydrological years of 1987 and 1988, this period of above-average rainfall is likely to explain the observed landslide occurrence in the air photograph of 1989. However, the simulated failure falls well short of the observed landslide occurrence, which is represented as the total over the period preceding the flight of 1989 (Figure 7.14). The actual pore pressures that triggered the instability

observed in the air photograph of 1989 are not reached in the simulation, which can be attributed to the accumulated soil moisture deficit that has built up in the model over the precursory drought.

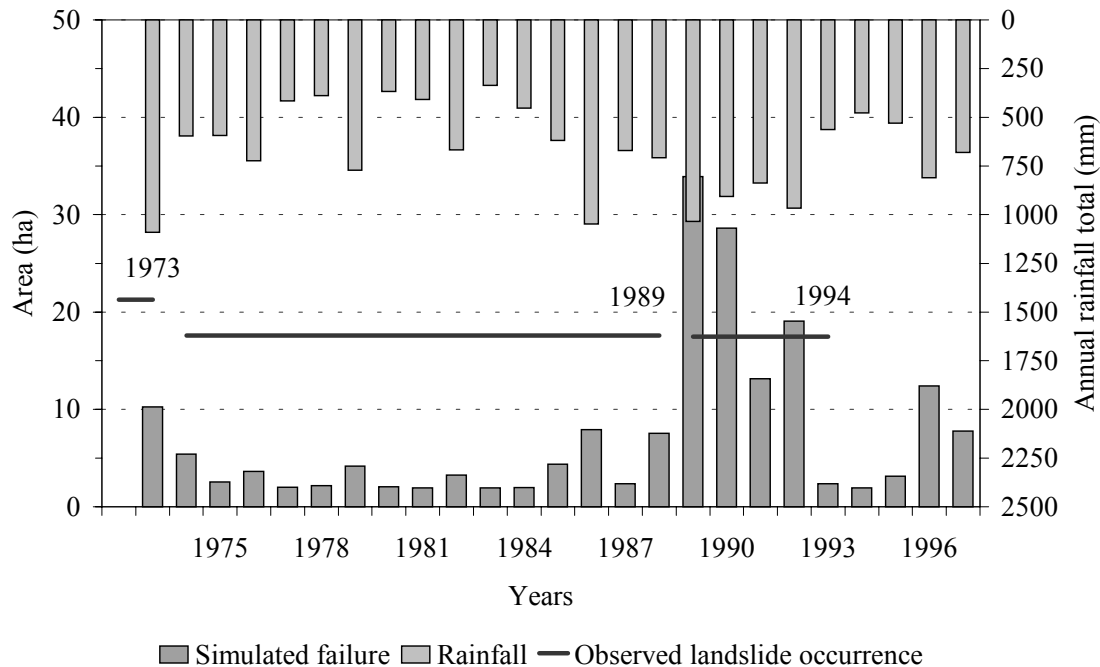


Figure 7.14: Total rainfall, area of observed landslide occurrence and simulated failure per year

Although the rainfall totals of 1990 and 1991 are similar to that of 1986, the amount of simulated failure is much higher (Figure 7.14). The area of simulated failure exceeds that of observed landslide occurrence and, in contrast to 1989, the mismatch is mainly due to the category with simulated failure only (Table 7.4). This period covers the hydrological years during which landsliding appeared to be the most frequent (La Roca, 1992).

The influence of antecedent rainfall appears to be due to higher moisture contents that favour the generation of perched water tables for the hydrological year under consideration. The rainfall deficit over summer has a levelling influence on any perched water tables, which is underlined by the fact that simulated failure does never extend beyond the limits of the hydrological year. There is little evidence that the antecedent rainfall affects the area of simulated failure on an annual scale. Over the validation period, the annual rainfall total explains 0.47 and 0.63 of the variance in the area of simulated failure in respectively linear and exponential relationships. These values do not change appreciably if the rainfall over the preceding hydrological years is included or when the period from 1986 until 1994 is considered separately. So, it can be concluded that the time lag in the simulated ground water levels has no significant influence on the simulated failure on an inter-annual scale and does not explain the poor performance of the model for the sub-periods.

The amount of simulated failure over the period after 1994 is erroneous as only an insignificant number of small landslides occurred. This overestimation can be explained by the rainfall characteristics for this period (see also Section 4.2.4). Although rainfall totals are close to the average for the years 1995-1997 (respectively 529.1 mm, 810.1 mm and 679.9 mm), the number of raindays exceeds the annual average of 38 days (respectively 51, 58 and 45 days). This results in small but numerous rainfall events, which are distributed evenly over the seasons. They apparently favour the generation of critical groundwater levels in the simulation but their occurrence is not witnessed by any substantial activity over this period. Although the conditions were near-critical in the year 1996-1997, the extreme rainfall that would have been required to lead to substantial landslide activity in the Barranco de la Coloma did not happen.

It can be concluded that the antecedent moisture conditions are the major source of error in the simulated hydrology that explains the poor agreement between observed landslide activity and the simulated failure. The influence of droughts is more serious than that of periods of above-average or persistent rainfall as the former leads to an underestimation of landslide activity.

The parameter k_r has a direct influence on the antecedent moisture conditions and accounts for the disparity between observation and simulation. Therefore, the calibrated value of k_r is not representative for the actual evapotranspiration that occurred during the drought of 1977-1985 and the validity of the calibrated hillslope model under such conditions can be questioned.

During the drought of 1977-1985, the average rainfall total was 492 mm over nine consecutive hydrological years. Over the entire validation period, 26% of rainfall totals do not exceed this amount of 492 mm. Based on a gamma-distribution of the annual rainfall totals, the probability of such a year is slightly lower with 21%. According to this distribution, the likelihood of a drought similar to the event of 1977-1985 is once every 377 years. So, such extreme droughts are relatively rare although this likelihood ignores the possibility that their occurrence is the result of an anomalous climatic situation of a higher incidence. Notwithstanding, the statistical probability is applicable to the stochastic weather generator, which provides the meteorological input for the scenario modelling. The average length of a drought of equal or less rainfall than 492 mm per year is 4 years for the duration of validation period (recurrence interval of once every 29 years). The calibration and validation of the hydrological model component STARWARS demonstrated that the hydrological response was not severely affected by droughts of this length and intensity (e.g. the years 1993-1995, see Section 6.3). Therefore, the conclusion is that the calibrated value of k_r only limits the validity of the coupled hillslope model for periods of extreme drought. Therefore, its performance to simulate slope failure will generally not be violated by the meteorological input of the scenario modelling.

7.6 Environmental conditions

For a meaningful forecast of landslide activity under hypothetical land use conditions, it is essential that the coupled hillslope model simulates failure consistently for the land use units of the present configuration (see also Section 5.2).

In the validation of the model performance with respect to land use, a complication arises as land use itself is conditioned by the slope angle. This is reflected in the susceptibility of the different land use units, which has been expressed as the critical pore pressure ratio, $r_{u \text{ crit.}}$ (Figure 7.15). The gentlest and consequently the least susceptible slopes are the preferred localities for cultivation (unit I). For this unit, 78% of the area coincide with slopes that are modelled as non-susceptible (*NS*). Because of their steepness, the most susceptible slopes are deemed unsuitable for cultivation. They are mainly abandoned or covered with semi-natural vegetation (respectively units III and IV). There is little difference between these units in terms of susceptibility. Respectively 64% and 65% of these units cover susceptible or marginally susceptible slopes. More recently abandoned slopes (unit II), however, are less susceptible and they occupy an intermediate position between the cultivated area and the semi-natural slopes.

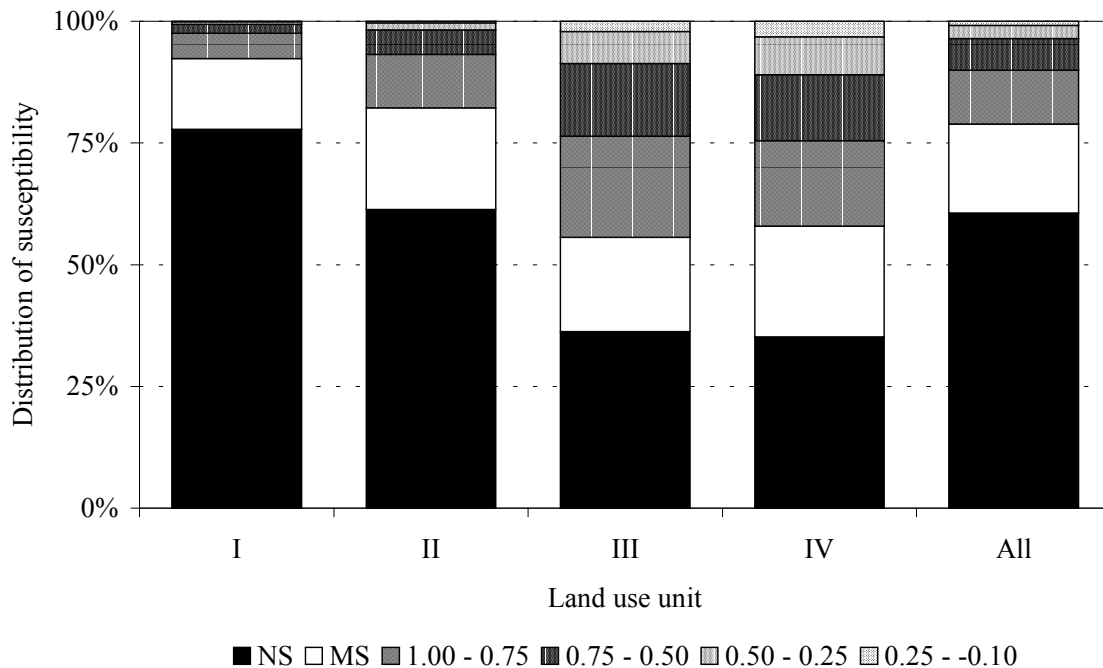


Figure 7.15: Distribution of susceptibility in relation to land use. See text for explanation

Only the marginally susceptible slopes (*MS*) are more or less equally frequent for all land use units (between 15% and 23%). Combined with the difference in size (Table 7.7), the area of the class *MS* roughly is twice as large for the land use units I and II than for the units III and IV. For the susceptible slopes, with $r_{u \text{ crit.}} \leq 1$, the absolute representation is more equal for the various land use units. The model performance can thus be compared for the various land use units. Moreover, the findings can be extrapolated to the changed

land use configurations of the scenario modelling if the imposed changes do not depart from the present distribution of susceptibility. Because of the fair distribution of susceptibility over the land use units this condition is easily met as long as cultivation is kept confined to the gentler slopes.

Table 7.7: Total area, landslide density and reactivation in relation to land use

Land use unit	Area (ha)	Area (%)	Landslide density (-)	Reactivation (-)
I Cultivated	62.7	41	0.08	0.36
II Abandoned – grass and herbs	46.2	30	0.14	0.54
III Abandoned – shrubs	27.4	18	0.39	0.60
IV Semi-natural vegetation	17.5	11	0.51	0.63
All units	153.7	100	0.20	0.56

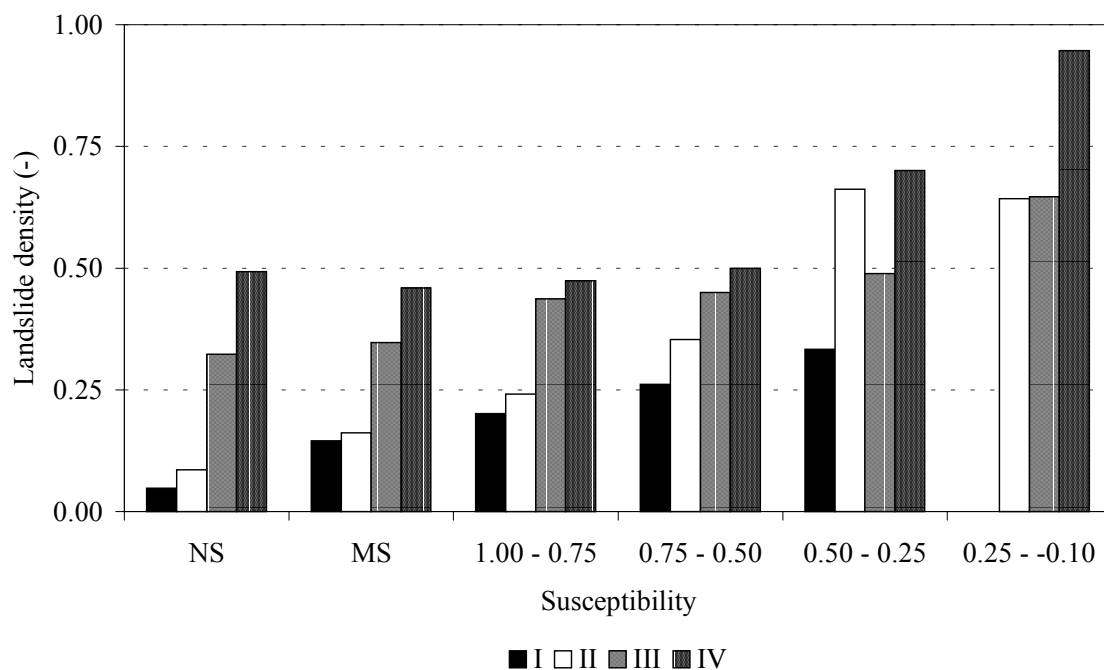


Figure 7.16: Landslide density in relation to modelled susceptibility, expressed by the critical pore pressure ratio, per land use unit

The landslide activity corresponds to the susceptibility of the different land use units (Table 7.7). Clearly, the presently cultivated area is the least sensitive to triggering rainfall as the observed landslide density, ld , is only 0.08 over the validation period, compared to 0.20 for the Barranco de la Coloma as a whole. Slopes with semi-natural vegetation have the highest landslide density ($ld= 0.51$). A similar relation is found for

the reactivation, which is more common under semi-natural vegetation than under any other land use type.

The observed difference in landslide activity, however, is not merely caused by the difference in susceptibility, as it is reflected by the respective susceptibility classes (Figure 7.16). The conclusion is, therefore, that the hydrological response is different for the land use units and results in a different temporal sensitivity to potential triggering rainfall events; independent of the susceptibility, slopes under cultivation are the least sensitive to landsliding whereas those under semi-natural vegetation are the most sensitive. Thus, the role of the hydrology in the triggering of landslides must be simulated adequately under the different land use conditions.

The distribution of landslide occurrence over the different categories of susceptibility and land use units affects the model performance as calculated by Equation 7.3. For the land use units I and II, the model performance is below the value for the entire Barranco de la Coloma over the validation period (Table 7.8). This poorer model performance can be attributed to the low sensitivity of these land use types to landsliding. For the less susceptible slopes, the observed landslide density is underestimated by the probability of failure. This particularly applies for Unit II. The model performance is also impaired by the overestimation of the landslide occurrence in the classes with $1.00 \geq r_{u \text{ crit.}} > 0.50$, which affects both units (see Figure 7.7).

Table 7.8: Model performance per land use unit

Land use unit	I	II	III	IV	All
Model performance (%)	37.1	36.1	42.1	42.7	41.2

For the units II and IV, underestimation of landslide occurrence in the class *NS* also impairs the model performance. However, due to the better performance for the higher susceptibility classes that contain a larger share of the observed landslide occurrence, the model performs above average and exceeds the overall value of 41.2%.

The discrepancies between observed landslide occurrence and simulated failure arise partly because the maximum probability of failure does not account for the persistence or recurrence of critical pore pressure conditions (Section 7.4.6). These temporal characteristics are basic measures for the simulated hydrological response and are evaluated in relation to land use.

The temporal characteristics of simulated failure are based on the range $P(F \leq 1) \geq 0.10$. Consequently, all areas for which the maximum probability of failure did not exceed this level have been excluded. This corresponds with the susceptibility class *NS* in its entirety and some of the areas for which the modelled susceptibility is low ($r_{u \text{ crit.}} > 0.50$). The resultant changes in the total area under consideration, model performance, *mp*, and observed landslide density, *ld*, are listed in Table 7.9. Because of the exclusion of the class *NS*, for which landslide occurrence is underestimated, the model performance increases for all landslide units. This class has relatively a large influence on the model performance for the units III and IV and the consequent increase in model performance is

larger than for the units I and II. Of the total area of observed landslide occurrence, 57% is considered in Table 7.9.

Table 7.9: Area used for the calculation of the temporal characteristics of simulated failure with consequent changes in landslide density and model performance

	Land use unit			
	I	II	III	IV
<i>Total area: 153.7 ha</i>				
ld (-)	0.08	0.14	0.39	0.51
mp (%)	37.1	36.1	42.1	42.7
<i>Area $P(F \leq 1) \geq 0.10$: 48.4 ha</i>				
ld (-)	0.21	0.26	0.44	0.54
mp (%)	37.6	41.0	53.1	60.8
Area (%)	15	29	56	56
Occurrence (%)	43	53	64	58

With respect to the temporal characteristics of simulated failure, it is interesting that the recurrence interval is not related to the observed landslide density for the land use units III and IV. These units cover most of the more susceptible slopes, for which a similar behaviour was observed in Section 7.4.6. This implies that for these units, persistence of simulated failure following a triggering event is a better indicator of landslide occurrence than frequency. This becomes apparent from the average duration that has been listed for the respective land use units in Table 7.10.

For the units III and IV, the storage capacity and permeability of the topsoil, which are higher than for the other units, could explain the persistence of the critical pore pressures. They allow for a rapid transfer of infiltration to the lithic contact when rainfall surplus is large. In the lower layers, the permeability decreases and the slower lateral drainage of the accumulated water result in persistent perched water tables. Since the steeper, more susceptible slopes under these types of vegetation require only a small absolute rise to be triggered, this mechanism could account for the simulated behaviour. On less susceptible slopes, the required absolute increase in pore pressure conditions is larger. Consequently, it becomes less likely that the threshold is exceeded as more water is lost to evapotranspiration under the denser vegetation cover of the land use units III and IV.

Table 7.10: Relative frequency, F, of total area (100% per land use unit) and observed landslide density, ld, in relation to the average duration of simulated failure

Land use unit	I		II		III		IV	
	F (%)	ld (-)	F (%)	ld (-)	F (%)	ld (-)	F (%)	ld (-)
> 0 days	25	0.03	22	0.13	14	0.29	11	0.24
$\geq 2\frac{1}{2}$ days	25	0.17	27	0.17	24	0.43	18	0.41
≥ 5 days	24	0.24	27	0.31	26	0.45	27	0.53
≥ 10 days	22	0.37	22	0.41	29	0.50	35	0.65
≥ 25 days	4	0.54	3	0.59	7	0.50	8	0.77

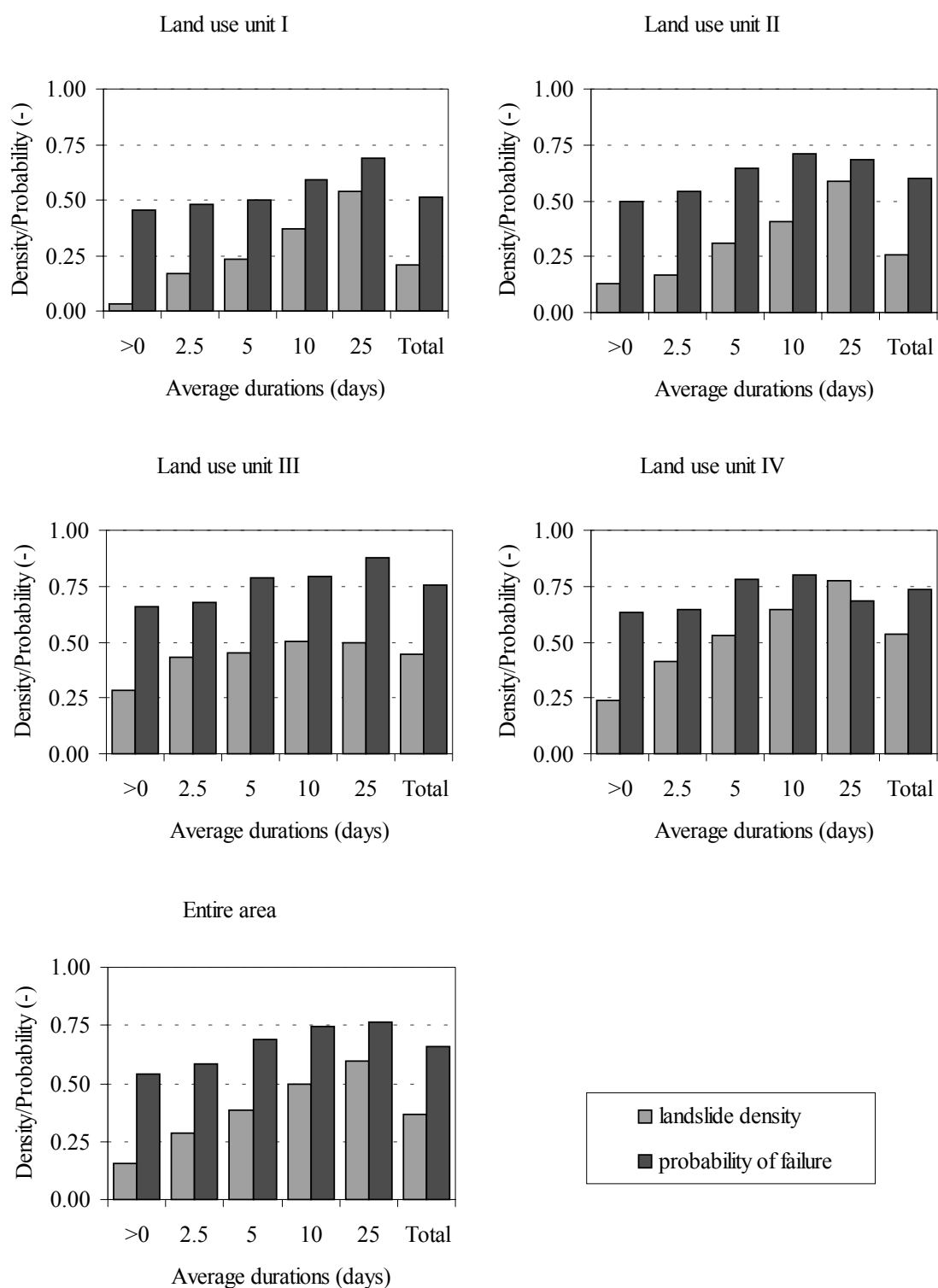


Figure 7.17: Spatial average of the maximum probability of failure and observed landslide density per land use unit in relation to the average duration of simulated failure (entire area $P(F \leq 1) \geq 0.10$)

For the land use units I and II, the observed landslide density is lower and a larger part of the area $P(F \leq 1) \geq 0.10$ falls in the categories that represent a lower average duration. For unit II, this lower average duration corresponds to longer recurrence intervals. This indicates that the required increase in pore pressure for failure is not easily achieved and the associated peaks persist only for a short time. For unit I, however, critical pore pressures recur frequently but do not persist. A possible explanation for the rapid hydrological response in the simulation is the seasonal fluctuation in the crop factor (Section 5.2.4). Over winter, the dormancy of the fruit trees reduces the actual evapotranspiration and the antecedent moisture conditions become more favourable for percolation. Yet, because of the lower permeability of the topsoil, the amount of infiltration and the subsequent accumulation along the lithic contact are insufficient to raise the pore pressure conditions above the threshold for a prolonged period. In the spring, the increased evapotranspiration rapidly reduces the antecedent moisture content and the favourable conditions for the generation of a perched water table are lost.

The simulated hydrology thus accounts for the observed differences in frequency and landslide density between the land use units. The standardised temporal characteristics of simulated failure, however, can not explain the observed difference in landslide density, which depends on the absolute level of the pore pressure conditions.

To analyse this relation, the spatial average of the maximum probability and the observed landslide density have been compared for each land use unit (Figure 7.17 and Table 7.11).

Although the observed landslide density is consistently overestimated for the area $P(F \leq 1) \geq 0.10$, it is positively related to the maximum probability of failure (Table 7.11). Land use unit IV has the poorest correlation between landslide density and the probability of failure, which can be attributed to the fact that the observed landslide density is higher than the probability of failure ($\rho = 0.54$). For the other units, the correlation is in excess of 0.80.

Table 7.11: Regression of the data of Figure 7.17

Land use unit	Intercept, Y_0 (-)	Slope, α (-)	R^2 (-)
I	0.41	0.48	0.95
II	0.48	0.44	0.77
III	0.40	0.83	0.65
IV	0.60	0.20	0.29
All	0.45	0.55	0.95

Because of the overestimation, the regression of the probability of failure on the landslide density returns an intercept for all land use units. This intercept, which is the probability of failure at which $ld = 0$, varies between 0.40 and 0.60. This value only applies to the area $P(F \leq 1) \geq 0.10$, for which landslide occurrence is overestimated. It implies that estimates of landslide occurrence based on the average duration and the probability of failure result in a structural but similar error that is independent of the land use conditions. Therefore, it can be used to assess the changes in landslide activity under

altered land use conditions for this area. However, it does not consider the model performance for the area $P(F \leq 1) < 0.10$. The overall model performance is influenced by the observed landslide occurrence in the susceptibility class *NS*, for which no failure can be simulated. This class includes a similar fraction of the observed landslide occurrence for each land use unit, ranging between 36% and 57% (Table 7.9). A similar fraction will probably be underestimated by the forecast of landslide occurrence in the Scenario Modelling. So, the inherent underestimation and overestimation of the actual landslide occurrence by the simulated failure prevent an assessment in quantitative terms of the landslide activity under the imposed changes. Yet, this does not impair the capacity of the calibrated hillslope model to assess the consequences of changes in climate or land use for the relative landslide activity in the study area.

7.7 Summary and conclusions

The susceptibility of the area to slope failure can be expressed by means of the critical pore pressure ratio. The critical pore pressure ratio results in a cut-off, the topographical threshold, at which complete saturation is insufficient to induce failure. By means of a probabilistic analysis, marginally susceptible slopes can be included that increase the amount of observed landslide occurrence that can be matched with simulated failure. The probabilistic version of the infinite slope model, *PROBSTAB*, includes 64% of the observed landslide occurrence that occur at slopes above 14° . By excluding spurious observations of landslide occurrence and the area for which the modelled susceptibility is erroneous, this fraction increases to 73%. The small overestimation in the modelled susceptibility arises because the soil cover is already exhausted in some areas.

The susceptibility does not include the effect of the hydrology on landslide activity and a dynamic simulation of the hydrology is required to simulate the temporal activity of landsliding. The temporal activity is partly mimicked but the coupling does not alleviate the observed discrepancies between the observed activity and the simulated failure. It overestimates the observed landslide occurrence on the more susceptible slopes over the validation period. The estimated soil depth appears to be a crucial factor in the overestimation through its influence on the modelled susceptibility and the simulated hydrological response.

The overestimation arises from the use of the maximum probability of failure, which, as extreme, is sensitive to short-lived peaks in the simulated pore pressure conditions. The temporal characteristics of simulated failure provide additional information that can be used as an indicator to assess landslide activity.

The observed landslide occurrence is underestimated on the non-susceptible and marginally susceptible slopes. The landslide complexes near *Almudaina* account for a large share of this underestimation. Here, the undercutting leads to lateral destabilisation of the slope and probably a loss of shearing resistance after prolonged displacement. The static susceptibility and the one-dimensional nature of the slope stability model can not accommodate these processes.

Because of the disagreement of the probability of failure with the observed landslide density, the simulated probability of failure is not an exact estimator for landslide

occurrence. Notwithstanding, the coupled hillslope model is capable to simulate the spatial distribution of landslide occurrence adequately.

Although the hydrology is simulated adequately, the model suffers from prolonged droughts such as that of 1977-1985. Consequently, it fails to attain the observed landslide occurrence over the period 1986 and 1989. Thus, the calibrated parameter k_r , the reduction factor for the reference potential evapotranspiration, is not representative for the true evapotranspiration over such periods. Such droughts are, however, extreme and unlikely to affect the Scenario Modelling as the meteorological input is parameterised by statistical distributions.

Differences in the temporal sensitivity of the different land use units to triggering rainfall events are reproduced by the coupled hillslope model. Thus, it can be extrapolated and applied to the scenarios of the Chapter 8. The assessment of landslide activity from the scenarios, however, is subject to structural errors. These errors arise from the discrepancy between the probability of failure and the observed landslide density and the landslide occurrence in the class of non-susceptible slopes for which failure can not be simulated. Consequently, only relative assessments of the changes in landslide activity under the impact of climate and land use change can be made on a regional scale.

8 ASSESSMENT OF THE TEMPORAL SENSITIVITY TO LANDSLIDING UNDER CHANGED ENVIRONMENTAL CONDITIONS BY MEANS OF SCENARIO MODELLING

8.1 Introduction

In the study area of the Barranco de la Coloma, land use is mainly agricultural (Section 2.4). Over the past century, this agricultural land use has adapted itself to the changing socio-economic demands as reflected in market prices and agricultural policy, to the improved technology and to the availability of natural resources. It is plausible that land use will continue to change although scenarios that describe these changes are entirely hypothetical (Section 8.2). These scenarios can be used to evaluate the effects of land use change on landslide activity under the present climate and under the expected elevated temperatures at the moment of CO₂-doubling (2·CO₂).

The impact of the environmental changes that are imposed by these hypothetical scenarios is evaluated on the basis of the model results. The Scenario Modelling simulates the hydrology dynamically over periods that are sufficiently long to represent the temporal variability in potential triggering rainfall events (30 years). The simulated hydrology is calculated for a static land use configuration and coupled to a constant susceptibility to landsliding (Section 7.3). Under the assumption that the present susceptibility is inherited under new environmental conditions, model results for the respective scenarios are used to assess the change in the temporal sensitivity of the study area to landslide activity.

The first section of this Chapter, Section 8.1, considers the development of possible land use scenarios. Section 8.2 treats the analysis of the rainfall characteristics of the synthetic weather series for the present 1·CO₂- and future 2·CO₂ climates that have been applied in the Scenario Modelling. There are three purposes for this analysis. Firstly, it is intended to establish whether the two synthetic rainfall series are mutually comparable in terms of potential triggering rainfall events. Secondly, the rainfall characteristics of the synthetic weather series should be similar to those of the validation period for the same reason. Thirdly, extreme droughts, which violate the validity of the calibrated model through the simulated actual evapotranspiration (Section 7.5), should be avoided.

To establish whether the results of the Scenario Modelling reflect the true landslide activity, the model outcome of the scenario reflecting the present land use and climate is related to that for the validation period in Section 8.3. In Section 8.4, the simulated landslide activity for the various scenarios is presented as a measure for the temporal sensitivity of the study area to landsliding. In this section, the possible explanations for the observed differences between the scenarios are also presented before the implications and limitations of the outcome of the Scenario Modelling are discussed in Section 8.5. In Section 8.6, the conclusions of this Chapter are summarised.

8.2 Development of land use scenarios

Given the socio-economic constraints and production limitations, changing land use aims – at the farm level - at maximising the profitability of agricultural practices. The resulting changes in land use and agricultural practices are subject to the perception of the individual farmer and to cultural patterns. It is this combination of large- and small-scale processes that makes land use change difficult to foresee. It clearly surpasses the scope of this modelling exercise to forecast future land use changes in the study area but realistic land use scenarios are needed. Under this consideration, it appears reasonable to assume that the same processes, which led to land use change in the past, will be reflected in future, altered land use conditions. Recapitulating the processes mentioned in Chapters 1 and 2, these are

- Mechanisation;
- Reduced importance of agriculture as the primary source of sustenance;
- Absolute population decrease and rural exodus;
- Globalisation and agricultural policy on the national and European level.

Changes in land use are generally gradual. A recent exception occurred when the altered geo-political situation of the Cold War ended abruptly the period of enforced autarky under Franco's regime during and after World War II. Consequently, the intensive land use, extending cultivation even on marginal land, was rapidly abandoned in favour of the more profitable production of fruits and olives that covers nearly all presently cultivated fields. Changes of this kind are unlikely to occur and certainly impossible to predict. Furthermore, it can be expected that the process of mechanisation is complete; any technological improvement will result in better performance and profitability but will not be comparable to the change from donkey to tractor in the 1950s. This means that land use changes in the near future, i.e. on a temporal scale of decades considered here, are gradual and probably governed by political decisions and socio-economic demands.

On the instrumental level, the *Common Agricultural Policy* (CAP) of the EU has a strong influence. Currently it supersedes the national agricultural policy of all EU member states. In response to global free trade pacts and overproduction, the tendency is to limit and abolish existing protective measures like subsidies. For important, subsidised crop types, in casu olives, this reduces the income of farmers in the Alcoy region. The alternative aim is to create new opportunities for deficient agricultural regions, for example by means of the LEADER program. The rural area of the Alcoy region satisfies the criteria for an 'Objective 1'-classification as defined in the CAP, which means that the Gross Domestic Product per capita is below 75% of the EU average for the 15 member states. In the framework of the LEADER program, initiatives are developed to restructure its economy and to improve the well-being of its inhabitants.

The net results of the political instruments are difficult to assess. On the long term, the loss of subsidies could lower the income of full-time farmers in the area and the attractiveness of agriculture as the primary source of income. In this respect, the expected policy will strengthen the ongoing rural exodus. Alternative employment is often found in the nearby industries of Alcoy and Cocentaina, although most of the local residents keep their land partly in cultivation as an additional source of income and pastime. This is possible because of the decreased labour costs (mechanisation) and because of the

reduced area under cultivation that is planted with late and early crops. So, labour-intensive activities as harvesting can be done by a relatively small group, in most cases one's relatives. Even people with a distant occupation (e.g. Valencia, Alicante) often continue to cultivate several parcels. In this manner agriculture may be intensified on several locations, but, overall, the area under cultivation decreases. Agriculture as a full-time occupation is left to a decreasing number of greying men; already in 1993, 58% of all Spanish farmers was over 55 years (CAP Working document, 1997).

In the case that agriculture does not benefit from better conditions to compete –better transport, storage etc.- or does not open new markets, the eventual consequence could be that more and more land is taken out of production and agriculture becomes an activity without priority. If no alternative means of existence can be found in the rural villages themselves, this change would affect the population, the secondary employment and the quality of life of the rural community as a whole. In the bleakest situation, the loss of population in Almudaina will equal that experienced over the period 1960-1999 namely a decrease of 52 %, from 245 to 118 inhabitants (section 2.4). This equals the average 50% decrease experienced by all rural areas of Spain between 1960 and 1996 (Censo de Población and Padrón Municipal I.N.E.). The decline of number of farms may then well exceed the 19% decrease that the European Union is expecting over the period 1993 – 2003 (CAP working document, 1997). This decrease is smaller than the decrease in the agricultural population and labour force as presented in Figure 2.13.

Within the framework of the LEADER program, local action to counteract these developments is co-ordinated by the *Centro de Desarrollo Rural Aitana*. In this body, the 24 rural municipalities, amongst which Almudaina, two agricultural co-operations and the Federación Valenciana de Montañismo participate. According to the LEADER directives, the actions concern the consolidation of the present agriculture, development of alternative occupations (agriculture, tourism and artisanal industries), and improvement of the human and natural environment. Investments made until 1998 amounted to a total of 11.1 million ECUs of which 32% was furnished by the EU. Most measures are consistent with the pursuit of the LEADER program to adapt the activities in the rural areas to the local demands. This reorientation of the economy on local and traditional demands offers a protection against ongoing globalisation ('niche markets') and squares with the strong regional policy of the Valencian autonomy. On the basis of this tendency it is probable to expect a continuation of traditional agriculture in the area, which combines the cultivation of fruit and olives as cash crop with the limited production of vegetables for local use.

The continuation of traditional agriculture is also favoured by the ongoing technical improvements that are introduced by the aforementioned co-operations. The acquisition of new machinery and the presence of co-operative services for information, transport and administration reduce the labour costs per hectare on the one hand and increase the yield and profit on the other. For example, the yield of olives – expressed as average over three years – doubled in 1995 compared to that in 1950. Over the same period, the demand and accessibility of the European market favoured a similar increase in the produce of cherries (MAPA, 1997). This increase, however, is accompanied by a relative extensivisation in manual labour as more cultivated land is replanted with cherries. Some of these plots are less suitable than the original plantations in the region and, as a result, the yield per hectare decreases. The expansion of cherries in the region occurs at the

expense of the cultivation of almonds. This traditional crop is becoming less attractive because of the collapse of global market prices and its vulnerability to frost in the flowering period.

In the future, land use will be just as dependent on the limitations of the natural resources as it is now. Although man can resist adverse conditions for some time, profitable land use is eventually impaired. Therefore, land use must be sustainable and adapt itself to the present and anticipated availability of natural resources. It is open to debate whether the changes in the natural resources are perceptible on the spatio-temporal scale under consideration for the interactions between the different biotic and abiotic components occur on a global instead of the local and regional scale. This makes it unlikely that any – farmer induced – land use change will indeed anticipate the expected global changes in the natural resources. It is for this reason that land use is evaluated under the present climatic conditions and under those at the moment of CO₂-doubling (2·CO₂) regardless of the evolving natural constraints. This approach is only justified when the changed climatic conditions do not decrease the profitability of the present crop types. This is, however, not ensured, even under the limited change envisaged in the climate change scenario. Direct changes in the expected temperature can affect the yield of cherry trees that need average daily temperatures of below 7°C to recover in winter (pers. com. A. Gill). In contrast, such a rise in temperature could increase the profitability of citrus fruits that under the current conditions suffer from the widespread occurrence of night frost. Similar direct effects could be expected from the changed frequencies of extreme precipitation, hail storms, droughts *et cetera*. Yet, these direct effects of climatic change can be assessed. The secondary effects of the expected climatic change – like plagues and diseases – are less predictable (Rosenberg, 1997).

In the development of the land use scenarios, only the current natural factors are taken into account. This means that future land use changes are limited to natural water resources and large-scale irrigation is not feasible. Given the conservative nature of agricultural societies, this implies that the current land use of olive groves and orchards *en secano*, i.e. without irrigation, is likely to last for this century. The activities of sheep herding and horticulture will remain marginal compared to this principal land use.

Under these constraints, the following land use scenarios are designed to reflect the land use change over the period to the presumed date of 2·CO₂ (≤ 100 years):

1. Business as usual (*BAU*):

Land use is continued on the present footing and with the current practices. This scenario is tenable whenever agriculture continues to function as an additional source of income with a social and cultural merit. Low-cost technological improvements reduce the labour requirements for profitable yields and returns below the optimum values are taken for granted.

2. Continued rural exodus (*CRE*):

This scenario complies with the *Conventional Wisdom Scenario* of Brouwer & Chadwick (1991) although they assume a different rate of decline (75% in 50 years). It is assumed here as a worst case-scenario that the current demographic trend of population decrease in the rural areas continues at the observed rate of – 50% in 40 years. Assuming that the ratio between full-time and part-time farming

does not change, this would result in a 50% decrease of the presently cultivated fields. Extrapolating the present situation even further, most full-time farmers will be over 55 and derive their sustenance partly from state pensions. As a consequence, large-scale investments are omitted and the distribution of properties and practices remain the same. This scenario is simulated by the random abandonment of cultivated parcels at any time, equal to the proportional loss of 50% per 40 years.

3. Professional slimming (*PS*):

Present agricultural land use remains profitable and in spite of the population decrease a considerable number of the existing farms continue to function (8 out of the present 14 full-time farmers). Average farm size is expanded to 20 ha and investments can be made to increase the present parcel size to 1 ha. This upscaling is independent of current property rights and the professional farmers own or rent the areas with the lowest slopes and easiest access. This results in an improved arrangement of cultivated fields. Of the remaining, presently cultivated fields, a fraction of 50% is lost over a period of 40 years.

This scenario is also tenable when the population decrease is less pronounced than expected under scenario 2.

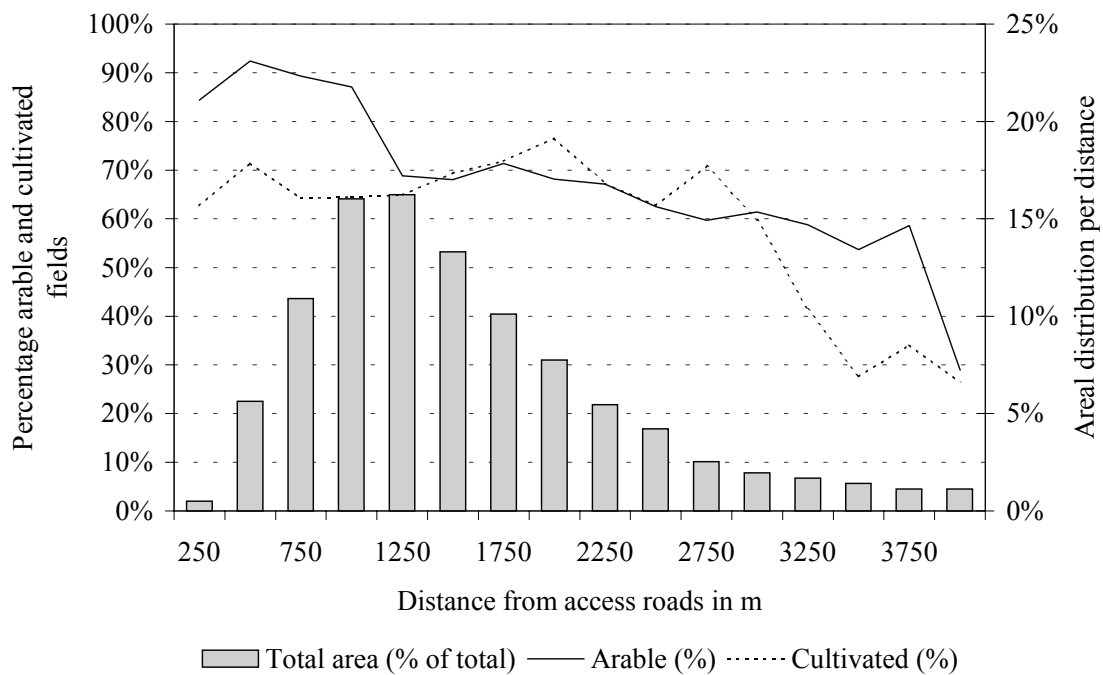


Figure 8.1: Relation between the area of potentially arable land and travel distance

The three land use scenarios are subject to the hypothetical climatic conditions as outlined in Section 4.4.4. This binds the land use configuration to the presumed date of CO₂-doubling, which is set to 70 years from 1990 (2060), or, approximately, 60 years from the situation in 1998. For a half-time of 40 years, 35% of the presently cultivated fields will then remain. For the Scenario Modelling itself, only the catchment of the

Barranco de la Coloma is considered. For the generation of the new configuration, the catchment of the Mollo has been included to avoid boundary effects. The combined area covers most of the presently cultivated fields in the municipality of Almudaina. It is accessible by several paved roads. The main road along the southern margin of the area connects Almudaina with the village of Benillup whilst other roads run over the pediment. From the two villages, the travel distance over these roads is used to calculate the accessibility of the arable area in the PS scenario. The relation between the travel distance, the area of potentially arable land and the presently cultivated fields is given in Figure 8.1. The more accessible 160 ha have been selected and reclaimed as new terraces.

Table 8.1: Changed land use based under the hypothetical scenarios on the moment of 2·CO₂ (2060) as percentage of the present situation (BAU) for the Barranco de la Coloma

Unit		BAU	CRE	PS
I	Cultivated	41	14	51
II	Recently abandoned	30	15	6
III	Abandoned: shrubland	18	17	7
IV	Semi-natural: open pine stand	11	54	36

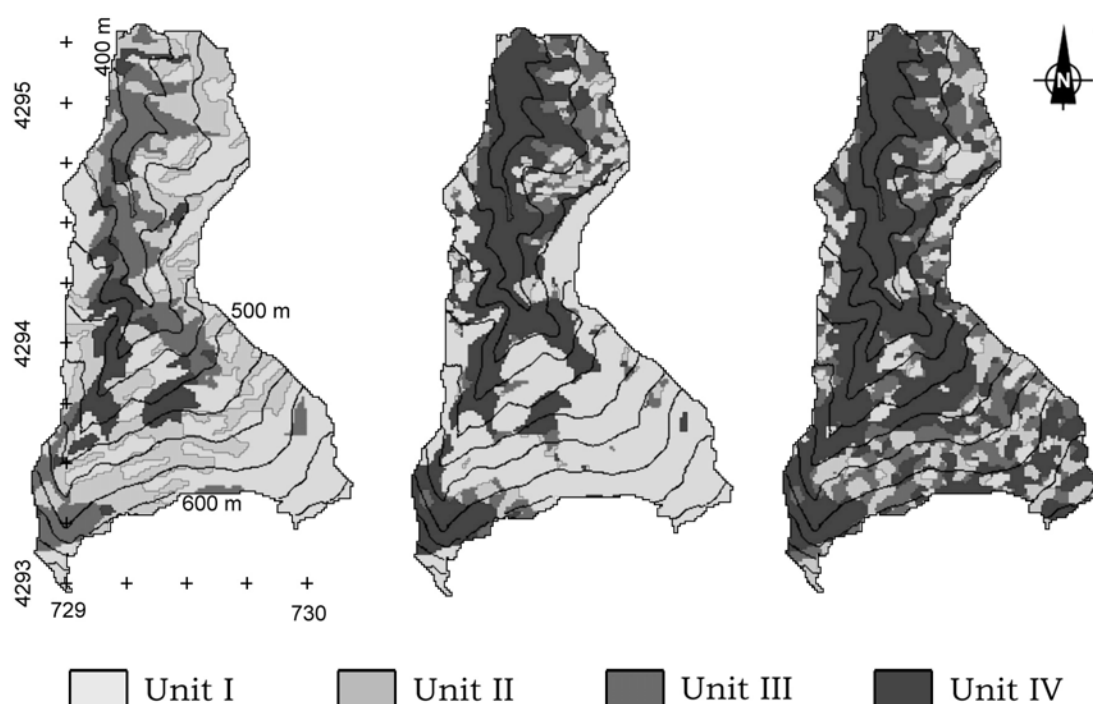


Figure 8.2: Present land use configuration (BAU) and simulated land use conditions according to the CRE and PS scenarios (see text and Table 8.1 for details)

In the CRE and PS scenarios, the abandonment has been simulated by placing random seeds in the presently cultivated area and expanding the selection until a decrease to 35%

of the present fraction has been achieved. For the Coloma, the land use configurations that are generated according to the above scenarios are depicted in Figure 8.2. The changes are listed in Table 8.1.

It is simulated that the regeneration of abandoned fields to semi-natural vegetation evolves over periods of ten years. Based on the developments since the abandonment in the 1950's, the transition frequency has been set to a value of 0.4 for all classes. According to this rule, the state of revegetation has been determined at the time of CO₂-doubling. Here, a concluding remark should be made on the implied static character of land use change; although land use change is a gradual process, the complex interactions between soil-vegetation-atmosphere and man have been neglected, considering them as imperceptible on the spatio-temporal scale studied. As a result, objective comparisons can be made on the basis of the expected hydrological and geomechanical behaviour at the moment of full vegetation recovery. Transitions from the present to the inferred future land use configuration can be simulated, e.g. Sidle (1995), but they will invariably suffer from the lack of information to parameterise accurately the changes in soil properties over time.

8.3 Scenario implementation

8.3.1 Scenario ensembles

The land use scenarios have been applied to the calibrated model for the present climate and for the expected warmer climate at CO₂-doubling (1.2 °C increase in annual temperature; Section 4.4.4). This results in 3 x 2 scenario ensembles, which are summarised in Table 8.2. These different ensembles offer the possibility to compare the effect of changes in land use and climate both jointly and separately. The scenario with the present land use and climate serves as a reference to evaluate the predicted results. The proposed limited land use scenarios do not violate the long-term validity of the calibrated parameters (Section 6.4), nor do they project land use into areas where the conditions are extremely different from the current situation (Section 7.6).

Table 8.2: Scenario ensembles

Climate change scenarios	Land use scenarios		
	Business as usual (BAU)	Continued rural exodus (CRE)	Professional slimming (PS)
Present, cool 1·CO ₂ -climate (CP)	BAU – CP	CRE – CP	PS – CP
Future, warmer 2·CO ₂ -climate (WF)	BAU – WF	CRE – WF	PS – WF

The implementation of the scenarios is similar to the approach for the validation of the model. Equilibrium conditions are calculated starting from the measured average soil moisture content over a period of 20 hydrological years with average daily rainfall and potential evapotranspiration under the appropriate land use and climatic conditions of the scenario. This equilibrium is subsequently exposed to a random succession of variable meteorological conditions generated by the stochastic weather generator described in Section 4.4. The generated synthetic series applied extend over 30 hydrological years.

This length is comparable to that of the historical record analysed in Chapter 4. This period is likely to generate a sequence of extreme events with recurrence periods that are comparable to those observed over the validation period. Two independent series, one for the cooler present (CP) and one for the warmer future climate (WF) around the date of $2\cdot\text{CO}_2$, have been generated randomly. The two scenarios are reused for the land use scenarios so that they are exposed to the same potential triggering rainfall events. Hence the land use scenarios under the same climatic scenario are directly comparable.

Between the climatic scenarios, the comparison is less straightforward as the frequency of the potential triggering rainfall events could be different. The climate change scenario developed in Section 4.4.4 presupposes only a change in the average daily temperature; the rainfall characteristics under the present $1\cdot\text{CO}_2$ and the future warmer $2\cdot\text{CO}_2$ climate are assumed to remain unchanged. Therefore, in order to make a comparison between the land use scenarios under the different climate scenarios, it is required that the precipitation in both series represents more or less the same mean conditions and variability.

8.3.2 Rainfall characteristics of the generated weather series

For the evaluation of landslide sensitivity under the hypothetical environmental conditions of the scenarios, it is essential that the generated weather series for the CP- and WF-climate contain a comparable number of extreme rainfall events of similar magnitude. Moreover, the rainfall characteristics should approximate those over the validation period in order to relate simulated failure to actual landslide occurrence. Not only concerns this the extreme events but also the interannual variability as antecedent rainfall is essential for the simulated hydrological response (Section 7.5).

Based on Section 4.4.3, the performance of the stochastic weather generator seems to ensure the generation of statistically homogeneous precipitation series. Hence the mean conditions and the variability are reproduced adequately as long as the generated sample is large enough. This is confirmed by the rainfall characteristics generated for the two climate scenarios that are summarised in Table 8.3. The two generated series have been tested on the homogeneity of the rainfall characteristics. Between the generated 30-year series no significant differences for the mean and variances at the 95% confidence level were found. Yet, the WF-series are more variable for all rainfall characteristics.

On average, the temporal characteristics of the observed rainfall at Almudaina are duplicated without deviations. In both series, however the mean annual rainfall is overestimated. This is caused by the slightly biased estimates of the monthly rainfall by the parameterised two-parameter gamma-distribution for November and February. For the CP-series, the average annual rainfall is overestimated by 13% (Table 8.3). For the WF-series, the overestimation reduces to 8%. Between the CP- and WF-series the differences in annual rainfall totals is -5% whilst the difference in the numbers of raindays is -3%. The generated series of annual rainfall are shown in Figure 8.3. Over the entire period of 30 years, the extreme annual rainfall is reproduced accurately although the above-average rainfall is overestimated (Table 8.4). The maximum annual rainfall

totals of the CP- and WF-series are comparable to the observed maximum of 1186.4 mm (Table 8.3).

Table 8.3: Rainfall characteristics for the 30-year synthetic CP- and WF-series and as observed over the validation period (1971-1998)

Scenario	Mean	S.D.	Min.	Max.	T_E (yrs) ^A	N^B
<i>Annual rainfall (mm)</i>						
Validation	697.7	244.4	335.6	1186.4	16.1	27 yrs
CP	788.4	231.2	295.1	1440.9	50.0	30 yrs
WF	752.4	250.2	321.0	1175.4	15.4	30 yrs
<i>Raindays (days)</i>						
Validation	38.2	10.1	22	58		27 yrs
CP	39.1	7.9	17	55		30 yrs
WF	37.8	8.6	23	55		30 yrs
<i>P 24-hr (mm)</i>						
Validation	18.3			240.5	37.5	1032 days
CP	20.2			277.8	86.1	1172 days
WF	19.9			245.2	41.6	1133 days
<i>Event rainfall (mm)</i>						
Validation	31.7	54.3		553.2	40.8	595 events
CP	34.4	42.0		341.9	6.5	688 events
WF	34.3	44.8		406.8	11.3	659 events
<i>Duration (days)</i>						
Validation	1.7	1.1		9		22.0 events ^C
CP	1.7	1.1		7		22.9 events
WF	1.7	1.2		10		22.0 events

A: Theoretical recurrence interval for the maximum mentioned (Gumbel-distribution)

B: Number of observations

C: Mean number of events per year

The overestimation of above-average rainfall can be explained by the absence of a prolonged period of drought in the generated weather series, such as over the years 1977-1985. This drought was extreme with the mean annual rainfall not exceeding 500 mm for 9 consecutive years. This extreme drought affected the model performance as the actual evapotranspiration was overestimated (Section 7.5). Because of the extreme nature of this event, it is to be expected that extreme droughts are absent in the generated weather series. In the generated weather series, the longest period over which the mean fell below 500 mm is two years. This occurs only once in the CP-series and three times in the WF-series. Droughts of this intensity will not impair the model performance to the same extent as the drought of 1977-1985. Consequently, it can be concluded that the generated weather series do not violate the validity of the calibrated hillslope model (Section 7.5).

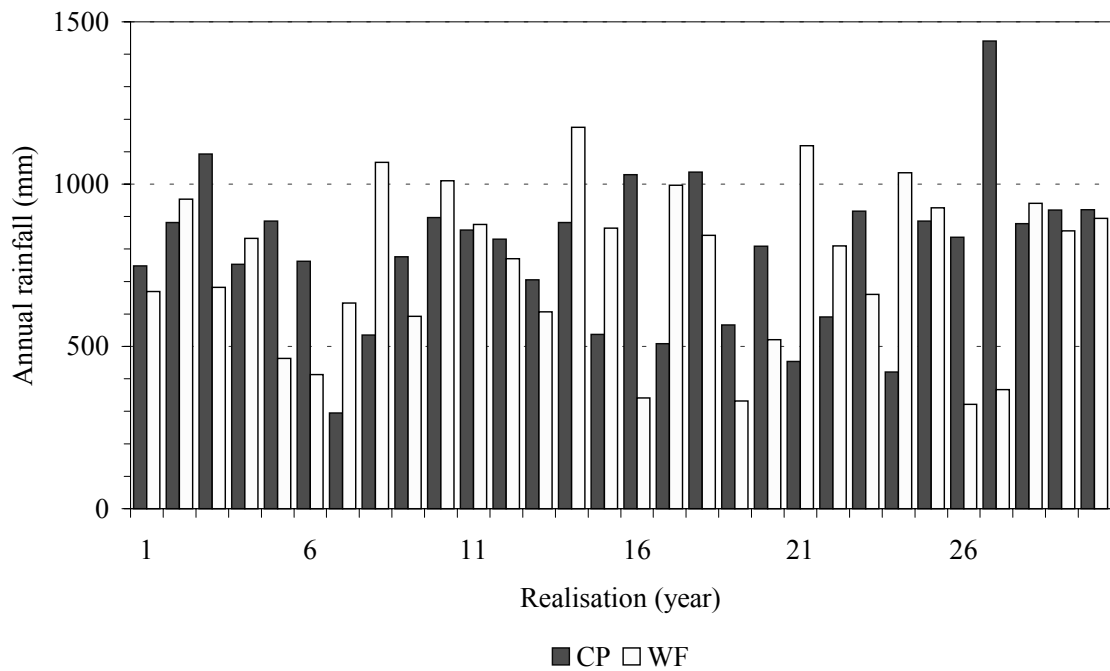


Figure 8.3: Simulated annual rainfall over 30 years for the CP- and WF-series

Table 8.4: Frequency (%) of annual rainfall totals for the synthetic weather series and as observed over the validation period (1971-1998)

Series	CP	WF	Validation period
Below-average rainfall (≤ 600 mm)	27	27	41
Average rainfall ($600 < P \leq 800$ mm)	17	20	26
Above-average ($800 < P \leq 1000$ mm)	43	36	18
Extreme rainfall (> 1000 mm)	13	17	15

The stochastic weather generator is unable to reproduce the frequency of extreme events accurately (≥ 250 mm; Table 8.5). As a result, the estimated recurrence interval for such events is an order of magnitude higher than that calculated from the Gumbel-distribution for the observed event rainfall totals (respectively $T_E = 10.5$ and 3.2 years; Section 4.2.2). The absolute number of events ≥ 100 mm of the WF-series is closer to the expectation of 56 events than the CP-series. However, the WF-series contain a larger number of relatively low magnitude events (< 150 mm) relative to the CP-series and the observations. More events are contained by the CP-series (688 compared to 659 events), but a smaller number of these events exceeds the total of 100 mm. Since the mean event rainfall is the same (Table 8.3), this implies that the CP-series contain more high-frequency low-magnitude events. Consequently, the antecedent moisture conditions will tend to be more favourable for the CP-series. This agrees with the lower frequency of droughts for the CP-series.

For the triggering of landsliding by extreme rainfall, event totals in the order of 200 mm are required (La Roca, 1992). The maxima are respectively 341.9 and 406.8 mm for the CP- and WF-series (Table 8.3). Using the Gumbel-distribution fitted to the observed rainfall events, the maximum event of the WF-series has a recurrence interval, T_E , of 11 years. The maximum event in the CP-series is less extreme ($T_E \approx 7$ years).

For both series, the maxima occurred in February. In neither case do these events coincide with the longest events in each series or with the maximum 24-hour rainfall total. The observed maximum, which also occurred in February, is 553.2 mm ($T_E \approx 41$ years). So, both the generated maxima and the number of extreme events are lower than observed. Notwithstanding, the event maxima are representative for the upper 1% of the observed events. Moreover, events ≥ 200 mm are equally present in both series of generated rainfall in sufficient numbers to mask the influence of slight differences in the antecedent moisture conditions (8 events over the 30 generated hydrological years). Consequently, the generated weather series contain sufficient extreme rainfall events to compare the simulated failure under the different climatological conditions. Moreover, the generated event totals are similar to the observed totals over the hydrological years 1971-1997 and the simulated failure of the respective climate series CP and WF can be compared and related to the observed landslide activity over the validation period.

Table 8.5: Absolute and relative frequency of rainfall event totals and recurrence, T_E , for the synthetic weather series and as observed over the validation period (1971-199)

<i>Series</i>	<i>CP</i>			<i>WF</i>			<i>Observed 1971-1997</i>		
	Abs. (N)	Rel. (%)	T_E (yr)	Abs. (N)	Rel. (%)	T_E (yr)	Abs. (N)	Rel. (%)	T_E (yr)
≥ 100 mm	14	36	1.4	21	39	1.2	13	26	1.3
≥ 125 mm	6	15	1.8	16	30	1.5	12	24	1.4
≥ 150 mm	5	13	2.1	5	9	2.3	6	12	1.6
≥ 175 mm	6	15	2.7	4	7	3.0	3	6	1.9
≥ 200 mm	2	5	4.3	3	6	4.3	4	8	2.2
≥ 225 mm	3	8	5.5	2	4	6.5	3	6	2.6
≥ 250 mm	3	8	10.5	3	6	10.5	9	18	3.2
Total	39 events in 30 years			54 events in 30 years			50 events in 27 years		

8.3.3 Correlation between simulated failure for the validation period and the BAU-CP scenario

The BAU-CP scenario represents the present land use and climate conditions. If the synthetic weather series for the 1·CO₂ climate is an acceptable replica of that of the validation period, the simulated failure of the scenario should be similar to that over the validation period. Measures by which the simulated failure of the BAU-CP scenario and the validation period can be compared have been defined in Section 7.4 and include the probability of failure and the temporal characteristics.

Differences between the BAU-CP scenario and the validation period, however, arise due to the variations in the (generated) weather series. In particular the difference in rainfall characteristics will affect the simulated failure. Since the duration of the BAU-CP is

slightly longer, covering 30 years instead of the 27 years of the validation period, it is also important to ascertain that no large differences in the temporal characteristics of the simulated failure occur.

The similarity between the model outcome for the two periods, i.e. the validation period and the 1·CO₂ climate, has been expressed by the correlation coefficient and the slope of the linear regression equation that has been forced through the origin (intercept= 0). These statistics have been calculated on a cell-by-cell basis (10x10 m). If both the correlation coefficient and the slope were at unity, the values of the independent and dependent variables would be exactly the same for each cell. The different measures of simulated failure of the BAU-CP scenario have been regressed on those of the validation period (Table 8.6). The probability of failure, $P(F \leq 1)$, used in the regression is the maximum of each cell for either the validation period or the BAU-CP scenario. The regression of the maximum probability of failure considers the entire range of simulated probability of failure and for the range $P(F \leq 1) \geq 0.10$. This restricted range coincides with the majority of the occurred landslides over the validation period and has been used for the calculation of the temporal characteristics of simulated failure as defined in Section 7.4.

Over the range $P(F \leq 1) \geq 0.10$, the temporal characteristics of simulated failure are calculated from the duration or the frequency over which a pre-set level of the probability of failure is exceeded. This pre-set level is the first decimal of the maximum probability of failure over the entire period under consideration (see also Figure 7.10). Thus, the dependency on the absolute level of the probability of failure is partly removed and the temporal characteristics normalised.

Table 8.6: Similarity between the simulated failure for the BAU-CP scenario (dependent variable) and that for the validation period (independent variable). Given are the correlation coefficient, ρ , and the slope of the linear regression, α .

Range Area	$P(F \leq 1) \geq 0$	$P(F \leq 1) \geq 0.10$			
	153.7 ha	48.5 ha	Persistence	Frequency	Average duration
	$P(F \leq 1)$	$P(F \leq 1)$	(-)	($\text{yr} \cdot \text{yr}^{-1}$)	(days)
ρ (-)	0.96	0.88	0.97	0.88	0.90
α	0.91	0.91	1.45	1.18	0.91

The temporal characteristics used in the regression are the persistence, the recurrence and the average duration. The persistence is the dimensionless fraction of the period with instability or simulated failure and the total duration. The recurrence is the number of years that this level is exceeded whilst the average duration is the average number of days that this level is exceeded for each of these recurring years. By definition, the persistence and the average duration are relative measures and the values of the BAU-CP scenario and the validation period can be directly compared in spite of the difference in length. The recurrence, however, is the integer number of the years that the pre-set level is exceeded. Consequently, it is limited by the total length of the period. As the lengths of the BAU-CP scenario and the validation period differ, the recurrence can not be

regressed directly on each other. To overcome this problem, the recurrence has been divided by the total length in years. This returns the frequency of simulated failure, which, like the other temporal characteristics, is directly comparable.

The maxima of the probability of failure, as simulated for the validation period and the BAU-CP scenario, are very similar, whether the entire range or only that of $P(F \leq 1) \geq 0.10$ is considered. Overall, the maximum probability of failure is slightly higher for the validation period as the slope in both cases is below unity. The slope of the linear regression remains the same but the correlation coefficient decreases when only the range $P(F \leq 1) \geq 0.10$ is considered. The exclusion of all probabilities below $P(F \leq 1) = 0.10$, which constrains the linear regression equation in the lower region, emphasises the differences between the BAU-CP scenario and the validation period. Of the area under consideration (48.5 ha), 9% or 4.2 ha have a maximum probability of failure below 0.10 in the BAU-CP scenario. For this fraction, the maximum probability of failure exceeds this level for the validation period. In contrast, the area for which only the BAU-CP scenario exceeds the level of $P(F \leq 1) = 0.10$ is negligible (0.2%). The differences between the validation period and the BAU-CP scenario are reflected in the average probability of failure (Table 8.7). When the maxima of both periods exceeds $P(F \leq 1) \geq 0.10$, the average and standard deviation are highly similar. When the maxima of the BAU-CP scenario falls below this level, the averages are much lower and the standard deviation increases relatively for the validation period. This implies that maximum probability of failure is generally lower but still varies over the entire range $P(F \leq 1) \geq 0.10$. Thus, the maximum probability of failure of the BAU-CP scenario is nearly identical to that of the validation period in 91% of the cases for the range $P(F \leq 1) \geq 0.10$.

Table 8.7: Average and the standard deviation (S.D.) of the maximum probability of failure for the range $P(F \leq 1) \geq 0.10$

	Validation		BAU-CP	
	Average	S.D.	Average	S.D.
BAU-CP, $P(F \leq 1) < 0.10$	0.35	0.25	0.05	0.02
BAU-CP, $P(F \leq 1) \geq 0.10$	0.69	0.32	0.64	0.33

As all temporal characteristics are relative to the total length of the period under consideration, the values for the BAU-CP scenario and the validation period are directly comparable by means of regression. The results from the regression indicate that the persistence and the frequency are generally higher for the BAU-CP scenario than for the validation period (Table 8.6). For the frequency, the spread is large as expressed by the lower correlation coefficient and originates from the discrete nature of the recurrence. The trend itself is linear and the frequency of the BAU-CP scenario is positively related to that over the validation period. For the persistence, the relation is also linear and the spread lower, as the higher correlation coefficient indicates. The average duration, which pairs persistence and frequency, is in closer agreement. For the range $P(F \leq 1) \geq 0.10$, the slope of the linear regression is the closest to unity. The correlation factor is, however, lower as it combines the small deviations of the persistence with the larger spread of the frequency. Thus, triggering occurs more often in the BAU-CP scenario than in the

validation period. Notwithstanding, these events last shorter and are associated with lower values of the probability of failure as the slopes of both statistics indicate (Table 8.6).

The explanation for the differences between the validation period and the BAU-CP scenario lies in the synthetic weather series of the latter. In Section 8.2, it was observed that the annual rainfall is on average higher and that the event rainfall was less extreme. The first factor, which is associated with the absence of prolonged droughts, explains the longer persistence and frequency in the BAU-CP scenario in which the antecedent moisture conditions are more favourable for triggering. The second factor explains the lower maxima of the probability of failure for the BAU-CP scenario. The events of the validation period are more extreme and able to raise $P(F \leq 1) \geq 0.10$ in an area of 4.2 ha for which this level has not been attained in the BAU-CP scenario. This area of 4.2 ha represents 3% of the total area under consideration and 9% of the area with $P(F \leq 1) \geq 0.10$. The recurrence interval of these events, as calculated with the Gumbel-distribution, is 41 and 7 years for respectively the validation periods and the BAU-CP scenario (see Section 8.2). Despite this large difference, only a limited area of the potentially unstable area is affected by it. Consequently, it can be concluded that the simulated failure of the BAU-CP scenario is similar to that of the validation period when the probability of failure and the average duration are considered. This implies that the BAU-CP scenario is a valid measure for the landslide activity under the present environmental conditions and can be used as reference for the other hypothetical scenarios.

8.4 Simulated changes in landslide activity under environmental change

8.4.1 Possible changes in landslide activity under environmental change

For the six scenarios of Section 8.2, changes in landslide activity are entirely due to changes in the propensity of the system, *in casu* the Barranco de la Coloma, to potentially triggering rainfall events (Brunsdon, 1993 & 2001). These changes in the propensity are defined by the static land use conditions that are superimposed on the constant level of modelled susceptibility (Section 7.3). Thus, the changes in landslide activity reflect the temporal sensitivity of the landscape to landsliding for the various environmental conditions (Chapter 1).

The possible changes in the landslide activity are approximated by the changes in simulated failure of the Scenario Modelling. These changes in simulated failure affect both its temporal characteristics and its spatial distribution. Changes in the temporal characteristics occur as the result of shifts in the period or frequency that the critical pore pressure conditions are exceeded and the failure is simulated locally. Changes in the spatial distribution of landslide activity result from absolute differences in the local pore pressure that controls failure. So, despite the inherent simplification of the Scenario Modelling, the simulated response is still complex. This precludes the definition of a single measure to express the changes in landslide activity under the imposed environmental conditions. Rather, it has been preferred to express the change in landslide activity under the hypothetical environmental conditions relative to the present situation.

These present conditions are contained by the BAU-CP scenario of which the area and temporal characteristics of simulated failure have been used as reference.

Evidently, the forecasted changes in the landslide activity are based on the simulation only and consequently subject to the constraints on the validity of the coupled hillslope model that have been identified in the Chapters 6 and 7. The implications of the limited model validity and the static nature of land use conditions are addressed in detail in the Discussion (Section 8.5).

8.4.2 *Changes in the area of simulated failure*

The area of simulated failure is calculated from the probability of failure from the slope stability assessment (see Sections 3.2.3 and 7.4). It is the product of the total catchment area, 153.7 ha, and the spatial average of the maximum probability of failure over the 30-year period. In addition, the deterministic prediction, the area for which the factor of safety, F , falls below unity, has been used despite its drawbacks; so is it incapable of predicting instability below the deterministic topographical threshold of 18° and does not differentiate the level of instability above it. Notwithstanding, it provides a graphic example of the change that occurs relative to the BAU-CP scenario (Figure 8.4).

The changes in the area of simulated failure are listed in Table 8.8. All scenarios predict a decrease with respect to the present conditions of the BAU-CP scenario. The change in the probabilistic forecast is very similar to that of the deterministic prediction (Figure 8.4). The changes are small for the land use changes under the present climate (CP scenarios). Likewise, the climate change scenario does not result in an appreciable change under the present land use conditions (BAU-WF scenario). By comparison, the combined changes in land use and climate (CRE-WF and PS-WF scenarios) result in a dramatic fall in the order of 20% or more in the area of simulated failure.

These changes are reflected by the cumulative frequency distributions in which the probability of failure is plotted against the cumulative, relative area (Figure 8.5). These plots reveal a decrease over the entire range of the probability of failure for the CRE-WF and PS-WF scenarios. This decrease in the probability of failure occurs predominantly on the less susceptible slopes with a critical pore pressure ratio, $r_{u \text{ crit.}}$ (see Equation 7.1), of more than 0.50 or a slope angle of less than 27° . These changes become apparent in Figure 8.6, in which the absolute areas of simulated failure are plotted per scenario and susceptibility class. The change for the less susceptible slopes implies that under these hypothetical land use conditions the maximum groundwater levels that are attained over the respective 30-year periods decrease. In contrast, no appreciable changes occur for the more susceptible slopes where the critical pore pressure levels are readily exceeded.

In order to relate the predicted changes to the validation period, the predicted and observed areas are also plotted in Figure 8.6 (Val-Obs. & Val-Sim. respectively). As observed in Section 7.4 it is clear that the area of simulated failure overestimates the observed landslide occurrence above the deterministic threshold, $r_{u \text{ crit.}} \leq 1.00$. Below this threshold, which contains the non-susceptible and marginally susceptible slopes (classes *NS* and *MS* respectively), the area of simulated failure underestimates the observed landslide occurrence. Because of the limitation of the coupled hillslope model, no

changes can be assessed for the range of non-susceptible slopes. Although the observed decrease is weaker for the marginally susceptible slopes than for $r_{u \text{ crit.}} > 0.50$, it seems plausible that a similar decrease might be expected for the non-susceptible slopes.

Change in predicted slope failure, $P(F < 1) > 0.5$

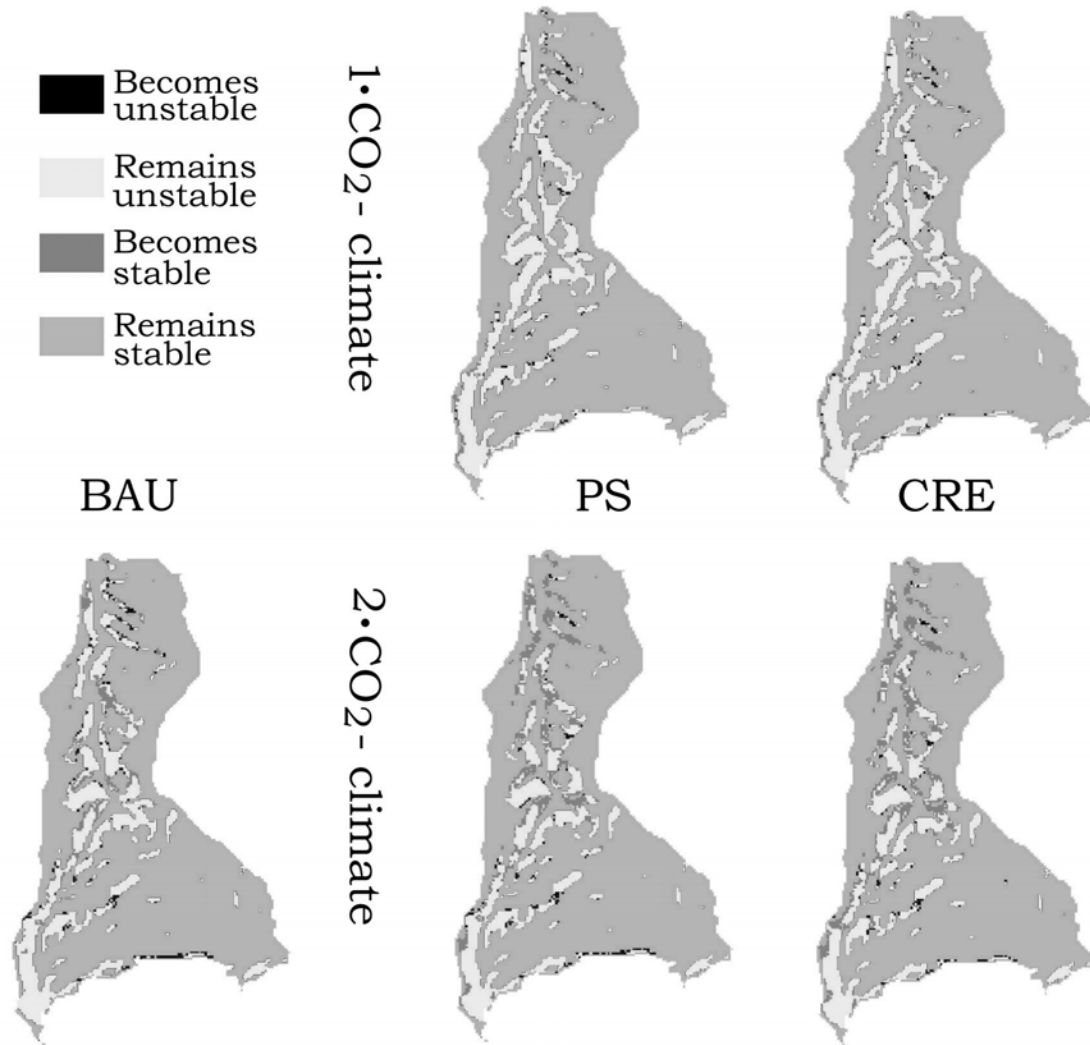


Figure 8.4: Changes in the predicted instability relative to the BAU-CP scenario, based on the deterministic model outcome ($F \leq 1$)

The changes in stability in the scenarios are both positive, i.e. stabilising, and negative, i.e. destabilising (Figure 8.4), which is due to local variations in the simulated pore pressures. This raises the question on the consistency of the predicted trend. As a tentative measure for the consistency, the direction and magnitude of the change of the deterministic prediction may be used. The change in area of simulated failure is the largest for the CRE-WF and PS-WF scenarios and respectively 90% and 85% of the change is directed towards stabilisation. In comparison to this marked decrease in

landslide activity, the changes for the CP- and BAU-WF scenarios are less conclusive. All in all, the hypothetical scenarios predict a general decrease in the area of simulated failure that is considerable in the case of the CRE-WF and PS-WF scenarios. This change is attributable to the decrease in the likelihood of failure on the less susceptible slopes ($< 27^\circ$). On the more susceptible, steeper slopes there is no indication of decreased landslide occurrence.

Table 8.8: Change in the area of simulated failure based on the probabilistic forecast

Scenario	Area (ha)	Relative change (%)
BAU-CP	30.7	0
BAU-WF	29.1	-5
CRE-CP	29.3	-5
CRE-WF	24.0	-25
PS-CP	29.6	-4
PS-WF	25.2	-20

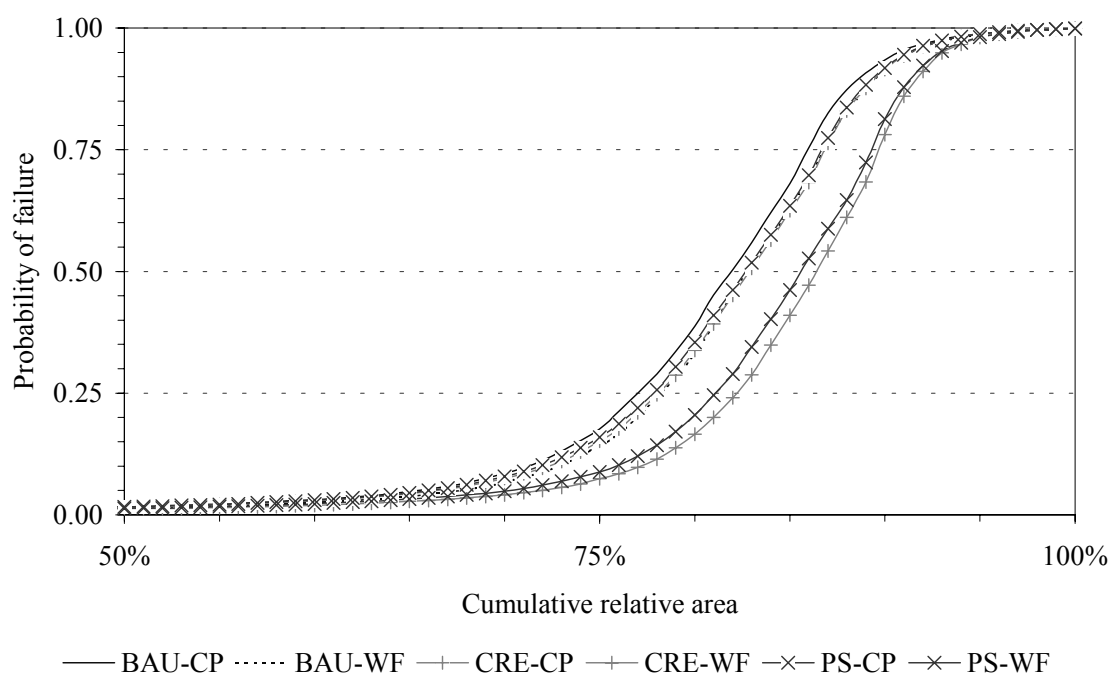


Figure 8.5: Probability of failure against the cumulative relative frequency of the area $P(F \leq 1)$

Table 8.9: Absolute change in the area of simulated failure between the respective scenarios and the BAU-CP scenario based on the deterministic prediction (area with $F \leq 1 = 27.7$ ha). Percentage gives the fraction of the area that becomes stable.

Scenario	BAU-WF	CRE-CP	CRE-WF	PS-CP	PS-WF
Area(ha)	5.1	3.2	8.7	3.0	8.1
Stabilisation (%)	63	73	90	69	85

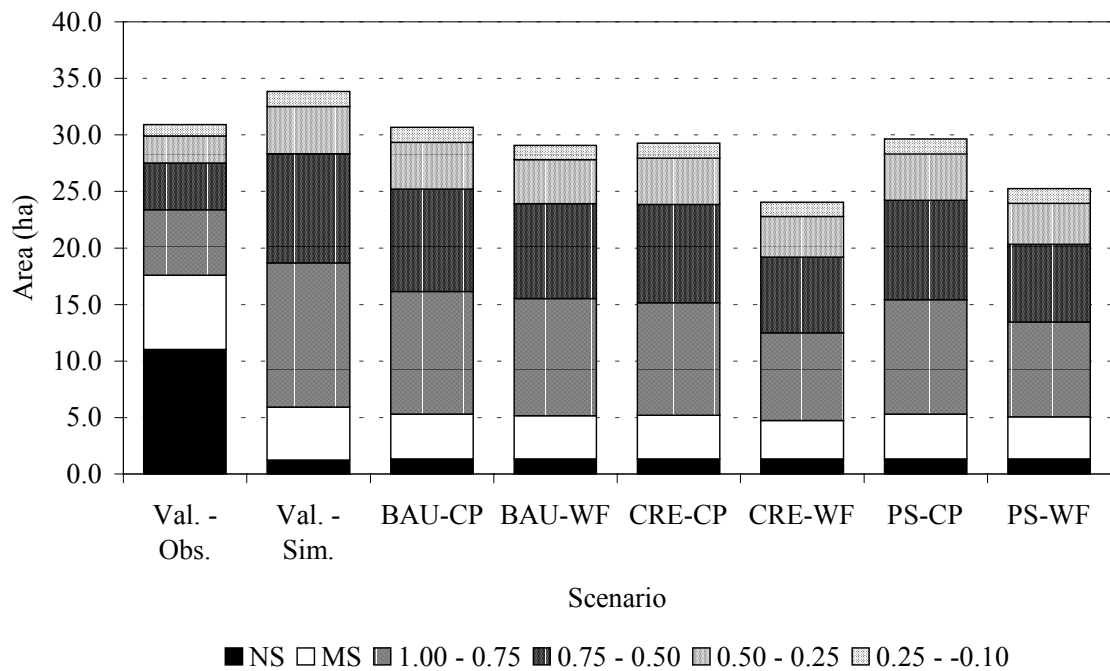


Figure 8.6: Area of simulated failure per scenario and for the validation period (Sim.: simulation, Obs.: observed landslide occurrence). Legend classes represent the susceptibility as expressed by the critical pore pressure ratio, ru . The classes NS and MS represent respectively the non-susceptible and marginally susceptible slopes (Section 7.3.3).

8.4.3 Changes in the temporal characteristics of simulated failure

The change in the area of simulated failure reflects the alteration in the maximum groundwater levels that have been achieved over the 30-year periods of each scenario. It provides, however, no information on the frequency or the duration by which these maximum levels are approximated in the simulation. This information is provided by the temporal characteristics of simulated failure, as defined in Section 7.4. The temporal characteristics analysed are the persistence, average duration and the recurrence or frequency that have been normalised with respect to the maximum probability of failure (Section 8.3.3).

Table 8.10: Change in the area of $P(F \leq 1) \geq 0.10$, average persistence and total duration relative to the BAU-CP scenario

Scenario	BAU-CP	BAU-WF	CRE-CP	CRE-WF	PS-CP	PS-WF
Area (%)	44.2 (ha)	-6	-4	-21	-2	-16
Duration (%)	313288 (days)	-14	-27	-41	-12	-22
Persistence (%)	0.0065 (-)	-9	-24	-25	-10	-7

In Table 8.10, the relative changes in the total duration, persistence and the area under consideration are listed for the respective scenarios. The change in area is just below the

values of Table 8.8 as areas with $P(F \leq 1) < 0.10$ have been excluded from the analysis. The relative change in total duration is larger than that in the area of simulated failure. So, parts of the area that remain prone to landsliding under the changed environmental conditions are likely to experience a drop in landslide activity. Remarkably, the change in the persistence under the different land use conditions is very similar, regardless of the climate. The largest change occurs for the CRE scenarios in which the current trend of land abandonment is extrapolated. Shifts in the absolute levels of the probability of failure that result from the changes in the environmental conditions have apparently no influence on the duration over which they persist once the pre-set threshold of $P(F \leq 1)$ is exceeded.

Table 8.11: Change in average duration relative to the BAU-CP scenario. Changes are determined from data classified according to Table 7.5.

Scenario	BAU-WF	CRE-CP	CRE-WF	PS-CP	PS-WF
Increase (%)	29	20	20	22	24
No change (%)	49	52	38	54	39
Decrease (%)	22	28	41	25	37

Local changes are reflected by the average duration, which possesses a strong but empirical relationship with the observed landslide density (Section 7.4.6). Changes in the classified average duration (Table 7.5) are summarised in Table 8.11. Compared to the BAU-CP scenario, there is little change for the BAU-WF, CRE-CP and PS-CP scenarios. In about 50% of the cases, there is no change at all whilst the observed change is equally divided over the categories of change. For all scenarios, the fraction of increased average duration remains in the order of 20%. For the WF scenarios, this general increase can be explained by the extreme event, which results in a single but prolonged period of elevated pore pressure conditions. For the PS-WF- and, in particular, the CRE-WF scenario is there a substantial decrease in the average duration. For the others, however, the average duration changes little in most cases.

The average duration implicitly includes the recurrence. The recurrence of simulated failure, i.e. the number of years that the pre-set level of the probability of failure is exceeded, is listed in Table 8.12. The recurrence shows that, in the simulation, failure is the most frequent for the BAU-CP scenario. The recurrence remains high for the different land use scenarios under the present climate conditions (CP series). However, it decreases sharply under the hypothetical future conditions, when the evapotranspiration increases (WF series). Yet, despite the lower recurrence, the WF scenarios have a larger cohort with a recurrence of 2 out of the 30 years that must be attributed to the higher number of large rainfall events (Table 8.5).

From the changes in the temporal characteristics of simulated failure, it emerges that landslide activity will decrease under the environmental conditions of the scenarios. This decrease is the clearest for the duration and the persistence. Relative to the present situation, the alteration in land use results in a stronger decrease in landslide activity than those in climate conditions alone. In turn, changes in land use alone have little effect on the average duration and the recurrence of simulated failure. For the affected area, the

frequency and the duration by which the normalised, pre-set threshold of $P(F \leq 1)$ is exceeded, remains the same. An absolute decrease in the probability of failure occurs for all altered conditions as lower pore pressures are simulated. This is consistent with the observed changes in the area of simulated failure and the decreases are marked when both land use and climate change are altered (CRE-WF – and PS-WF scenarios). Under the warmer, future climate (WF), the larger evapotranspiration lowers the simulated absolute pore pressure levels, which leads to a drop in the area and frequency of simulated failure. The changes in simulated failure can be explained by the altered hydrological triggering in the scenarios. Potential hydrological triggers are defined by the hydrological response, which is considered in relation to the temporal sensitivity in the next section.

Table 8.12: Cumulative relative frequency in % of the area $P(F \leq 1) \geq 0.10$ with recurrence

R (yrs)	Scenario					
	BAU-CP	BAU-WF	CRE-CP	CRE-WF	PS-CP	PS-WF
1	34	21	39	28	36	24
2	49	50	52	53	50	43
4	67	71	74	77	70	68
8	84	91	88	93	85	89
16	96	98	98	99	97	99
Max. recurrence (yrs)	27	24	25	22	26	22

8.4.4 Hydrological response and temporal sensitivity

In the CP- and WF series, the relationship between event rainfall and the annual rainfall totals is equally weak whilst that between the annual rainfall total over the preceding and the present year is non-existent. Thus, the relation between rainfall and the area of simulated failure can be compared for the two series

The correlation coefficients between the area of simulated failure and rainfall are listed for the scenarios in Table 8.13. The area of simulated failure has been correlated with the event rainfall, and the annual rainfall totals, both over the present, t , and preceding year, $t-1$. From these correlations, the following observations can be made:

- The correlation between event rainfall and the area of simulated failure is only significant at $\alpha = 0.05$ (-) for the WF-scenarios;
- Significant correlations exist between the annual rainfall totals of the present year, t , and the simulated area of failure for both the CP- and WF-scenarios;
- Significant correlations, although marginal, exist between the annual rainfall totals over the preceding year, $t-1$, for the CP-scenarios. No significant correlations, however, exist for the WF-series;
- The correlations are similar for the scenarios of the CP- and WF climates but not between them.

The fact that the correlations for the various land use scenarios remain the same under the different climates indicates that the dominant hydrological processes on susceptible

slopes remain the same and only the magnitude of the simulated pore pressure levels changes.

Table 8.13: Correlation, ρ , between the area of simulated failure and rainfall on the series of 30 hydrological years. P is the probability that $\rho=0$.

Scenario		Event rainfall		Annual rainfall			
Climate	Land use	ρ (-)	P (-)	present year, lag($t=0$)		preceding year, lag($t=-1$)	
				ρ (-)	P (-)	ρ (-)	P (-)
CP	BAU	0.16	0.386	0.69	0.000	0.37	0.045
	CRE	0.13	0.489	0.65	0.000	0.39	0.035
	PS	0.15	0.417	0.67	0.000	0.38	0.037
WF	BAU	0.44	0.015	0.56	0.001	0.01	0.950
	CRE	0.41	0.025	0.55	0.002	0.03	0.879
	PS	0.42	0.022	0.58	0.001	0.02	0.916

The correlation coefficients between the area of simulated failure and the annual rainfall totals of the CP-series are identical to those found for the validation period (Section 7.5). Because of the slightly longer period, the correlation coefficient of the area of simulated failure with the annual rainfall total over the preceding year is marginally significant at $\alpha=0.05$ (-) whereas this was not the case over the validation period. The correlation with event rainfall is lower for the CP scenarios than for the validation period although it is insignificant for both series. In contrast, the correlation with event rainfall is significant for the WF-scenarios. The correlation with the annual rainfall totals decreases, in the case of that over the antecedent year to imperceptible levels. Since the relation between event rainfall and annual totals is equally weak for the two climates, the observed differences in the correlation between the area of simulated failure can not be attributed to the particular combinations of annual rainfall totals and extreme event rainfall (Section 8.2). The significant relationship between the area of simulated failure and the event rainfall for the WF climate can not be explained by the higher frequency of extreme events (Table 8.5), as the absolute number is identical to that of the validation period for which no significant correlation with event rainfall was found.

The relationships between the rainfall and the area of simulated failure stem from the hydrological response by which the net rainfall is transformed into pore pressure at the potential slip plane. The hydrological response is determined by the soil moisture deficit that must be replenished before percolation becomes significant. Over summer, the soil moisture deficit increases due to evapotranspiration. Because of this dependence, land use and climate -and possible changes therein- control the soil moisture deficit. The resulting soil moisture deficit forms the initial setting at the start of the hydrological year. In Appendix 6, the hydrological response is given for two locations. These points represent nearly identical physiographic conditions with the exception of the vegetation (see Figure 8.7). The two points represent different land use units that remain the same for the respective scenarios. For all scenarios, the hydrological response is shown. The change in the volumetric moisture content (VMC) is shown per layer and for three types of annual rainfall: below-average, average and above-average. The latter type is represented by the maximum annual rainfall total for the generated weather series. The

rainfall over the preceding years varies but is never extreme. The differences in the hydrological response that arise due to differences in climate or land use are discussed here from the examples of the BAU-CP and BAU-WF scenarios.

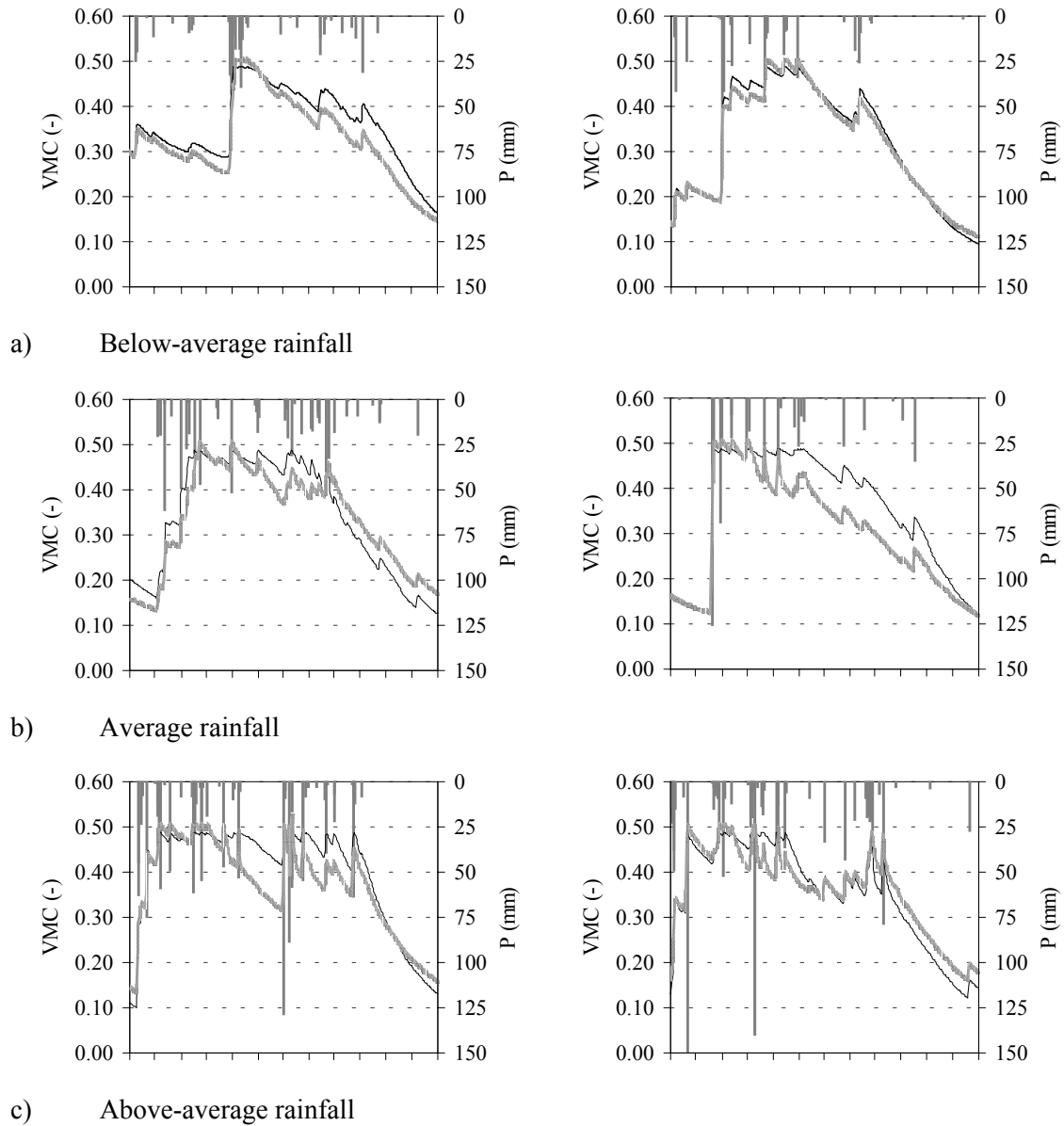


Figure 8.7: Hydrological response for the topsoil (< 50 cm): simulated change in the volumetric moisture content for a hydrological year with below-average (a), average (b) and extreme rainfall (c) under the CP and WF climates. Represented are a recently abandoned location (Unit II) and one under *Pinus halepensis* (Unit IV) of the present land use configuration (BAU)

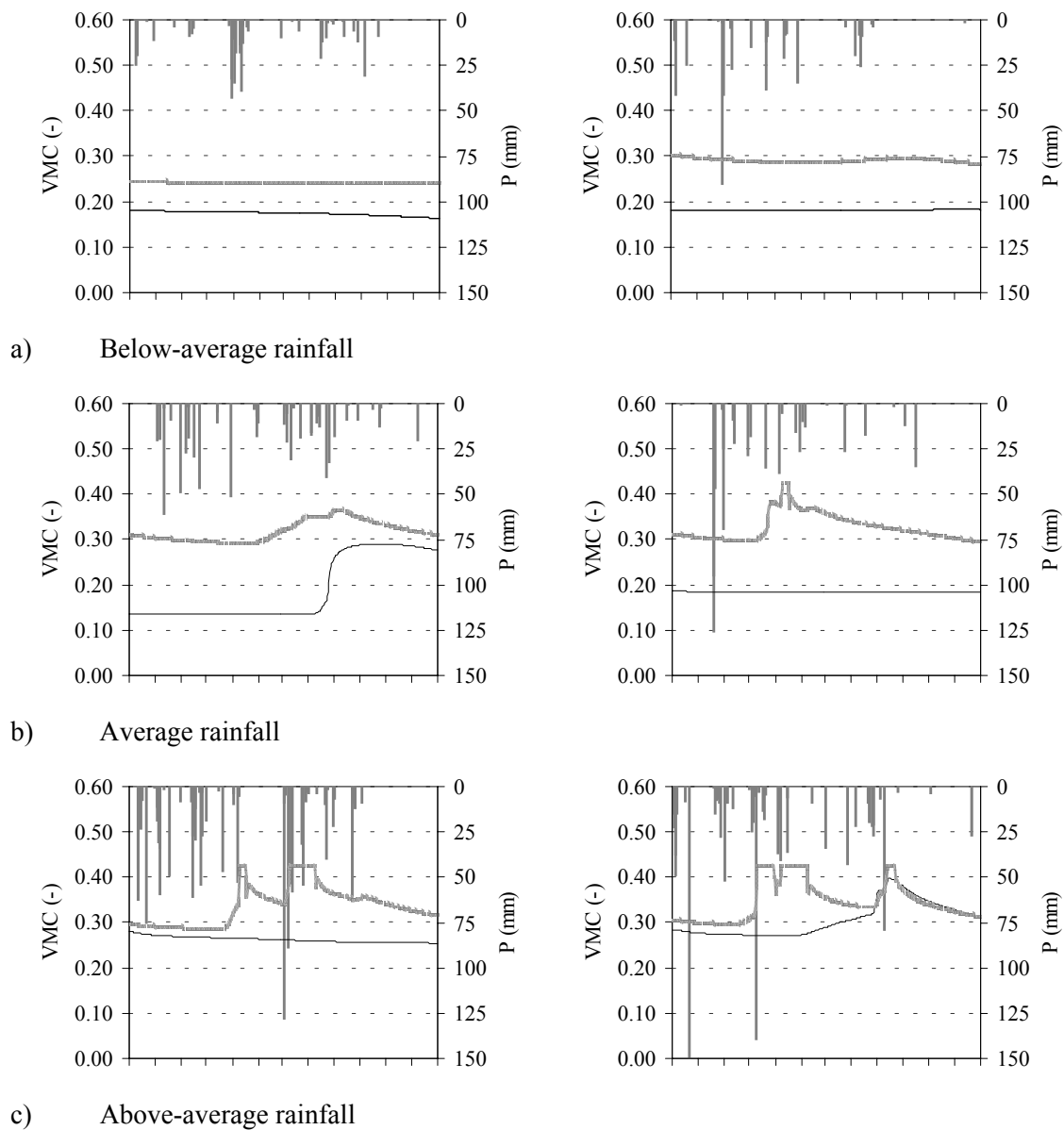


Figure 8.8: Change in the volumetric moisture content (VMC) above the lithic contact (> 1.00 m) for the different rainfall types under the CP and WF climates (see Figure 8.7 for explanation)

The influence of the climate explains the disconnection of the area of simulated failure from the annual rainfall over the preceding year for the WF series. The larger evapotranspiration results in a constant moisture deficit that recurs every hydrological year, irrespective of the land use conditions (Figure 8.7). For the CP climate, the initial soil moisture deficit still varies from year to year and between land use conditions. Consequently, the amount of rainfall that is required to compensate the soil moisture deficit varies accordingly.

The disconnection for the WF series is restricted to the top soil only, which is the direct result of the hydrological effects of land use. All other factors remaining equal, the differences in the percolation of water to the deeper layers of Figure 8.8 can be attributed to the actual evapotranspiration, infiltration, drainage and the available storage, which are all higher for soils under semi-natural vegetation. For this type of vegetation, the response in the topsoil is more accentuated and the response in the deeper layers is earlier and more pronounced. In this layer, also the cumulative percolation along the slopes becomes apparent for the location under semi-natural vegetation as saturated conditions, i.e. perched water tables, occur in some years. This cumulative effect also explains the differences for the deeper layers for the various scenarios of Appendix 6.

For the deeper layers, there is no clear difference in the summer moisture contents between the CP and WF climate. The response in these layers depends not only on the rainfall totals but also on the recurrence of the rainfall events. It is feeble for the years with below-average rainfall and fails to penetrate to the deepest layer for both the CP and WF climate. The response becomes more vigorous under average and above-average rainfall conditions although it still fails to generate a response for the recently abandoned location (Unit II) under the WF climate. Important factors that attenuate the response to the concentrated rainfall are the limited storage capacity and percolation of the topsoil for this unit. So, the available storage is readily exceeded and the rainfall excess treated as surface detention. Under the semi-natural vegetation, the response is stronger. The larger storage capacity and the higher hydraulic conductivity ensure a rapid transfer of to the deeper layers and primes them for later events. Under such conditions, the response to rainfall becomes instantaneous and perched water tables are formed. This is the case for the above-average rainfall, when a rapid rise in moisture content is observed after the extreme rainfall events in winter and spring. In the case of the average rainfall for the CP climate, however, the response is more subdued as more water from the smaller rainfall events is lost by evapotranspiration.

The spatial aggregate of the hydrological response determines the area of simulated failure in the simulation for each hydrological year. The area of simulated failure ranges from a small area of steep, frequently failing slopes to the complete mobilisation of the susceptible area. Because of the influence of these extremes, a fundamental relationship should exist between the area of simulated failure and the recurrence intervals of the annual rainfall totals. The recurrence interval, T_E , is based on the extreme event series of the Gumbel-distribution and pertains to the rainfall depth that is on average exceeded once over this period. It is understandable that this relationship is a better descriptor than that between the area of simulated failure and annual rainfall totals. The relationships explain between 44% and 56% of the variance against a range from 30% to 33% for the rainfall totals over the hydrological years.

The relationship between the recurrence interval and the area of simulated failure can be used to express the change in temporal sensitivity of the entire catchment of the Barranco de la Coloma for the scenarios (Figure 8.9). Around the relationship, the 95% confidence limits have been drawn that are indicative for the variability (Table 8.14). In all cases, the band of uncertainty is large and does not enclose all data points. Clearly, the area of simulated failure is not defined by the annual rainfall alone and the part of the

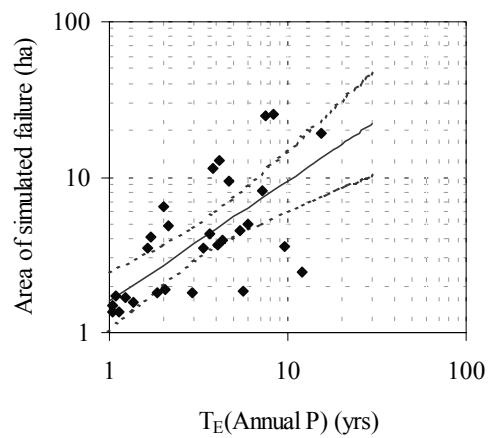
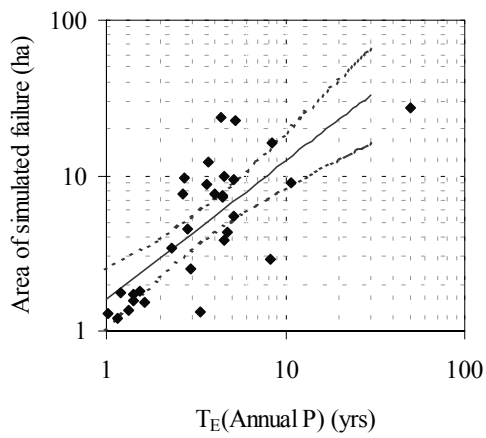
unexplained variance will be due to local differences in the antecedent moisture conditions and the consequent hydrological response. The spread of the data points is therefore especially large for the moderately frequent events with recurrence periods between 2 and 20 years. It is important to realise that the confidence limits are defined by a statistical model for the variability of this range. Thus, the confidence limits confine the extremes adequately but may be unrealistic for large recurrence intervals as the area of simulated failure will be truncated by the modelled susceptibility.

Table 8.14: Relationship between area of simulated failure, A , and the recurrence interval, T_E , per scenario of the form $\ln(A) = Y_0 + \alpha \cdot \ln(T_E)$. Given are the mean Y and 95% confidence limits $\pm \varepsilon$, for $T_E = 30$ years

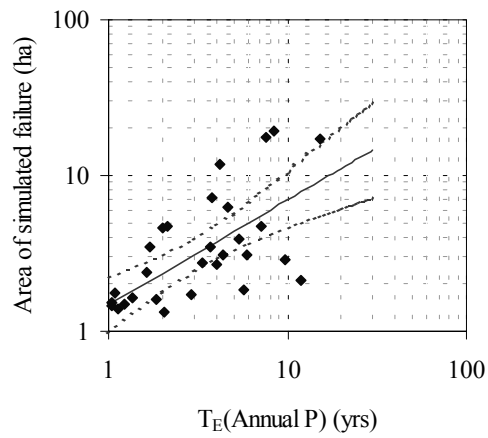
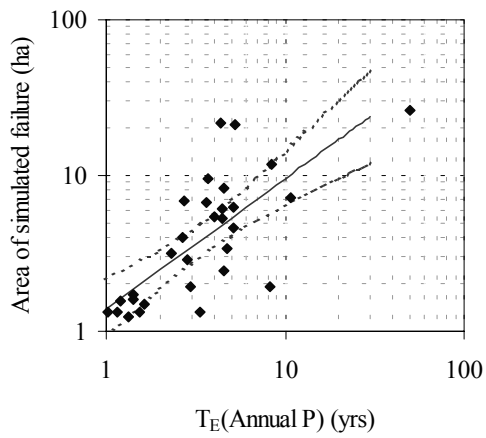
Scenario	Y_0	α	R^2 (-)	Y	$Y - \varepsilon$	$Y + \varepsilon$
BAU-CP	5.07	0.89	0.56	33.0	16.3	66.9
BAU-WF	5.07	0.78	0.47	22.2	10.3	47.8
CRE-CP	4.94	0.84	0.54	23.9	12.0	47.6
CRE-WF	5.00	0.67	0.44	14.6	7.2	29.7
PS-CP	4.98	0.87	0.56	27.7	13.9	55.1
PS-WF	4.98	0.75	0.048	18.8	9.1	38.7

Because of the uncertainty, the regions around the relationships overlap to a large extent. However, the changes in the area of simulated failure are consistent between the land use and climate change components of the scenarios and result primarily from a change in slope (Table 8.14). This change follows the observed tendency with the largest changes occurring for the CRE scenario, both under the CP and WF climates (Table 8.14). In spite of the overlap and the similar degree of uncertainty, the uncertainty bands are partly exclusive which evidences that the differences between the scenarios are substantial.

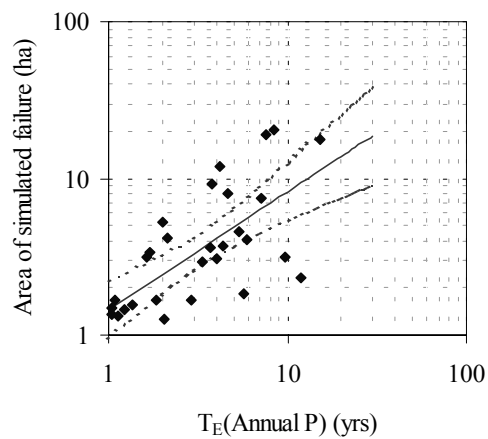
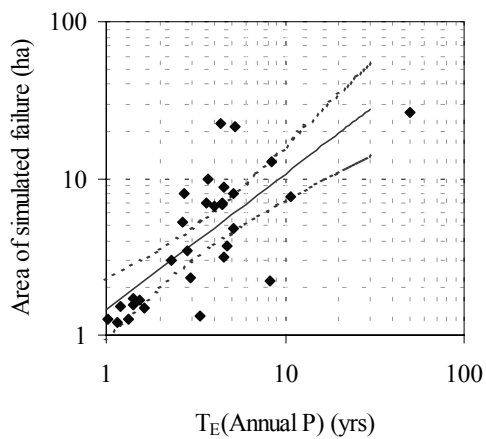
Recapitulating, the simulated failure decreases under all scenarios with respect to the present environmental conditions (BAU-CP). The change in the area is smaller than the decrease in the temporal activity. This can be attributed to the changes in the simulated hydrological response. For the present climate (CP), changes in the area and temporal characteristics are the direct result of the changed distribution of land use of the area. The land use changes of the CRE and PS scenarios lead to an increase in the area under semi-natural vegetation (unit IV) and, for the PS scenario, in an expansion and concentration of the area under cultivation (unit I). Both units have a larger actual evapotranspiration, which accounts for the decrease in persistence (Section 8.4.3). However, the land use change does not affect the absolute pore pressure levels over the 30-year period as the recurrence and the area of simulated failure remains virtually the same (see Table 8.12 and Figure 8.6).



a) BAU



b) CRE



c) PS

Figure 8.9: Relation between the area of simulated failure and recurrence interval of the Gumbel-distribution, T_E , for the annual rainfall totals per scenario (respectively CP and WF)

Under the changed climate of the WF series, the combined effect of land use and climate change accounts for the disconnection between the rainfall over the preceding hydrological year and the area of simulated failure. It also increases the propensity of the system to event rainfall as the dependence of landslide activity on the timing and the magnitude of event rainfall increases (Table 8.13). The changes in area and in the temporal characteristics of simulated failure are marked as the evapotranspiration increases and the soil moisture deficit at the end of the summer deepens. More rainfall is needed to accumulate drainable pore water in the topsoil, which shifts the moment at which the soil moisture might start to percolate to the deeper layers forward. When this moment occurs on average later in the hydrological year, less rainfall events will be available to raise the ground water in the deeper layer to critical levels. Meanwhile, the magnitude of these significant rainfall events that can trigger landslides will increase as more water is lost to evapotranspiration. Under these conditions, large storage capacities and rapid drainage favour percolation. These variables are the highest for the semi-natural vegetation of Unit IV but this unit is also the most sensitive to an increase in potential evapotranspiration (Figure 8.7).

The decrease in the temporal sensitivity of the Barranco de la Coloma to landsliding is the largest when the current trend of abandonment continues (CRE scenario). This trend effectuates the largest decrease in simulated failure under both climate conditions (Table 8.10). On average, the simulated failure for the CRE-WF scenario is less than the half of the BA-CP scenario for a 30-year event (Table 8.14).

8.5 Discussion

The assessment of the change in temporal sensitivity as presented above is based entirely on the results of the Scenario Modelling. These results have been treated as representative for the landslide activity in the study area and only briefly a reference was made to the performance of the coupled hillslope model as discussed in Chapter 7. In that Chapter, it was concluded that the simulated failure could not account for all of the observed landslide occurrence. Thus, the changes in simulated failure will also represent only a fraction of the probable landslide occurrence under the changed environmental conditions. In Section 8.4.2 it was stated that for the non-susceptible slopes for which no failure could be simulated, the same decrease in landslide occurrence can be extrapolated for the various scenarios. This assumption is of course only valid if the mechanisms that control the landslides on these non-susceptible slopes remain the same. In Section 7.4, the poor performance for the model on these slopes was explained by the modelled susceptibility, which was too optimistic to simulate failure on slopes below 14°. The observed landslide occurrence on these slopes, which included the large landslide complexes near Almudaina, was attributed to the development of a lower shearing resistance under periodic displacement in combination with lateral destabilisation. For these periodic displacements, the frequent recurrence of critical pore pressures is required. The expected decrease in hydrological triggering, however, makes the full development of residual strength less likely as increased periods of rest may lead to strength regain. Consequently, the lower incidence of critical pore pressures may initiate

to a positive feedback mechanism that increases the stability to an extent that is larger than that explained by an attenuated hydrological response alone.

In order to safeguard the validity of the coupled hillslope model, the imposed environmental changes of the scenarios are limited and based on the present conditions. Notwithstanding, the forecasts will still be hampered by the model performance under the present conditions. It was observed that the simulated failure overestimates the landslide occurrence on the susceptible slopes. The proportion between simulated failure and observed landslide occurrence varied (Section 7.6), but generally a ratio of one half can be applied. The only differences were observed for the steep slopes under land use units III and IV but their occurrence on these slopes is not changed. This would imply that the relative changes in simulated failure could be extrapolated to the real world under the assumption that the process system of the coupled hillslope model remains valid. This assumption is embodied in the static susceptibility and land use conditions that have been used in the simulation. This, in turn, restricts the validity of the forecasts to the relatively short period that the present susceptibility is inherited under new, environmental conditions. Over longer periods, the susceptibility will change and result in an adaptation of the temporal sensitivity. Under the WF climate, such adaptations include the exhaustion or degradation of the soil, changed rates of soil formation and a decrease in vegetation density as water stress might become more frequent. The feedback mechanisms that accompany such changes are still incompletely understood and the interactions too complex to model in order to make reliable forecasts on the transitions that may occur under transient environmental change. Yet, it is an essential problem to understand the changes in the sensitivity over time from both a geomorphological and a practical perspective. The decrease of landslide occurrence and the increased dependence on event rainfall predicted here will generally be advantageous to the human activities in the area. An additional favourable effect, which this study briefly touches, is that overland flow may become less frequent under the changed environmental conditions. Especially under the WF climate, the excess rainfall that generates runoff will decrease whilst the storage capacity of the present soil mantle will still be large. So, the overall risk of mass wasting can be expected to decrease initially.

However, such a decrease in the temporal sensitivity of inherited systems, could lead to a more brittle behaviour. The decreased frequency of potential triggers will result in a situation where a larger fraction of the geomorphic work is done by low frequency-high magnitude events. Once the resistance of the landscape is exceeded by these events, the inherited landscape is likely to be in a larger state of disequilibrium with the actual conditions and the resulting adaptation more dramatic with all the possible consequences for human activities in the affected area.

8.6 Conclusions

The Scenario Modelling indicates a general decrease in the temporal sensitivity to rainfall-induced slope failure as assessed from the changes in the simulated failure. The relative changes give an estimate for the actual changes in landslide occurrence that are likely to occur in the study area under conditions that are similar to the changes imposed

by the five hypothetical scenarios of Table 8.2. The changes are caused by alterations in the hydrological response; under the present climate, the different rates of actual evapotranspiration of the land use units account for the decrease. The absolute increase of the area with semi-natural vegetation in both the CRE and PS scenarios leads to an attenuation of the hydrological response on these slopes. Consequently, the persistence of slope failure decreases by 24% and 10% for the CRE-CP and PS-CP scenarios respectively. The attenuation of the hydrological response has less influence on the absolute groundwater levels that were obtained. The decrease in the area of simulated failure is in the order of 5% for both scenarios.

Under the WF climate, the increased potential evapotranspiration has a large impact on the simulated failure. Especially in the case of the CRE-WF scenario are the changes substantial. Both the area and the persistence decrease with 25%. In terms of absolute duration, the change is even larger as the model results show a decrease of 41% in the days that $P(F \leq 1) \geq 0.10$. For the PS-WF scenario, these changes are respectively 20%, 7% and 22%. For the BAU-WF scenario, the changes are much smaller (respectively 5%, 9% and 14%). The conclusion is, therefore, that under the present CP climate mainly the temporal activity is affected by the imposed land use changes but the sensitivity in terms of landslide occurrence does not change noteworthy. In contrast, the compounded effect of climate and land use change leads to a large decrease in the sensitivity to slope failure, both in terms of temporal activity and spatial occurrence.

APPENDIX 1: LOCATION OF THE STUDY AREA

This appendix specifies the location of the study area and the equipment. The study area, comprising the Barranco de la Coloma and the Barranco del Mollo, is enclosed by the square of the local UTM co-ordinates of the zone 30S between 728000-4293000 and 730000- 4295000 (Figure A1.1). In the figures of the text, these co-ordinates are indicated on the maps as units of thousands (e.g. 729-4294). Indicated on this map are the Barranco del Mollo and the Coloma, as well as the villages of Planes and Almudaina (see Figure 2.1 for general reference).

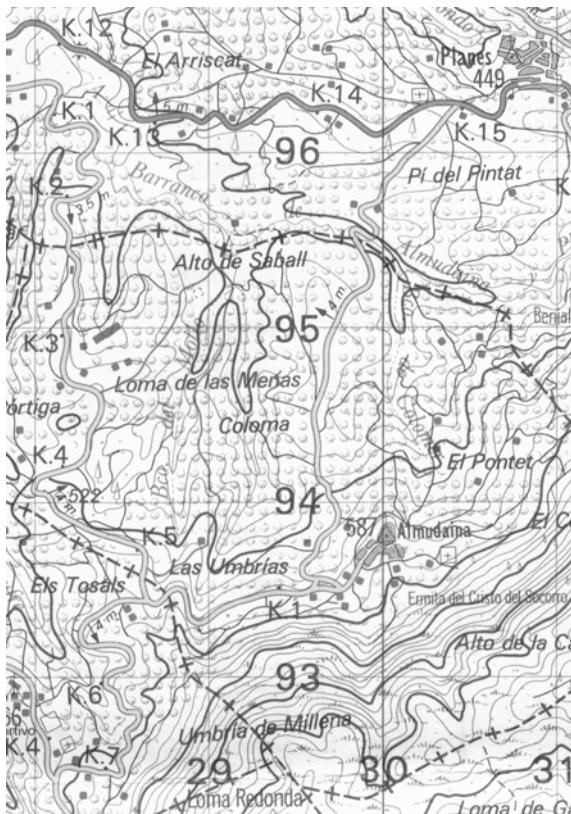


Figure A1.1: Topographical map (original scale 1:50,000) of the study area and adjacent area (Sheet 821, Mapa militar de España, Seria L, 1991)

Figure A1.2 specifies the location of the equipment within the Barranco de la Coloma. The darker area represents the 30-ha large sub-area.

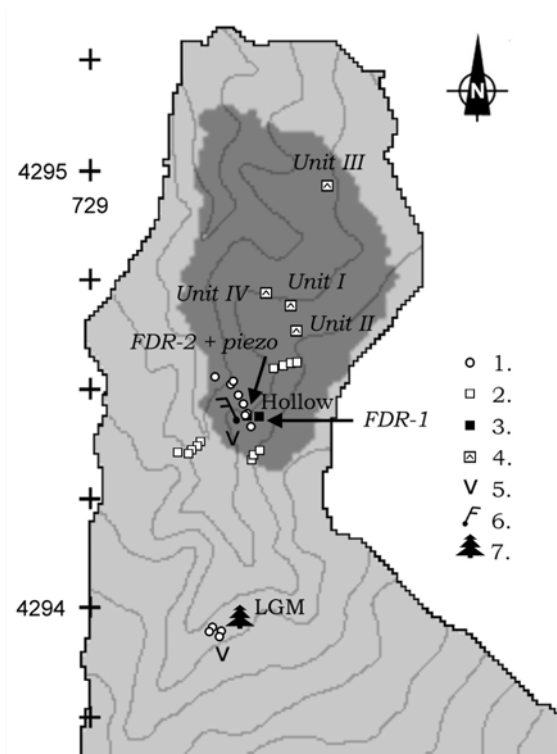


Figure A1.2: Location of field equipment & tests: 1: Piezometers; 2: TDR-pits; 3: Automated FDR-sensors; 4: Rainfall simulations; 5: Tipping bucket rain gauge; 6: meteorological station; 7: Interception plot

APPENDIX 2: DERIVATION OF THE PENMAN EQUATION

The potential rate of evapotranspiration is controlled by the energy budget at the soil surface and by the effectiveness of vertical air movements to transfer vapour into the atmosphere.

The energy budget is subject to the fluxes of long- and short-wave radiation. Most of the energy that is transferred to the soil surface comes from solar or global radiation, which consists of both direct beam and indirect, scattered radiation (short-wave radiation, R_S). The additional source of radiation is the long-wave radiation, R_L , emitted by cold bodies on the earth (Hanks & Ashcroft, 1986). The actual incoming radiation is dependent on the atmospheric conditions. Clouds will decrease the amount of global radiation that reaches the surface. At the same time the presence of clouds will increase the total of emitted long-wave radiation that can be absorbed. The net amount of absorbed radiation, R_N , at the surface is the sum of the absorbed incoming global radiation, total minus reflected, and the net long-wave radiation, which is the difference between the absorbed and emitted quantities

$$R_N = R_S(1 - \rho) + R_L. \quad (\text{A2.1})$$

In this equation the reflected short-wave radiation is determined by the albedo of the surface, ρ , which is the ratio of the scattered and incoming radiation as measured by two pyranometers looking in down- and upward directions. The radiation flux is expressed as energy per unit time and surface. In the *SI*, the units are $\text{J}\cdot\text{s}^{-1}\cdot\text{m}^{-2}$ what corresponds to $\text{W}\cdot\text{m}^{-2}$.

Usually the influence of the long-wave radiation is considered of little importance compared to that of the global radiation. If the net radiation is known, the energy budget equation can be written as

$$R_N = H + \lambda \cdot \rho_w \cdot ET + G, \quad (\text{A2.2})$$

in which G is the quantity of radiation used to heat the soil or water body and H that for heating the air, often called the sensible heat. This contrasts it against the term $\lambda \cdot \rho_w \cdot ET$ or *latent heat*, L , which represents the amount of energy that is used to evaporate or transpire water from the soil and vegetation. Most of the incoming net energy is consumed as latent heat for evapotranspiration when the water supply is unrestricted.

The vapour, released at the surface, is transferred to higher air layers by the prevailing vapour pressure difference and by the turbulent air movements over irregularities as vegetation. If no energy is advected, transport is entirely vertical and measurements at two heights are sufficient to define the effectiveness of the turbulent eddies.

The already mentioned energy balance and aerodynamic profile methods utilise this principle of vertical transport to calculate the potential evapotranspiration from the sensible heat flux, H . The aerodynamic profile method requires measurement of the temperature, the wind speed and the vapour difference at the surface and a given height. Moreover, it applies an estimate of the vertical eddy transfer coefficient, K_V , that varies widely under different conditions (Hanks & Ashcroft 1986). The same holds for the

energy budget approach in which the Bowen ratio, H/L , is used to estimate H what, again, requires knowledge of the temperature and vapour pressure difference at two heights and an additional assumption on the horizontal eddy transfer coefficient, e.g. $K_h = K_v$.

Penman avoided the problem of defining H by using an empirical aerodynamic equation and assuming isothermal conditions (Hanks & Ashcroft, 1986, Dingman, 1994). He assumed that the vapour pressure in a boundary layer over the surface is at its saturated value, $e_s(T_a)$, under the actual air temperature T_a . At the same time, he assumed the vapour pressure of the overlying air, e_a , to be directly proportional to the relative humidity RH (i.e. $e_a = e_s(T_a) \times \text{RH}$). This assumption reduces the number of measurements but it limits the applicability of the Penman equation to areas of unrestricted water supply only.

Consequently, the vertical gradient is known and the removal of vapour from the saturated boundary layer is only dependent on the effectiveness of the air to transport it. Penman originally used an empirical relation for the vertical transport of water vapour. Van Bavel (1966) replaced this relation by a physical description for the eddy transfer coefficient, giving the equation a sound physical and dimensionally balanced basis. Here it suffices to state that the additional assumptions of the modified Penman equation are that there is no advected energy and that there is no change in heat storage present in the equation. This implies that there is no heat exchange with the ground although the term G of the energy budget can, if measured, be included as a flux density in the adapted Penman equation.

By combining the energy budget, as measured by the net radiation, with the vertical mass transfer by the turbulence, the Penman equation becomes

$$ET = \frac{\delta \times \text{"net radiation"} + \gamma \times \text{"mass transfer"}}{L(\delta + \gamma)}, \quad (\text{A2.3})$$

in which δ is the slope of the function of the saturation vapour versus the air temperature T_a ($\text{Pa} \cdot ^\circ\text{C}^{-1}$; see Figure A2.1).

The parameter γ is the psychrometric constant ($\text{Pa} \cdot ^\circ\text{C}^{-1}$) which relates the sensible to the latent heat by means of the Bowen ratio, B (Dingman, 1994)

$$B = H/L = \gamma \frac{T_s - T_a}{e_s - e_a}, \quad (\text{A2.4})$$

and

$$\gamma = \frac{c_a \cdot P}{0.622\lambda}, \quad (\text{A2.5})$$

in which T_s is the surface temperature ($^\circ\text{C}$), e_a and e_s are respectively the actual vapour pressure of the air and the saturated vapour pressure at the surface (both in Pa), c_a is the specific heat capacity of air ($1004 \text{ J} \cdot \text{kg}^{-1} \cdot ^\circ\text{C}^{-1}$), P is the atmospheric pressure (Pa) and λ is the latent heat of vaporisation ($\text{J} \cdot \text{kg}^{-1}$). The constant 0.622 represents the ratio of the molecular weight of water vapour and dry air. The psychrometric constant is not a true constant as both the latent heat λ and the pressure P vary with the temperature and with

the elevation respectively. The variation in the atmospheric pressure, P , is, however, generally low and the calculated potential evapotranspiration is relatively insensitive to it.

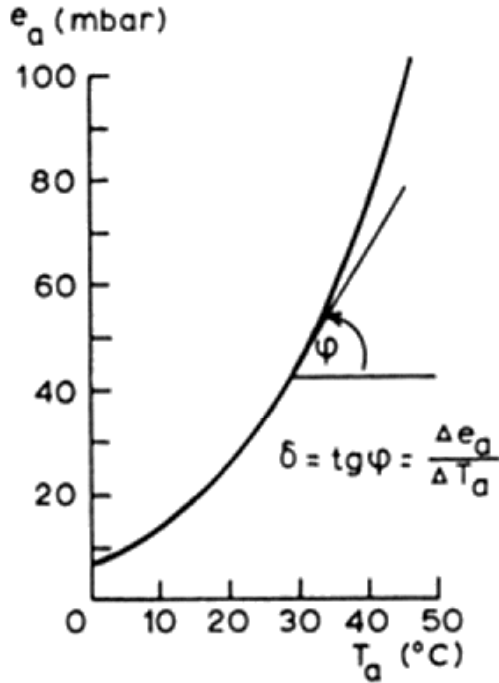


Figure A2.1: Saturated vapour pressure e_s as function of temperature T_a and its first derivative δ ($\text{Pa} \cdot ^\circ\text{C}^{-1}$). After Feddes *et al.* (1978)

The rate of evapotranspiration is different under crops than for an open water surface (Feddes *et al.*, 1978). This is not only because of the different albedos and the resistance of the stomata on the plants' leaves but also because of the larger surface roughness from the vegetation stand what influences the rate of evapotranspiration due to the aerodynamic turbulence. This surface roughness is most times represented by the canopy resistance term, R_a ($\text{s} \cdot \text{m}^{-1}$). The mass transfer term, which is also called the isothermal evapotranspiration because of the assumption that $T_a = T_s$ and which is denoted by $L \cdot E_a$, can then be replaced by

$$Ea = \frac{\rho_a \cdot c_a \cdot (e_s - e_a) / R_a}{L(\gamma + \delta)}, \quad (\text{A2.6})$$

where ρ_a is the density of air, $1.205 - 1.293 \text{ kg} \cdot \text{m}^{-3}$ and Ea has units of ($\text{m} \cdot \text{s}^{-1}$) (Feddes *s.*, 1978).

In the adapted equation of Van Bavel (1966), R_a is obtained from a parabolic wind sprofile above an irregular surface. Wind speed distributions show a clear logarithmic increase above a point $Z_d + Z_0$ at which the velocity is zero. These elevations, Z_d and Z_0 , are called the zero plane displacement and the roughness height respectively. These heights are proportional to the average height of the irregularities, like vegetation. For Z_0 a value of 0.1 of the vegetation height is common, whereas Z_d is fixed at a value of 0.75 of this height (Dingman, 1994). The resulting turbulence determines the diffusivity of

momentum that leads to the vertical redistribution of vapour and heat. The effectiveness of the vertical transport is given by the friction velocity u^* of the eddies. When the wind speed V_m at a height Z_m is known, the friction velocity is given by

$$u^* = \frac{k V_m}{\ln[(Z_m - Z_d)/Z_0]}, \quad (\text{A2.7})$$

where k is the *Von Karman* constant (0.41 -).

As the diffusivity of momentum is directly proportional to the square of the friction velocity, R_a is, for the finite difference approximation de/dv . $(e_s - e_a)/(V_m - 0)$, given by

$$R_a = \left[\frac{1}{u^*} \right]^2 \cdot \frac{1}{V_m} = \frac{\ln[(Z_m - Z_d)/Z_0]^2}{[k^2 V_m]}. \quad (\text{A2.8})$$

This gives the following formula for Penman's equation

$$ET = \frac{\delta \cdot R_N + \gamma \cdot E_a}{L(\delta + \gamma)}, \quad (\text{A2.9})$$

where the evapotranspiration rate is given in units of $\text{m} \cdot \text{s}^{-1}$.

APPENDIX 3: METEOROLOGICAL DATA OF NON- PRECIPITATION VARIABLES FOR COCENTAINA 1991-1997

The automatic station of the Instituto Nacional de Meteorología at Cocentaina is located at 560 m.a.s.l. (No. 45 in Figure 4.10). Since November 1991, this station has been collecting meteorological data on the relative humidity, temperature, wind speed and atmospheric pressure (respectively abbreviated to RH, T, V and P). The concerned data are registered as averages over the periods between 0, 7, 13 and 18 hours. For the temperature and atmospheric pressure, the daily extremes are given as well while for the wind speed the total distance covered between 0 and 24 hours is listed. For this study, the data from November 1991 until December 1997 have been used.

Table A3.1: Data recovery INM-station Cocentaina 1991-1997

Year	1991	1992	1993	1994	1995	1996	1997
Recovery (%)	72	58	55	78	83	91	78

The availability of data from Cocentaina is listed in Table A3.1. When only those periods over which all four variables are available are considered complete, the recovery is nearly 75% over the period 1992-1997. For the individual variables, about 90% is recovered. For the years 1992 and 1993, the recovery is low. For 1992, this is caused by an overall data scarcity. In 1993, the low recovery can be attributed to the lack of pressure data.

In the original data set, the temperature is given with a resolution of 0.1°C, the relative humidity in multiples of 1% and the atmospheric pressure with a resolution of 10 Pa, what agrees with the resolution of 0.1 mb in the original records. The average atmospheric pressure and the temperature are obtained from the extreme values over the period between 0 and 24 hours. In the case of the atmospheric pressure, the measured values have been used without the usual reduction to sea level. The average relative humidity has been calculated from the observations at the regular recording intervals. Only those days are considered as complete when at least three of the four observations are present. The average wind speed over the day has been calculated from the total distance covered over the 24 hours period. This distance is given in units of kilometres, what brings the accuracy of the average wind speed to $\pm 0.01 \text{ m}\cdot\text{s}^{-1}$.

The averages for the four meteorological data are presented in Table A3.2 and Figure 4.13. Based on these observations, the relative humidity appears to be fairly constant over the year. The average values range from 59% during the summer to 69% in the winter. The regularity of the daily course explains this small seasonal difference; in the winter and summer, the RH is respectively 77% and 66% at sunrise. The lowest values are observed in the late afternoon when the values decrease to 67% and 51%. This continuity reflects the relation of the absolute humidity with temperature, which has a strong seasonal fluctuation in addition to its daily course as well. On average, the daily

temperature is 10.5°C during winter, compared to 23.5°C in summer over the period 1991-1997. The diurnal course in temperature is lower during the summer than in winter. In contrast to temperature, the average atmospheric pressure and the wind speed do not exhibit a seasonal trend. For the atmospheric pressure, the range over which the pressure varies, is limited to 20 mb for the average daily values and to 40 mb on the entire data set. Given the average of 953.5 mb, the range is less than 5% of this value. With respect to the wind speed, it must be observed that the variability is much lower during the summer than for the other seasons. In combination with the slightly lower average wind speed (1.9 m·s⁻¹ vs. 2.1 m·s⁻¹ in winter), this confirms the general observation that more stable conditions prevail during the summer.

Table A3.2: Seasonal and yearly statistics based on the daily averages of RH, T, V and P at the INM-station Cocentaina 1991-1997

Period	N	Average	COV (-)	Median	Min.	Max
<i>RH: Relative humidity (%)</i>						
SON	538	65	0.21	64	30	99
DJF	484	69	0.20	67	38	98
MAM	482	59	0.23	57	27	99
JJA	464	58	0.23	58	26	96
Year	1968	63	0.23	62	26	99
<i>T: Temperature (°C)</i>						
SON	545	16.7	0.26	16.4	5.9	27.4
DJF	513	10.5	0.30	10.5	1.3	18.5
MAM	495	14.4	0.26	14.4	3.1	24.0
JJA	466	23.5	0.15	23.8	13.5	34.7
Year	2019	16.1	0.37	15.4	1.3	34.7
<i>V: Windspeed (m·s⁻¹)</i>						
SON	532	2.05	0.44	1.86	0.47	6.49
DJF	515	2.07	0.55	1.74	0.15	6.97
MAM	496	2.10	0.40	1.89	0.12	6.37
JJA	474	1.92	0.23	1.88	0.31	4.64
Year	2017	2.04	0.43	1.85	0.12	6.97
<i>P: Atmospheric pressure (Pa)</i>						
SON	455	95330	0.01	95350	93250	96700
DJF	441	95560	0.01	95690	93530	97320
MAM	495	95230	0.01	95210	93350	96750
JJA	401	95280	0.00	95290	93970	96080
Year	1792	95350	0.01	95340	93250	97320

APPENDIX 4: GENERATION OF THE STANDARDISED NON- PRECIPITATION VALUES

The simulation of the standardised non-precipitation values z_k as included in the stochastic weather generator is based on a multivariate weakly stationary generating process as defined by Matalas (1967) and applied by Richardson (1981).

The generation of the k standardised non-precipitation variables is defined as

$$z_k(t) = [\beta] \cdot z_k(t-1) + [\zeta] \cdot \varepsilon(t), \quad (\text{A4.1})$$

where $z(t)$ and $z(t-1)$ are k -dimensional vectors of the standard normal variable z_k for the present and the previous day (t and $t-1$ respectively), and $\varepsilon(t)$ is the k -dimensional vector of uncorrelated, standard normal white noise. The $k \times k$ -dimensional matrices $[\beta]$ and $[\zeta]$ are coefficients relating the vector $z(t)$ to those of $z(t-1)$ and $\varepsilon(t)$ respectively. This model is a first-order linear autoregression model that resembles the Markov chain used for rainfall occurrence (Section 4.4).

The problem is to define the entries of $[\beta]$ and $[\zeta]$ that will generate synthetic sequences that resemble the values of Z_k in the historical record. Since the expected value of the standard normal white noise at t and $t-1$, $E[\varepsilon]$, equals zero, the terms on both sides of the matrix equation A4.1 can be postmultiplied by the transpose of the vector $z(t-1)$. The expectations of the various matrix products then become

$$M_1 = \beta \cdot M_0. \quad (\text{A4.2})$$

In this equation, M_1 is the expected product $E[z(t-1)z(t-1)^T]$ and M_0 is $E[z(t)z(t-1)^T]$. Both M_0 and M_1 are $k \times k$ matrices that contain the variances as diagonal and the covariances as the off-diagonal elements. As the standardised variables, have a zero mean and unit variances, the entries of the matrices M_0 and M_1 are reduced to the lag 0 or *simultaneous* serial correlation and the lag 1 serial crosscorrelations. For the four non-precipitation variables simulated here, it results in the 4x4 matrices

$$M_0 = \begin{bmatrix} \rho_0 1,1 & \rho_0 1,2 & \rho_0 1,3 & \rho_0 1,4 \\ \rho_0 2,1 & \rho_0 2,2 & \rho_0 2,3 & \rho_0 2,4 \\ \rho_0 3,1 & \rho_0 3,2 & \rho_0 3,3 & \rho_0 3,4 \\ \rho_0 4,1 & \rho_0 4,2 & \rho_0 4,3 & \rho_0 4,4 \end{bmatrix}, \quad (\text{A4.3a})$$

and,

$$M_1 = \begin{bmatrix} \rho_1 1,1 & \rho_1 1,2 & \rho_1 1,3 & \rho_1 1,4 \\ \rho_1 2,1 & \rho_1 2,2 & \rho_1 2,3 & \rho_1 2,4 \\ \rho_1 3,1 & \rho_1 3,2 & \rho_1 3,3 & \rho_1 3,4 \\ \rho_1 4,1 & \rho_1 4,2 & \rho_1 4,3 & \rho_1 4,4 \end{bmatrix}. \quad (\text{A4.3b})$$

In Equation A4.3, $\rho_0(j,k)$ and $\rho_1(j,k)$ denote the lag 0 and lag 1 serial and cross-correlations. Since $\rho_0(j,k) = \rho_0(k,j)$, M_0 is a symmetrical matrix. However, for the lag 1 correlations the values are different and all entries must be defined separately (see Table 4.24).

By definition, the standard white noise is independent and has zero mean and unit variance. Hence, $E(\varepsilon(t)\varepsilon(t)^T)$ is an $k \times k$ identity matrix, I . If both sides of Equation A4.1 is postmultiplied by $z(t)^T$, the expectations of the various matrix products leads to (Matalas, 1967)

$$M_0 = \beta M_1^T + \zeta \zeta^T. \quad (A4.4)$$

The elements of $[\beta]$ are equal to the beta weights of the multiple regression of $z(t)$ on $z(t-1)$, and in matrix form, are obtained by

$$\beta = M_1 M_0^{-1}, \quad (A4.5)$$

where M_0^{-1} is the inverse of the non-singular matrix M_0 .

The matrix $[\zeta]$ can be solved from

$$\zeta \zeta^T = M_0 - M_1 M_0^{-1} M_1^T. \quad (A4.6)$$

According to Matalas (1967), principal component analysis can be used to solve A4.6 for $[\zeta]$. If determined in this manner,

$$\zeta^T \zeta = \lambda, \quad (A4.7)$$

where λ is a diagonal $k \times k$ matrix with the eigenvalues of Equation A4.6.

Table A4.1: Beta weights of $[\beta]$ for the non-precipitation variables Z_k

		X, t-1			
		RH	T	V	P
Y, t	RH	0.486	-0.010	-0.141	-0.005
	T	0.090	0.715	-0.029	0.061
	V	-0.072	0.070	0.335	-0.216
	P	0.055	-0.044	0.079	0.797

Table A4.2: Elements of $[\zeta]$ for properly correlated forcing of Z_k

		X, t-1			
		RH	T	V	P
Y, t	RH	0.508	-0.605	-0.220	0.094
	T	-0.015	0.609	-0.352	-0.199
	V	0.378	0.479	0.604	-0.056
	P	-0.034	0.046	-0.121	0.607

The elements of $[\zeta]$ have no physical meaning and is not unique for it can be postmultiplied by any $k \times k$ matrix θ as long as $\theta \cdot \theta^T = I$. This is in agreement with the requirement that the values of matrix $[\zeta]$ only have to ensure properly correlated forcings of Equation A4.1 from the white noise $\varepsilon(t)$.

The values of $[\beta]$ and $[\zeta]$ for the simulated standardised non-precipitation variables of relative humidity (RH), temperature (T), wind speed (V) and atmospheric pressure (P) are given in Table A4.1 and Table A4.2.

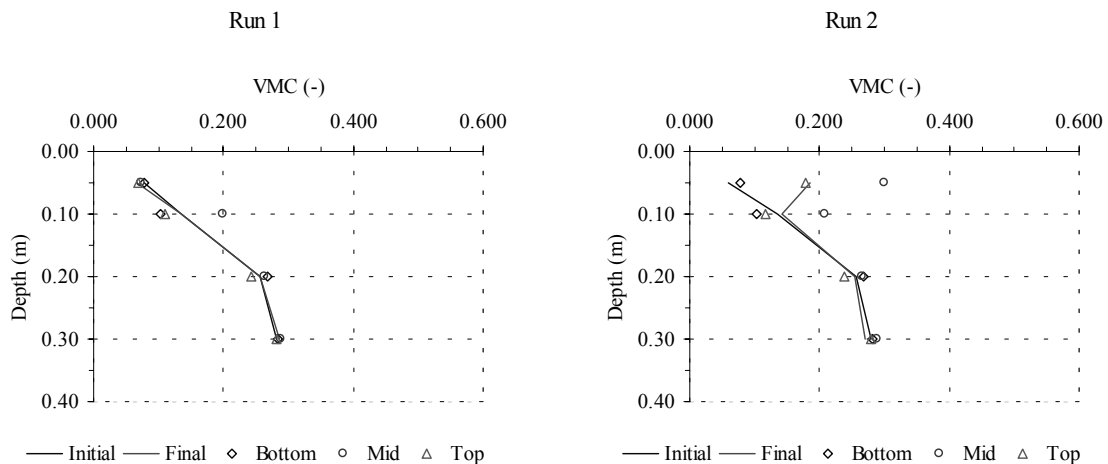
APPENDIX 5: INFILTRATION AND REDISTRIBUTION OF SOIL MOISTURE UNDER DIFFERENT LAND USE UNITS AS OBSERVED WITH TDR DURING BROADSCALE RAINFALL SIMULATIONS

This appendix summarises the information of the broadscale rainfall simulations for the four land use units. For the runs of each simulation, the start, duration and the intermediate period are given. In addition, the amount of rainfall is given. The average intensity is $34.4 \text{ mm}\cdot\text{hr}^{-1}$. The graphs show the distribution of the volumetric moisture content (VMC) with depth. The observations were made with time domain reflectometry (TDR) with sensors installed at three locations (top, middle and bottom of the plot). Both the individual readings and the average at the start and end of each run are shown.

Land use unit I: Cultivated

Table A5.1: Timing and amount of water applied during the rainfall simulation on land use unit I

Run	Rain applied Amount (mm)	Start (hh:mm)	Duration	Redistribution Intermediate period
1	8.8	00:00	00:15	01:03
2	10.6	01:03	00:17	02:11
3	17.5	03:14	00:30	01:41
4	9.7	04:56	00:20	20:38
5	16.6	25:33	00:30	01:50
6	17.1	27:23	00:30	



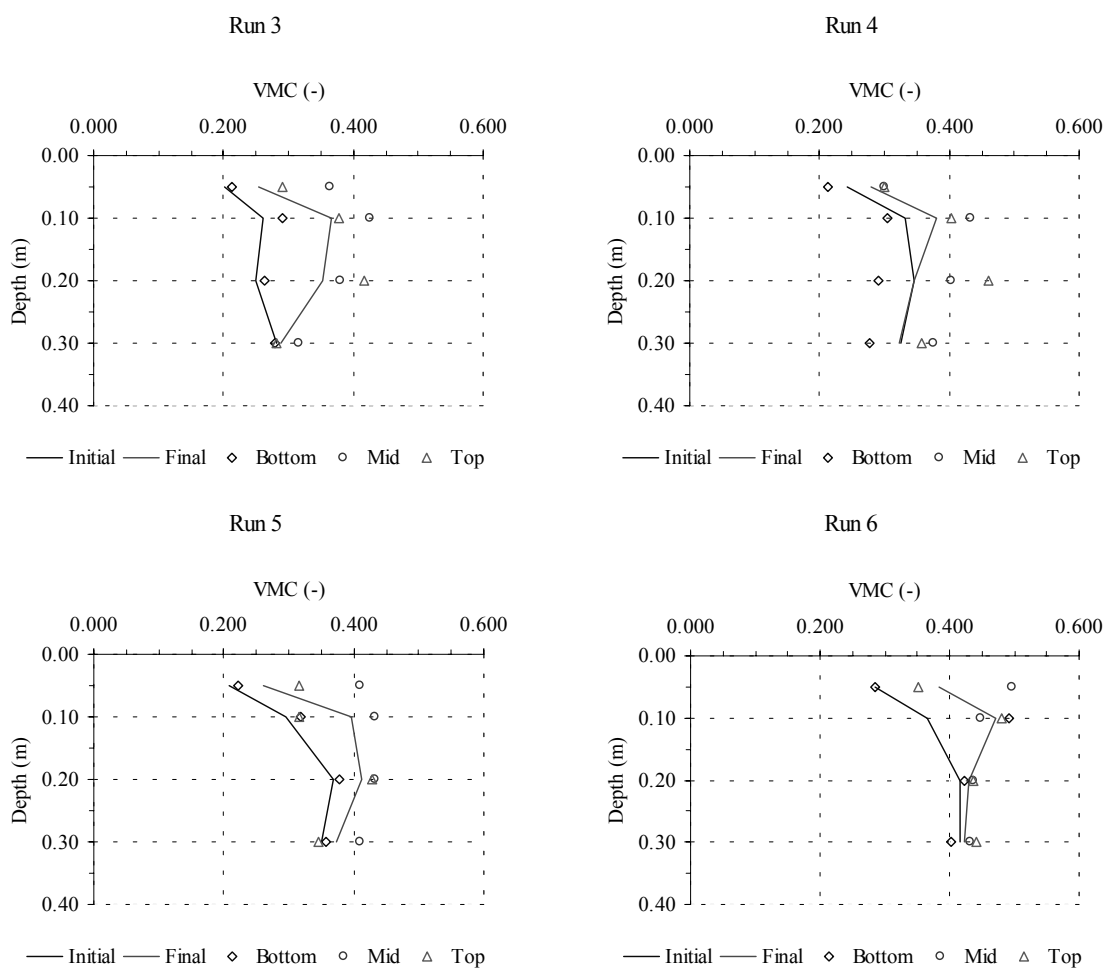


Figure A5.1: Change in VMC as observed with TDR during the rainfall simulation for land use unit I

Land use unit II: Abandoned – grasses & herbs

Table A5.2: Timing and amount of water applied during the rainfall simulation on land use unit II

Run	Rain applied Amount (mm)	Start (hh:mm)	Duration	Redistribution Intermediate period
1	11.5	00:00	00:20	01:20
2	11.2	01:20	00:22	01:20
3	10.8	02:40	00:23	03:30
4	16.1	06:10	00:30	17:02
5	24.6	23:13	00:45	
6				

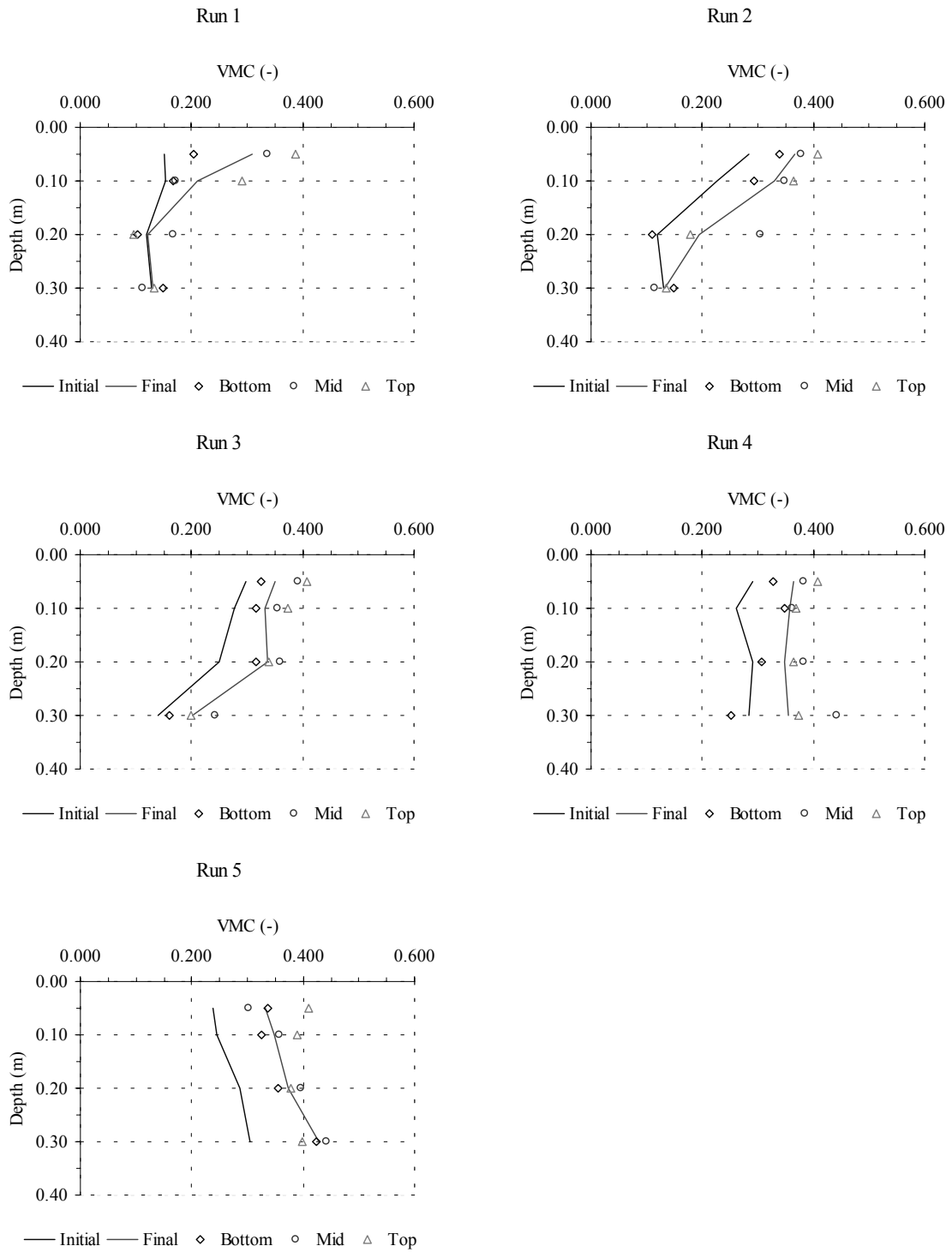
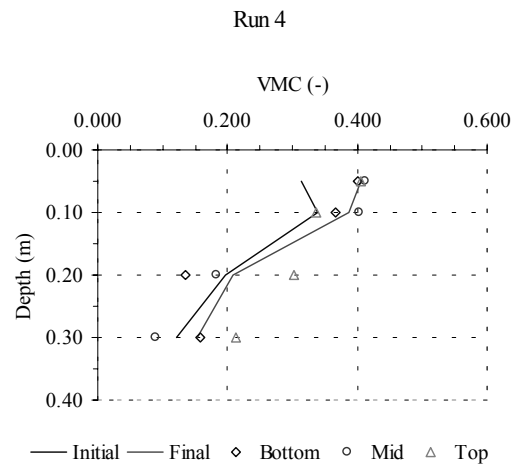
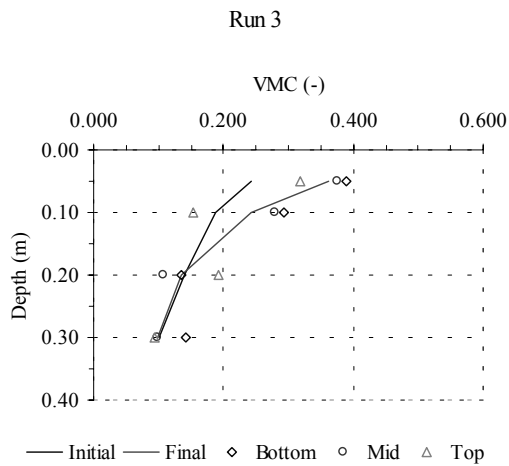
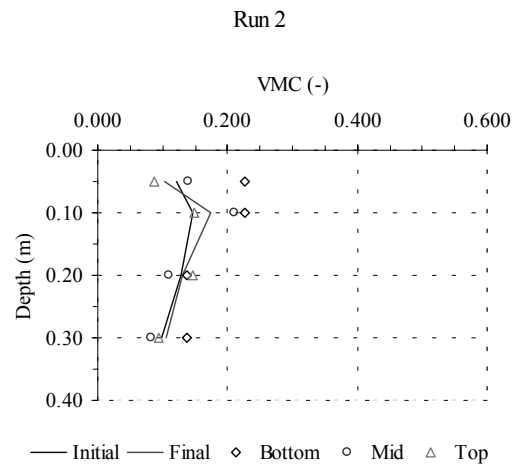
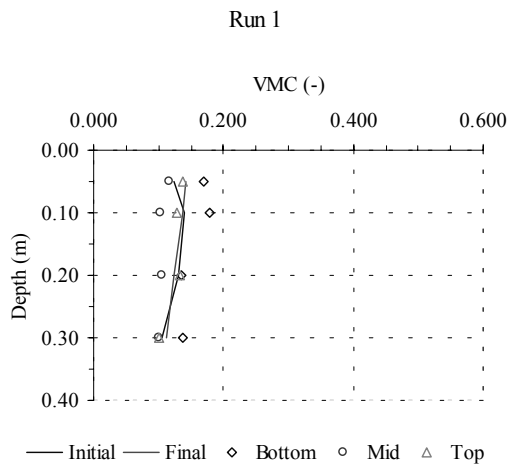


Figure A5.2: Change in VMC as observed with TDR during the rainfall simulation for land use unit II

Land use unit III: Abandoned – shrubs

Table A5.3: Timing and amount of water applied during the rainfall simulation on land use unit III

Run	Rain applied Amount (mm)	Start (hh:mm)	Duration	Redistribution Intermediate period
1	9.1	00:00	00:15	01:46
2	11.6	01:46	00:20	01:39
3	11.3	03:25	00:20	04:34
4	10.4	07:59	00:20	01:27
5	15.9	09:26	00:30	11:09
6	17.1	20:35	00:25	



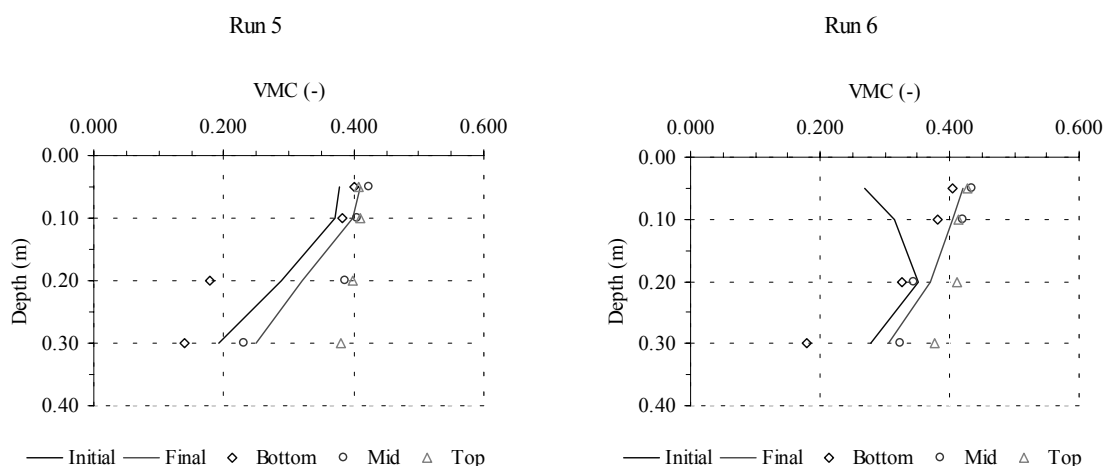
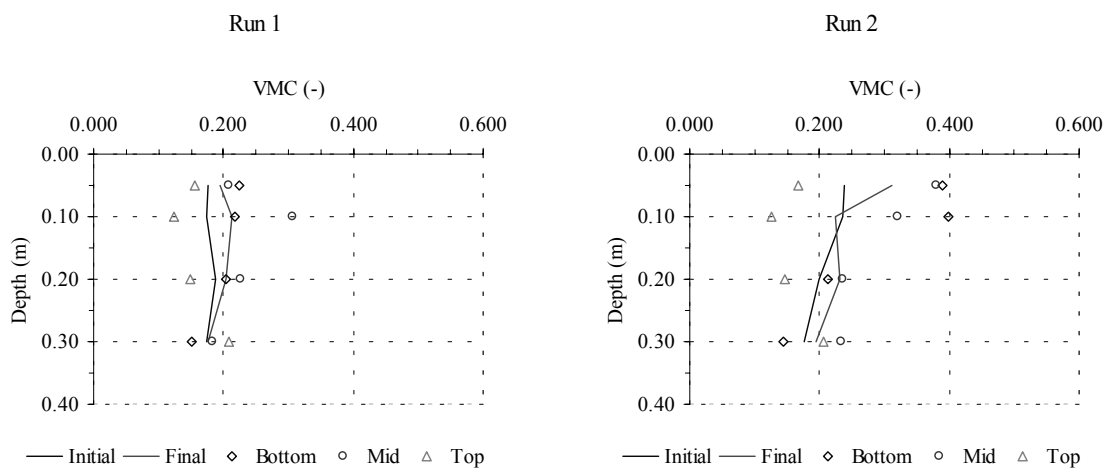


Figure A5.3: Change in VMC as observed with TDR during the rainfall simulation for land use unit III

Land use unit IV: Semi-natural – *Pinus halepensis*

Table A5.4: Timing and amount of water applied during the rainfall simulation on land use unit IV

Run	Rain applied Amount (mm)	Start (hh:mm)	Duration	Redistribution Intermediate period
1	8.6	00:00	00:15	03:36
2	8.7	03:36	00:15	01:34
3	8.7	05:10	00:15	03:31
4	16.5	08:42	00:30	15:32
5	8.4	24:15	00:15	02:35
6	21.8	26:50	00:45	



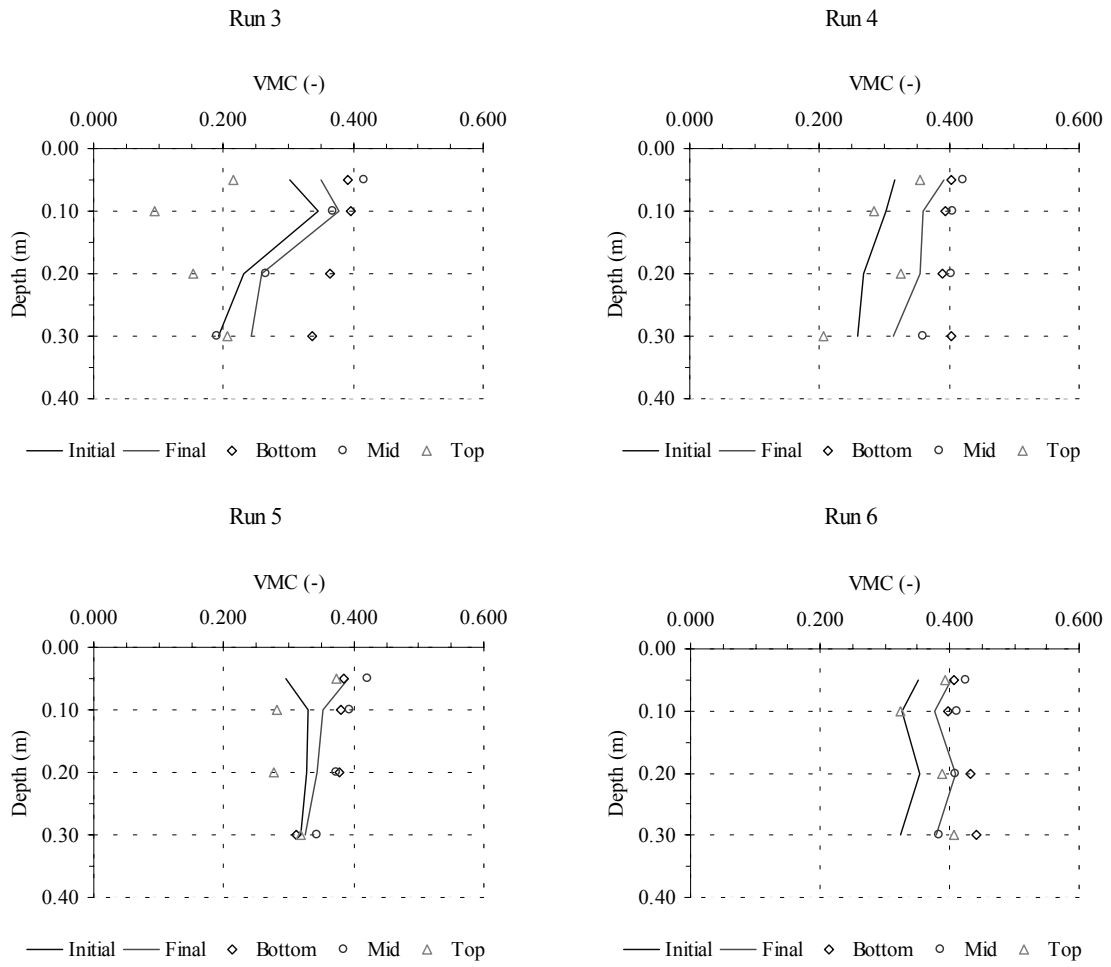


Figure A5.4: Change in VMC as observed with TDR during the rainfall simulation for land use unit IV

APPENDIX 6: SIMULATED HYDROLOGICAL RESPONSE FOR THE DIFFERENT CLIMATE CONDITIONS

The following graphs contrast the simulated hydrological response under the present land use conditions for the different climates (CP: cool present, WF: warmer future).

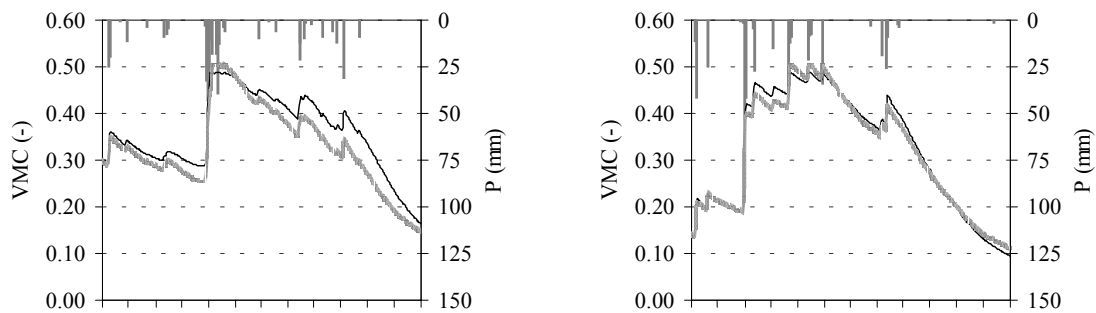
Two points are shown. The first point is situated in recently abandoned land (land use unit II), the second under semi-natural open pine wood (Unit IV; see Section 5.2 for classification). The solid black line represents the point under Unit II, the grey line the location under Unit IV. At these points, land use remains the same for the three land use scenarios.

The physiographic setting of the points is roughly the same (soil depth, slope and incoming radiation), except that the slope length above the point under semi-natural vegetation has a longer contributing slope.

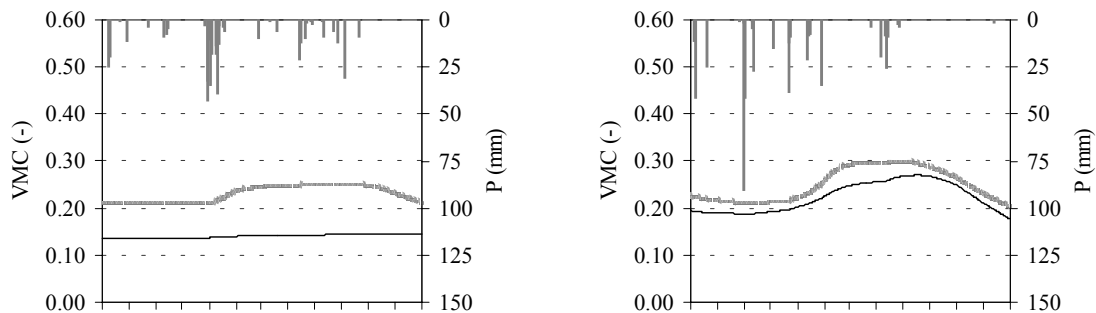
Per climate, the response over a hydrological year is shown for all three layers (0-50 cm, 50-100 cm and 100-150 cm). Three conditions of annual rainfall are contrasted: below-average, average and maximum as generated for the 30-year weather series. In the following, the left-hand graphs always represent the CP climate, the right-hand graphs the WF climate.

Below-average rainfall

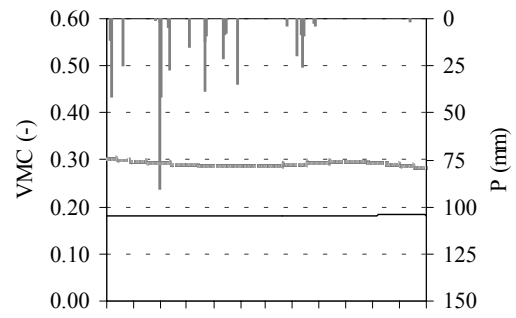
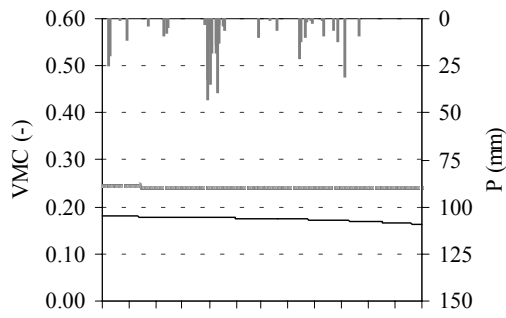
Layer 0.0 – 0.5 m



Layer 0.5 – 1.0 m

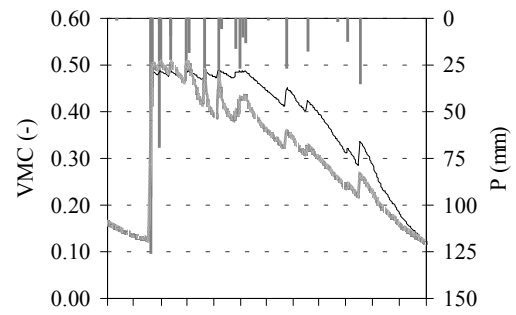
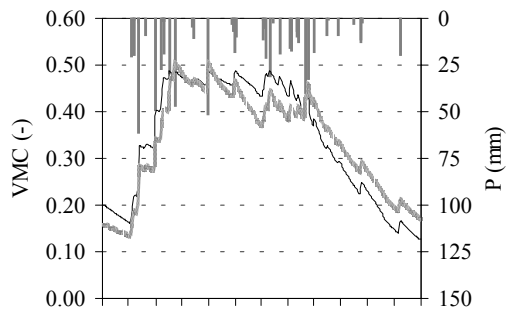


Layer 1.0 – 1.5 m

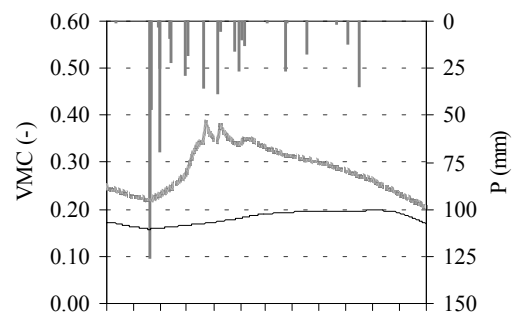
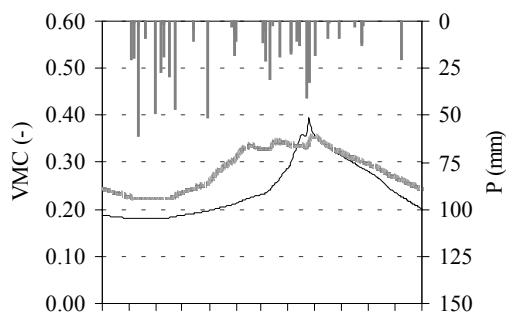


Average rainfall

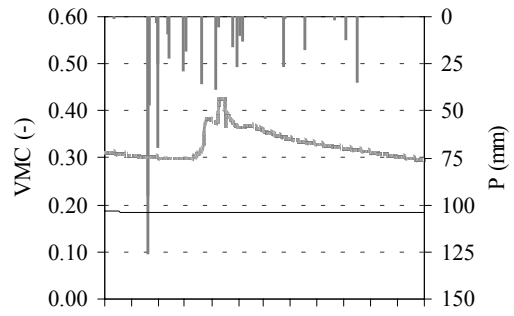
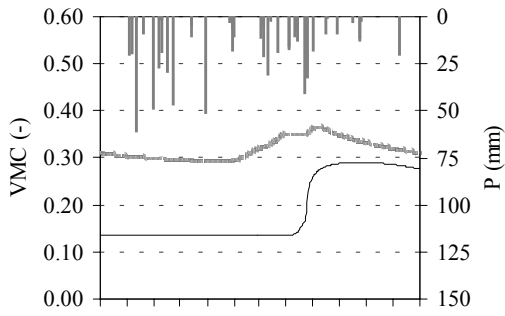
Layer 0.0 – 0.5 m



Layer 0.5 – 1.0 m

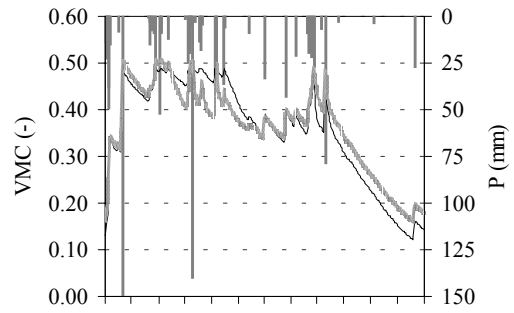
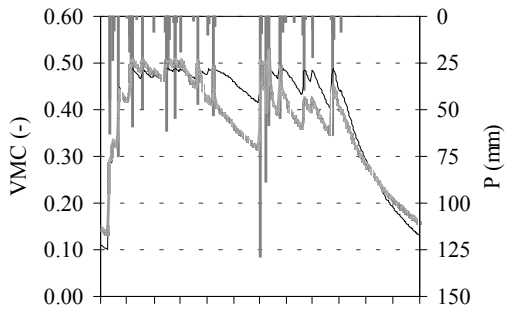


Layer 1.0 – 1.5 m

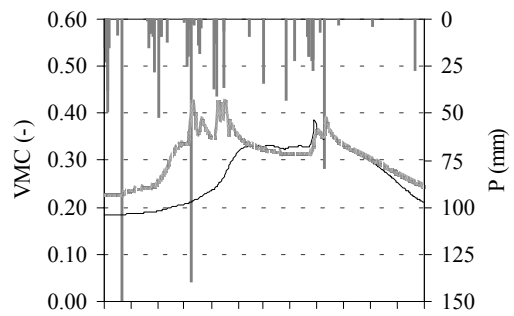
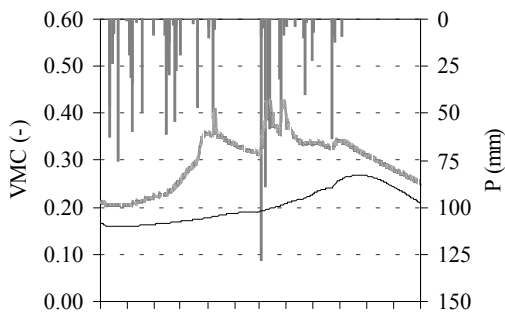


Above-average rainfall (maxima)

Layer 0.0 – 0.5 m



Layer 0.5 – 1.0 m



Layer 1.0 – 1.5 m

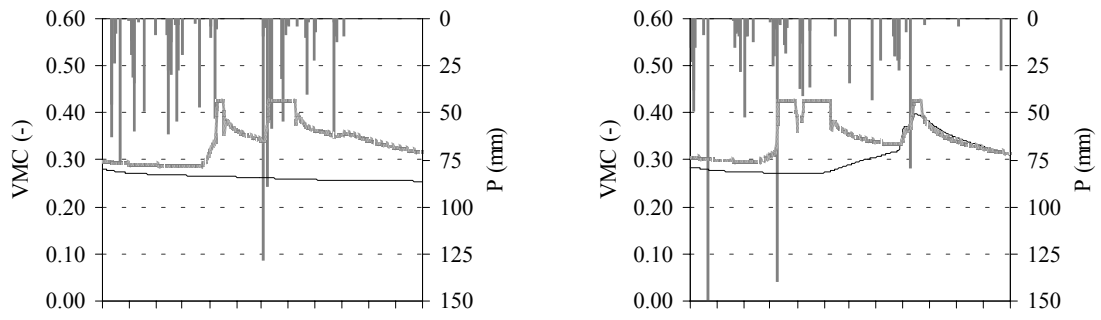


Figure A6.1: Change in volumetric moisture content for the BAU-CP and BAU-WF scenarios

SUMMARY

Introduction

Chapter 1: Problem definition, aim and methodology

Rainfall-induced landslides contribute directly to land degradation by the displacement of material and indirectly by destroying the vegetation cover that prevents surface wash. In humid to sub-humid Mediterranean environments, where a continuous vegetation cover can be supported, it can consequently be considered as a key process in the process system of land degradation. As part of the NWO research program *Hierarchy of Land Degradation Processes in a Mediterranean Environment*, the aim is to evaluate the role of landsliding within the integrated system of erosion processes in a quantitative manner. Hydrological processes that trigger landslides fluctuate temporally and are imposed on spatial variations in susceptibility. Hence, landslide activity can be considered in terms of its spatial extent and temporal frequency. On medium temporal scales (10-100 years), environmental conditions and the changes thereof influence the hydrological controls of landslide activity. The objectives of this study are, therefore, to

- Evaluate the spatial and temporal variations in potentially triggering rainfall events;
- Assess local variations in landslide susceptibility;
- Evaluate the role of the hydrology on landslide activity in the area;
- Assess the change in landslide activity under the impact of changes in land use and climate on medium temporal scales (10-100 years).

Because of the hypothetical nature of anticipated environmental change, a strong emphasis has been placed on modelling as a tool to assess the effects of land use and climate change on landslide activity (Section 1.4). The imposed changes are described by scenarios and static in nature. The fundamental assumption is made that on the medium temporal scales considered the susceptibility does not change. Consequently, the simulated changes in landslide activity reflect in essence those in temporal sensitivity.

Chapter 2: Physiography of the Valles de Alcoy

As study area, a small catchment has been chosen in the Valles de Alcoy (Spain), where rainfall-induced landslides occur frequently. In this region, landslide activity is favoured by the strong gradients of slopes underlain by incompetent marl of Miocene age. These unstable slopes are formed and maintained by the ongoing incision of the Río Serpis. Landslides are initiated by extreme rainfall events. However, such events are scarce and must alleviate the soil moisture deficit that builds up over summer.

In the Valles de Alcoy, land use is predominantly agricultural. Agriculture as source of sustenance, however, is on the decline. Abandonment of fields leads to regeneration of semi-natural vegetation. The regenerated vegetation cover is denser and has a more structured root zone. Due to the resulting larger infiltration capacity and changes in

interception and evapotranspiration, this regeneration can be expected to affect the effective rainfall that drives landslide activity.

Model development

Chapter 3: A coupled model of hillslope hydrology and slope stability

Given the aim and constraints of the area, a simple physically based model has been constructed that couples hydrology with stability. It is applicable to all cases in which percolation stagnates on a less permeable layer. This model is dynamic, i.e. it simulates the hydrology over time and evaluates the effects on the stability. The groundwater levels and moisture contents that are generated for every timestep are used as input for the stability assessment (Section 3.2). This stability assessment consists of a probabilistic version of the infinite slope model. Since the model is intended to evaluate changes in land use, it is embedded in a GIS to facilitate data exchange and the implementation of a land use dependent parameterisation (Figure 3.9).

Model implementation

Chapter 4: Climatic controls of landsliding

The coupled hillslope model aims to simulate the influence of antecedent moisture conditions and event rainfall on landslide activity. Because of this deterministic relationship, spatial and temporal patterns of rainfall and evapotranspiration can be considered as climatic controls on landslide activity on a regional scale.

The local weather system of the *temporal de Levante* defines the temporal activity of rainfall in the Valles de Alcoy. Although this system is not the only source of rainfall, it is the more important as droughts resulting from its absence demonstrate.

On a regional scale, the orographic effect of the parallel-aligned mountain ranges leads to a spatial difference between the northfaces that are exposed to the incoming rain from the Mediterranean and the leesides. It also favours the seclusion of fronts and the formation of convection cells. Inland from the Mediterranean, the decrease of orographic rainfall and the change towards more persistent rainfall will be reflected in landslide activity of the Valles de Alcoy. At the scale of the study area, no spatial differences in rainfall depth or occurrence could be found. Apparently the distribution is fairly homogeneous as long as the same exposure in the same basin is considered (Section 4.2).

Because of the large seasonal differences in temperature and radiation, the potential evapotranspiration mirrors the temporal distribution of rainfall over the year. Hence a soil moisture deficit is built up during summer that is not compensated until substantial rainfall in the fall or winter has occurred. Although most of the meteorological variables determining evapotranspiration can be considered as homogeneous over the study area or even on regional scales, the topography has again a strong influence. In the model, this is included by the spatial distribution of the incoming global radiation (Section 4.3).

The expected global warming is likely to have a great impact on the effective rainfall by changes in rainfall and increased evapotranspiration. These changes can be inferred from the output of global circulation models (GCMs) that simulate the global weather adequately. Their application, however, on the local scale is not straightforward. The output can not be transferred directly because of the low-resolution of GCMs and must be downscaled – here by a simple regression model – to the local level. Based on the downscaled output of three GCM models, the local rise in the average annual temperature in the 20-year period before CO₂-doubling is in the order from 1.2 to 2 °C. The increased temperature is not evenly divided over the year but predicts larger rises in winter and summer. The temperature rise in winter is relatively the largest and associated with an increase in variability. Thus, the higher temperature range will strengthen the moisture deficit in the area but the variability will not entirely eliminate those soil moisture conditions favouring landslide occurrence in the wetter part of the year between autumn and spring (Section 4.4). The net effect of climatic change will depend on the accompanying changes in rainfall. However, downscaling of precipitation has proven unsuccessful. Based on literature, it appears that the change is mainly an increase in variability.

The application of the coupled hillslope model under future conditions clashes with the deterministic nature of the historical rainfall record. To overcome this problem, a stochastic weather generator has been constructed (Figure 4.19). The observed interannual variability in precipitation and non-precipitation variables was satisfactorily reproduced by the stochastic weather generator. This makes it a valuable tool to obtain unbiased, synthetic timeseries of the climatic conditions controlling landslides for the recent past and the near future.

Chapter 5: Site investigation and parameterisation

This Chapter describes the experiments and results that have been used to parameterise the coupled hillslope model. For the definition of land use dependent parameters an inventory was made that resulted in a classification of four units representing stages of abandonment (Table 5.2). For these units, interception parameters and factors for crop-specific evapotranspiration (crop factors) were determined from field experiments and literature review (Tables 5.5 & 5.6).

Results of hydrological studies indicate a decrease in the saturated hydraulic conductivity with depth (Table 5.8). Given this relation with depth, it is likely that the increase in the porosity and bulk density is due to sampling disturbance (Tables 5.9 & 5.10). With the soil water retention curve, these variables may be taken as homogeneous throughout the profile below the root zone. This influence of land use was attested for the saturated hydraulic conductivity, the total porosity and the soil water retention curve. Broad-scale rainfall simulations indicate that the vertical saturated hydraulic conductivity over the root zone is in the order of the values measured by bore-hole tests and that infiltration is restricted by the storage capacity rather than the infiltration capacity. The distinction between the root zone and the regolith gives rise to the parameterisation as given in Tables 5.23 and 5.24.

The shearing resistance of the weathered marl has been determined by saturated and unsaturated direct shear tests. These tests show that the marl behaves as a purely frictional material under saturated conditions (Figure 5.22). Under unsaturated conditions, an apparent cohesion exists dependent on the matric suction, which is well described by the model of Fredlund (1987). The values of the friction angle, ϕ' , and Fredlund's parameter, ϕ^b , of respectively 34.8° and 16.1° correspond well with literature values (Tables 5.18 & 5.22).

Chapter 6: Implementation of the hydrological component of the coupled hillslope model

Calibration of the coupled hillslope model in order to optimise its performance has been restricted to the hydrological component. No optimisation of the slope stability model has been performed to avoid bias towards a certain landslide type.

Calibration of the hydrology is necessary because the potential evapotranspiration exceeds the available rainfall on long-term scales. A reduction factor similar to the crop factor was introduced to which the model is the most sensitive (Figure 6.1). In addition, the loss to bedrock was optimised as information on its value was scarce.

The calibration period covered a period of several years and model performance was optimised by comparing water level and moisture content over the years 1997-1998.

The calibrated model was successively applied over a longer period from 1971 to 1998 to assess the model validity. For the validation, additional information over a larger area was used to evaluate the performance under different environmental conditions (Tables 6.5 to 6.7). Over the validation period, the model performance was lower as errors were accumulated over space and time. A time lag between simulated and observed groundwater levels was found. However, the absolute levels are reasonably well estimated and this does not impair the model performance with respect to slope stability assessment severely. Likewise, local differences have been found that should be attributed to errors in the estimated soil depth. This problem arises from the disparity in scale between the measurement and application of the model (Figure 6.5). A structural error was found in the model response after severe droughts. It was found that the actual response to rainfall after such periods is quicker than simulated. This should be attributed to the constant reduction of the evapotranspiration by the calibrated reduction factor that reflects the average conditions. It is likely that this assumption is violated under such conditions due to a loss of vitality in the vegetation (Section 6.5).

Chapter 7: Simulation of landslide activity under the present environmental conditions

This Chapter considers the validity of the simulated failure as indicator for actual landslide occurrence over the period 1971 to 1998. For the comparison, a landslide inventory is used based on aerial photographs (Section 7.2). The validation considers the spatial distribution and the temporal activity by comparing simulated failure and landslide occurrence over the entire validation period and over several sub-periods. Also,

differences in slope and land use are considered to evaluate whether model predictions will hold under different environmental conditions in the Scenario Modelling (Chapter 8).

The simulated failure is determined by the modelled susceptibility, on which the hydrological triggering is superimposed. This susceptibility is expressed by the critical pore pressure ratio (Equation 7.1). The modelled susceptibility can simulate failure on slopes over 14°, which corresponds with 69% of the observed landslide occurrence (Section 7.3). The discrepancy between observation and simulation is due to landslides occurring on non-susceptible slopes and by spurious simulation of failure on steep slopes where the soil cover has been exhausted.

The agreement between the area of simulated failure and observed landslide occurrence limits the model performance for the coupled hillslope model (Table 7.4). Against the expectation is the probability of failure not an exact estimator of landslide density (Figure 7.7). Landslide density is generally overestimated for the susceptible slopes whereas it is underestimated for the non-susceptible and marginally susceptible slopes. This problem can only be partly explained by the neglect of lateral forces and strain-dependent changes in the shearing resistance (Figure 7.4.5).

Model performance is particularly low for the subperiods, which is due to the sensitivity of the model to prolonged droughts (Sections 7.4.4 & 7.5). The model is capable, however, to simulate the implied relationship between susceptibility and reactivation adequately (Table 7.6).

Temporal characteristics of simulated failure provide essential information on the actual activity of landslides and reflect the differences in hydrological triggering mechanisms for the land use units (Section 7.6). The conclusion, therefore, should be that although the model is not a replicate of the actual process system, it can be extrapolated and applied to hypothetical scenarios.

Scenario Modelling

Chapter 8: Assessment of the temporal sensitivity to landsliding under changed environmental conditions

The influence of changes in land use and climate on the temporal sensitivity has been assessed by Scenario Modelling. The scenarios extrapolate the current trends of abandonment and global warming. Three land use configurations are considered: the present configuration (BAU), continued abandonment (CRE) and a limited reorganisation of the agriculture in the area (PS). In addition, the present climate (CP), and a future, warmer climate (WF) at the moment at the moment of CO₂-doubling are included. This results in six scenario ensembles (Table 8.2), in which the departure in the conditions is modest and does not invalidate the calibration of the hydrological model component. These ensembles have been applied over a 30-year period.

The imposed climates are generated with the stochastic weather generator. For the comparison of landslide activity it is essential that the imposed meteorological conditions are comparable (Section 8.3). The synthetic weather series are, due to their statistical nature, less extreme than the observed weather. Consequently, the synthetic weather

series generate higher mean annual rainfall amounts than observed. So, the limited validity of the model after prolonged droughts does not apply. The number of extreme rainfall amounts is smaller but sufficient to compare landslide activity between the scenarios.

The BAU-CP scenario serves as benchmark to evaluate the changes in the other scenarios. To determine whether the scenario is representative for the present conditions, it has been compared to the simulated failure over the validation period (Section 8.3.3). Because of the higher mean rainfall, simulated failure in the BAU-CP scenario is more frequent and persistent than over the validation period. Likewise, the less frequent extreme events result in lower groundwater levels, which is reflected in the probability of failure (Tables 8.6 & 8.7). However, the probability of failure still varies over the same range and the change in the affected area is small. Consequently, the BAU-CP scenario can be used as reference although the same restrictions on model performance as signalled in Chapter 7 will apply.

Under the hypothetical scenarios, landslide activity decreases relative to the BAU-CP scenario. The changes between the scenarios are caused by alterations in the hydrological response; under the present climate, the different rates of actual evapotranspiration of the land use units account for this decrease. The absolute increase of the area with semi-natural vegetation in both the CRE and PS scenarios leads to an attenuation of the hydrological response on these slopes. Consequently, the persistence of slope failure decreases by 24% and 10% for the CRE-CP and PS-CP scenarios respectively. The attenuation of the hydrological response has less influence on the absolute maximum groundwater levels that are reached. The decrease in the area of simulated failure is in the order of 5% for both scenarios (Tables 8.4 & 8.10).

Under the WF climate, the increased potential evapotranspiration has a large impact on the simulated failure. Especially in the case of the CRE-WF scenario are the changes substantial. Both the area and the persistence decrease with 25% (Table 8.4). In terms of absolute duration, the change is even larger as the model results show a decrease of 41% in the days that $P(F \leq 1) \geq 0.10$ (Table 8.9). For the PS-WF scenario, these changes are respectively 20%, 7% and 22%. For the BAU-WF scenario, the changes are much smaller (respectively 5%, 9% and 14%). The conclusion is, therefore, that under the present CP climate mainly the temporal activity is affected by the imposed land use changes but the sensitivity in terms of landslide occurrence does not change noteworthy. In contrast, the compounded effect of climate and land use change leads to a large decrease in the sensitivity to slope failure, both in terms of temporal activity and spatial occurrence.

Synthesis and recommendations for future research

The central objective of this study to quantify landslide activity within the system of erosion processes with inclusion of possible environmental changes asked for the development of a methodology by which the influence of such changes on landslide activity can be assessed. Here, this influence is determined from changes in the temporal sensitivity, i.e. the frequency of triggering hydrological events that is superimposed on the static susceptibility to landsliding. Changes in the temporal sensitivity can be

assessed from Scenario Modelling. The significance of the changes depends on the validity of simulated failure as measure for actual landslide occurrence under the present environmental conditions. To determine this, the performance of the model should be rigorously tested. In order to ensure this validity under hypothetical conditions, it is imperative that the hypothetical conditions that are imposed do not depart too strongly from the present situation.

The results show that land use and climate have a strong influence through the hydrology on the activity of landsliding in the Mediterranean environment of the Valles de Alcoy. Land use has predominantly an effect on the hydrological response to event rainfall whilst the climate determines the magnitude of the soil moisture deficit at the end of the summer. Combined, the anticipated changes in land use and climate induce a large decrease in landslide activity for the hypothetical scenarios. The influence is strongly felt on the less susceptible slopes. Generally, such changes are advantageous to human activities. However, it is important to realise that the decrease in temporal sensitivity could lead to a more brittle behaviour of the system. The decreased frequency of potential triggers will result in a situation where a larger fraction of the geomorphic work is done by low frequency-high magnitude events. Once the resistance of the inherited landscape is exceeded by these events, the inherited landscape is likely to be in a larger state of disequilibrium with the actual conditions and the resulting adaptation more dramatic with all the possible consequences. From a practical perspective, it is recommended, therefore, that the effects of environmental change and inheritance are explicitly considered in hazard assessments. This requires the integration of detailed process and modelling studies like the one presented to research on the long-term behaviour of landscapes.

In order to increase the performance of the model it is essential that the influence of vegetation dynamics on the hydrology is better understood. In particular the role of vegetation on evapotranspiration should be considered and included in more detail. From a geotechnical perspective, the sources for the inequality between the simulated probability of failure and the observed landslide density deserve attention. Especially the effect of variability in the local slope and soil depth should be evaluated as they have a large influence on the modelled instability.

DE INVLOED VAN VERANDERINGEN IN LANDGEBRUIK EN KLIMAAT OP AARDVERSCHUIVINGSRISICO IN HET MIDDELLANDSE ZEEGEBIED

SAMENVATTING

Introductie

Hoofdstuk 1: Probleemschets, doelstelling en aanpak

Aardverschuivingen na neerslag dragen bij aan bodemdegradatie. Deze bijdrage is zowel direct, door het verplaatsen van materiaal, als indirect, door de verstoring van het vegetatiedek dat tegen oppervlakkige erosie beschermt. In humide tot subhumide Mediterrane gebieden, waar complete bedekking door vegetatie mogelijk is, kunnen aardverschuivingen als een sleutelproces binnen het processysteem van bodemdegradatie te zijn. Als onderdeel van het NWO onderzoeksprogramma *Hierarchy of Land Degradation Processes in a Mediterranean Environment*, is het doel van deze studie om de rol van aardverschuivingen binnen het totale systeem van erosieprocessen kwantitatief te evalueren.

Hydrologische processen die tot aardverschuivingen aanzetten fluctueren over tijd en komen bovenop op de ruimtelijke variabiliteit in de ontvankelijkheid (*susceptibility*) voor hellingsinstabiliteit. Aardverschuivingsactiviteit kan beschouwd worden in termen van haar ruimtelijke verbreiding en temporele frequentie. Op middellange tijdschalen (10-100 jaar), omgevingsfactoren en de veranderingen hierin beïnvloeden de hydrologische processen die aardverschuivingen bepalen. Om de invloed van veranderingen in omgevingsfactoren, met name landgebruik en klimaat, te bepalen, worden de volgende aspecten beschouwd

- De ruimtelijke en temporele variaties van mogelijk initiërende neerslaggebeurtenissen (*triggers*);
- Lokale variaties in de ontvankelijkheid voor aardverschuivingen;
- De invloed van de hydrologie op de aardverschuivingsactiviteit;
- De vaststelling van de verandering in deze activiteit ten gevolge van veranderingen in landgebruik en klimaat op middellange tijdschaal.

Gezien de denkbeeldige aard van toekomstige veranderingen in omgevingsfactoren ligt de nadruk sterk op de toepassing van modellen om de effecten van landgebruiks- en klimaatsveranderingen vast te stellen (§ 1.4). De opgelegde veranderingen worden omschreven in scenario's en statisch van aard. De grondveronderstelling is dat op de beschouwde temporele schaal de ontvankelijkheid niet verandert. Derhalve geven de voorspelde veranderingen in aardverschuivingsactiviteit in essentie de veranderende temporele sensitiviteit weer.

Hoofdstuk 2: Fysiografische beschrijving van de Valles de Alcoy

Het studiegebied ligt in de Valles de Alcoy (Spanje), waar aardverschuivingen veelvuldig optreden na neerslag. De steile hellingen in zachte mergels van miocene ouderdom zijn zeer ontvankelijk voor het ontstaan van aardverschuivingen. Deze instabiele hellingen worden in stand gehouden door de voortschrijdende insnijding van de Río Serpis. Aardverschuivingen worden geïnitieerd door extreme neerslaggebeurtenissen. Zulke gebeurtenissen zijn echter schaars en moeten het vochttekort overwinnen dat over de zomer opbouwt.

Landbouw is het voornaamste landgebruik in het gebied maar wordt als inkomstenbron steeds minder belangrijk. Verlating van velden leidt tot de regeneratie van semi-natuurlijke vegetatie. Het geregenereerde vegetatiedek is dichter en bezit een meer gestructureerde opbouw. Tengevolge van de toegenomen infiltratiecapaciteit en veranderingen in de interceptie en verdamping mag het verwacht worden dat de regeneratie van vegetatie de effectieve neerslag, die het optreden van aardverschuivingen bepaald, zal beïnvloeden.

Modelontwikkeling

Hoofdstuk 3: Een gekoppeld model voor de hydrologie en stabiliteit van hellingen

Gegeven het doel van deze studie en de eigenschappen van het gebied, is een simpel fysisch gebaseerd model ontwikkeld dat de hellingstabiliteit aan de hydrologie koppelt. Het is toepasbaar in alle gevallen waar percolatie stagneert boven een minder doorlatende bodemlaag. Het model is dynamisch in de zin dat het de hydrologie over de tijd nabootst en de gevolgen voor de hellingstabiliteit evalueert. De grondwaterstand en vochtgehalten die voor iedere tijdstap gegenereerd worden dienen als invoer voor de stabiliteitsbepaling (§ 3.2). Deze bepaling bestaat uit een probabilistische versie van het oneindig helling model. Daar het model dient om de gevolgen van landgebruiksveranderingen te evalueren, is het genesteld in een Geografisch Informatie Systeem dat de uitwisseling van data en de invoer van gegevens gerelateerd aan landgebruik vergemakkelijkt (Figuur 3.9).

Toepassing van het model voor het studiegebied

Hoofdstuk 4: Klimaatsfactoren voor aardverschuivingen

Het gekoppeld hellingmodel is gebouwd om de invloed van antecedente vochtcondities en neerslaggebeurtenissen op aardverschuivingsactiviteit na te bootsen. Vanwege deze invloed kunnen ruimtelijke en temporele patronen van neerslag en verdamping beschouwd worden als klimaatsfactoren die deze activiteit bepalen.

In de Valles de Alcoy is het lokale weersysteem van de *temporal de Levante* het belangrijkste voor het optreden van neerslag. Hoewel het niet de enige bron van neerslag is, is het van doorslaggevend belang zoals droogtes in zijn afwezigheid aantonen. Op een

regionale schaal leidt het orografisch effect van parallel georiënteerde gebergteruggen tot een ruimtelijke verschil in neerslag tussen noordelijke loef- en zuidelijke lijzijdes. Dit bevordert ook de isolatie van regenfronten en het ontstaan van convectiecellen. Landinwaarts van de Middellandse Zee wordt de invloed van stuwingsregen minder en die van persisterende neerslag groter. Deze tendens kan zijn weerslag hebben op de aardverschuivingsactiviteit in de Valles de Alcoy. Op de schaal van het studiegebied is er geen ruimtelijk verschil gevonden in de hoeveelheid en voorkomen van neerslag. De verdeling is vrij uniform voor dezelfde expositie in hetzelfde bekken (§ 4.2).

Door de grote seizoensverschillen in temperatuur en inkomende straling is de potentiële verdamping gespiegeld aan de neerslagsverdeling over het jaar. Hierdoor ontstaat een bodemvochttekort over de zomer dat niet opgeheven wordt totdat voldoende neerslag in de herfst of winter is gevallen. Hoewel de waarden van de meteorologische variabelen weinig verschillen op de regionale schaal, ontstaan lokaal verschillen door de topografie. In het model zijn deze lokale verschillen in microklimaat weergegeven middels een ruimtelijke verdeling van de inkomende straling (§ 4.3).

De verwachte temperatuurstoename op wereldschaal zal waarschijnlijk een grote invloed hebben op de effectieve neerslag door veranderingen in neerslag en toegenomen verdamping. Zulke veranderingen kunnen afgeleid worden uit de voorspellingen van generale circulatie modellen (GCMs) welke het globale klimaat nabootsen. Deze voorspellingen zijn echter niet direct toepasbaar op lokaal niveau vanwege hun beperkte resolutie. In dit geval zijn lokale waarden voor de klimaatsverandering verkregen door terugschaling van de voorspellingen middels een simpel regressiemodel (§ 4.4). Op grond van de voorspellingen van drie GCMs zou de verwachte toename in de gemiddelde jaarlijkse temperatuur, berekend over een periode van 20 jaar voorafgaand aan het moment van CO₂-verdubbeling, in de orde van 1.2 tot 2°C zijn. Deze toename is niet gelijkelijk verdeeld over het jaar maar het grootst in de winter en zomer. De toename in de winter is relatief het grootste en gaat vergezeld met een toename in de variabiliteit. De hogere temperatuur zal leiden tot een groter bodemvochttekort maar door de toegenomen variabiliteit in de winter zullen de antecedente vochtcondities die het optreden van aardverschuivingen bevorderen niet geheel verdwijnen. Het netto effect van de veranderingen in temperatuur zal afhangen van de begeleidende veranderingen in neerslag. Echter, het terugschalen van neerslag was onbevredigend. Uitgaande van literatuurgegevens schijnt de verandering in neerslag vooral uit een toename van de variabiliteit bestaan.

De vaste opeenvolging van neerslaggebeurtenissen in de historische reeks is onverenigbaar met de toepassing van het model onder hypothetische omstandigheden. Om dit probleem te vermijden is een stochastische weergenerator gebouwd (Figuur 4.19). Deze simulator reproduceert de waargenomen variabiliteit over de jaren in de neerslags- en niet-neerslagsvariabelen naar behoren. Dit maakt het een waardevol instrument om kunstmatige weerreeksen voor het recente en toekomstige klimaat te maken die niet naar een bepaalde volgorde van initiërende neerslaggebeurtenissen neigen.

Hoofdstuk 5: Veldstudie en parameterisatie

Dit hoofdstuk beschrijft de testen en resultaten welke gebruikt zijn om het gekoppeld hellingmodel te parameteriseren. Om de aan landgebruik gerelateerde parameters vast te stellen is een inventarisatie van het huidig landgebruik gebruikt. Dit resulteerde in een classificatie in vier eenheden die opeenvolgende stadia van verlating weergeeft (Tabel 5.2). Voor deze eenheden zijn parameters voor interceptie en soort-specifieke verdamping (*crop factors*) bepaald middels veldexperimenten en een literatuurstudie (Tabellen 5.5 & 5.6).

De gegevens van hydrologische experimenten geven aan dat de verzadigde doorlatendheid afneemt met de diepte (Tabel 5.8). Op grond van dit gegeven lijkt het waarschijnlijk dat de toename in porositeit en bulkgewicht toe te schrijven is aan verstoring bij de monsternamen (Tabellen 5.9 & 5.10). Samen met de bodemvochtkarakteristiek zijn deze variabelen als uniform beschouwd beneden de wortelzone. De invloed van landgebruik was waargenomen voor de verzadigde doorlatendheid, de totale porositeit en de bodemvochtkarakteristiek. Regenvalsimulaties over grote oppervlakken geven aan dat de verticale verzadigde doorlatendheid over de wortelzone de waarde zoals gemeten met de omgekeerde boorgattest benaderen en dat de infiltratie in de eerste plaats beperkt wordt door de bergingscapaciteit van de bodem. De gevonden verschillen tussen de wortelzone en het dieper verweringsdek ligt ten grondslag aan de parameterisatie zoals weergegeven in Tabellen 5.23 & 5.24.

De schuifweerstand van de verweerde mergel is bepaald middels verzadigde en onverzadigde directe schuiftesten. Deze testen geven aan dat de mergel zich als een zuiver wrijvingsmateriaal gedraagt onder verzadigde condities (Figuur 5.22). Onder onverzadigde condities, treedt er een schijnbare cohesie op die afhangt van de zuigspanning, welke goed beschreven wordt door het model van Fredlund (1987). De waarde voor de wrijvingshoek, ϕ' , en Fredlund's parameter, ϕ^b , van respectievelijk 34.8° and 16.1° stroken met die uit de literatuur (Tabellen 5.18 & 5.22).

Hoofdstuk 6: Toepassing van de hydrologische component van het gekoppelde hellingmodel

De kalibratie van het gekoppeld hellingmodel om zijn voorspellende waarde te vergroten is beperkt tot de hydrologische component. Op de stabiliteitscomponent is geen kalibratie toegepast om te voorkomen dat voorspellingen naar een bepaald type aardverschuivingen zouden gaan tenderen.

Kalibratie van de hydrologie is noodzakelijk aangezien de potentiële verdamping de neerslag overstijgt op de lange termijn. Een reductiefactor, vergelijkbaar met de crop factor, is gebruikt om neerslag en verdamping in overeenstemming te brengen. De hydrologische modelcomponent is zeer gevoelig voor deze reductiefactor (Figuur 6.1). Bovendien is het verlies naar het onderliggende vaste gesteente geoptimaliseerd aangezien de voorradige kennis over deze parameter schaars was.

De kalibratieperiode overspande een periode van meerdere jaren waarbij de prestatie van het model geoptimaliseerd werd door de gesimuleerde en waargenomen grondwaterstand en vochtgehalten over de kalenderjaren 1997-1998 te vergelijken. Het gekalibreerde model werd hierna gevalideerd over een langer periode (1971 tot 1998). Voor de validatie werd aanvullende informatie van een groter gebied gebruikt om de prestatie van

het model onder verschillende omgevingsfactoren vast te stellen (Tabellen 6.5 t/m 6.7). Over de validatieperiode presteerde het model slechter ten gevolge van de fouten die opeengestapeld werden over ruimte en tijd. Een verschuiving over de tijd tussen de nagebootste en waargenomen grondwaterstand werd waargenomen. De absolute waterstand werd echter redelijk goed benaderd waardoor de prestatie van het model voor het voorspellen van aardverschuivingen niet geschaad wordt. Lokale verschillen zijn waargenomen die aan fouten in de geschatte bodemdikte toegeschreven moeten worden. Dit probleem treedt op ten gevolge van het verschil tussen de waarnemingschaal en de schaal waarop het model toegepast wordt (Figuur 6.5). Een structurele fout treedt op na periode van ernstige en voortdurende droogte. Het bleek dat de werkelijk respons na zulke droogtes sneller was dan nagebootst. Dit moet toegeschreven worden aan de vaste reductie die op de verdamping wordt toegepast. De gekalibreerde waarde is in overeenstemming met de gemiddelde condities maar niet toepasbaar tijdens extreme droogtes wanneer de verdamping lager zal zijn tengevolge van de verminderde levensvatbaarheid van de vegetatie (§ 6.5).

Hoofdstuk 7: Simulatie van aardverschuivingsactiviteit onder de huidige omgevingsfactoren

Dit hoofdstuk beschouwt de validiteit van het nagebootste bezwijken van hellingen als maat voor het werkelijk optreden van aardverschuivingen over de periode 1971 tot 1998. Voor de vergelijking is een inventarisatie van aardverschuivingen gebruikt die gebaseerd was op luchtfoto's (§ 7.2). De validatie gaat uit van de ruimtelijke en temporele verbreiding van aardverschuivingen over de gehele periode en enkele deelperiodes. Ook is bekeken of er verschillen in prestatie optreden met hellingshoek en landgebruikseenheid om vast te stellen of de voorspellingen geldig zijn onder de verschillende omgevingsfactoren welke tijdens de modellering van de scenario's opgelegd worden (Hoofdstuk 8).

Het nagebootste bezwijken wordt bepaald door de gemodelleerde ontvankelijkheid, waar overheen de hydrologische initiërende mechanismen werken. Deze ontvankelijkheid kan weergegeven worden door het kritische poriedruk getal (Vergelijking 7.1). Het model kan instabiliteit voorspellen op hellingen boven de 14° , wat 69% van het waargenomen aardverschuivingen omvat (§ 7.3). Het verschil tussen het werkelijke optreden en model komt voor uit het voorkomen van aardverschuivingen op niet-ontvankelijke hellingen en de voorspelling van bezwijken op steile hellingen waar de bodem reeds verdwenen is.

De overeenstemming tussen het gebied met nagebootst bezwijken en waargenomen aardverschuivingen limiteert de prestaties van het gekoppeld hellingmodel (Tabel 7.4). Tegen de verwachting in is de probabiliteit van bezwijken geen exacte schatter van de aardverschuivingsdichtheid (Figuur 7.7). Deze wordt overschat voor de ontvankelijke hellingen en onderschat voor niet- en marginaal ontvankelijke hellingen. Dit probleem kan slechts gedeeltelijk verklaard worden door de verwaarlozing van de laterale krachten en rek-afhankelijke veranderingen in schuifweerstand (Figuur 7.4.5).

De modelprestatie is bijzonder laag voor de sub-perioden, wat toegeschreven moet worden aan de ontvankelijkheid van het model voor langdurige droogten. (§ 7.4.4 & §

7.5). Toch is het model in staat om de impliciete relatie tussen ontvankelijkheid en reactivatie te simuleren (Tabel 7.6).

Temporele eigenschappen van nagebootst bezwijken bieden belangrijke informatie over het werkelijke optreden van aardverschuivingen en weerspiegelen de verschillen in de hydrologische bezwijkmechanismen tussen de verschillende landgebruikseenheden (§ 7.6). De conclusie moet dientengevolge zijn dat, alhoewel het model geen exacte replica van het werkelijke processysteem is, het toegepast kan worden voor de hypothetische scenario's.

Scenariomodellering

Hoofdstuk 8: Bepaling van de temporele sensitiviteit voor aardverschuivingen onder veranderde omgevingsfactoren

De invloed van veranderingen in landgebruik en klimaat op de temporele sensitiviteit is bepaald met behulp van scenariomodellering. De scenario's extrapoleren de huidige trend van verlating en temperatuurstoename. Drie landgebruikscenario's zijn beschouwd: de huidige verdeling (BAU), voortschrijdende verlating (CRE) en een beperkte reorganisatie van de landbouw in het gebied (PS). Bovendien worden twee klimaatscenario's meegenomen: het huidige klimaat (CP) en een warmer, toekomstig klimaat (WF) op het moment van CO₂-verdubbeling. Dit geeft zes combinaties van scenario's (Tabel 8.2), welke in een beperkte mate van de huidige situatie afwijken en de validiteit van het gekalibreerde hydrologische model niet schaden. Deze combinaties zijn geëvalueerd over een periode van 30 jaar.

Voor de opgelegde klimaatscondities worden synthetische weerreeksen gegenereerd met de stochastische generator. Voor de analyse is het belangrijk dat deze reeksen vergelijkbaar zijn (§ 8.3). De synthetische weerreeksen zijn door hun statistische aard minder variabel dan het waargenomen weer. De gemiddelde jaarlijkse neerslag wordt hierdoor groter dan waargenomen. Dit maakt de beperking van de validiteit door langdurige droogte minder belangrijk. Het aantal extreme neerslaggebeurtenissen is kleiner maar voldoende om de nagebootste activiteit tussen de scenario's te vergelijken.

Het BAU-CP scenario dient als uitgangspunt om de veranderingen in de andere scenario's te evalueren. Om te bepalen of dit scenario de huidige condities weergeeft, is het vergeleken met het nagebootst bezwijken over de validatieperiode (§ 8.3.3). Doordat de jaarlijkse neerslag gemiddeld hoger is wordt nagebootst bezwijken meer frequent en persisterend dan over de validatieperiode. Evenzo leidt de minder frequent voorkomende extreme neerslag tot lagere grondwaterstanden, wat zijn weerslag heeft op de probabiliteit van bezwijken (Tabellen 8.6 & 8.7). Echter, de probabiliteit van bezwijken bestrijkt nog steeds hetzelfde bereik en de verandering treft slechts een klein gebied. Hierdoor kan het BAU-CP scenario gebruikt worden als referentie ofschoon dezelfde beperkingen voor de prestatie van het model als vermeld in Hoofdstuk 7 blijven gelden.

Voor de hypothetische scenario's neemt de aardverschuivingsactiviteit in vergelijking met het BAU-CP scenario af. De verschillen tussen de scenario's worden veroorzaakt door veranderingen in de hydrologische respons; onder het huidige klimaat verklaren verschillen in verdamping tussen de landgebruikseenheden verklaren deze afname. De

toename in het gebied onder semi-natuurlijke vegetatie voor het CRE en PS scenario's leidt tot een demping van de hydrologische respons. Hierdoor neemt de persistentie van bezwijken af met 24% en 10% voor het CRE-CP en het PS-CP scenario. De demping heeft minder vat op de absolute waterstand die over de periode bereikt worden. De afname in het gebied waarvoor bezwijken voorspeld wordt, is in beide gevallen minder dan 5% (Tabellen 8.4 & 8.10).

Voor het WF-klimaat heeft de toegenomen verdamping een grote invloed op de gesimuleerde activiteit. Vooral voor het CRE-WF scenario zijn de veranderingen groot. Zowel het gebied en persistentie van gesimuleerd bezwijken nemen met 25% af (Tabel 8.4). De absolute duur waarover $P(F \leq 1) \geq 0.10$ daalt zelfs met 41%. (Tabel 8.9). Voor het PS-WF scenario zijn deze veranderingen respectievelijk 20%, 7% and 22%. Voor het BAU-WF scenario zijn de veranderingen veel kleiner (5%, 9% and 14%). De conclusie is dus dat onder het huidige CP klimaat vooral de temporele activiteit afneemt onder de opgelegde veranderingen in landgebruik maar dat de gevolgen voor de ruimtelijke verbreiding klein zijn. Daarentegen leidt het samengestelde effect van klimaats- en landgebruiksveranderingen tot een substantiële afname in de sensitiviteit voor aardverschuivingen, zowel in termen van temporele activiteit als in ruimtelijke verbreiding.

Synthese en aanbevelingen voor aanvullend onderzoek

De centrale doelstelling van deze studie om aardverschuivingsactiviteit binnen het processysteem van erosieprocessen te kwantificeren en de verandering in omgevingsfactoren hierbij te betrekken vereiste de ontwikkeling van een methodologie waarmee de invloed van deze veranderingen op de aardverschuivingsactiviteit kan worden vastgesteld. Hier is deze invloed bepaald aan de hand van veranderingen in de temporele sensitiviteit, de frequentie van triggers die op een veronderstelde statische ontvankelijkheid voor aardverschuivingen inwerken. Veranderingen in de temporele sensitiviteit kunnen door scenariomodellering vastgesteld worden. Het belang van de veranderingen hangt af van de validiteit van de nagebootste instabiliteit als maat voor het werkelijke optreden van aardverschuivingen onder de huidige condities. Om dit vast te stellen, moet het model grondig geëvalueerd worden. Om deze validiteit onder de hypothetische condities te bewaren, is het noodzakelijk dat de opgelegde condities niet te zeer van de huidige situatie afwijken.

De resultaten geven aan dat landgebruik en klimaat door de hydrologie een sterke invloed op de aardverschuivingsactiviteit hebben in het Mediterrane milieu van de Valles de Alcoy. Landgebruik heeft vooral invloed op de hydrologische respons na een neerslaggebeurtenis terwijl het klimaat vooral de grootte van het vochttekort aan het eind van de zomer bepaalt. Samen leiden de verwachte ontwikkelingen tot een grote afname in aardverschuivingsactiviteit voor de hypothetische scenario's. Deze afname is het sterkst op de minst ontvankelijke hellingen. Gewoonlijk zullen zulke veranderingen gunstig zijn voor de menselijke activiteiten in het gebied. Echter, het is belangrijk om te realiseren dat de afname in temporele sensitiviteit kan leiden tot een brosser gedrag van het systeem. De afgenomen frequentie van mogelijke triggers kan leiden tot een situatie

waarin meer geomorfologische arbeid verricht wordt door gebeurtenissen met een lage frequentie en grote magnitude. Wanneer de weerstand van het overerfde landschap overschreden wordt door deze gebeurtenissen, zal het in een grotere staat van onevenwichtigheid verkeren onder de dan heersende omstandigheden. De hieruit volgende aanpassing zal waarschijnlijk heviger zijn met alle mogelijke, hieruit voortvloeiende gevolgen. Vanuit een praktisch perspectief, dient het aanbeveling dat de gevolgen van veranderingen en omgevingsfactoren en overerving voor risicostudies expliciet in overweging genomen worden. Dit vereist de integratie van gedetailleerde proces- en modelstudies zoals deze met onderzoek naar landschapsontwikkeling over langere perioden.

Om de prestatie van het model te verhogen is het noodzakelijk dat de invloed van de vegetatiedynamiek op de hydrologie beter begrepen wordt. Met name de rol van vegetatie in de verdamping zou beschouwd moeten worden en in meer detail in het model opgenomen worden. Vanuit een geotechnisch perspectief verdienen de mogelijke oorzaken van de ongelijkheid tussen de waargenomen aardverschuivingsdichtheid en de probabiliteit van bezwijken aandacht. Met name de gevolgen van variabiliteit in de lokale hellingshoek en bodemdikte zouden geëvalueerd moeten worden aangezien zij een grote invloed hebben op de gemodelleerde instabiliteit.

RESUMEN

Introducción

Capítulo 1: Formulación del problema, objetivo y metodología

Los deslizamientos, que son inducidos por la lluvia, contribuyen directamente a la degradación de la tierra por el movimiento de suelo e indirectamente por el destrozamiento de la cubierta vegetal que previene el escurrimiento. En consecuencia, la actividad de deslizamientos puede ser reconocida como un proceso clave en el sistema de la degradación de la tierra en los ambientes mediterráneos húmedos y sub-húmedos, en los cuales una cubierta vegetal continua se puede sostener normalmente. Como parte del programa de investigación de la Organización Científica de los Países Bajos llamado *Jerarquía de procesos de degradación de la tierra en un ambiente mediterráneo*, el objetivo de este estudio es cuantificar la importancia de la actividad de deslizamientos en el sistema integral de procesos erosivos.

Los procesos hidrológicos que inducen deslizamientos fluctúan por el tiempo y se ponen encima de las variaciones espaciales en la susceptibilidad del terreno a la inestabilidad de laderas. Por lo tanto, la actividad de deslizamientos debe ser evaluada en virtud de su distribución espacial y frecuencia temporal.

Sobre escalas temporales medianas (10-100 años), las condiciones ambientales y los cambios en esas afectan los procesos controlados hidrológicos de la actividad de deslizamientos. Por eso, los temas de este estudio son

- La evaluación de las variaciones espaciales y temporales en eventos de lluvia que en potencia pueden inducir deslizamientos;
- La determinación de variaciones locales en la susceptibilidad del terreno a la inestabilidad de laderas;
- La evaluación del papel importante de la hidrología sobre la actividad de deslizamientos en ambientes mediterráneos;
- Sobre escalas temporales medianas (10-100 años), la determinación del impacto de cambios en aprovechamiento y cambios climáticos sobre la actividad de deslizamientos.

Por el carácter hipotético de los cambios supuestos, énfasis ha sido dado a la modelación como herramienta analítica para determinar los efectos del aprovechamiento y clima sobre la actividad de deslizamientos. (Sección 1.4). Combinaciones estáticas de condiciones climáticas y aprovechamiento (“escenarios”) definen los cambios impuestos en la modelación. La suposición fundamental es que sobre la escala temporal contemplada la susceptibilidad del terreno a la inestabilidad de laderas es invariable. Por lo tanto, todos los cambios simulados en la actividad de deslizamientos representan cambios posibles en su frecuencia temporal.

Capítulo 2: El ambiente físico de los Valles de Alcoy

Como área de investigaciones una cuenca pequeña ha sido elegida en los Valles de Alcoy (España), donde deslizamientos son inducidos frecuentemente por la lluvia. En la zona de Alcoy, las laderas empinadas en margas flojas de una edad miocena (Tap) favorecen la actividad de deslizamientos. La incisión continua del Río Serpis ha formado y mantiene esas laderas.

Los deslizamientos son iniciados por eventos extremos de lluvia. Sin embargo, tales eventos son escasos y tienen que suplir el déficit de la humedad en el suelo que se eleva durante el verano.

Agricultura, en la forma de cultivo en seco, es el aprovechamiento principal en los Valles de Alcoy. No obstante, agricultura como el único fuente de sustento está disminuyendo. En campos abandonados la vegetación se está regenerando hasta un cubierto semi-natural. La vegetación regenerada está más densa y tiene una capa de raíces más elevada. Gracias a la capacidad de infiltración alargada y cambios en la interceptación y evapotranspiración, esa revegetación influye en la lluvia neta que controla la actividad de deslizamientos.

Desarrollo del modelo

Capítulo 3: Un modelo combinado para simular la hidrológica y la estabilidad de laderas

Dado el objetivo de este estudio y el área de investigación, un modelo simple con una base física ha sido desarrollada que junta procesos de hidrológica y estabilidad de laderas. Se puede aplicar en todas las situaciones en cuales la percolación se detiene sobre una capa inferior que es menos permeable. El modelo es dinámico, que significa que simula la hidrológica por el tiempo y evalúa los efectos sobre la estabilidad de laderas: La capa freática y los contenidos de humedad en el suelo que están generados, se utilizan como entrada para la calculación de la estabilidad de ladera (Sección 3.2). La estabilidad es calculada por una versión probabilística del modelo para una ladera infinita. Ya que el modelo tiene por objeto la evaluación de cambios en aprovechamiento, está encajado en un Sistema de Información de Geografía (SIG) para facilitar el intercambio de datos y llevar a cabo una parameterización dependiente del aprovechamiento (Figura 3.9).

Ejecución del modelo

Capítulo 4: Controles climáticos de deslizamientos

El modelo combinado de laderas intenta simular la influencia de la humedad antecedente en el suelo y eventos de lluvia sobre la actividad de deslizamientos. Por esa relación causal, patrones espaciales y temporales de lluvia y evapotranspiración pueden ser entendidos como los controles climáticos de la actividad de deslizamientos sobre una escala regional.

El sistema local del *temporal de Levante* dispone la distribución de lluvia en los Valles de Alcoy. Aunque ese sistema no es el único fuente de lluvia, él es lo más importante como las sequías en su ausencia demuestran.

Sobre una escala regional, las sierras colocadas paralelamente tienen un efecto orográfico que da lugar a una diferencia entre las laderas más secas expuestas al sur y las al norte que reciben la lluvia proveniente del Mediterráneo. También favorece la seclusión de frentes meteorológicos y la formación de células convectivas. Hasta el interior del mediterráneo, el cambio de lluvia orográfica hasta un tipo más persistente se representa en la actividad de deslizamientos en los Valles de Alcoy. Sobre la escala del área de investigaciones, ninguna diferencia espacial en los totales o ocurrencia de lluvia se puede constatar. Por lo visto, la distribución de lluvia está bastante homogénea por cuanto se considere la misma exposición en la misma cuenca. (Sección 4.2).

Por las grandes diferencias en temperatura y radiación, la evapotranspiración potencial refleja la distribución temporal de la lluvia por el año. Por eso el déficit de la humedad en el suelo se eleva durante el verano que no estará suplido hasta bastante lluvia haya caído durante el otoño o el invierno. Aunque la mayoría de los variables meteorológicos se pueden ser considerado homogéneo sobre la escala del área de investigaciones o también de la región, la topografía tiene otra vez una influencia importante; el modelo incluye la distribución espacial de la radiación global recibida en el área (Sección 4.3).

El calentamiento global tendría probablemente un impacto fuerte sobre la lluvia neta por un cambio en la lluvia misma y un aumento en la evapotranspiración. Esos cambios se pueden inferir por los resultados de Modelos Generales de la Circulación (MGCs) que simulan el tiempo sobre una escala mundial adecuadamente. Sin embargo, no son aplicables directamente sobre una escala local por la resolución baja de MGCs: Hay que desagregar los resultados de MGCs a la escala local por métodos estadísticas, en este caso por un modelo simple de regresión. Basado en los resultados desagregados de tres MGCs la temperatura se aumenta con aproximadamente 1.2 o 2°C en los 20 años que preceden el momento de la duplicación del CO₂. El calentamiento no está distribuido igualmente por el año pero es más grande en el verano y invierno. Relativamente, el calentamiento es más grande en el invierno y más variable. Entonces, la temperatura elevada aumentará el déficit de la humedad en el suelo pero por la variabilidad las condiciones en el invierno y primavera que favorecen la ocurrencia de deslizamientos no serían eliminadas. (Sección 4.4). El efecto neto del cambio climático dependerá no solo del cambio en la temperatura pero también de él en la lluvia. Sin embargo, la desagregación de la lluvia se quedó sin éxito. Evidencia de literatura demuestra sobre todo un cambio probable en la variabilidad de la lluvia.

La aplicación del modelo combinado de laderas a condiciones futuras es contraria a la secuencia fija contenido por los datos históricos de la lluvia. Como solución, un generador estocástico del tiempo ha sido construido (Figura 4.19). La variabilidad en lluvia y los otros medidos meteorológicos (temperatura, humedad relativa, viento y presión atmosférica) entre los años se reproduce satisfactoriamente. Eso rende el generador útil para obtener secuencias sintéticas objetivas de las condiciones climáticas que controlan la actividad de deslizamientos por el presente y en el futuro cercano.

Capítulo 5: Trabajo de campo y parameterización

Este capítulo describe los ensayos y resultados empleados en la parameterización del modelo combinado de laderas. Para relacionar los variables al aprovechamiento, se utilice una clasificación que incluye las cuatros fases del abandono (Tabla 5.2). Para esas fases, parámetros de intercepción y factores de cultivo para la evapotranspiración han sido determinados por ensayos y a base de la literatura. Los factores de cultivo relacionan la evapotranspiración a un tipo específico del aprovechamiento en el área (Tablas 5.5 y 5.6).

Los resultados de los estudios hidrológicos indican un decrecimiento en la permeabilidad del suelo con la profundidad (Tabla 5.8). Por esa relación con la profundidad, es probable que el aumento en porosidad con la profundidad resulta de una disturbancia en las muestras recogidas (Tablas 5.9 y 5.10). Así como la curva de la retención del agua en el suelo, esas variables se consideran como constante por todo el perfil del suelo abajo de la capa de raíces. La influencia del aprovechamiento se demuestra en la permeabilidad, la porosidad total y la curva de la retención. Sobre una escala más amplia, simulaciones de lluvia indican que la permeabilidad vertical en la capa de raíces es en el orden de ella determinada por ensayos en pozos perforadas en el suelo y que la capacidad de almacén determina sobre todo la infiltración en el suelo. La diferencia entre la capa de raíces y el suelo da lugar a la parameterización de las Tablas 5.23 y 5.24.

La resistencia de corte de la marga meteorizada ha sido determinada por ensayos saturados y insaturados de corte directo (“direct shear tests”). Demuestran que la marga se comporta como un material friccional en condiciones saturadas (Figura 5.22). En condiciones insaturadas, una cohesión aparente existe que depende de la succión de la matriz del suelo. Esa cohesión esta bien descrito por el modelo de Fredlund (1987). Los valores del ángulo de fricción, ϕ' , y el parámetro, ϕ^b , de Fredlund son respectivamente 34.8° y 16.1° y corresponden bien a valores mencionados en la literatura (Tablas 5.18 y 5.22).

Capítulo 6: Ejecución del componente hidrológico del modelo combinado de laderas

Solo el componente hidrológico del modelo de laderas ha sido calibrado para optimalizar la facultad pronostica del modelo. Ninguna calibración ha sido aplicada al componente de la estabilidad de laderas para evitar a una predisposición a un tipo particular de deslizamientos.

Se necesita una calibración de la hidrológia ya que la evapotranspiración potencial sobre tres veces a la lluvia disponible por temporadas largas. Se utiliza una reducción parecido a los factores de cultivo a cual el modelo esta muy sensitivo (Figura 6.1). Además, el perdido del agua al almacén de roca madre ha sido optimalizado por que información sobre eso proceso está escaso.

El periodo de calibración cubre una temporada de unos años y la facultad pronostica del modelo ha sido optimalizado por corroborar la capa freática y los contenidos de humedad en el suelo para los años 1997-1998.

El modelo hidrológico calibrado se aplicó con éxito a una temporada más larga que se extiende de 1971 hasta 1998 para determinar su validez. Para la validación, información

adicional de un área mas largo ha sido utilizado para evaluar el comportamiento del modelo en condiciones ambientales diferentes (Tablas 6.5, 6.6 y 6.7). En la temporada de validación, la facultad pronostica está más baja porque más errores se acumulan por el tiempo y espacio. Se observe un aplazamiento entre la simulación y la observación de la capa freática. Sin embargo, los niveles absolutos se reproducen bien y por eso el aplazamiento no está muy grave para la facultad pronostica del modelo respecto al inicio de deslizamientos. Igualmente, diferencias locales son observadas que se atribuyan a errores en la profundidad de suelo estimada. Ese problema procede de la desproporción entre escales de medidas en el campo y la ejecución del modelo (Figure 6.5). Se observa un error estructural en la reacción del modelo después sequías de larga duración. Después tales sequías, la reacción actual debe ser más rápida que simulada. Eso se atribuye a la reducción constante que se aplica a la evapotranspiración potencial por el factor calibrado; el factor representa condiciones medianas que no son validas en caso de sequías de larga duración cuando la vegetación pierde su vitalidad (Sección 6.6).

Capítulo 7: Simulación de la actividad de deslizamientos para las condiciones ambientales actuales

Se considera la validez de la rotura simulada como indicador de la ocurrencia actual de deslizamientos en la temporada desde 1971 hasta 1998. Para la comparación, un inventario ha sido hecho a partir de fotos aéreas de la zona. (Sección 7.2). La validación compara la actividad espacial y temporal simulada con la ocurrencia actual de deslizamientos por la temporada entera y unos intervalos inferiores. También, se consideran diferencias en pendiente y aprovechamiento para determinar si las predicciones serán validas en condiciones ambientales alteradas como aplicadas en la modelación de situaciones hipotéticas (Scenario Modelling; Capítulo 8).

La susceptibilidad del terreno a inestabilidad de laderas y influye en primer lugar la rotura simulada. Sobre la susceptibilidad, se pone la influencia de la hidrológia sobre la actividad de deslizamientos. La susceptibilidad se expresa por el valor critico de la proporción de la presión de poros. (Ecuación 7.1). La susceptibilidad calculada puede simular rotura para laderas inclinadas a mas que 14° que corresponde a 69% de la ocurrencia observada de deslizamientos (Sección 7.3). La discrepancia entre observación y simulación se causa por la ocurrencia de deslizamientos en laderas con pendientes menos que 14° y la simulación errónea de rotura en laderas empinadas donde en realidad el cubierto de suelo esta agotado ya.

La correspondencia entre el área con rotura simulada y ocurrencia observada de deslizamientos restringta la facultad pronostica del modelo (Tabla 7.4). Contra previsión, la probabilidad de rotura no estuvo un estimador exacto de la frecuencia especial de deslizamientos (Figura 7.7). La frecuencia especial de deslizamientos está sobreestimada para laderas susceptibles a inestabilidad y subestimado para laderas insusceptible o poco susceptible. Este problema se explica solo en parte por el descuido de las fuerzas laterales y cambios en la resistencia del suelo durante la deformación (Sección 7.4.5).

El modelo tiene poca facultad pronostica para los intervalos inferiores que se explica por la sensibilidad del modelo a sequías de larga duración (Secciones.4.4 y 7.5). No obstante,

el modelo es capaz de simular la relación entre la susceptibilidad del terreno y la reactivación de deslizamientos adecuadamente (Tabla 7.6).

Las características temporales de la rotura simulada proveen información esencial sobre la actividad actual de deslizamientos y reflejen las diferencias entre las clases de aprovechamiento en el comportamiento hidrológico relevante a deslizamientos. (Sección 7.6). Por lo tanto, la conclusión debe ser que el modelo se puede aplicar a las condiciones hipotéticas aunque no es una replica del sistema actual de procesos.

“Scenario Modelling”

Capítulo 8: Evaluación de la frecuencia temporal de deslizamientos para condiciones ambientales alteradas

La influencia de cambios en aprovechamiento y clima en la frecuencia temporal de deslizamientos ha sido evaluada por “Scenario Modelling”. Escenarios significan aquí combinaciones estáticas de condiciones climáticas y aprovechamiento que extrapolan tendencias actuales o previstas del abandono y el calentamiento global. Se tratan de tres configuraciones de aprovechamiento: el presente (BAU), el abandono avanzado (CRE) y una reorganización limitada de la agricultura en la zona (PS). Además, se incluyen el clima de hoy (CP) y un clima con temperaturas más elevadas en el momento de la duplicación de CO₂ (WF). Resulta en seis combinaciones de escenarios (Tabla 8.2), en cuales los cambios son modestos y no afecten la validez del componente hidrológico calibrado. Las combinaciones han sido aplicadas por un periodo de 30 años.

Los datos climáticos por esos periodos han sido generados por el generador estocástico del tiempo. Para la comparación de la actividad de deslizamientos es esencial que las condiciones meteorológicas impuestas son parecidas. (Sección 8.3). Las secuencias sintéticas son, por su carácter estadístico, menos extremos que el tiempo observado. Por eso, las secuencias sintéticas generan un medio de lluvia anual que sobre al valor observado. El número de eventos extremos es menos pero basta para comparar la actividad de deslizamientos entre los escenarios.

El escenario BAU-CP sirve como piedra de toque para evaluar los cambios en la actividad de deslizamientos abajo de las condiciones hipotéticas. Para determinar si el escenario BAU-CP represente las condiciones actuales adecuadamente, la rotura simulada ha sido comparado con ella por el periodo de validación (Sección 8.3.3). Debido a la lluvia mediana más alta, la rotura simulada del escenario BAU-CP es más frecuente y persistente que ella en la validación. Los eventos extremos, que son menos frecuentes, resultan en capas freáticas menos elevadas, que se reflejen como una probabilidad de rotura más baja (Tablas 8.6 y 8.7). Sin embargo, la probabilidad todavía cubre el mismo alcance que en la validación y el área afectado por la disminución es pequeño. Por lo tanto, el escenario BAU-CP se puede utilizar como referencia aunque las mismas restricciones en la facultad pronóstica del modelo aplican como señaladas en Capítulo 7.

En los escenarios hipotéticos, la actividad de deslizamientos disminuye relativa a ella en el BAU-CP. Cambios en el comportamiento hidrológico provocan las diferencias entre los escenarios; sobre todo diferencias en evapotranspiración entre las clases de

aprovechamiento explican la disminución en caso del clima actual (CP). El aumento absoluto en el área con vegetación semi-natural en también el escenario CRE y PS resulta en un apagamiento en la respuesta hidrológica en esas laderas. En consecuencia, la persistencia de inestabilidad de laderas disminuye respectivamente por 24% y 10% en los escenarios de CRE-CP y PS-CP. El apagamiento tiene menos importancia para el máximo absoluto del nivel freático en los 30 años considerados. La disminución en el área afectado por deslizamientos es alrededor de 5% para los dos escenarios (Tablas 8.4 y 8.10).

En caso del clima WF, la evapotranspiración elevada tiene un papel importante en la rotura simulada. Especialmente en el caso del escenario CRE-WF, los cambios son sustanciales. También el área y la persistencia disminuyen con 25% (Tabla 8.4). Expresado en duración absoluta, el cambio es más grande porque los resultados del modelo muestran una reducción con 41% en el número de días que $P(F \leq 1) \geq 0.10$ (Tabla 8.9). Para el escenario PS-WF, los cambios, todas reducciones en actividad, son respectivamente 20%, 7% y 22%. En caso del escenario BAU-WF, las reducciones son mas bajas con 5%, 9% y 14%. Por eso, se concluye que en el clima CP cambios en aprovechamiento afectan principalmente la frecuencia temporal de deslizamientos pero que la extensión no se altera insignificante. Al contrario el efecto compuesto de cambios en clima y aprovechamiento causa una reducción notable en la sensibilidad de laderas a inestabilidad, también considerado por extensión y frecuencia temporal.

Síntesis y recomendaciones para investigaciones futuras

El tema central de este estudio era cuantificar la actividad de deslizamientos en el sistema de procesos erosivos incluso los efectos posibles de cambios ambientales. Requiso por el desarrollo de una metodología por cual el impacto de tales cambios hipotéticos se podría evaluar. Aquí, el impacto ha sido evaluado como cambios en la frecuencia temporal de deslizamientos. Esa frecuencia temporal es determinada por la frecuencia de eventos de lluvia que son capaz de inducir deslizamientos. La inducción de deslizamientos por la lluvia actúa encima de la susceptibilidad estática del terreno a inestabilidad. Cambios en la frecuencia temporal de deslizamientos se pueden percibir en los resultados de la modelación de situaciones hipotéticas (“Scenario Modelling”). La significación de los cambios depende de la validez de rotura simulada como medida de la ocurrencia observada de deslizamientos abajo de las condiciones actuales. Para determinar la validez, la facultad pronostico debe ser puesto a prueba rigurosamente. Para conservar la validez en condiciones hipotéticas, es imperativo que los cambios impuestos no difieran demasiado de la situación actual.

Los resultados muestran que aprovechamiento y clima tiene por la hidrológica un papel importante en la actividad de deslizamientos en el ambiente mediterráneo de los Valles de Alcoy. Aprovechamiento influye sobre todo en la respuesta hidrológica a eventos de lluvia. El clima determina el déficit de la humedad en el suelo a los finales del verano. Combinados, los cambios previstos en aprovechamiento y clima resultan en una reducción notable en la actividad de deslizamientos para las condiciones hipotéticas. La influencia se nota mas en las laderas menos susceptibles a inestabilidad. En el área la

disminución en la actividad de deslizamientos es generalmente favorable al hombre pero la realización que deslizamientos ocurran menos frecuente es muy importante; en el terreno eventos del tipo baja frecuencia-alta magnitud estarían responsables para un parte más grande de la acción erosiva. Si la resistencia esté excedida, el paisaje heredado será en un estado mas fuerte de desequilibrio con las condiciones vigentes y las adaptaciones que resultarán estarán mas violentas con todas las consecuencias. Se recomienda por eso que los efectos de cambios ambientales son considerados explícitamente en estudios sobre el riesgo de deslizamientos. Requiere la integración de estudios detallados de procesos y aplicaciones de modelos como el presente con investigaciones sobre el comportamiento del paisaje sobre temporadas largas.

Para mejorar la facultad pronostica del modelo una comprensión mas clara de la influencia dinámica de la vegetación sobre la hidrológia es necesario. Sobre todo la importancia de la vegetación para le evapotranspiración debe ser considerado y incluido con mas detalle. Respecto a la geotecnología, las fuentes de la discrepancia entre la probabilidad de rotura simulada y la frecuencia especial de deslizamientos merecen la atención. Sobre todo la influencia de la variabilidad en la pendiente local y la profundidad del suelo deben ser evaluada ya que tienen una influencia grande sobre la estabilidad calculada.

REFERENCES

- Aleotti, P. & R. Chowdhury (1999): Landslide hazard assesment: summary review and new perspectives. *Bulletin of Engineering Geology and the Environment* 58, pp. 21-44.
- Anderson, M.G. & K. S. Richards (1987): *Slope stability*. Chichester: Wiley.
- Anderson, M.G. & S. Howes (1985): Development and application of a combined water-slope stability model. *Quarterly Journal of Engineering Geology* 18, pp. 225-236.
- Aston, A.R. (1979): Rainfall interception by eight small trees. *Journal of Hydrology* 42, pp. 383-396.
- Bardossy, A. & E. Plate (1991): Modelling daily rainfall using a semi-Markov representation of circulation pattern occurrence. *Journal of Hydrology* 122, pp. 33-47.
- Barling, R. D. Moore & R. Grayson (1994): A quasi-dynamic wetness index for characterising the spatial distibution of zones of surface saturation and soil water content. *Water Resources Research* 30, pp. 1029-1044.
- Bates, P.D., M.G. Anderson & M. Horrit (1998): Terrain information in geomorphological models: stability, resolution and sensitivity. In: Lane *et al.* (Eds.).
- Bear, J. (1972): *Dynamics of fluids in porous media*. New York: Elsevier.
- Belmonte Serrato, F. (1997): Interceptación en bosque y matorral mediterráneo semiárido: balance hídrico y distribución de la lluvia neta. *Doct. Thesis Universidad de Murcia*.
- Benda, L. & T. Dunne (1997): Stochastic forcing of sediment routing and storage in channel networks. *Water Resources Research* 33, pp. 2865-2880.
- Beven, K. (1982): On subsurface stormflow: Predictions with simple kinematic theory for saturated and unsaturated flows. *Water Resources Research* 18, pp. 1627-1633.
- Beven, K. (1989): Changing ideas in hydrology – the case of physically-based models. *Journal of Hydrology* 105, pp. 157-172.
- Beven, K. & M. Kirkby (1979): A physically based variable contributing area model of catchment hydrology. *Hydrological Sciences Bulletin* 24, pp. 43-69.
- Beven, K. & P. German (1982): Macropores and water flow in soils. *Water Resources Research* 18, pp. 1311-1325.
- Beven, K. & A. Binley (1992): The future of distributed models – Model calibration and uncertainty in predictions. *Hydrological Processes* 6, pp. 279-298.
- Bishop, A.W. (1954): The use of the pore pressure coefficient in practice. *Geotechnique* 4, pp. 148-152.
- Bishop, A.W., I. Alpan, G.E. Blight & I.B. Donald (1960): Factors controlling the strength of partly saturated cohesive soils. *Proceedings American Society of Civil Engineers. Research Conference on Shear Strength on Cohesive Soils (Boulder)*, pp. 503-532.
- Bishop, A.W. & G.E. Blight (1963): Some aspects of effective stress in saturated and partly saturated soils. *Geotechnique* 13, 177-197.
- Blalock, H.M. (1981): *Social statistics*. Auckland: McGraw-Hill.
- Boas, M. (1983): *Mathematics in Physical Sciences*. 2nd edition, New York: Wiley.
- Bogaard, T.A. (2001): *Analysis of hydrological processes in unstable clayey slopes*. *Doct. Thesis, Utrecht University*.
- Boorman, D.B. & C.E.M. Sefton (1993): Recognising uncertainty in the quantification of effects of climate change on the hydrological response. *Climate Change* 35, pp. 415-434.
- Brooks, S.M, K.S. Richards & M.G. Anderson (1993): Approaches to the study of hillslope development due to mass movements. *Progress in Physical Geography* 17, pp. 32-49.
- Brouwer, F.M. & M.J. Chadwick (1991): Future land use patterns in Europe. In: Brouwers, F.M. *et al.* (Eds.): *Land use changes in Europe*. Dordrecht: Kluwer, pp. 49-78.

- Brunsdon, D. (1993): Barriers to geomorphological change. In: Thomas, D.S.G. & R.J. Allison (Eds.): Landscape sensitivity. Chichester: Wiley, pp. 7-12.
- Brunsen, D. (1999): Some geomorphological considerations for the future development of landslide models. *Geomorphology* 30, pp. 13-24.
- Brunsdon, D. (2001): A critical assessment of the sensitivity concept in geomorphology. *Catena* 42, pp. 99-123.
- Brunsdon, D. & J.B. Thornes (1979): Landscape sensitivity and change. *Transactions of the Institute of British Geographers* 4, pp. 463-484.
- Brutsaert, W. (1982): Evaporation into the atmosphere. Dordrecht: Kluwer.
- Buishand, T.A. (1978): Some remarks on the use of daily rainfall models. *Journal of Hydrology* 36, pp. 295-308.
- Buishand, T.A. & C.A. Velds (1980): Neerslag en Verdamping. *Klimaat van Nederland 1*. De Bilt: KNMI.
- Bull, W.B. (1991): Geomorphic responses to climatic change. Oxford: Oxford University Press.
- Buma J. & M. Dehn (1998): A method for predicting the impact of climate change on slope stability. *Environmental Geology* 35, pp. 190-96.
- Burgy, R. & C. Pomeroy (1958): Interception losses in grassy vegetation. *Transactions American Geophysical Union* 39, pp. 1095-1100.
- Burrough, P.A. & R.A. McDonnell: Principles of geographical information systems. Oxford: Oxford University Press.
- Burton, A., T.J. Arkell & J.C. Bathurst (1998): Field variability of landslide model parameters. *Environmental Geology* 35, pp. 100-114.
- Camarasa Belmonte, A.M. (1991): La intensidad de las lluvias extremas mediterráneas a partir de la red S.A.I.H. XII Congreso Nac. de Geogr. (Valencia), AGE y Univ. de Valencia, 127-133, Valencia.
- Carrara A., M. Cardinali, R. Detti, F. Guzzetti, V. Pasqui & P. Reichenbach (1991): GIS-techniques and statistical-models in evaluating landslide hazard. *Earth Surface Processes and Landforms* 16, pp.427-445.
- Carrara A., M. Cardinali F. Guzzetti & P. Reichenbach (1995): GIS-based techniques for mapping landslide hazard. In Carrara, A. & F. Guzzetti (Eds.): Geographical information systems in assessing natural hazards. Dordrecht: Kluwer, pp. 135-176.
- Carson, M.A. (1971): The mechanics of erosion. London: Pion.
- Carson, M.A. & M.J. Kirkby (1972): Hillslope form and process. Cambridge: Cambridge University Press.
- Casti, J.D. (1990): Searching for certainty. New York: William Morrow.
- Chandler, D. (1996): Monte Carlo Simulation to evaluate slope stability. *Uncertainty in the Geologic Environment*, 474-493.
- Christian, J., Ladd, C., & G.B. Baecher. (1994). Reliability applied to slope stability analysis. *Journal of Geotechnical Engineering* 120, 2180-2207.
- Christian, J.T. & G.B. Beacher (1999): Factor of safety and reliability in geotechnical engineering: discussion. *Journal of Geotechnical and Geoenvironmental Engineering ASCE* 125, pp..
- Clarke, R.T. (1994): Statistical modelling in hydrology. Chichester: Wiley.
- Coccosis, H.N. (1991): Historical land use changes: Mediterranean regions of Europe. in Brouwers, F.M. *et al.* (Eds.): Land use change in Europe. Dordrecht: Kluwer, pp. 441-461.
- Conselleria d'Obres Publiques, Urbanisme i Transports (1994): Atlas Climàtic de la Generalitat Valenciana. Digital database and treatise, Valencia.
- Craig, R.F. (1987): Soil mechanics 4th edition. London: Van Nostrand Reinhold International.

- Crozier, M. J. (1973): Techniques for the morphometric analysis of landslips. *Zeitschrift für Geomorphologie N.F.*, 17 pp. 78-101.
- Crozier, M.J. (1986): Landslides: causes, consequences and environment. London: Croom Helm.
- Crozier, M.J., E.E. Vaughan & J.M. Tippet (1990): Relative instability of colluvium-filled bedrock depressions. *Earth Surface Processes and Landforms* 15, pp. 326-339.
- Crozier, M.J. & B.J. Pillans (1991): Geomorphic events and landform response in SE Taranaki, New Zealand. *Catena* 18, pp. 471-487.
- Crozier, M.J. (1996): Magnitude/Frequency issues in landslide hazard assessment. In: Mäusbacher, R. & a. Schulte (Eds.): *Beitrage zur Physiogeographie. Heidelberger Geographische Arbeiten* 104, pp. 221-236.
- Crozier, M.J. & N.J. Preston (1999): Component of landform evolution in unstable hill country. In: Hergarten, S. & H.J. Neugebauer (Eds.): *Process modelling and landscape evolution. Earth Lecture Notes in Earth Sciences* 78, pp. 267-284.
- Crozier, M.J. (1999): Prediction of rainfall-triggered landslides: a test of the antecedent water status model. *Earth Surface Processes and Landforms* 24, 825-833.
- Cubasch, U., H. von Storch, J. Waskewitz & E. Zorrita (1996): Estimates of climate change in Southern Europe using different downscaling techniques. Hamburg: Max-Planck-Institut für Meteorologie (183).
- Cuenca Payá, A. & M.J. Walker (1995): Terrazas fluviales de la zona bética de la Comunidad Valenciana. *El Cuaternario del País Valenciana*, pp. 105-114.
- Davis, J. (1986): *Statistics and data analysis in geology*. 2nd edition, New York: Wiley.
- De Boer, D.H. (1992): Hierarchies and spatial scale in process geomorphology: a review. *Geomorphology* 4, pp. 303-318.
- Dehn, M. (1999): Szenarien der klimatischen Ausösung alpiner Hangrutschungen. *Bonner Geographische Abhandlungen* (99).
- Dehn, M., G. Bürger, J. Buma & P. Gasparetto (2000): Impact of climate change on slope stability using expanded downscaling. *Engineering Geology* 55, pp. 193-204.
- Delta-T Devices (1995): Theta probe. User manual.
- DeRose, R.C., N.A. Trustrum & P.M. Blaschke (1991): Geomorphic change implied by regolith-slope relationships on steepland hillslopes, Taranaki, New Zealand. *Catena* 18, 489-514.
- De Wit, A. (2001): Runoff controlling factors in various sized catchments in a semi-arid Mediterranean environment in Spain. *Doct. Thesis, Utrecht University*.
- Dietrich, W.E. & R. Dorn (1984): Significance of thick deposits of colluvium on hillslopes, a case study involving the use of pollen analysis in the coastal mountains of California. *Journal of Geology* 92, pp. 147-158.
- Dingman, S.L. (1994): *Physical Hydrology*. New York: McMillan.
- Dolman, A. (1987): Summer and rainfall interception in an oak forest. Predictions with an analytical and numerical simulation model. *Journal of Hydrology* 90, pp. 1-9.
- Doorenbos, J. & W.O. Pruitt (1977): *Crop water requirements*. Rome.: FAO
- Eagleson, P. (1982): Ecological optimality in water-limited natural soil-vegetation systems: I. Theory and hypothesis. *Water Resources Research* 21, pp 1483-1493.
- Escario, V. & J. Sáez (1986): The shear strength of partially saturated soils. *Géotechnique*. 36, 453-456.
- Esteban Parra, M.J., F.S. Rodrigo & Y. Castro Diez (1998): Spatial and temporal patterns of precipitation in Spain for the period 1880-1992. *International. Journal of Climatology* 18, pp. 1557-1574.
- European Union (1997) CAP Working Document.
- Evans, I. (1996): What do terrain statistics really mean? In: Lane *et al.* (Eds.), pp. 119-138.

- Eybergen, F.A. & A.C. Imeson (1989): Geomorphological processes and climate change. *Catena* 16, 307-319.
- Farrel, D. & W. Larson (1972): Modeling the pore structure of porous media. *Water Resources Research* 8, pp. 699-705.
- Feddes, R., P. Kowalik & H. Zaradny (1978): Simulation of field water use and crop yield. Wageningen: Pudoc.
- Fredlund, D.G. (1987): Slope stability analysis incorporating the effect of soil suction. In: Anderson & Richards (Eds.), pp. 113-144.
- Fredlund, D.G. & H. Rahardjo (1993): Soil Mechanics for unsaturated soils. New York: Wiley.
- Fumanal, M.P. (1990): Dinamica sedimentaria Holocena en valles de cabecera del País Valenciano. *Cuaternario y Geomorfología* 4, pp. 93-106.
- Gabriel, K.R. & Neumann, J. (1962): A Markov chain model for daily rainfall occurrence at Tel Aviv. *Quarterly Journal of the Royal Meteorological Society* 88, pp. 90-95.
- Gallart, F. (1995): The relative geomorphic work effected by four processes in rainstorms: a conceptual approach to magnitude and frequency. *Catena* 25, pp. 353-364.
- Gan, J.K., D.G. Fredlund, H. Rahardjo (1988): Determination of the shear strength parameters of an unsaturated soil using the direct shear test. *Canadian Geotechnical Journal* 25, pp. 500-510.
- Gash, J.H.C. (1979): An analytical model of rainfall interception in forests. *Quarterly Journal of the Royal Meteorological Society* 105, pp. 43-55.
- Gens, A. (1993): Unsaturated soils: Recent developments and applications-shear strength. *Civil Engineering European Courses*. UPC Barcelona, 1-13.
- Gindel, I. (1964): Transpiration of the Aleppo pine (*Pinus halepensis* Mill.) as a function of the environment. *Ecology* 45, pp 868-873..
- Giorgi, F., M. Marunici & G. Visconti (1992): A 2xCO₂ climate change scenario over Europe generated using a limited area model nested in a general circulation model. 2 Climate change scenario. *Journal of Geophysical Research* 97, pp. 10011-10028.
- Gleick, P.H. (1986): Methods for evaluating the regional hydrologic impacts of global climatic changes. *Journal of Hydrology* 88, 97-116.
- Goodess, C. & J. Palutikof (1998): Development of daily rainfall scenarios for southeast Spain using circulation-type approach to downscaling. *International Journal of Climatology* 10, pp. 1051-1083.
- Gray, D.H. & W.F. Megahan (1981): Forest vegetation removal and slope stability in the Idaho Batholith. *Research Papers INT-97, USDA*, pp. 34.
- Grayson, R.B., I.D. Moore & T.A. McMahon (1992): Physically based modelling 2.: Is the concept realistic? *Water Resources Research* 26, pp. 2659-2666.
- Greenway, D. (1987): Vegetation and slope stability. In: Slope stability, M. Anderson & K. Richards (Eds.). pp 187-230.
- Haff, P.K. (1996): Limitations on predictive modelling in geomorphology. In: Rhoads, B.L. & C.E. Thorn (Eds.): The scientific nature of geomorphology. *Proceedings 27th Binghampton Symposium on Geomorphology*. Chichester: Wiley, pp. 337-357.
- Hanks, R.J. & G.L. Ashroft (1986): *Applied soil physics*: 2nd printing. Berlin: Springer.
- Hattendorff, I., S. Hergarten & H.J. Neugebauer (1999): Local slope stability analysis. In Hergarten, S. & H.J. Neugebauer (Eds.): *Process modelling and landform evolution*. *Lectures notes in earth sciences* 78. Berlin: Springer.
- Hay, L., G. McCabe, D. Wollock & M. Ayers (1992): Simulation of precipitation by weather type analysis. *Water Resources Research* 27, pp. 493-501.
- Heimovaara, T. J. (1993): Time domain reflectometry in soil science: theoretical backgrounds, measurements and models. *Doct. Thesis, University of Amsterdam*.

- Heuvelink, G. & E. Pebesma (1999): Spatial aggregation and process modelling. *Geoderma* 89, pp. 47-65.
- Hillel, D. (1986): Modelling in soil physics.: a critical review. In: Future developments in soil science research. Soil Science Society of America, pp. 35-42.
- Hooghart, J. & W. Lablans (1988): Van Penman naar Makkink. The Hague: CHO-TNO.
- Houghton, J., G. Jenkins & J. Ephraums Eds. (1990): Climate Change: the IPCC scientific assessment. Cambridge: IPCC.
- Imeson, A.C. & I.M. Emmer (1992): Implications of climatic change on land degradation in the Mediterranean. In: Jeftic *et al.* (Eds.), pp. 95-128.
- Imeson, A.C. *et al.* (1994): Hierarchy of land degradation processes in a Mediterranean environment. NWO proposal.
- Instituto Geológico y Minero de España (1975): Mapa geológico de España: Alcoy H. 821 1:50,000. Madrid.
- Instituto Geológico y Minero de España (1981): Mapa geotécnico de riesgos geológicos para la ordenación urbana de Alcoy. I: Mapa Geotécnico 1:25,000 and 1:5,000. Madrid.
- Instituto Tecnológico Geominero de España (1990): Estudio de Riesgos Naturales en la Ciudad de Alcoy. Madrid.
- Jackson, C.R. (1992): Hillslope infiltration and lateral downslope unsaturated flow. *Water Resources Research* 28, pp. 2533-2539.
- Jeftic, L., J. Milliman & G. Sestini (1992): Climatic changes in the Mediterranean. London: Arnold.
- Joffre, R. & S. Rambal (1993): How tree cover influences the water balance of Mediterranean rangelands. *Ecology* 74, pp 570-582.
- Katz, R. & B. Brown (1992): Extreme events in a changing climate: variability is more important than averages. *Climate Change* 21, pp. 289-302.
- Katz, R. (1996): Use of conditional stochastic models to generate climate change scenarios. *Climate Change* 32, pp. 237-255.
- Kessler J. & R. Oosterbaan (1974): Determining hydraulic conductivity of soils. In: Drainage principles and applications. International Institute for Land Reclamation and Improvement 16 (3), pp. 253-256.
- Kirkby M.J. (1993): Computer simulation in physical geography. Chichester: Wiley.
- Kirkby M.J. (1989): A model to estimate the impact of climatic change on hillslope and regolith form. *Catena* 16, pp. 321-341.
- Klaassen, W., F. Bosveld & E. de Water E (1998): Water storage and evaporation as constituents of rainfall interception. *Journal of hydrology* 213, pp. 36-50.
- Konikow, L.F. & J.D. Bredehoeft (1992): Groundwater models cannot be validated. *Advances in Water Resources* 15, pp. 75-83.
- Kutilek, M. & D.R. Nielsen: Soil Hydrology. Cremlingen: Catena.
- Lambe, R, K. Beven & S. Myrabbø (1998): A generic topographical soils hydrological index. In: Lane *et al.* (Eds.).
- Lambe, T.W. & R.V. Whitman (1979): Soil mechanics, SI version. New York: Wiley.
- Lane, S.N., K.S. Richards and J.H. Chandler (1998): Landform monitoring, modelling and analysis. Chichester: Wiley.
- Lankreijer, H.J.M., M.J. Hendriks & W. Klaassen (1993): A comparison of models simulating rainfall interception of forests. *Agricultural and Forest Meteorology* 64, pp. 187-199.
- La Roca, N. & A. Calvo-Cases (1989): Slope evolution by mass movements and surface wash (Valls d'Alcoi, Alicante, Spain) *Catena Supplementband*, pp. 95-102.

- La Roca, N. (1991^a): La sismicidad en la mitad sur del País Valenciano desde el punto de vista de los movimientos de masa. XII Congreso Nac. de Geogr. (Valencia), AGE y Univ. de Valencia, pp. 179-186.
- La Roca, N. (1991^b): Untersuchungen zur räumlichen und zeitlichen Variabilität der Massenbewegungen in Einzugsgebiet des Riu d'Alcoi (Alicante, Ostspanien). *Die Erde* 122, pp. 221-236.
- La Roca, N. (1992): Precipitaciones mediterráneas y movimientos de masa en margas de los Valles de Alcoi. *Saitabi Separ.*, 26 p.
- Lautensach, H. (1964): *Iberische Halbinsel*. München.
- Le Houérou, N. (1996): Vegetation and land use in the Mediterranean basin by the year 2050: a prospective study. In: Jeftic *et al.* (Eds.), pp. 175-232.
- Lee, I.K, W. White & O.G. Ingles (1983): *Geotechnical engineering*. Boston: Pitman.
- Lumb, P. (1970): Safety factors and probability distributions of soil strength. *Canadian Geotechnical Journal* 17, 225-242.
- Matalas, N.C. (1967): Mathematical assessment of synthetic hydrology. *Water Resources Research* 3, pp. 937-945
- Merriam, R. (1960): A note on the interception loss equation. *Journal of Geophysical Research* 65, pp. 380-385.
- Miller, D.J. & J. Sias (1998): Deciphering large landslides: linking hydrological, groundwater and stability models through GIS. *Hydrological Processes* 12, pp. 923-941.
- Millington, R.J. & J.P. Quirk (1959): Permeability of porous media. *Nature* 183, pp. 387-388.
- Millington, R.J. & J.P. Quirk (1961): Permeability of porous media. *Transactions of the Faraday Society* 57, pp. 1200-1207.
- Ministerio de Agricultura, Pesca y Alimentación (1981): Mapa de Cultivos y Aprovechamientos; Alcoy H. 821 1:50,000. Madrid.
- Ministerio de Agricultura, Pesca y Alimentación (1986): Mapa de Cultivos y Aprovechamientos de la Provincia de Alicante 1: 200,000. Madrid.
- Montgomery D.R. & W.E. Dietrich (1994): A physically based model for topographic control on shallow landsliding. *Water Resources Research* 30, 1153-1171.
- Montgomery, D.R., K. Sullivan & H.M. Greenberg (1998): Regional test of a model for shallow landsliding. *Hydrological Processes* 12, pp. 943-955.
- Mood, A.M., F.A. Gaybill & D.C. Boes (1974): *Introduction to the theory of statistics*. Auckland: McGraw-Hill.
- Mosely, F. (1990): *A geological field guide to the Costa Blanca, Spain*. London: Geologists' Association.
- Mulder, H.F.M. (1991): Assessment of landslide hazard. *Doct. Thesis*, Utrecht University.
- Mulligan, M. (1998): Modelling the geomorphological impact of climatic variability and extreme events in a semi-arid environment. *Geomorphology* 24, pp. 59-78.
- Nandakumar, N. & R.G. Mein (1997): Uncertainty in rainfall-runoff model simulations and the implication of predicting the hydrologic effects of land use change. *Journal of Hydrology* 192, pp. 211-232.
- Nash, D. (1987): A comparative review of limit equilibrium methods of stability analysis. In: Anderson & Richards (Eds.), pp. 11-75.
- Noirfalise, A. (1959): Sur l'interception de la pluie par le couvert dans quelques forêts belges *Bulletin de la Société Royale Forestière Belge* 66, pp. 433-439.
- Oreskes, N., K. Schaderfrehette & K. Belitz (1994): Verification, validation and confirmation of numerical models in earth sciences. *Science* 263, pp. 641-646.
- Palutikof, J. & T. Wigley (1996): Developing climate change scenarios for the Mediterranean region. In: Jeftic, L. *et al.* (Eds.), pp. 27-56.

- Patton, P.C. & V.R. Barker (1977): Geomorphic response of central Texas stream channels to catastrophic rainfall and runoff. In: Doehring, D.O. (Ed.): Geomorphology in arid and semi-arid regions. Binghamton: State University N.Y., pp. 189-217.
- Pebesma, E. & C. Wesseling (1998): GSTAT: a program for geostatistical modelling, prediction and simulation. *Computer & Geosciences* 24, pp 17-31.
- Penman, H.L. (1948): Natural evaporation from open water, bare soil and grass. *Proceedings of the Royal Society A* 193, pp. 120-145.
- Philip, J.R. (1990): Hillslope infiltration: planar slopes. *Water Resources Research* 27, pp. 109-117.
- Pierson d'Autrey, L. (1987): Sedimentation et structuration synsedimentaire dans le basin neogene d'Alcoy. *Doct. Thes. Université de Paris-Sud (Orsay)*.
- Price, D. (1992): Static and dynamic loading. *Technical University Delft, Delft*.
- Quereda Sala, J. (1989): Ciclogénesis y gotas frías del Mediterráneo occidental. *Diput. Castellón de la Plana, Castellón*.
- Rebel, P.J. (1988): Het tertiair ten Z. van Alcoy. *Unpublished Msc. Thes., University of Amsterdam*.
- Refsgaard, J.C. (1997): Parameterisation, calibration and validation of distributed hydrological models. *Journal of Hydrology* 198, pp. 69-97.
- Rice, J.A. (1995): *Mathematical statistics and data analysis*. Belmont: Duxbury Press.
- Richardson, C.W. (1981): Stochastic simulation of daily precipitation, temperature and solar radiation. *Water Resources Research* 17, pp. 182-190.
- Richardson, C.W. (1985): Weather simulation for crop management models. *Transactions of the American Society of Agricultural Engineers*. 28, pp. 1602-1606.
- Rodda, H.J.E., M.J. Stroud, U. Shankar & B.S. Thorrold: A GIS based approach to modelling the effects of land use change in New Zealand. *Soil use and management* 17, pp. 30-40.
- Rodriguez Estrella (1977^a): Síntesis geológico del Prebético de la Provincia de Alicante: I) Estratigrafía. *Bol. Geol. Min. T. LXXXVIII-III* pp 183-214.
- Rodriguez Estrella (1977^b): Síntesis geológico del Prebético de la Provincia de Alicante: II) Tectónica. *Bol. Geol. Min. T. LXXXVIII-IV* pp 273-299.
- Romero, R., J.A. Guijarro, C. Ramis & S. Alonso (1998): A 30-year (1964-1993) daily rainfall data base for the Spanish Mediterranean regions: first exploratory study. *International Journal of Climatology* 18, pp 541-560.
- Romero, R., C. Ramis & J.A. Guijarro (1999): Daily rainfall patterns in the Mediterranean area: an objective classification. *International Journal of Climatology* 19, pp. 95-112.
- Rosenberg, N.J., B.L. Blad & S.B. Varma (1983): *Microclimate: the biological environment*. New York: Wiley.
- Rosenberg, N.J. (1992): Adaptation of agriculture to climatic change. *Climatic change* 21, pp. 385-405.
- Rutter, A.J., K.A. Kershaw, P.C. Robins, & A.J. Morton (1971): A predictive model of rainfall interception in models. 1. Derivation of the model from observations in a plantation of Corsican pine. *Agricultural Meteorology* 9, pp. 367-384.
- Santos Deltell, M.J. (1991): Estudio de las precipitaciones extraordinarias (100 mm/24 hr) en la provincia de Alicante, 1914-1989. *XII Congreso Nac. de Geogr. (Valencia), AGE y Univ. de Valencia* pp 205-213.
- Sanz de Galdeano, C. (1983): La neotectónica de las Cordilleras Béticas. *Libro Jubilar J.M. Ríos IGME, II* pp 469-486, Madrid.
- Schiller, G. & Y. Cohen (1998): Water balance of *Pinus halepensis* Mill. afforestation in an arid region. *Forest Ecological Management* 105, pp 121-128.

- Semenov, M. & E. Barrow (1997): Use of a stochastic weather generator in the development of climatic change scenarios. *Climate Change* 35, pp. 397-414.
- Siddle, H.J., D.B. Jones & H.R. Payne (1991): Development of a methodology for in the Rhondda Valley, In: Chandler, R.J. (Ed.) *Slope Stability Engineering*. London: Telford, pp. 137-142.
- Sidle, R.C., A.J. Pearce & C.O. O'Loughlin (1985): Hillslope stability and land use. American Geophysical Union (Water Resources Monograph 11).
- Sidle, R.C. (1992): A theoretical model of the effects of timber harvesting on slope stability. *Water Resources Research* 28, pp. 1897-1910.
- Skempton, A.W. (1964): The long-term stability of clay slopes. *Géotechnique*, 14, 95-102.
- Taylor, R. & J. Crips (1987): Weathering effects slopes in mudrocks and overconsolidated clays. In Anderson & Richards (Eds.).
- Terlien, M.T.J., Th.W.J. Van Asch & C.J. van Westen (1995): Deterministic modelling in GIS-based landslide hazard assessment in Carrara, A. & F. Guzzetti (Eds.): *Geographical information systems in assessing natural hazards*. Dordrecht: Kluwer.
- Terlien, M.T.J. (1996): Modelling spatial and temporal variations in rainfall-triggered landslides. *I.T.C. Publ.* 32, 254 pp..
- Terlien, M.T.J. (1998): The determination of statistical and deterministic hydrological landslide-triggering thresholds. *Environmental Geology* 35, pp. 124-130.
- Thomas, M.F. (2001): Landscape sensitivity in time and space – and introduction. *Catena* 42, pp. 83-98.
- Thornes, J.B. & I. Alcántara-Ayala (1998): Modelling mass failure in a Mediterranean mountain environment: climatic, geological, topographical and erosional controls. *Geomorphology* 24, 87-100.
- Tong, H. (1978): Determination of the order of a Markov chain by Aikake's information criterion. *Journal of Applied Probability* 12, pp. 488-497.
- Topp, G.C., J.L. Davis & A.P. Annan (1980): Electromagnetic determination of soil water content: Measurements in coaxial transmission cables. *Water Resources Research* 16, pp. 574-582.
- Tsukamoto, Y. & O. Kusakabe (1984): Vegetative influences on debris slide occurrences on steep slopes in Japan. In: *Proc. Symp. Effects Forest Land use on Erosion and Slope Stability, Environment and Policy Institute, Honolulu*.
- U.S. Department of Agriculture, Soil Conservation Service (1975): *Soil Taxonomy*. Agricultural Handbook Nr. 436, Washington.
- Valente, F., J. David & J. Gash (1997): Modelling interception loss for two sparse eucalypt and pine forests in central Portugal using reformulated Rutter and Gash analytical models. *Journal of Hydrology* 190, pp 141-162.
- Van Asch, Th.W.J. (1980): *Water erosion on slopes and landsliding in a Mediterranean landscape*. Doct. Thesis, Utrecht University.
- Van Asch, Th.W.J. & H. van Steijn (1991): Temporal patterns of mass movements in the French Alps. *Catena* 18, pp. 515-527.
- Van Asch, Th.W.J., Kuipers, B. & Van der Zanden, D.J (1993): An information system for large scale quantitative hazard analyses of landslides. *Zeitschrift für Geomorphologie N.F. Suppl.* Bd. 87, pp. 133-140.
- Van Asch, Th. W. J., J. Buma & L. P. H. Van Beek (1998): A view on some hydrological triggering systems in landslides, *Geomorphology* 30, pp. 25-32.
- Van Asch, Th.W.J., S.J.E. van Dijck & M.R. Hendriks (2001): The role of overland flow and subsurface flow on the spatial distribution of soil moisture in the topsoil. *Hydrological processes* 15, 2325-2340.

- Van Bavel, C.H.M. (1966): Potential evaporation: the combination concept and its experimental verification. *Water Resources Research*, 2 pp. 455-467.
- Van Beek, L.P.H. & Th.W.J. van Asch (1998): Quantification of diffuse landsliding by derivation of a general hydrological slope instability threshold. In Moore, D.P. & O. Hungr (Eds.): 8th International Congress of the International Association of Engineering Geologists (IAEG, Vancouver), pp. 896-906.
- Van Dam, O. (2001): Forests filled with gaps. Doct. Thesis, Utrecht University.
- Van der Wateren-De Hoog, B. (1998): Quantification of catchment discharge sensitivity to climate variability. Doct. Thesis, Utrecht University.
- Van Deursen, W. (1995): GIS and dynamic models. Doct. Thesis, Utrecht University.
- Van Genuchten, M. Th. & D.R. Nielsen (1985): On describing and predicting the hydraulic properties of unsaturated soils. *Annales Geophysicae* 3, pp. 615-628.
- Varnes, D.J. (1984): Landslide hazard zonation. a review of principles and practice. Commission on landslides of the IAEG 3: Paris: UNESCO.
- Veldkamp, A. & L.O. Fresco (1996): *CLUE*: A conceptual model to study the conversion of land use and its effects. *Ecological Modelling* 85, pp. 253-270.
- Von Storch, H., E. Zorrita & U. Cubasch: Downscaling of global climate change estimates to regional scales: an application to Iberian rainfall in wintertime. *Journal of Climate* 6, pp. 1161-1171.
- Ward, T.J. , R.M. Li & D.B. Simons (1981): Use of a mathematical model for estimating potential landslide sites in steep forested drainage basins. In: Davies, T.R.M. & A.J. Pearce (Eds.): *Erosion and sediment transport in Pacific Rim steeplands*. (IAHS, 132), pp. 21-41.
- Watermark Computing (1994): *PEST Manual*.
- Wigley, T.M.L. (1992): Future climate in the Mediterranean basin with particular emphasis on precipitation. In: Jeftic *et al.* (Eds.), pp. 15- 44.
- Wilby, R. (1994): Stochastic weather type simulation for regional climate change impact assessment. *Water Resources Research* 30, pp. 3395-3403.
- Wilby, R. & T. Wigley (1997): Downscaling general circulation model output: a review of methods and limitations. *Progress in Physical Geography* 21, pp. 530-548.
- Wilks, D. (1992): Adapting stochastic weather generation algorithms for climate change studies. *Climate Change* 22, pp. 67-84.
- Wilks, D.S. & R.L. Wilby (1999): The weather generation game: a review of stochastic weather models. *Progress in Physical Geography* 23, pp. 329-357.
- Wolman, M.G. & P. Miller (1960): Magnitude and frequency of forces in geomorphic processes. *Journal of Geology* 68, pp. 54-74.
- Wood, E.F. (1995): Scaling behaviour of hydrological fluxes and variables: empirical studies using a hydrological model and remote sensing data. In Kalma, J.D. & M. Sivapalan (Eds.): *Scale issues in hydrological modelling*. New York: Wiley.
- Zhang, W. & D.R. Montgomery (1994): Digital elevation model gridsize, landscape reproduction and hydrological simulation. *Water Resources Research* 30, pp. 1019-1028.
- Zinke, P. (1965): Forest interception studies in the United States. In Sopper, W.E. & H.W. Lull: *Forest Hydrology*. Oxford.

CURRICULUM VITAE

Rens van Beek was born on the 24th of March 1969 in Breda (The Netherlands). He obtained his gymnasium diploma at the Stedelijk Gymnasium, Breda, in May 1987. From 1987 until 1993, he studied Physical Geography at Utrecht University. His specialisation was “process systems in mountainous areas” with additional courses in geomorphology, quaternary geology, soil mechanics, engineering geology and prehistory. As part of this specialisation, his final year project concerned the mobility of the La Valette landslide near Barcelonnette in the French Alps. After graduation, in August 1993, he worked as assistant at the Department of Physical Geography on the Nourtec (Mast III project) on the experimental suppletion of the Dutch coast from the Isle of Terschelling. In 1995, he started as Ph.D. researcher at the Department of Physical Geography of Utrecht University for the NWO-funded project the *Temporal Frequency of Landsliding as an Integrated Sub-System in the Process of Land Degradation in a Mediterranean Environment*. Of this research, this thesis is the result.

In April 2000, he accepted a short-term contract as research assistant at the School of the Built Environment of Coventry University (UK). Here, he worked on a feasibility study on the use of volcanic materials as alternative building materials and the potential of revegetation for slope stabilisation in the volcanic environment of Montserrat (West Indies).

Since September 2001, he is employed at the IBED-Physical Geography of the University of Amsterdam (NL), where he works as post-doc on the EU- project Eco-Slopes that examines the potential of vegetation for slope stabilisation.